

SURFACE TURBULENCE AND THE TENSILE PROPERTIES, REPRODUCIBILITY AND RELIABILITY OF CAST IRONS – A STUDY OF ENTRAINMENT DEFECTS

By

ZAKAREYA SALEM MOHAMED HASSAN NASHWAN

A thesis submitted to the University of Birmingham for the degree of
DOCTOR OF PHILOSOPHY

School of Metallurgy and Materials
College of Engineering and Physical Sciences
University of Birmingham
June 2022

UNIVERSITY OF
BIRMINGHAM

University of Birmingham Research Archive

e-theses repository

This unpublished thesis/dissertation is copyright of the author and/or third parties. The intellectual property rights of the author or third parties in respect of this work are as defined by The Copyright Designs and Patents Act 1988 or as modified by any successor legislation.

Any use made of information contained in this thesis/dissertation must be in accordance with that legislation and must be properly acknowledged. Further distribution or reproduction in any format is prohibited without the permission of the copyright holder.

Abstract

Mechanical properties, and their reproducibility and reliability, of several cast alloys are negatively influenced by surface turbulent filling as a result of entrainment defect formation. It is therefore important to examine the effect of entrainment defects and surface turbulent filling on the mechanical properties, reproducibility and reliability of cast irons. Resin-bonded sand castings were made of three types of cast irons, spheroidal graphite iron (SGI), lamellar graphite iron (LGI), and compacted graphite iron (CGI) in testbar moulds with three filling designs: quiescently-filled (QFM); surface turbulently-filled (TFM); and very (surface) turbulently-filled (VTFM). Subsequently the castings were tensile tested, and the fracture surfaces examined.

Regrading SGI, the tensile test showed a negative effect on surface turbulence. The ultimate tensile strength of the QFM samples had a Weibull modulus 92% higher than TFM, and 212% higher than VTFM. The %Elongation of QFM samples had a Weibull modulus 63% higher than TFM, and 131% higher than VTFM. Samples with low tensile properties were found to contain entrainment defects that formed due to the folding over of surface films during casting. The entrainment defects were either oxide bifilms (magnesium as the main constituent), lustrous carbon bifilms, inflated bifilms (nucleated by shrinkage or gas pore), and bifilm entraining inclusions (sand, slag, or both). The magnesia bifilms were only a nanometre in thickness.

Regarding LGI, the tensile tests performed on TFM and QFM samples showed mixed evidence for the effect of surface turbulence on LGI casting. However, the Ultimate Tensile Strength of the VTFM samples had a Weibull modulus 60% lower than the average between QFM and TFM Weibull modulus. Samples with low tensile properties were found to contain no evidence of entrainment defects that could be the cause of deterioration. Limited evidence of entrainment defects was found in LGI tensile testbars, either oxide bifilms (silicate as the main constituent), or bubble trail defects. Further, a reduced pressure test was employed to examine evidence of entrainment defects in LGI, and no evidence was found. LGI die cast in an oxygen-rich environment contained evidence of oxide bifilm formation.

Regarding CGI, the tensile test results showed mixed evidence of the effect of surface turbulence. The Ultimate Tensile Strength of QFM samples had a Weibull modulus that was on average 26% higher than TFM, but surprisingly, VTFM had a Weibull modulus 108% higher than QFM. The %elongation values followed the same trend, QFM had a Weibull modulus on average 44% higher than TFM samples, and VTFM had a Weibull modulus 120% higher than QFM. Samples with low tensile properties were found to contain no evidence of entrainment defects that could explain the deterioration. Novel defects with plate structures were observed in several samples with low tensile properties that were cast in TFM. The defects were only observed in one melt.

Entrainment defects in cast iron behaved similarly to entrainment defects in aluminium by exhibiting the following: they could form from several constituents, they could act as nucleation sites for shrinkage and gas pores, they could entrain different types of inclusions, the wetted surfaces of the defect could act as a nucleation site for precipitates, and the entrapped atmosphere in the defect might gradually be consumed by reaction with the surrounding liquid metal. Finally, due to its stable oxide surface film, SGI is the main cast iron alloy similar to aluminium in regards to the negative effect of surface turbulence on casting quality.

Contents

1 Introduction **27**

2 Literature Review **29**

2.1 Entrainment defects 29

2.1.1 Entrainment process 29

2.1.2 Types of entrainment defects 33

2.1.3 The evolution of entrainment defects (furling and unfurling) . 40

2.2 The evidence for entrainment defects 44

2.2.1 The evidence for entrainment defects in non-ferrous alloys . . 44

2.2.2 The evidence for entrainment defects in ferrous alloys 51

2.3 The reduction of entrainment defects 59

2.4 The deactivation of entrainment defects 60

2.5 The Weibull probability distribution statistical analysis of the mechanical properties of cast components 64

2.6 Cast irons reaction with gases 74

2.7 Surface films in cast irons 75

2.7.1 Oxide films 76

2.7.2 Nitride films 77

2.7.3 Carbon films (lustrous carbon) 78

2.8 Summary 79

3 Experimental Procedure **80**

3.1 Tensile testbars casting experiment 80

3.1.1 Mould preparation 80
3.1.2 Mould filling verification 81
3.1.3 Mould feeding verification 81
3.1.4 Melt preparation and casting 83
3.1.5 Chemical composition 86
3.2 Reduced pressure test experiment 88

4 Validation Results of the Ingate Velocity, Feeding, and Filling Modes 95
4.1 Feeding verification 97
4.1.1 Thermal Analysis 97
4.1.2 Porosity formation modelling 97
4.2 Filling modes verification 98
4.2.1 Initial ingate velocity 98
4.2.2 Real time X-ray radiography 99
4.2.3 Filling modes modelling 101

5 Results for Spheroidal Graphite Iron 114
5.1 The effect of quiescently-filled, surface turbulently filled, and very (surface) turbulently-filled moulds on the tensile properties, reproducibility and reliability of SGI 114
5.1.1 Statistical analysis of SGI UTS data 115
5.1.2 Statistical analysis of SGI %Elongation data 123
5.1.3 Weibull distribution analysis for SGI UTS and El data 126
5.2 Microscopy analysis of SGI fracture surfaces 138
5.2.1 Optical microscopy of fracture surfaces 138
5.2.2 SEM and EDX analysis of the fracture surfaces 141
5.2.3 Focused Ion Beam and Transmission electron microscopy analysis 193
5.3 The relation between SGI defect size and tensile properties 199
5.4 Summary 201

6 Results for Lamellar Graphite Iron **203**

6.1 The effect of quiescently-filled, surface turbulently filled, and very (surface) turbulently-filled moulds on the tensile properties, reproducibility and reliability of LGI 204

6.1.1 Statistical analysis of LGI UTS data 204

6.1.2 Weibull Distribution analysis of LGI UTS data 209

6.2 SEM and EDX examination of LGI fracture surfaces 214

6.2.1 LGI fracture surface topography 214

6.2.2 Testbars containing sand inclusions 215

6.2.3 Evidence of entrainment defects in LGI 216

6.3 Testbars die casting in an O-rich environment 231

6.4 Reduced pressure test 239

6.5 Industrial Data 241

6.6 Summary 242

7 Results for Compacted Graphite Iron **243**

7.1 The effect of quiescently-filled, surface turbulently filled, and very (surface) turbulently-filled moulds on the tensile properties, reproducibility and reliability of CGI 243

7.1.1 Statistical analysis of CGI UTS data 244

7.1.2 Statistical analysis of CGI %Elongation data 249

7.1.3 Weibull distribution analysis for UTS and %El CGI data . . . 255

7.2 SEM and EDX examination of CGI fracture surfaces 260

7.3 The relation between CGI defect size and tensile properties 274

7.4 Summary 276

8 Discussion **277**

8.1 Entrainment defects in cast irons 277

8.1.1 Entrainment defects in SGI 277

8.1.2 Entrainment defects in LGI 288

8.1.3 Entrainment defects in CGI 293
8.2 The effect of surface turbulence on the tensile properties, reproducibility and reliability of cast irons 295
8.2.1 The effect of surface turbulence on the tensile properties, reproducibility and reliability of SGI 295
8.2.2 The effect of surface turbulence on the tensile properties, reproducibility and reliability of LGI 297
8.2.3 The effect of surface turbulence on the tensile properties, reproducibility and reliability of CGI 299
8.3 The relationship between cast iron tensile properties and defect size . 301
8.4 Entrainment of surface films due to mould design features, and the potential of entrainment defect flotation 303
8.4.1 Effect of mould design features on surface turbulence and entrainment of surface film in cast iron 303
8.4.2 Entrainment defects flotation in cast irons 306

9 Conclusions **312**
9.1 Cast iron alloys and mould designs 312
9.2 Spheroidal graphite iron 313
9.3 Lamellar graphite iron 314
9.4 Compacted graphite iron 315

10 Future Work **316**

A **336**
A.1 Tensile test results for SGI 336
A.2 Tensile test results for LGI 342
A.3 Tensile test results for CGI 346
A.4 MATLAB^{TM}code for plotting the 3-parameter Weibull distribution . 350

List of Figures

2.1 A sketch of the entrainment process (3) 30

2.2 The balance of forces acting on a sessile drop (4) 31

2.3 (a) The behaviour profile of liquid metal entering a mould cavity at zero, critical and super critical velocities; (b) experimental profiles for cast iron and Al at different ingate velocities (5) 32

2.4 Calculated critical ingate velocities for the major cast elements (4) . . 33

2.5 Different types of entrainment defects: (a) bifilm, (b) inflated bifilm, (c) bifilm with trapped liquid flux, (d) bifilm entraining surface debris, (e) bifilm entraining sand inclusions, and (f) complex bifilm entraining multiple inclusions (4) 34

2.6 A web of bifilms on the polished surface of an Al-7Si-0.4Mg alloy (10) 35

2.7 Types of oxides by age in Al alloys (11) 35

2.8 Oxide bifilms with different topographies on fracture surfaces: (a) thin film on Al-7Si-0.4Mg (12), (b) thick and flexible film on Al-5Mg (13), and (c) thick and granular spinel film on Al-7Si-0.5Mg (14) . . . 35

2.9 The process of detrainment of liquid surface films; they do not cause entrainment defects as no bifilm is formed (4) 37

2.10 Schematic illustration of bubble trail defect formation (4) 38

2.11 Bubble trail defect (15) 38

2.12 Extrinsic inclusions due to bifilm entrainment 39

2.13 SE image of an oxide bifilm entraining sand inclusions in an Al alloy (16) 39

2.14 On the left, a sketch when bifilms are furled with a compacted configuration, and on the right the same bifilms are unfurled as planner cracks 41
2.15 A sketch of the mechanism of gas unfurling a bifilm; (a) bifilm is fully unfolded and (b) bifilm is inflated into a spherical pore (4) . . . 42
2.16 Bifilms unfurling due to the driving force of shrinkage 42
2.17 Bifilms unfurling due to the driving force of dendrite growth 43
2.18 Primary Fe-rich phase growing of the wetted sides of a bifilm in an Al alloy (14) 43
2.19 Secondary electron (SE) image of of a halved oxide bifilm on the fracture surface of Al-Si-Mg alloy (29), the blue lines added by the author to illustrate the symmetry 44
2.20 X-ray radiography showed the increase of bifilms size under reduced pressure (30) 45
2.21 Oxide films with different morphologies (10) 47
2.22 MgO bifilm on the fracture surface of commercial purity Mg alloy tensile testbar (39) 47
2.23 An alumina bifilm was found symmetrical on both sides of the fracture surface of nickel-aluminium bronze testbar (44) 48
2.24 Evidence of oxide films in TiAl investment casting (45) 48
2.25 Evidence of oxide films in Ni-based super alloys grade 8933 (47) . . . 50
2.26 A flat alumina bifilm containing some wrinkles was found both sides of the fracture surface of laser-powder bed fusion IN719 Ni-based super alloy (53) 51
2.27 The subsurface defects that caused the premature failure of 34CrN-iMo6 quenched and tempered steel drive axle during operation (57) 53
2.28 Surface and sub-surface lustrous carbon defects in LGI castings . . . 54
2.29 Lustrous carbon defects in SGI castings 55

2.30 Examples of mislabelled oxide bifilms in SGI castings 57

2.31 On the top right corner a SEM image of Ti inclusions agglomerate; the schematic diagram presents the step of formation (85). Note, Campbell stated that surface films cannot be entrained in an open form, as the process of entrainment will always fold the films dry sides 58

2.32 Silicate folded film in high alloyed Si cast iron (86) 58

2.33 A reported magnesium oxide bifilm which does not bear any resemblance to previously reported magnesium oxide bifilms (87) . . . 58

2.34 Filling system designs showed to affect the entrainment process (88) . 60

2.35 A schematic illustration of the mechanism of oxide bifilm healing in the liquid state (94) 61

2.36 The experimental results of entrapped air bubble in aluminium melt . 62

2.37 The rate of change of atmospheric gases entrapped inside an oxide bifilm (102) 63

2.38 Weibull parameters unbiased probability estimators a and b (113) . . 67

2.39 An example of Weibull mixtures in tensile test results of IN939 alloy casting 68

2.40 A comparison between Weibull probability plots of the tensile strength results of 319 Al alloy showed a better fit with the 3-parameter Weibull distributions 71

2.41 When the correct Weibull probability distribution is chosen, a better representation of the data is achieved 71

2.42 The distribution of the ratio of two estimated Weibull moduli for the 2.5 and 97.5 percentile. The first number in the intersection is for 2.5 and the second for 97.5 percentile (119) 73

2.43 The distribution of the ratio of two estimated Weibull moduli for the 5 and 95 percentile. The first number in the intersection is for 5 and the second for 95 percentile (119) 73

2.44 Effect of temperature on the diffusion coefficient for elements in solution in iron (134) 75
2.45 Effect of temperature on the solubility of hydrogen and nitrogen in iron (135) 75
2.46 Ellingham Diagram (144) 77
2.47 A schematic illustration showing the mechanism of formation of lustrous carbon films as suggested by Campbell and Naro (62) 79

3.1 The location of thermocouples in TFM 82
3.2 The location of thermocouples in VTFM/QFM 83
3.3 The apparatus used to cast LGI testbars in an oxygen-rich environment, (a) a permanent metal die, (b) a resin bonded sand pouring basin, (c) a vacuum pump, (d) an oxygen tank, and (e) a gas non-return valve 86
3.4 Tensile testbar sketch 87
3.5 RPT vacuum chamber and mould 89
3.6 Geometry and dimensions of the surface turbulently-filled mould (TFM) 91
3.7 Geometry and dimensions of the very (surface) turbulently-filled and quiescently-filled moulds (VTFM/QFM) 93
3.8 Geometry and dimensions of the cast iron permanent mould 94

4.1 TFM cooling curve 97
4.2 VTFM/QFM cooling curve 98
4.3 Measurement of the ingate velocity through the runner bar of TFM and VTFM/QFM using two thermocouples RB1 and RB2 99
4.4 SGI TFM shrinkage porosity locations 102
4.5 LGI TFM shrinkage porosity locations 102
4.6 CGI TFM shrinkage porosity locations 103
4.7 SGI VTFM/QFM shrinkage porosity locations 103

4.8 LGI VTFM/QFM shrinkage porosity locations 104
4.9 CGI VTFM/QFM shrinkage porosity locations 104
4.10 Frames from the real time X-ray video of the VTFM showing surface turbulent filling, including splashing, several waves and back-waves generated in the filter print. Red arrows point to examples of localised surface turbulence and green arrows point to examples of localised quiescent filling 105
4.11 Frames from the real time X-ray video of the TFM showing surface turbulent filling, including splashing, several back-waves and jetting in the mould cavity. Entrained air bubbles are captured flowing in through the runner bar and the testbar. Red arrows point to examples of localised surface turbulence and green arrows point to examples of localised quiescent filling 106
4.12 Frames from the real time X-ray video of the QFM showing quiescent filling. Green arrows point to examples of localised quiescent filling . 107
4.13 MAGMASOFT^{TM} simulation of the VTFM filling showed surface turbulent filling mainly generated in the filter print, and filling time = 2.3 s 108
4.13 MAGMASOFT^{TM} simulation of the VTFM filling showed surface turbulent filling mainly generated in the filter print, and filling time = 2.3 s 109
4.14 MAGMASOFT^{TM} simulation of the TFM filling showed surface turbulent filling, and filling time = 1.3 s 110
4.14 MAGMASOFT^{TM} simulation of the TFM filling showed surface turbulent filling, and filling time = 1.3 s 111
4.15 MAGMASOFT^{TM} simulation of the QFM filling showed quiescent flow and filling time = 2.3 s 112
4.15 MAGMASOFT^{TM} simulation of the QFM filling showed quiescent flow and filling time = 2.3 s 113

5.1 The Fitted Gaussian distributions for UTS data from each mould type for different SGI melts 116

5.2 Separate histograms for UTS data showed the trend of negative skewness. The x-axis represent the range of bins in MPa, and the y-axis represents the number of data points in each bin 117

5.3 Probability plots for AD test for SGI1 TFM UTS. The y-axis represents the cumulative probability in percent. The x-axis represents the UTS in MPa, except for the 3-parameter Weibull plot, it is the threshold value in MPa 119

5.4 Probability plots for AD test for SGI1 VTFM UTS. The y-axis represents the cumulative probability in percent. The x-axis represents the UTS in MPa, except for the 3-parameter Weibull plot, it is the threshold value in MPa 120

5.5 Probability plots for AD test for SGI2 TFM UTS. The y-axis represents the cumulative probability in percent. The x-axis represents the UTS in MPa, except for the 3-parameter Weibull plot, it is the threshold value in MPa 120

5.6 Probability plots for AD test for SGI2 QFM UTS. The y-axis represents the cumulative probability in percent. The x-axis represents the UTS in MPa, except for the 3-parameter Weibull plot, it is the threshold value in MPa 121

5.7 Probability plots for AD test for SGI3 VTFM UTS. The y-axis represents the cumulative probability in percent. The x-axis represents the UTS in MPa, except for the 3-parameter Weibull plot, it is the threshold value in MPa 121

5.8 Probability plots for AD test for SGI3 TFM UTS. The y-axis represents the cumulative probability in percent. The x-axis represents the UTS in MPa, except for the 3-parameter Weibull plot, it is the threshold value in MPa 122

5.9 Probability plots for AD test for SGI3 QFM UTS. The y-axis represents the cumulative probability in percent. The x-axis represents the UTS in MPa, except for the 3-parameter Weibull plot, it is the threshold value in MPa 122

5.10 The Fitted Gaussian distributions for %El. (pct) data from each mould type for different SGI melts 123

5.11 Separate histograms for %El. data showed the trend of positive skewness. The x-axis represent the range of bins in %El (pct.), and the y-axis represents the number of data points in each bin 124

5.12 Probability plots for AD test for SGI1 TFM %El. The y-axis represents the cumulative probability in percent. The x-axis represents the %El in pct., except for the 3-parameter Weibull plot, it is the threshold value in pct. 127

5.13 Probability plots for AD test for SGI1 VTFM %El. The y-axis represents the cumulative probability in percent. The x-axis represents the %El in pct., except for the 3-parameter Weibull plot, it is the threshold value in pct. 127

5.14 Probability plots for AD test for SGI2 TFM %El. The y-axis represents the cumulative probability in percent. The x-axis represents the %El in pct., except for the 3-parameter Weibull plot, it is the threshold value in pct. 128

5.15 Probability plots for AD test for SGI2 QFM %El. The y-axis represents the cumulative probability in percent. The x-axis represents the %El in pct., except for the 3-parameter Weibull plot, it is the threshold value in pct. 128

5.16 Probability plots for AD test for SGI3 VTFM %El. The y-axis represents the cumulative probability in percent. The x-axis represents the %El in pct., except for the 3-parameter Weibull plot, it is the threshold value in pct. 129

5.17 Probability plots for AD test for SGI3 TFM %El. The y-axis represents the cumulative probability in percent. The x-axis represents the %El in pct., except for the 3-parameter Weibull plot, it is the threshold value in pct. 129

5.18 Probability plots for AD test for SGI3 QFM %El. The y-axis represents the cumulative probability in percent. The x-axis represents the %El in pct., except for the 3-parameter Weibull plot, it is the threshold value in pct. 130

5.19 2-prameter Weibull probability plot for SGI1 UTS data 131

5.20 2-prameter Weibull probability plot for SGI1 %El. data 131

5.21 2-prameter Weibull probability plot for SGI2 UTS data 132

5.22 2-prameter Weibull probability plot for SGI2 %El. data 133

5.23 3-prameter Weibull probability plot for SGI2 %El. data 134

5.24 2-prameter Weibull probability plot for SGI3 UTS data 135

5.25 2-parameter Weibull probability plot for SGI3 %El. data 136

5.26 2-prameter Weibull probability plot for SGI UTS (MPa) data 137

5.27 2-prameter Weibull probability plot for SGI %El. (pct) data 138

5.28 Optical images of the first type of defects found on SGI test bars fracture surfaces (diameter = 6.7 mm). The image shows the two sides of the fracture surfaces 139

5.29 Optical image of bifilm defects that were revealed by machining . . . 140

5.30 Optical image of the first type of defects revealed its film topography 140

5.31 Optical image of the smallest double film defect (L = 1 mm, W = 0.25 mm) 141

5.32 Optical image of a shiny thick black corrugated film found symmetrically on both sides of the fracture surfaces of the upper grip section of two testbars 142

5.33 Optical image of the second type of defects 143

5.34 A closer view of the second type of defect revealed that the dark areas were dense clusters of spheroidal graphite 143
5.35 SE image of a small bifilm found on an SGI testbar fracture surface . 145
5.36 BSE image of the bifilm defect in figure 5.35 revealed its light elements composition 145
5.37 EDX element maps of the bifilm defect in figure 5.35 showed it contained C, Si, Mg and O 146
5.38 A close up SE image of the bifilm defect in figure 5.35 showed a combination of smooth and rough topography 147
5.39 BSE image of the same area shown in figure 5.38 revealed that each texture corresponds to a different elemental composition 148
5.40 EDX analysis of area 1 and 2 of the bifilm texture in figure 5.39 . . . 148
5.41 SE image of a big bifilm defect with a smooth structure (the red circles show locations of gaps between the bifilm and the matrix) . . 150
5.42 BSE image of the bifilm in figure 5.41 revealed its light composition and the high density of spheroidal graphite surrounding it 150
5.43 SE image of the area shown in figure 5.44 where the nitride and oxide film overlap, area 1 is a part of nitride film, and area 2 is a part of the oxide film 151
5.44 EDX element maps of the bifilm in figure 5.41 showed it contained C, Si, Mg, O, N and Al 152
5.45 EDX analysis of area 1 and 2 of the bifilm texture in figure 5.43 . . . 153
5.46 A layered EDX map generated from the EDX mapping of the bifilm in figure 5.41, with each color in the spectrum representing an element (i.e. C in red, Fe in blue, Si in yellow) 154
5.47 SE image of one of the largest oxide bifilm defects on the fracture surface of SGI testbar showing that it had a chaotic topography . . . 155
5.48 BSE image of the defect in figure 5.47 revealed the bifilm light composition 155

5.49 EDX element maps of the bifilm in figure 5.47 showed that it contained C, Si, Mg, O and Al 156
5.50 SE image of the largest oxide bifilm defects on the fracture surface of SGI testbar revealed its chaotic topography 157
5.51 BSE image of the bifilm in figure 5.50 revealed its light composition . 157
5.52 EDX element maps of the bifilm in figure 5.50 revealing it contained C, Si, Mg, O and Al 158
5.53 SE image of a bifilm with entrained sand particles 160
5.54 BSE image of the bifilm in figure 5.53 revealed its light constituents and several sand particles between its folds 160
5.55 SE image of the surface of the bifilm in figure 5.53 showed its rough surface 161
5.56 A close-up SE image the surface shown in figure 5.55 revealed two types of textures 161
5.57 EDX element maps of the bifilm shown in figure 5.53 defined the sand particles and showed that the bifilm contained Si, Mg, O and Al 162
5.58 EDX element maps of the bifilm surface shown in figure 5.56 revealed an under layer of C 163
5.59 EDX analysis of the bifilm texture shown in figure 5.56 164
5.60 BSE image of a bifilm with a bright area 165
5.61 A close-up SE image of the bright area circled in red shown in figure 5.60 166
5.62 EDX analysis of the bifilm and slag lump shown in figure 5.60 166
5.63 SE image of a bifilm with its features masked due to the brightness of the surrounding SGI matrix 168
5.64 BS image of the bifilm shown in figure 5.63 revealed it had five different features 169
5.65 EDX mapping of the bifilm in figure 5.64 revealed that it contained areas high in C, Si, Mg, O, Al, Ca and K 170

5.66 SE image of a bifilm blocking dendrite growth 172
5.67 SE image of the bifilm surface with the primary dendrites trying to penetrate the surface 172
5.68 SE image of the bifilm surface showing its creased surface 173
5.69 EDX spectrum from the bifilm in figure 5.66 showing that it mainly consisted of C 173
5.70 EDX element maps of the graphitic film shown in figure 5.66 revealed that its main constituent was C (as pointed to by the red arrow) . . . 174
5.71 EDX element maps of the graphitic film showing its folded bottom side, (marked by a red oval), contained O, Si and Fe 175
5.72 SE image of a dendrite arm near the bifilm in figure 5.66 showed fragments on the surface of the dendrite 175
5.73 EDX spectrum from the fragments shown in figure 5.72 showed that the fragments were mainly C 176
5.74 SE image of the second type of defects found on SGI fracture surfaces 178
5.75 EDX layered elements map of the defect shown in figure 5.74 revealed a zone depleted from graphite (marked in red) 178
5.76 A close-up SE image of the defect shown in figure 5.74 showed what appears to be a hole in the middle of the defect with plates surrounding it 179
5.77 A close-up SE image of the areas marked in red in figure 5.76 showed perturbations and fragments on the surface of the plates 179
5.78 Close-up SE image of the fragments in figure 5.77 180
5.79 EDX analysis of the defect features shown in figure 5.77 180
5.80 SE image of a particle nucleating on the plate of the defect shown in figure 5.74 181
5.81 EDX spectrum of the particle shown in figure 5.80 confirmed that it was a graphite sphere 181
5.82 BSE image of a different plate defect marked by the red circle 182

5.83 A close-up SE image of the defect shown in figure 5.82 revealed that it formed from horizontal plates 183
5.84 SE image of a shrinkage pore with fragments between the dendrite arms 183
5.85 EDX spectrum of the fragments shown in figure 5.84 revealed they contained Mg and O 184
5.86 SE image of an inflated oxide bifilm 186
5.87 BSE image of the defect in figure 5.86 showed aligned light element particles between its folds 187
5.88 EDX spectrum from the surface of the defect shown in figure 5.87 revealed that it contained Mg, O and Si 187
5.89 EDX spectrum of the particles shown in figure 5.87 revealed that they mainly composed of C 188
5.90 SE image of a lodged particles between the bifilm's corrugated folds . 188
5.91 EDX spectrum of the particles shown in figure 5.90 revealed they are composed of Cu and Sn 189
5.92 SE image of a corrugated thick black layer on the defect's surface . . 189
5.93 EDX spectrum of the dark layer shown in figure 5.92 showed that it is fully graphitic 190
5.94 A BSE image of aligned graphite next to a bubble 191
5.95 EDX spectrum from the area surrounding the bubble shown in figure 5.94 revealed that it contained Mg and O 192
5.96 SE image of the milling location from which the TEM sample were removed, marked with a red box 195
5.97 The location of the FIB milled bifilm section 196
5.98 SE image of the FIB milled section of the film attached to a TEM grid 196
5.99 STEM analysis of the bifilm shown in figure 5.98 197
5.100 STEM analysis of the bottom section of the same bifilm 198
5.101 Graph between bifilm area vs UTS for SGI testbars 200

5.102Graph between bifilm area vs %El. for SGI testbars 200
5.103Optical image of the fracture surface of the testbar, with a bifilm defect and the highest %El. value in table 4.17, revealed a large area with a high density of spheroidal graphite around the defect 200

6.1 The fitted Gaussian distributions for UTS data from each mould type for different LGI melts 205
6.2 Separate histograms for UTS data. The x-axis represent the range of bins in MPa, and the y-axis represents the number of data points in each bin 206
6.3 Probability plots of AD test for LGI1 TFM. The y-axis represents the cumulative probability in percent. The x-axis represents the UTS in MPa, except for the 3-parameter Weibull plot, it is the threshold value in MPa 209
6.4 Probability plots of AD test for LGI1 QFM. The y-axis represents the cumulative probability in percent. The x-axis represents the UTS in MPa, except for the 3-parameter Weibull plot, it is the threshold value in MPa 210
6.5 Probability plots of AD test for LGI2 VTFM. The y-axis represents the cumulative probability in percent. The x-axis represents the UTS in MPa, except for the 3-parameter Weibull plot, it is the threshold value in MPa 210
6.6 Probability plots of AD test for LGI2 TFM. The y-axis represents the cumulative probability in percent. The x-axis represents the UTS in MPa, except for the 3-parameter Weibull plot, it is the threshold value in MPa 211
6.7 Probability plots of AD test for LGI2 QFM. The y-axis represents the cumulative probability in percent. The x-axis represents the UTS in MPa, except for the 3-parameter Weibull plot, it is the threshold value in MPa 211

6.8 LGI1 UTS data 3-parameter Weibull probability plot 212
6.9 LGI2 UTS data 2-parameter Weibull probability plot 213
6.10 BSE image of LGI fracture surface showing the graphite flakes in black 215
6.11 SE image of LGI fracture surface showing fracture through pearlite and graphite/matrix interface. The red arrow points to the fracture through the pearlite phase, the green arrow points to the fracture through the graphite/matrix interface looking at the graphite side, and the blue arrow points to the fracture through the graphite/matrix interface looking at the matrix side 216
6.12 SEM imaging of the two LGI fracture surface excluded from LGI2 VTFM due to sand inclusions 219
6.13 EDX element maps of the fracture surface confirmed the particles as silica sand 220
6.14 Location of a defect (red circle) on both sides of the fracture surface . 221
6.15 A closer view of the defect on both sides of the fracture surfaces . . . 222
6.16 A closer view of the defect on both sides of the fracture surfaces confirmed it is a bifilm nature 223
6.17 EDX spectrum from the bifilm 224
6.18 EDX element maps of the one side of the bifilm 225
6.19 EDX element maps of the other side of the bifilm 226
6.20 A bifilm defect symmetrical on both sides of the fracture surface. Note the folds and creases of the surface pointing to the inside direction 227
6.21 A close view of the surface of the folded bifilm surface 228
6.22 A the inclusion lodged between the bifilm and LGI matrix 229
6.23 EDX analysis from different areas marked in figure 6.22 230
6.24 The casting appearance indicated a very surface turbulent filling . . . 232
6.25 X-ray radiography images of the casting showed evidence of casting defects 233

6.26 SE image of a film defect and its EDX element maps contained areas high in Si and O 234
6.27 Another film defect and its EDX element maps which contained areas high in Si, O and Mn 235
6.28 The fracture surfaces contained areas covered with creased and translucent films 236
6.29 EDX analysis of the bifilms shown in figure 6.28 237
6.30 Different features of entrainment defects were also detected on fracture surfaces 238
6.31 EDX spectrum from the fragments 239
6.32 LGI RPT sample 240
6.33 Droplets and a thin layer of solidified metal was found on the surface of the vacuum chamber 240
6.34 A skin defect resembles a bubble with an attached tail was the reason behind scarping LGI engine block 241

7.1 The fitted Gaussian distribution for UTS data from each mould type for different CGI melts 245
7.2 Separate histograms for UTS data. The x-axis represent the range of bins in MPa, and the y-axis represents the number of data points in each bin 246
7.3 Probability plots for AD test for CGI1 TFM UTS. The y-axis represents the cumulative probability in percent. The x-axis represents the UTS in MPa, except for the 3-parameter Weibull plot, it is the threshold value in MPa 247
7.4 Probability plots for AD test for CGI1 QFM UTS. The y-axis represents the cumulative probability in percent. The x-axis represents the UTS in MPa, except for the 3-parameter Weibull plot, it is the threshold value in MPa 247

7.5 Probability plots for AD test for CGI2 VTFM UTS. The y-axis represents the cumulative probability in percent. The x-axis represents the UTS in MPa, except for the 3-parameter Weibull plot, it is the threshold value in MPa 248

7.6 Probability plots for AD test for CGI2 TFM UTS. The y-axis represents the cumulative probability in percent. The x-axis represents the UTS in MPa, except for the 3-parameter Weibull plot, it is the threshold value in MPa 248

7.7 Probability plots for AD test for CGI2 QFM UTS. The y-axis represents the cumulative probability in percent. The x-axis represents the UTS in MPa, except for the 3-parameter Weibull plot, it is the threshold value in MPa 249

7.8 The fitted Gaussian distributions for %El. data from each mould type for different CGI melts 250

7.9 Separate histograms for %El. data. The x-axis represent the range of bins in %El (pct.), and the y-axis represents the number of data points in each bin 251

7.10 Probability plots for AD test for CGI1 TFM %El. The y-axis represents the cumulative probability in percent. The x-axis represents the %El in pct., except for the 3-parameter Weibull plot, it is the threshold value in pct. 252

7.11 Probability plots for AD test for CGI1 QFM %El. The y-axis represents the cumulative probability in percent. The x-axis represents the %El in pct., except for the 3-parameter Weibull plot, it is the threshold value in pct. 253

7.12 Probability plots for AD test for CGI2 VTFM %El. The y-axis represents the cumulative probability in percent. The x-axis represents the %El in pct., except for the 3-parameter Weibull plot, it is the threshold value in pct. 253

7.13 Probability plots for AD test for CGI2 TFM %El. The y-axis represents the cumulative probability in percent. The x-axis represents the %El in pct., except for the 3-parameter Weibull plot, it is the threshold value in pct. 254

7.14 Probability plots for AD test for CGI2 QFM %El. The y-axis represents the cumulative probability in percent. The x-axis represents the %El in pct., except for the 3-parameter Weibull plot, it is the threshold value in pct. 254

7.15 2-parameter Weibull probability plot for CGI1 UTS data 256

7.16 3-parameter Weibull probability plot for CGI1 %El. data 257

7.17 2-parameter Weibull probability plot for CGI2 UTS data 258

7.18 3-parameter Weibull probability plot for CGI2 %El. data 259

7.19 SE image of a fracture surface of CGI testbar showed four areas of defects 261

7.20 BSE image of the fracture surface shown in figure 7.19 showed four areas of defects with light elements composition, notice the areas around the defects are depleted from CG 261

7.21 Close up SE image of the defects shown in figure 7.20 showed plate structures with perturbations on top 262

7.22 SE image of the fracture surface of the other half of the testbar showed a mirroring of the defects shown in figure 7.19 262

7.23 SE image of two groups of plate defects on CGI testbar fracture surface 263

7.24 BSE image of the of plate defects shown in figure 7.23 showed the plates were covered with a light element 264

7.25 EDX layered map of the plate defects in figure 7.24 showed the plate chemical composition to be graphite 264

7.26 SE image of a thin film covering a plate defect 265

7.27 Close-up SE image of the film in figure 7.26 showed half of it to be transparent, and the other half almost transparent. The red arrows point to the star-shaped configurations on the thick side of the film. The blue arrows point to the star-shaped configurations on the almost transparent side of the film 265
7.28 EDX analysis of the film in figure 7.27 showed it was graphitic 266
7.29 A SE image of the bright star-like configuration found on a graphite film 266
7.30 EDX spectrum of the stars configuration shown in figure 7.29 267
7.31 EDX element maps of the stars configuration 268
7.32 SE image of a of what looks like a micro-shrinkage defect with a graphite film 269
7.33 BSE image of a of graphite film covering the defect shown in figure 7.32 269
7.34 A close-up SE image of the defect shown in figure 7.32 showed a film covering part of the plates with the iron matrix impinge from it . . . 270
7.35 EDX spectrum of the film and the dendrite arm shown in figure 7.34 270
7.36 SE image of the scattered and folded graphite films 271
7.37 BSE image of the scattered and folded graphite films shown in figure 7.36 272
7.38 Close up SE image of folded graphite film revealing the empty space between its folds 272
7.39 EDX spectrum of the folded graphite films 273
7.40 Graph between defect area vs UTS for CGI testbars 275
7.41 Graph between defect area vs %El. for CGI testbars 275
7.42 BSE image of a CGI fracture surface demonstrates the difficulty of finding small defects between the dense web of vermicular graphite . . 275

8.1 SE image of a recorded SGI plate defect (166), note the bright area that resembles a light film covering a part of the dendrites 284

8.2 A schematic illustration showing the shape transformation from a bubble trail to a collapsed surface bubble 291
8.3 A schematic illustration showing head of the bubble splitting into two sections. The top section is in figure 6.15a, and the bottom section is in figure 6.15b 292

Chapter 1

Introduction

Cast iron mainly consists of Fe and C, but it contains more alloying elements than superalloys (e.g., Si, Mn, P, S, Cu, Sn, Ni, Cr, Mo, V, Mg, Al, etc.), making it one of the most complex alloys used. Depending on the composition and cooling rate, its matrix will be an either stable or metastable eutectic, and the graphite phase will occur in a variety of morphologies. The main types of cast irons, classified by the shape of graphite, are lamellar graphite iron (LGI), spheroidal graphite iron (SGI), and compacted graphite iron (CGI). The combination between the different microstructural constituents gives cast iron a wide range of properties. This explains why cast iron is the most widely produced cast alloy in the world. In 2019, the total worldwide production of cast iron was 74.8 million metric tons, about 69% of the total world castings (1). This amount is 7 times that of cast steel, and more than 4 times that of cast aluminium. These figures reflect the wide functionality and adaptability of cast iron to a range of engineering applications spanning construction, automotive, railway, energy generation and aerospace.

Despite casting being one of the main manufacturing processes of metal components, the main disadvantage of cast alloys is their scatter of mechanical properties. It reduces the reproducibility and reliability of cast components, and could lead to premature failure during service. Starting with aluminium alloys, a large amount of research has been conducted previously to investigate the reasons behind this phenomena. The research has shown that during casting with surface turbulent filling,

(a widely acceptable practice), different sizes and shapes of entrainment defects will form inside the cast component. These defects will act as pre-existing hidden cracks, reducing properties and increasing the scatter of their mechanical properties. Subsequently, the effect of surface turbulent filling and entrainment defects on mechanical properties, reproducibility, and reliability of castings was examined in several alloys; including copper, magnesium, titanium, steel and nickel alloys. Nevertheless, the effect has not yet been researched in cast iron.

The objectives of this study were to examine whether surface turbulence negatively affected the tensile properties, reproducibility and reliability of cast irons; if entrainment defects formed in cast irons; and what role they played concerning the quality of castings. Three types of mould, designed to produce castings with different levels of surface turbulence, were used to produced tensile testbars from spheroidal graphite iron (SGI), lamellar graphite iron (LGI) and compacted graphite iron (CGI). Tensile testing and statistical analysis was conducted to determine the effect of surface turbulence on the tensile properties, reproducibility and reliability of these castings. In addition, the fracture surfaces were examined for evidence of entrainment defects. Furthermore, LGI castings were produced in an oxygen-rich environment and under reduced pressure to examine the formation of entrainment defects in the alloy.

Chapter 2

Literature Review

2.1 Entrainment defects

2.1.1 Entrainment process

Entrainment defects are formed by the folding over of a surface solid film on liquid metal, mostly oxide films, due to surface turbulence, resulting in entraining of a pocket of gas. The entrained gas, which is usually largely air, is sandwiched between the two un-wetted sides of an oxide film, forming a gas filled pocket. Therefore the entrained surface films are always double in nature. Surface turbulence events could happen at any point during the casting process: melting, transfer, pouring and mould filling. The double film defect will float suspended in the liquid metal and will be engulfed by solidification and entrained in the bulk of the cast component. As the bonding between the un-wetted (dry) sides of the double film is negligible, these defects will behave as cracks (2). The double films could be oxide, nitride or graphite. Figure 2.1 is a sketch of the mechanism of formation of bifilm defects (3).

Campbell (4) suggested that surface turbulence due to pouring and mould filling is driven by the liquid's metal internal pressure; this is defined by the following equation:

$$P = \frac{1}{2}V^2\rho \tag{2.1}$$

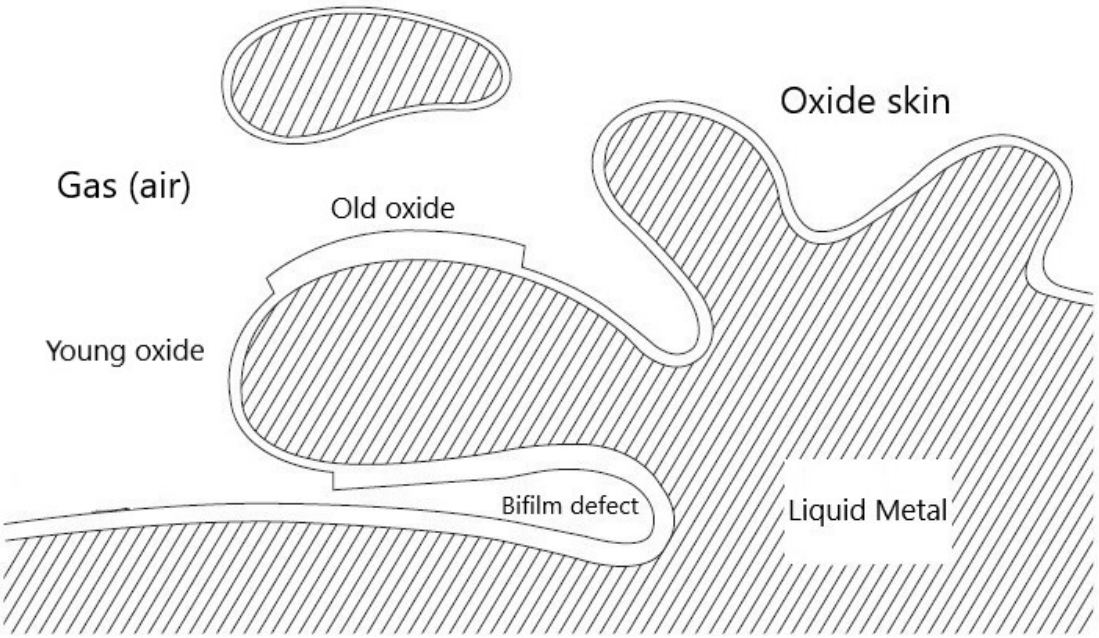


Figure 2.1: A sketch of the entrainment process (3)

Where ρ is the density, and V is the local flow velocity. The liquid's surface tension will counter the internal pressure according to the following equation:

$$\frac{1}{2}V^2\rho = 2\gamma/L \tag{2.2}$$

where γ is the surface tension and L is the radius of the deformed hemisphere. In this case, the local velocity to overcome the surface tension will be:

$$V = 2\sqrt{\gamma/L\rho} \tag{2.3}$$

Campbell denoted this parameter as the critical ingate velocity. To simplify the equation, the author assumed L to be the radius of a sessile drop on a non-wetted surface. Gravity and surface tension are the two forces keeping the sessile drop in equilibrium, as described in the following equation: $\frac{1}{2}\rho g h^2 = 2\gamma L$, see figure 2.2. Assuming h = 2L will result in:

$$V_{critical} = 2(\gamma g/\rho)^{1/4} \tag{2.4}$$

For liquid Al, $\rho = 2.4 * 10^3\ Kg/m^3$ and $\gamma = 0.9 Nm^{-1}$, the critical ingate velocity was calculated to be 0.5 m/s. The author suggested that when the ingate velocity was higher than $V_{critical}$, surface turbulence will fold over the opposing dry sides of the film, entraining gas and forming a bifilm structure, as shown in figure 2.3. Runyoro (5) confirmed the value for Al using a high speed camera and showed experimental liquid profiles at different ingate velocities, as shown in figure 2.3 . Lai (6) confirmed the result when comparing ingate velocities of 0.5 m/s and 1.1 m/s for Al. No folding action occurred for ingate velocity 0.5 m/s , while for ingate velocity of 1.1 m/s the liquid metal folded over upon itself and the surface film was entrained. Using computational fluid dynamics modelling (CFD), Lai (6) confirmed the same value for the critical ingate velocity. Figure 2.4 contains the calculated critical ingate velocities, using equation 2.4, for the significant elements with values ranging from 0.4 m/s to 0.5 m/s. Note that for Fe $V_{critical}$ is 0.45 m/s.

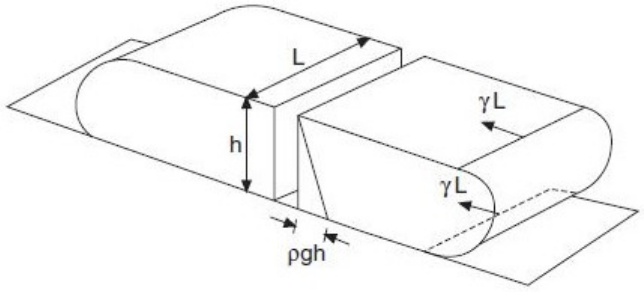


Figure 2.2: The balance of forces acting on a sessile drop (4)

According to Campbell (4), surface turbulence could be described with the following three dimensional quantities:

$$\text{The Weber number } (We) = V^2 L\rho/\gamma \tag{2.5}$$

$$\text{The Froude number } (Fr) = V^2/gh \tag{2.6}$$

$$\text{The Reynolds number } (Re) = VL\rho/\mu \tag{2.7}$$

V: liquid velocity, L: characteristic length (i.e. the hydraulic radius of the channel), h: wave height, g: gravity, μ: dynamic viscosity, and γ: surface tension.

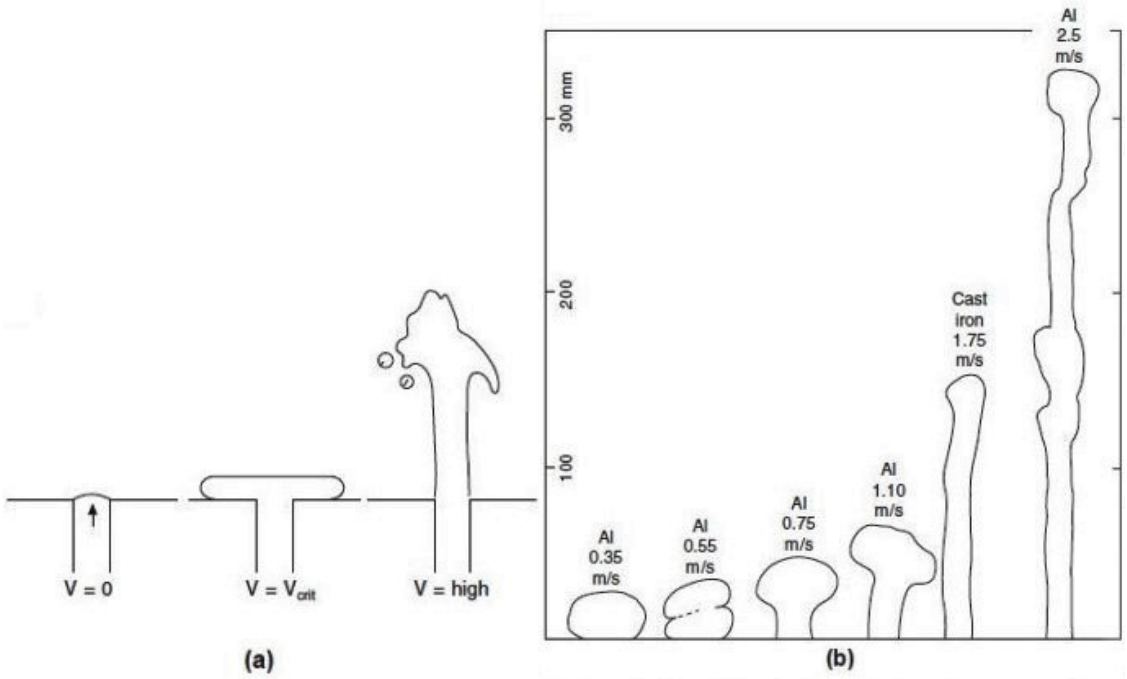


Figure 2.3: (a) The behaviour profile of liquid metal entering a mould cavity at zero, critical and super critical velocities; (b) experimental profiles for cast iron and Al at different ingate velocities (5)

The We number represents the ratio of liquid pressure to the surface tension, and is used to assess small-scale surface turbulence, (e.g. ripples). Campbell (4) suggested that surface turbulence is likely to occur when We > 1, but studies examining the We number effect on surface turbulence found the critical We number to be 12.3 (7, 8). On the other hand, Fr number deals with large-scale surface turbulence such as waves and slopping. It describes the ratio between internal pressure (potential for surface break) and the pressure asserted by gravity (potential for surface restraint). When Fr > 2000, turbulence is likely to occur. Thus, the We and Fr numbers are used to assess *surface turbulence*. Contrastingly, the Re number is used to describe *bulk turbulence* and it represents the ratio between liquid pressure to viscous pressure. Re values larger than 2000 describe bulk turbulent flow. In relation to entrainment defects, the Re number is not important as it does not affect the process of incorporating the defects. However, it indicates that, as soon as an entrainment defect forms, the defect will be carried into the casting by the subsurface turbulent flow. Flows in running systems are typically turbulent, with Re numbers up to 10^6 in industrial castings. Re will reach 7000 even for a small casting

with a very narrow running system (i.e. wall to wall filling) designed to minimize surface turbulence (4).

Liquid	Density (kgm^{-3})	Surface Tension (Nm^{-1})	Critical Height h (mm)	Critical Velocity (ms^{-1})
Ti	4110	1.65	12.8	0.50
Al	2385	0.914	12.5	0.50
Mg	1590	0.559	16.0	0.42
Fe	7015	1.872	10.4	0.45
Ni	7905	1.778	9.6	0.43
Cu	8000	1.285	8.1	0.40

Figure 2.4: Calculated critical ingate velocities for the major cast elements (4)

2.1.2 Types of entrainment defects

The folding-in of the surface film can result in a variety of entrainment defects. If a solid film is folded over, the defect will be called a bifilm (figure 2.5a). An example of a oxide bifilm defect on a polished surface of an Al alloy is shown in figure 2.6; note the double and convoluted nature of the film defect. Bifilms exist in a wide spectrum of topographies, thickness and size. Their thickness ranges from tens of nm to a few μm, depending on growth time (as shown in figure 2.7). Growth times as low as 10 ms were quoted by Birch (9) for Zn-Al pressure die casting. The growth of the bifilm is a one-way process; as turbulence passes, the film surface will break, reform and wrinkle. Surface crinkles and folds are a characteristic and common feature to identify bifilm defects on the fracture surface. Figure 2.8 is an example of bifilm defects seen on the fracture surface of Al alloys with different topographies, (a) is an example of a young thin bifilm, (b) is a thicker bifilm with larger features, and (c) is an old, thick and granular bifilm.

When a liquid film (slag), (figure 2.5c), is entrained, bifilm defects are not to be expected. Due to the high surface energy and low viscosity of the liquid metal, entrained liquid films should spheroidize in seconds and buoyancy will carry it to the surface; a sketch of the detrainment process is shown in figure 2.9. This phenomena applies to irons and steels because of the liquid nature of their slag.

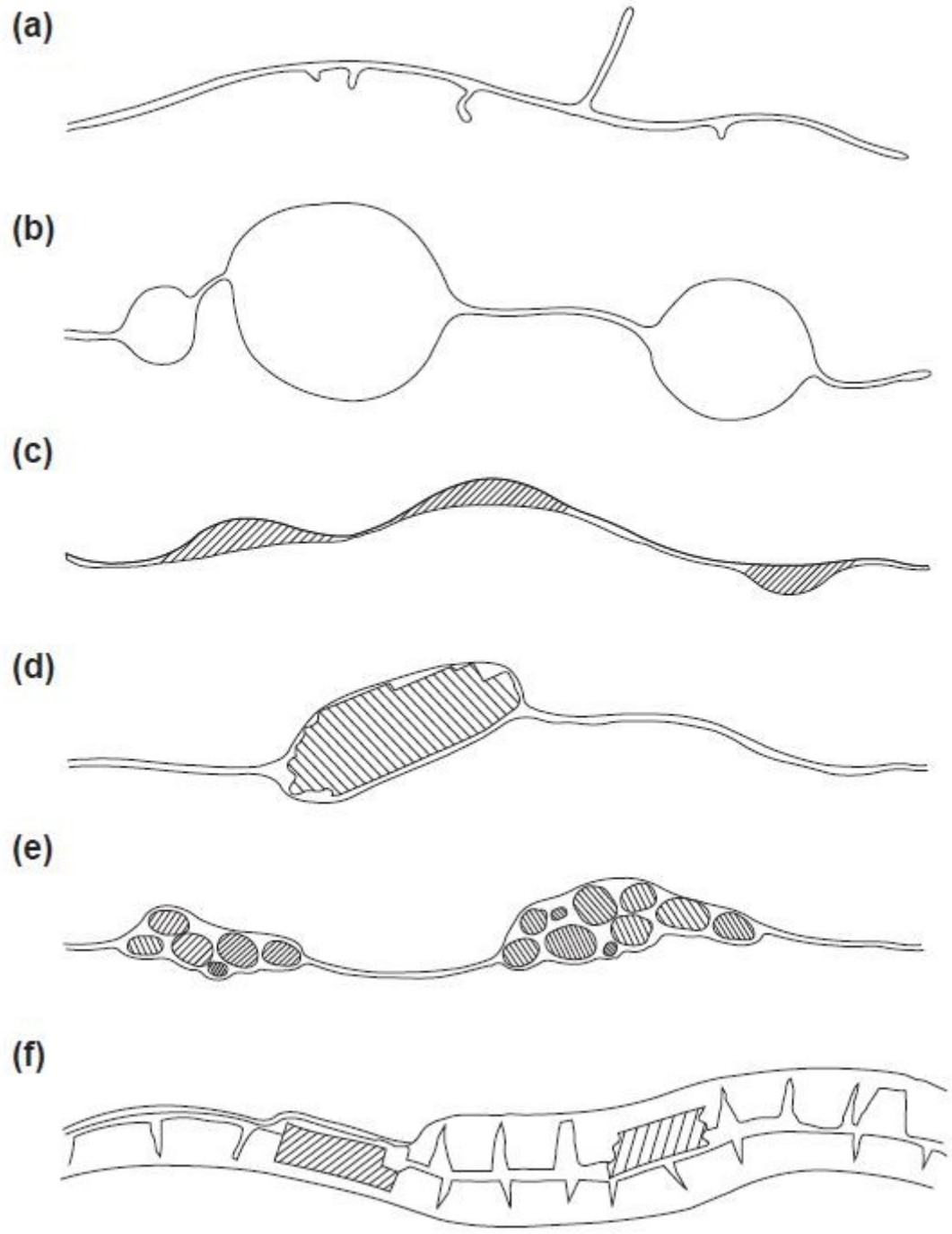


Figure 2.5: Different types of entrainment defects: (a) bifilm, (b) inflated bifilm, (c) bifilm with trapped liquid flux, (d) bifilm entraining surface debris, (e) bifilm entraining sand inclusions, and (f) complex bifilm entraining multiple inclusions (4)

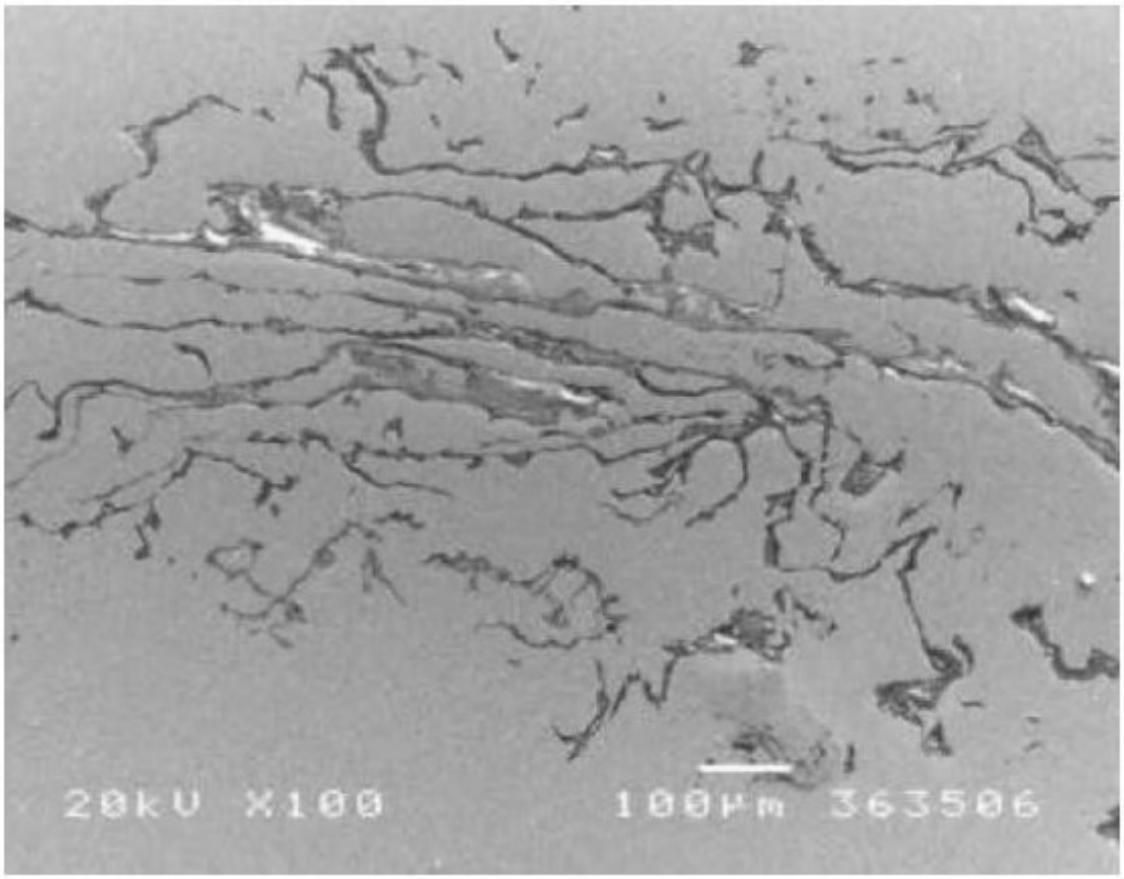


Figure 2.6: A web of bifilms on the polished surface of an Al-7Si-0.4Mg alloy (10)

Growth Time	Thickness	Type	Description	Possible Source
0.01 s	1 nm–1 µm	New	Confetti-like fragments	Pour and mould fill
10 s–1 min	10 µm	Old 1	Flexible, extensive films	Transfer ladles
10 min–1 h	100 µm	Old 2	Thicker films, less flexible	Melting furnace
10 h–10 days	1000 µm	Old 3	Rigid lumps and plates	Holding furnace

Figure 2.7: Types of oxides by age in Al alloys (11)

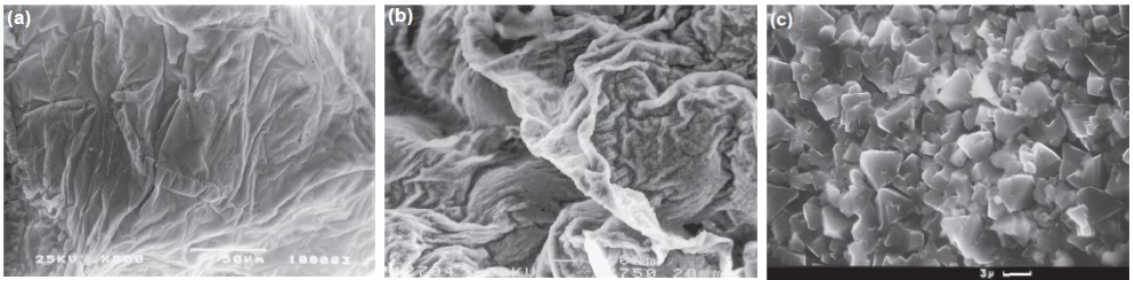


Figure 2.8: Oxide bifilms with different topographies on fracture surfaces: (a) thin film on Al-7Si-0.4Mg (12), (b) thick and flexible film on Al-5Mg (13), and (c) thick and granular spinel film on Al-7Si-0.5Mg (14)

Surface turbulence will also lead to the entrainment of air bubbles between the oxide film layers. Small bubbles with low buoyancy will not be able to escape to the surface and will be trapped between the bifilm folds and act as a source of microporosity. Severe surface turbulence will also cause larger bubbles, with a diameter larger than 5 mm, to be entrained, but their greater buoyancy will overcome the resistance of the oxide film and will float to the surface. During their floatation, the oxide layer at the crown of the bubble will split and reform at the base while leaving a trail of oxide film, see figure 2.10. This defect is a form of oxide bifilms called bubble trail defects and was first observed by Divandari and Campbell (15) in Al alloys. The solidification front could capture the bubble with its tail, as seen in figure 2.11a of a preserved bubble with its attached tail in an Al-Zn alloy, or the bubble could escape leaving the trail as the defect, seen in figure 2.11b. Thus, even though the bubble itself has escaped, the process could leave a long oxide trail that might reduce mechanical properties.

Beside bifilms and bubbles, extrinsic inclusion defects could also be entrained into the liquid metal. They are different from second phases, which precipitate from the melt during solidification and cooling, as they are externally introduced into the melt. Extrinsic inclusions could be slag, old oxides, surface debris, moulding sand or grain refiners. They will be wrapped into the oxide bifilm either during addition or surface turbulence. Figure 2.5d represent the entrainment of an old oxide between the folds of a young oxide film. Sand inclusions wrapped between the folds of an Al oxide bifilm were observed by Fox (16) in Al-7Si-0.4Mg alloy. Emamy et al. (17) found that with the addition of alumina particles in 356 Al alloy matrix to produce MMC, oxide bifilms were found to control the failure of MMCs due to entrainment as seen in figure 2.12a. Figure 2.12b is the fracture surface of an Al-Si alloy revealing bifilms associated with inclusions at the base of a ductile dimple (18). Finally, all the above features, from figure 2.5a to 2.5e, could be entrained as integral parts of the surface film.

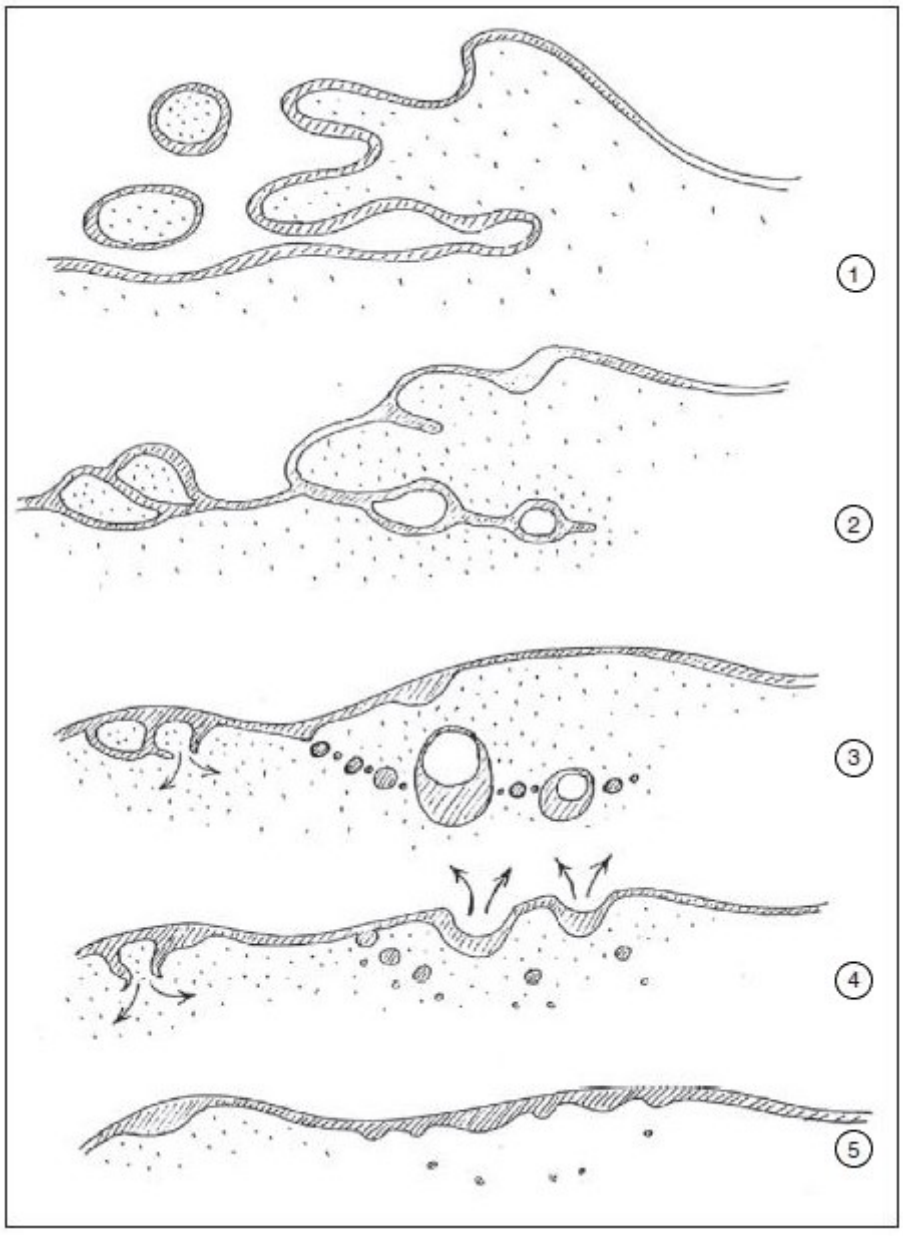


Figure 2.9: The process of detrainment of liquid surface films; they do not cause entrainment defects as no bifilm is formed (4)

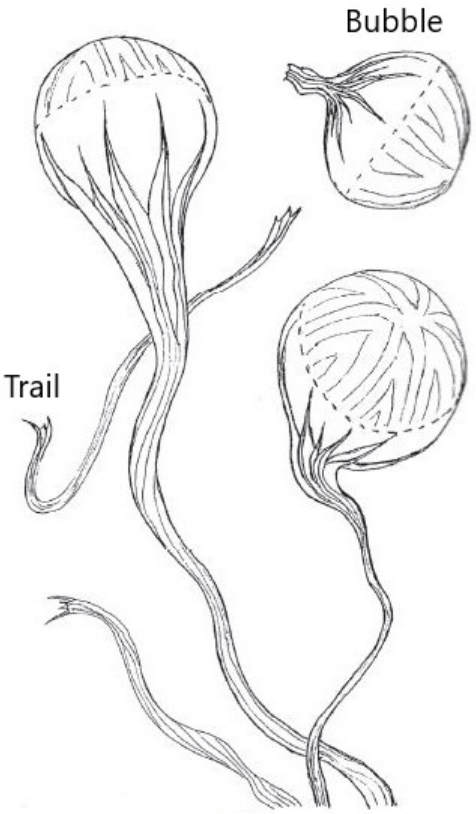
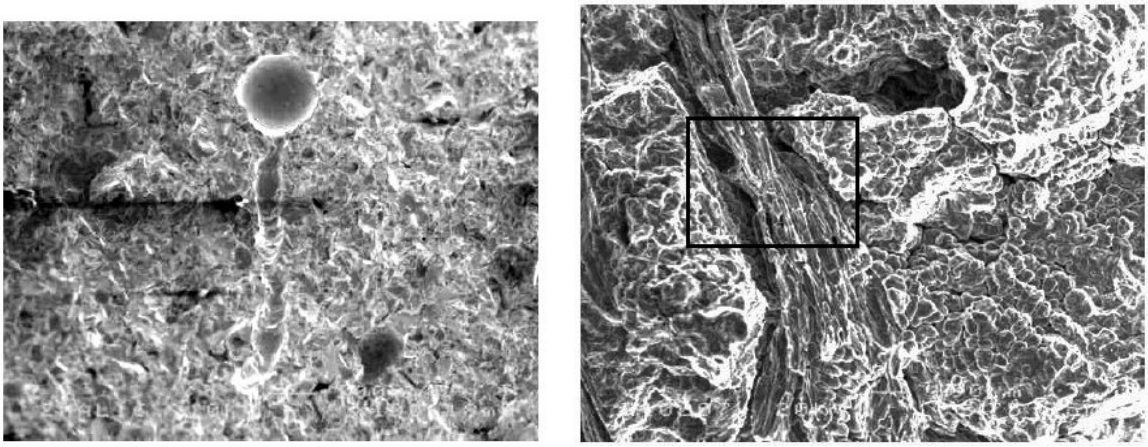


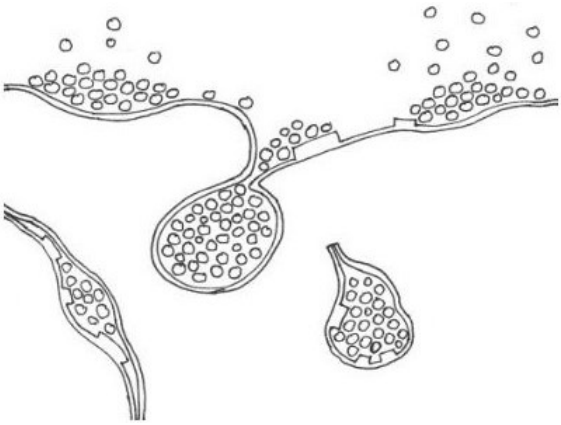
Figure 2.10: Schematic illustration of bubble trail defect formation (4)



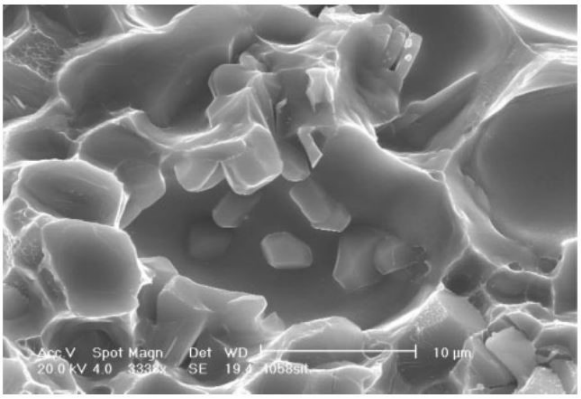
(a) SE image of a bubble with its trail in Zn-Al alloy

(b) SE image of a trail defect caused by a bubble passage in an Al-Mg alloy

Figure 2.11: Bubble trail defect (15)



(a) Sketch of the mechanism agglomerates entrainment by bifilms in MMCs (17)



(b) Fracture surface of Al alloy showing inclusion entrainment as a result of bifilms (18)

Figure 2.12: Extrinsic inclusions due to bifilm entrainment

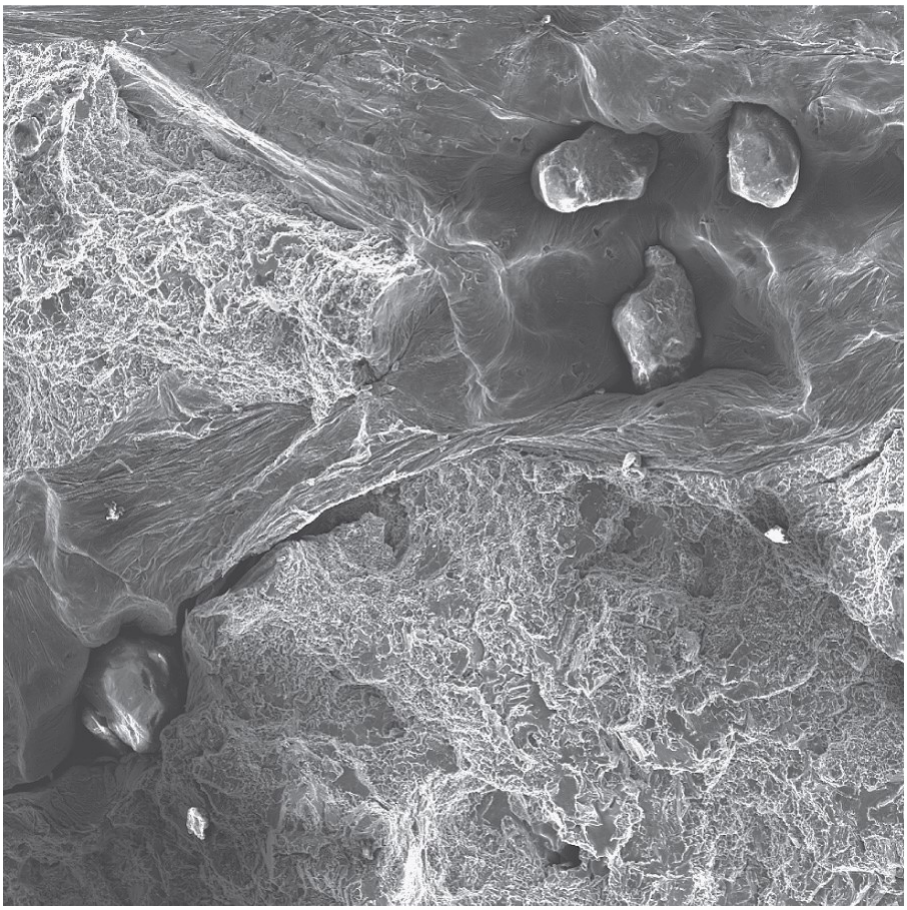


Figure 2.13: SE image of an oxide bifilm entraining sand inclusions in an Al alloy (16)

2.1.3 The evolution of entrainment defects (furling and unfurling)

Campbell (19) suggested that during the lifetime of a bifilm it experiences a series of geometrical changes. After the bifilm entrainment due to surface turbulence, it will be carried under conditions of bulk turbulence. The forces of the turbulent bulk flow, depending on the strength of the bifilm, will tear, pummel, and ravel the bifilm into a convoluted form. This will effectively change the shape and size of the bifilm to a convoluted, crumpled and raveled inclusion in a random manner. The outcome of this process will be a net reduction in shape and size; called "furling". Despite the changes and reduction in geometry, the bifilm will not lose its crack-like feature. On the contrary, after the filling is complete, the forces of bulk turbulence will disappear and the bifilm will be in a quiescent environment. This, as Campbell observed during his work on Al alloys, will open the way to the "unfurling" of the bifilm. During unfurling, the bifilm will open and unfold progressively, growing in size and establishing itself as a planar crack. A sketch illustrating the phenomena is shown in figure 2.14. The unfurling of bifilms could be driven by the following forces (20):

1. The inflation of the bifilm due to precipitation of hydrogen into the gas layer entrained by oxide films (21). Inflation will act separately on each fold, then the inflated section will exert unfolding pressure on adjacent folds. This will be in the form of irregular jerks, until the bifilm is fully unfolded (figure 2.15a). If gas precipitation continues during the liquid phase, and with sufficient time, the bifilm will inflate into a spherical pore, as seen in figure 2.15b. If gas diffusion continues during freezing, the bifilm morphology will be in an interdendritric form. Both mechanisms could cause the bifilm to be irregular in thickness or tear it up into fragments.

2. Shrinkage could also drive the unfurling of bifilms. It will cause pressure reduction in localized areas, sucking the two halves of the bifilm apart, as shown in figure 2.16a. The withdrawal of the residual liquid would stretch the bifilm over the

dendrites and pull its halves into the interdendretic regions. Eventually, the bifilm will either be sucked completely, or its fragments will be scattered over the dendrites, as seen in figure 2.16b. Gas precipitation and shrinkage could work together to drive the unfurling of bifilms.

3. Dendrite growth is another force driving the unfurling of bifilms (18). Growing dendrites will push bifilms ahead, as they are unable to grow through the layer of gas within the films. As a result, the bifilms will be flattened and unraveled, and arranged into planar regions among the dendrites (figure 2.17a). This process could be more effective if the bifilms are anchored to the side walls of the casting. Moreover, the bifilms will be pushed into the grain boundary and interdendritic regions. The effect of this mechanism will appear as large flat facets on the fracture surface. The evidence of dendrite straining of bifilms caused by grain growth is seen on the tensile fracture of Al-4.5Cu alloy (figure 2.17b). Note the lack of ductile dimples on the fracture surface.

4. Finally, the nucleation and growth of intermetallics on the wetted surface of the bifilm could lead to the unfurling of bifilms, shown in figure 2.18. Initially, the nanometer-thick intermetallic crystals will follow the crevasses of the crumpled bifilm. However, the crystal will become rigid as it grows and thicken, forcing the bifilm to straighten (22). Cao (23) confirmed the phenomena when he observed beta iron precipitates growing on the oxide bifilms in Al-11.5Si-0.4Mg, as shown in figure 2.18. He also found correlation in planar disregistry between α-iron rich phase and Al oxide bifilms.

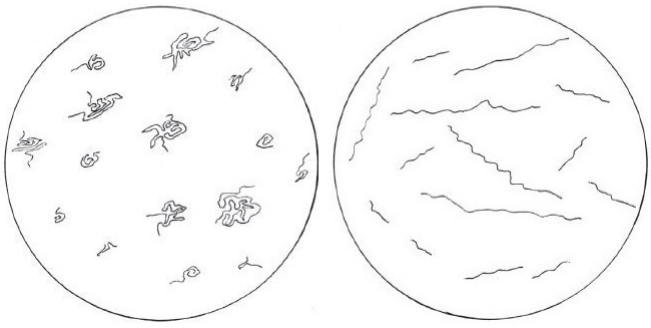


Figure 2.14: On the left, a sketch when bifilms are furled with a compacted configuration, and on the right the same bifilms are unfurled as planner cracks

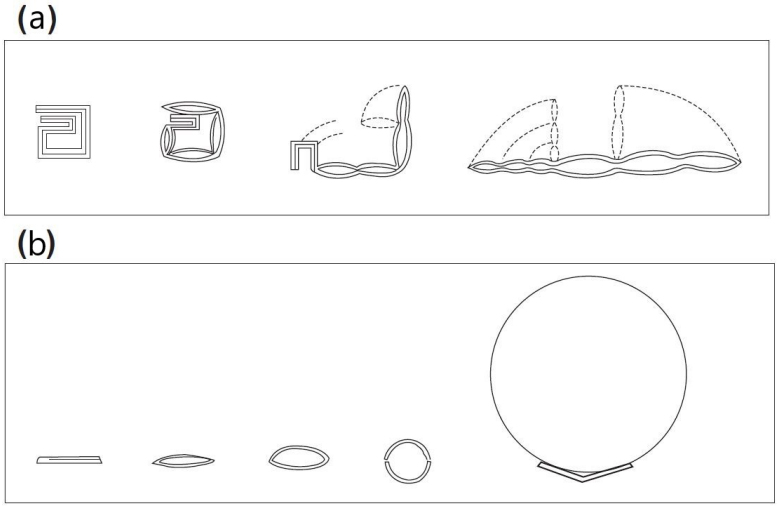
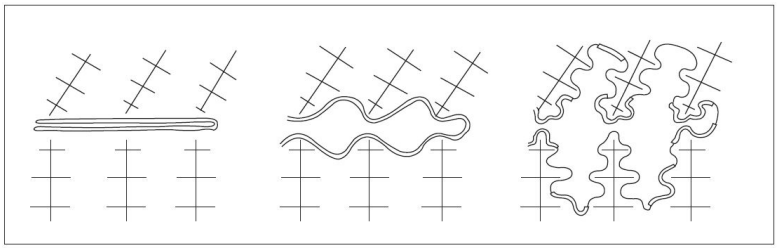
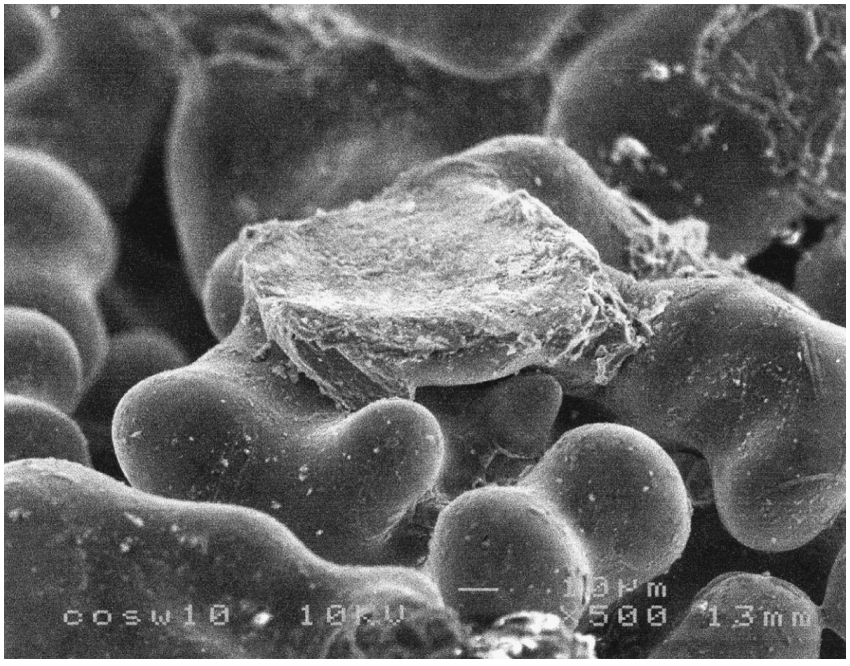


Figure 2.15: A sketch of the mechanism of gas unfurling a bifilm; (a) bifilm is fully unfolded and (b) bifilm is inflated into a spherical pore (4)

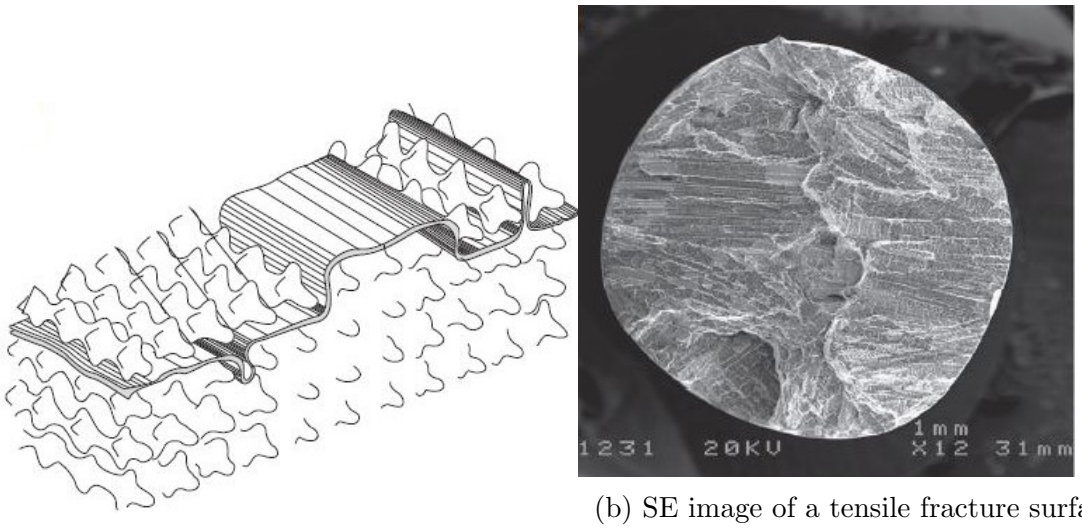


(a) Sketch illustrating the steps of shrinkage unfurling a bifilm (24)



(b) SE image of the remains of a thick oxide bifilm on the dendrite arms of a shrinkage pore, the remains of the bifilm was withdrawn into the dendrite mesh (25)

Figure 2.16: Bifilms unfurling due to the driving force of shrinkage



(a) Sketch illustrating the flatting of a bifilm by dendrites

(b) SE image of a tensile fracture surface of Al alloy showing large bifilms straightened by grain growth (26)

Figure 2.17: Bifilms unfurling due to the driving force of dendrite growth

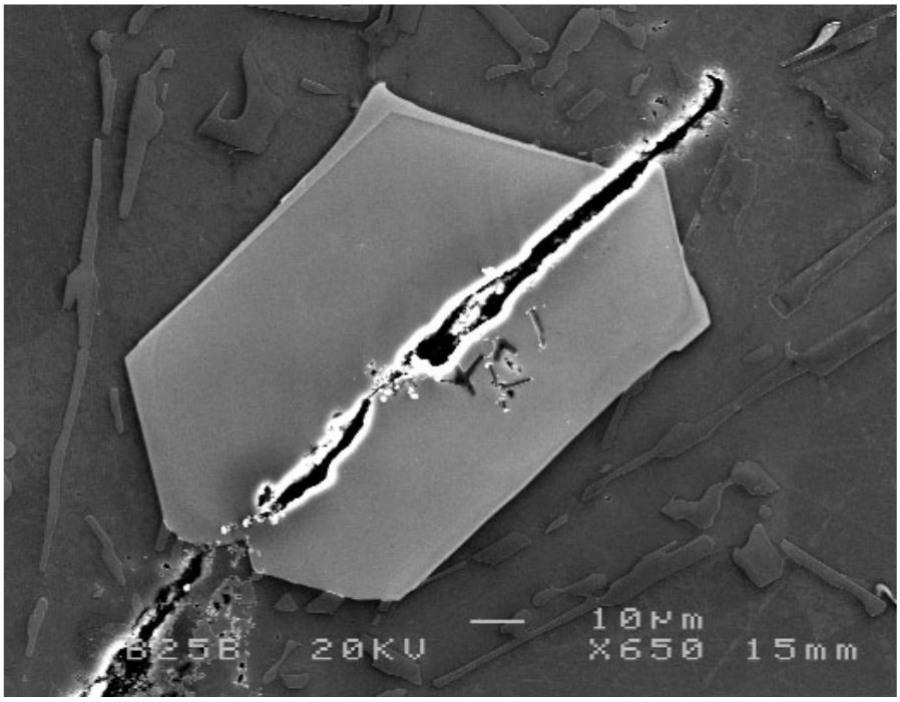


Figure 2.18: Primary Fe-rich phase growing of the wetted sides of a bifilm in an Al alloy (14)

2.2 The evidence for entrainment defects

2.2.1 The evidence for entrainment defects in non-ferrous alloys

Entrainment defects in the form of double oxide films were first mentioned in a publication by Campbell (27) when examining Al-Si alloy thin wall castings. Their forming mechanism and its relation to critical ingate velocities was discussed by Runyoro et al. in 1992 (5) when studying commercially pure aluminium (99.5 Al). Oxide bifilms were then observed in Al-Si-Mg alloy (13, 28). Oxide bifilms' distinctive symmetrical features on the fracture surface of cast specimens was first captured by Cao and Campbell (29) when studying the effect of mould-filling turbulence on the tensile properties of Al-Si-Mg alloys, shown in figure 2.19.

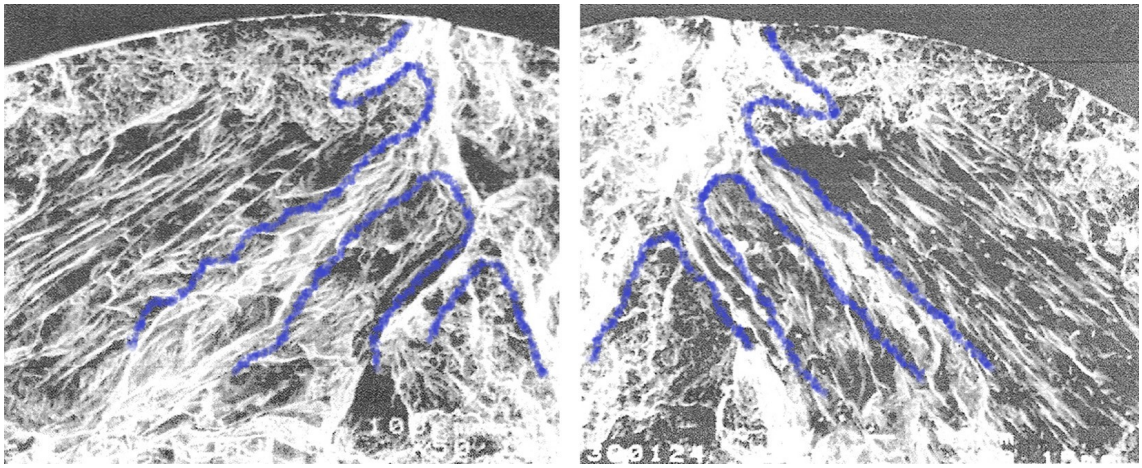


Figure 2.19: Secondary electron (SE) image of of a halved oxide bifilm on the fracture surface of Al-Si-Mg alloy (29), the blue lines added by the author to illustrate the symmetry

Bifilms are so thin that they cannot be detected by non-destructive tests like x-ray radiography. Fox and Campbell (30) developed a technique that utilise a combination of X-ray radiography and a reduced pressure test to examine the quality of liquid metal. In this technique, the liquid metal goes through solidification under a reduced atmospheric pressure, ranging from 5 mbar to 250 mbar. The negative pressure around the casting allows the internal atmosphere inside the oxide bifilm to expand, leading to the unfolding and enlargement of the defect (this is an unfurling

process, is discussed in section 2.1.3). As the bifilm defect is now more visible as a planar defect, X-ray imaging can be used to detect it, as shown in figure 2.20. Additionally, the hydrogen content of the melt will lead to the inflation of the oxide bifilms. The hydrogen in solution utilizes the entrained bifilm as a nucleation site, and migrates into the internal gas layer increasing the internal pressure. If the melt hydrogen content is high, the increase in the internal pressure will be enough to transform the bifilms into expanded spheres (16). The RPT was used as a part of technique developed to create a bifilm index for aluminium castings by visual assessment (24, 31). A sample solidified under reduced atmospheric pressure of 100 mbar is sectioned and the length of bifilms are measured to determine the quality of liquid aluminium. The procedure was detailed by Dispinar and Campbell (32) and its validity was assessed by Esfahani et al (33).

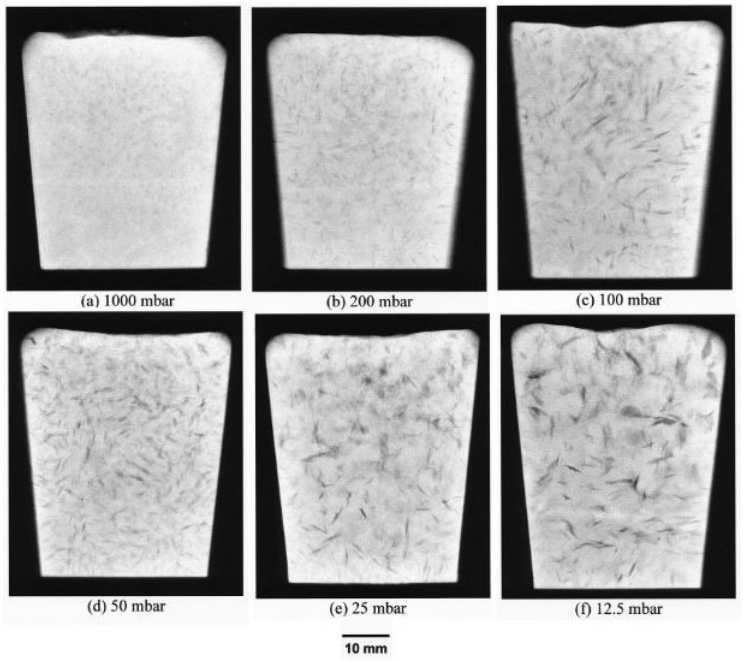


Figure 2.20: X-ray radiography showed the increase of bifilms size under reduced pressure (30)

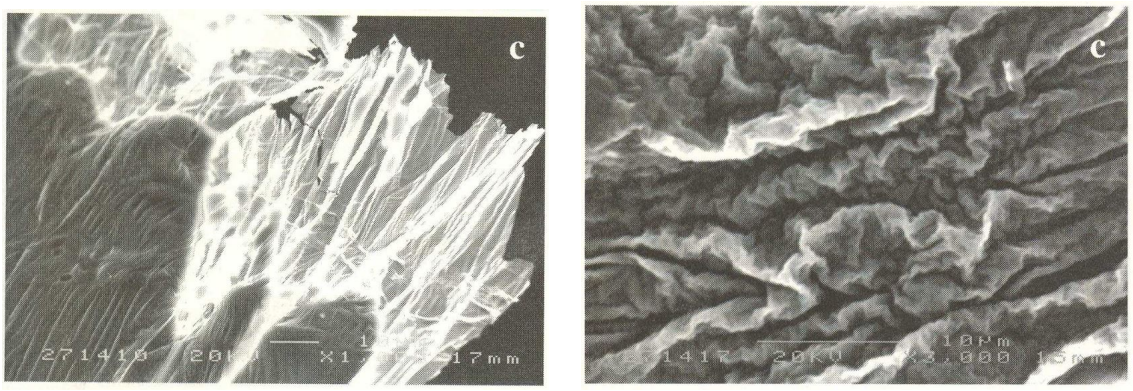
Divandari and Campbell (10) developed an experiment to study aluminium-alloy oxide bifilm features such as morphology, thickness and chemical composition. They introduced bubbles into molten Al-7Si-Mg and Al-5Mg alloys to generate an oxide-metal sandwich, consisting of a triple layer of metal and oxide films. The results of the experiment showed that the nature of oxide bifilms varied in different aluminium

alloys. Depending on the oxide film strength, it was either wrinkled, convoluted with deep folds, or shredded into smaller particles (10). They also found that the oxides seen in Al-7Si-Mg were more brittle than the ones seen in Al-5Mg, and that there was a relationship between the thickness of the oxide bifilm and its morphology (34). The thin and rigid oxide films are shown in figure 2.21a and 2.21b, respectively.

The precipitation of intermetallic compounds on the wetted surface of oxide bifilms in aluminium cast alloys was recorded by Cao and Campbell (35, 36). They observed iron rich phases and titanium aluminium crystals growing on the oxide bifilms in Al-11.5Si-0.4Mg alloy. These observations explained the common sighting of cracks in and around such particles as shown in figure 2.18. Furthermore, Sr-rich compounds were found precipitating on the wetted side of oxide bifilms in Sr-modified A356 alloy (22). The growth of secondary phases on the wetted side of entrainment defects is another distinctive feature of the defect. The mechanical effect exerted by the growth of such phases on the morphology of bifilm defects, shown in section 2.1.3, cause it to be more deleterious to mechanical properties and the reliability of cast alloys. Such negative effects were noted by Zahedi el al. (37) when studying the effect of iron-rich intermetallics on the tensile fracture of Mn and Sr modified type 319 Al alloy.

The main types of oxide bifilms observed in Al-Si-Mg cast alloys were $MgAl_2O_4$ (spinel), Al_2O_3, and MgO. Spinel bifilms formed due to the intermediate content of magnesium. Alumina bifilms formed as a result of magnesium local depletion, or originated from the charge material, and the magnesium oxide bifilms were found to have originated from the original ingots. Additionally, SiO_2 inclusions were found entrained between the folds of oxide bifilms (14).

Oxide bifilms were also identified in magnesium casting alloys. Bahreinian et al. found that, with the increase of ingate velocity, the bend strength of ZK51A decreased as a result of the entrainment of oxide bifilms (38). Griffiths and Lai (39, 40) found that the density of oxide bifilms, arising from different levels of surface turbulent filling, controlled the strength of unfluxed commercial purity magnesium



(a) SE image of a thick folded oxide film found covering the dendrites

(b) SE image of a thin transparent oxide film

Figure 2.21: Oxide films with different morphologies (10)

alloy. MgO films were found symmetrically on either sides of the fracture surface of tensile testbars, shown in figure 2.22. In addition, oxide bifilms were observed in magnesium alloy AZ91 castings. MgO bifilms caused a high density of porosity in gravity cast plate ingots of AZ91 alloy. Oxide bifilms with lengths more than 1 mm were found on the fracture surfaces of tensile and four point bend test samples (41). Mirak et al. (42) found a relationship between MgO bifilms entrained by surface turbulence during mould filling and the mechanical properties and reliability of AZ91 alloy castings.

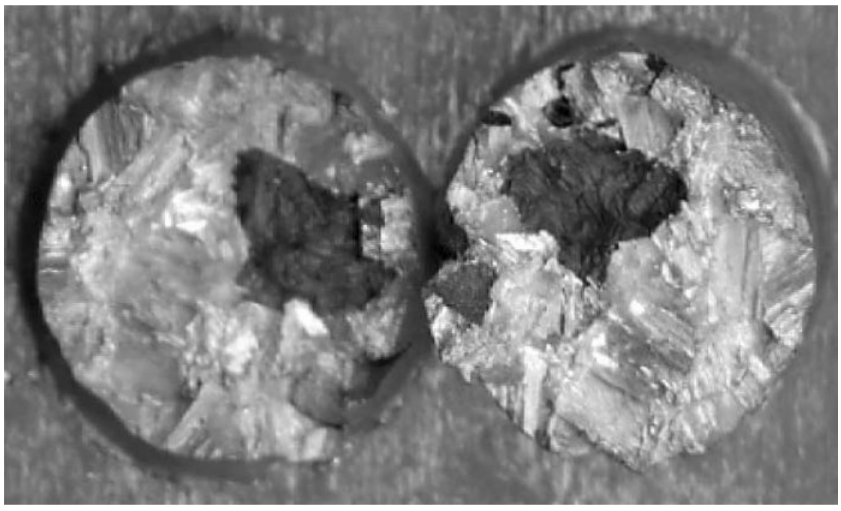


Figure 2.22: MgO bifilm on the fracture surface of commercial purity Mg alloy tensile testbar (39)

Oxide bifilms were identified as a source of failure in copper alloys when they were found draped over shrinkage pores while examining different ingate velocities

for aluminium bronze castings (Cu-10Al and AB2) (43). Entrainment defects were also found in gravity cast nickel-aluminium bronze castings (44). Moulds filled with reduced surface turbulence produced better reliability and mechanical properties. Old and young alumina bifilms were observed on the fracture surfaces of testbars, showin in figure 2.23, and were identified as the source of failure, and scatter of strength and ductility.

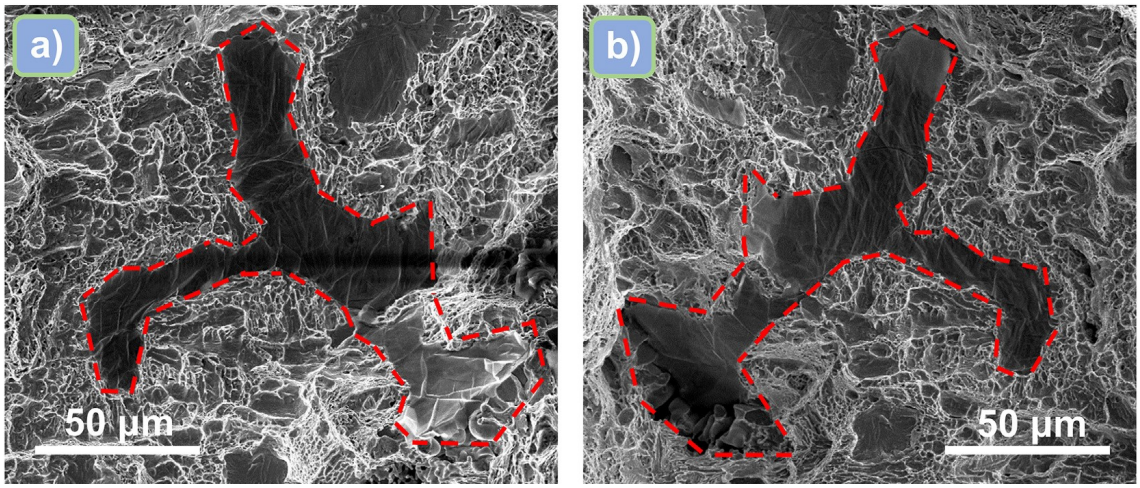
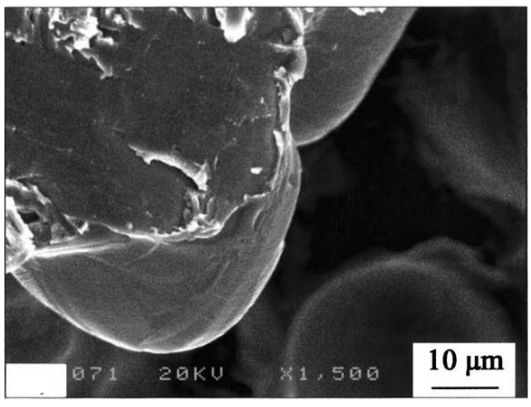
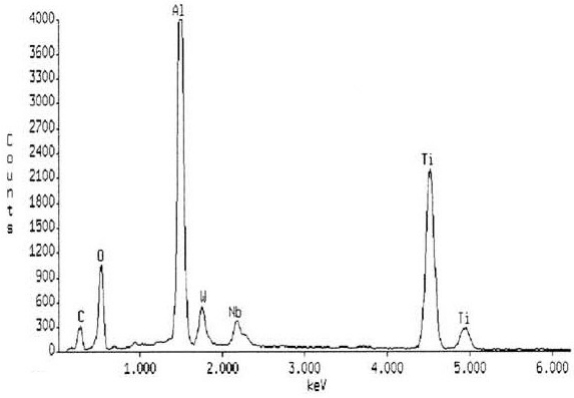


Figure 2.23: An alumina bifilm was found symmetrical on both sides of the fracture surface of nickel-aluminium bronze testbar (44)

Oxide bifilms draped over shrinkage pores were detected in TiAl alloy tilt poured investment casting, shown in figure 2.25. The oxide bifilms were attributed to be the nucleation sites for the formation of center-line porosity in castings (45).



(a) SE image of a film draped over a dendrite on the fracture surface of TiAl testbar

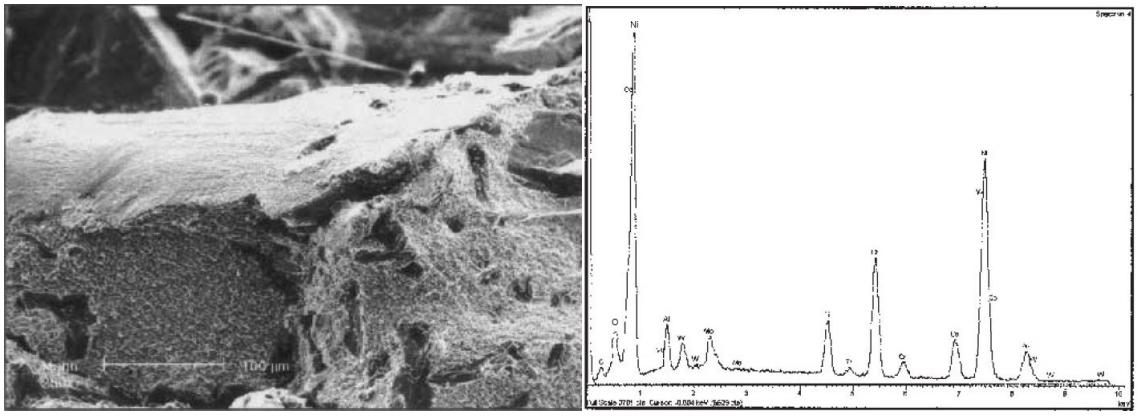


(b) EDX spectra of the film suggest this is a Ti/Al oxide

Figure 2.24: Evidence of oxide films in TiAl investment casting (45)

As for nickel alloys, Cox et al. (46) was the first to examine the effect of surface turbulence and entrainment defect formation on the mechanical properties of nickel based alloys. They found that the ultimate tensile strength of vacuum melted IN939 and IN738LC nickel based alloy investment castings increased with the reduction of surface turbulence. Rashid and Campbell (47) found evidence of oxide and nitride bifilms on the fracture surface of turbine blades vacuum cast from TLV 8933-grade nickel based superalloy (figure 2.25). The wetted side of the bifilms acted as nucleation sites for the growth of carbides, and as a path for a network of cracks. The oxygen content of the oxide bifilms was diluted as a result of the vacuum casting. Campbell and Tiryakioglu (48) attributed the catastrophic failure of a Ni-based super alloy IN100 high-pressure turbine blade in a single engine plane to entrainment defects leading to fatalities. They found what seemed to be an oxide bifilm pushed by growing grains into the grain boundaries (i.e. dendrite straightening). The entrained bifilm allowed the rapid propagation of fatigue failure causing the premature failure of the turbine blade. A study (49, 50) was carried on the same Ni-based super alloy, IN100, to verify the claims made by the previous authors. Samples were cast under different atmospheric conditions, air, argon, and vacuum, and under different levels of surface turbulence, top fill, bottom fill, filter top fill and filter bottom fill. The tensile and fatigue properties were examined under room temperature. The authors found that the tensile and fatigue properties of IN100 were not influenced by surface turbulence. Though heterogeneous non-metallic inclusions, alumina and stringy Ti/Mo carbides, were observed on the fracture surfaces of testbars, they were not interpreted as entrained oxide bifilms with precipitated compounds. The authors suggested that the findings in this study clearly conflict with Campbell and Tiryakioglu (48) interpretation of the source of premature failure on IN100 turbine blade. And they suggested that there was not enough evidence to support the claim that bifilm defects arising from surface turbulence are a source of significant risk in Ni-based super alloy castings. Campbell (51) then noted that the research done by Kaplan and Fuchs (49, 50) actually presented multiple forms of evidence of the for-

mation of bifilms in IN100 alloy, especially in the air-cast samples. He pointed out that the unconventional (high) addition of boron (0.02 wt. pct) transformed surface films from solid to liquid reducing the deleterious effect of entrainment defects, but when the casting is carried out in air, the abundant oxygen content overwhelms the added boron. Moreover, the author of this research criticises the design of the experiment, mainly the designs of filling systems and the lack of their verification. That could have led to a comparison between castings with equal densities of entrainment defects, which would obscure differences. Finally, the number of samples and statistical method used to represent the mechanical property results lack the sensitivity discussed in section 2.5, which would also add to the obscureness of differences.



(a) SE image of a film covering a part of the fracture surface of Ni-based super alloy casting

(b) EDX spectra of the film showed presence of oxygen, aluminium and chromium

Figure 2.25: Evidence of oxide films in Ni-based super alloys grade 8933 (47)

Evidence of oxide bifilms were also found in Ni-based super alloys produced by different additive manufacturing techniques. Zhang et al. (52) found Al_2O_3 and Cr_2O_3 bifilms on the fracture surfaces of direct laser deposited IN718. The bifilms were nucleation sites for crack propagation, and their wetted sides nucleated several intermetallic compounds. Young aluminium oxide bifilms were found on both sides of the tensile fracture surface of test samples made of IN719 laser-powder bed fusion, shown in figure 2.26. Though there was less than 1% of aluminium in the alloy, the entrained oxide bifilms reduced the mechanical properties below the required standards. It was suggested that the source of entrainment was the laser hitting

the melt pool, causing a wave that folded the surface oxide film on itself entraining it in the bulk (53). In high-entropy alloys, streams of oxide bifilms were the cause of separation of splats and sites of porosity in plasma-sprayed MnCoCrFeNi and AlCoCrFeNi (54).

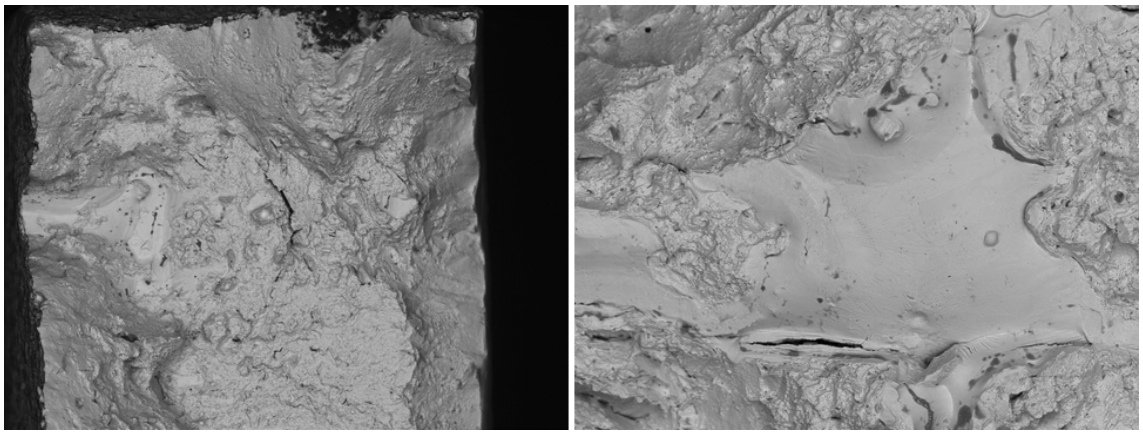


Figure 2.26: A flat alumina bifilm containing some wrinkles was found both sides of the fracture surface of laser-powder bed fusion IN719 Ni-based super alloy (53)

2.2.2 The evidence for entrainment defects in ferrous alloys

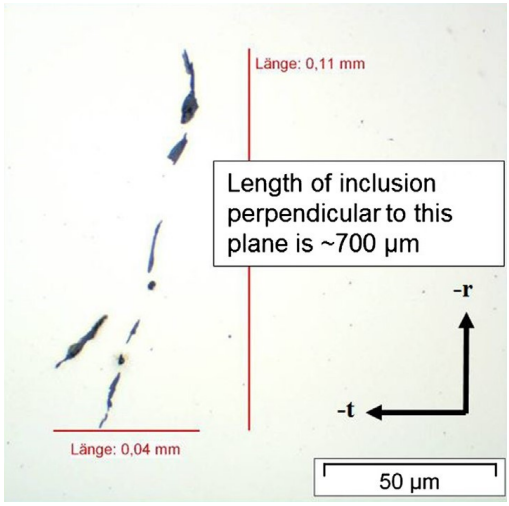
In steels, Cox et al. (46) found no change in the reliability of air-cast 254-SMO stainless steel investment castings, produced using bottom or top filling with or without ceramic filter inserts. This suggested either the lack of entrainment defects in the alloy or that both filling modes produced a high density of entrainment defects. which obscured the difference. The latter could be the reason according to the findings of Hardin (55) who conducted a study to examine the effect of surface turbulence of the mechanical properties and reliability of CLA 11 steel investment castings. It was found that top-filled, and bottom-filled with filter castings produced the same reliability. But when a centrifugal counter gravity casting technique was employed to eliminate surface turbulence, the reliability increased by two orders of magnitude. Griffiths et al. (56) conducted the same study on low alloy steel investment casting and recorded the same behaviour; the centrifugal counter gravity casting technique increased the reliability of the castings by two orders of magnitude. Additionally, inclusions were found on the fracture surfaces of testbars produced with

surface turbulent filling.

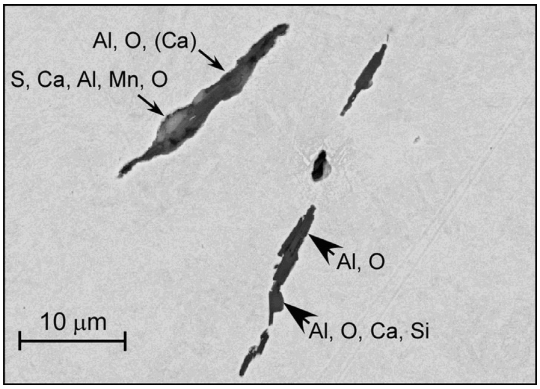
In 2008 a high speed train, with a speed of up to 330 km/h, derailed during departure from Cologne, Germany, as a result of a premature fatigue failure of one of the driving axles. A study commissioned by the public attorney's office was carried out by the Federal Institute for Materials Research and Testing to investigate the incident (57). The axle was made of 34CrNiMo6 quenched and tempered steel and, while in-service, it was inspected every 300,000 km with ultrasonic testing. The last inspection took place 150,000 km before fracture and, according to the operator, no crack indications were found. After no issues were found on the neighbouring components relevant to the axle loading, it was concluded that loading conditions did not play a role in failure. After fractography, micro-computer tomography and metallography it was concluded that one of multiple sub-surface defects was the source of high cycle fatigue crack initiation. The defects appeared to be stretched cracks nearly along the axial direction, with a length ranging from 0.5 mm to 1 mm, an example of which in shown in figure 2.27a. After scanning electron microscopy (SEM) and energy dispersive X-ray (EDX) analysis the defects were designated as non-metallic inclusions, mainly mixed oxides (figure 2.27b). This study is an example of the mislabelling of entrainment defects as "non-metallic inclusions". The defects shown in figure 2.27 are double oxide bifilms that were entrained as a result of surface turbulence and were subsequently stretched. As a result of the study findings, the inspection interval was reduced to 30,000 km, the operator then decided to replace all 1200 driving axles made from the same alloy, and increased the size of the new design; the final costs were estimated to be 350 Million Euro.

The evidence of entrainment defects in cast irons

Formation and control of carbonaceous surface films (lustrous carbon) in sand castings have been a subject of research as surface defects (wrinkling) in cast irons (58), shown in figure 2.28a, and their entrained metallographic appearance was reported as an anomaly by Goodrich (59). Their effect on the mechanical properties of grey



(a) μCT result show one of the bifilms found near the fatigue crack propagation site

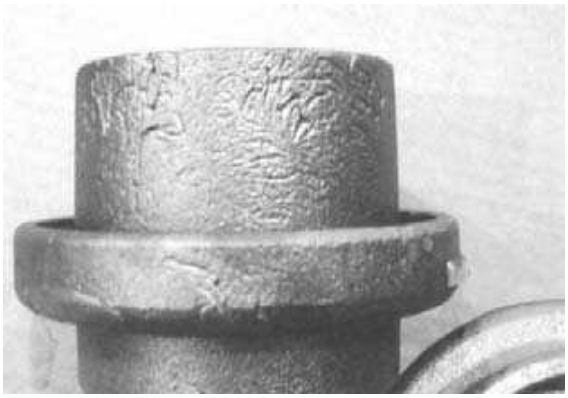


(b) EDX analysis of the bifilm showed presence of oxygen, aluminium and silicon

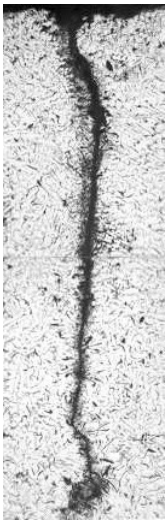
Figure 2.27: The subsurface defects that caused the premature failure of 34CrNiMo6 quenched and tempered steel drive axle during operation (57)

cast iron was examined by Fasoro (60). Naro (61) found that when lustrous carbon bifilms were entrained in grey iron, as shown in figure 2.28b, they could be an issue; especially in thin sections where pressure tightness and hydraulic soundness is required as entrained bifilms could be leak paths. In thick sections and heavy castings, the long solidification time will allow the carbon to go into solution, dissolving the defect, thus lustrous carbon defects are not seen in such castings. When not entrained, lustrous carbon films improve the surface finish of cast iron castings (62). With surface quiescent filling conditions the carbon lustrous surface film is trapped between the mould and the metal and held in place by friction with the sand. While the melt advances, it will deposit more of the film on the mould surface bridging the sand grains. The mechanical rigidity of the deposited carbon films will improve the smoothness of the cast surface. Habibollahzadeh and Campbell (63) also reported the improvement in surface finish of grey iron castings due to lustrous carbon films formed due to the decomposition of hydrocarbons in phenolic urethane binders, as did Sun (64). They also observed entrained carbon films on the internal surface of entrained bubbles. Types of sand binders, their content and amount, and the sand's chemical constituent effect the formation of lustrous carbon films (65, 66).

High casting temperatures (1480°C) have been reported to eliminate lustrous carbon defects in grey iron (67).



(a) Surface wrinkling on an automotive part cast with lost foam process (58)



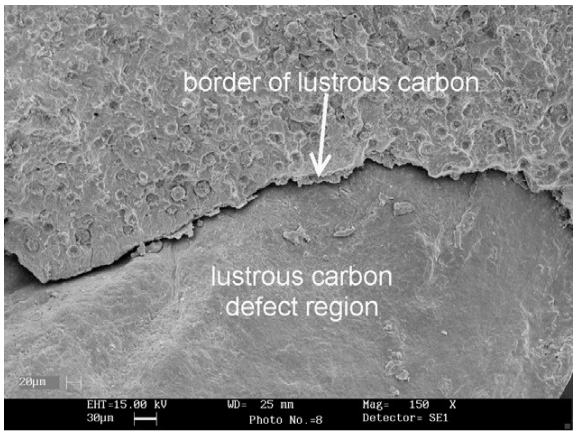
(b) Entrained lustrous carbon bifilm (61)

Figure 2.28: Surface and sub-surface lustrous carbon defects in LGI castings

Lustrous carbon bifilms were also observed in SGI castings. In lost foam SGI castings, lustrous carbon bifilms, shown in figure 2.29a, were found by Chakherlou et al. (68) to have acted as a site for fatigue crack propagation reducing the fatigue properties of the castings. Unrecorded low pouring temperature was used to promote the formation of lustrous carbon defects in SGI lost foam castings to compare it to green sand castings. The same defect was also recorded by Jezierski et al. (69) during the production of SGI castings using the lost foam process, shown in figure 2.29b. In their experiment they used low pouring temperatures to cast their test samples, between 1236°C and 1360°C, and as stated by Naro (61) lustrous carbon defects increased with the reduction of pouring temperature, which is the same result Jezierski et al. arrived to. Lustrous carbon films were also found on the surface of shrinkage porosities in SGI casted in phenolic resin sand moulds and green sand moulds (70, 71).

Bubble trail defects were reported as the source of leakage in LGI automotive castings by Campbell (72). The trails originated from the out-gassing of poorly vented cores. The blows of gas oxidised the silicon in the iron forming entrained silicate films. More serious out-gassing events caused lustrous carbon surface films

to be dragged into the bubble trails. In a study conducted on LGI castings to examine oxide defects caused by mould filling, Modaresi et al. (73) tested the effect of different gating system designs on defect formation. Unfortunately, the premise of the study was flawed, it made the mistake of substituting the concept of surface turbulence with bulk turbulence without making the distinction. As a result, the study used the Reynolds number as the factor to evaluate the quality of the gating system designs. As explained in section 2.1.1 the Reynolds number describe bulk turbulence which is not representative of the entrainment process of surface films. The Froude and Weber numbers should have been used instead to evaluate the gating system designs as they describe the forces acting to entrain surface films. The study contained some examples of silicate defects on micrographs taken from an area next to the passage of air bubbles.



(a) SE image of a lustrous carbon film on the fatigue fracture surface of SGI casting (68)



(b) Entrained lustrous carbon surface film in SGI lost foam casting (69)

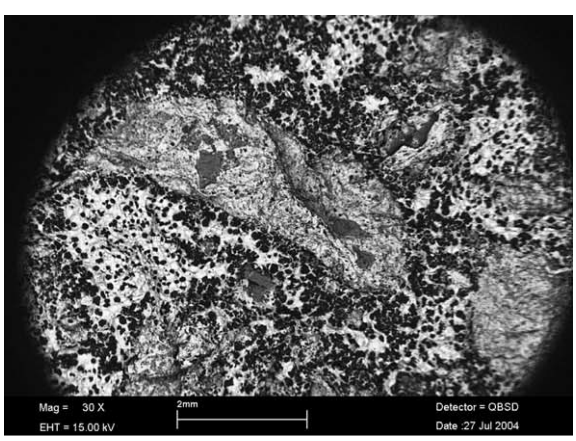
Figure 2.29: Lustrous carbon defects in SGI castings

Dross or slag inclusions, mainly oxides, were a common defect reported in cast irons (74), and were sometimes referred to as non-metallic inclusions. They have a filamentary shape and resemble stringers on polished micrographs (75). Haque et al. (76) reported the sighting of an entrained oxide slag and identified it as the source of fracture in a SGI tensile testbar. Campbell (77) interpreted some light shades

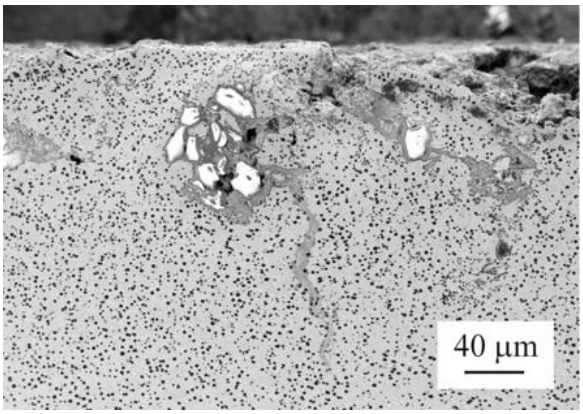
on SEM images of the surface of a fatigue fractured continuously cast SGI testbars as oxide bifilms. He attributed the brightness of the shades to be the accumulation of electrons on the non-conductive oxide films. When examining the behaviour of SGI wind turbine components, Shirani and Harkegard (78) found that fatigue cracks nucleated on shrinkage pores but that fatigue crack propagation was favoured by oxide inclusions.

Evidence of entrainment defects were recorded in a serious of studies conducted to examine the mechanical properties of SGI nuclear waste canisters (79-84). The canister had a length of 4,835 mm and a diameter of 1,050 mm. Samples were extracted from the top and bottom slabs of the canister body and mechanically tested. The results showed a wide scatter and the samples extracted from the bottom slab exhibited better mechanical properties than the samples extracted from the top slab. One of the reasons attributed for the variation in mechanical properties was the observation of oxide films on the fracture surface of testbars. The image of the fracture surface, shown in figure 2.30a, and the description of the defect did not mention if the oxide film was symmetrical on both sides of the fracture surface. The testbars extracted from the top slab had a higher density of oxide films. This meant that most of the defects were observed near the top of the castings. Impinged oxide surface films were also found on surface breaking cracks, the film entrained surface debris (figure 2.30b). The oxide films were categorized as areas of secondary phases or large slag/dross. To improve the quality of the upper part of the canisters, one of the studies recommended increasing the thickness of the top slab and then cutting the extra top layer as it will contain most of the oxide defects. Though this solution will work as intended, the study did not point to the effect of surface turbulent filling of the casting. As the cannister was long, it is fair to assume that the metal fall hight resulted in a very surface turbulent filling; thus entraining bifilms. The long solidification time will allow the bifilms to float to the upper section of the casting which will be removed with subsequent machining. The same behaviour is observed in cast irons in the flotation of graphite, especially chunky graphite, which was one

of the defects observed in the top slab of the canister under investigation.



(a) The fracture surface of SGI testbar showed a large oxide slag defect (79)



(b) Impinged surface oxide films entraining debris, referred to as inclusions and agglomerates (82)

Figure 2.30: Examples of mislabelled oxide bifilms in SGI castings

Agglomeration of titanium carbide inclusions surrounded by cracks were observed in Ti-inoculated chromium white cast iron, and were assumed to be entrained by bifilms (figure 2.31) (85). The non-homogeneous distribution of agglomerates were explained to be the result of dendrite pushing of entrained bifilms, which in turned were wrapped around the Ti inclusions. This mechanism of formation assumed that inclusions were entrained during solidification by the wetted side of a closed folded bifilm. This assumption contradicted Campbells' explanation of the process of bifilm formation (4). A better explanation was the assumption of nucleation of the secondary phases on the wetted side of bifilms, as observed in Al alloys (20), the proceeded by geometrical changes due to dendrite growth. Dendrite pushing of entrained oxide films were also observed in Si high alloyed cast iron (86). Folded sheets of silicate and carbon films, shown in figure 2.32, were found between, but not on top, of dendrites in shrinkage pores. Figure 2.33 is an SEM image of what was presented as a magnesium oxide bifilm in a SGI support bracket casting (87). The defect string shape does not have resemblance to any recorded magnesium oxide bifilms in any alloy. The authors claimed that the defect was the source of tensile failure of a test sample, but the defect orientation was not representative of a bifilm planar crack.

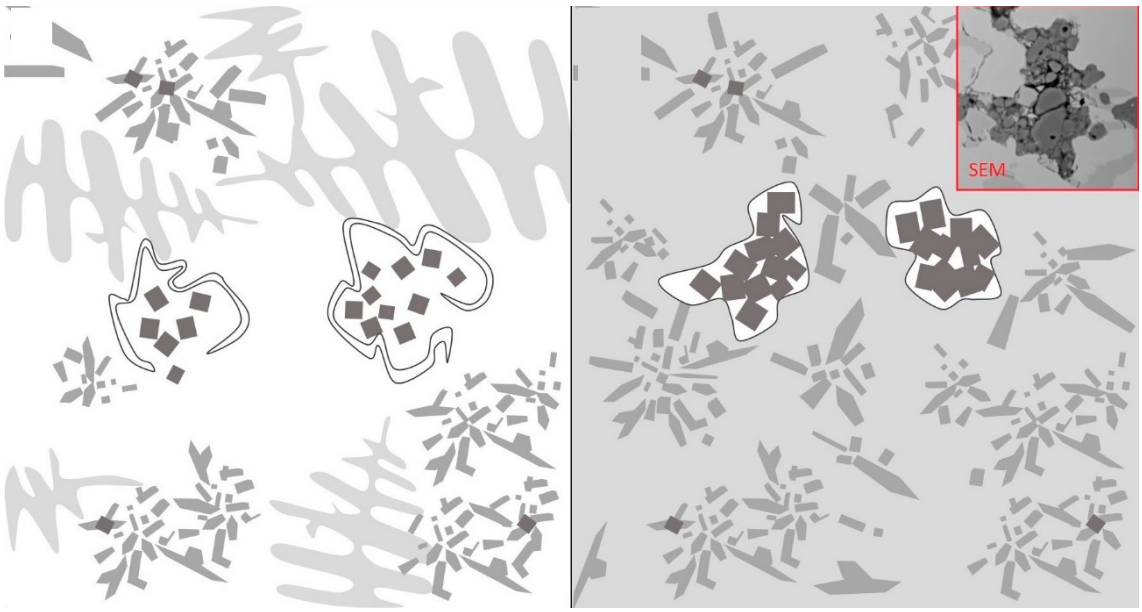


Figure 2.31: On the top right corner a SEM image of Ti inclusions agglomerate; the schematic diagram presents the step of formation (85). Note, Campbell stated that surface films cannot be entrained in an open form, as the process of entrainment will always fold the films dry sides

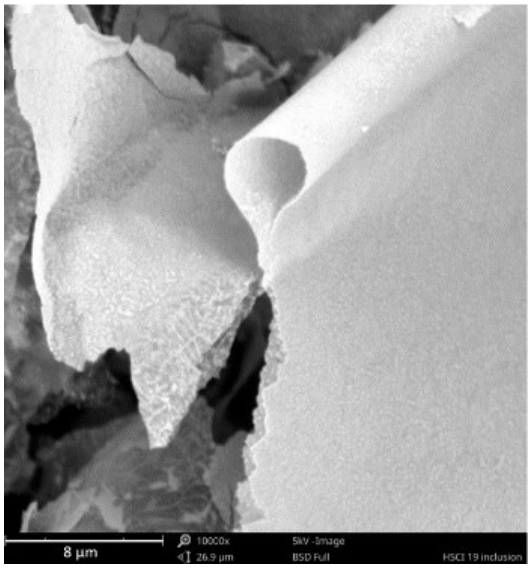


Figure 2.32: Silicate folded film in high alloyed Si cast iron (86)

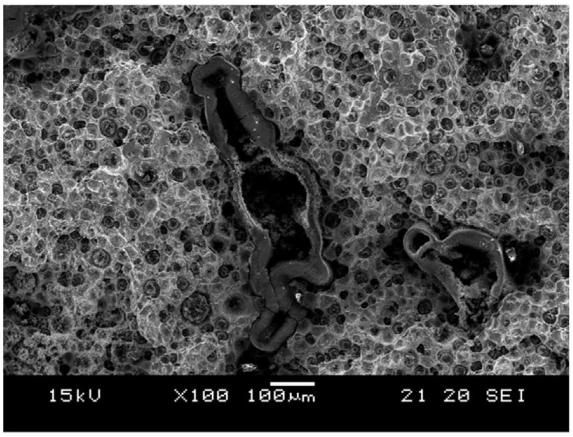
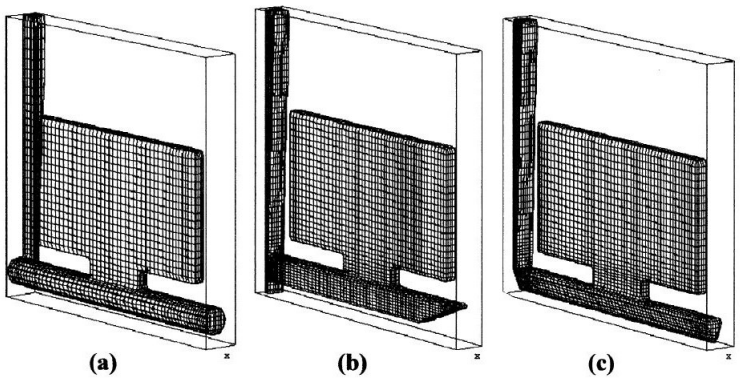


Figure 2.33: A reported magnesium oxide bifilm which does not bear any resemblance to previously reported magnesium oxide bifilms (87)

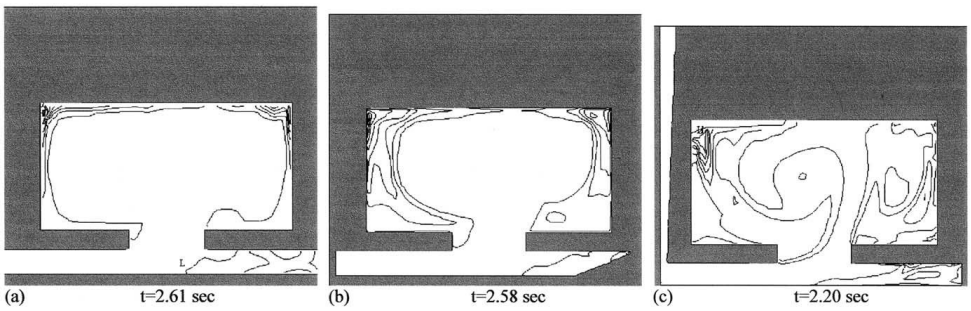
2.3 The reduction of entrainment defects

Two methods have been reported as factors in reducing entrainment defects in casting. The first revolve around the re-design of mould filling systems to ensure the ingate velocity will not exceed the critical velocity for the alloy, (for iron $V_{critical} = 0.4m/s$). Critical heights, values of which are shown in figure 2.4, also affect the critical ingate velocity, so the melt fall hight during filling has to be considered too. Cox et al. (46) compared the mechanical properties and reliability of castings produced with top-gated and bottom-gated moulds and found that top-gated castings contained more entrainment defects compared to bottom-gated casting, leading to reduced mechanical properties and reliability. Figure 2.34a contains three different types of runner system design, a vortex flow runner (cylindrical cross-section), a triangular flow runner (triangular cross-section), and rectangular flow runner (rectangular cross-section), they were investigated by Dai (88) to examine the effect of runner systems design on the ingate velocity of aluminium alloys. The simulation result, shown in figure 2.34b , showed that the vortex flow runner effectively controlled the ingate velocity below $V_{critical} = 0.5m/s$ and caused less surface-turbulence during filling, improving the mechanical properties and reliability (89).

The other method used to control entrainment defect content in casting was the use of filters. It was first suggested by Aubrey et al. that filters could be used before liquid metal entered casting to clean the melt from inclusions (90). Sirrel and Campbell (91) claimed that the use of filters would not have a profound effect on the filtration of entrained oxide bifilm defects. That being said, filters would act as a choke point and reduce the velocity of liquid metal filling the mould, which would reduce surface turbulence and splashing of the liquid metal surface. The claim was experimentally confirmed by Bäckman et al. (92). The authors suggested that the main effect of the use of a filter was the reduction of the melt velocity, and the priming of the filling system before the liquid metal enters the ingate. Due to the friction in the filter, a back-pressure will build up filling the downsprue. The early



(a) The three runner system designs, (a) vortex runner, (b) rectangular runner, and (c) triangular runner



(b) The numerical simulation result showed the vortex runner produced the least surface turbulent filling

Figure 2.34: Filling system designs showed to affect the entrainment process (88)

filling of the downsprue (priming) and slowing velocity would reduce the entrainment of surface films. Ardekhani and Raiszadeh (93) found that the number and size of oxide biflms decreased with the addition of a ceramic foam filter. Moreover, they found a relation between the pore size of the filter and the density of oxide bifilms. They stated that a 30 ppi filter size could eliminate almost all oxide biflim defects, but if the filter caused the liquid metal to jet, entrainment defects would reappear.

2.4 The deactivation of entrainment defects

Though precautions could reduce bifilm defects, the formation of oxide skin and surface turbulence events that lead to entrainment are somehow inevitable; especially in industrial processes such as inoculation, degassing and injection in high pressure die casting. Hence, it is important to examine the life-cycle of oxide biflm defects before solidification.

Nyahumwa et al. (94) hypothesised that oxide bifilm defects could rupture due to the following factors: the transformation of the oxide structure from amorphous to crystalline, the stress exerted by solidification, or the nucleation and growth of secondary phases on the film. When rupture occurs, the entrapped gas will react almost instantaneously with the liquid metal, resealing the bifilm. The repetition of the process of rupture and reseal will consume the entrapped atmospheric gas, starting with oxygen, then nitrogen. When most of the atmospheric gases are depleted, only a small amount of argon will remain between the layers of the bifilm (1 vol. %). At this point the two layers may bond together. A schematic of the hypothesised process is shown in figure 2.35.

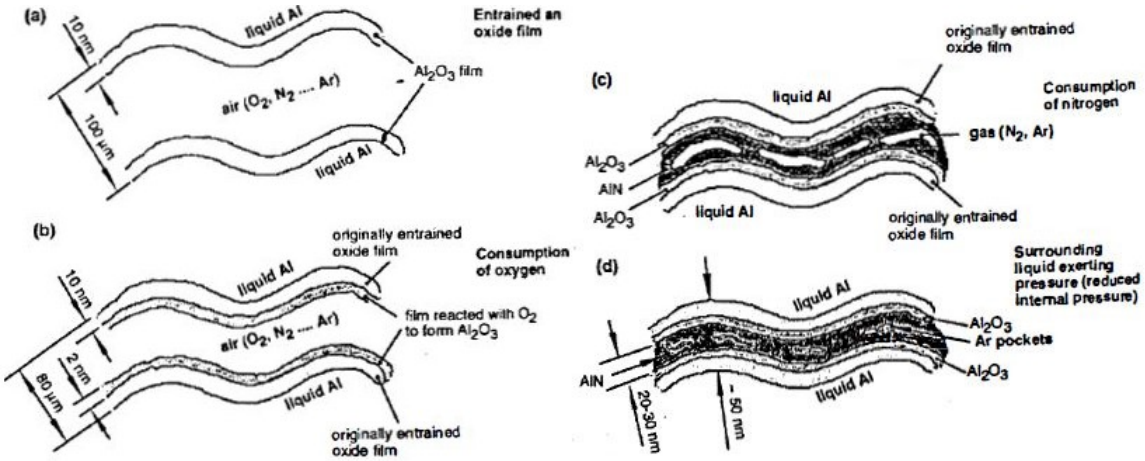
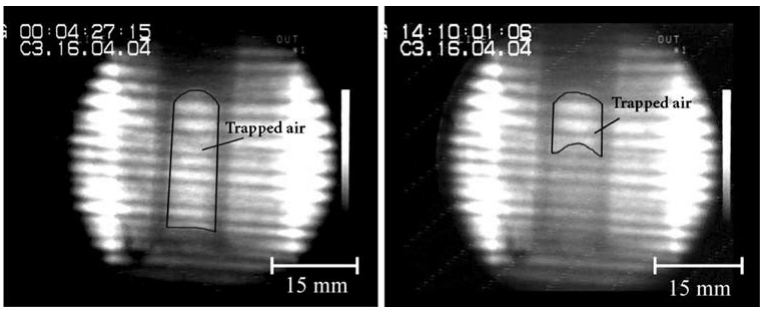


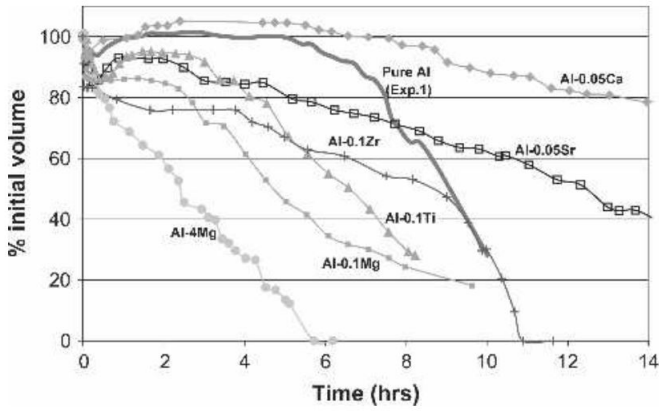
Figure 2.35: A schematic illustration of the mechanism of oxide bifilm healing in the liquid state (94)

Built on the assumption of Nyahumwa et al., Raeiszadeh (95) performed an experiment to examine the consumption of air entrapped inside a bifilm. He trapped an air bubble inside a pure aluminium melt by immersing a SiAlON tube with a blind hole at one end. The consumption of air was monitored by real-time X-ray radiography for 8 hours, (shown in figure 2.36a). The sample containing the reaction product between the liquid metal and entrapped air was examined by SEM and EDX, and the results showed that for the first three to four hours the oxygen reacted with the liquid aluminium forming aluminium oxide. Then the N in the bubble reacted with the aluminium and formed aluminium nitride (AlN). The experiment was repeated for different aluminium alloys and the rate of consumption

was recorded, shown in figure 2.36b. Alloys containing magnesium had a higher consumption rate. Also, only aluminium nitride was detected in all of the alloys.



(a) Real time X-ray radiography showing the consumption of entrapped air bubble by melt reaction (96)

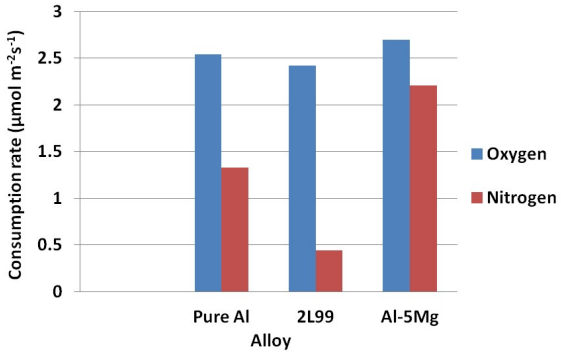


(b) The consumption rate of the entrapped air bubble in different aluminium alloys (97)

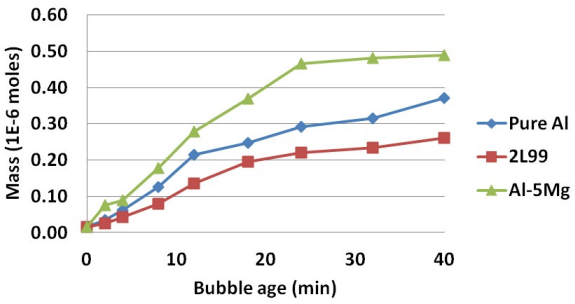
Figure 2.36: The experimental results of entrapped air bubble in aluminium melt

El-Sayed (98) conducted a similar experiment to investigate the rate of change in gas composition in a trapped bubble. Steel strips with a blind hole on each side were immersed in three different aluminium alloys (commercial purity aluminum, 2L99 and Al-5Mg). The melt was allowed to react with the entrapped air before solidification, then the composition of the air bubbles was analysed by mass spectrometer. The results showed the same conclusions reached by Raeiszadeh (95). The oxygen was the first to be consumed in the entrapped atmosphere, followed by the nitrogen. Al-5Mg alloy had the fastest gas consumption rate in the three alloys, for both oxygen and nitrogen, followed by commercial purity aluminium and 2L99 alloy, respectively (figure 2.37a). It was also suggested that hydrogen continued to diffuse into oxide bifilms. Al-5Mg had the faster diffusion rate of hydrogen, followed by pure aluminium then 2L99 (figure 2.37b).

Aryafar et al. (99) suggested that if most of the entrapped oxygen and nitrogen were consumed, the un-wetted oxide/nitride surface could bond together, closing the crack. The bonding will reduce the deleterious effect caused by entrainment defects. The phenomena was created in A356 alloy using two oxidized aluminium bars that were pressed together and melted, then held for different amounts of time. The results showed that after holding for a few minutes, the ponding process started to occur when the first MgO was observed. The bonding was attributed to two different mechanisms, the transformation of alumina to spinel, and the transformation of spinel to MgO. The second mechanism gave a stronger bond than the first. The experiment was expanded to examine the effect of different amounts of Mg. It was found that with the increase in Mg content, the bonding process started earlier (100). Bonding would not occur unless a transformation that involves rearranging of atoms took place at the surface of the oxide film (101).



(a) The consumption rate of entrained oxygen and nitrogen



(b) The diffusion rate of hydrogen into oxide biflms

Figure 2.37: The rate of change of atmospheric gases entrapped inside an oxide bifilm (102)

2.5 The Weibull probability distribution statistical analysis of the mechanical properties of cast components

As an outcome of mechanical properties test results, if no low results, "outliers", were removed from the outcome of mechanical testing, and all results were retained, a histogram could be plotted. The shape of the Gaussian curve is usually not symmetrical, but is either negatively skewed (in the case of strength distributions), or positively skewed (in the case of fatigue life and elongation)(103). A close approximation of the curve shape was initially developed by Weibull in 1939 (104), and greatly expanded in 1951 (105). The Weibull statistical distribution is an empirical method used to study the failure properties of metals. It was developed on the "weakest link" theory, derived by Pierce in 1926 (106), which described the probability of failure of a chain comprised of many links based on the probability of the weakest link failing. The Weibull distribution is widely employed to model the reliability and lifetime of an engineered component (107- 109). The following equation expresses the Weibull cumulative distribution function:

$$F_w = 1 - exp[-(\frac{x - x_T}{x_0})^m] \tag{2.8}$$

F_w is the cumulative fraction of failures up to a given value of x (e.g. strength) and m, x_T and x_0 are the Weibull parameters, where:
m: the Weibull modulus of the data set
x_T: is a lower strength threshold, or threshold parameter, where no specimen fails
x_0: is the scale (or position parameter) within which $\sim 63\%$ of data might fail.

The Weibull distribution is an ideal statistical tool to model the failure of defect containing castings, suggested Campbell (103). At the higher end of the distribution there is a cut-off value where the limit to the mechanical property of a material exists, and this behaviour is consistent with cast components. For example, in

tensile testing, the results usually accumulate at the higher end, but for test bars containing large defects resulting in poor values, the results will end up at the tail end of the distribution.

To simplify the use of the Weibull distribution, the unknown variables are reduced from three to two by assuming the threshold (x_T) is zero. In this case the distribution is called the 2-parameter Weibull, and its cumulative distribution function is:

$$F_w = 1 - exp[-(\frac{x}{x_0})^m] \tag{2.9}$$

And the above equation could be rearranged to:

$$ln[ln(1/(1 - F_w))] = mln(x) - mln(x_0) \tag{2.10}$$

Now the equation is in a linear form and could be presented as a straight line. The values of the 2-parameter Weibull, the scale parameter (x_0) and Weibull modulus (m), can be obtained when $\ln[\ln(1/(1-F_w))]$ is plotted as a function of $ln(x)$, resulting in m as the slope, and - $\mathrm{mln}(x_0)$ as the intercept. For the castings mechanical properties (e.g., UTS, %Elongation or fatigue life) the values (x_n) are sorted into an ascending order as follows:

$$x_1 < x_2 < x_3 < \ldots < x_{n-1} < x_n \tag{2.11}$$

and a probability of failure (P_n) between 0 and 1 is assigned to each value using the following equation:

$$P_1 < P_2 < P_3 < \ldots < P_{n-1} < P_n \tag{2.12}$$

As the probability values need be estimated, the often-used equation is expressed as:

$$P_n = \frac{n - a}{N + b} \tag{2.13}$$

Moreover, another four commonly used equations are (110, 111):

$$P_n = \frac{n - 0.5}{N} \tag{2.14}$$

$$P_n = \frac{n}{N + 1} \tag{2.15}$$

$$P_n = \frac{n - 0.3}{N + 0.4} \tag{2.16}$$

$$P_n = \frac{n - 0.5}{N + 0.25} \tag{2.17}$$

Khalili (112) suggested that equation 2.15 had the least reliable outcome, while equation 2.17 gave a better estimation for the assigned probability of failure. With the help of Monte Carlo simulation, Tiryakioglu et al. (113) found a combination of unbiased estimators, a and b, listed in figure 2.38, assigned to different sample size for equation 2.13. Tiryakioglu et al. (114) also suggested a criteria to determine if the mechanical property test values followed a Weibull distribution. For sample size ranging 5 to 100, a critical value for the coefficient of determination R^2, calculated from equation 2.18 for 95% confidence, can be used to conduct a goodness-of-fit test. This value is compared to the R^2 of the linear regression from the Weibull probability plot. If $R^2 < R^2_{0.05}$, it can be concluded that the data does not follow the 2-parameter Weibull distribution. If $R^2 > R^2_{0.05}$, then the data does follow a 2-parameter Weibull distribution.

$$R^2_{0.05} = 1.0637 - \frac{0.4174}{n^{0.3}} \tag{2.18}$$

The 2-parameter Weibull distribution was used by Green and Campbell to describe the distribution of fracture strength of Al-7Si-0.35Mg alloy (28). They suggested that the 2-parameter Weibull distribution had a better data fit than Type 1 extreme value distribution and thr Normal distribution. Nyahumwa et al. applied the same method when examining the effect of surface turbulence filling and different defect distributions on the fatigue life of cast Al-Si-Mg alloy (94, 115). Byczynski (116) reached a similar conclusion for A319 alloy (Al-Si-Cu-Mg) when he

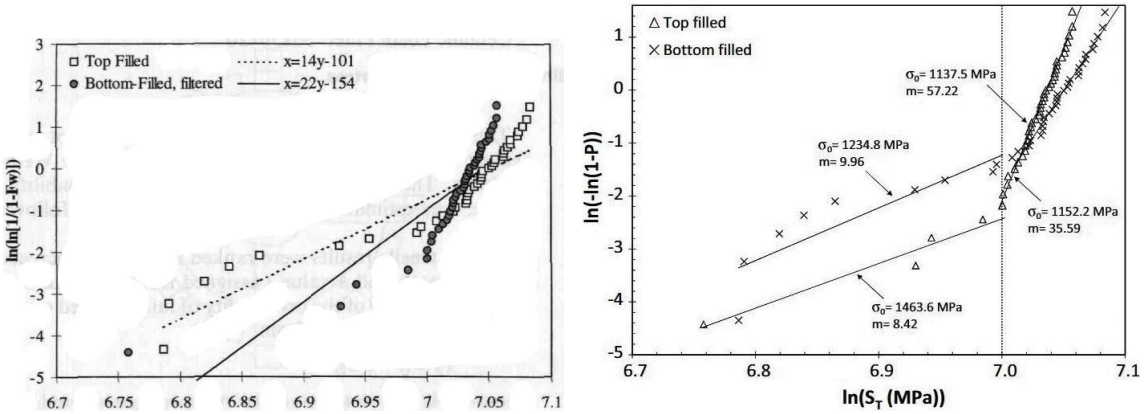
N	a	b	N	a	b
5	0.173	0.500	27	0.448	0.000
6	0.243	0.390	30	0.455	0.000
7	0.280	0.310	32	0.460	0.000
8	0.309	0.251	35	0.465	0.000
9	0.322	0.210	40	0.472	0.000
10	0.348	0.190	45	0.481	0.000
11	0.367	0.160	50	0.486	0.000
12	0.371	0.130	55	0.499	0.000
13	0.382	0.110	60	0.503	0.000
14	0.388	0.100	65	0.509	0.000
15	0.394	0.080	70	0.518	0.000
17	0.407	0.050	75	0.522	0.000
20	0.417	0.030	80	0.516	0.000
22	0.430	0.000	90	0.518	0.000
25	0.443	0.000	100	0.519	0.000

Figure 2.38: Weibull parameters unbiased probability estimators a and b (113)

compared the 2-parameter Weibull distribution to log-normal and Normal distributions. Campbell (3) claimed that the Weibull modulus (m) is often between 1 and 10 for pressure die casting, and for gravity-filled casting it is between 10 and 30. Whereas for high quality aerospace castings m is expected to lie between 50 and 100.

It was proposed that when the goodness-of-fit criteria is not satisfied, the data set can still follow a 2-parameter Weibull distribution. Weibull plots could contain two distinctive Weibull distributions (Weibull mixtures) (117). The bimodal distribution could be detected when the data trend contains inflection points, see figure 2.39b. Two distinct types of defect distributions are the reason behind this inflection, and as a result, when data sets were evaluated as a single group, the R^2 value was lower than than $R^2_{0.05}$ (figure 2.39a). Thus, two different Weibull distributions with different slopes has to be adopted to better describe the data, as shown by Cox et al. (46) in HIPed Ni IN939 alloy tensile strength results. The result was validated through the analysis of the fracture surfaces, and the two defect populations were

identified as young and old oxide bifilms. Old bifilms caused prior to mould filling were responsible for the lower distribution; whereas young bifilms were responsible for the upper distribution. Nyahumwa et al. (118) reported the same behaviour when investigating the fatigue life of Al-7Si-0.35Mg alloy. The author suggested that multiple sources of failure in the alloy were responsible for the Weibull mixtures, compromised of young oxide bifilm defects, old oxide bifilm defects, oxide bifilms inflated into pores, and slip planes (the alloy metallurgical strength limit).



(a) A 2-parameter Weibull plot with $R^2 < R^2_{0.05}$ (46)

(b) Reanalysis with an assumption of a bimodal 2-parameter Weibull distribution showed a good fit (117)

Figure 2.39: An example of Weibull mixtures in tensile test results of IN939 alloy casting

Hudak and Tiryakioglu (119) used Monte Carlo simulation to compare between two different Weibull moduli. The authors generated two groups of data points that contained n_1 and n_2 data points with $n_1 > n_2$. The Weibull modulus of the two groups was estimated with 2-parameter Weibull distribution, and were denoted m_1 and m_2. The ratio between the two Weibull moduli (m_1/m_2) was recorded, then the process was repeated 10,000 times to achieve a clear distribution. Figures 2.42 and 2.43 contains the results for the 2.5 and 97.5 percentiles, and 5 and 95 percentiles, respectively, for groups of sample size ranging from 10 to 100. Practically, the mechanical property results of two casting groups of n_1 and n_2 can be treated as having different Weibull moduli if the value of m_1/m_2 fall outside the percentile range.

Although the 2-parameter Weibull distribution is widely used to asses the reliability of the mechanical test results of castings, if the 2-parameter Weibull plot is not a straight line, the goodness-of-fit criteria will not be satisfied. One of the reasons could be the assumption that $x_T = 0$ in equation 2.8 is not valid. Hence the data set minimum limit to strength could not be assumed to be zero. The plot then becomes a 3-parameter Weibull distribution represented by the following equation (103):

$$ln[-ln(1 - F_w)] = mln(x - x_T) - mln(x_0) \tag{2.19}$$

The Weibull plot becomes $ln[-ln(1-F_w)]$ as the vertical axis, and $ln(x-x_T)$ as the horizontal axis. The data set then have to be fitted with a curve which optimizes the values for the three unknowns: m, x_0 and x_T. Weibull (104) gave the first known fits of the 3-parameter Weibull distribution to mechanical data; it was applied to the tensile strength data of Al die casting (120). Tiryakioglu and Campbell (121) studied the correlation between the threshold value (x_t) and the critical flaw size. They found that with a positive threshold value the critical flaw size should be small. This can occur when the quality of the melt is high, and contains low damage from prior processing and ingot preparation; which in turn will negate the forming of old oxides. Moreover, the filling system has to be well designed to eliminate the creation of any young bifilms.

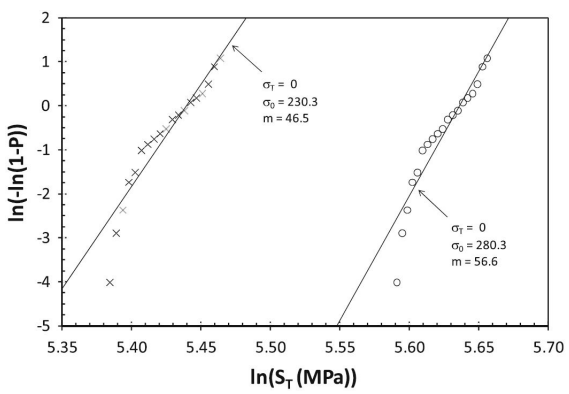
A negative threshold value indicates the existence of a second defect distribution that impairs the property of the casting. The effect is illustrated by the reduction of the slope of the 3-parameter Weibull distribution curve at low values of x. An inflection point can be detected, and a 3-parameter Weibull mixture can be used to better describe the data set, see figure 2.41b.

The threshold value can be taken as zero when the Weibull cumulative distribution function, shown in equation 2.8, solution does not converge to zero. This result was reached experimentally by Holland and Zarestsky (122) while investigating a large sample size of A357-T6 fracture stress.

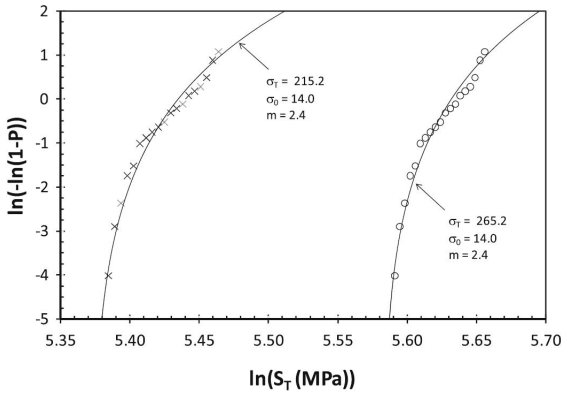
Fok et al. (123) found that the Weibull modulus derived from a 2-parameter Weibull fit to data originating from a 3-parameter Weibull distribution is strongly affected by the threshold value. The Weibull modulus can be two orders of magnitude higher than the one obtained from the 3-parameter Weibull distribution. Zahedi et al. (37) confirmed this difference in the Weibull modulus sensitivity to the threshold value between the 2-parameter Weibull and 3-parameter Weibull distributions, as shown in figure 2.40.

Zahedi et al. also demonstrated the importance of the threshold and its' effect on the statistical analysis of mechanical property test data for the development of design values (tolerances). 2-parameter and 3-parameter Weibull distributions were fitted to the tensile strength of 319 Al alloy castings that underwent four different types of melt treatments. Then the analysis procedure for metallic materials outlined in the Military Handbook 5F (124) were followed to calculate the design tolerances. The result demonstrated that the tolerances for the 3-parameter Weibull distribution fits are higher than those of the 2-parameter Weibull fits. The difference in tolerances would then translate into weight savings, leading to the realization of the practical benefit of using the right Weibull distribution. It is desirable to use the 2-parameter Weibull distribution when both distributions represent the data equally well, as it is easier to estimate its parameters. Nevertheless, it is advised that the two distribution be considered and small details receive attention, especially for threshold values close to zero (125).

The reliance on the accuracy of the Weibull modulus obtained from a limited number of tests has to be regarded with caution. Tiryakioglu and Hudak (113) have shown that with the reduction of sample size (from n = 100 to n = 5) the Weibull modulus confidence limit spread will increase; leading to the estimated value of m to be less accurate. Campbell (103) stated that a sample size of 30 has often been considered enough to obtain a valid Weibull plot as the accuracy of results do not further deteriorate too drastically. However, to increase the accuracy more tests are needed depending on the level of precision required.

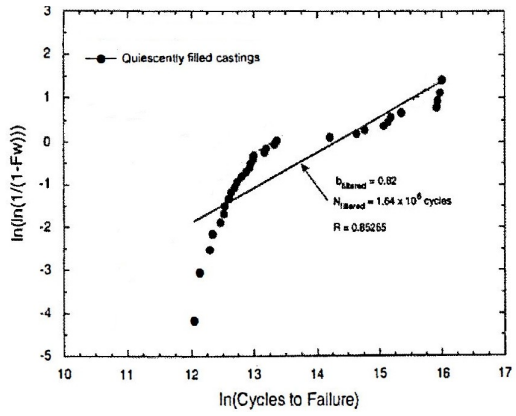


(a) The original 2-parameter Weibull probability plot (37)

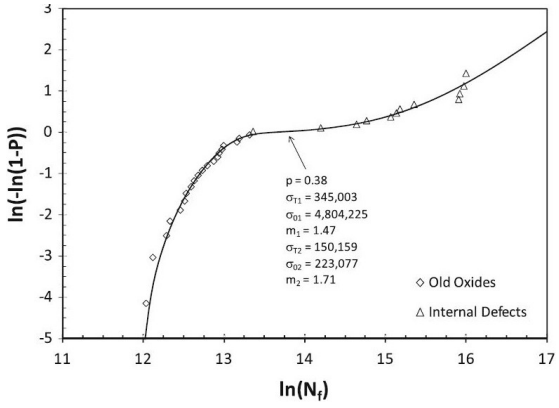


(b) 3-parameter Weibull probability plot with $x_T = 50$ MPa (121)

Figure 2.40: A comparison between Weibull probability plots of the tensile strength results of 319 Al alloy showed a better fit with the 3-parameter Weibull distributions



(a) 2-parameter Weibull probability plot for fatigue life of Al-7Si-Mg alloy casting (94)



(b) 3-parameter Weibull mixture probability plot for the same data set. The two distributions represent two population of defects (121)

Figure 2.41: When the correct Weibull probability distribution is chosen, a better representation of the data is achieved

The Anderson-Darling goodness-of-fit test, developed in 1954, (126) measures how well a data set follow a certain distribution. The less the value of the Anderson-Darling score, the higher the confidence and the better fit the data set has to the distribution. Nonetheless, in some cases that requires comparing different distributions, the calculated Anderson-Darling goodness-of-fit test values may not be directly comparable. Hence, small differences in the values may not indicate practical relevance. It is then recommended to use probability plots to compare the goodness-of-fit of different distributions (127). The Anderson-Darling goodness-of-fit test values is calculated according to the following equation (128, 129):

$$A^2 = -n - \frac{1}{n}\sum_{n}^{i=1}[(2i-1)lnP_i + (2n-1-2i)ln(1-P_i)] \tag{2.20}$$

The Anderson-Darling test was used to compare between log-normal, normal, 3-parameter log-Weibull and 3-parameter Weibull distributions when estimating the Weibull modulus (m) by the moments and maximum likelihood methods (130). It was selected due to to its sensitivity to the tails of the distributions.

		n_1												
		10	15	20	25	30	35	40	50	60	70	80	90	100
	10	0.412 2.434	0.453 2.262	0.475 7 777	0.488 7 151	0.494 2.124	0.505 7 100	0.507 2.089	0.517 2.058	0.524 2.049	0.535 2.042	0.534 2.027	0.536 2.011	0.540 2.030
	15		0.489 2.069	0.511 1 976	0.531 1 951	0.543 1 906	0.550 1 881	0.559 1.877	0.574 1.854	0.581 1 877	0.591 1 871	0.594 1 873	0.599 1 798	0.595 1 798
	20			0.526 1 889	0.553 1 851	0.571 1.799	0.575 1 798	0.585 1.767	0.600 1.722	0.609 1.708	0.614 1.703	0.621 1.690	0.629 1.693	0.629 1.693
	25				0.567 1 771	0.581 1 778	0.598 1 770	0.599 1.677	0.615 1 661	0.624 1.647	0.632 1 630	0.639 1 670	0.644 1 618	0.649 1 600
	30					0.596 1.677	0.608 1 667	0.621 1.622	0.634 1.612	0.643 1.597	0.653 1.583	0.660 1.573	0.661 1.559	0.668 1.549
	35						0.614 1 674	0.632 1 605	0.643 1 568	0.658 1 560	0.671 1.545	0.674 1 573	0.683 1.516	0.684 1.505
n_2	40							0.636 1.569	0.655 1.552	0.668 1.531	0.674 1.515	0.685 1.510	0.693 1.492	0.694 1.489
	50								0.665 1.504	0.678 1 483	0.689 1.466	0.694 1.458	0.702 1.447	0.708 1 437
	60									0.690 1.444	0.702 1.439	0.709 1.420	0.713 1.412	0.721 1.402
	70										0.710 1.415	0.714 1.399	0.724 1.389	0.731 1.380
	80											0.722 1.384	0.731 1.382	0.739 1.360
	90												0.737 1.361	0.741 1.355
	100													0.752 1.331

Figure 2.42: The distribution of the ratio of two estimated Weibull moduli for the 2.5 and 97.5 percentile. The first number in the intersection is for 2.5 and the second for 97.5 percentile (119)

		n_1												
		10	15	20	25	30	35	40	50	60	70	80	90	100
	10	0.477 2.109	0.518 1.981	0.548 1 875	0.557 1.909	0.563 1.890	0.572 1.879	0.577 1.852	0.582 1.825	0.593 1.819	0.597 1.823	0.605 1.827	0.605 1.815	0.605 1.805
	15		0.548 1.825	0.574 1 770	0.590 1.759	0.602 1.713	0.610 1 696	0.617 1 693	0.630 1 678	0.636 1 665	0.648 1 650	0.649 1 643	0.655 1 637	0.650 1.641
	20			0.589 1 695	0.608 1 666	0.628 1 63?	0.631 1 6?4	0.641 1 603	0.650 1.576	0.661 1.571	0.668 1 563	0.672 1.548	0.678 1.548	0.679 1.547
	25				0.624 1.604	0.639 1.580	0.648 1.564	0.655 1.535	0.666 1.521	0.675 1.513	0.682 1.496	0.691 1.497	0.693 1.492	0.699 1.479
	30					0.651 1 538	0.662 1 533	0.671 1.504	0.681 1.485	0.694 1.476	0.700 1.471	0.706 1.449	0.706 1.455	0.717 1.444
	35						0.666 1.497	0.678 1.477	0.695 1.454	0.705 1.445	0.713 1.432	0.719 1.424	0.726 1.415	0.729 1.411
n_2	40							0.687 1.459	0.702 1.439	0.717 1.430	0.719 1.414	0.727 1.410	0.734 1.403	0.739 1.391
	50								0.711 1.406	0.724 1 389	0.734 1 378	0.739 1 367	0.746 1 356	0.749 1.350
	60									0.735 1.356	0.744 1.352	0.749 1.338	0.754 1.337	0.760 1.328
	70										0.749 1.332	0.753 1.319	0.762 1.311	0.766 1.306
	80											0.763 1.313	0.770 1.305	0.778 1.293
	90												0.776 1.293	0.778 1.288
	100													0.788 1.271

Figure 2.43: The distribution of the ratio of two estimated Weibull moduli for the 5 and 95 percentile. The first number in the intersection is for 5 and the second for 95 percentile (119)

2.6 Cast irons reaction with gases

It is important to understand the reaction expected between liquid cast irons and different gases, in order to understand the formation of porosity. Oxygen, hydrogen and nitrogen are the significant gases that can react with liquid cast iron and change their contribution to the total pressure in equilibrium in the liquid metal. Their typical concentration ranges are: oxygen 0.005-0.01%, hydrogen 0.00005-000025% and nitrogen 0.0015-0.015% (131).

Oxygen is absorbed in the liquid iron during melting. The absorption rate is connected to the concentration of oxygen in equilibrium, which is controlled by C, Si, Al de-oxidation reactions (132), and graphite nucleation (133). The main source of Al in cast iron is the inoculation with FeSi. Increasing Si content decreases oxygen solubility but the effect of temperature is greater (131). Soluble Oxygen in cast iron reacts with the carbon content to produce CO. Oxide slag was assumed to cause the release of Carbon dioxide bubbles in cast iron as a result of reaction between the oxygen content in the slag and the carbon in the melt. Due to their size the bubbles observed could not have been formed by diffusion-controlled reaction (figure 2.44). Campbell suggested that the source of the the bubbles and the the oxide slag was surface turbulent filling of the casting (19).

Carbon monoxide is observed in low silicon cast irons as a froth of bubbles known as carbon boil. The release of CO could be instigated by blowing air into the melt. Thought the melt is saturated by carbon, the oxygen goes into solution to react with C to form CO. During solidification carbon and oxygen will have a high concentration in the area ahead of the solidification front (136).

Hydrogen is also soluble in cast iron, but if a carbon boil takes place it will flush it out to negligible levels. Unlike aluminium, hydrogen does not seem to cause major issues in cast irons due to its low solubility (figure 2.45). Unusually high hydrogen contents are not caused by melting, rather by the reaction of the reactive elements in iron with moisture in the mould (136).

Nitrogen is soluble in liquid iron and picked up mainly during melting. Its' equi-

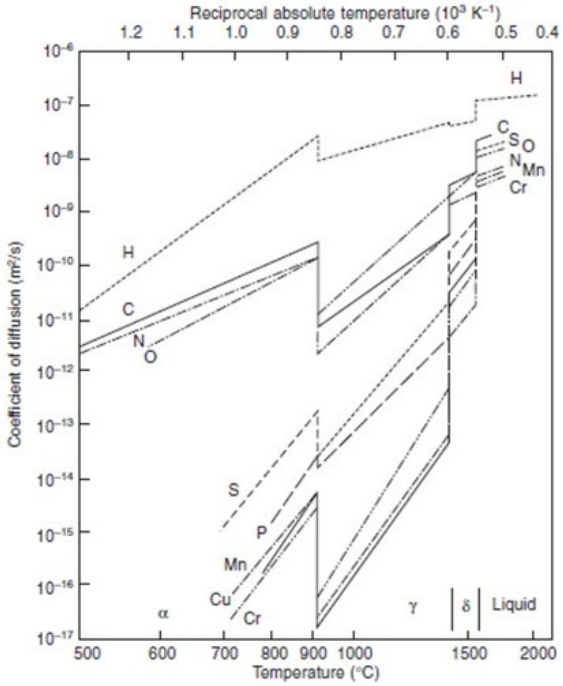


Figure 2.44: Effect of temperature on the diffusion coefficient for elements in solution in iron (134)

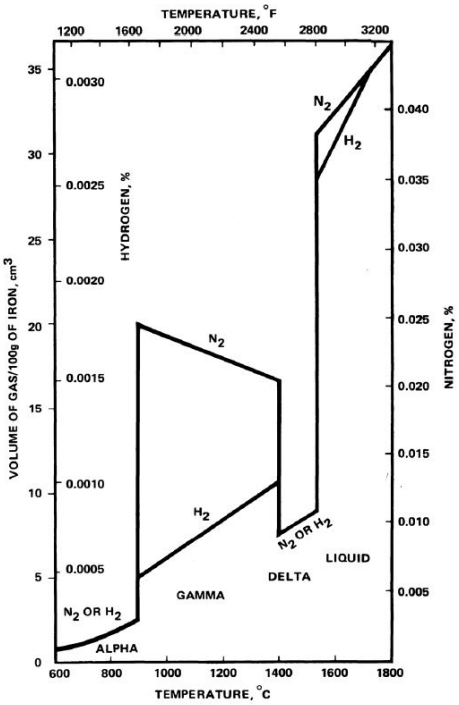


Figure 2.45: Effect of temperature on the solubility of hydrogen and nitrogen in iron (135)

librium content is a function of temperature and composition (figure 2.45). Similar to hydrogen, nitrogen does not seem to be a source of porosity in iron. Nitrogen could be picked from the decomposition of amines in high-nitrogen binders used in cores and mould sands, which might lead to defects such as nitrogen fissures (137).

2.7 Surface films in cast irons

Slag layers start to accumulate on the surface of liquid cast iron held at high temperature, 1500°C, in a ladle or furnace lined with refractory materials. The composition of the slag will change rapidly with high temperature, and its unstable oxide content. Fe, Mn, and Si, will dissolve into solution of liquid iron. On the other hand, stable oxides such as Al and Ca, will accumulate as dry slag or dross. The thickness of the slag layer can be from 0.1 mm to upto 100 mm (in cupola furnaces). These macroscopic slags originate from the lining material of vessels, and can be reduced and removed, but in regard to entrainment defects they are not a cause of concern

(138, 139). The concern is about the microscopically thin surface films that will form automatically regardless of the quality of melting and transfer vessels.

2.7.1 Oxide films

Work done by Heine and Loper (140), and later expanded on by Merz and Marinek (141) explained the complex formation of surface films on cast irons when temperature falls. The Ellingham diagram, shown in figure 2.46, indicate that at 1550°C CO is more stable than SiO_2. Hence, the carbon oxidises preferentially at a higher rate than Si, but after the C is consumed the Si content start to decline. Thus, at this temperature the surface of the melt will be film free. The oxidation behaviour will change at around 1420°C as the stability of carbon and silicon oxide is reversed. The exact temperature will depend on the composition of the melt, although the Ellingham digram puts the temperature at 1500°C, this was based on pure Fe-C alloys (figure 2.46). Below 1400°C, a SiO_2 grey, dry and solid film will appear on the surface of the melt. If wiped, the film will reform constantly. At 1300°C, and if the alloy contains Mn, it is seen from the Ellingham diagram that MnO is the least stable, then followed by SiO_2, and CO is the most stable. Thus Mn is oxidised away preferentially contributing to the film, and reducing its melting point, converting it to liquid. Around 1200°C, FeO will further lower the melting point. If the iron contains S, MnS will lower the complex ternary eutectic temperature, (between FeO, MnO and SiO_2) to 1066°C.

In lamellar graphite iron, the temperature fall during casting will ensure the surface film will be liquid during the filling of the mould. If the filling was surface turbulent and the film became entrained in the melt, it will spherodise into droplets. The droplets have a lower density than the melt, thus they will agglomerate and rapidly float out, as shown in figure 2.9. Then they will mutually assimilate by the surface liquid film and cover the casting surface. This phenomena is not troublesome, except when the accumulation of liquid surface films exceeds the required machining allowance (142).

In spheroidal graphite iron, contrary to LGI, the entrainment of a surface film is usually a cause for concern. The small amount of Mg added to convert the graphite morphology from flakes to spheres changes the nature of the oxide film. Heine and Loper (140) found that, above 1454°C, the surface of liquid SGI contained no films, but below that temperature a film was observed. With temperature decrease the film increases in thickness, and at 1350°C the film will exhibit solidified particles. When the temperature falls to 1290°C the entire surface of the melt will be covered with a dry film. As the melt is above the boiling temperature of Mg, the Mg vapour distils off through the film layer and turns to powdery MgO which will settle on the surface. This process will grow a stable surface film quickly (figure 2.46), and if entrained, could cause defects (143).

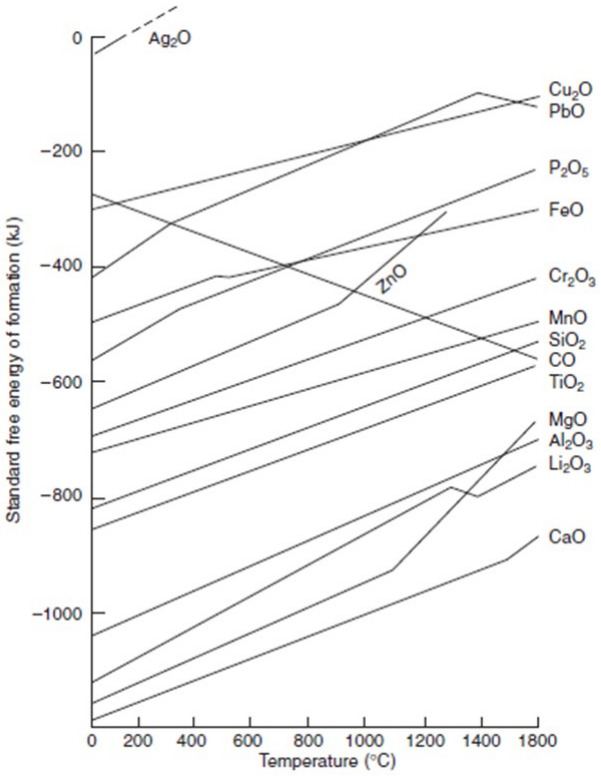


Figure 2.46: Ellingham Diagram (144)

2.7.2 Nitride films

Nitride films could form on the surface of liquid cast irons and cause nitrogen fissure defects. This type of defect was attributed to the decomposition of high-nitrogen

binders (145), but the defect does not always form with the use of such binders. Campbell (142) suggested that the cause of nitrogen fissures defects is the entrainment of nitride surface films. Thus, in addition to the nitrogen content of the binder, the design of the filling system will play an influential role in the formation of the defect. The combination of high hydrogen and nitrogen pressure resulting from the decomposition of the binder would inflate the nitride bifilms transforming it into visible cracks. Such cracks were observed in LGI castings.

2.7.3 Carbon films (lustrous carbon)

Lustrous carbon films have a shiny black skin like appearance that can cause wrinkling on the surface of the casting, shown in figure 2.28a. They started to appear with the use of early resin-bonded sand, especially with polyurethane-based resins. They were also observed in green sand with high amounts of volatile additions (hydrocarbons) (146). Draper (147) examined lustrous carbon films using X-ray diffraction patterns and found that the film was pyrolytic carbon with a microcrystalline form. This meant it was unlike crystallographic graphite and similar to carbon black. He found that the lustrous carbon film was deposited, in temperatures of a range of 650-1000°C, from the gas phase to hot surfaces. At first the hot surface was assumed to be the sand mould surface where the film is deposited and pushed ahead of the advancing liquid (58). This explanation is problematic for two reasons, films were usually found detached from the complex and rough sand grains, and the sand surface does not have enough heat to break down the gases. Bindernagel (146) observed lustrous carbon defects on the fracture surface of cast components that suffered brittle fracture and found that the defect originated from a surface film on the liquid metal. This observation gave a rise to the assumption that the molten metal provides the hot surface where the breakdown of hydrocarbons takes place. Campbell and Naro (62) claimed that lustrous carbon films form on the front of the advancing liquid, and as it breaks and reforms, it is laid down by the advancing melt and trapped between the melt and the mould, as shown in figure 2.47. The film

will then form a rigid mechanical barrier bridging the sand grains. They also added that the carbon film could have deposited on a precursor oxide film. If the mould filling was surface turbulent, the lustrous carbon film would fold in the bulk liquid and cause a carbon film crack, as shown in section 2.2.2, but if the casting was filled without surface turbulence, the lustrous carbon film will improve the surface finish.

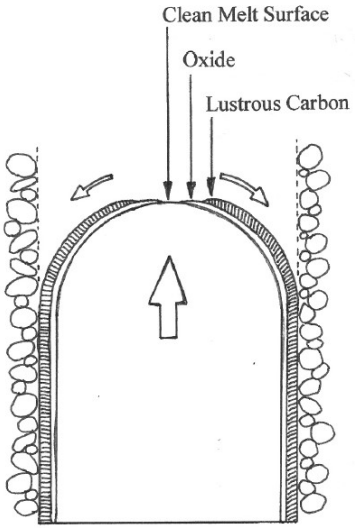


Figure 2.47: A schematic illustration showing the mechanism of formation of lustrous carbon films as suggested by Campbell and Naro (62)

2.8 Summary

This section has reviewed the key aspects of entrainment defects: their formation process, types, morphology evolution (i.e. furling and unfurling), reduction parameters and deactivation. Furthermore, the section has examined evidence of entrainment defects in non-ferrous alloys such as Al, Mg, Cu, Ti and Ni; in ferrous alloys such as steel and cast irons; and the statistical characterization of castings using the Weibull distribution. Finally, the section reviewed cast irons reaction with gases, and the different types of surface films in cast irons; which were found to be either oxide, nitride or lustrous carbon.

Chapter 3

Experimental Procedure

3.1 Tensile testbars casting experiment

In this study three types of cast irons were used, spheroidal graphite iron (SGI), lamellar graphite iron (LGI), and compacted graphite iron (CGI). For SGI, there were three melts denoted SGI1, SGI2 and SGI3. For LGI, there were two melts denoted LGI1 and LGI2. For CGI, there were two melts denoted CGI1 and CGI2. Melts SGI1, SGI3, LGI2, CGI1 and CGI2 were cast at a commercial foundry (Grainger and Worrall). SGI2 and LGI1 were cast at the University of Birmingham laboratory. SGI was grade 500/7 for SGI1 and SGI3, and grade 700/2 for SGI2. LGI castings were two melts grade 220. CGI castings were two melts of grade 400. An extra melt of LGI grade 220 was cast at the University of Birmingham to examine the formation of entrainment defects in LGI. The testbars were cast in an O-rich environment, and this melt was denoted LGIO.

3.1.1 Mould preparation

All testbar castings in this study were cast in sand moulds, apart from LGIO which was cast in a cast iron permanent mould. The sand moulds were made from resin bonded silica sand (grade HST 60). The binder used was Novathane three part resin of E12, E25, and a catalyst 3550. The addition of resin was per 1% wt. of

sand, a mix of 60% E12 to 40% E25, and catalyst amount 2% wt. E12. The moulds were made at least one week before casting to allow volatiles to dissipate to reduce mould blows and gas pick-up by the liquid metal. The sand moulds had three designs, quiescently-filled (QFM), surface turbulently filled (TFM), and very (surface) turbulently-filled (VTFM). The QFM contained a FOSECO SEDEX 20 ppi ceramic foam filter located at the end of the downsprue. The VTFM had the same design as the QFM but did not contain a filter. A sketch of QFM and VTFM is shown in figure 3.7, TFM is in figure 3.6, and the permanent mould is in figure 3.8.

3.1.2 Mould filling verification

The mould filling conditions of quiescently-filled, surface turbulently-filled, and very (surface) turbulently-filled were verified using real time X-ray radiography YXLON (YXLON International GmbH) X-ray booth. In the X-ray booth, the X-ray source was rated 160 kV but only 92 kV at 12.5 mA was used to allow enough contrast between the mould and the liquid alloy. The moulds were placed between the X-ray source, an X-ray image intensifier and the X-ray camera. A robot arm conducted the casting, while a real-time video image of the mould cavity was generated showing the filling. The filling pattern was recorded using a high-speed X-ray camera at a frame rate of 100/s at a resolution of 800 x 600 pixels, giving a field of view of 250 x 190 mm of the mould. Due to the limitation of the field view, only half of the mould, including the whole of the downsprue, could be captured. Computer modelling with MAGMASOFT^{TM}, a widely used casting process simulation software, was used to verify the filling conditions of the whole mould.

3.1.3 Mould feeding verification

The feeding of the testbars was verified by thermal analysis. K-type thermocouples were inserted in a ceramic insulator, and positioned in the mould cavity with their extension wires connected to a data-logger to store the time-temperature history of

the solidifying metal. The stored data was used to generate cooling curves.

For the TFM, two thermocouples, denoted TB1 and TB2 were inserted through the mould wall at mid-length in the testbar cavity. As the TFM design uses the runner bar as a feeder, two thermocouples, denoted RB1 and RB2, were inserted in the section of the runner bar cavity underneath the testbars, as shown in figure 3.1.

The VTFM and QFM designs contained two vertical feeders connected to the ends of the runner bar. The same configuration of thermocouples in the testbars and runner bar in the TFM was followed, and an extra two thermocouples were added in the feeder cavity. They were positioned at one-third and two-thirds of the length, denoted F1 and F2, respectively. A sketch of the mould with the locations of the thermocouples is shown in figure 3.2. MAGMASOFT^{TM}was also used to model shrinkage porosity formation in the moulds.

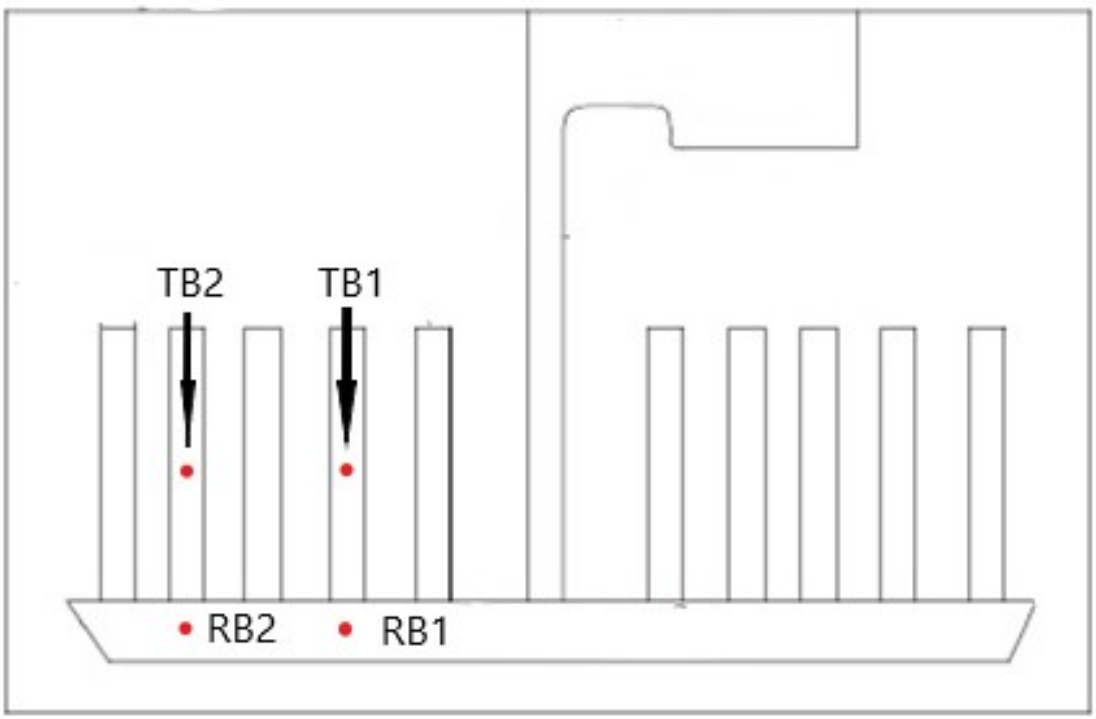


Figure 3.1: The location of thermocouples in TFM

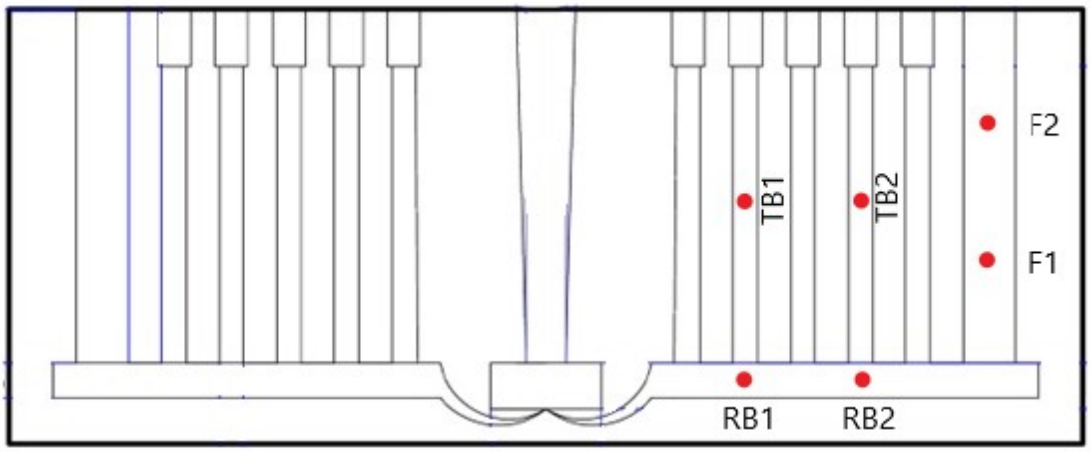


Figure 3.2: The location of thermocouples in VTFM/QFM

3.1.4 Melt preparation and casting

Charge

The charge for the different melts consisted of the following:

- SGI1: charge made up of pig iron, steel returns, SGI 500/7 returns, graphite, and copper to the ratio of 1 : 1 : 1.3 : 0.03 : 0.01.
- SGI2: the charge was made up of CGI 400 returns.
- SGI3: the charge was made up of steel returns, SGI 500/7 returns, graphite, and copper to the ratio of 1 : 1 : 0.015 : 0.005.
- LGI1, LGI2 and LGIO: the charge was made up of LGI 220 returns.
- CGI1 and CGI2: the charge was made up of pig iron, steel returns, CGI returns, graphite, Fe-Si (75%), copper, and tin to the ratio of 1 : 1 : 1 : 0.04 : 0.045 : 0.02 : 0.01.

Melting

The melting was done an induction furnace, in an inserted clay-graphite crucible at the University of Birmingham, and in the furnace's refractory crucible at the commercial foundry. The capacity of the furnaces were 60 kg, and 1000 kg, respectively.

The pouring temperatures of all castings were recorded with a Heraeus Electro-Nite Pt Rh positherm Multi-stik thermocouple connected to an immersion lance. The lance was used to dip the thermocouple into the molten metal and the temperatures were recorded using a Heraeus Electro-Nite Digilance III portable temperature measuring instrument.

Treatment and casting

- SGI was produced using the sandwich process according to the following steps:

    1. 2.2% of the charge weight of magnesium ferro silicon (Mg-Fe-Si) nodulariser was packed tightly into one side of the ladle and covered with approximately twice its weight with steel returns.
    2. When the liquid metal reached the treatment temperature (approximately 1550°C), it was poured quickly into the ladle.
    3. A vigorous bubbling reaction coupled with magnesium flare took place.
    4. When the reaction subsided, a 0.9% of the charge weight of ferro silicon (Fe-Si) inoculant was added to the ladle and plunge-mixed.
    5. The pouring temperature was recorded, see table 3.1, and the melt was cast.

- LGI did not require treatment because it was a remelted alloy. The pouring temperature was recorded before casting, see in table 3.1.

- CGI was produced according to the following steps:

    1. The ladle was flushed by putting 0.25% of the charge weight of magnesium ferro silicon (Mg-Fe-Si) tightly packed into one side of the ladle and covered with approximately twice its weight with steel.
    2. When the metal in the furnace reached a temperature of 1540°C, it was poured quickly into the ladle.

3. The ladle was covered with a ceramic fibre blanket, and the metal stood in the ladle for five minutes.

4. The melt was then put back in the furnace, and the ladle flush procedure was finished.

5. A coin sample was taken from the melt, for chemical composition, measured using an emission optical spectrometer.

6. The sulphur content, melt weight, and required pouring temperature was entered into a Sintercast^{TM} unit, and the unit gave the amount of Mg-Fe-Si and cerium mischmetal (rare-earth mischmetal) to be added.

7. The treatment was packed tightly into one side of the ladle and covered with approximately twice its weight with steel, then the melt was poured into the ladle.

8. Two minutes after the treatment reaction subsided a sample was taken for Sintercast^{TM} analysis.

9. The unit showed that the base treatment was accurate, the melt did not require further correction, and the required amount of corrective magnesium and inoculante wire addition was made.

10. The wire was plunged into the melt, and a violent reaction took place.

11. When the reaction subsided, the pouring temperature was recorded, see table 3.1, and the melt was cast.

- The LGIO melt did not require treatment, however, the casting was carried out in an oxygen-rich environment under a positive pressure of oxygen. Figure 3.3 shows the apparatus used to conduct the casting, (a) a permanent metal die, with (b) a resin bonded sand pouring basin, was connected to (c) a vacuum pump, (d) an oxygen tank, and (e) a gas non-return valve. First the mould was vacuumed, then the oxygen was allowed to follow from the tank into the mould cavity. The oxygen flow was then shut after the non-return valve showed a

sign that the die was full of oxygen. Finally, the pouring temperature was recorded, see table 3.1, and the melt was cast into the pouring basin.

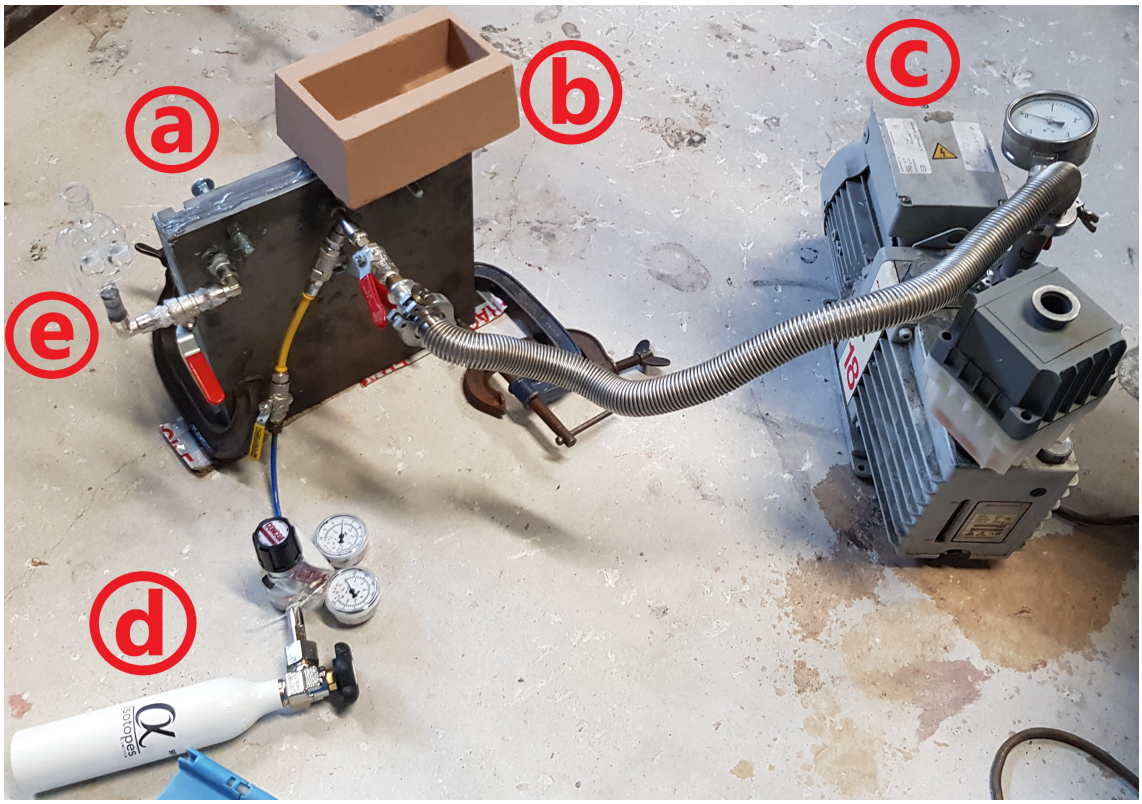


Figure 3.3: The apparatus used to cast LGI testbars in an oxygen-rich environment, (a) a permanent metal die, (b) a resin bonded sand pouring basin, (c) a vacuum pump, (d) an oxygen tank, and (e) a gas non-return valve

Melt	Pouring temperature (°C)
SGI1	1393
SGI2	1426
SGI3	1437
LGI1	1423
LGI2	1430
LGI0	1443
CGI1	1431
CGI2	1436

Table 3.1: The pouring temperature for each melt

3.1.5 Chemical composition

The final chemical composition was obtained from a coin sample that was taken from the melt just before casting to ensure a homogeneous chemical composition.

For the castings carried out in the commercial foundry, the chemical composition was obtained with a HILGER analytical POLYVAC 2000 emission optical spectrometer (EOS). As for the casting carried in the University of Birmingham, the chemical analysis was obtained by LECO GDS-750 QDP glow discharge optical emission spectrometer (GDEOS). The carbon equivalent (C.E.) was calculated according to the following equation:

$$C.E. = \%C + \frac{\%Si + \%P}{3} \tag{3.1}$$

The final chemical compositions of the castings are shown in tables 3.2, 3.3, and 3.4 for SGI, LGI and CGI, respectively.

Tensile testbar machining and testing

All castings, except LGIO, were machined into tensile testbars according to ASTM E8/E8M-15a (148). The total length of the testbar was 100 mm, the gauge length was 37 mm, and the radius of the shoulder was 26 mm, as shown on the sketch of the testbar in figure 3.4. The casting produced from LGIO were square testbars and did not require machining.

The tensile testing was conducted on a Zwick^{TM} machine equipped with a touch micro extensometer, using a strain rate of 1 mm/min.

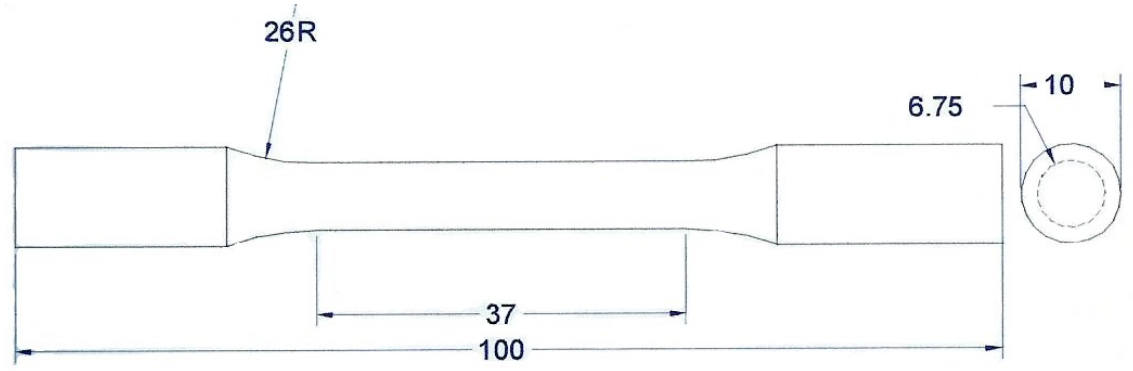


Figure 3.4: Tensile testbar sketch

Microscopy imaging

The optical images were captured using an ALBENTH HD Lite 1080 camera connected to a trinocular stereo microscope. The electron images were captured using a Philips XL30 field emission gun (FEG) scanning electron microscope (SEM) equipped with an INCA Oxford Dispersive X-ray spectrometer (EDX). A Dual Beam SEM FEI Quanta 3D FEG focused ion beam (FIB)-SEM was used to mill cross-sections from the fracture surface. A layer of Pt was initially deposited on the required location to protect its features. A Ga beam was used for cross sectional milling. In regards to transmission electron microscopy (TEM) imaging, a thin section was cut, fabricated and thinned using the Ga beam. Then the section was lifted-out with an OmniProbe^{TM} nano manipulator and attached to a TEM grid. TEM imaging and element mapping was conducted using a Philips Tecani F20 TEM.

The quantitative measurements of C were collected using EDX analysis, and could have been affected by hydrocarbon contamination. Hydrocarbon based contaminates can be decomposed and deposited on the sample surface by the electron beam. Contamination could arise from the hydrocarbons previously deposited on the surface of the sample or in the SEM/TEM itself (149, 150, 151).

3.2 Reduced pressure test experiment

The reduced pressure test (RPT) was conducted in an aluminium cylindrical chamber connected to a vacuum pump. The chamber, shown in figure 3.5a, had a diameter of 20 cm and a hight of 30 cm. LGI grade 220 bars were melted in an induction furnace with an inserted clay-graphite crucible. When the melt reached a temperature around 1420°C, it was poured into a resin-bonded sand cylindrical ingot mould, shown figure in 3.5b, positioned inside the vacuum chamber. The mould cavity had a diameter of 6 cm and a height of 10 cm, and the mould thickness was 3 cm. As soon as the mould was filled, the chamber was closed, the vacuum pump started, and the casting allowed to solidify under a reduced pressure. The sample was then

sectioned, and the surface examined.



(a) Vacuum chamber



(b) Resin bonded ingot sand mould

Figure 3.5: RPT vacuum chamber and mould

Melt	Element	C	Si	Mn	P	S	Mg	Cu	Sn	Cr	Ni	Al	Ce	Fe	C.E.
SGI1	EOS	3.79	0.85	0.157	0.015	0.013	0.048	0.418	0.003	0.027	0.026	0.015	0.011	Bal.	4.01
SGI2	GDEOS	3.761	3.597	0.212	0.005	0.003	0.053	0.761	0.012	0.027	0.037	0.02	0.02	Bal.	4.96
SGI3	EOS	3.64	1.32	0.18	0.001	0.003	0.06	0.221	0.001	0.034	0.03	0.01	0.013	Bal.	3.98

Table 3.2: The compositions of SGI melts in wt.%

Melt	Element	C	Si	Mn	P	S	Mg	Cu	Sn	Cr	Mo	Ni	Al	Ti	Fe	C.E.
LGI1	GDEOS	3.28	2.474	0.493	0.091	0.0505	0.004	0.049	0.0145	0.0275	0.057	0.0205	0.0045	0.0195	Bal.	4.1
LGI2	EOS	3.01	2.2	0.58	0.039	0.109	0.002	0.532	0.072	0.156	0.03	0.13	0.01	0.01	Bal.	3.8

Table 3.3: The compositions of LGI melts in wt.%

Melt	Element	C	Si	Mn	P	S	Mg	Cu	Sn	Cr	Ni	Al	Ce	Ti	Fe	C.E.
CGI1	EOS	3.77	2.1	0.357	0.018	0.0107	0.012	0.918	0.087	0.027	0.037	0.007	0.021	0.011	Bal.	4.27
CGI2	EOS	3.81	1.94	0.3	0.005	0.013	0.011	0.971	0.107	0.024	0.02	0.01	0.02	0.01	Bal.	4.31

Table 3.4: The compositions of CGI melts in wt.%

Melt	Element	C	Si	Mn	P	S	Mg	Cu	Sn	Cr	Mo	Ni	Al	Ti	Fe	C.E.
LGIO	GDEOS	3.35	2.8	0.475	0.079	0.037	0.003	0.035	0.001	0.052	0.001	0.044	0.006	0.019	Bal.	4.31

Table 3.5: The compositions of LGIO melt in wt.%

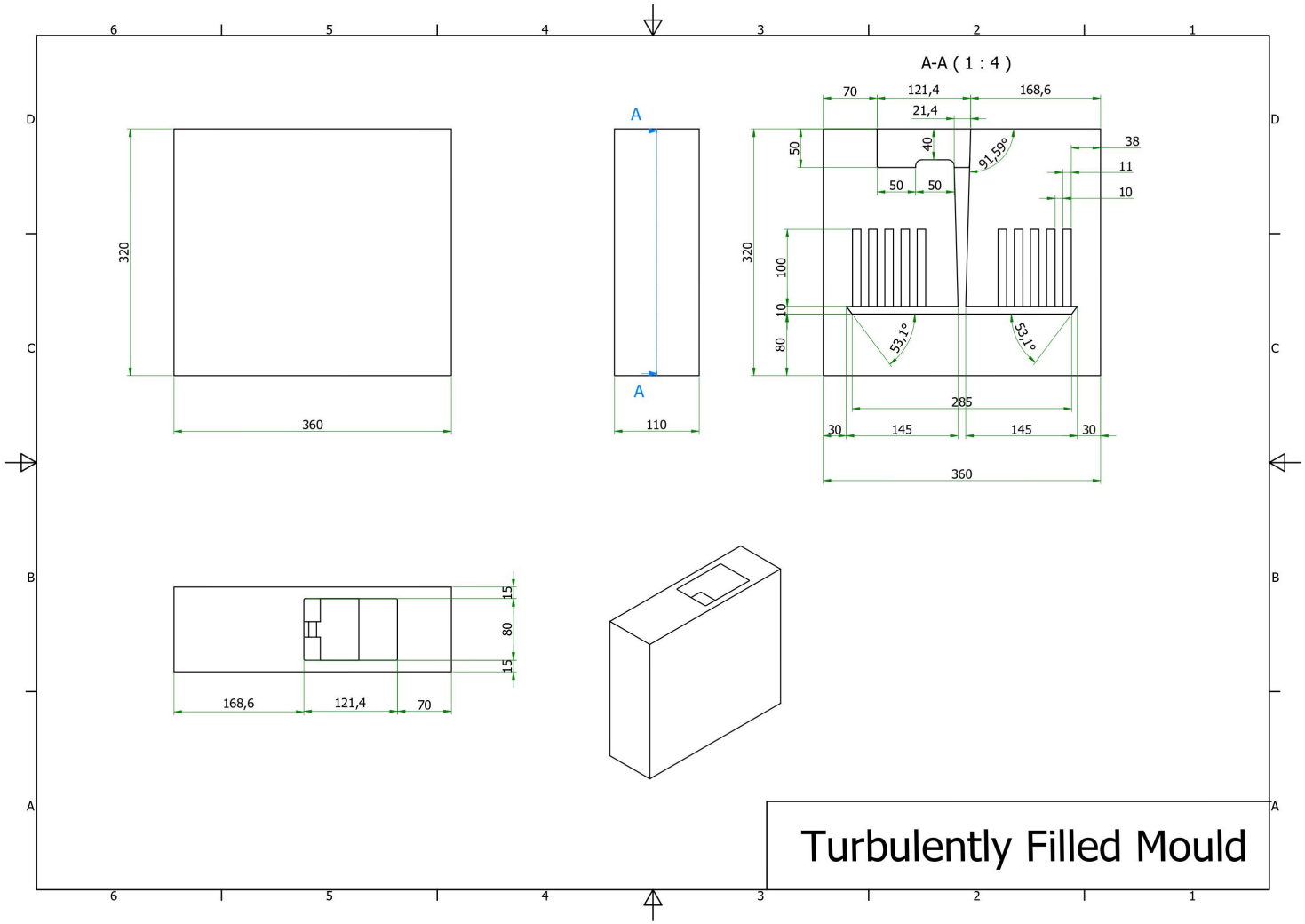
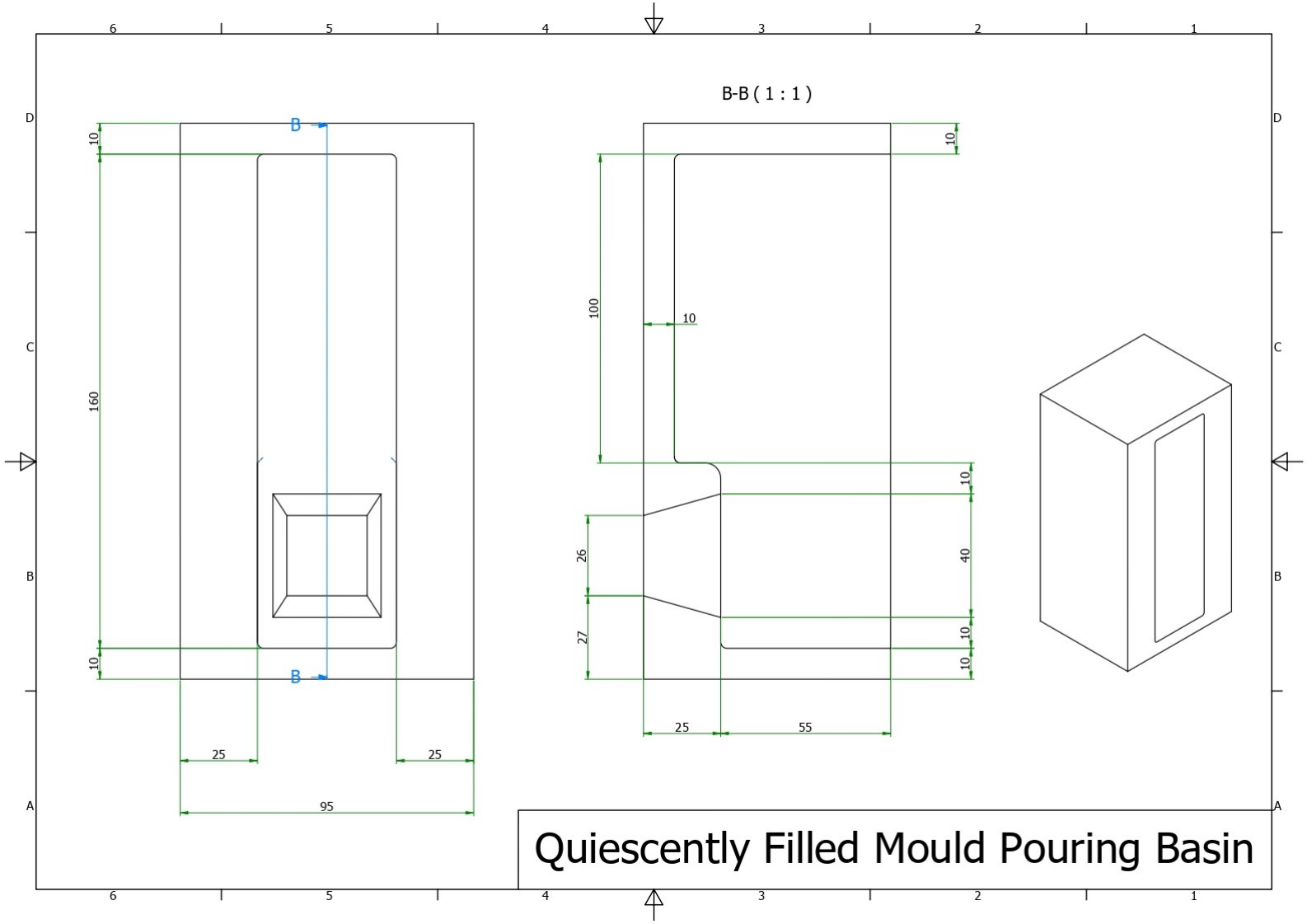
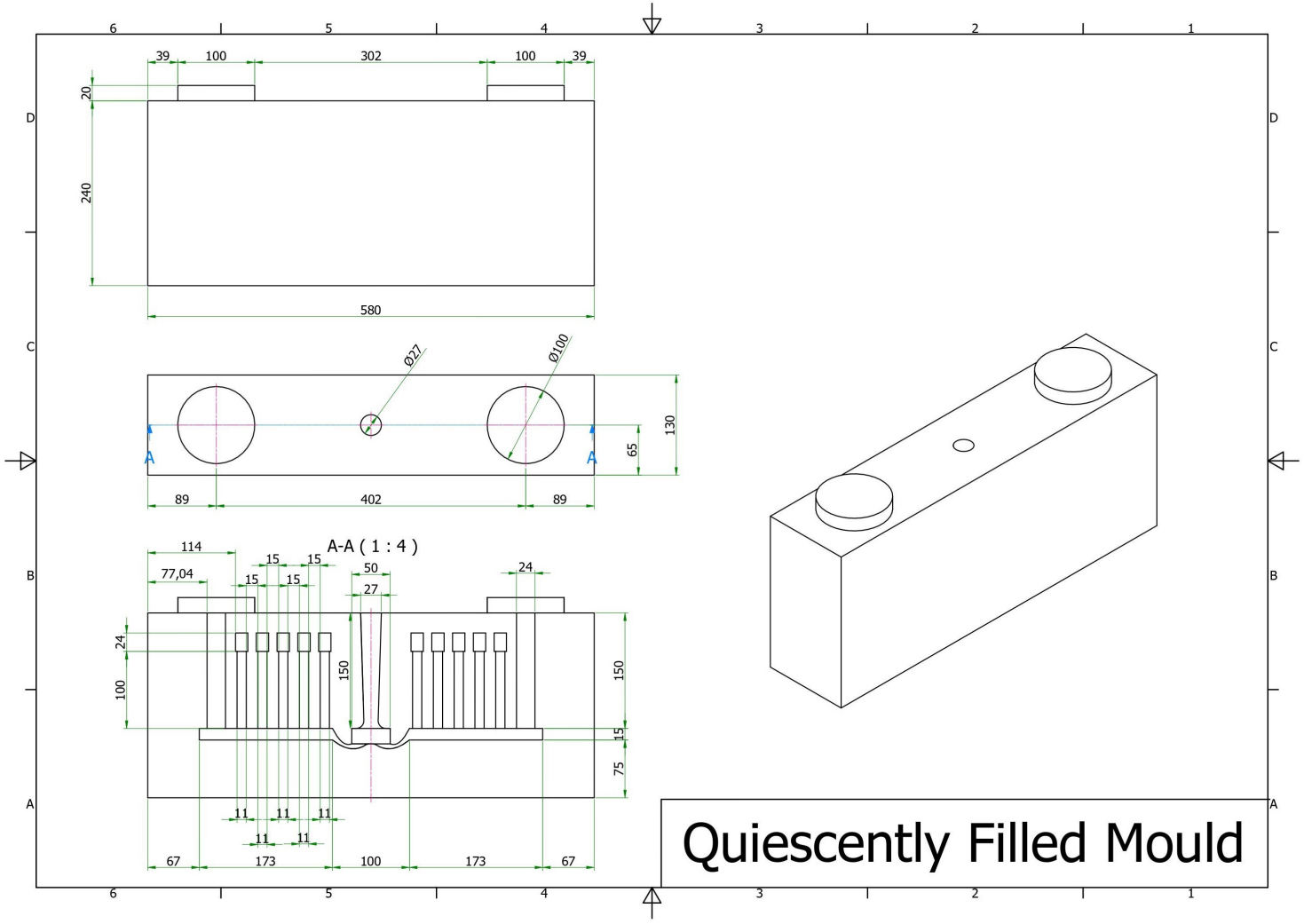


Figure 3.6: Geometry and dimensions of the surface turbulently-filled mould (TFM)



(a) pouring basin



(b) running system

Figure 3.7: Geometry and dimensions of the very (surface) turbulently-filled and quiescently-filled moulds (VTFM/QFM)

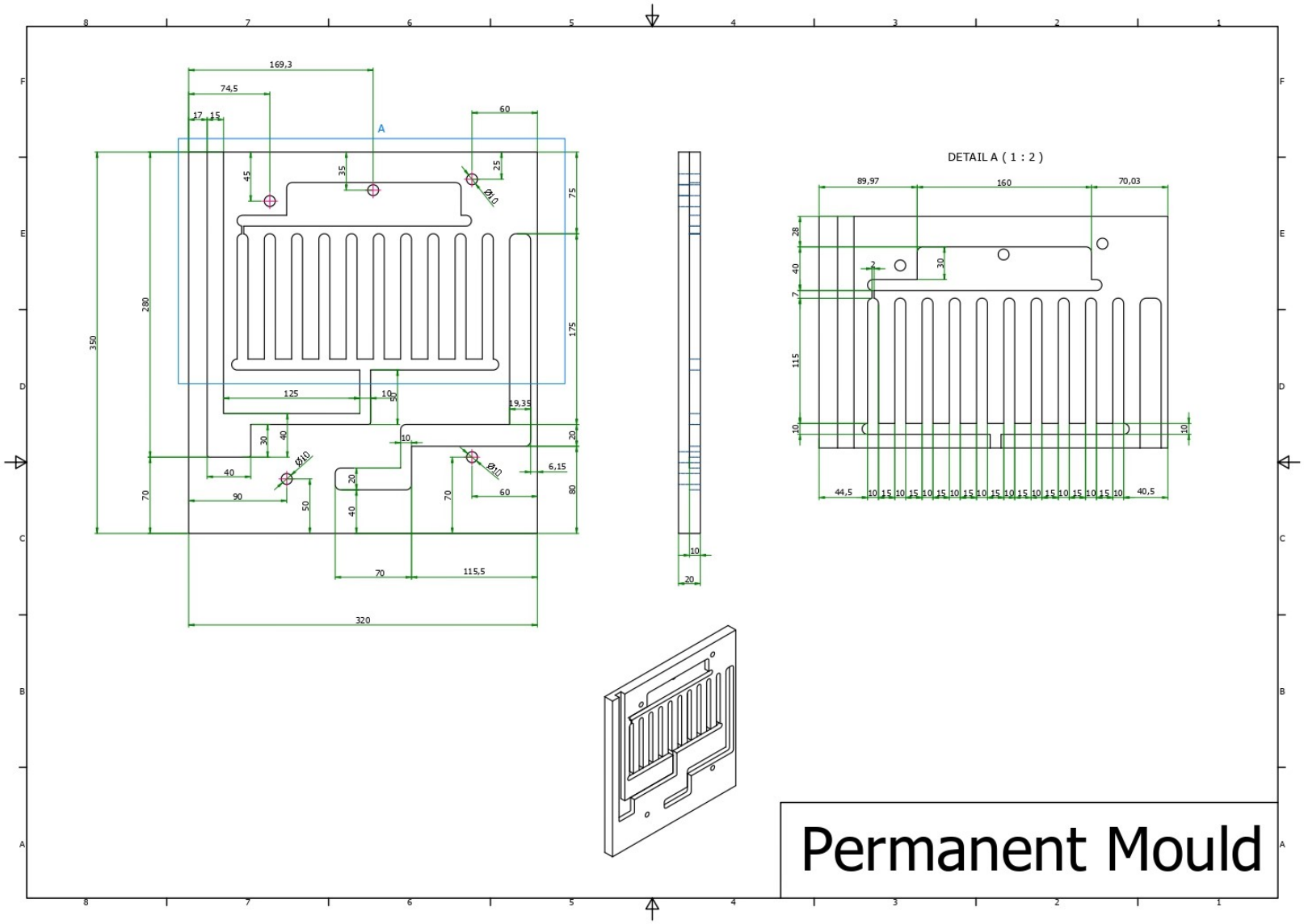


Figure 3.8: Geometry and dimensions of the cast iron permanent mould

Chapter 4

Validation Results of the Ingate Velocity, Feeding, and Filling Modes

The chapter below describes the validation results for the ingate velocity, metal feeding and filling modes generated by the quiescently-filled mould (QFM); surface turbulently-filled mould (TFM); and very (surface) turbulently-filled (VTFM) mould.

The TFM and QFM were specifically designed to study the effect of running system designs and entrainment defects on the mechanical properties, reliability and reproducibility of cast aluminium alloys. The TFM was designed to generate ingate velocity more than the critical ingate velocity of aluminium, and the QFM was designed to generate an ingate velocity less than the critical ingate velocity for aluminium. The critical ingate velocity for iron is almost equal to that of aluminium, 0.45 and 0.5 m/s, respectively, thus the moulds will theoretically produce the same intended effects for liquid cast iron. The VTFM design was not previously used. It had the same design as the QFM but without installing the filter. The VTFM, TFM and QFM were never used for cast irons. Thus, in order to see the actual liquid flow behaviour, and to study entrainment defects and the effect of the filling

modes on tensile properties, reproducibility and reliability of cast irons, the moulds feeding design and running systems were examined to be fit for purpose.

Regarding the moulds feeding, it was verified to ensure adequate feeding for the testbars, in order to produce porosity-free castings. Any major casting defects, as shrinkage porosity, may be the main source of failure, negatively affecting mechanical properties and scatter, which in turn would obscure the effect of filling modes and the search for entrainment defects. Since the filter in QFM has no effect on feeding, VTFM should have the same solidification behaviour as QFM. Hence, the solidification results for VTFM and QFM were combined. The feeding of the testbars was verified by two methods, first by thermal analysis, recording and evaluating cooling curves and insuring that the testbars were the last part to solidify, which would indicate adequate feeding. The second method was computer modelling of porosity formation with MAGMASOFT^{TM}, a widely used casting process simulation software.

With regards to the runner system designs, they were verified to guarantee that they generated the same filling profile as was intended. The ingate velocities of TFM and VTFM/QFM were measured, and the values were compared to the critical ingate velocity of Fe. Moreover, the VTFM, TFM and QFM filling modes were verified separately by real time X-ray radiography and MAGMASOFT^{TM} modelling. Due to technical limitations, LGI was the only alloy used for real time X-ray radiography of moulds filling. The VTFM, TFM and QFM filling simulation results were the same for SGI, LGI and CGI, hence only one version is shown. A copy of the videos of moulds filling captured with real time X-ray radiography, and MAGMASOFT^{TM} modelling results of the filling are attached with this work. They show every frame of the process revealing the full effect of the filling modes.

4.1 Feeding verification

4.1.1 Thermal Analysis

The TFM cooling curve, shown in figure 4.1, showed that the runner bar had a higher over all temperature profile, and a lower rate of cooling than the testbars. This indicated that the testbars in TFM were adequately feed.

The VTFM/QFM moulds cooling curve, see figure 4.2, showed that the testbars had a an over all temperature profile lower than the feeder, and the runner bar. This in turn indicated that the testbars in VTFM/QFM were adequately feed.

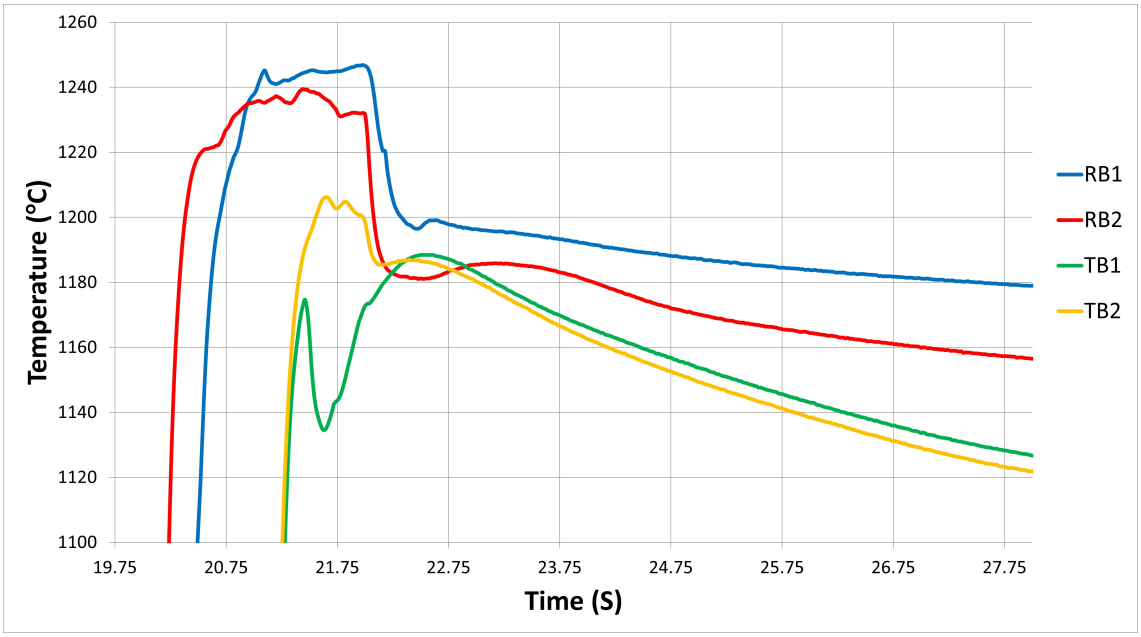


Figure 4.1: TFM cooling curve

4.1.2 Porosity formation modelling

The porosity formation of TFM was modelled for SGI, LGI and CGI, and the results are shown in figures 4.4, 4.5 and 4.6; respectively. The modelling results showed the testbars had no shrinkage porosity in the case of LGI and CGI. Shrinkage porosity was shown to be only present in the runner bar. Note, even though shrinkage was detected in the LGI modelling, this contradicts the reality of the alloy's solidification expansion. In the case of SGI, the simulation results showed that the TFM contained

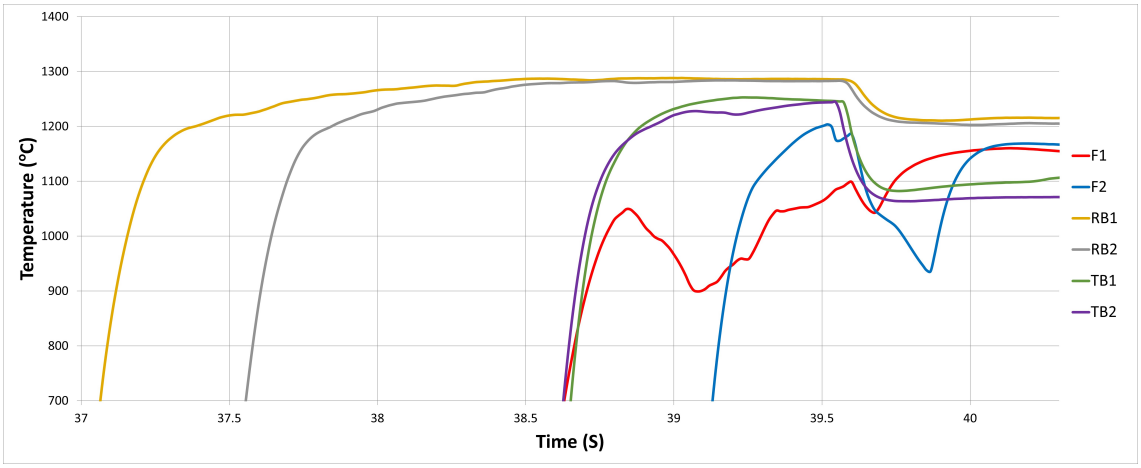


Figure 4.2: VTFM/QFM cooling curve

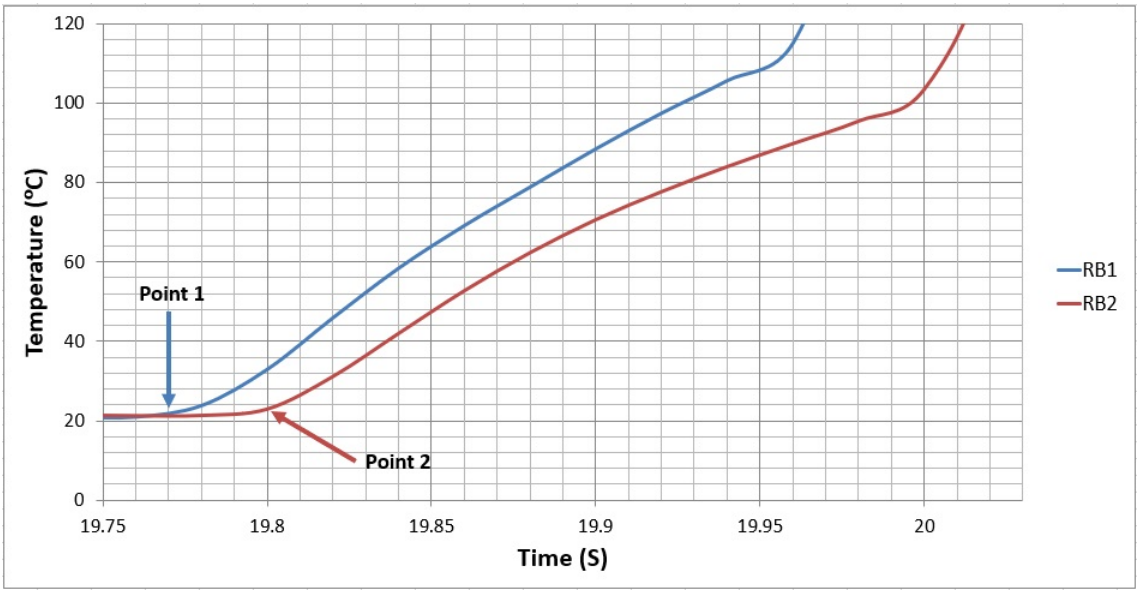
major shrinkage porosity in 9 out of the 10 testbars and in the runner bar. This result did not agree with the inspection of the actual casting, as TFM SGI testbars did not contain any major or minor shrinkage porosity.

The porosity formation of VTFM/QFM was modelled for SGI, LGI and CGI, and the results are in figure 4.7, 4.8 and 4.9; respectively. There were no shrinkage porosity in the testbars. Shrinkage porosity was only found in the runner bar and feeders.

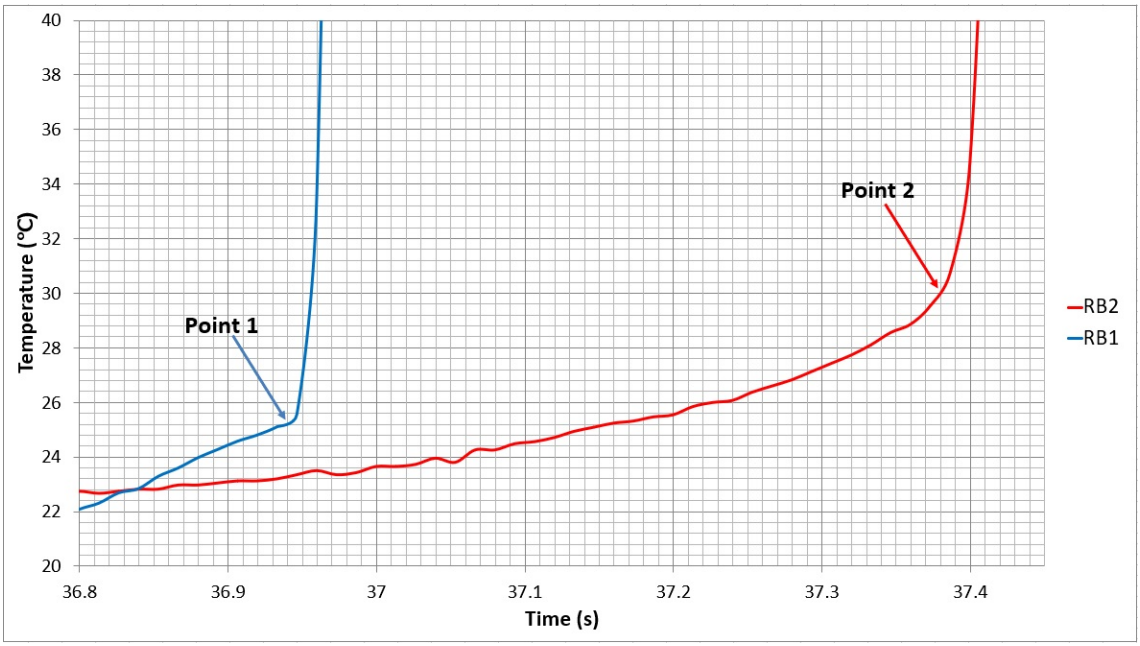
4.2 Filling modes verification

4.2.1 Initial ingate velocity

Figure 4.3 shows the velocity of the liquid metal passing through the ingate/runner bar determined by two thermocouples denoted RB1 and RB2 in figures 3.1 and 3.2, shown in section 3.1.3. Initial ingate velocity of 1.46 m/s ± 0.06 m/s (time = 0.03 s and distance = 44 mm) was obtained for TFM, and 0.12 m/s ± 0.004 m/s (time = 0.44 s and distance = 52 mm) was obtained for VTFM/QFM (the error was determined from estimated ±2 mm error in the positioning of the thermocouples).



(a) TFM ingate velocity = 1.46 m/s ± 0.06 m/s



(b) VTFM/QFM ingate velocity = 0.12 m/s ± 0.004 m/s

Figure 4.3: Measurement of the ingate velocity through the runner bar of TFM and VTFM/QFM using two thermocouples RB1 and RB2

4.2.2 Real time X-ray radiography

Figure 4.10 shows real time X-ray radiography frames of the filling of LGI 220 alloy in the VTFM. The molten metal came through the downsprue, hit the empty filter print generating splashes and churning the metal around. The moving liquid metal hit the walls of the filter print and rolled back on itself. Every plunge of the liquid metal into the filter print created a driving force that pushed the liquid metal into the

runner bar. The metal filled the first part of the runner bar wall-to-wall, and during, the forced generated in the filter print caused the surface to oscillate. The liquid metal then proceeded through the remaining part of the runner bar without any broken metal surface detected. After the filter print was filled, some splashing was detected in the downsprue. Afterwards the molten metal filled the testbar cavities with a continuous smooth flow following the sidewalls. No entrapped bubbles or splashing of the melt was seen in the testbar cavities. The filling action in the filter print lead to inevitable entrainment of the surface film.

Figure 4.11 shows images of LGI 220 alloy cast in the TFM obtained using real time X-ray radiography. The initial molten metal plunged through the downsprue and directly struck the runner bar generating splashing, surface turbulent waves, and a strong metal stream towards the end of the runner bar. A reflected wave of molten metal, overlaying fresh incoming metal, was observed at the mid-section of the runner bar. The back wave generated from hitting the end of the runner bar and as a result jetted the metal through the last testbar cavity. Then the metal jet collapsed back upon itself. Due to the collapsed metal front and the oscillation of the back waves, air bubbles were seen flowing through the latter part of the runner bar to the last testbar cavity. This caused a major wave inside the cavity, collapsing on itself and trapping air. The whole process displayed turbulent surface filling and broken free surfaces would be incorporated into the bulk metal.

Figure 4.12 shows real time X-ray radiography images of the filling of LGI 220 alloy in the QFM. At the beginning, the metal fell through the downsprue and primed the filter well. The filter acted as a damper to the falling liquid metal from the pouring basin. The metal seeped through the filter filling the beginning of the runner bar wall-to-wall and filling the rest of the runner bar. Afterwards the molten metal filled the testbar cavities with a continuous smooth flow following the sidewalls. No entrapped bubbles or splashing of the melt was seen. Although some oscillation of the surface of the molten metal was observed during filling, the free surface of the liquid metal was intact. No broken molten metal surface was seen and

surface film entrainment was reduced with this running system design.

4.2.3 Filling modes modelling

Figure 4.13 shows computer modelling results of VTFM filling. The falling metal interaction with the filter print generated considerable amounts of splashing and surface turbulence, this demonstrated good agreement with the flow patterns seen using real time X-ray radiography, see figure 4.10. Unlike the real time X-ray radiography, the metal flow after exciting the filter print exhibited surface turbulence. Some waves were detected at the testbar cavity inlet and along the runner bar. The testbar cavities filled with a continuous smooth flow following the sidewalls. The computer simulation displayed those regions of the casting not observed in the real time X-ray. The reflected wave generated by hitting the end of the runner bar was neutralized by filling of the feeder, and it did not overlay fresh incoming metal. The feeder in this location worked as an overflow to capture the initial stream and dissipate its energy.

With regards to computer modelling results of TFM, see figure 4.14, it showed the reflected liquid metal wave generated by hitting both ends of the runner bar. It also showed the recirculation of the liquid metal in the runner bar cavity and the jetting inside the testbar cavities. This demonstrated good agreement with the flow pattern seen using real time X-ray radiography, seen in figure 4.11.

In the case of QFM, the computer modelling shown in figure 4.15, showed good agreement with the real time X-ray results, shown in figure 4.12, up to the runner bar inlet. The metal plunging through the downsprue was dampened by the filter and started to seep out into the runner bar. Then the simulation deviated from the real time X-ray as it showed an increased ingate speed causing free surface break in the runner bar. The filling of the testbars and feeders followed the same behaviour described for the VTFM.

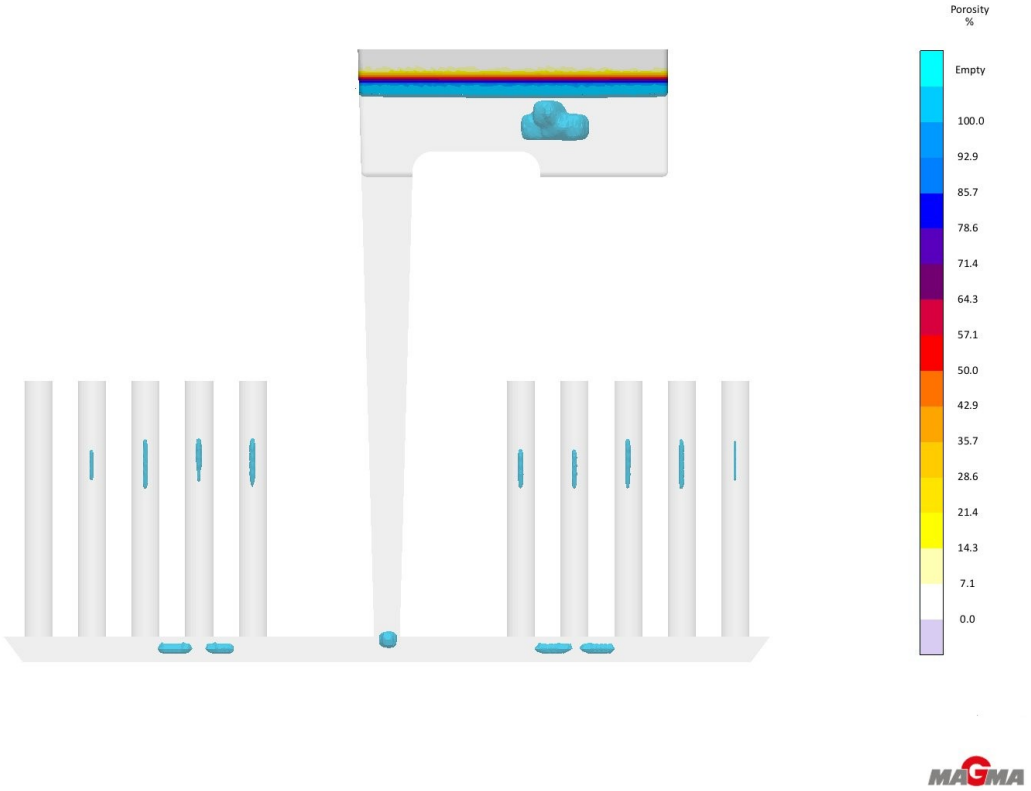


Figure 4.4: SGI TFM shrinkage porosity locations

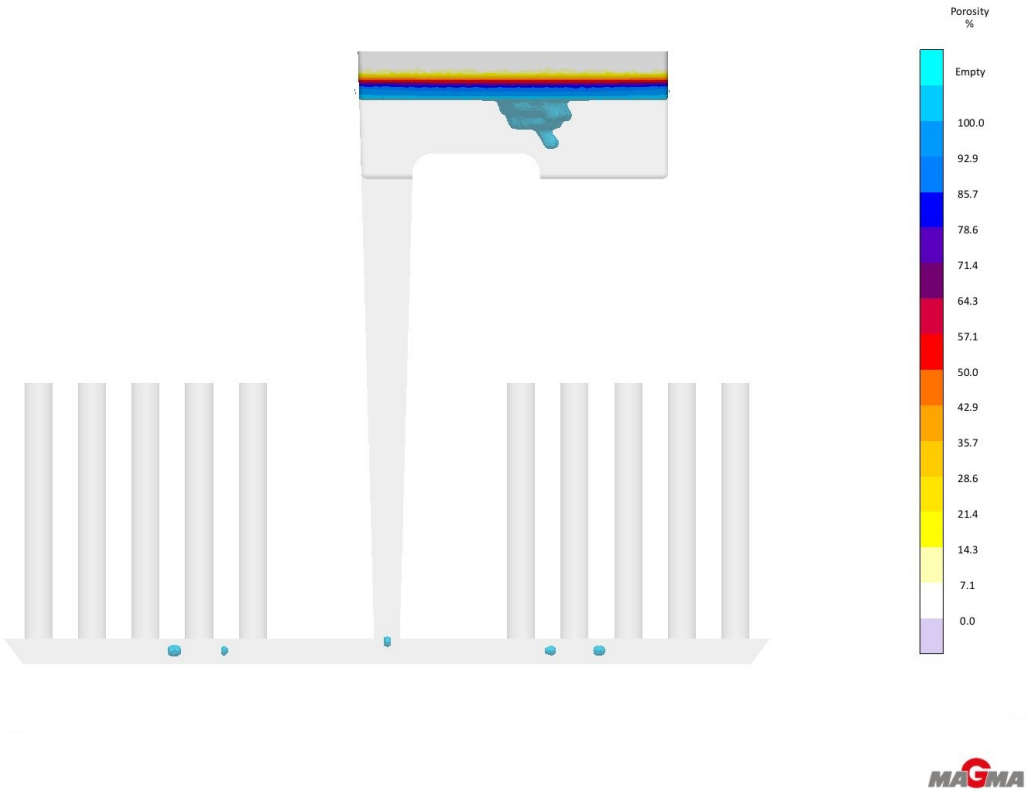


Figure 4.5: LGI TFM shrinkage porosity locations

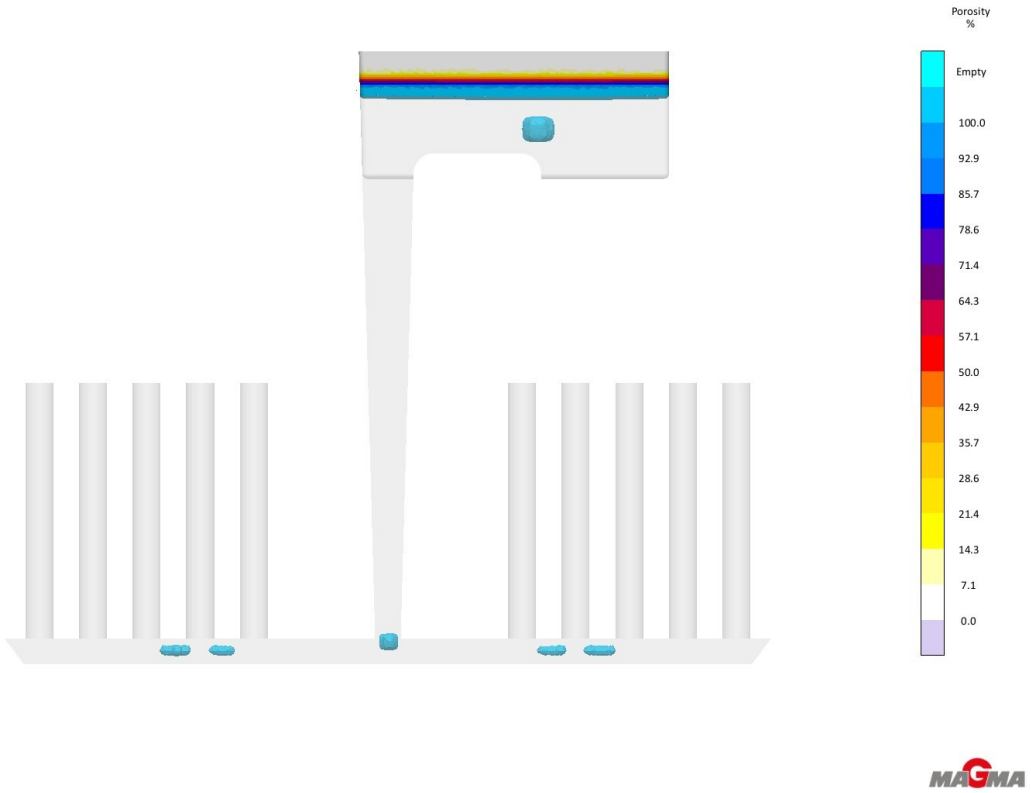


Figure 4.6: CGI TFM shrinkage porosity locations

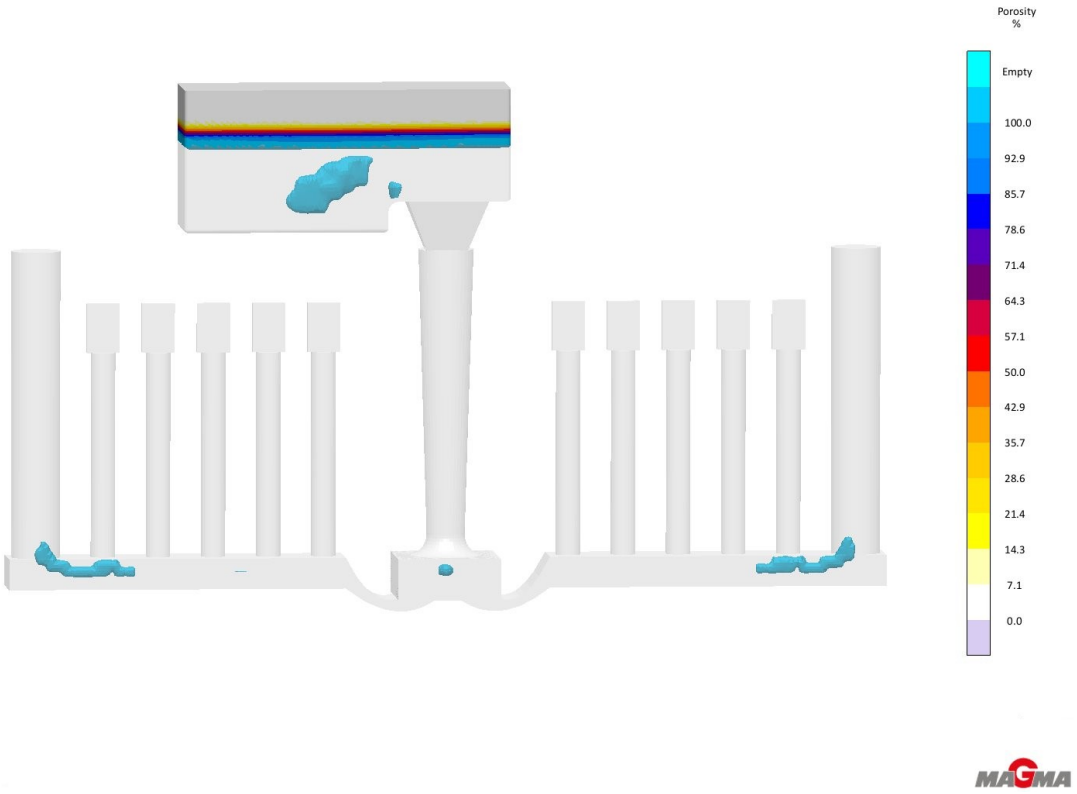


Figure 4.7: SGI VTFM/QFM shrinkage porosity locations

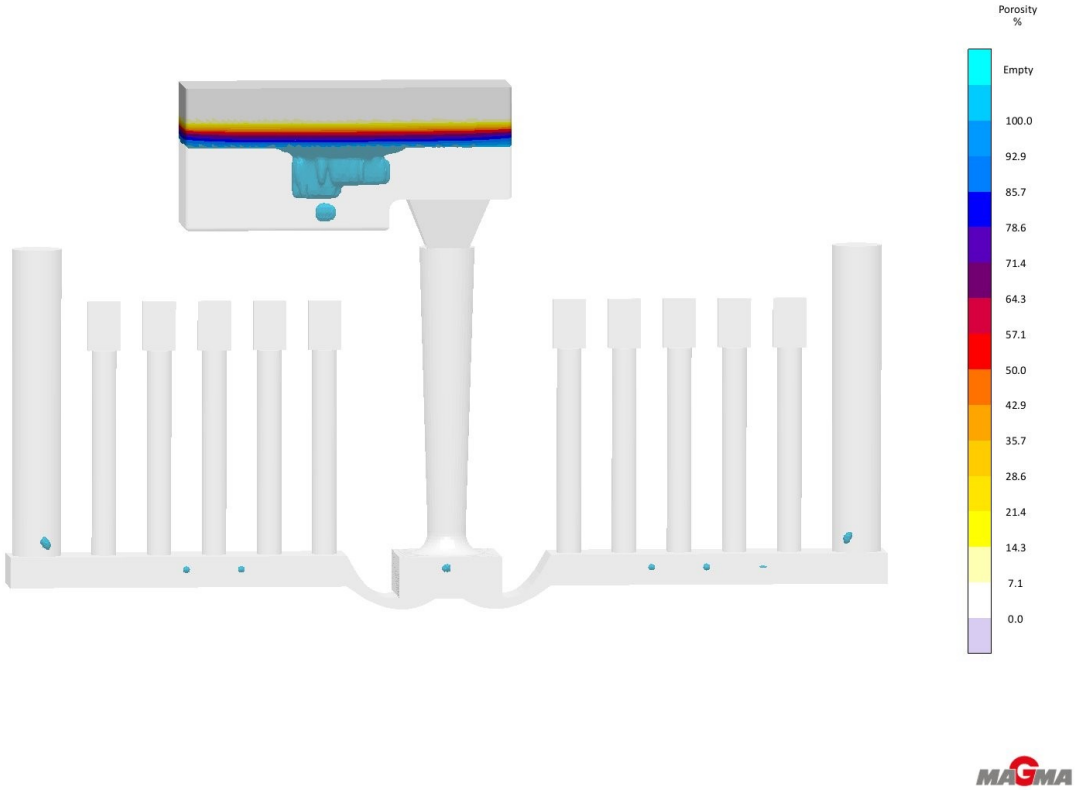


Figure 4.8: LGI VTFM/QFM shrinkage porosity locations

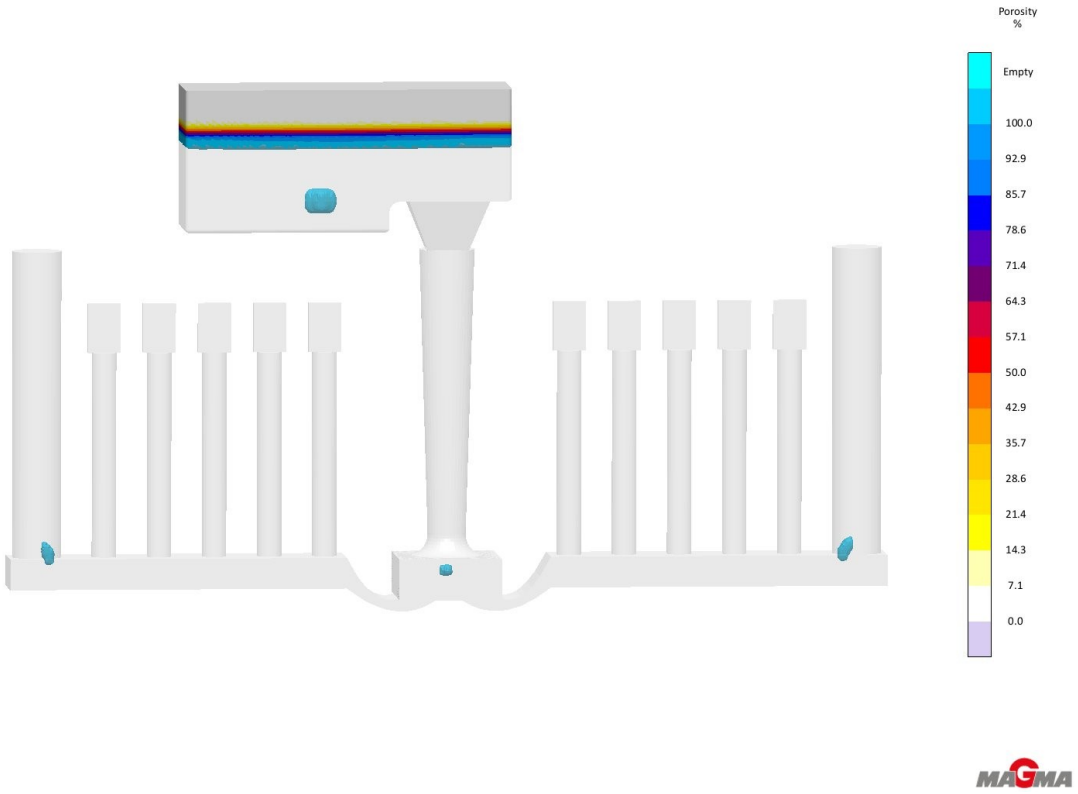


Figure 4.9: CGI VTFM/QFM shrinkage porosity locations

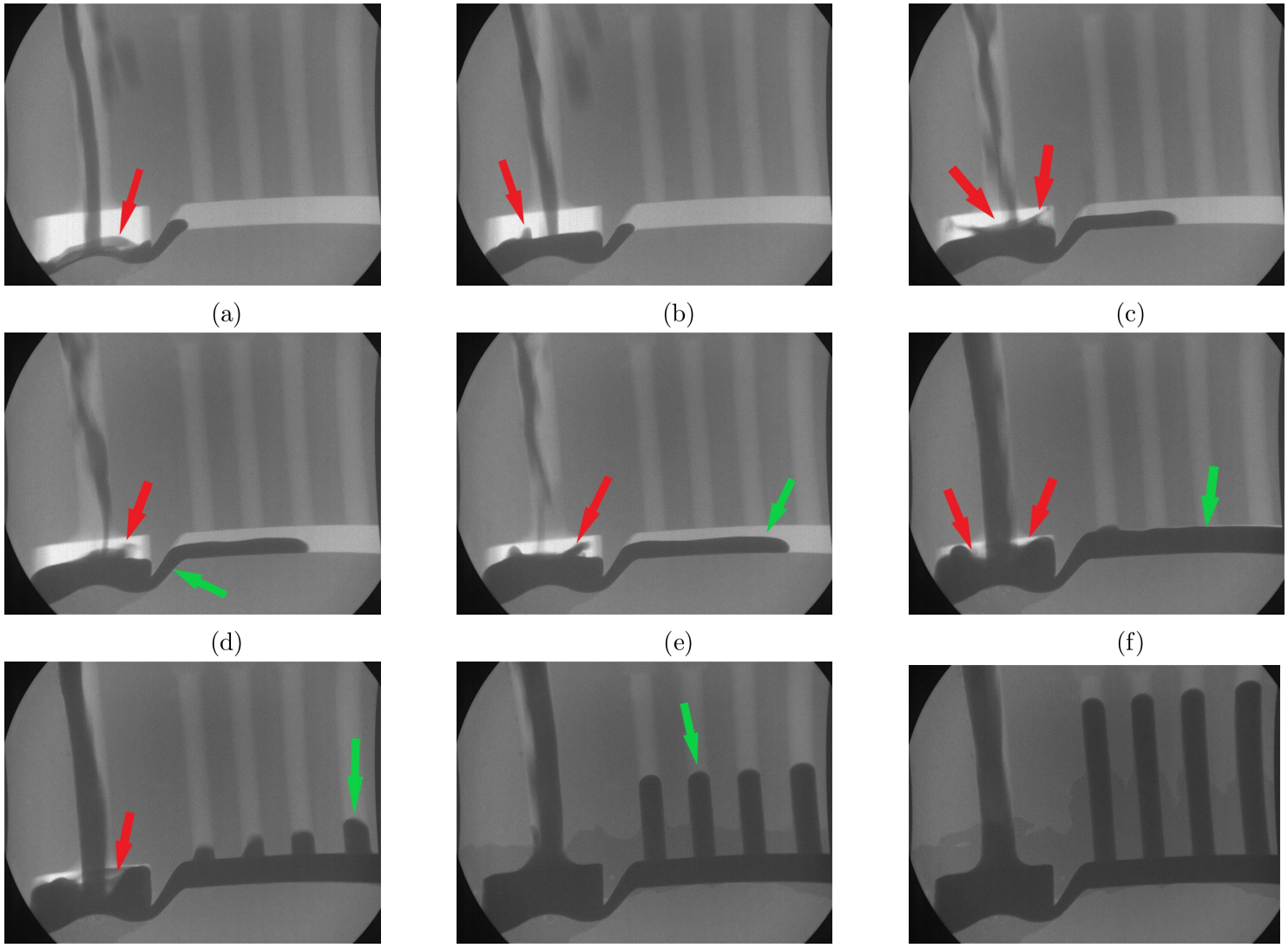


Figure 4.10: Frames from the real time X-ray video of the VTFM showing surface turbulent filling, including splashing, several waves and back-waves generated in the filter print. Red arrows point to examples of localised surface turbulence and green arrows point to examples of localised quiescent filling

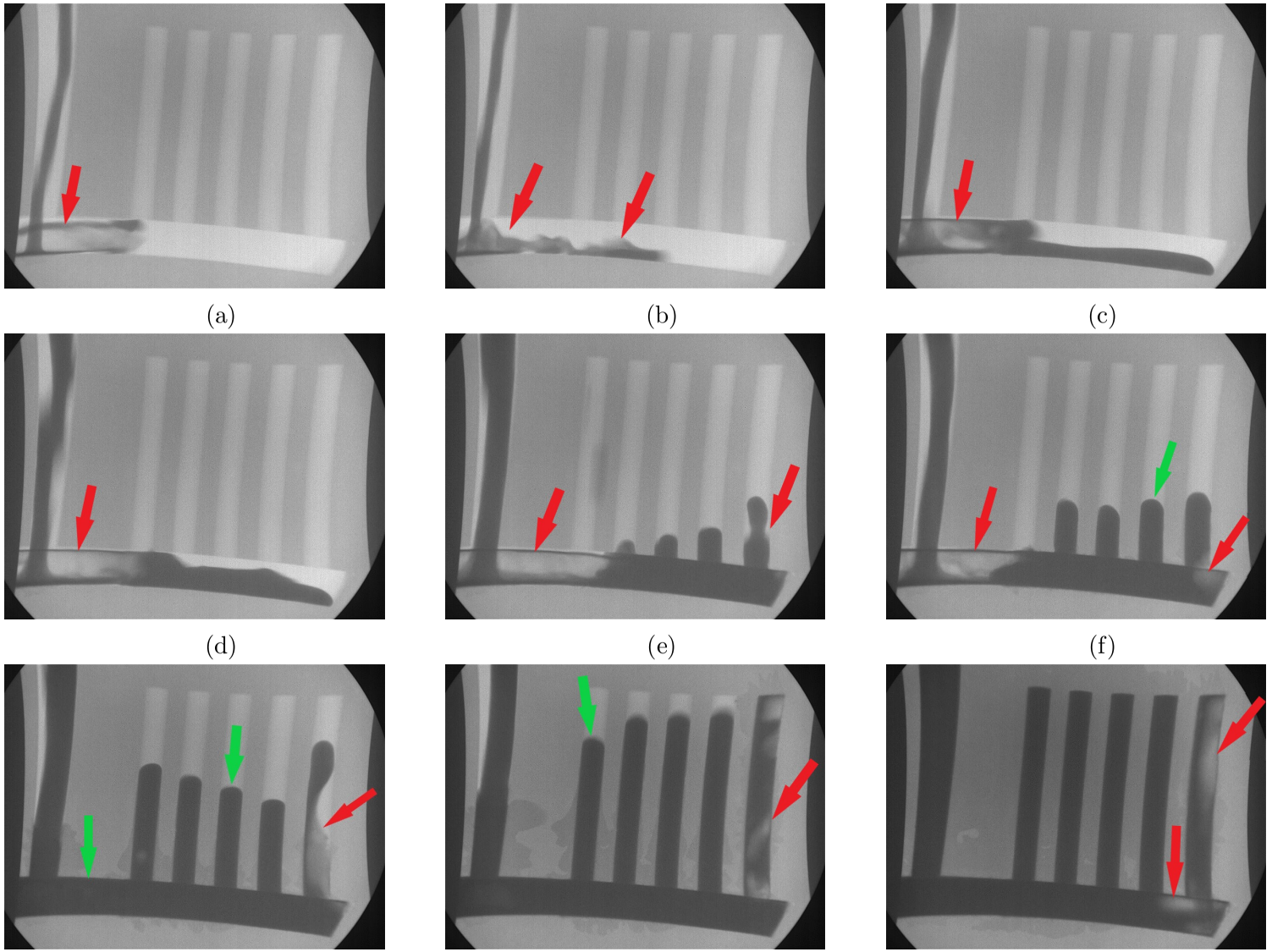


Figure 4.11: Frames from the real time X-ray video of the TFM showing surface turbulent filling, including splashing, several back-waves and jetting in the mould cavity. Entrained air bubbles are captured flowing in through the runner bar and the testbar. Red arrows point to examples of localised surface turbulence and green arrows point to examples of localised quiescent filling

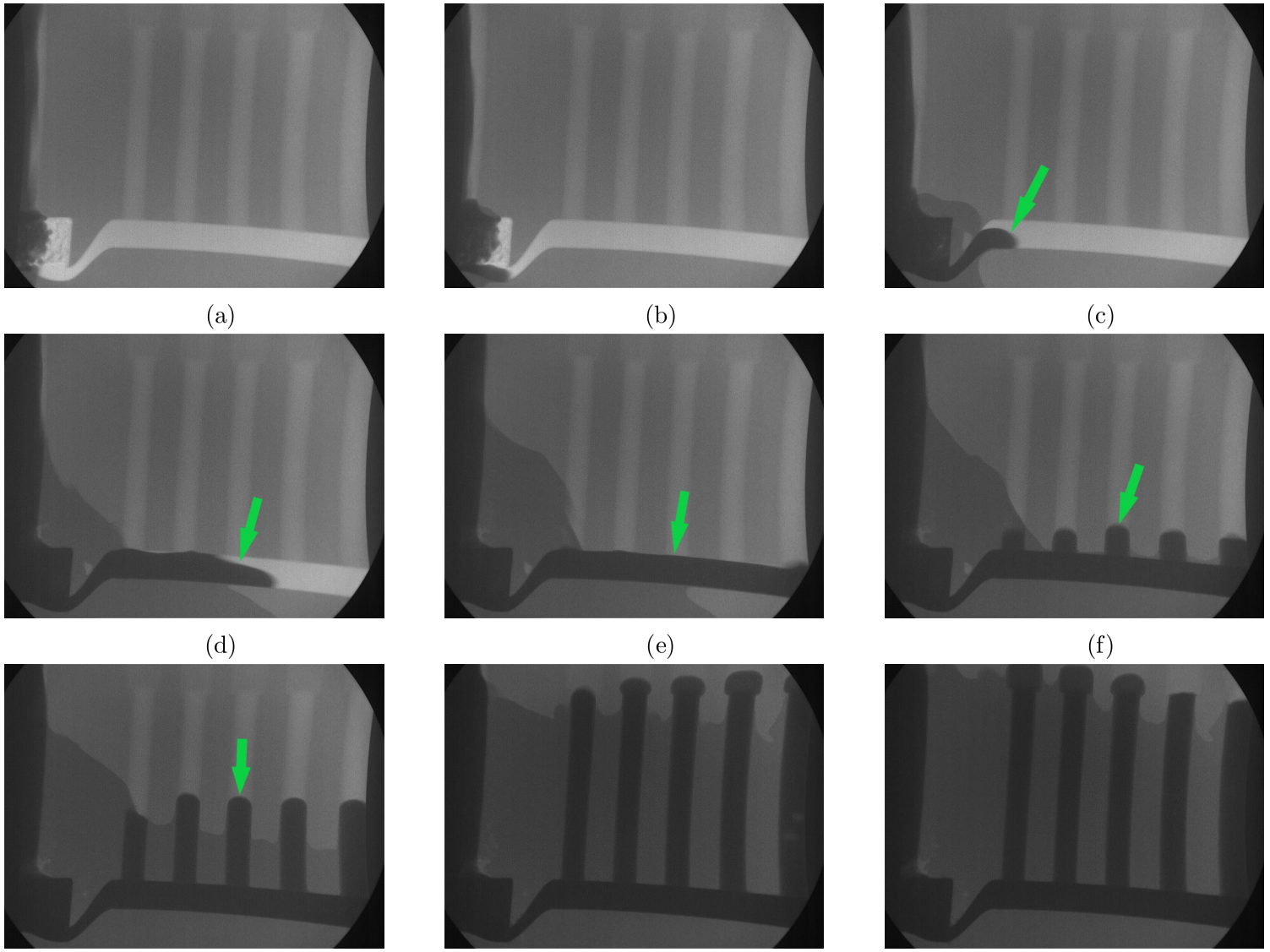
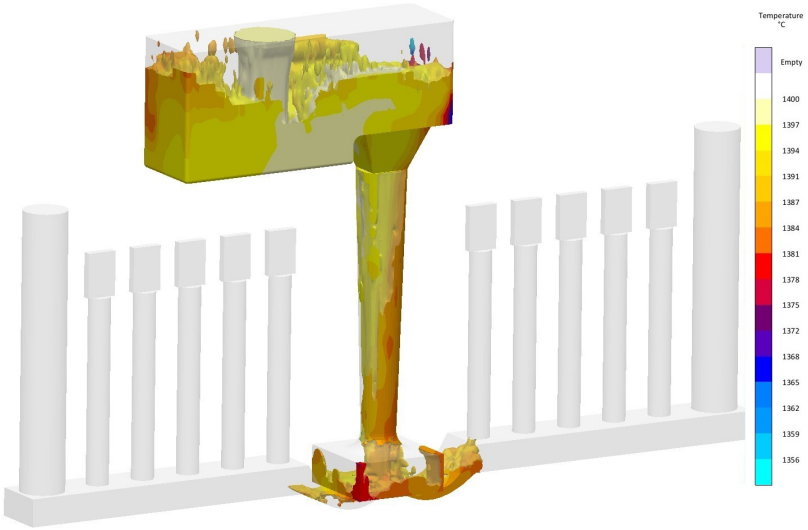
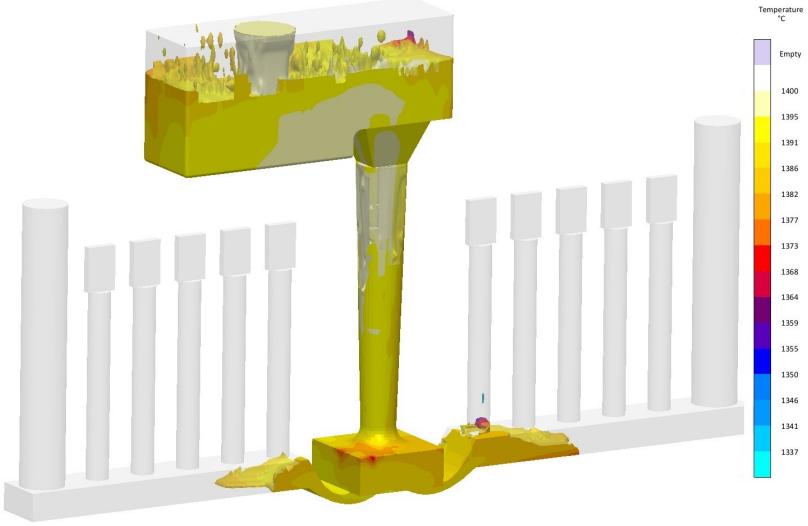


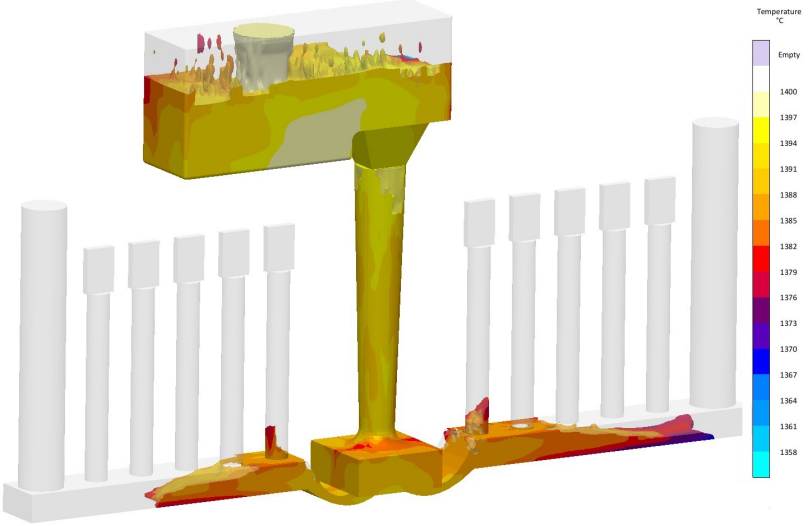
Figure 4.12: Frames from the real time X-ray video of the QFM showing quiescent filling. Green arrows point to examples of localised quiescent filling



(a)

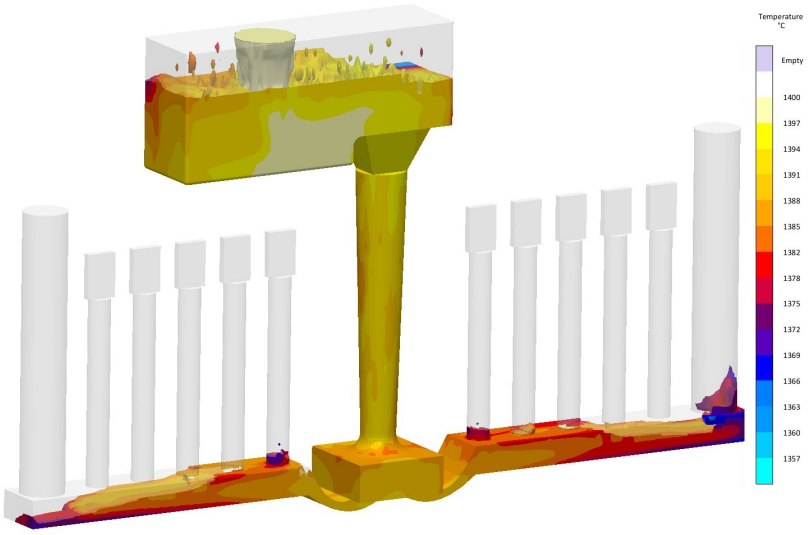


(b)

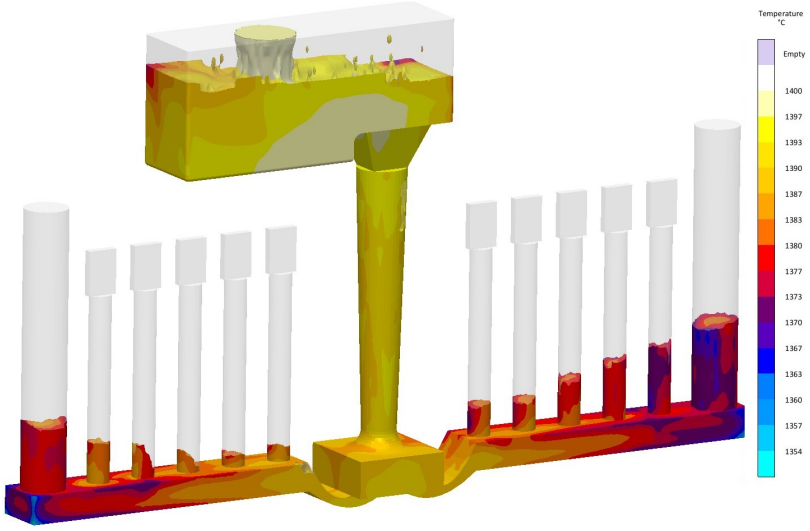


(c)

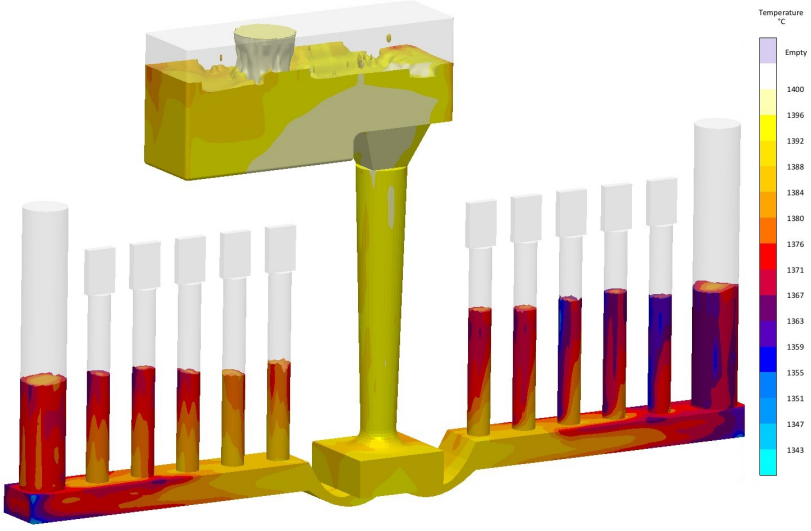
Figure 4.13: MAGMASOFT^{TM} simulation of the VTFM filling showed surface turbulent filling mainly generated in the filter print, and filling time = 2.3 s



(d)

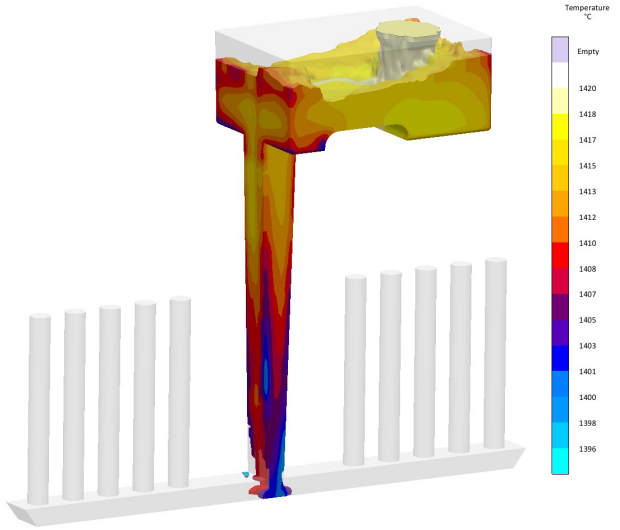


(e)

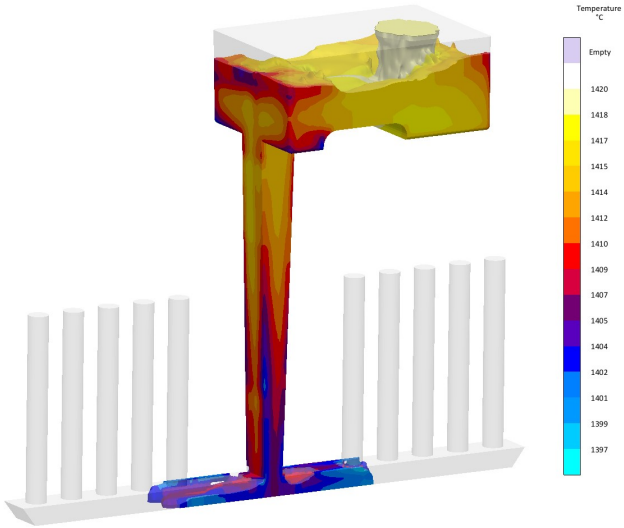


(f)

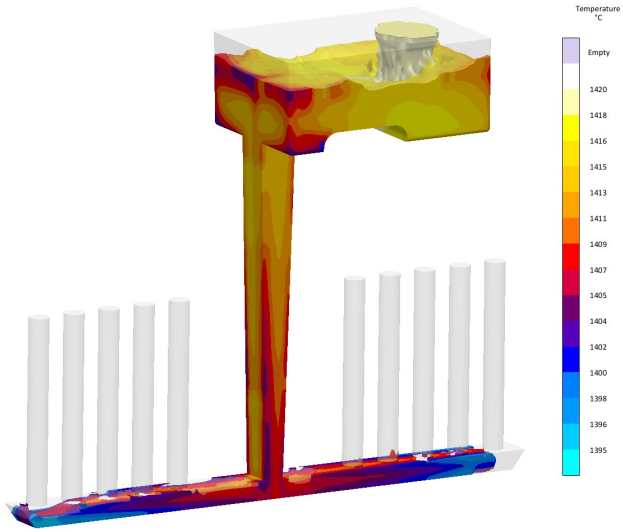
Figure 4.13: MAGMASOFT^{TM} simulation of the VTFM filling showed surface turbulent filling mainly generated in the filter print, and filling time = 2.3 s



(a)

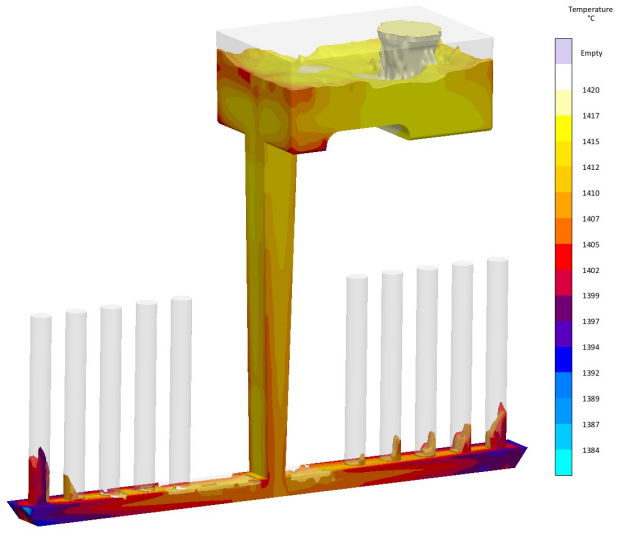


(b)

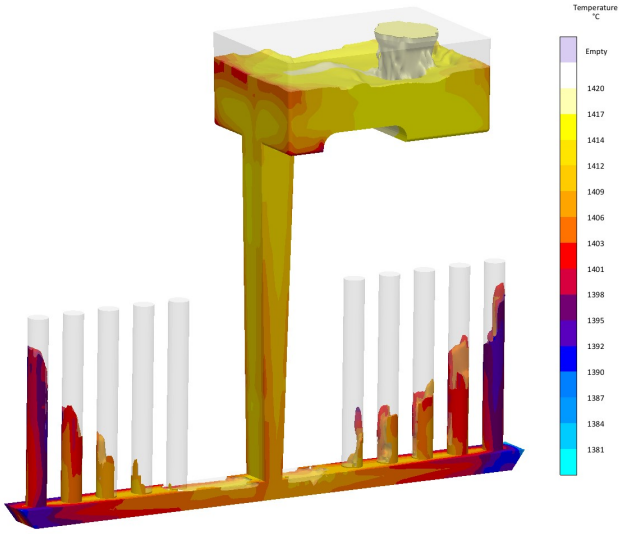


(c)

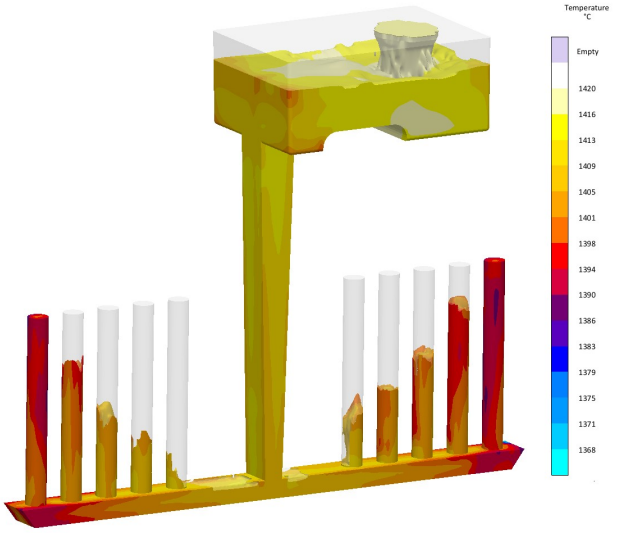
Figure 4.14: MAGMASOFT^{TM} simulation of the TFM filling showed surface turbulent filling, and filling time = 1.3 s



(d)

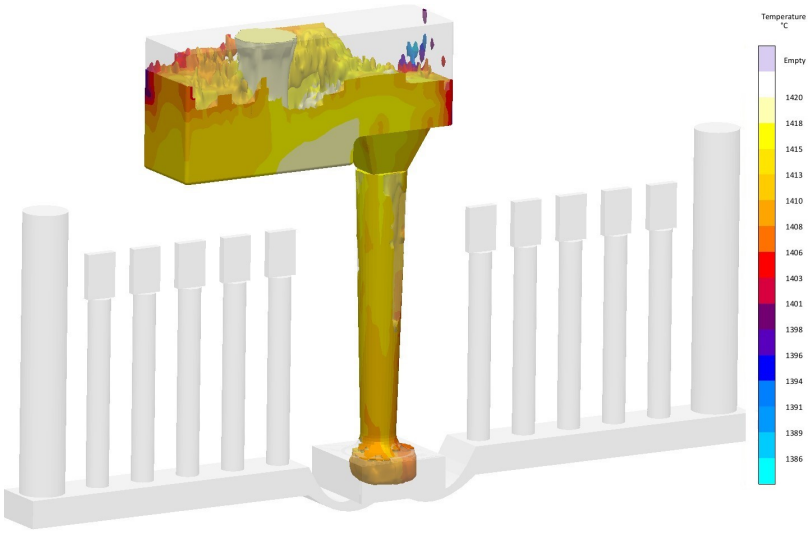


(e)

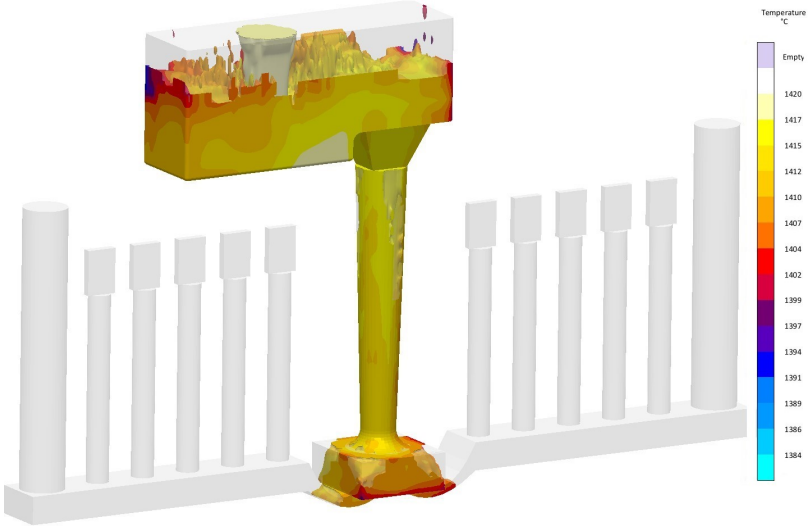


(f)

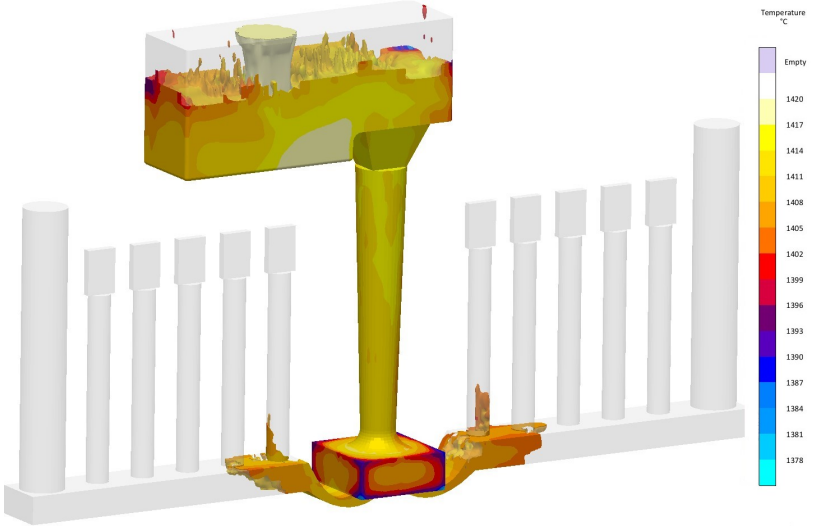
Figure 4.14: MAGMASOFT^{TM} simulation of the TFM filling showed surface turbulent filling, and filling time = 1.3 s



(a)

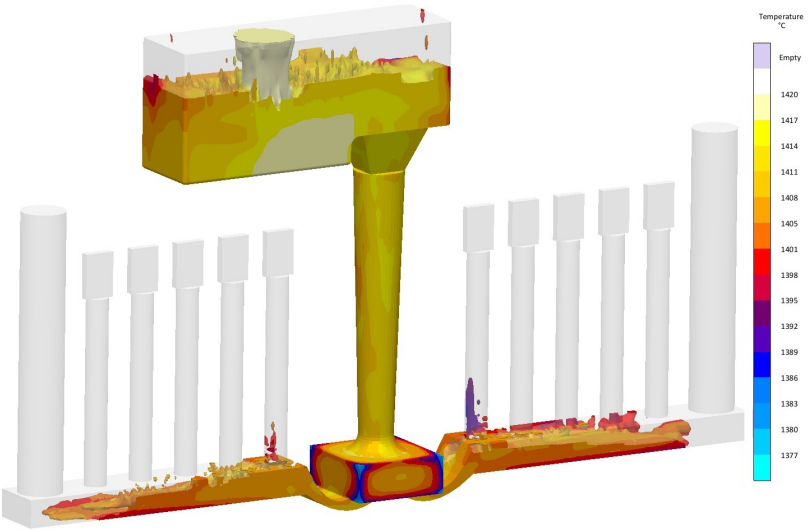


(b)

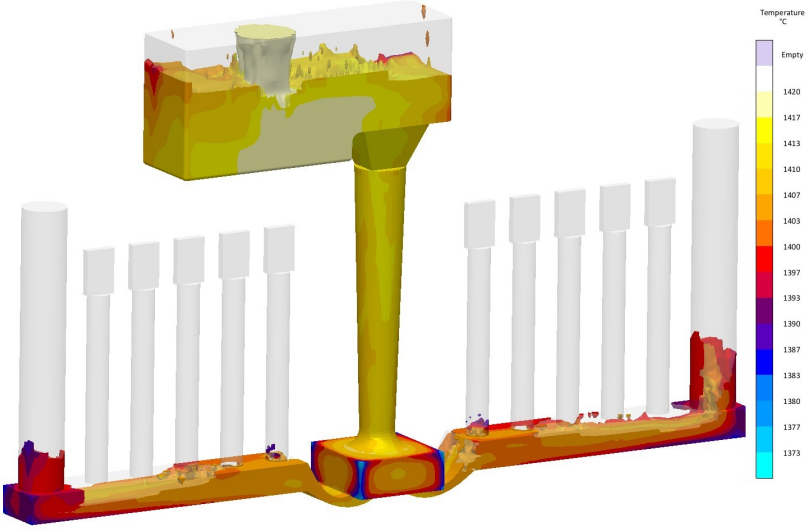


(c)

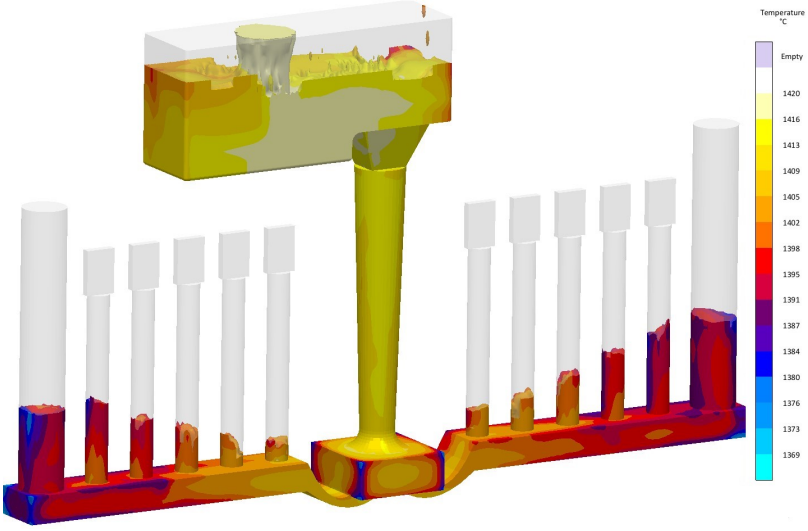
Figure 4.15: MAGMASOFT^{TM} simulation of the QFM filling showed quiescent flow and filling time = 2.3 s



(d)



(e)



(f)

Figure 4.15: MAGMASOFT^{TM} simulation of the QFM filling showed quiescent flow and filling time = 2.3 s

Chapter 5

Results for Spheroidal Graphite Iron

In this experiment, SGI testbars were gravity cast in three different running system designs of resin bonded sand moulds. The data was analysed statistically to determine the effect of the filling mode on the tensile properties, reproducibility and reliability of the castings. Subsequently the fracture surfaces were examined using SEM to determine the source of fracture. EDX was used to acquire the chemical composition of any defects. FIB milling, lift out technique and STEM elements mapping was also utilized to examine finer details.

5.1 The effect of quiescently-filled, surface turbulently filled, and very (surface) turbulently-filled moulds on the tensile properties, reproducibility and reliability of SGI

Three separate SGI melts were cast to produce a total of 240 test bars. The first melt was denoted SGI1, the second denoted SGI2 and the third denoted SGI3. The grade for SGI1 and SGI3 was SGI 500/7 and for SGI2 the grade was SGI 700/2.

The three filling modes used were quiescently-filled (QFM), surface turbulently filled (TFM), and very (surface) turbulently-filled (VTFM). SGI1 had 40 test bars from TFM and VTFM. SGI3 had 40 test bar from QFM, TFM and VTFM. SGI2 had only 20 test bars from QFM and TFM (table 5.1). Unlike SGI1 and SGI3, SGI2 was cast at the University of Birmingham. Hence the deviation in the chemical composition from grade SGI 500/7 to SGI 700/2. The reduced number of test bars was due to the casting capacity of the furnace at the University of Birmingham. The number of testbars from each type of mould for each melt are listed in table 5.1.

Melt	QFM	TFM	VTFM
SGI1	•	40	40
SGI2	20	20	•
SGI3	40	40	40

Table 5.1: Number of SGI test bars from each mould type for different melts

5.1.1 Statistical analysis of SGI UTS data

The statistics of all SGI UTS data from the tensile test have been shown in table 5.2. The UTS mean values for SGI2 TFM and SGI2 QFM highlighting the difference in grades between SGI2 vs. SGI1 and SGI3. The average UTS value in SGI2 was around 800 MPa. 55 MPa more than the average UTS for SGI1 and SGI3.

Variable	Total Count	Mean	StDev	Variance	Minimum	Maximum	Range
SGI1 VTFM	40	715	65	4208	519	823	304
SGI1 TFM	40	739	42	1768	641	811	171
SGI2 TFM	20	800	56	3126	664	904	240
SGI2 QFM	20	802	44	1897	722	881	158
SGI3 VTFM	40	760	25	646	674	800	126
SGI3 TFM	40	746	29	828	679	813	134
SGI3 QFM	40	769	19	355	730	806	75

Table 5.2: Descriptive statistics of SGI UTS (MPa) values

The Gaussian distribution plot for the SGI UTS data (figures 5.1 and 5.2) showed SGI1 VTFM data to have a significantly wider distribution than the rest of the data sets. SGI2 TFM and SGI2 QFM distributions, see figure 5.1, were almost

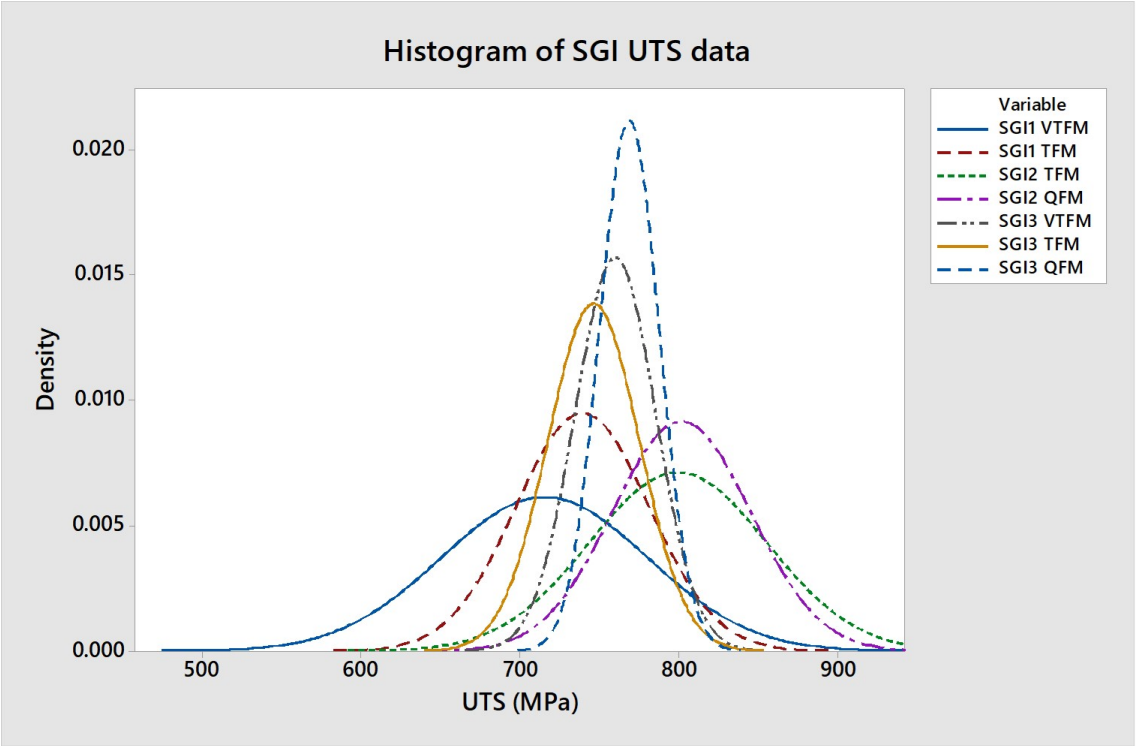


Figure 5.1: The Fitted Gaussian distributions for UTS data from each mould type for different SGI melts

identical, with SGI QFM showing less spread. Moreover, SGI2 TFM and SGI2 QFM had higher means as they belonged to a higher grade (SGI 700/2). For SGI3, the Gaussian distribution revealed that with the reduction of the surface turbulence from very turbulent to quiescent (i.e. VTFM to TFM to QFM), the mean increased and the distribution narrowed. The Gaussian distribution analysis also illustrated that the six data sets intersected and overlapped. Thus to determine if there was a significant difference between the data sets, a Student's t-test was carried out between the comparable data sets. The results are shown in the table 5.3.

Two Samples		T Value	P Value
SGI1 VTFM	SGI1 TFM	2	0.05
SGI2 TFM	SGI2 QFM	0.1	0.893
SGI3 VTFM	SGI3 TFM	2.25	0.027
SGI3 VTFM	SGI3 QFM	1.75	0.084
SGI3 TFM	SGI3 QFM	4.12	0

Table 5.3: Student's t-test results for SGI UTS data

The Student's t-test t-values and p-values (table 5.3) showed that there were significant difference in the means between all data sets, except for SGI2 TFM and

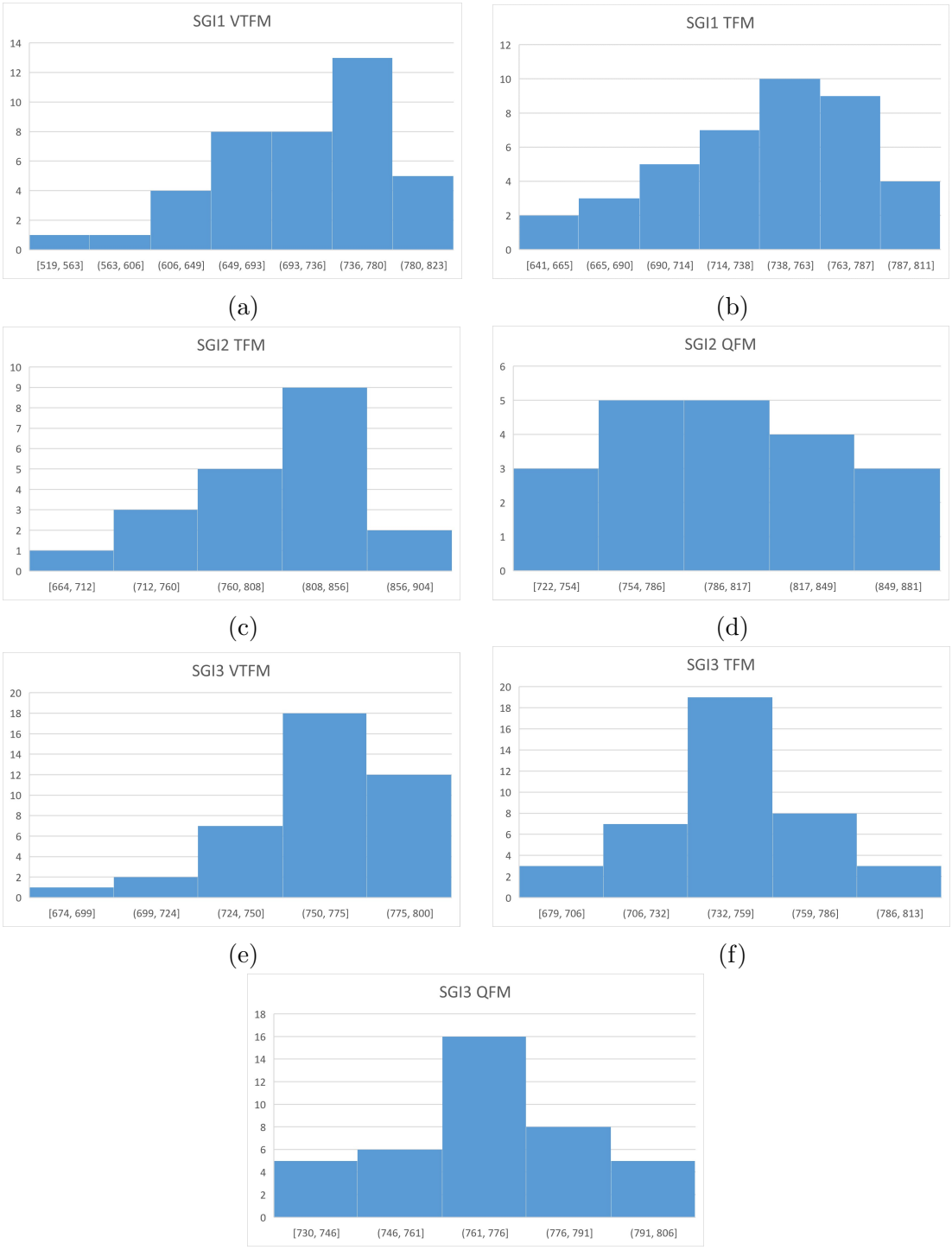


Figure 5.2: Separate histograms for UTS data showed the trend of negative skewness. The x-axis represent the range of bins in MPa, and the y-axis represents the number of data points in each bin

SGI2 QFM. With a t-value of 0.1 and a p-value of 0.893 (> the significant level of 0.05), it indicated that the null hypothesis cannot be rejected (the null hypothesis assumes the difference between the means = 0). Thus, it cannot be concluded that there is a significant difference between the means of SGI2 TFM and SGI2 QFM. The student's t-test for SGI3 VTFM and SGI3 QFM resulted in a t-value of 1.75 and a p-value of 0.084. The p-value is slightly > 0.05 which means the null hypothesis cannot be rejected, but on the other hand the t-value is almost 2, (the greater the magnitude of t, the greater the evidence against the null hypothesis).

The Anderson-Darling test was used to test the fit of UTS data sets against the normal, log-normal, 2-parameter and 3-parameter Weibull distribution. The criteria for determining the best fit was by comparing the AD scores, and the lowest the AD score, the better the goodness of fit. A slight difference in the score might not be practically relevant. The probability plot would determine the better fit by comparing the alignment of the data points on the regression line. The author aim was to use the same distribution for all data sets for ease of comparison, and to use the 2-parameter Weibull distribution so the work would conform to the literature. Thus, unless the data doesn't result in a goodness of fit test lower than $R^2_{0.05}$ the 2-parameter Weibull would be used. Moreover, the descriptive statistics and histograms assumed the data followed a normal distribution; hence there was no need to repeat the same analysis. The same aims and reason would be applied to the AD test for LGI and CGI data. Table 5.4 contains the resulting scores from the AD test. For SGI1 TFM the 2-parameter and the 3-parameter Weibull had the lowest AD score (AD = 0.5). The 3-parameter Weibull had the lowest AD score for SGI1 VTFM, but the 2-parameter was not far off with AD = 0.6. So the 2-parameter Weibull distribution was chosen for SGI1. SGI2 TFM had similar results to SGI1 TFM. The 2-parameter Weibull had a highest AD score for SGI2 QFM (AD = 0.9) but it was only 0.1 higher than the lowest score (AD = 0.8). Thus the 2-parameter Weibull was chosen for SGI2. The 2-parameter and 3-parameter Weibull distributions had the lowest AD score for SGI3 VTFM (AD = 0.5). On the

other hand, 2-parameter Weibull distribution had the highest AD score for SGI3 TFM and SGI3 QFM, AD = 1.2 and 1.8; respectively. The 2-parameter Weibull distribution was chosen for both data sets to conform with SGI3 VTFM, but on the condition $R^2 > R^2_{0.05}$. The AD probability plots for all data sets are shown in figures 5.3 to 5.9.

•	Normal	2-Parameter Weibull	3-Parameter Weibull	Log-normal
SGI1 VTFM	0.8	0.6	0.5	1
SGI1 TFM	0.7	0.5	0.5	0.8
SGI2 TFM	1.3	1.2	1.2	1.4
SGI2 QFM	0.8	0.9	0.8	0.8
SGI3 VTFM	0.9	0.5	0.5	1
SGI3 TFM	0.7	1.2	0.7	0.7
SGI3 QFM	0.6	0.8	0.6	0.7

Table 5.4: Anderson-Darling test results for SGI UTS values

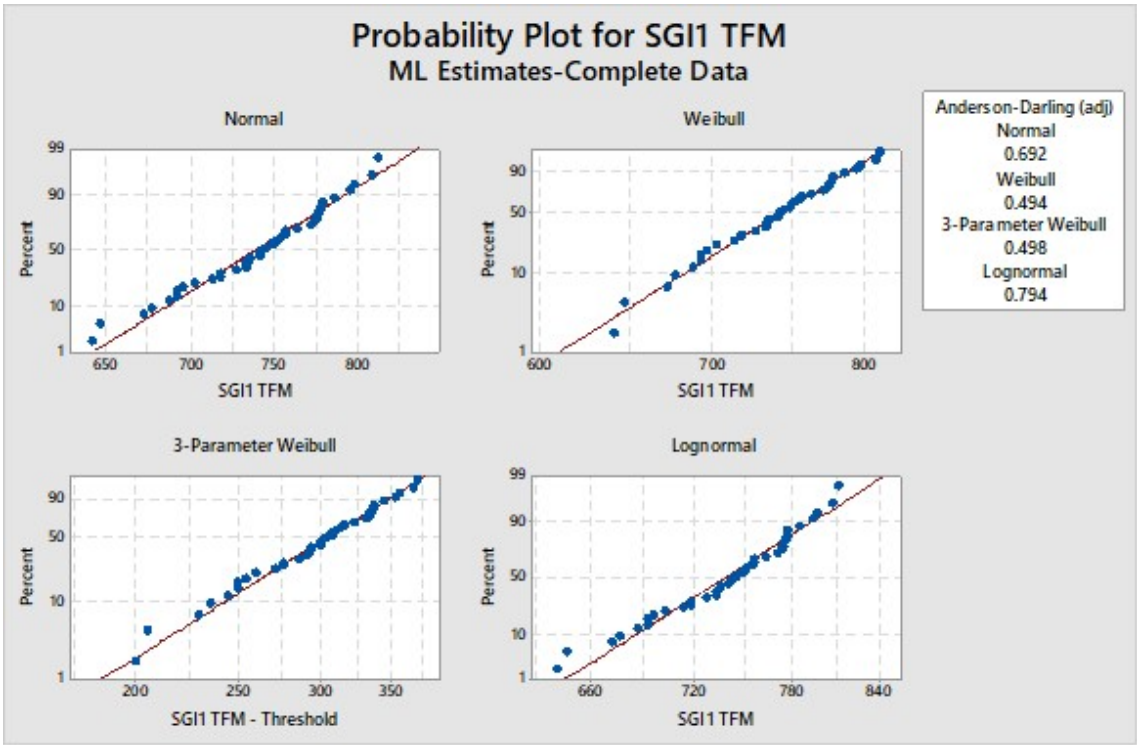


Figure 5.3: Probability plots for AD test for SGI1 TFM UTS. The y-axis represents the cumulative probability in percent. The x-axis represents the UTS in MPa, except for the 3-parameter Weibull plot, it is the threshold value in MPa

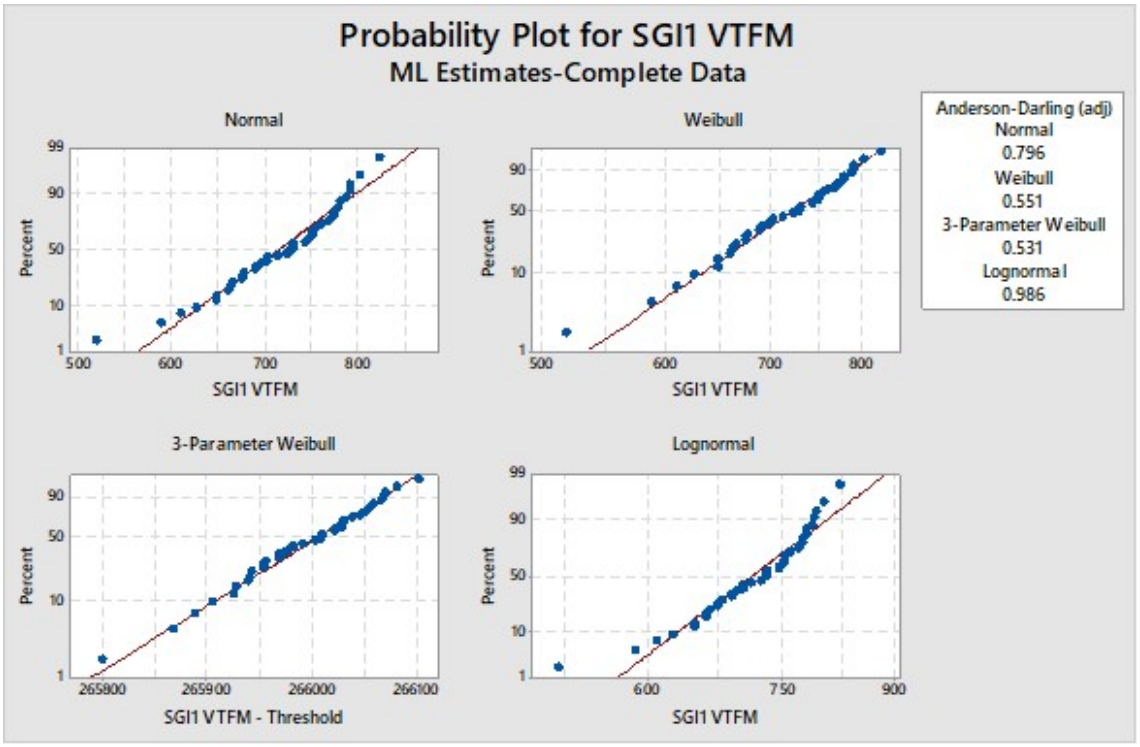


Figure 5.4: Probability plots for AD test for SGI1 VTFM UTS. The y-axis represents the cumulative probability in percent. The x-axis represents the UTS in MPa, except for the 3-parameter Weibull plot, it is the threshold value in MPa

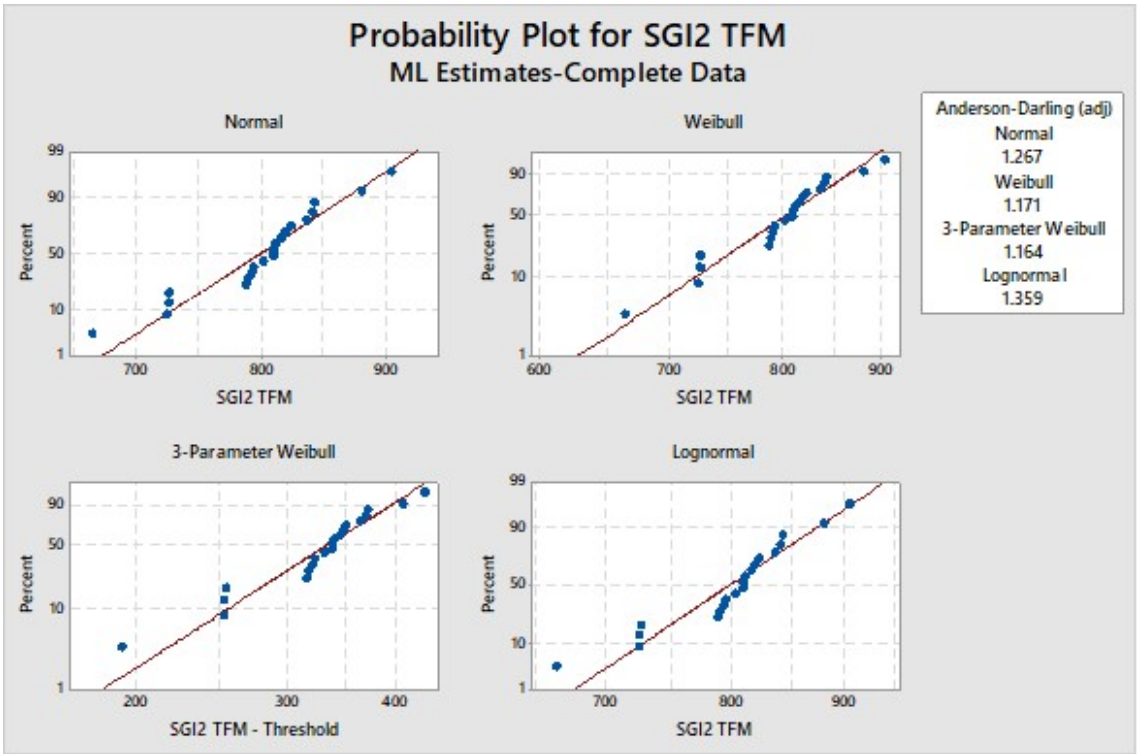


Figure 5.5: Probability plots for AD test for SGI2 TFM UTS. The y-axis represents the cumulative probability in percent. The x-axis represents the UTS in MPa, except for the 3-parameter Weibull plot, it is the threshold value in MPa

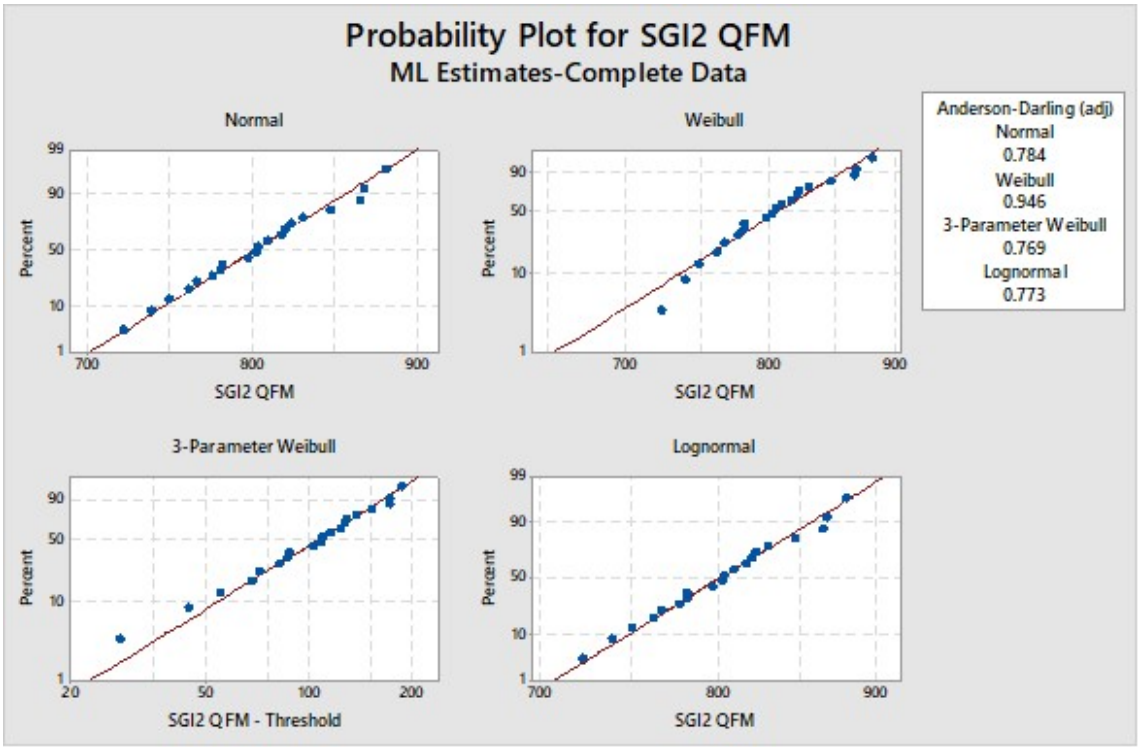


Figure 5.6: Probability plots for AD test for SGI2 QFM UTS. The y-axis represents the cumulative probability in percent. The x-axis represents the UTS in MPa, except for the 3-parameter Weibull plot, it is the threshold value in MPa

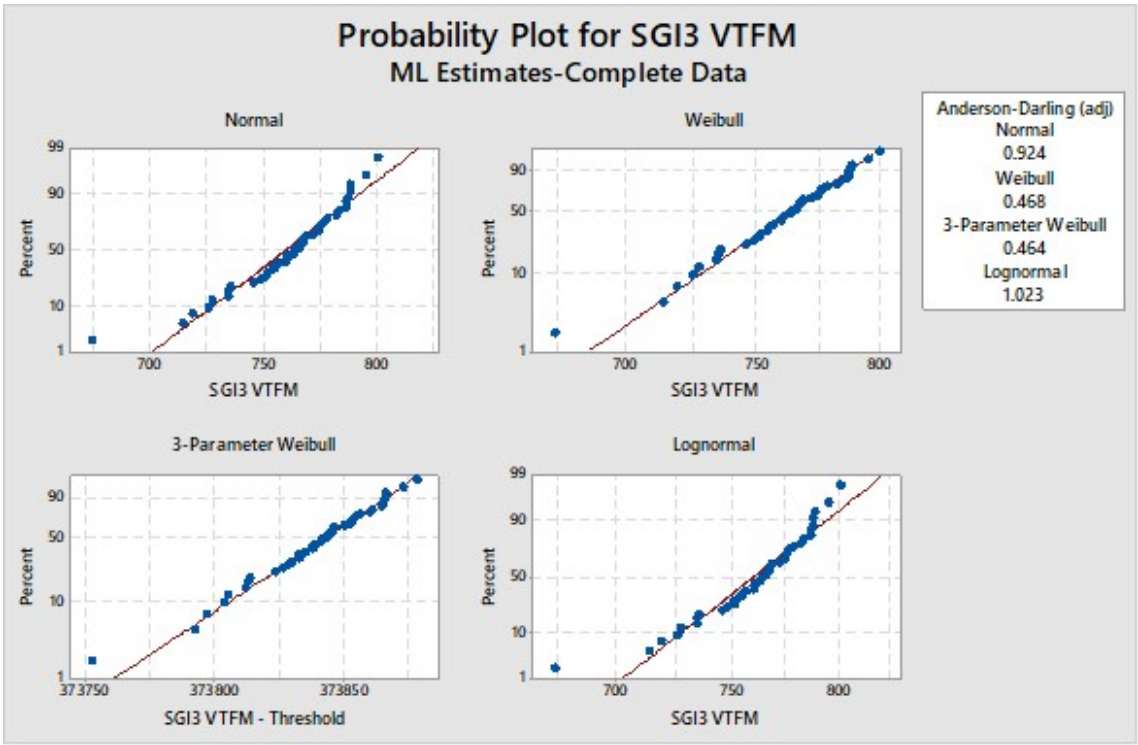


Figure 5.7: Probability plots for AD test for SGI3 VTFM UTS. The y-axis represents the cumulative probability in percent. The x-axis represents the UTS in MPa, except for the 3-parameter Weibull plot, it is the threshold value in MPa

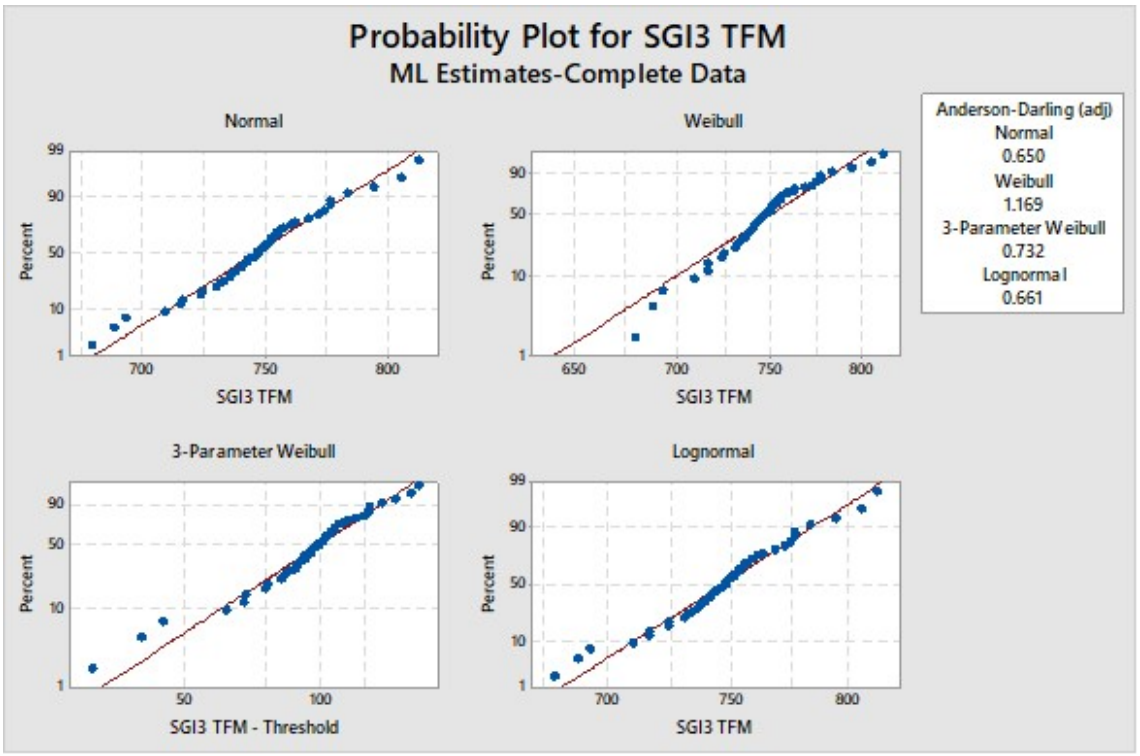


Figure 5.8: Probability plots for AD test for SGI3 TFM UTS. The y-axis represents the cumulative probability in percent. The x-axis represents the UTS in MPa, except for the 3-parameter Weibull plot, it is the threshold value in MPa

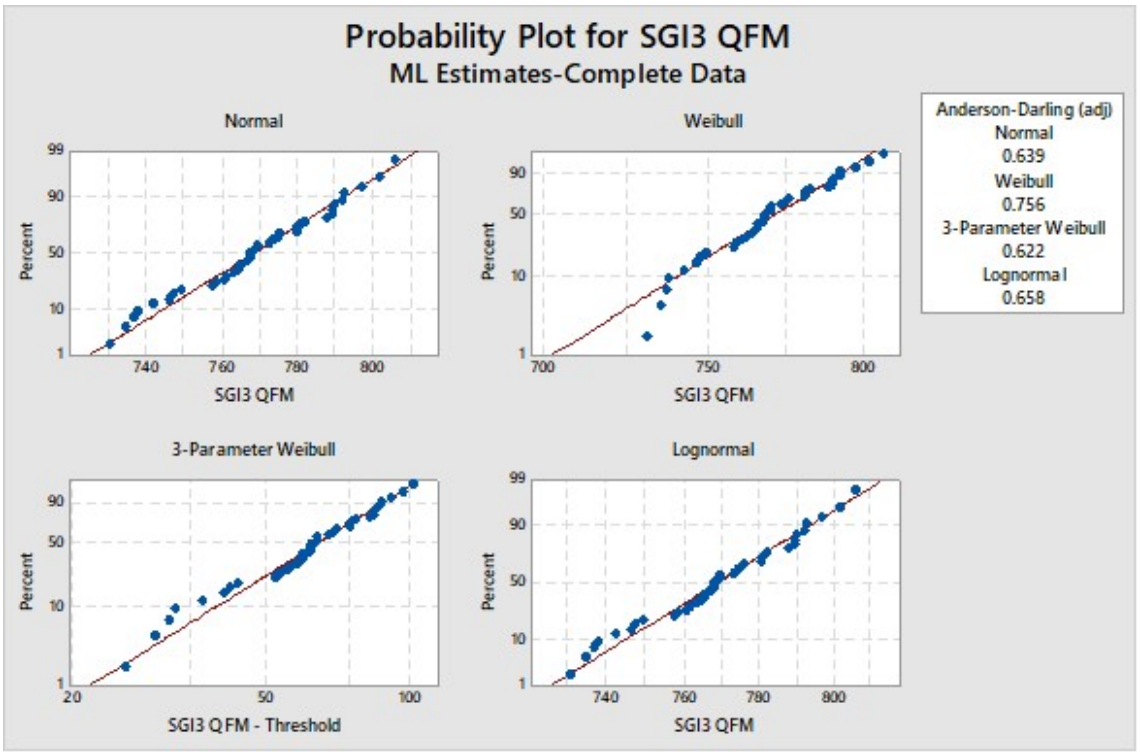


Figure 5.9: Probability plots for AD test for SGI3 QFM UTS. The y-axis represents the cumulative probability in percent. The x-axis represents the UTS in MPa, except for the 3-parameter Weibull plot, it is the threshold value in MPa

5.1.2 Statistical analysis of SGI %Elongation data

The same statistical analysis that was carried out for the UTS data was carried out for the %El. data. The descriptive statistics of %El. data are shown in table 5.5 and the Gaussian distribution is shown in figures 5.10 and 5.11.

Variable	Total Count	Mean	StDev	Variance	Minimum	Maximum	Range
SGI1 VTFM	40	2.2	0.9	0.8	0.6	4.0	3.5
SGI1 TFM	39	3.2	1	0.9	1.1	5.5	4.4
SGI2 TFM	20	1.2	0.5	0.3	0.5	2.7	2.2
SGI2 QFM	20	0.8	0.3	0.1	0.5	1.4	0.9
SGI3 VTFM	40	3.3	0.6	0.3	1.6	4.4	2.7
SGI3 TFM	40	3.4	0.8	0.7	1.9	5	3.2
SGI3 QFM	40	3.5	0.6	0.3	2.1	4.4	2.3

Table 5.5: Descriptive statistics of SGI %El. (pct.) values

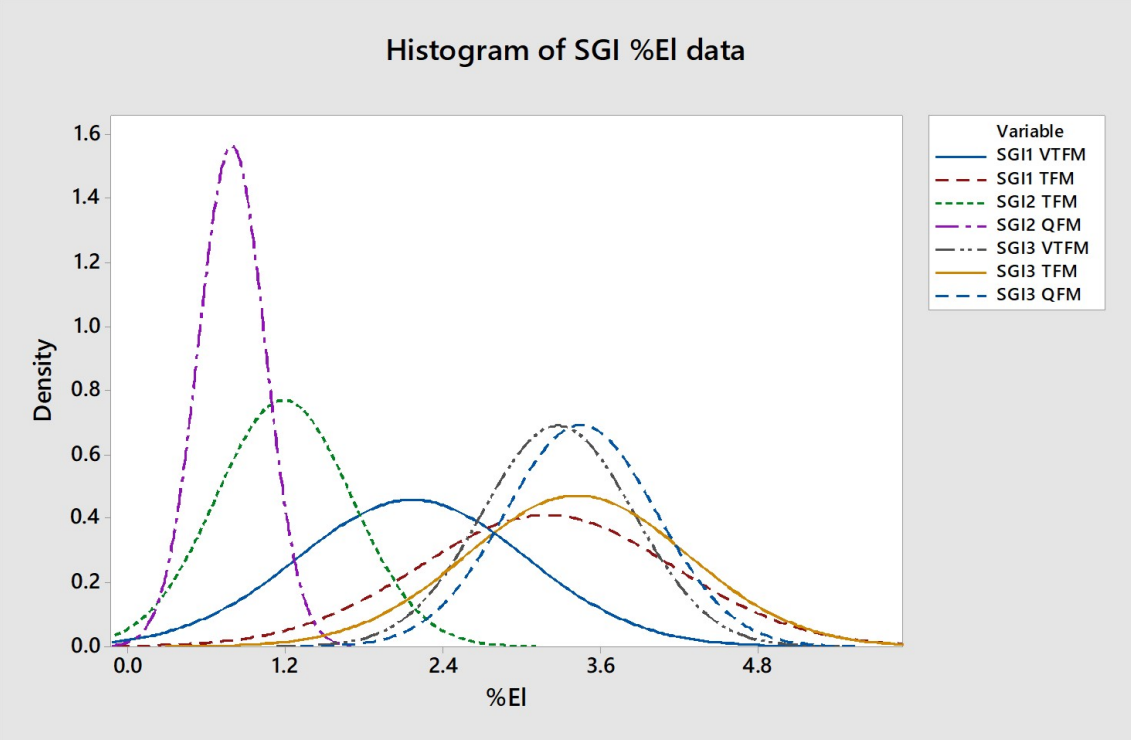


Figure 5.10: The Fitted Gaussian distributions for %El. (pct) data from each mould type for different SGI melts

Following the same behaviour as for the UTS data, the %El. mean values for SGI2 TFM and SGI3 QFM highlight the difference in grades between SGI2, and SGI1 and SGI3. Table 5.5 and Figure 5.10 showed SGI2 TFM and QFM have the lowest mean values for %El., and their respective Gaussian distributions were on the

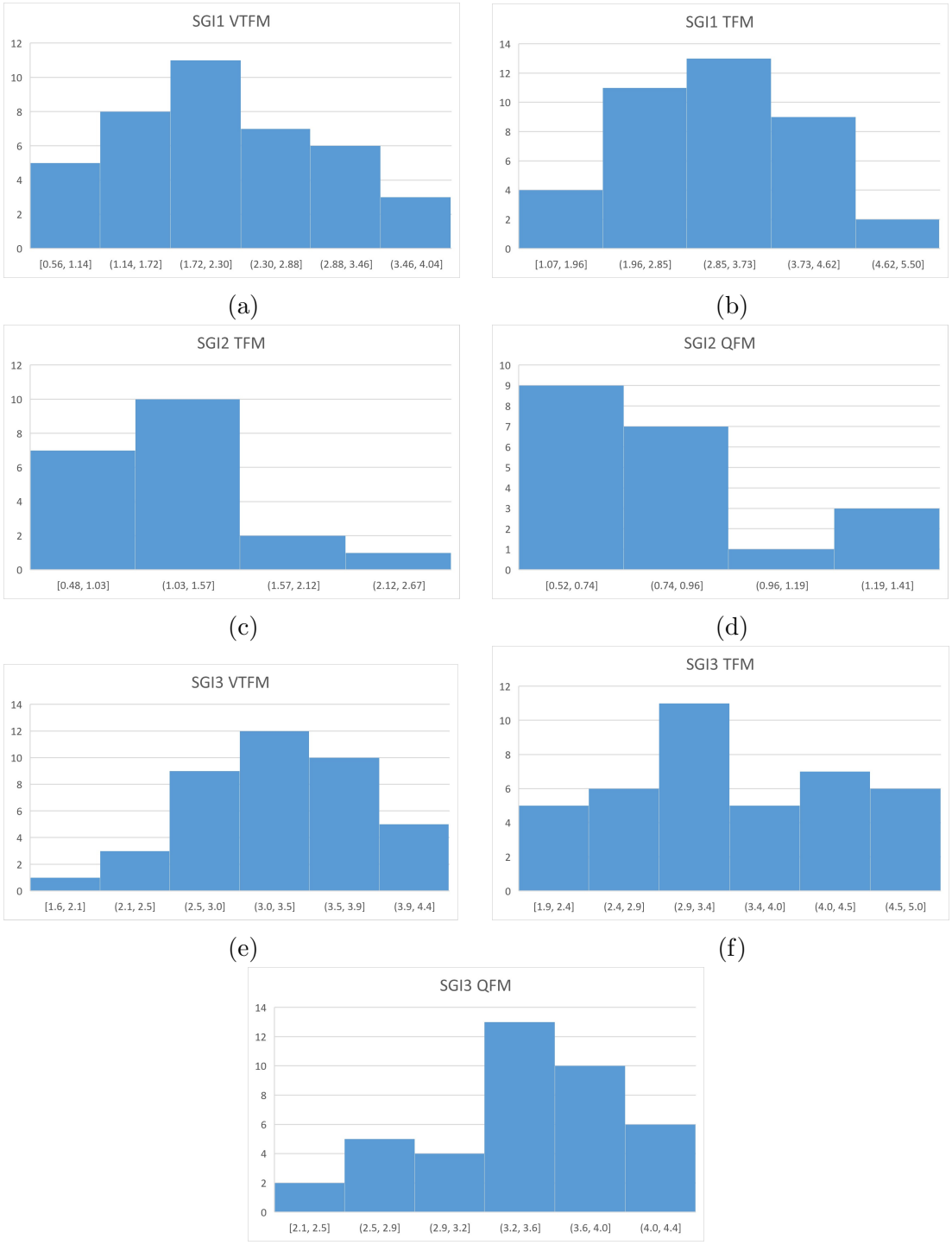


Figure 5.11: Separate histograms for %El. data showed the trend of positive skewness. The x-axis represent the range of bins in %El (pct.), and the y-axis represents the number of data points in each bin

low side of the spectrum. This was a result of the brittle nature of SGI grade 700/2 compared to SGI 500/7. Moreover, the distribution of SGI2 QFM had less spread than SGI2 TFM, but exhibited lower %El. values. For SGI1 data sets, SGI1 VTFM and SGI1 TFM, the Gaussian distribution showed a clear lag of VTFM %El. data from TFM %El. data. The remaining data set distributions (SGI3 VTFM, SGI3 TFM and SGI3 QFM) illustrated that SGI3 %El. values were higher than SGI1 and SGI2 %El. data. But the same data set distributions and SGI1 TFM distribution were almost entirely overlapping with slight differences in their spreads. Thus, the Student's t-test was carried out between the comparable data sets to ensure there was a significant difference between them.

The results of the Student's t-test are in table 5.6. For SGI1 and SGI3 the data sets showed a significant difference with T values of 4.9 and 3.1, respectively. Moreover, both P values were < 0.05 which meant rejecting the null hypothesis and concluding that the difference between the group means were statistically significant. On the other hand, the Student's t-test for the SGI3 data sets resulted in low T values, ranging from 0.17 to 1.36. With P values higher than the significant level of 0.05, the null hypothesis cannot be rejected, and it could not be concluded that the difference between the means was statistically significant.

Two Samples		T Value	P Value
SGI1 VTFM	SGI1 TFM	4.9	0
SGI2 TFM	SGI2 QFM	3.1	0.005
SGI3 VTFM	SGI3 TFM	0.9	0.366
SGI3 VTFM	SGI2 QFM	1.36	0.178
SGI3 TFM	SGI2 QFM	0.17	0.863

Table 5.6: Student's t-test results for SGI %El. data

The Anderson-Darling test was used to test the fit of the %El. data sets against the normal, log-normal, 2-parameter and 3-parameter Weibull distribution, to determine the best fitting distribution. The criteria is, the lowest the resulting AD score the better the goodness of fit, but taking in consideration the aims in section 5.1.1. From the results in table 5.7, the 2-parameter Weibull had the same score as the normal and the 3-parameter Weibull for SGI1 TFM. SGI1 VTFM had the

lowest and the same AD score for the 2-parameter and 3-parameter Weibull. Thus, the 2-parameter Weibull distribution was used to compare the %El. data in SGI1. In the case of SGI2 TFM data, the 2-parameter Weibull and the normal distributions had the lowest AD scores. For SGI2 QFM, the 3-parameter Weibull AD score was much lower than the rest of the distributions, with the lowest difference = 0.3. To follow to the literature, the 2-parameter Weibull distribution was used for comparison. But if the SGI2 QFM %El. data set had $R^2 < R^2_{0.05}$, the 3-parameter Weibull distribution will be used. For SGI3 VTFM and SGI3 TFM, the 2-parameter Weibull had the same AD score as the normal and the 3-parameter Weibull. As for SGI3 QFM, the 2-parameter Weibull had the second lowest score, with the lowest score going to the 3-parameter Weibull. As the two scores were close in value, the 2-parameter distribution was used to compare between SGI3 %El. data data sets. The AD probability plots for of all the data sets are shown in figures 5.12 to 5.18.

•	Normal	2-Parameter Weibull	3-Parameter Weibull	Log-normal
SGI1 VTFM	0.7	0.6	0.6	0.9
SGI1 TFM	0.5	0.5	0.5	0.9
SGI2 TFM	1.1	1.1	1.4	1.2
SGI2 QFM	1.7	1.6	0.9	1.2
SGI3 VTFM	0.6	0.6	0.6	0.8
SGI3 TFM	0.6	0.6	0.6	0.7
SGI3 QFM	1.1	0.7	0.5	1.8

Table 5.7: Anderson-Darling test results for SGI %El. values

5.1.3 Weibull distribution analysis for SGI UTS and El data

According to the outcome of the AD test, the 2-parameter Weibull distribution was used to evaluate and compare the UTS data. As for the %El. data, the 2-parameter was used for all data sets except SGI2. The 3-parameter Weibull distribution was used for SGI2. For each separate melt (SGI1, SGI2 and SGI3), the UTS and %El. data from the different filling modes were plotted and compared. To evaluate the effect of the filling modes on the tensile properties, reproducibility and reliability of SGI castings, the data from SGI1 and SGI3 were combined as they belonged to the

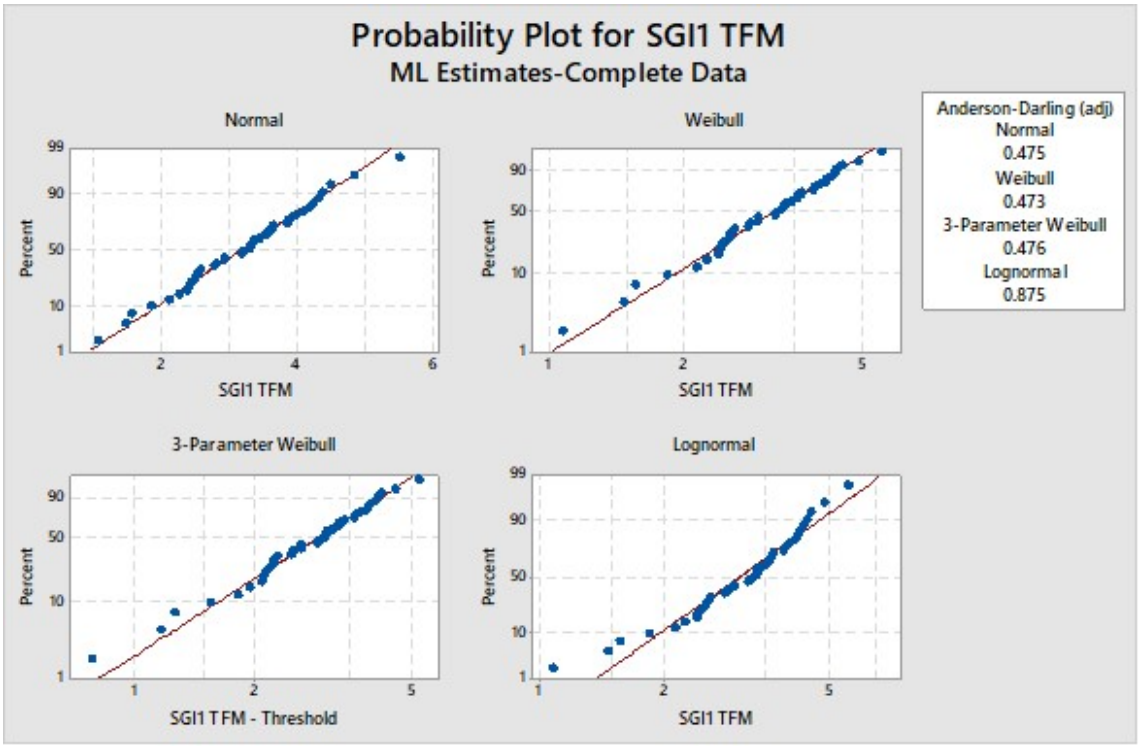


Figure 5.12: Probability plots for AD test for SGI1 TFM %El. The y-axis represents the cumulative probability in percent. The x-axis represents the %El in pct., except for the 3-parameter Weibull plot, it is the threshold value in pct.

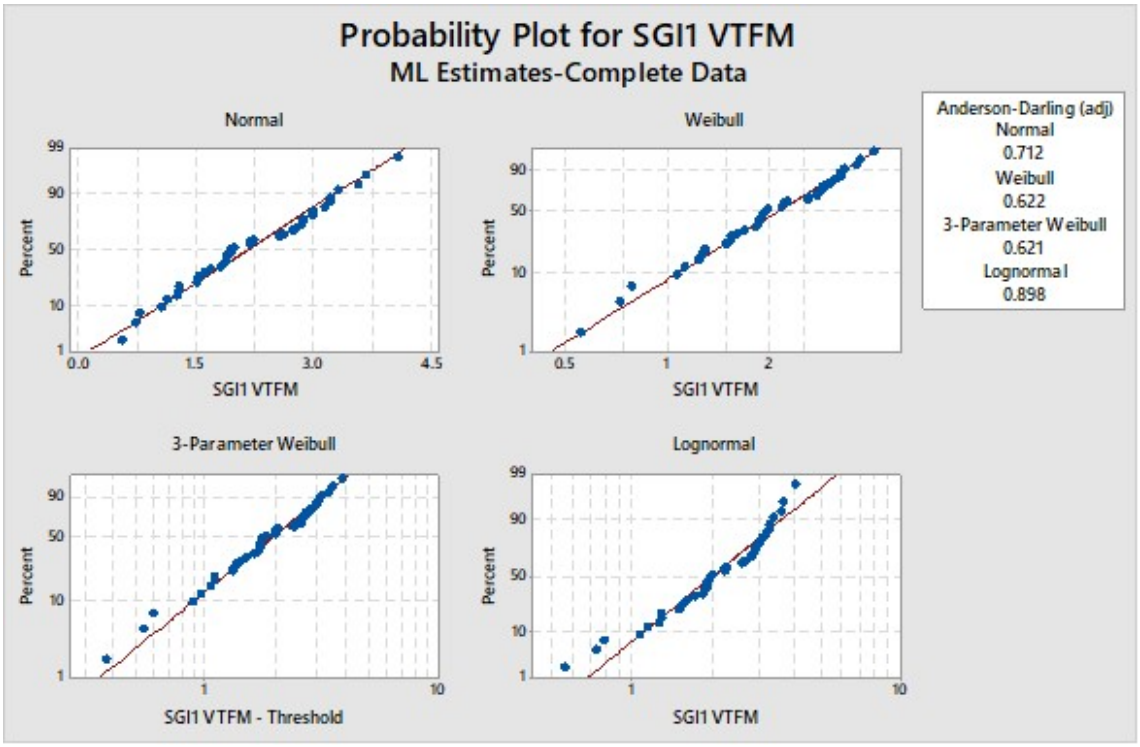


Figure 5.13: Probability plots for AD test for SGI1 VTFM %El. The y-axis represents the cumulative probability in percent. The x-axis represents the %El in pct., except for the 3-parameter Weibull plot, it is the threshold value in pct.

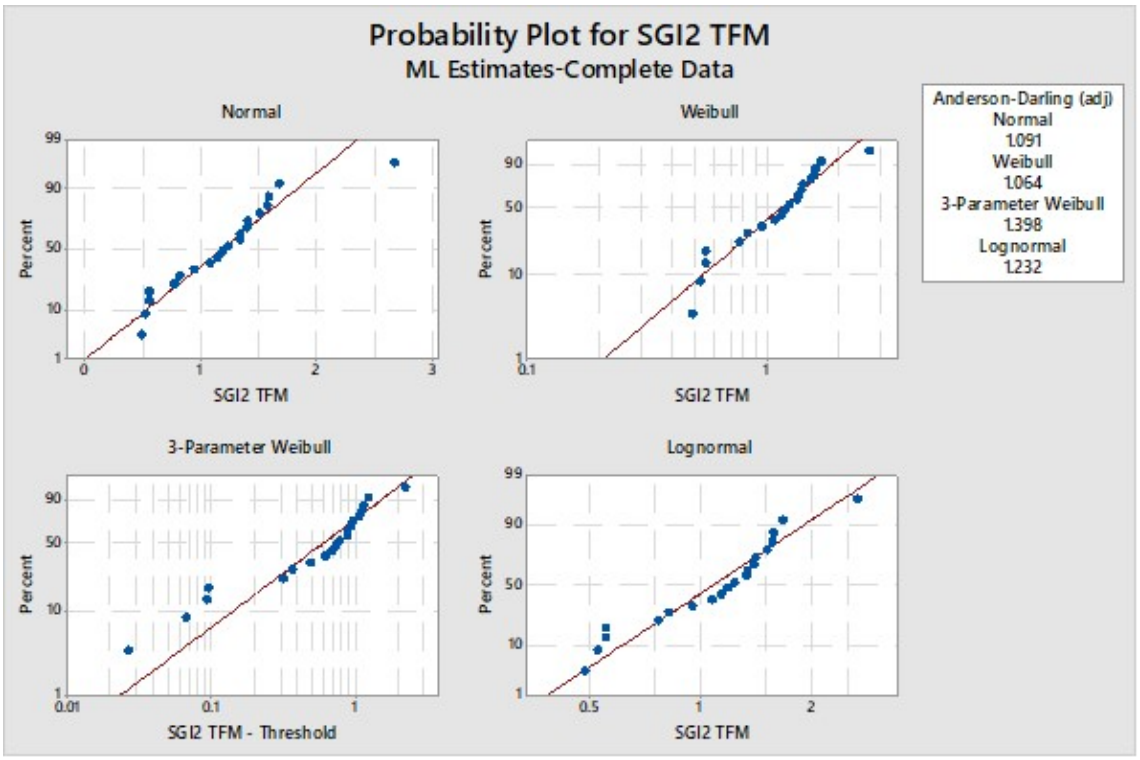


Figure 5.14: Probability plots for AD test for SGI2 TFM %El. The y-axis represents the cumulative probability in percent. The x-axis represents the %El in pct., except for the 3-parameter Weibull plot, it is the threshold value in pct.

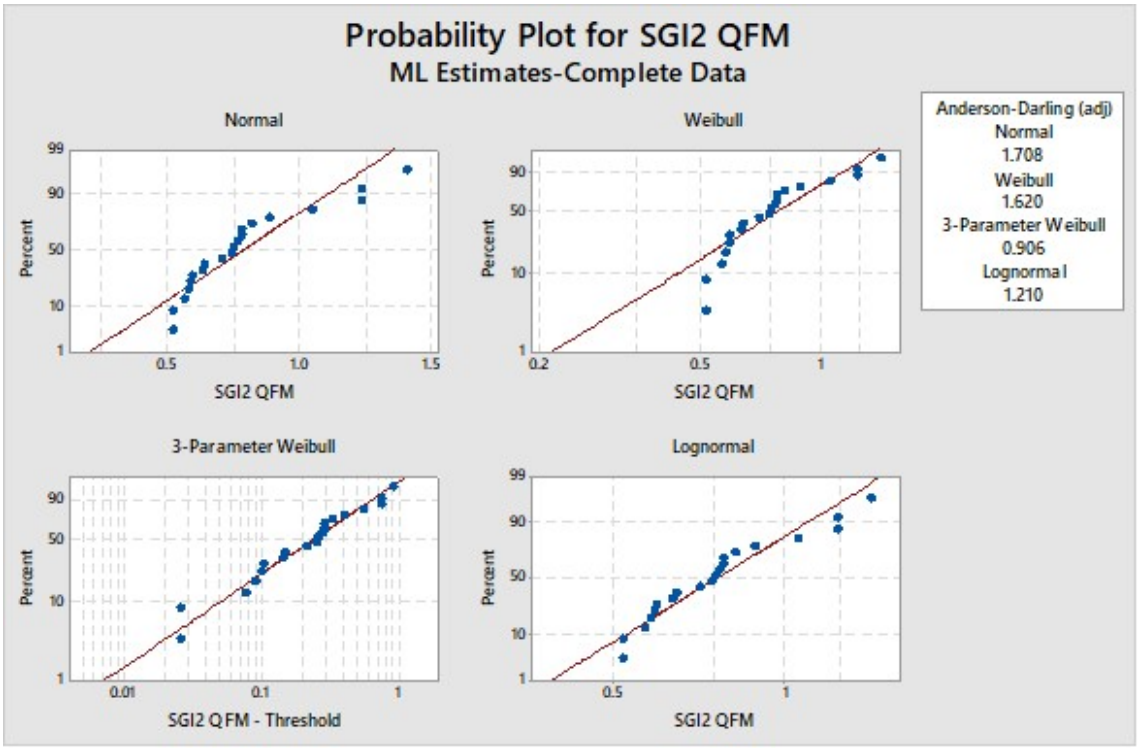


Figure 5.15: Probability plots for AD test for SGI2 QFM %El. The y-axis represents the cumulative probability in percent. The x-axis represents the %El in pct., except for the 3-parameter Weibull plot, it is the threshold value in pct.

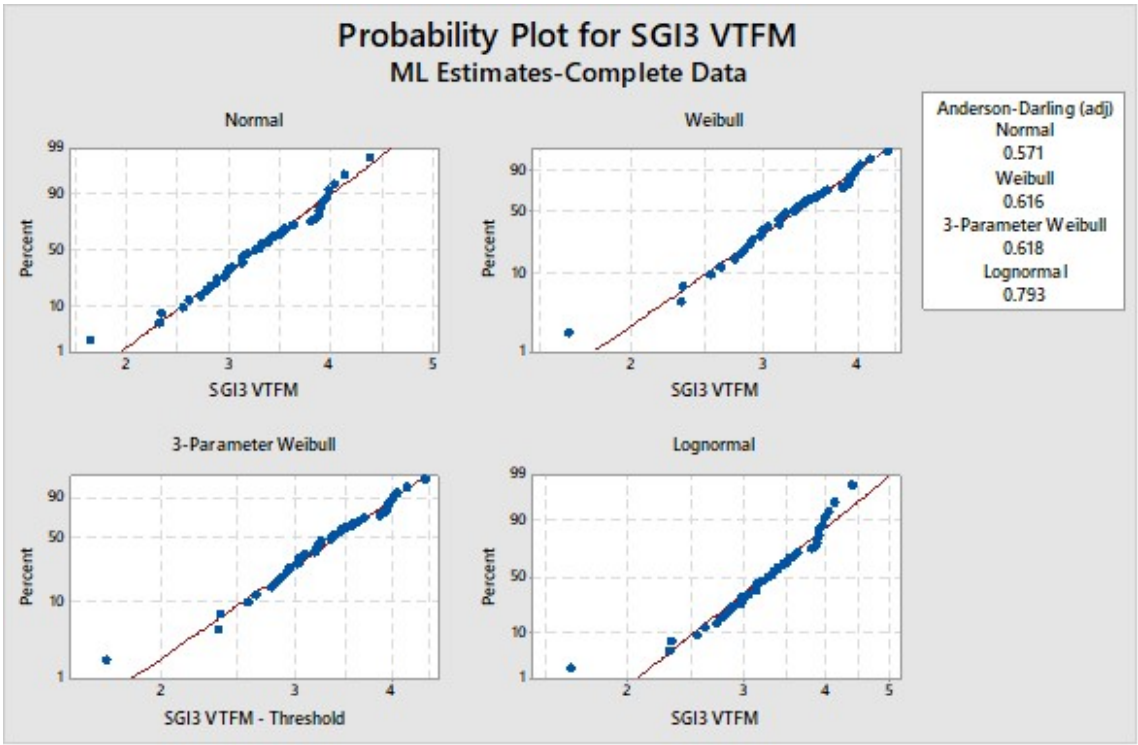


Figure 5.16: Probability plots for AD test for SGI3 VTFM %El. The y-axis represents the cumulative probability in percent. The x-axis represents the %El in pct., except for the 3-parameter Weibull plot, it is the threshold value in pct.

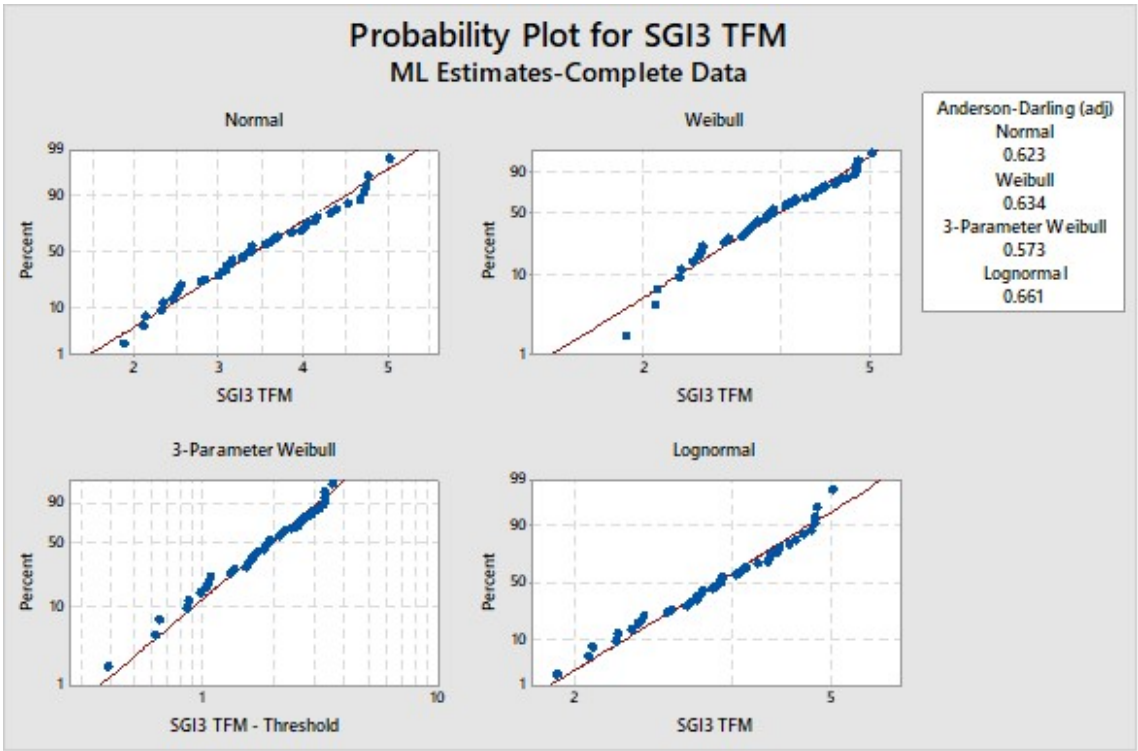


Figure 5.17: Probability plots for AD test for SGI3 TFM %El. The y-axis represents the cumulative probability in percent. The x-axis represents the %El in pct., except for the 3-parameter Weibull plot, it is the threshold value in pct.

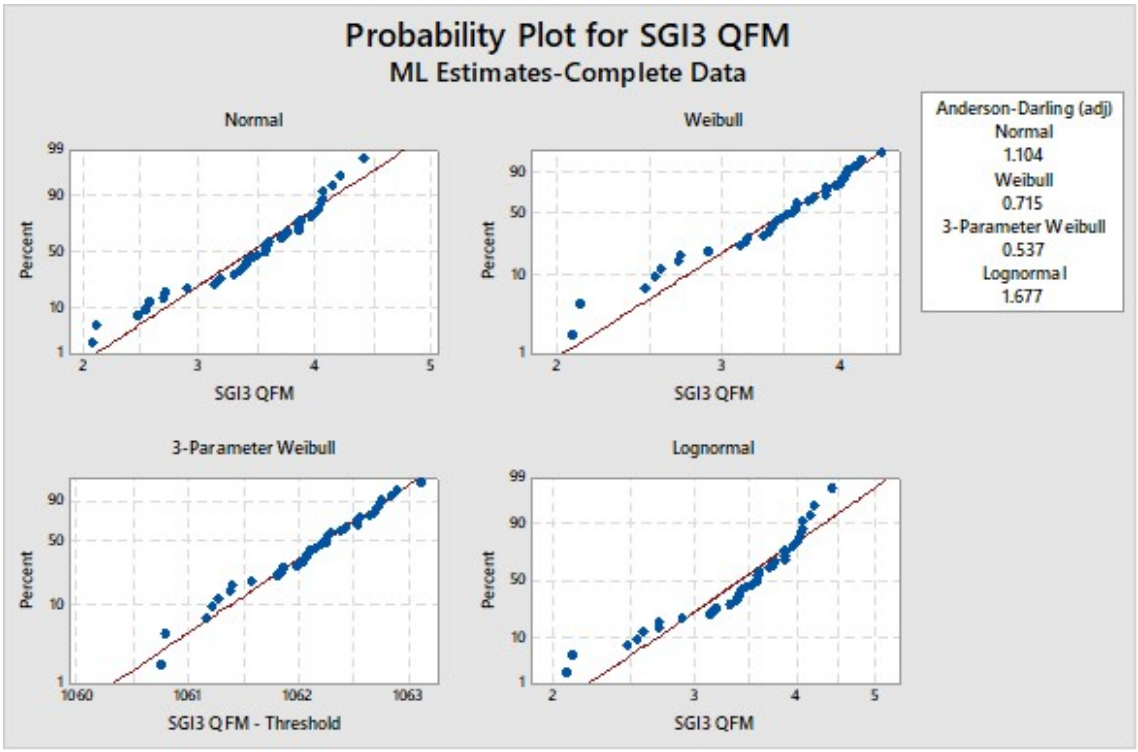


Figure 5.18: Probability plots for AD test for SGI3 QFM %El. The y-axis represents the cumulative probability in percent. The x-axis represents the %El in pct., except for the 3-parameter Weibull plot, it is the threshold value in pct.

same grade (SGI 500/7). The combined data sets were denoted VTFM, TFM and QFM. Then UTS and %El. data were plotted and compared once more. A table for the summary of results precedes each Weibull probability plot.

Figure 5.19 is the 2-parameter Weibull probability plot for SGI1 UTS data, with 40 data points in each group, and table 5.8 is the summary of the results. Both SGI1 VTFM and SGI1 TFM data sets showed a good fit to the 2-parameter Weibull distribution, as expected, with $R^2 > R^2_{0.05}$. SGI1 TFM had the higher Weibull modulus of 22 compared to 13 for SGI1 VTFM, equating to a 70% increase. SGI1 TFM also had a higher scale parameter of 783 MPa compared to 722 MPa for SGI1 VTFM.

Melt/Filling Mode	n	m	scale (MPa)	R^2	$R^2_{0.05}$
SGI1 VTFM	40	13	722	0.99	0.93
SGI1 TFM	40	22	783	0.98	0.93

Table 5.8: Results of 2-prameter Weibull probability plot for SGI1 UTS values

The 2-parameter Weibull probability plot for the %El. data of SGI1 and its

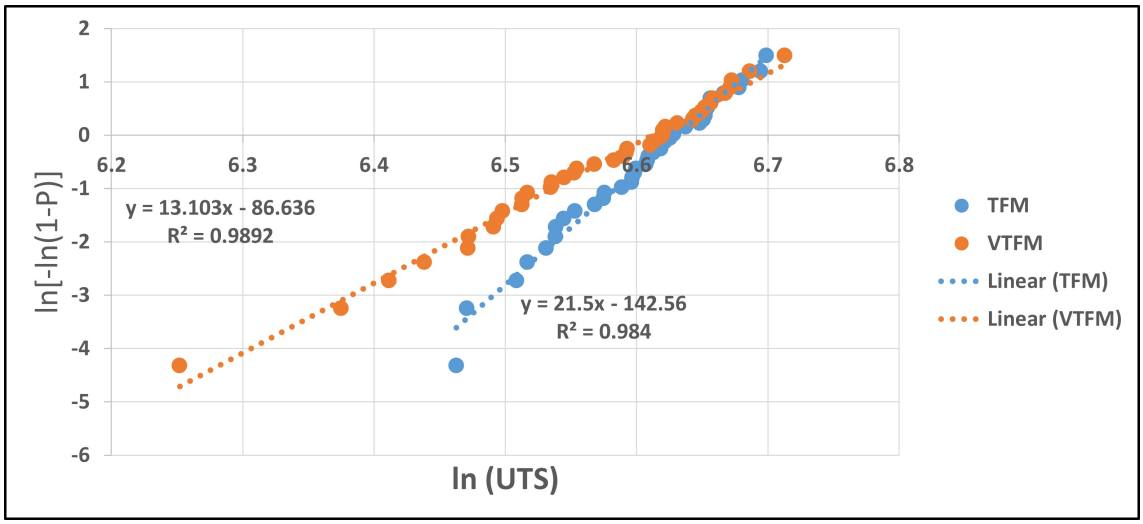


Figure 5.19: 2-prameter Weibull probability plot for SGI1 UTS data

summary of results are in figure 5.20 and table 5.9, respectively. The data sets had a good fit for the 2-Weibull distribution with $R^2 > R^2_{0.05}$. SGI1 TFM had a Weibull modulus of 3.6 which was higher than the 2.7 of SGI1 VTFM. This represented a 33% increase, compared to UTS values this was half the increased percentage. As for the scale parameter, SGI1 TFM was almost double that of SGI1 VTFM, with 3.5% and 1.8%, respectively.

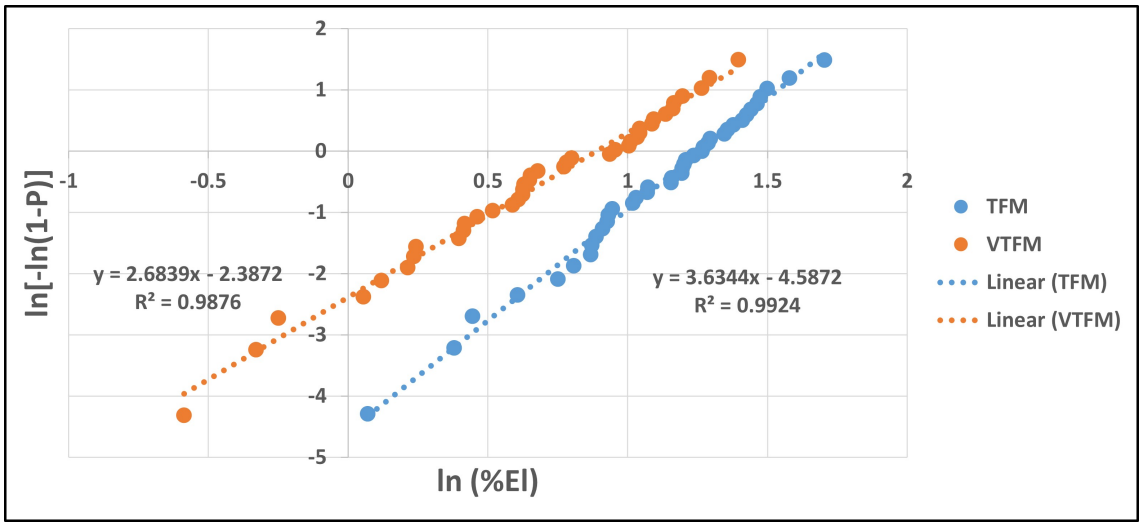


Figure 5.20: 2-prameter Weibull probability plot for SGI1 %El. data

In comparison to SGI1, SGI2 data analysis resulted in a less clear picture. The 2-parameter Weibull plot (fig 5.21 and table 5.10) showed SGI2 QFM had a higher Weibull modulus than SGI2 TFM, but with less significant difference than SGI1.

Melt/Filling Mode	n	m	scale	R^2	$R^2_{0.05}$
SGI1 VTFM	40	2.7	1.8	0.99	0.93
SGI1 TFM	39	3.6	3.5	0.99	0.93

Table 5.9: Results of the 2-parameter Weibull probability plot for SGI1 %El. values

The SGI2 QFM Weibull modulus was 22, for SGI2 TFM it was 17. The scale parameter for SGI2 TFM was 821 MPa and for SGI2 QFM it was 848 MPa, an increase of 3% . Both data sets had a good fit to the 2-parameter Weibull distribution with $R^2 > R^2_{0.05}$.

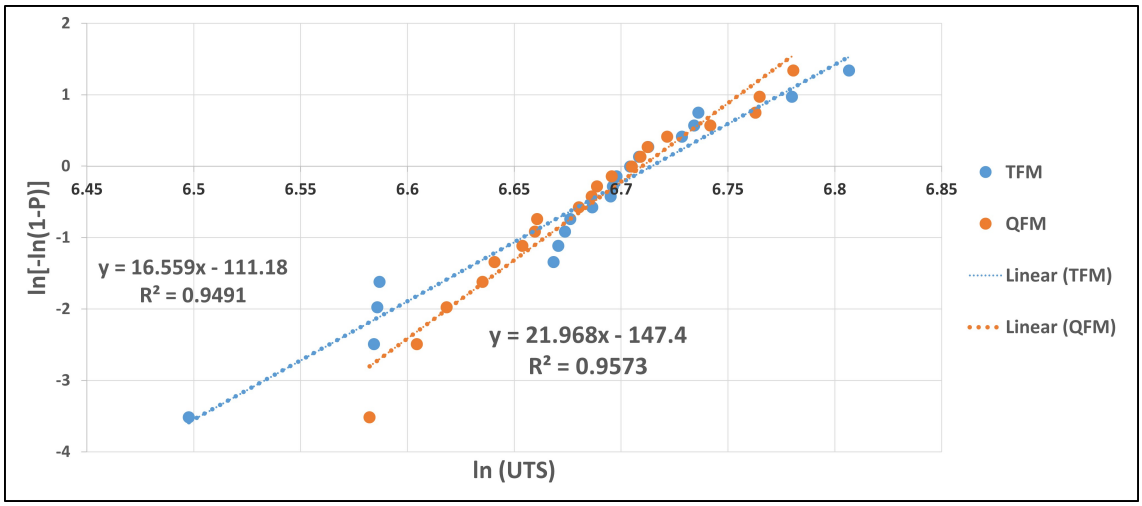


Figure 5.21: 2-prameter Weibull probability plot for SGI2 UTS data

Melt/Filling Mode	n	m	scale (MPa)	R^2	$R^2_{0.05}$
SGI2 TFM	20	17	821	0.95	0.89
SGI2 QFM	20	22	848	0.96	0.89

Table 5.10: Results of 2-parameter Weibull probability plot for SGI2 UTS data

In regards to the %El. data, the 2-parameter Weibull distribution was assumed for the two data sets. As seen from figure 5.22 and table 5.11 SGI2 TFM had a good fit to the distribution ($R^2 > R^2_{0.05}$) but SGI2 QFM did not show a good fit. With $R^2 = 0.82$, it was far less than 0.89 for $R^2_{0.05}$. Even though SGI2 QFM did not follow a 2-parameter Weibull distribution, the Weibull modulus was recorded in order to draw a contrast between the results of the 2-parameter and 3-parameter Weibull plots. The 2-parameter distribution of SGI2 QFM had a Weibull modulus

of 3.8, higher than that of SGI2 TFM which was 2.6. On the other hand, the scale parameter for SGI2 QFM was lower than SGI2 TFM with values of 0.3 and 0.8, respectively. Note that when comparing between cast metals using Weibull plots, if the Weibull modulus was higher in one group, the scale parameter should follow suit. Hence, there was discrepancy in the results from the 2-parameter Weibull plot for %El. of SGI2, with one data set having a higher Weibull modulus (SGI2 QFM) and the other having a higher scale parameter (SGI2 TFM).

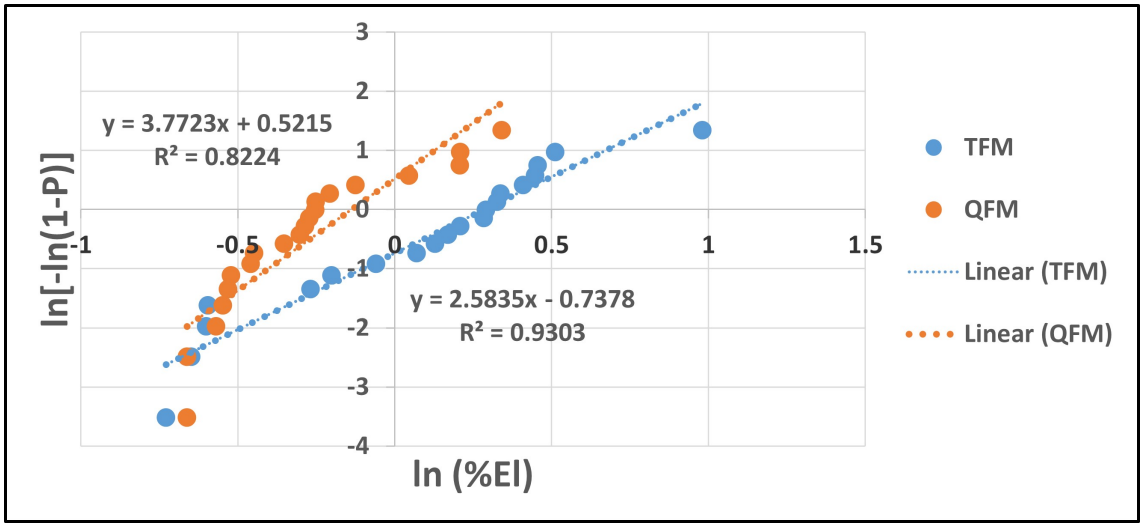


Figure 5.22: 2-prameter Weibull probability plot for SGI2 %El. data

Melt/Filling Mode	n	m	scale (pct)	R^2	$R^2_{0.05}$
SGI2 TFM	20	2.6	1.9	0.95	0.89
SGI2 QFM	20	3.8	1.3	0.82	0.89

Table 5.11: Results of 2-parameter Weibull probability plot for SGI2 %El. data

As a result of the poor fit of SGI2 QFM %El. data to the 2-parameter Weibull distribution, the 3-parameter Weibull distribution was used to evaluate SGI2 %El. data. Figure 5.23 is the 3-parameter Weibull probability plot for SGI2 QFM and SIG2 TFM %El. data. This showed SGI2 TFM Weibull modulus to be higher than that of SGI2 QFM (table 5.12). With SGI2 TFM m = 1.3 and SGI2 QFM m = 1.2, this was an opposite result to the 2-parameter Weibull plot. This could be due to the fact that SGI2 QFM data had a better fit to the 3-parameter Weibull distribution, thus the result was portrayed more accurately. This accuracy could

be detected from the values of the scale parameters. Unlike the results from the 2-parameter Weibull plot, they actually follow the same behaviour as the Weibull modulus. SGI2 TFM had a higher scale parameter, 0.8, than the 0.3 from SGI2 QFM. In addition, the 3-parameter Weibull distribution incorporates an additional parameter, the threshold, this parameter adjusts the sensitivity of the Weibull function to increase the goodness of fit, which gives more representative values of the parameters.

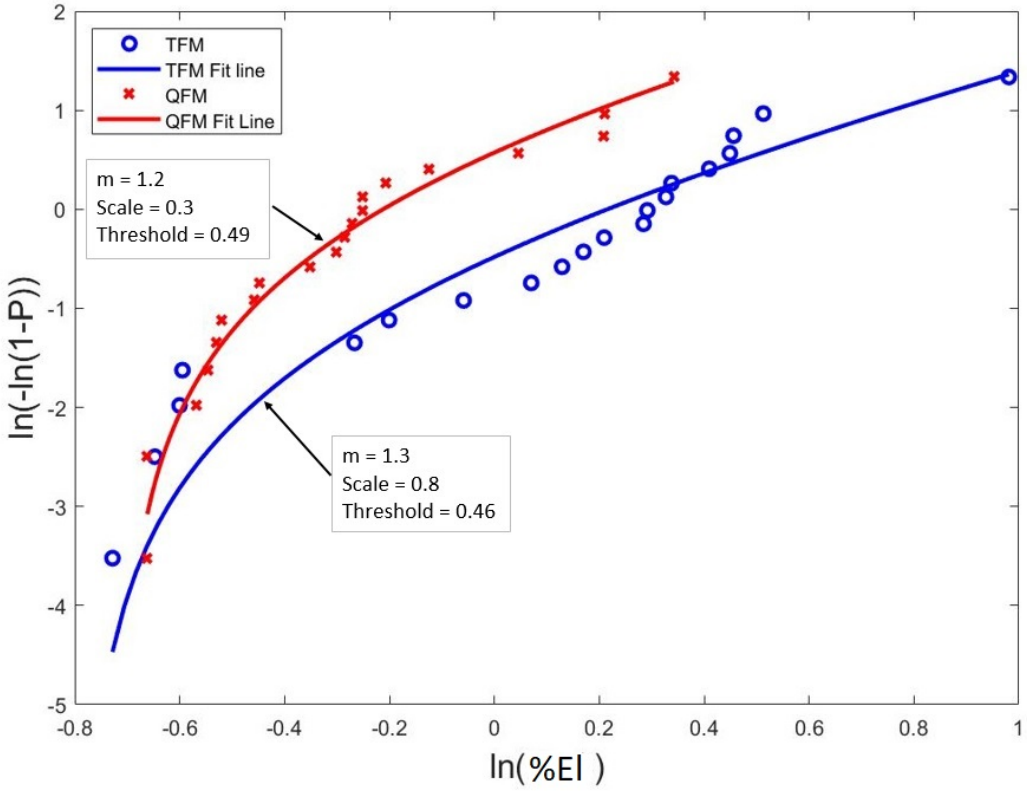


Figure 5.23: 3-prameter Weibull probability plot for SGI2 %El. data

Melt/Filling Mode	n	m	scale (pct)	threshold
SGI2 TFM	20	1.3	0.8	0.46
SGI2 QFM	20	1.2	0.3	0.49

Table 5.12: Results of 3-parameter Weibull probability plot for SGI2 %El. data from the two different filling modes

SGI3 2-parameter Weibull probability plot (figure 5.24) compared the three types of filling modes at once. The three data sets displayed a good fit for the distribution with $R^2 > R^2_{0.05}$. SGI3 QFM had the highest Weibull modulus of m = 50. SGI3

TFM and SGI3 VTFM had a considerably lower Weibull moduli of 32 and 36, respectively. The scale parameter values also mirrored the same behaviour of the Weibull modulus. With the highest value of 782 MPa for SGI3, succeeded by SGI3 VTFM with 767 MPa and SGI3 TFM with 756 MPa (table 5.13).

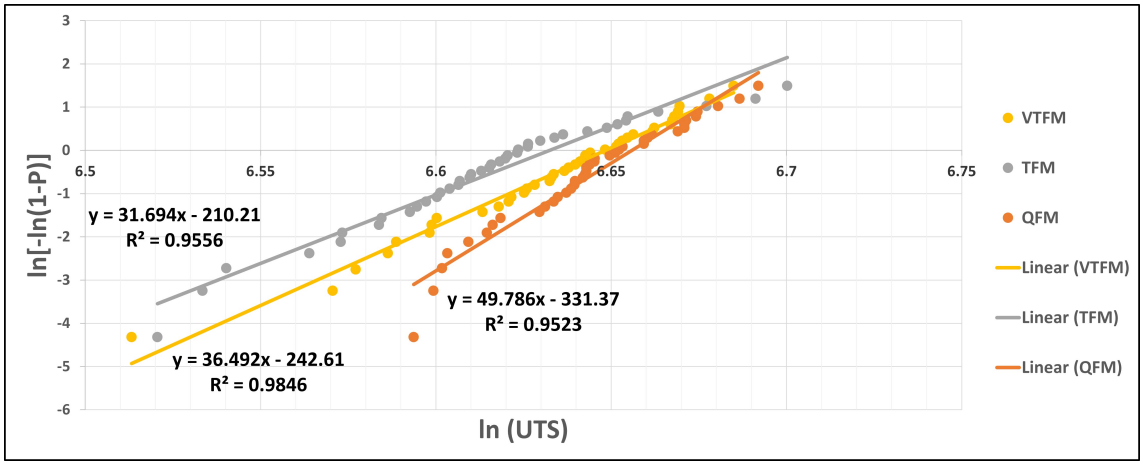


Figure 5.24: 2-prameter Weibull probability plot for SGI3 UTS data

Melt/Filling Mode	n	m	scale (MPa)	R^2	$R^2_{0.05}$
SGI3 VTFM	40	36	767	0.99	0.93
SGI3 TFM	40	32	756	0.96	0.93
SGI3 QFM	40	50	782	0.95	0.93

Table 5.13: Results of 2-parameter Weibull probability plot for SGI3 UTS data

From figure 5.25 and table 5.14 the data for SGI3 %El. followed the same behaviour as the UTS data. SGI3 QFM had the highest Weibull modulus and scale parameter with 7 and 3.9, respectively. Then followed SGI3 VTFM with a Weibull modulus of 6 and a scale parameter of 3.6, and finally the lowest values were for SGI3 TFM with m = 3.4 and a scale parameter = 3.4. Even though the %El. data followed the same behaviour as the UTS data, showing a significantly lower sensitivity to different filling modes. That was apparent from the small difference in the Weibull modulus between SGI3 VTFM and SGI3 TFM compared to SGI3 QFM.

To obtain a clear understanding of the effect of filling modes on the tensile properties, reproducibility and reliability of SGI castings, the data from SGI1 and SGI3 were combined due to their similar grade (SGI 500/7). The combined data

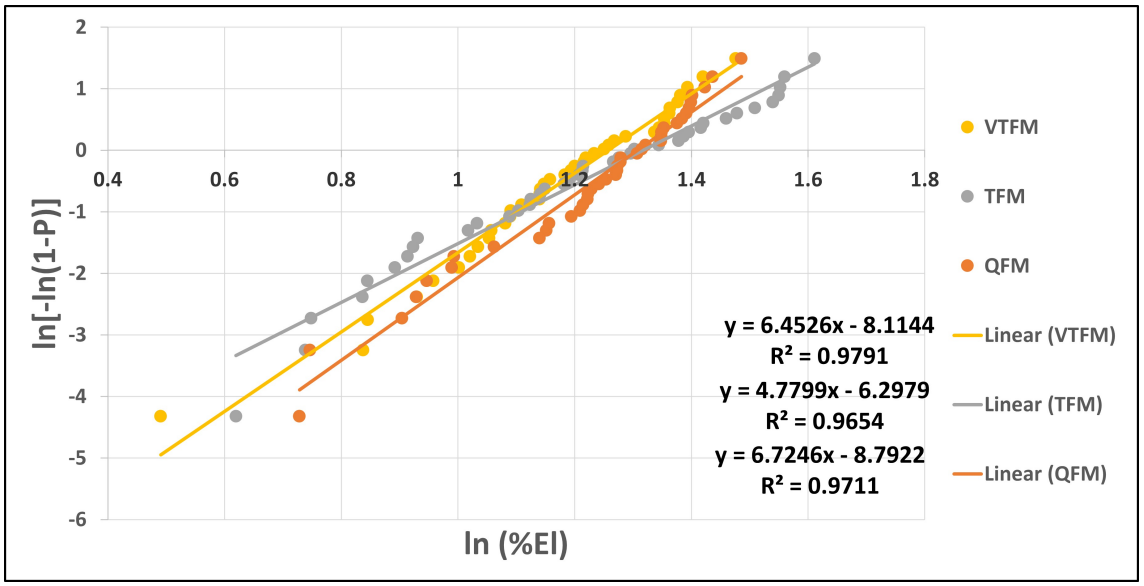


Figure 5.25: 2-parameter Weibull probability plot for SGI3 %El. data

Melt/Filling Mode	n	m	scale (pct)	R^2	$R^2_{0.05}$
SGI3 VTFM	40	6	3.6	0.98	0.93
SGI3 TFM	40	5	3.4	0.97	0.93
SGI3 QFM	40	7	3.9	0.97	0.93

Table 5.14: Results of 2-parameter Weibull probability plot for SGI3 %El. data

groups were denoted VTFM, TFM and QFM, and plotted once more with their descriptive statics in table 5.15. The 2-parameter Weibull plot for UTS data is in figure 5.26 and the summary of the results are in table 5.16. All data sets had a good fit to the 2-parameter distribution with $R^2 > R^2_{0.05}$. The 2-parameter Weibull plot revealed that with the reduction in surface turbulence the Weibull modulus increased significantly. From m = 16 for VTFM, to m = 26 for TFM, and finally m doubled to 50 for QFM. The scale parameter followed suit, from 756 MPa for VTFM, then a slight increase to 764 MPa for TFM, and finally a larger increase to 797 MPa for QFM.

Variable	Total Count	Mean	StDev	Variance	Minimum	Maximum	Range
SGI VTFM	80	734	56	2901	519	823	304
SGI TFM	80	745	36	1294	641	813	172
SGI QFM	40	769	19	355	730	806	75

Table 5.15: Descriptive statistics of the combined SGI1 and SGI3 UTS (MPa) values

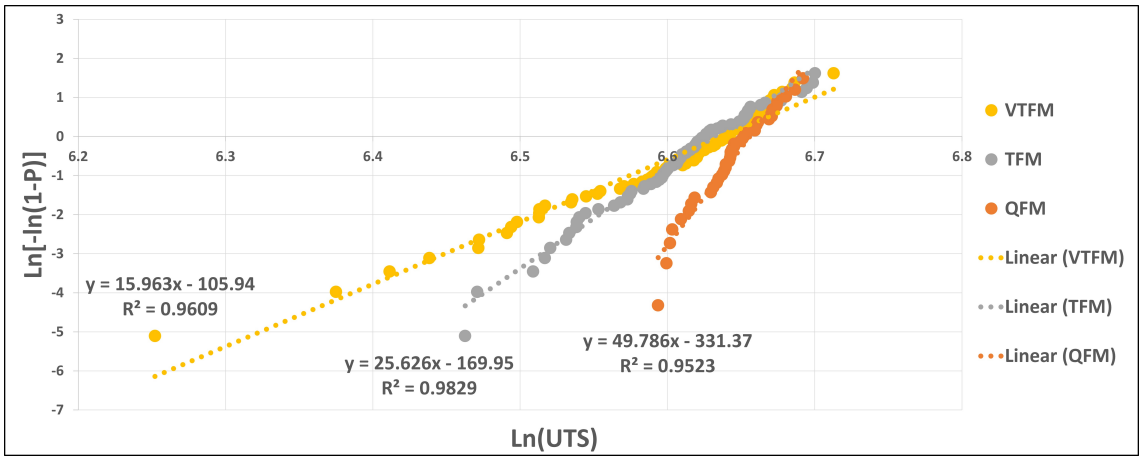


Figure 5.26: 2-prameter Weibull probability plot for SGI UTS (MPa) data

Filling Mode	n	m	scale (MPa)	R^2	$R^2_{0.05}$
VTFM	80	16	756	0.96	0.95
TFM	80	26	764	0.98	0.95
QFM	40	50	797	0.95	0.93

Table 5.16: Results of 2-parameter Weibull probability plot for SGI UTS data

When %El. data from SGI1 and SGI3 were combined, their descriptive statistics in table 5.17, the effect of the filling modes was also more apparent, and followed the UTS behaviour. The 2-parameter Weibull plot (fig 5.27) showed that with the reduction in surface turbulence the Weibull modulus increased. From m = 2.9 for VTFM, to m = 4.1 for TFM, and m = 6.7 for QFM. The scale parameter was the same for VTFM and TFM = 3.2, but increased to 3.7 MPa for QFM (table 5.18). The 2-parameter Weibull distribution of SGI3 %El. data showed a good fit to the distribution with $R^2 > R^2_{0.05}$.

Variable	Total Count	Mean	StDev	Variance	Minimum	Maximum	Range
SGI VTFM	80	2.7	0.9	0.8	0.6	4.4	3.8
SGI TFM	79	3.3	0.9	0.8	1.1	5.5	4.4
SGI QFM	40	3.5	0.6	0.3	2.1	4.4	2.3

Table 5.17: Descriptive statistics of the combined SGI1 and SGI3 %El. (pct.) values

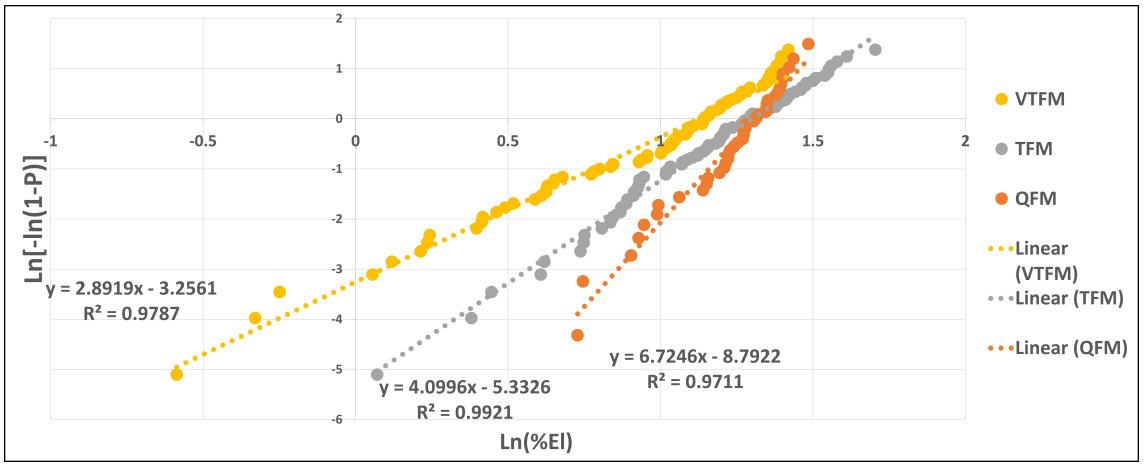


Figure 5.27: 2-prameter Weibull probability plot for SGI %El. (pct) data

Filling Mode	n	m	scale (pct)	R^2	$R^2_{0.05}$
VTFM	80	2.9	3.2	0.98	0.95
TFM	79	4.1	3.2	0.99	0.95
QFM	40	6.7	3.7	0.97	0.93

Table 5.18: Results of 2-prameter Weibull probability plot for SGI %El. data

5.2 Microscopy analysis of SGI fracture surfaces

5.2.1 Optical microscopy of fracture surfaces

Examining the SGI testbars' fracture surfaces with optical microscopy revealed several defects that was the source of failure. The defects can be grouped into two types depending on their appearance. The first type of defects (see figure 5.28) were a dull black thick films found symmetrically on both sides of the fracture surfaces (bifilms). The films were easily recognized by the naked eye and mostly occupied a considerable part of a fracture surface area. In the highest incidence, the film occupied 25% of the fracture surface, seen in the bottom image in figure 5.28. In the lowest incidence, the film occupied less than 1% of the area of the fracture surface (figure 5.31). The first type of defect was mostly found on the fracture surfaces of test bars cast with surface turbulence (i.e. TFM and VTFM). Only one was found in QFM test bars, and it was the defect with the smallest surface area (figure 5.31). It had a length of 1 mm and a width of 0.25 mm. Closer view of the first type of defects, seen in figure 5.30, it shows the thick and creased film topography of the

defect.

Another defect found symmetrically on both sides of the fracture surfaces is shown in figure 5.32 and was only observed in two testbars that were cast in QFM. The two testbars came from the same mould. The defect resembled the first type as it was a dark thick corrugated film, but its surface was shiny rather than dull. It was easily identified with the unaided eye as it was black and covered most of the fracture surface. Some areas of the defect had a corrugated black shiny film that had a length up to 5 mm, the other areas were dull. The defect was not the source of tensile failure as it was located in the upper grip section of the testbars.

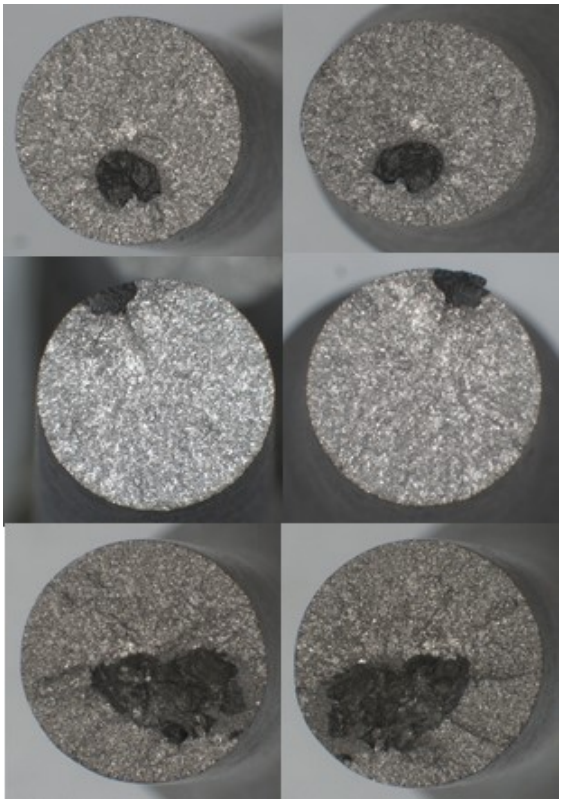
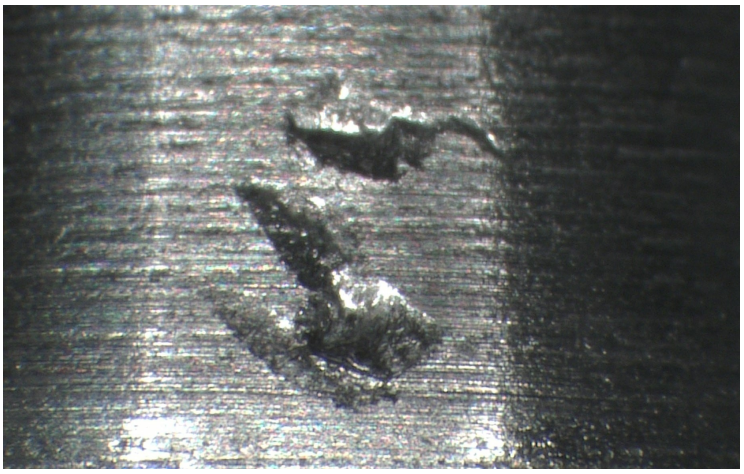


Figure 5.28: Optical images of the first type of defects found on SGI test bars fracture surfaces (diameter = 6.7 mm). The image shows the two sides of the fracture surfaces

The second type of defects found on SGI test bar fracture surfaces were also symmetrical on both sides of the fracture surfaces, but had a completely different appearance than the first type. Hence, separating and grouping the defects into two types was easily done using the naked eye. The second type of defects were identifiable due to their sharp contrast in color, which made them as apparent as



(a) The top bifilm dimensions L = 1.1 mm and W = 0.3 mm, and the bottom bifilm dimensions L = 1.3 and W = 0.3



(b) The bifilm dimensions L = 0.7 mm and W = 0.4 mm

Figure 5.29: Optical image of bifilm defects that were revealed by machining

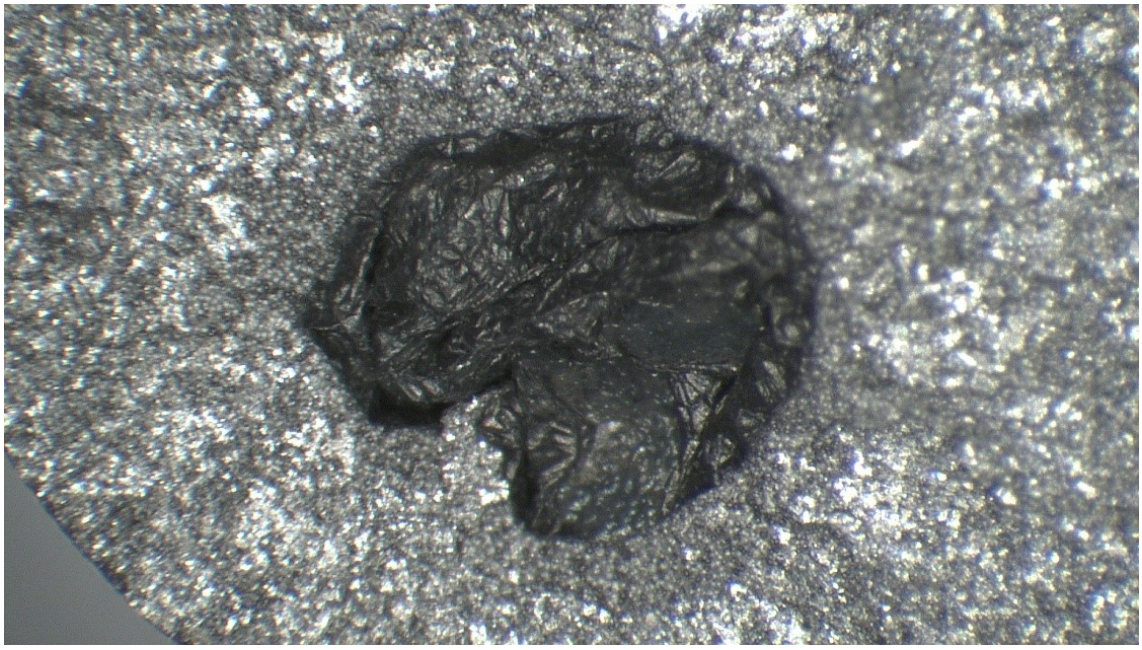


Figure 5.30: Optical image of the first type of defects revealed its film topography

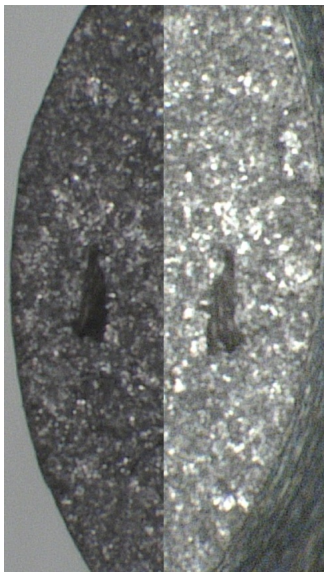
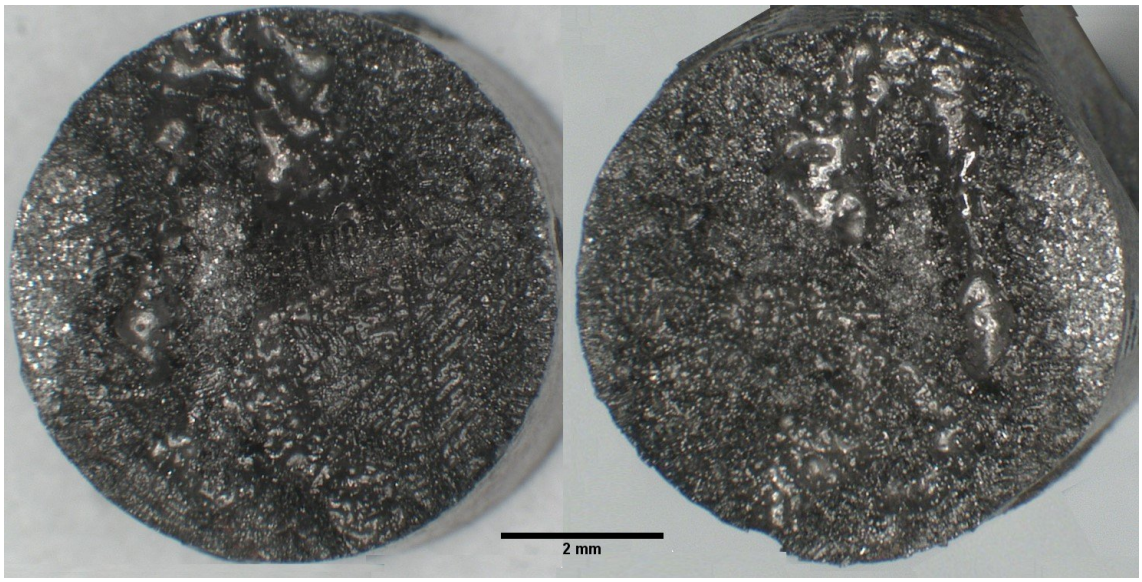


Figure 5.31: Optical image of the smallest double film defect (L = 1 mm, W = 0.25 mm)

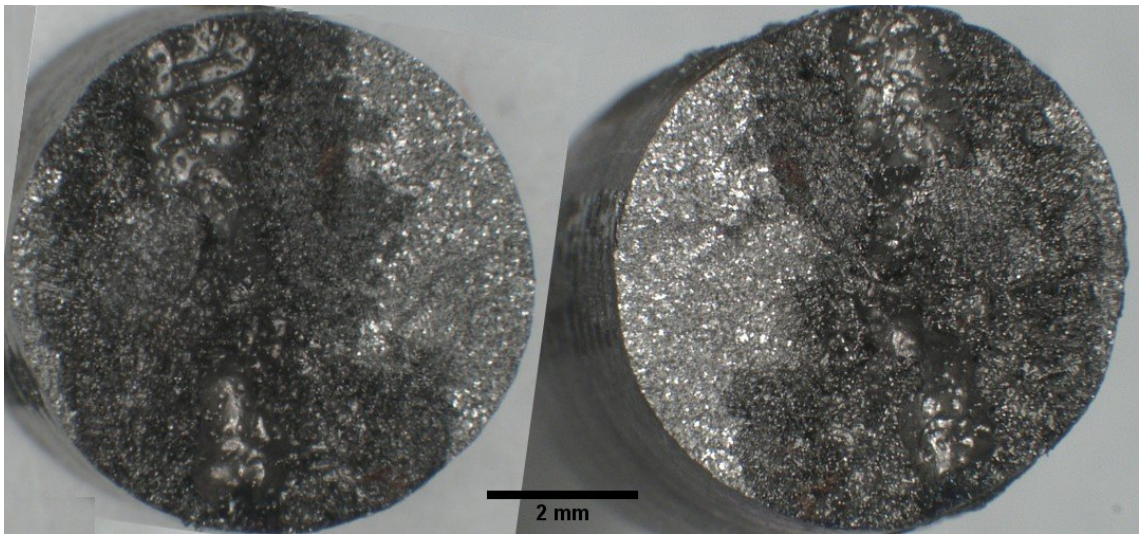
type one. The sharp contrast was attributed to the defect constituents. The defect had a small patch of bright surface, marked in figure 5.33, surrounded by a bigger dark patch. The two features made the testbar fracture surface look abnormal. In most cases the defect was located centrally on the fracture surface, as seen in the previous figure. In lesser cases the defect was towards the side of the fracture surface, as in figure 5.34. By magnifying the dark patch it was found that it comprised of high densities of spheroidal graphite (figure 5.34). As the magnification capability of the optical microscope used was limited, the nature of the bright areas could not be revealed, and SEM examination was needed.

5.2.2 SEM and EDX analysis of the fracture surfaces

Electron microscopy of the the first type of defects on SGI fracture surfaces confirmed the bifilm assumption made during the optical microscopy analysis. Moreover, it revealed the oxide nature of the bifilms. SGI oxide bifilms were found to be different in size, topography and entraining different extrinsic inclusions. In addition, lustrous carbon bifilms were also detected on SGI fracture surfaces. As to the second type of defects detected on SGI fracture surfaces, SEM and EDX revealed what seems to be a novel symmetrical defect which combines the appearance of bubble defect,



(a)



(b)

Figure 5.32: Optical image of a shiny thick black corrugated film found symmetrically on both sides of the fracture surfaces of the upper grip section of two testbars

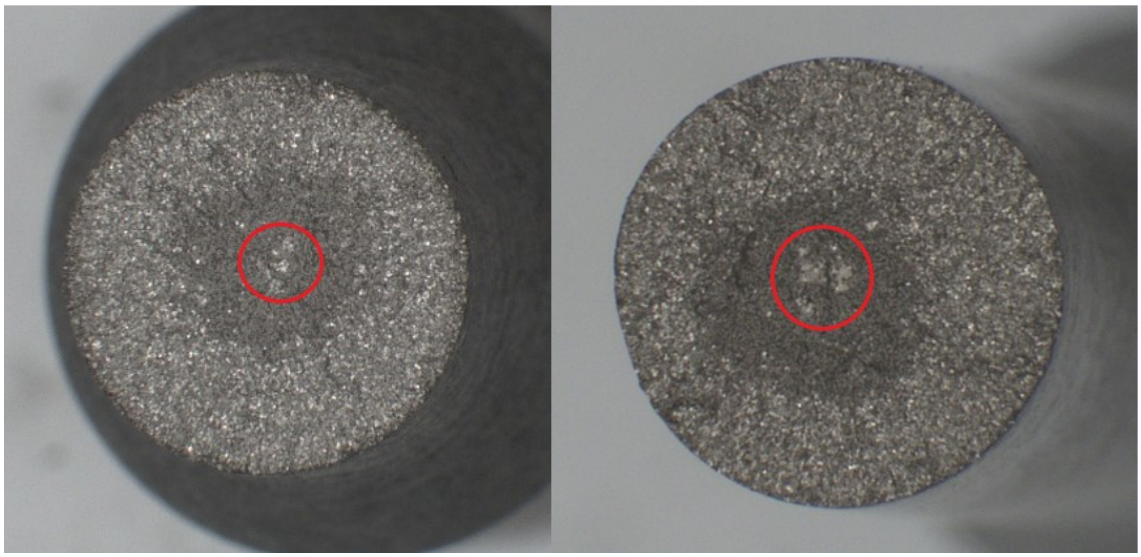


Figure 5.33: Optical image of the second type of defects

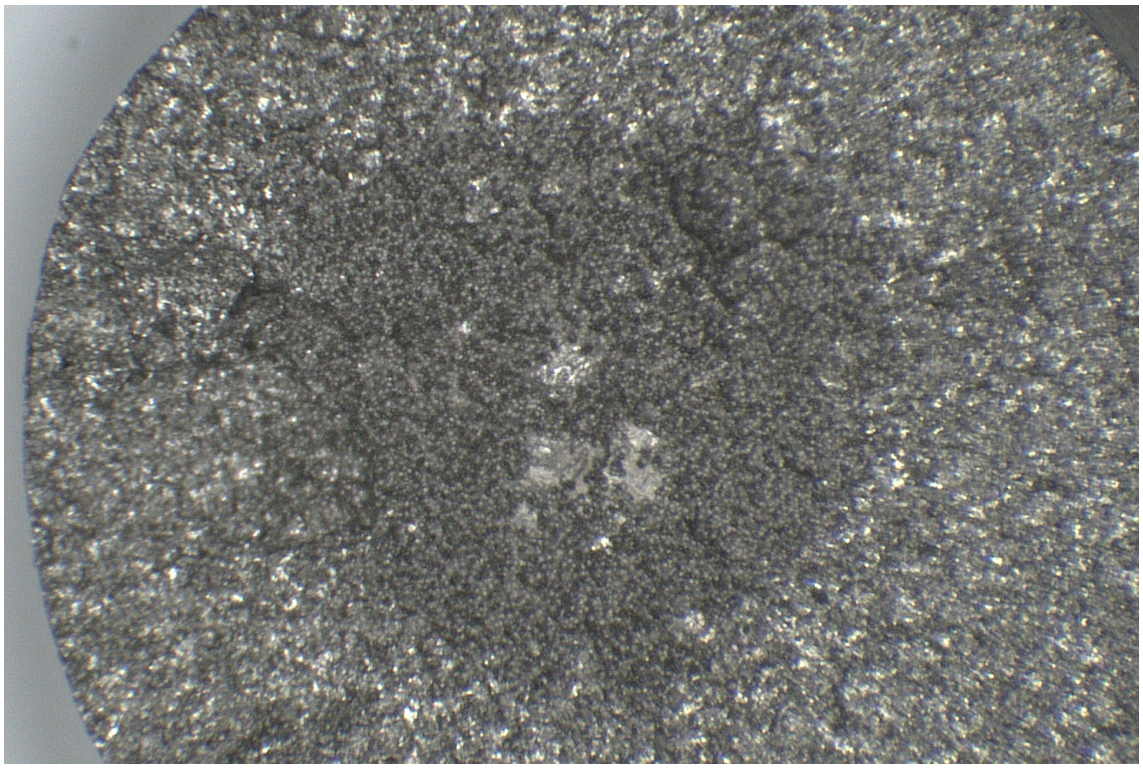


Figure 5.34: A closer view of the second type of defect revealed that the dark areas were dense clusters of spheroidal graphite

micro-shrinkage and plate defects. Finally, SEM and EDX examination revealed several casting defects that could be attributed to oxide bifilms.

Oxide bifilms

Figure 5.35 is a secondary electrons (SE) image of a small bifilm defect. Its dimensions were 500 µm in length, and at its widest it was 200 µm; this made it undetectable with the naked eye. The bifilm surface had a different topography than the surrounding pearlitic matrix and it contained folds. The back scattered electrons image (BSE), shown in figure 5.36, revealed the difference in the bifilm chemical composition compared to the rest of the matrix. The matrix was bright, because of the iron heavy, pearlite, and contained dark spheres of graphite, that made it easily distinguishable from the bifilm. The bifilm had a mostly dark surface with streaks of bright areas. This indicated that the bifilm consisted of light elements. EDX mapping of the bifilm showed the film consisted of 4 light elements (C, Si, Mg and O) and Fe, with the Mg and C prevalent over the whole area of the film (figure 5.37). The depth resolution of these elements couldn't be determined from EDX mapping as a result of the interaction volume of the electron beam.

A closer look at the film surface, (figure 5.38), revealed two types of surface textures, smooth swept surface and a more rugged granular one. In the higher magnification BSE image of the bifilm (figure 5.39) the smoother surface was bright, indicating heavier elements, and the rougher surface was dark, indicating lighter elements. This showed a correlation between bifilm topography and its chemical composition. The EDX analysis of area 1 against area 2, seen in figure 6.29, and summary of results are in table 5.19, showed area 1 had a high amount of C (75wt. %) and a low amount of Fe (11wt. %). The high amount of C explained the dark surface and contrast in BSE image. On the other hand, area 2 had a low amount of C (1.5wt. %) and high amount of Fe (1.5wt. %), and this explained the brightness in the BSE image. The amount of Mg in both locations were almost similar, only $\backsim$1wt. % difference. The difference amount of O between area 1 and 2 was $\backsim$5wt.%

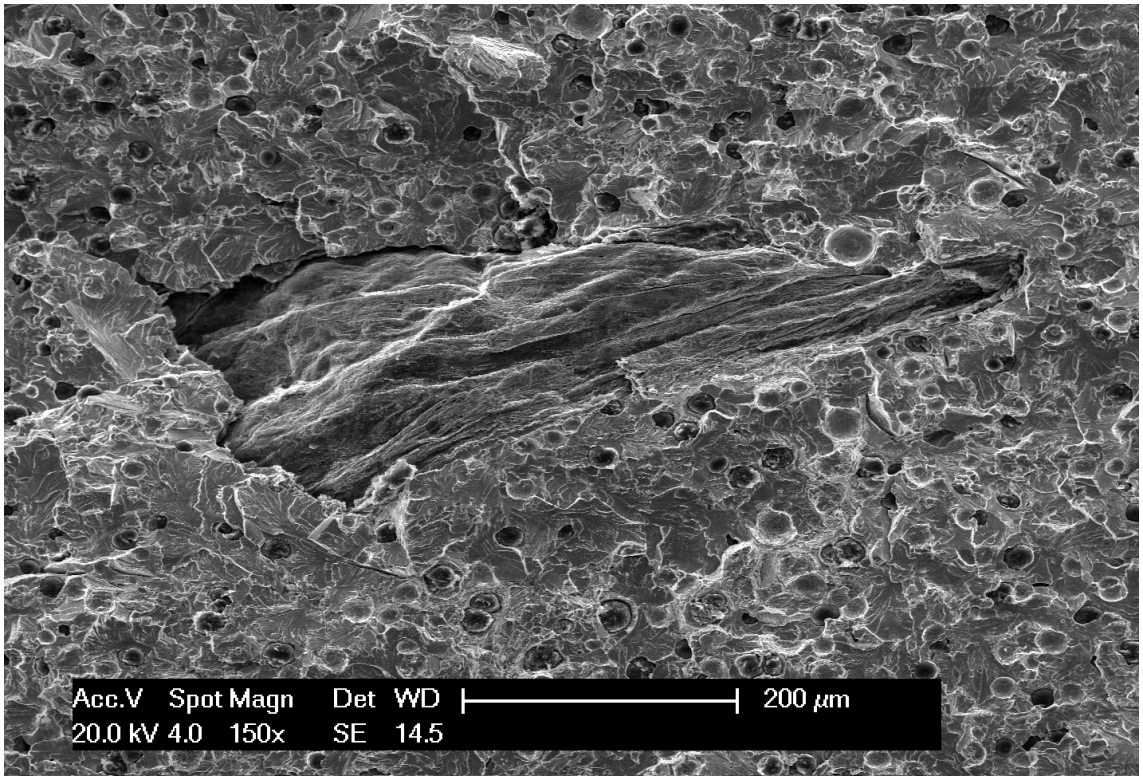


Figure 5.35: SE image of a small bifilm found on an SGI testbar fracture surface

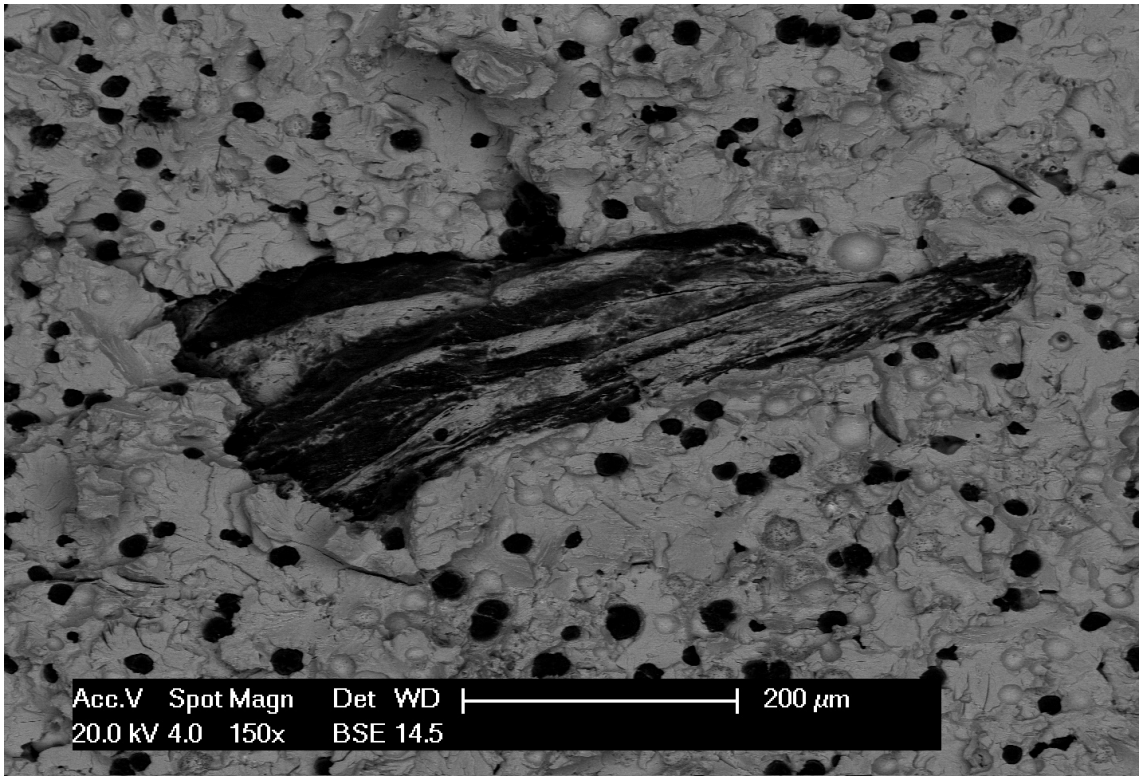


Figure 5.36: BSE image of the bifilm defect in figure 5.35 revealed its light elements composition

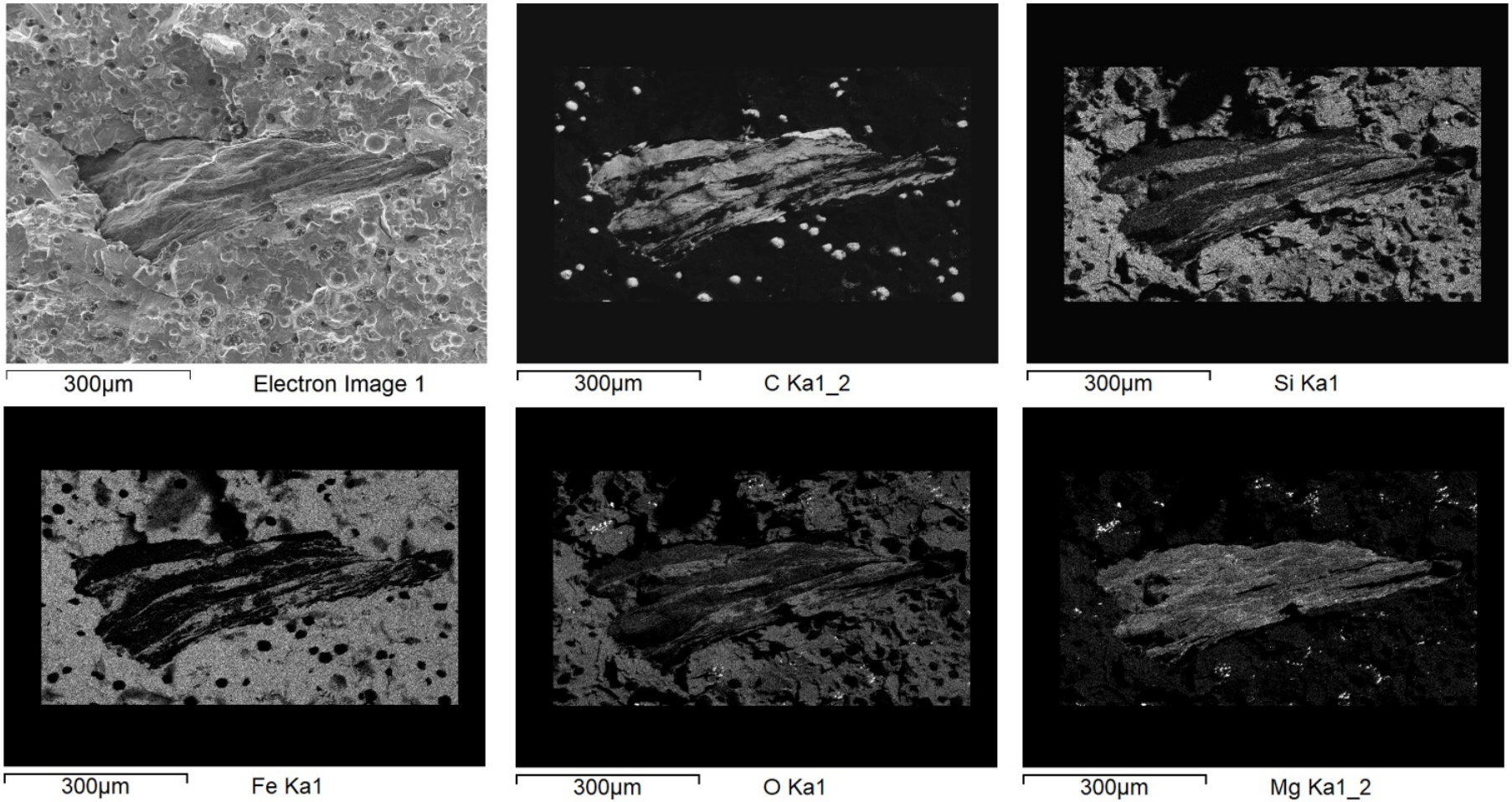


Figure 5.37: EDX element maps of the bifilm defect in figure 5.35 showed it contained C, Si, Mg and O

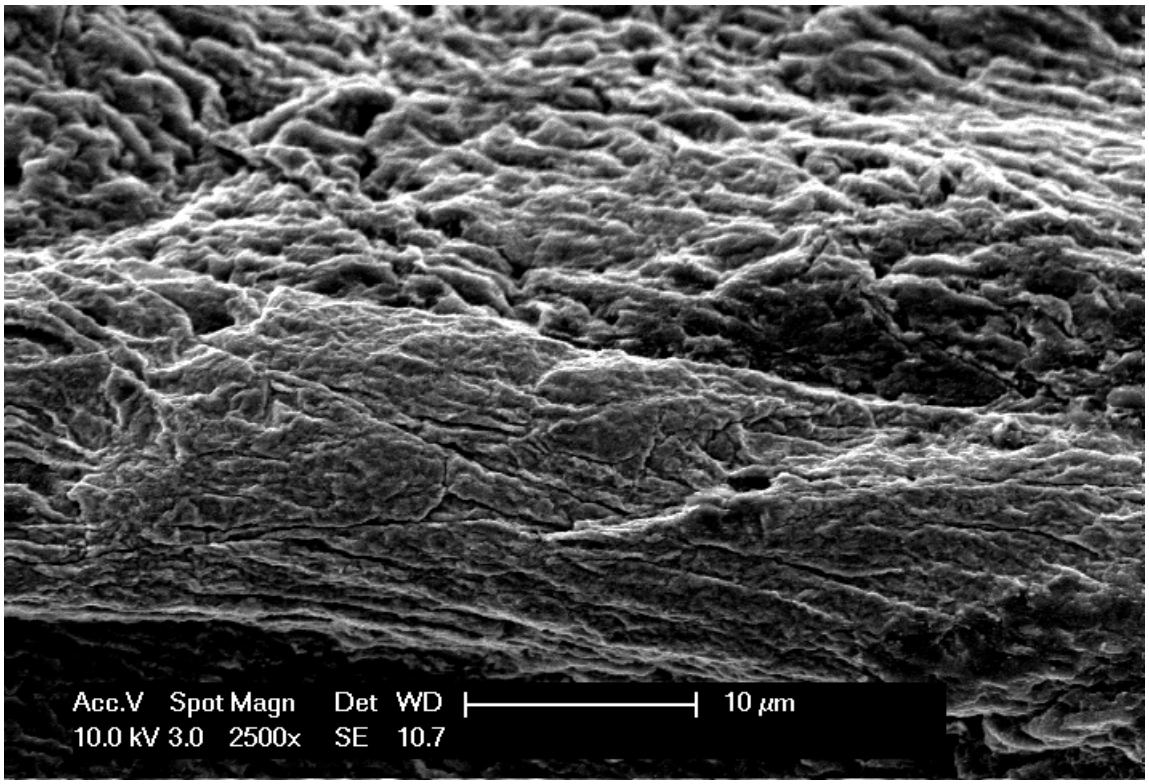


Figure 5.38: A close up SE image of the bifilm defect in figure 5.35 showed a combination of smooth and rough topography

•	Area 1		Area 2	
Element	Weight%	Atomic%	Weight%	Atomic%
C	75.96	87.23	1.69	6.33
O	8.98	7.74	3.26	9.18
Mg	3.72	2.11	4.7	8.7
Si	0.48	0.23	3.78	6.07
Fe	10.86	2.68	85.1	68.68
Cu	•	•	1.48	1.05
Total	100	•	100	•

Table 5.19: EDX elements composition in weight% and atomic% of area 1 and 2 in figure 5.39

Figure 5.41 is a SE image of another type of bifilm found on SGI fracture surfaces. The bifilm had a large surface and was almost circular shape. With a diameter of 1.5 mm, it was easily detected by the naked eye. The surface of the bifilm were full of folds and creases. The red circles in figure 5.41 showed areas where the bifilm was detached from the surrounding matrix. The BSE image revealed the bifilm had a lighter constituent than the rest of its surrounding (figure 5.42). Moreover, there seems to have been a high density of spheroidal graphite around the bifilm. This

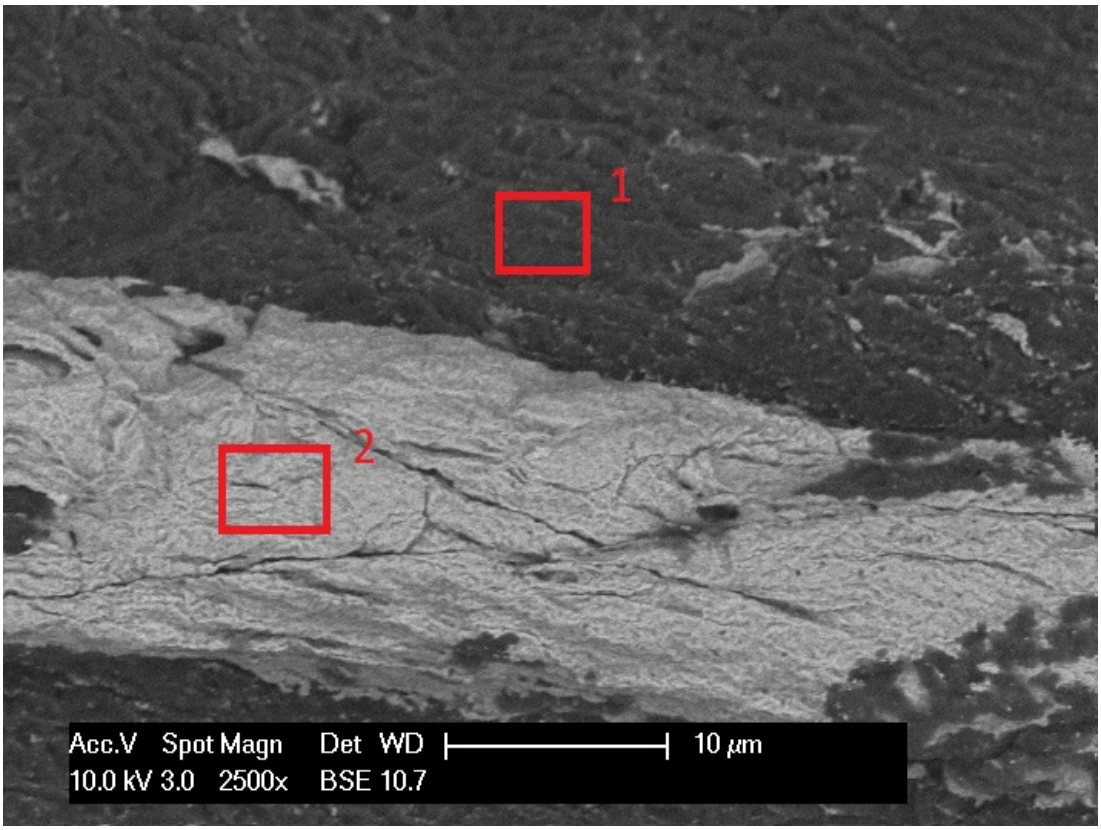
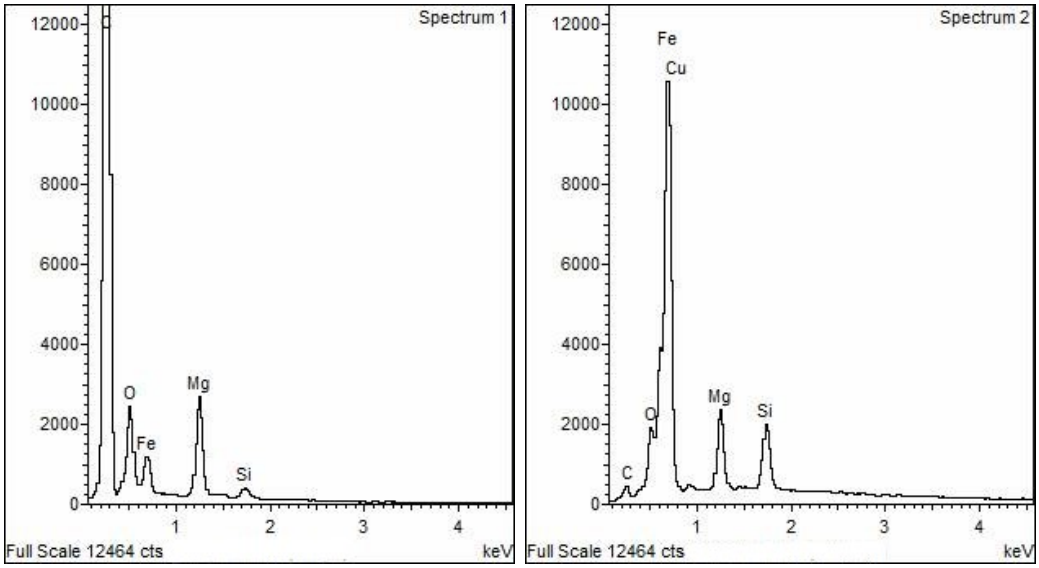


Figure 5.39: BSE image of the same area shown in figure 5.38 revealed that each texture corresponds to a different elemental composition



(a) EDX spectrum of area 1 (b) EDX spectrum of area 2

Figure 5.40: EDX analysis of area 1 and 2 of the bifilm texture in figure 5.39

behaviour resembled the case presented in figure 5.103. EDX mapping of the film revealed the complicatedly of its chemical composition as seen in figure 5.44. Unlike the previous example of the small bifilm, this bifilm hardly had any Fe in it. Most of the area of the film was high in C, but an area of Mg corresponded with the C. Moreover, there was a patch of the film high in Mg, Si and O, and to a lower extent Al. The area high in O was limited to this patch. further, N was detected over the whole area of the bifilm. Figure 5.46 was a result of assigning every element in the bifilm EDX map a different colour and overlaying the individual maps. The kaleidoscopic final result gave an idea of the complicity of the bifilm topography and chemical composition.

A closer look at the interface between the bifilm areas high in O and C, see figure 5.43, showed the difference in the topography between the two areas. The texture of the graphitic film was smoother and contained folds. On the other hand, the oxide film was thick and ragged. Figure 5.45a is the EDX spectrum from area 1 presented in figure 5.39, and figure 5.45b is the EDX spectrum from area 2 from the same figure; table 5.20 contain the corresponding chemical composition in weight%. Spectrum 1 had a higher concentration of C, but a lower concentration of Mg, Si and Al. Spectrum 2 had the opposite behaviour, it had less C and more Mg, Si and Al.

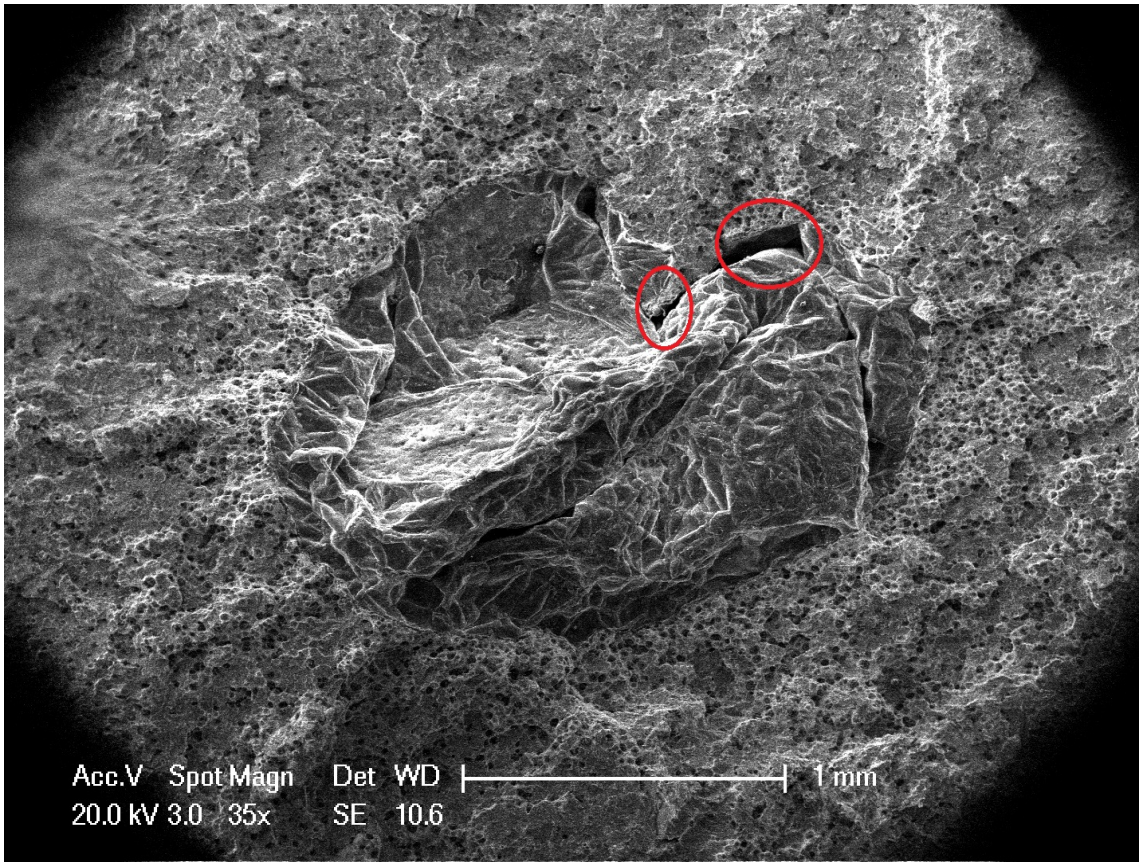


Figure 5.41: SE image of a big bifilm defect with a smooth structure (the red circles show locations of gaps between the bifilm and the matrix)



Figure 5.42: BSE image of the bifilm in figure 5.41 revealed its light composition and the high density of spheroidal graphite surrounding it

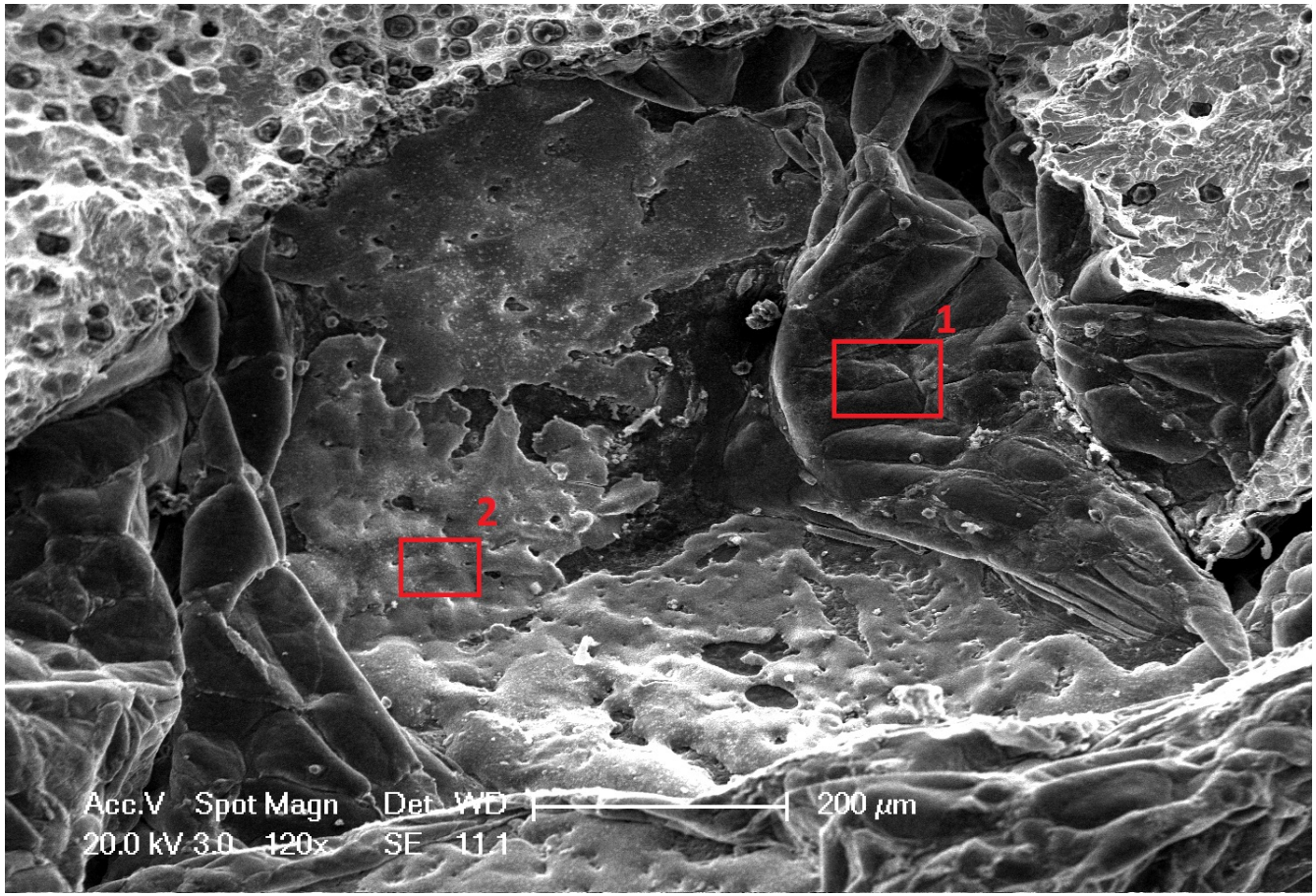


Figure 5.43: SE image of the area shown in figure 5.44 where the nitride and oxide film overlap, area 1 is a part of nitride film, and area 2 is a part of the oxide film

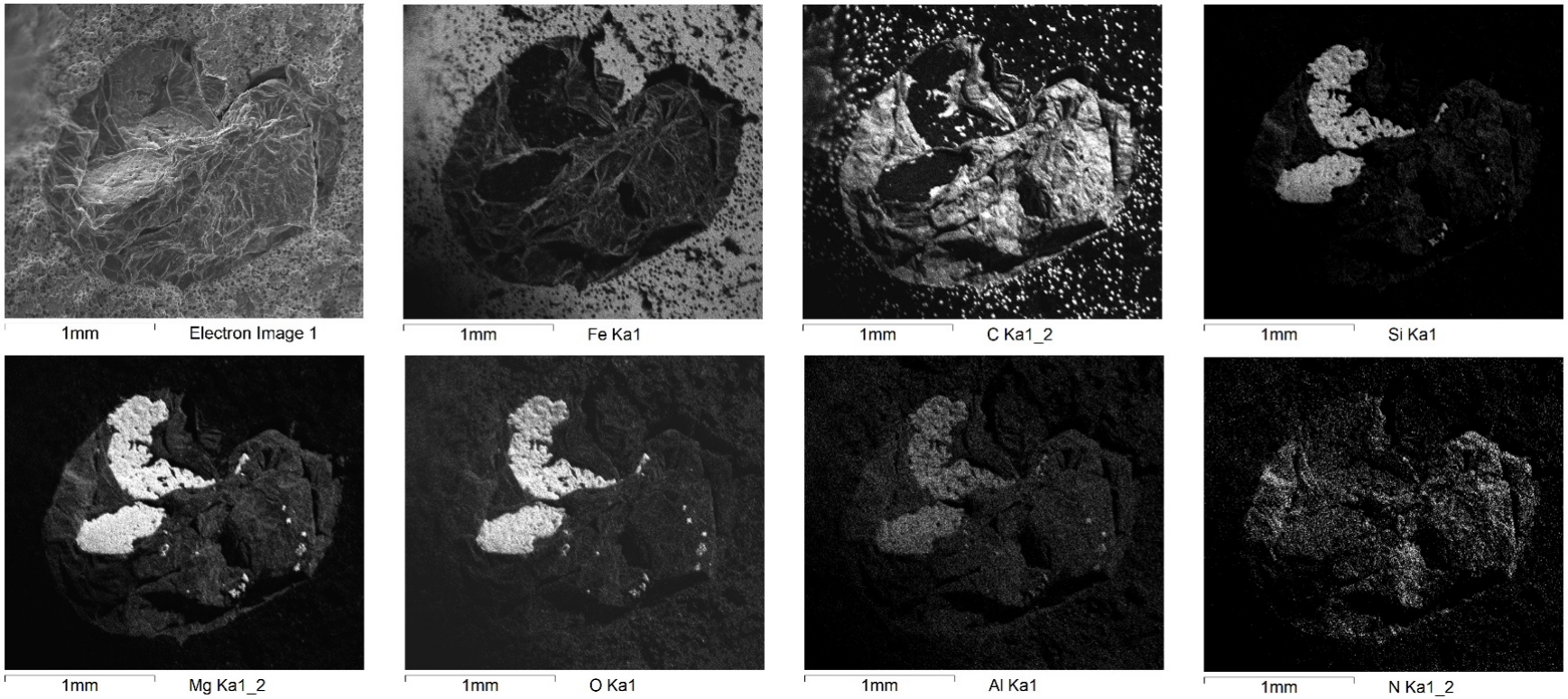
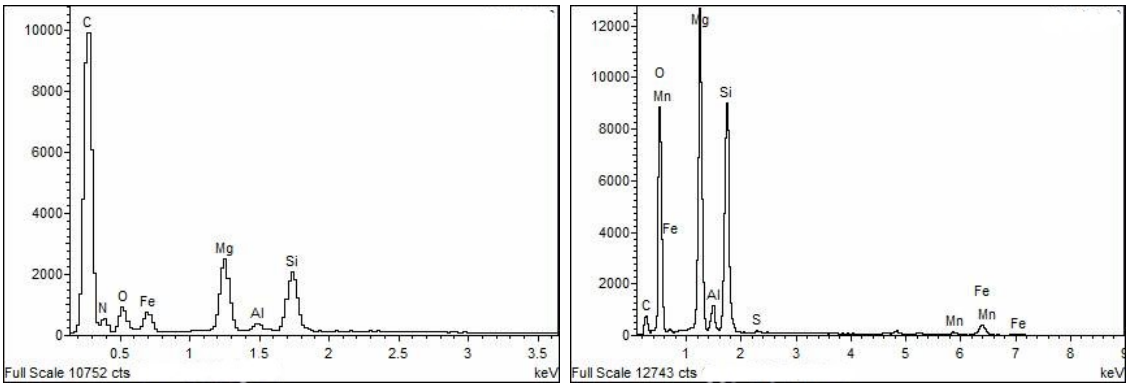


Figure 5.44: EDX element maps of the bifilm in figure 5.41 showed it contained C, Si, Mg, O, N and Al



(a) EDX spectrum of area 1 (b) EDX spectrum of area 2

Figure 5.45: EDX analysis of area 1 and 2 of the bifilm texture in figure 5.43

•	Spectrum 1		Spectrum 2	
Element	Weight%	Atomic%	Weight%	Atomic%
C	60.4	72.95	13.89	20.9
N	9.46	9.8	•	•
O	11.63	10.55	46.91	52.96
Mg	3.47	2.07	19.32	14.35
Al	0.3	0.16	1.71	1.14
Si	2.53	1.31	14.8	9.52
Fe	12.21	3.17	2.37	0.88
S	•	•	0.14	0.08
Mn	•	•	0.5	0.17
Total	100	•	100	•

Table 5.20: EDX elements composition in weight% and atomic% of area 1 and 2 in figure 5.43

The next two examples of SGI bifilms will be combined in analysis due to their similarity in size, shape and chemical composition. They were found in test bars cast in VTFM. The bifilms were large, 3 mm and 5 mm in length, as shown in figures 5.47 and 5.50 respectively. Their topography were chaotic in comparison to previous SGI bifilms examples. They also had some ridges which accumulated electrons from the SEM beam. This would explain the bright over charged areas that could be seen in figures 5.47 and 5.50. The BSE imaging revealed that the chemical composition of the bifilms were lighter than the surrounding SGI matrix (figures 5.48 and 5.51). Using EDX mapping, the resulting chemical composition of the bifilms were similar. The main body of the bifilm consisted of Mg, Si, and O with a small amount of Al (figures 5.52 and 5.52). In previous examples of SGI bifilms, the body of the bifilms

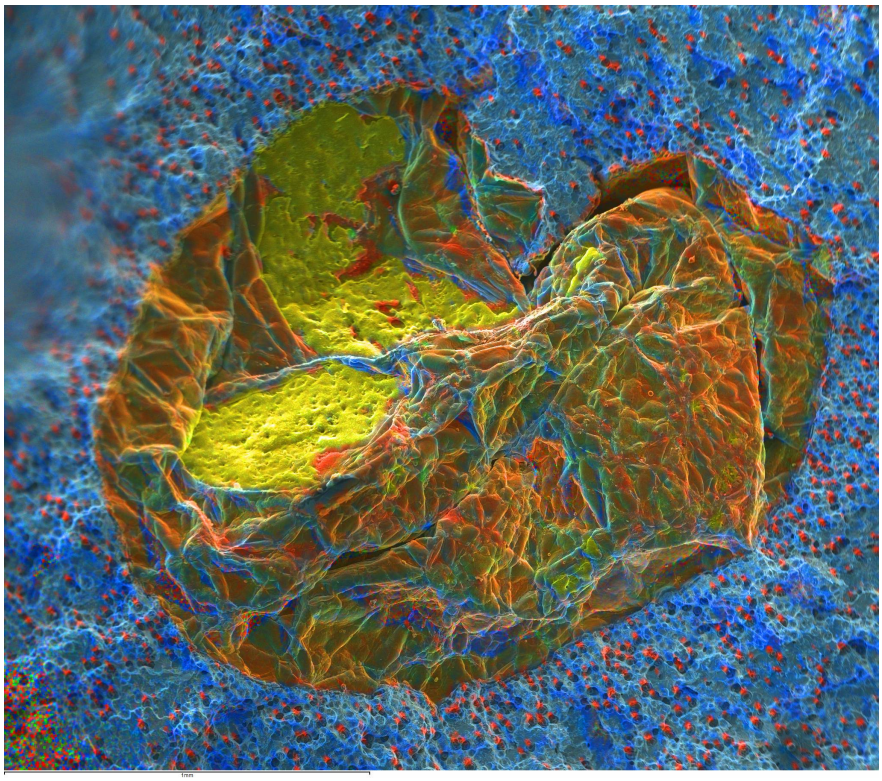


Figure 5.46: A layered EDX map generated from the EDX mapping of the bifilm in figure 5.41, with each color in the spectrum representing an element (i.e. C in red, Fe in blue, Si in yellow)

also contained Mg, Si and O. The difference in this type of bifilm was the behaviour of C. Previously, a C layer was noticed over the whole area of the bifilm, but here, the C layer was less significant, covering less area of the bifilm and it was patchy. Although two examples of maps have been provided in figures 5.49 and 5.52. It was easier to see the C behaviour in figure 5.49. Due to the extremely rough surface of the bifilm in figure 5.50, the EDX mapping was not able to cover all the area of the defect efficiently. Some of the high features of the bifilm were blocking the x-rays emitted from the bifilm, hence some areas of the map in figure 5.52 were dark.

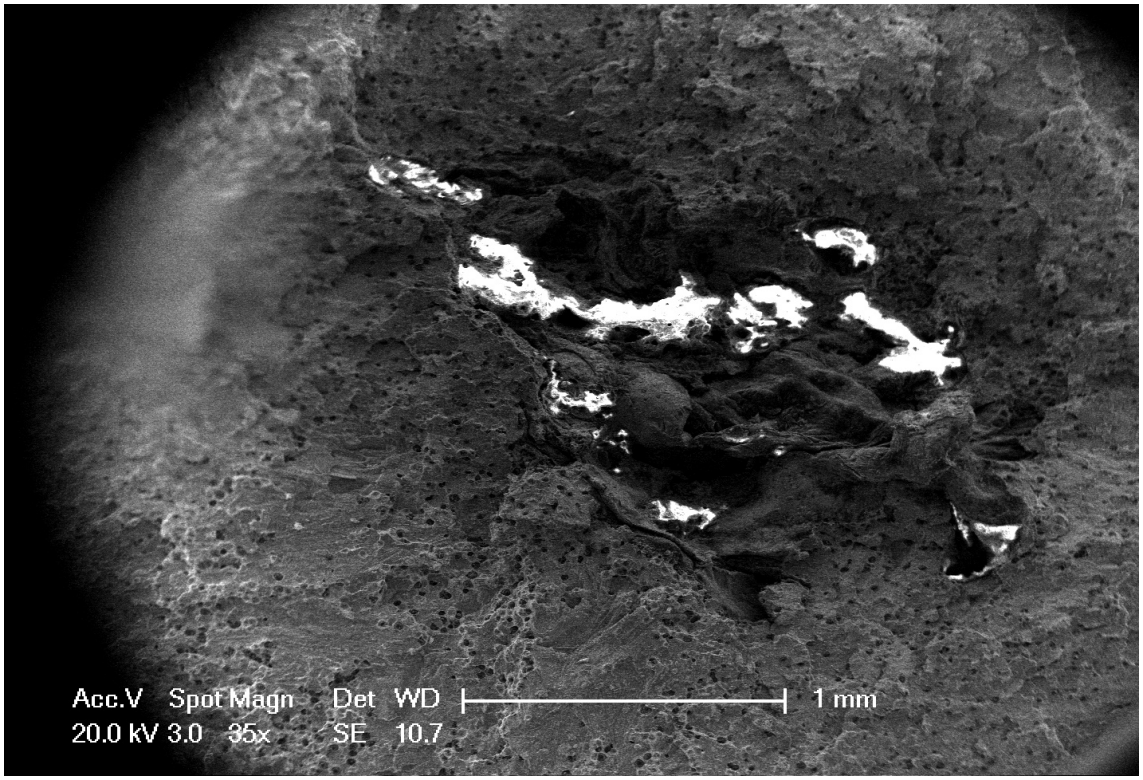


Figure 5.47: SE image of one of the largest oxide bifilm defects on the fracture surface of SGI testbar showing that it had a chaotic topography

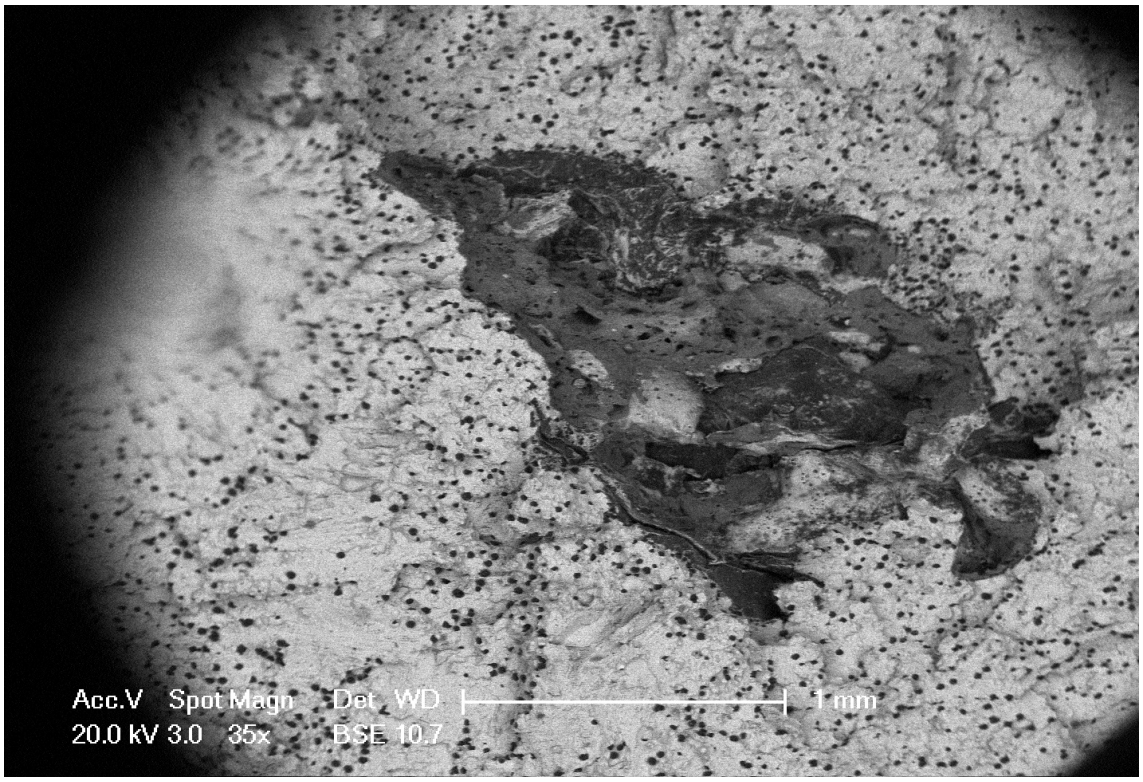


Figure 5.48: BSE image of the defect in figure 5.47 revealed the bifilm light composition

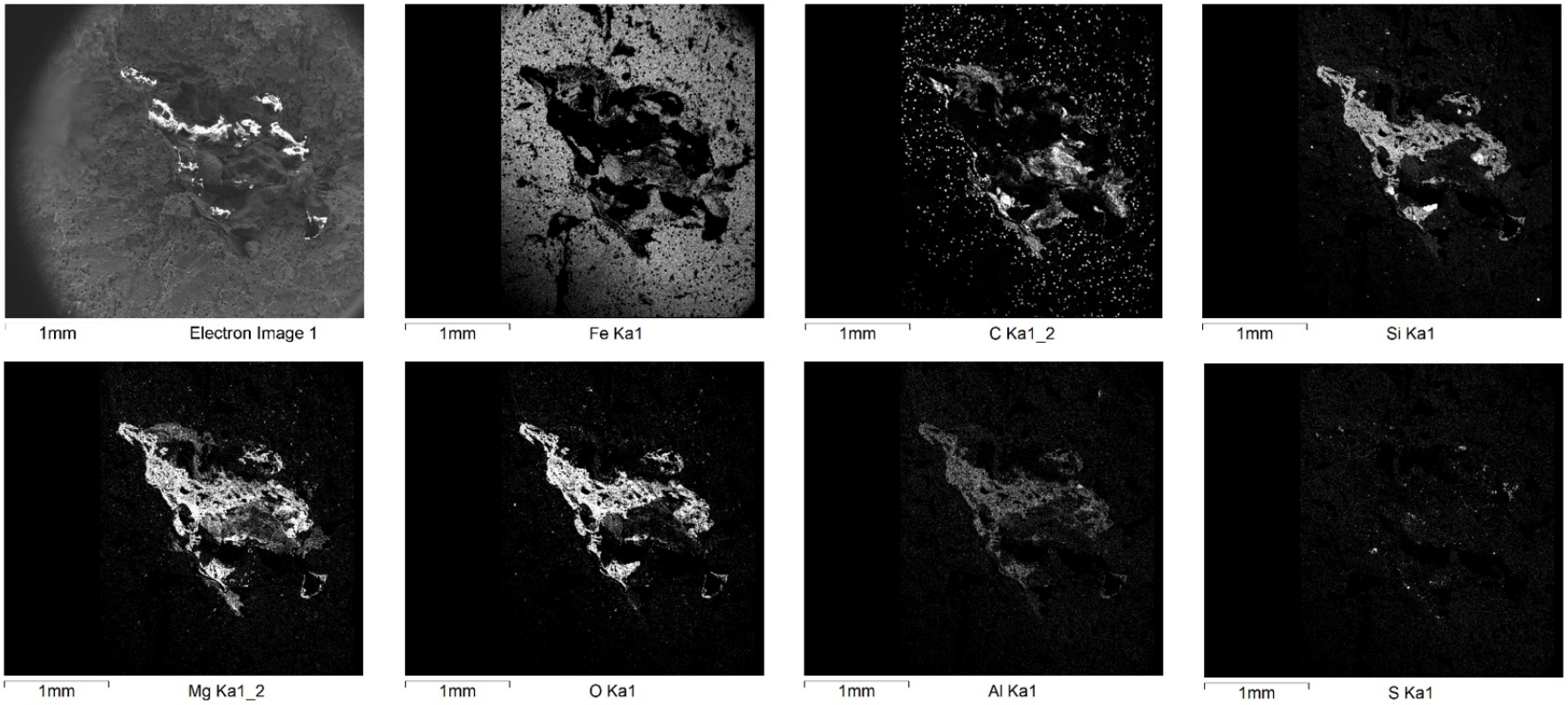


Figure 5.49: EDX element maps of the bifilm in figure 5.47 showed that it contained C, Si, Mg, O and Al

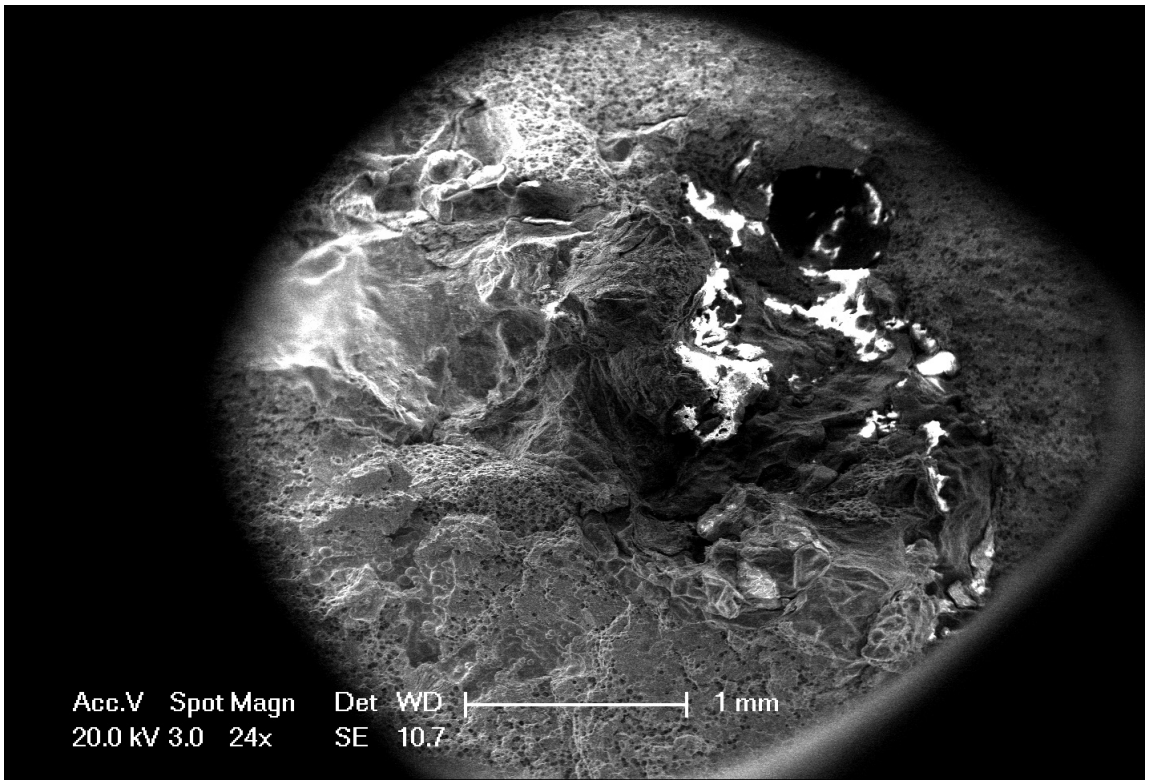


Figure 5.50: SE image of the largest oxide bifilm defects on the fracture surface of SGI testbar revealed its chaotic topography

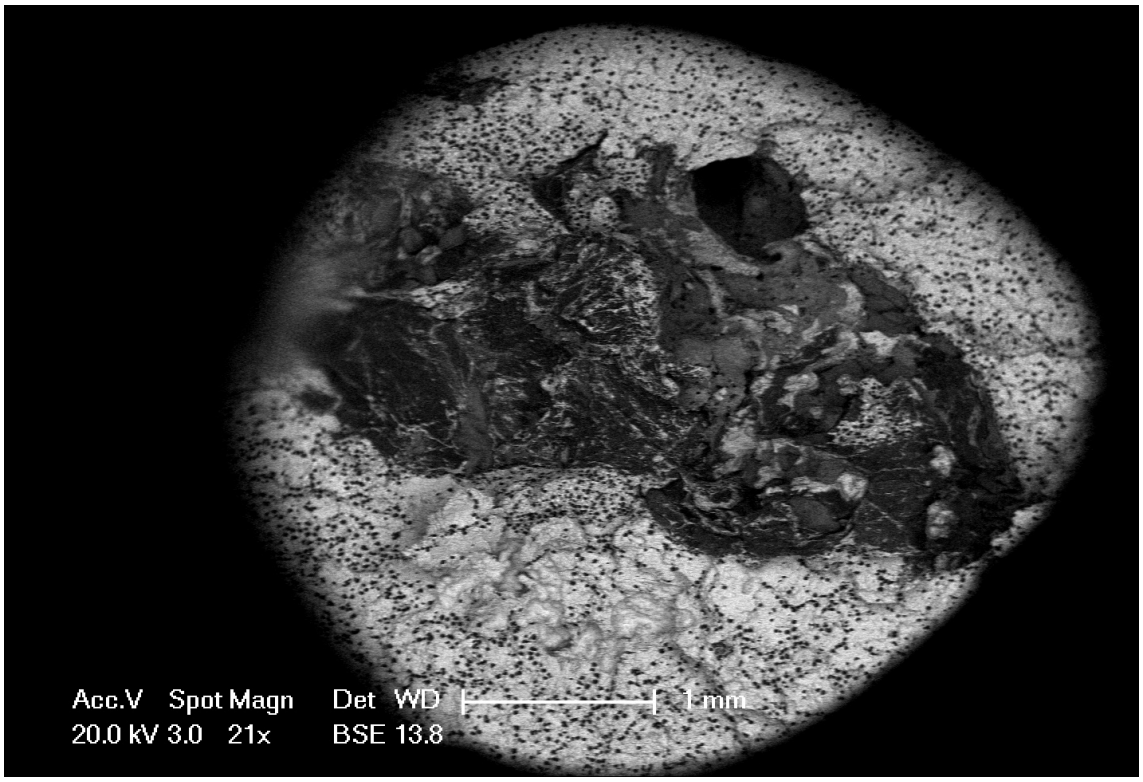


Figure 5.51: BSE image of the bifilm in figure 5.50 revealed its light composition

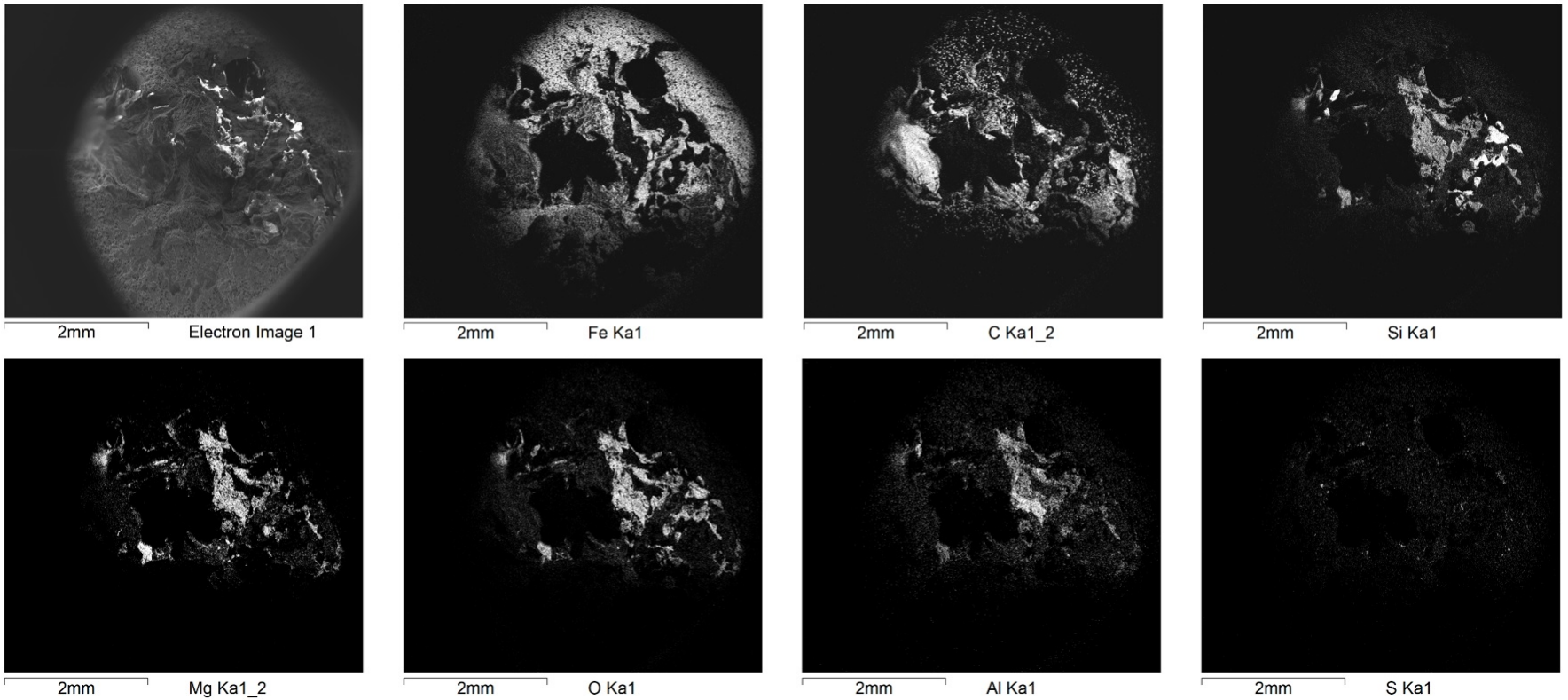


Figure 5.52: EDX element maps of the bifilm in figure 5.50 revealing it contained C, Si, Mg, O and Al

During the examination of SGI fracture surfaces a number of bifilms were found to have entrained some extrinsic inclusions. The next are examples of SGI bifilms with particles sandwiched between their folds. Figure 5.53 is a SE image of a bifilm around 1 mm in length with a bright surface as a results of electrons accumulation, which made it easily detectable. The bifilm had a different topography than the SGI matrix. At least three particles, resembling sand particles, could be noticed on the bifilm surface. The particles size ranged from 160 µm to 300 µm. BSE image of the bifilm (figure 5.54) showed the light constitute of the bifilm and particles. As the SE image was too bright, BSE image confirmed that the particles were tightly wrapped by the bifilm. EDX mapping revealed that the bifilm consist of Mg, Si, O and Al (figure 5.57). The entrained particles consisted of Si and O, which indicated that they were silica sand particles.

A closer look at the surface of the bifilm revealed its roughness (figure 5.55). The bifilm had two layers with different types of textures (marked in figure 5.55 by 1 and 2), with one layer covering the other. EDX mapping showed that the top layer consisted of Mg, Si and O, with a patchy layer of Al. The bottom layer was solely consisted of C (figure 5.57). Figures 5.59a and 5.59b are the EDX spectrum from spot 1 and 2, respectively. And table 5.21 is the chemical analysis in weight% from the spectrum. The results confirmed the data collected from the mapping, the top layer is formed of Mg, Si, O and Al; with clear peaks in the spectrum. On the other hand, the spectrum from the bottom layer had a large peak of C and significantly lower peaks of Mg, Si, O and Al. Even though the EDX map of the bifilm (figure 5.57) did not reveal a carbon layer, upon close examination the EDX map show the C under layer, seen in figure 5.58.

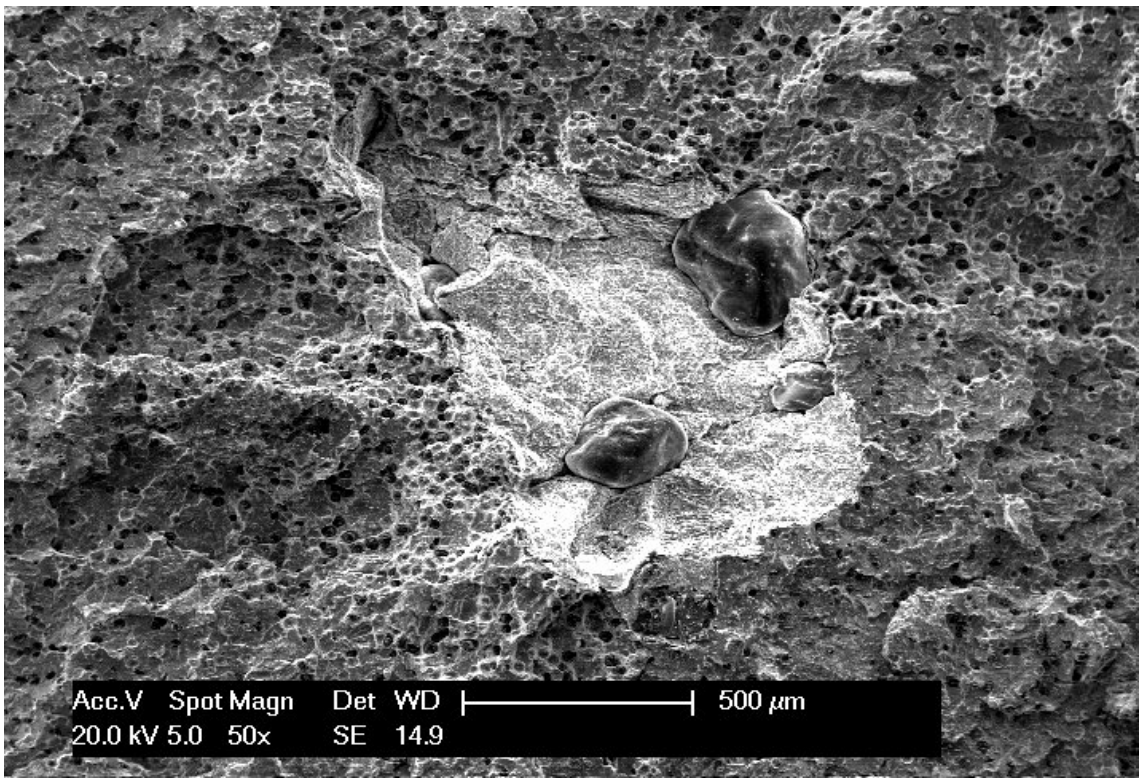


Figure 5.53: SE image of a bifilm with entrained sand particles

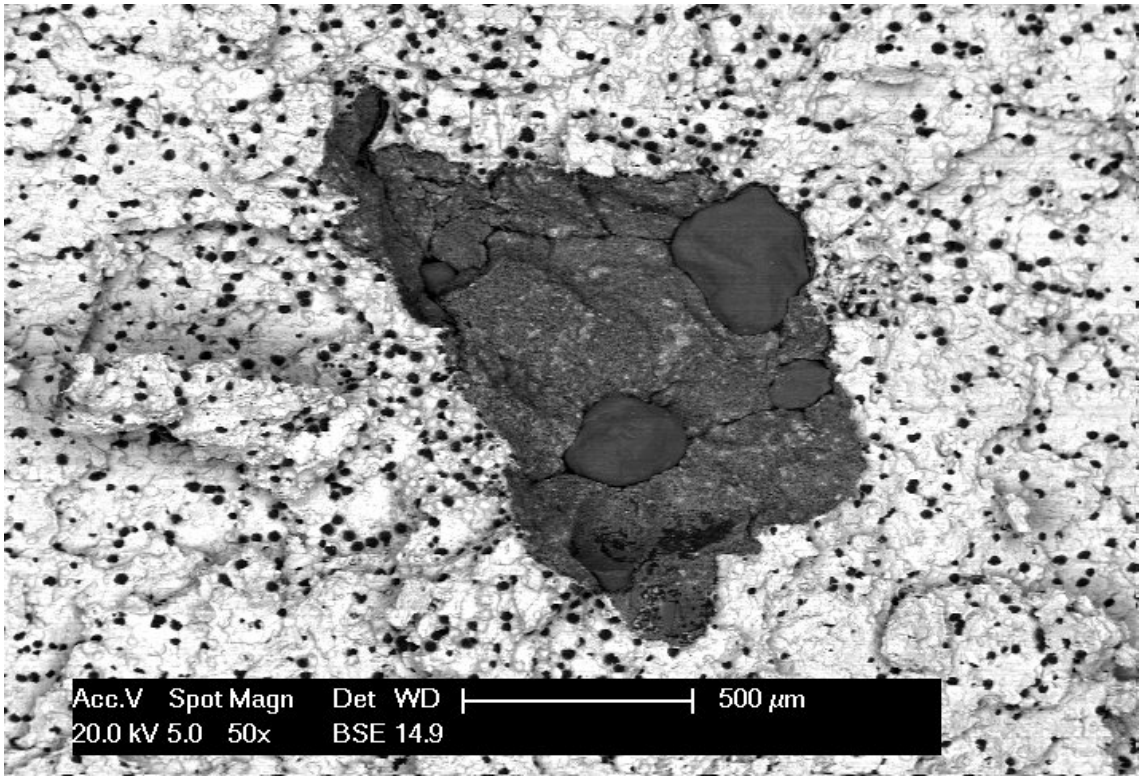


Figure 5.54: BSE image of the bifilm in figure 5.53 revealed its light constituents and several sand particles between its folds

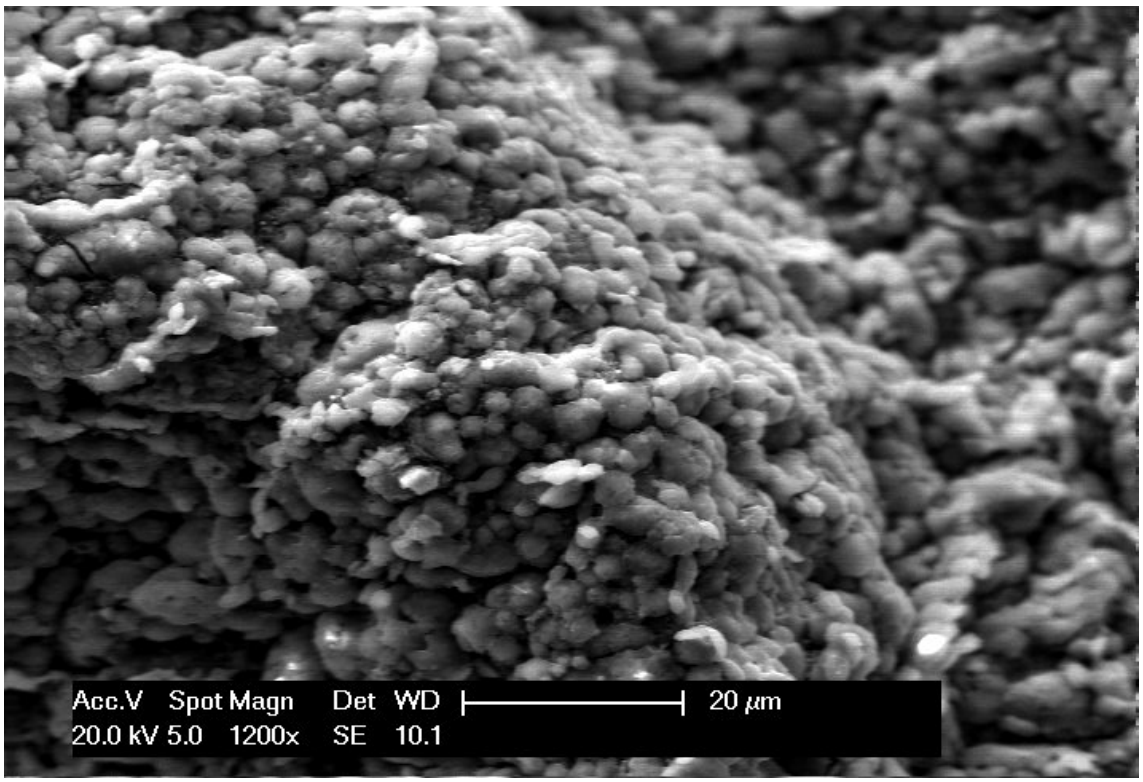


Figure 5.55: SE image of the surface of the bifilm in figure 5.53 showed its rough surface

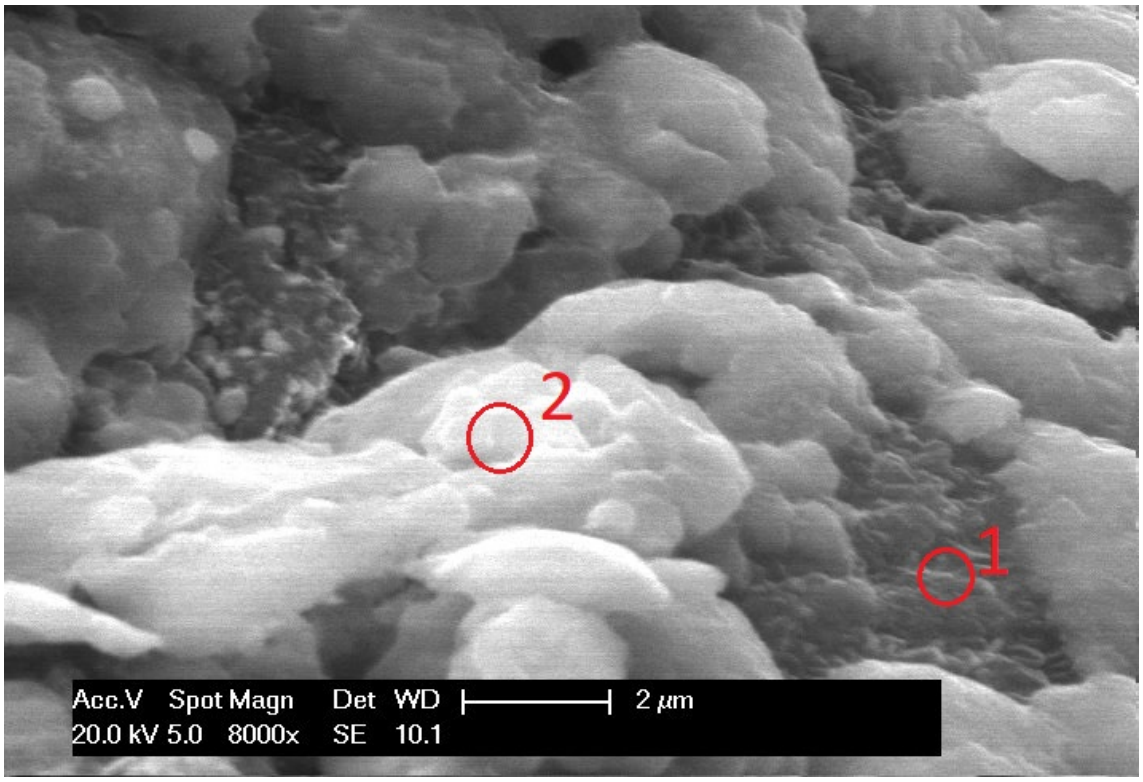


Figure 5.56: A close-up SE image the surface shown in figure 5.55 revealed two types of textures

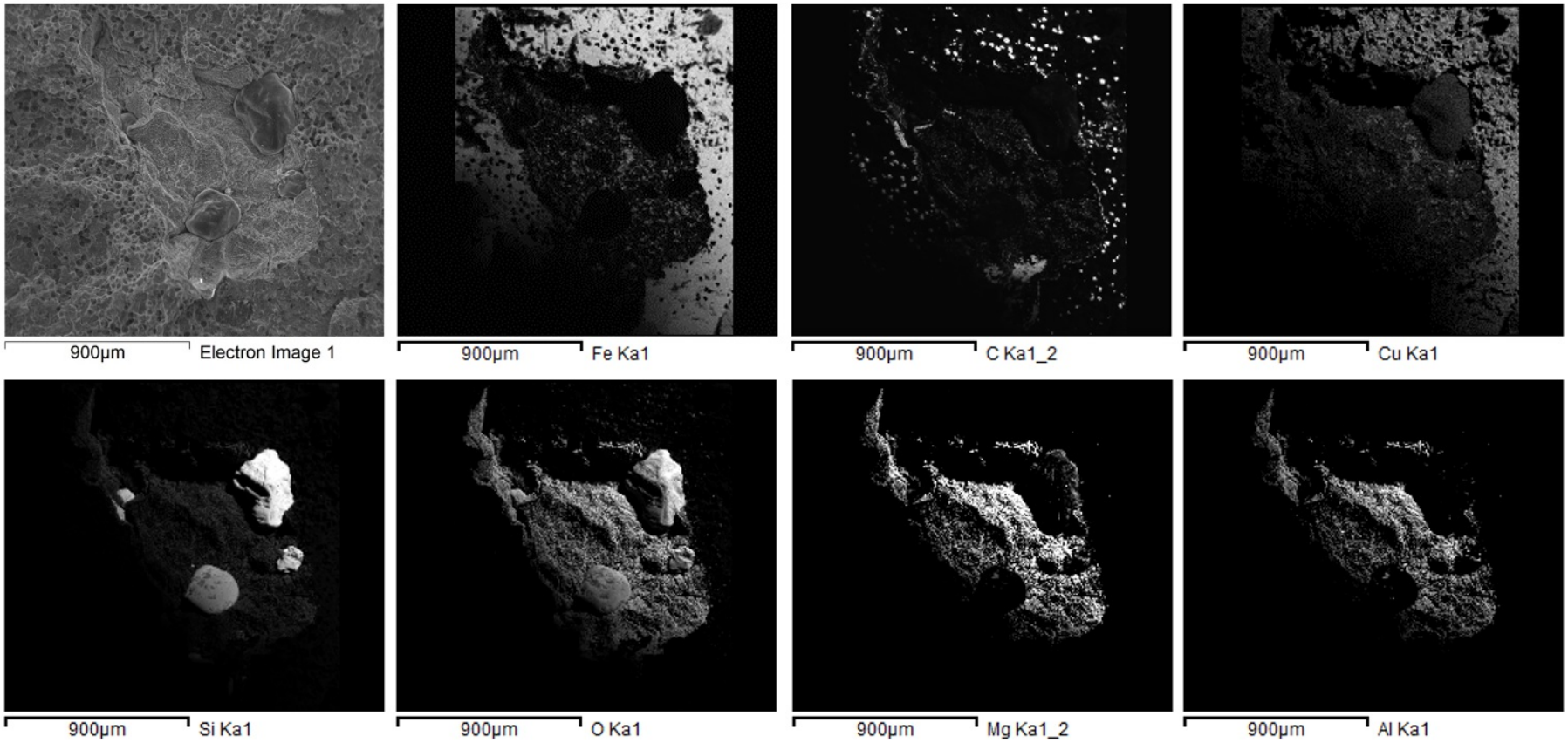


Figure 5.57: EDX element maps of the bifilm shown in figure 5.53 defined the sand particles and showed that the bifilm contained Si, Mg, O and Al

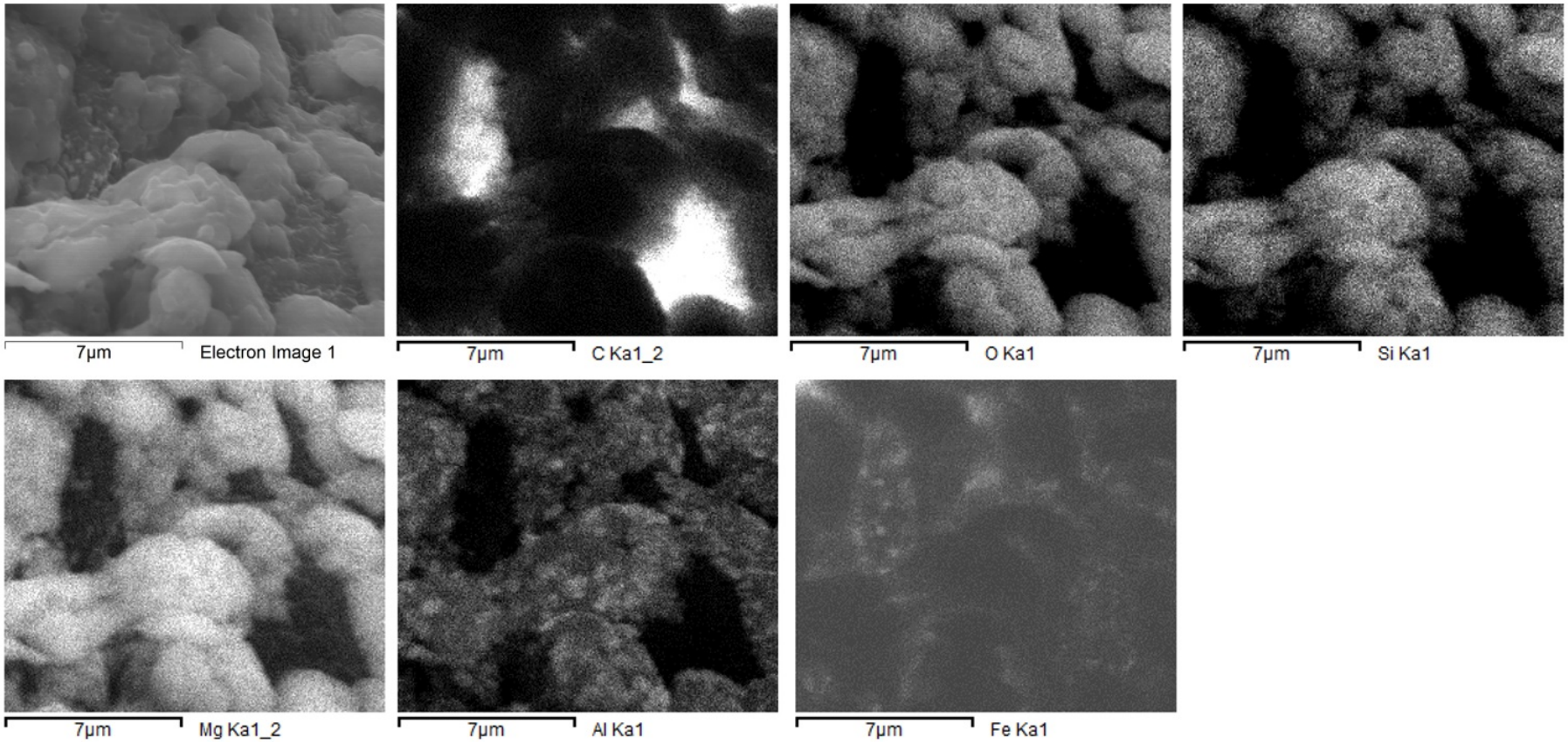
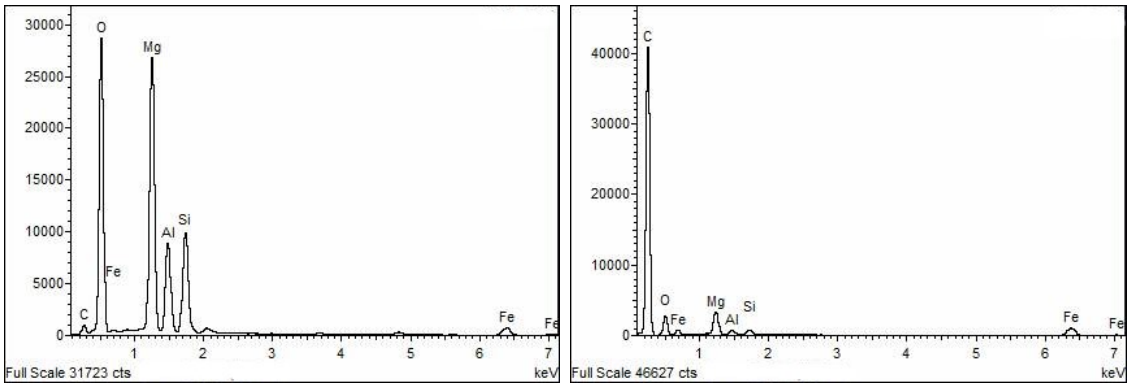


Figure 5.58: EDX element maps of the bifilm surface shown in figure 5.56 revealed an under layer of C



(a) EDX spectrum from the top layer of the bifilm (marked by 2)

(b) EDX spectrum from the bottom layer of the bifilm (marked by 1)

Figure 5.59: EDX analysis of the bifilm texture shown in figure 5.56

•	Spectrum 1		Spectrum 2	
Element	Weight%	Atomic%	Weight%	Atomic%
C	7.16	10.89	77.15	84.12
O	55.48	63.35	16.62	13.61
Mg	19.77	14.86	2.18	1.18
Al	7.07	4.79	0.27	0.13
Si	8.26	5.37	0.34	0.16
Fe	2.26	0.74	3.43	0.8
Total	100	•	100	•

Table 5.21: EDX elements composition in weight% and atomic% from area 1 and 2 in figure 5.56

Besides sand, slag was another endogenous inclusion that was found entrained inside SGI bifilms. Figure 5.60 is a BSE image of a bifilm with an area that was brighter than its surroundings. The brightness of the area compared to the the bifilm indicated that it was comprised of heavier elements than the surrounding bifilm. When the area was closely examined (figure 5.61) it appeared to have a different topography than the rest of the film surface. EDX analysis of the bifilm and the inclusion are in figures 5.62a and 5.62b, they showed the difference in chemical composition between the inclusion and the surrounding bifilm. The bifilm EDX spectrum had the same dominant peaks as previous SGI bifilms, with Mg, Si, O and Al comprising most of the resultant chemical composition (table 5.21). As for the inclusion, two major peaks of S and Ca were detected, plus an O peak. The corresponding chemical analysis in weight% is in table 5.21. The chemical analysis

indicated the particle sandwiched between the bifilm folds was composed of S and CaO slag.

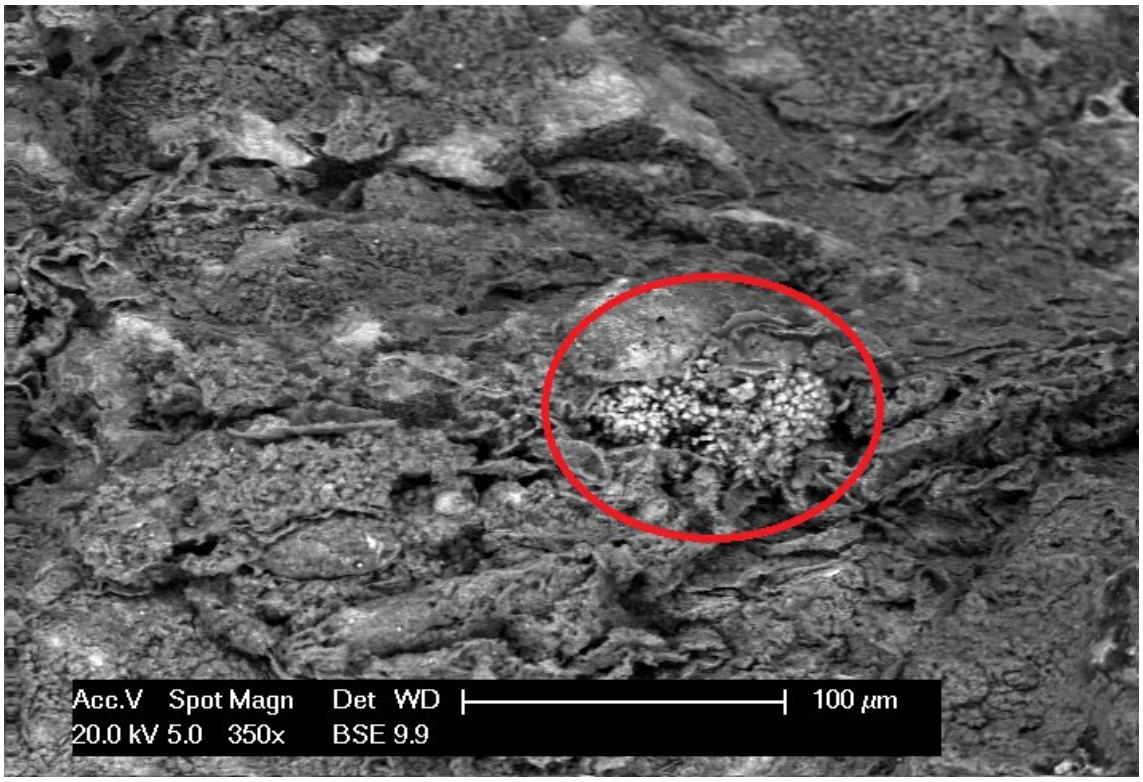


Figure 5.60: BSE image of a bifilm with a bright area

•	Bifilm		Slag	
Element	Weight%	Atomic%	Weight%	Atomic%
C	5.74	9.1	10.31	23.01
O	50.33	59.95	12.45	20.85
Mg	21.92	17.18	1.22	1.34
Al	6.76	4.77	0.18	0.18
Si	11.09	7.52	1.15	1.09
Ca	0.39	0.19	38.46	25.72
S	•	•	29.26	24.45
Fe	3.76	1.28	6.98	3.35
Total	100	•	100	•

Table 5.22: The bifilm and slag lump EDX elements composition in weight% and atomic%

As seen from the previous two examples, some cases of SGI bifilms were found that had entrained sand, and others had entrained slag. The next example was of a bifilm with multiple features entrained between its folds. The SE image of the bifilm in figure 5.63 captured the size of the bifilm (more than 1 mm in length) but it did

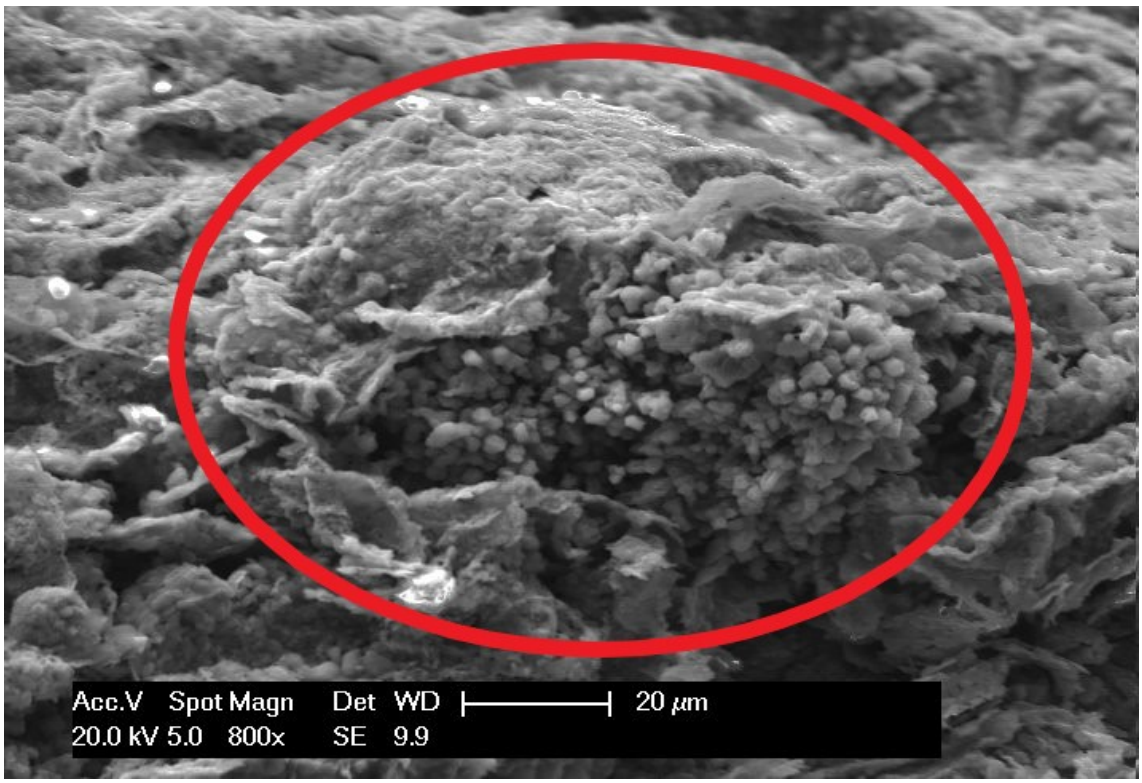
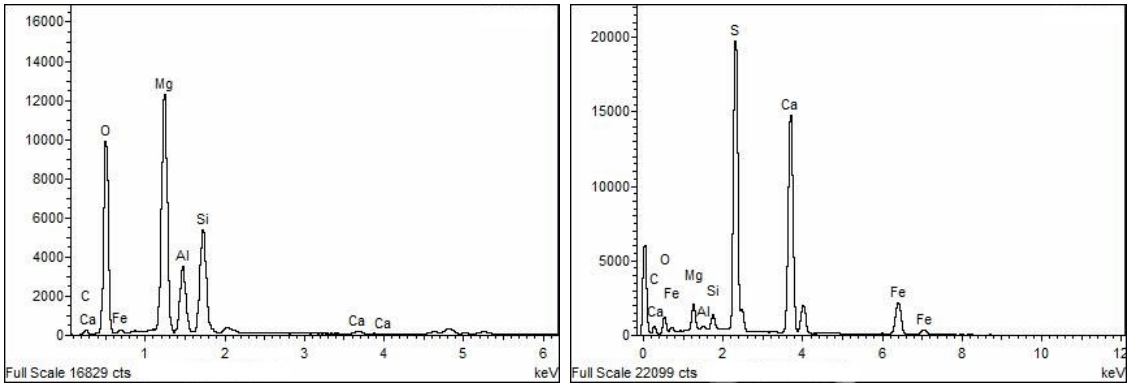


Figure 5.61: A close-up SE image of the bright area circled in red shown in figure 5.60



(a) Bifilm EDX spectrum (b) Slag lump EDX spectrum

Figure 5.62: EDX analysis of the bifilm and slag lump shown in figure 5.60

not reveal its features. This issue is one of the aspects that differentiate SEM study of Al alloys' bifilms from cast irons' bifilms. In Al alloys, the constituents of bifilms have an atomic number close to Al, which means their interaction with the electron beam would be similar to each other. This would translate to closer brightness levels and easier contrast control, resulting in a clear image. Thus any entrained features by the bifilm would be easily detected. In cast irons, the constituents of bifilms have an atomic number further from Fe, which means their interaction with the electron beam would be different from each other. For example, in figure 5.63 the bifilm was easily detected, but it's features were not, and they could not be revealed by altering the aspects of the image as the bifilm is much darker than its surrounding Fe matrix. Thus to see entrained features more clearly a switch to BSE imaging was needed. Figure 5.64 is the same bifilm captured with BSE imaging. It revealed the non-homogeneity of the bifilm surface and the fact that the bifilm contained 5 different features; they are marked from 1 to 5 in the same figure. The features were marked due to their difference in appearance and visibility, but just because they were marked separately, it does not mean that they were physically or chemically separate. Moreover, it also did not mean the features were only limited to the marked area.

The features revealed by the BSE imaging could be traced to different chemical compositions. Figure 5.65 is the EDX element maps of the bifilm. The locations marked by numbers on the maps correspond to the same numbers on the BSE image. The bifilm contained areas high in C, Si, Mg, Al, Ca, K and O. Most of these elements were a re-occurring sight when examining SGI bifilm defects. Location 1 was an area high in Mg and O, with a film-like surface that contained a large fold running through it. This indicated that location 1 was a Mg oxide bifilm. Location 2 was a familiar sight too, it had a gemstone looking particle, and a corresponding area high in Si and O. This indicated that it was an entrained silica sand grain. Location 3 was high in Ca and O, with a rough and grainy topography. CaO is a common constituent in SGI slag, which lead to identifying location 3 as an entrained

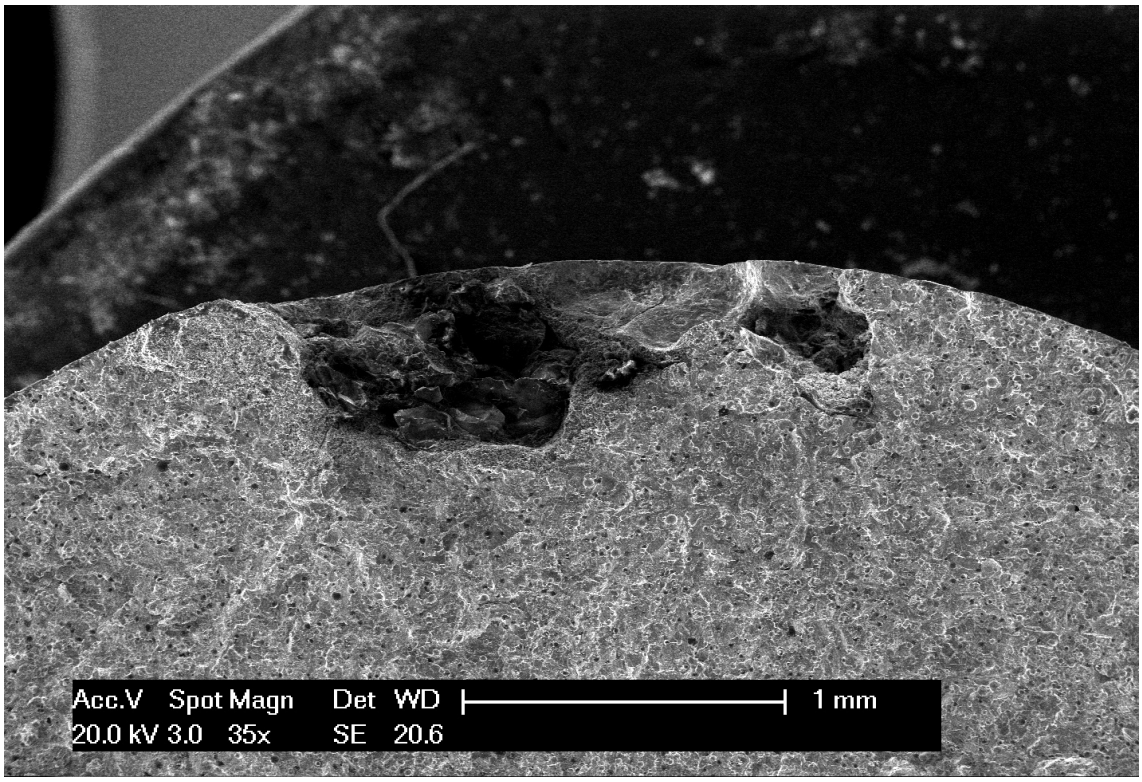


Figure 5.63: SE image of a bifilm with its features masked due to the brightness of the surrounding SGI matrix

CaO slag. EDX results showed location 4 to have a high concentration of Al, K and O. Its surface was faceted, granular and homogeneous, like a brittle grain boundary. The presence of Al, K and O coupled with its surface features indicated that it could be another entrained slag, but with a different chemical composition, for example: K_2O and Al_2O_3. The relation between SGI bifilms and C, and their co-existence has been seen in past examples (figure 5.44); and this was no different. In location 5, a large area of the bifilm had a high concentration of C with a dark and rough surface. Previously in figure 5.58, a layer of C was observed underneath SGI bifilm surface and this could be an example when the C layer is more visible. To summarize, the bifilm defect in figure 5.63 and 5.64 was a double oxide bifilm with multiple extrinsic inclusions entrained; sand particles and at least 2 types of slag.

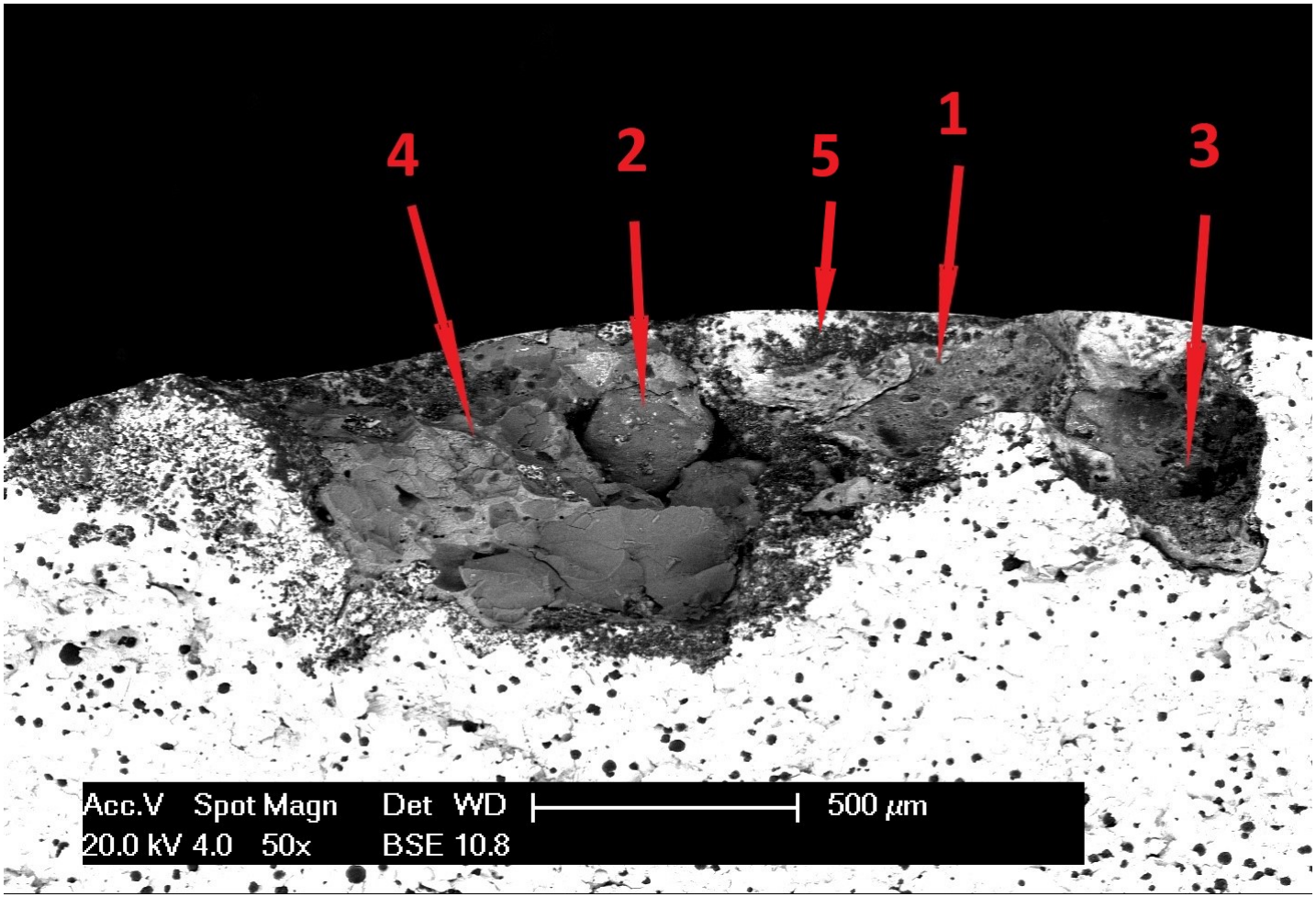


Figure 5.64: BS image of the bifilm shown in figure 5.63 revealed it had five different features

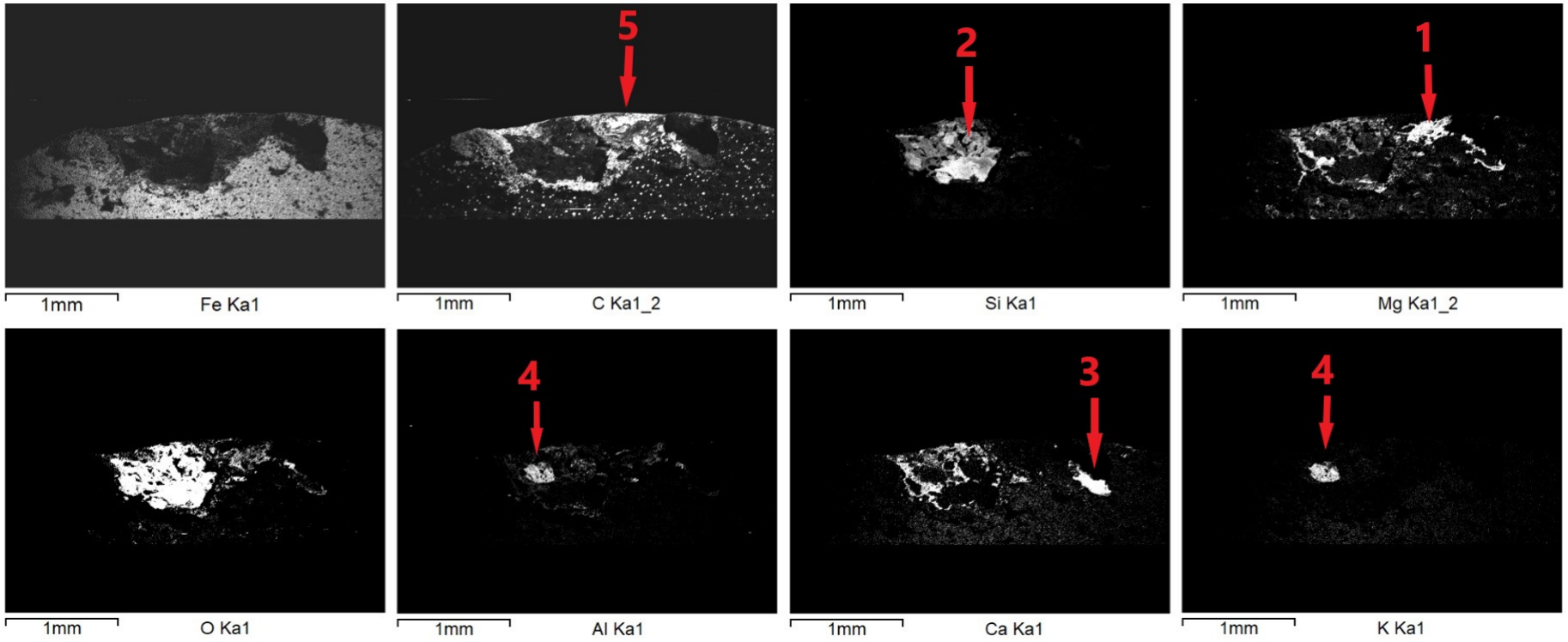


Figure 5.65: EDX mapping of the bifilm in figure 5.64 revealed that it contained areas high in C, Si, Mg, O, Al, Ca and K

Lustrous carbon bifilms

In addition to double oxide bifilms, graphitic bifilms were also identified on the fracture surfaces of SGI test bars. Figure 5.66 is a SE image of a large bifilm that was observed on one of the fracture surfaces. The bifilm was more than 3 mm in length and had multiple folds. Unlike previous examples of SGI bifilms, the area around this bifilm was not a normal ferritic/pearlitic matrix with SG; it was a fully dendritic structure. The EDX spectrum of the bifilm had a major C peak, comprised most of the spectrum, and small Fe, Si and O peaks (figure 5.69). The C peak indicated the graphitic nature of the bifilm. As for the Fe and Si, the signal could have been originated from the substrate. This would easily occur due to the light weight of C, which will allow the SEM beam to penetrate its surface and collect signal from the substrate.

Element maps of the film showed that the substrate containing O, Si and Fe expanded over the area of the film, as shown in figure 5.70. The element mapping of the bottom of the folded film, shown in figure 5.71, revealed that the substrate of the graphitc layer only comprises of O, Si and Fe. At the surface of the bifilm, the dendrite arms could be seen to be trying to penetrate the surface. The sight of bifilms next/near to a dendritic structure is a common occurrence. Note the area outside the image frame in figure 5.66 was a normal SGI fracture surface. However, the bifilm was surrounded by a large shrinkage porosity. Figure 5.68 is an SE image of the surface of the bifilm, which revealed the smooth surface and feint hollows within grains of graphite film. While examining different areas of the fracture surface, some smaller shrinkage defects were found. On the dendrite arms of the shrinkage porosity some fragments were observed (figure 5.72). EDX spectrum of the fragments in figure 5.73 was a mirror image of the EDX spectrum from the bifilm in figure 5.69. The spectrum comprised mostly of C, and small amounts of Fe, Si and O.

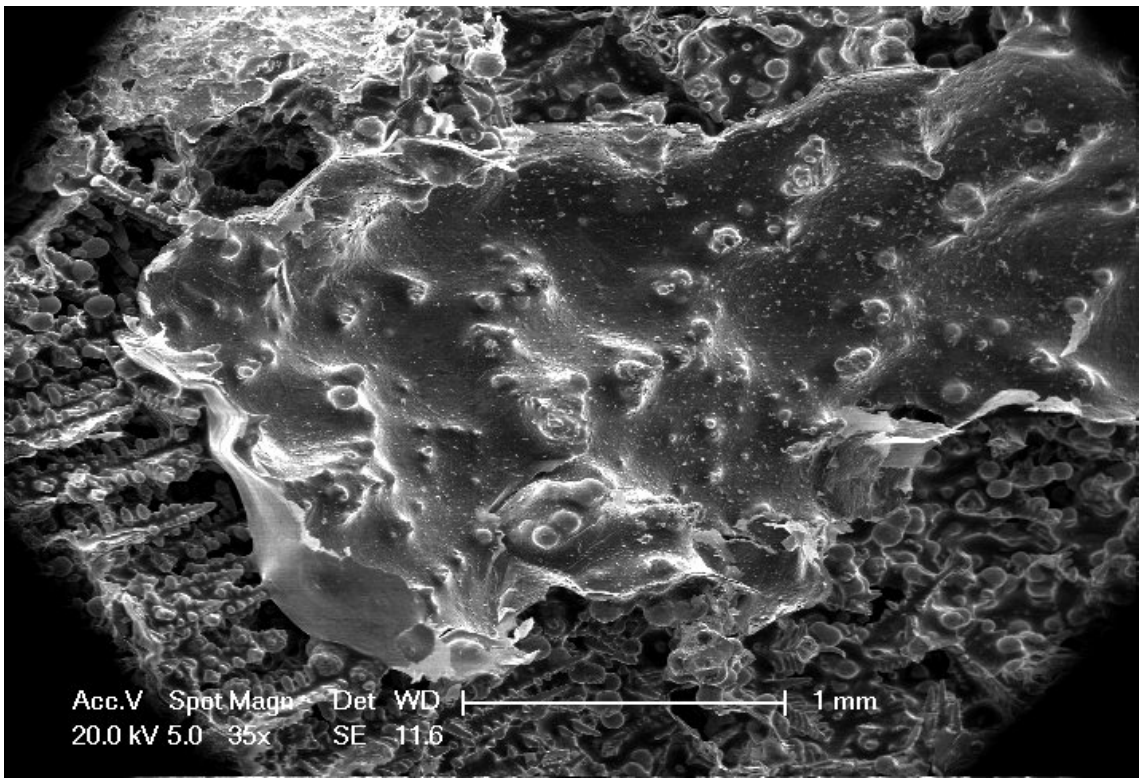


Figure 5.66: SE image of a bifilm blocking dendrite growth

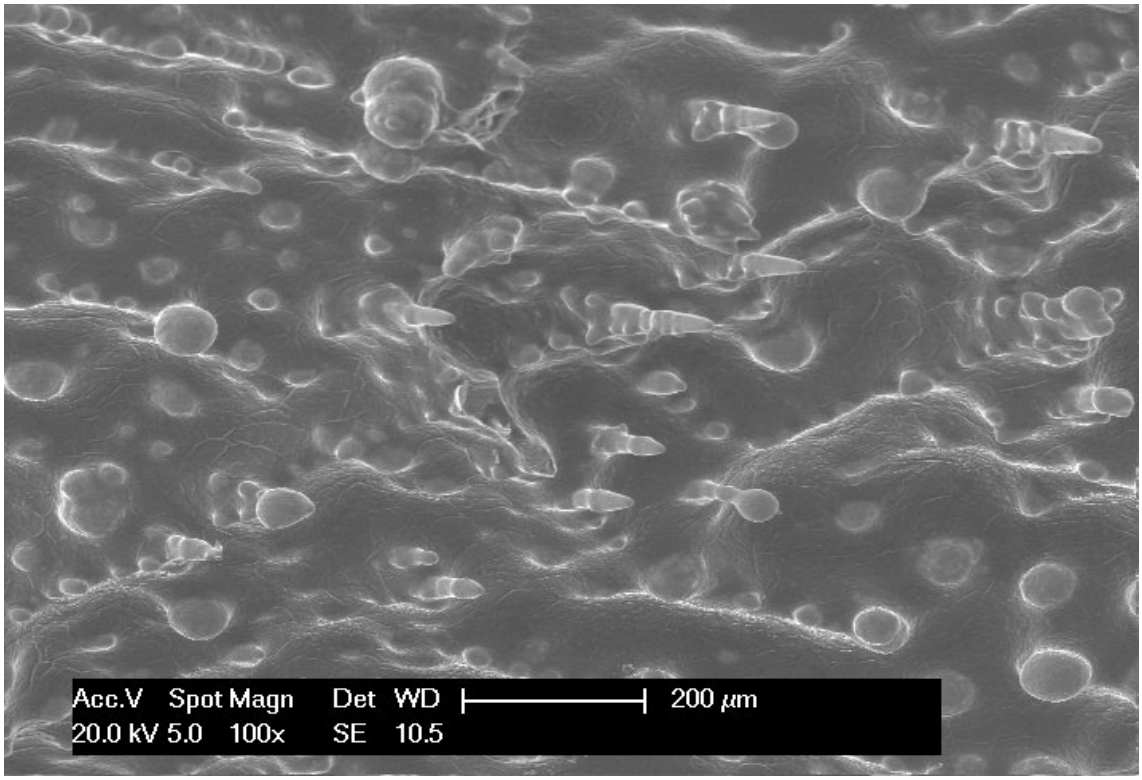


Figure 5.67: SE image of the bifilm surface with the primary dendrites trying to penetrate the surface

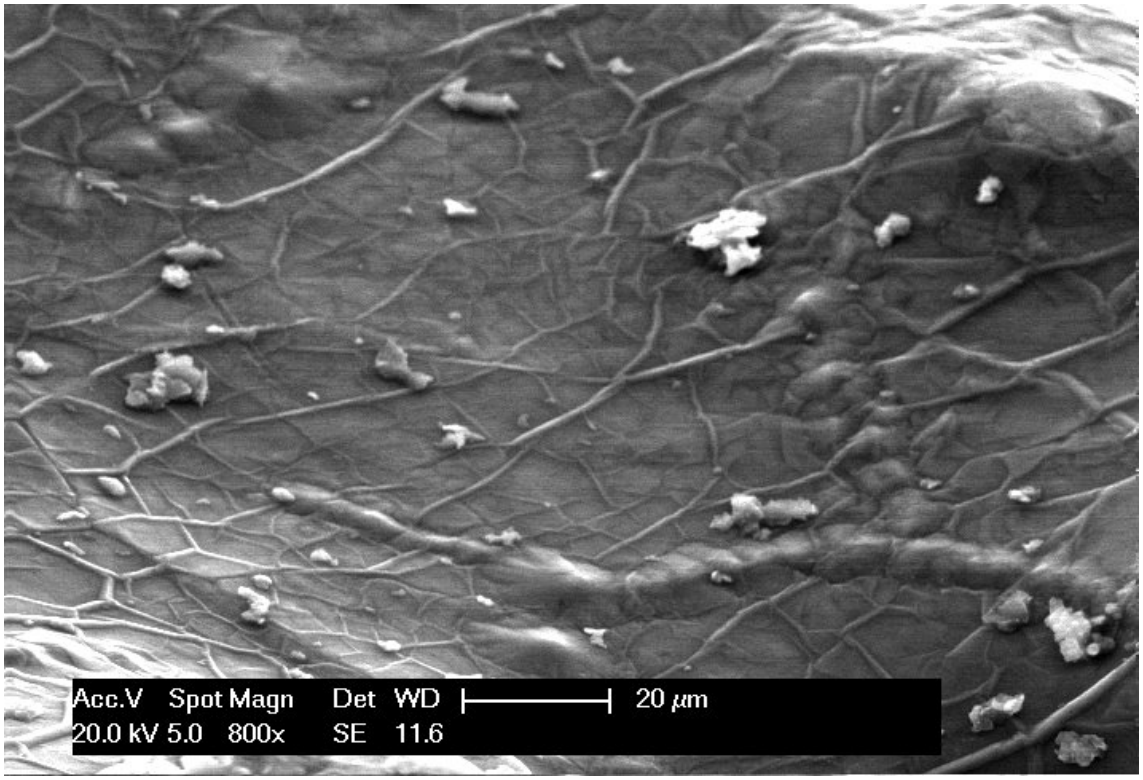


Figure 5.68: SE image of the bifilm surface showing its creased surface

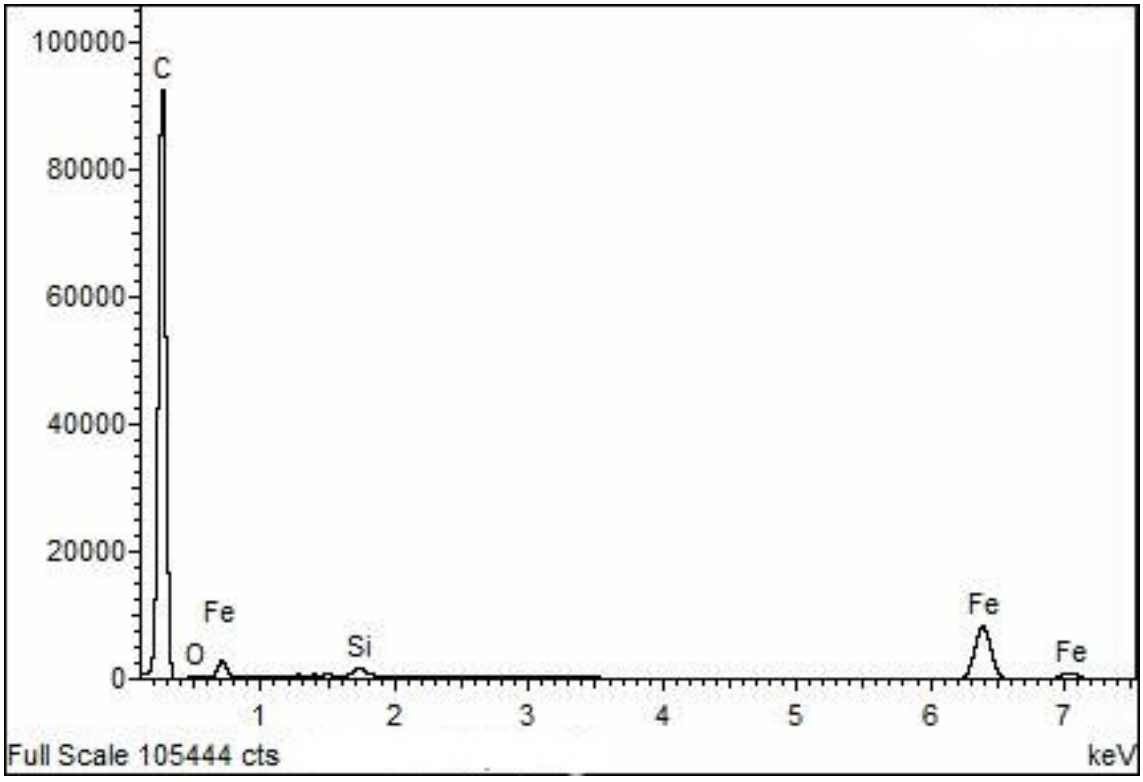


Figure 5.69: EDX spectrum from the bifilm in figure 5.66 showing that it mainly consisted of C

Element	Weight%	Atomic%
C	85.47	95.26
O	1.96	1.64
Si	0.37	0.18
Fe	12.2	2.92
Total	100	•

Table 5.23: EDX Chemical composition in weight% and atomic% of the graphitic film shown in figure 5.66

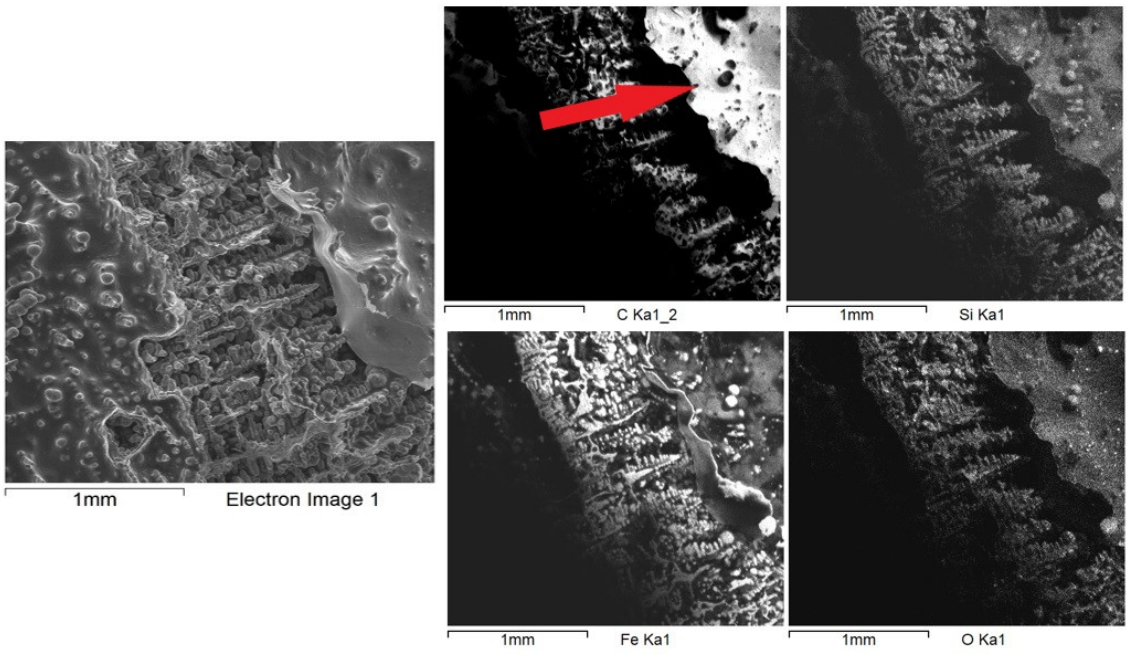


Figure 5.70: EDX element maps of the graphitic film shown in figure 5.66 revealed that its main constituent was C (as pointed to by the red arrow)

Element	Weight%	Atomic%
C	88.75	94.91
O	4.26	3.42
Si	0.24	0.11
Fe	6.74	1.55
Total	100	•

Table 5.24: The EDX Chemical composition in weight% and atomic% of the fragments shown in figure 5.72

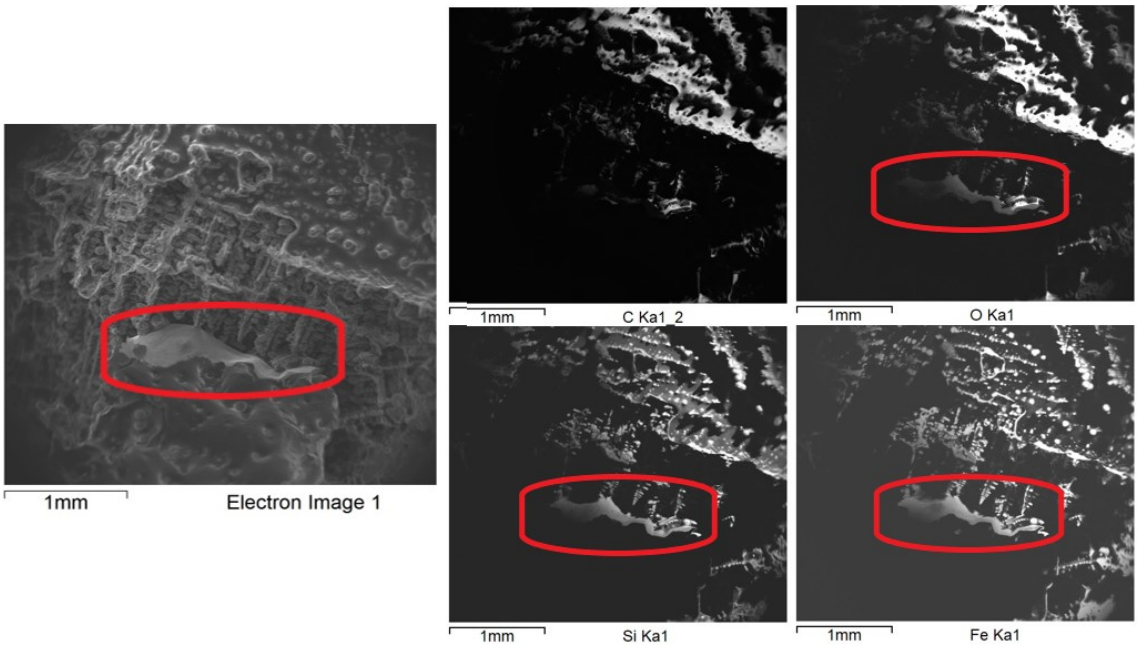


Figure 5.71: EDX element maps of the graphitic film showing its folded bottom side, (marked by a red oval), contained O, Si and Fe

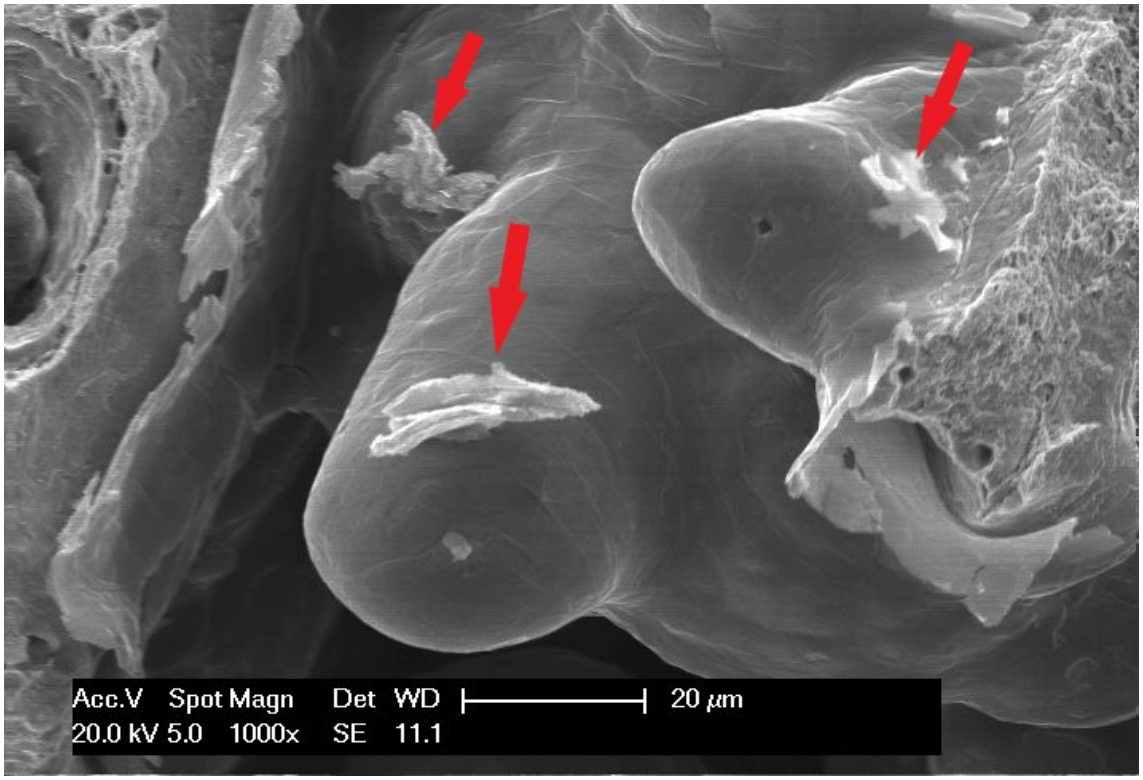


Figure 5.72: SE image of a dendrite arm near the bifilm in figure 5.66 showed fragments on the surface of the dendrite

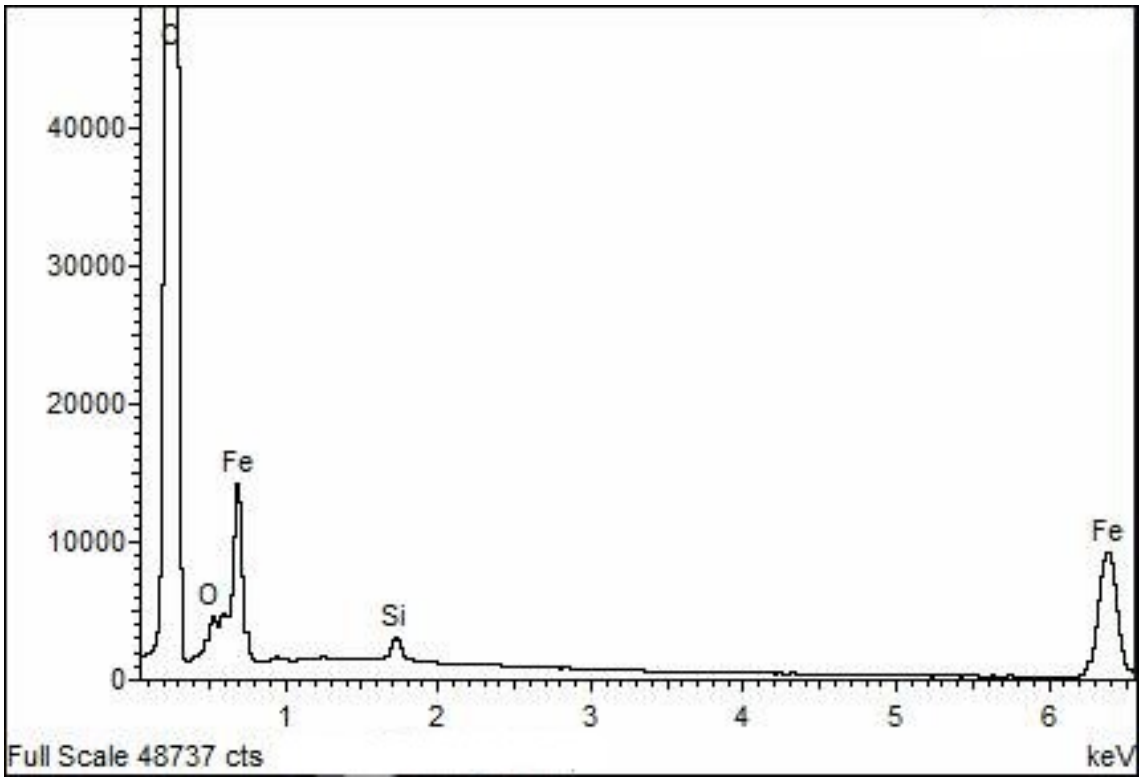


Figure 5.73: EDX spectrum from the fragments shown in figure 5.72 showed that the fragments were mainly C

Plate defects

The second type of defects detected with optical microscopy were grouped in the same category due to the shiny features on fracture surfaces. When examining the bright areas SE imaging revealed what appeared to be zones without any graphite spheres. Figure 5.74 is a SE image of one of the defects, which showed a circular zone with a diameter of 1 mm that did not contain any spheroidal graphite. This explained the shiny look of the defect. As seen from multiple examples of SE imaging of defect free SGI fracture surfaces, two features defined its appearance; dark spheroidal graphite and the surrounding pearlitic/ferritic matrix. The spheroidal graphite absorbs light, and the surrounding pearlitic/ferritic matrix reflect it. Hence, a large bright area would mean a lack of physical spheroidal graphite. EDX layered element mapping confirmed the information acquired from SE imaging. Figure 5.75 is a map of the defect with C marked in red and Fe in blue. The area of the defect was completely blue and did not contain any red areas.

Novel protruding plate-like structures were found in some areas of the defect. These areas were mostly located in the middle of the fracture surface, as in figure 5.74. A close examination of the area around the plates revealed several locations full of perturbations (figure 5.76). The perturbations resembled secondary dendrite arms and had several fragments scattered between them (fig 5.77). The fragments could only be found in the valleys of perturbations, as if they had been pushed aside. Figure 5.78 is a close-up low acceleration voltage (5 kev) SE image of the fragments and perturbations. The low acceleration voltage was used to enhance the topography of the area, as low acceleration voltage corresponds to a better edge resolution. The fragments were around 2 micron in size and resembled a crumpled piece of paper. To get a better understanding of the situation, EDX chemical analysis were carried on the defect surface and fragments, and the results were compared. The acceleration voltage for EDX was chosen to be the same as in imaging, (5 keV), but for a different reason. The signal for EDX comes from the interaction volume which is found mostly below the surface. Thus for fine features, the resulting EDX spectra would originate from the fine feature and its substrate, confusing the chemical analysis. To allow the chemical composition of the outer layer of the feature to be dominant and not diluted by the chemical composition of the substrate, a reduction in the acceleration voltage was required. With reducing the acceleration voltage the strength of the signal (i.e. number of counts) was also reduced. This would be an issue if the resulting spectrum peaks are not easily resolved. Spectrum 1 was generated from surface of the defects and spectrum 2 from the fragments. Spectrum 1 had a dominant Fe peak with smaller Si, Mg and O peaks. Spectrum 2 had a smaller Fe peak and a large Mg, Si and O peaks. Figure 5.80 is a SE image of a particle that was located on the surface of the plate defect. The particle was 15 μm in diameter and had a surface resembling those of graphite spheres. EDX spectrum, see figure 5.81, showed the particle comprised of C.

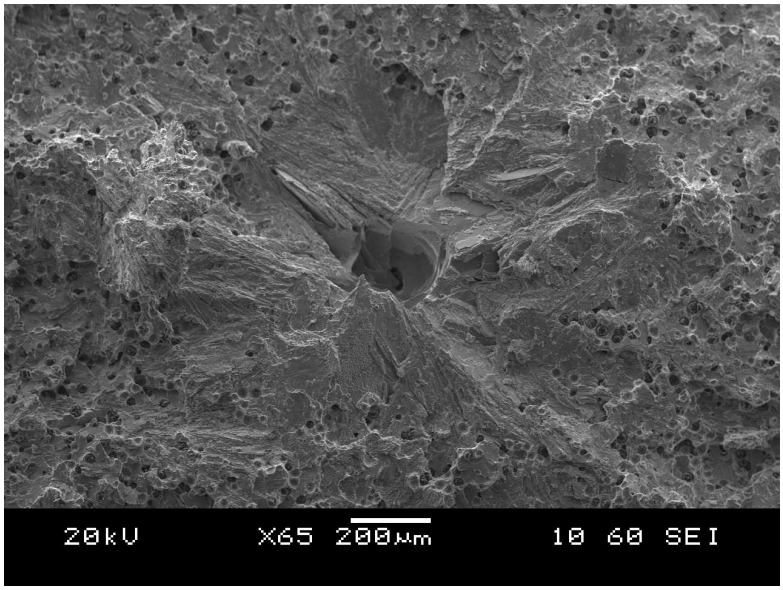


Figure 5.74: SE image of the second type of defects found on SGI fracture surfaces

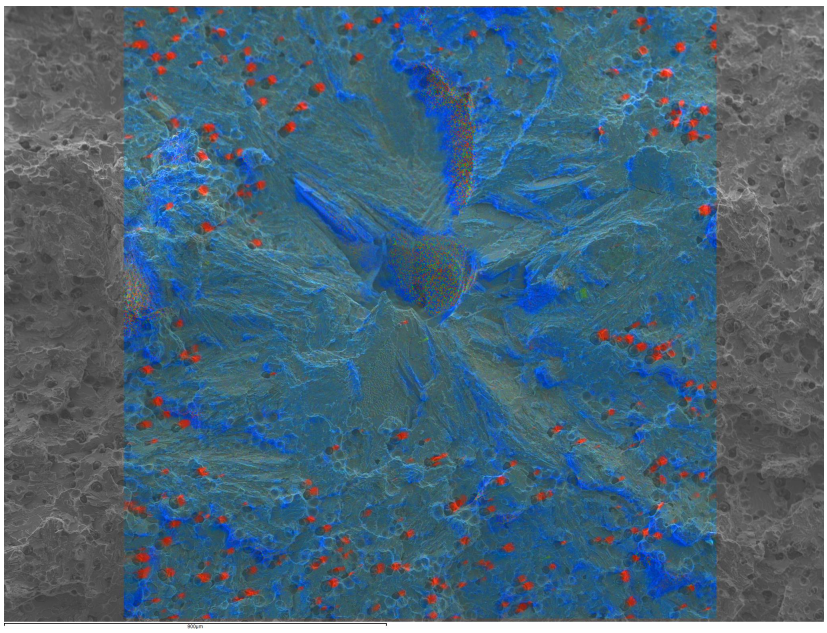


Figure 5.75: EDX layered elements map of the defect shown in figure 5.74 revealed a zone depleted from graphite (marked in red)

•	Surface		Fragment	
Element	Weight%	Atomic%	Weight%	Atomic%
C	2.19	8.73	3.05	9.84
O	2.06	6.14	9.42	22.83
Mg	0.57	1.11	4.17	6.65
Si	3.05	5.19	4.05	5.59
Fe	92.13	78.83	79.32	55.09
Total	100	•	100	•

Table 5.25: EDX elements composition in weight% and atomic% of the defect features shown in figure 5.77

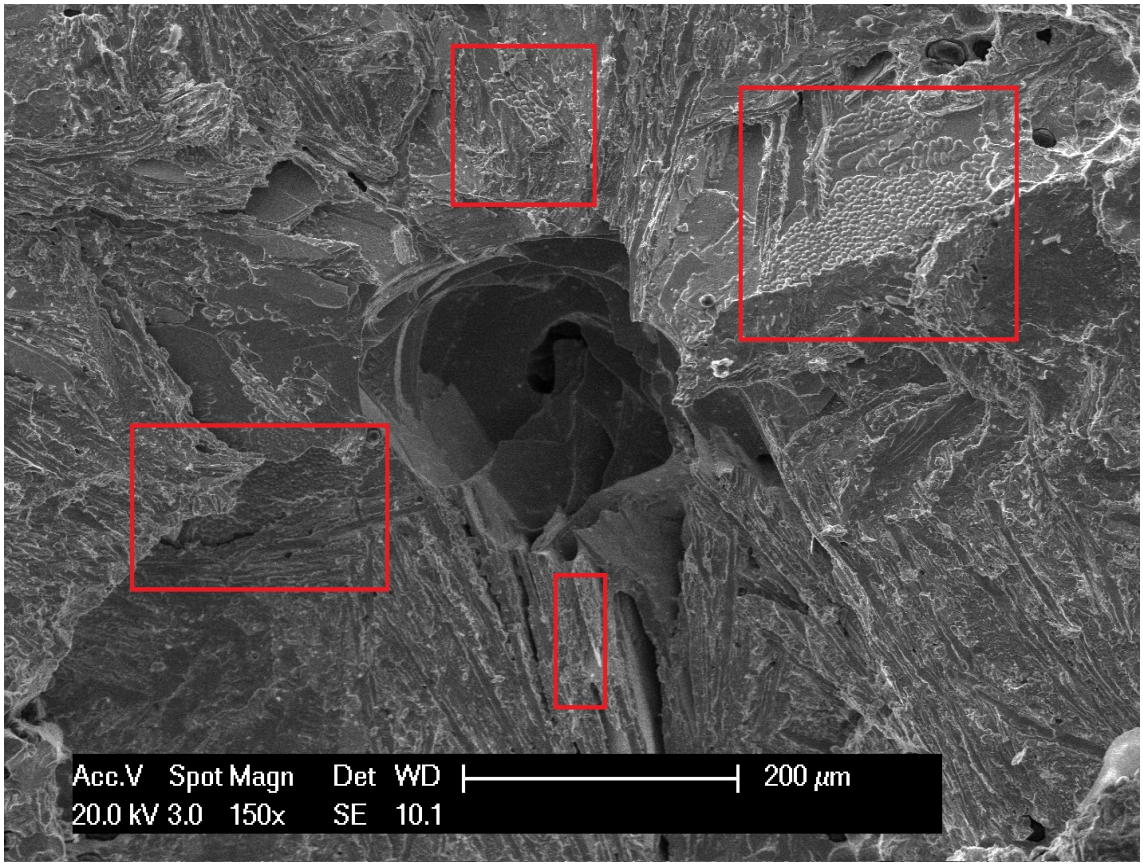


Figure 5.76: A close-up SE image of the defect shown in figure 5.74 showed what appears to be a hole in the middle of the defect with plates surrounding it

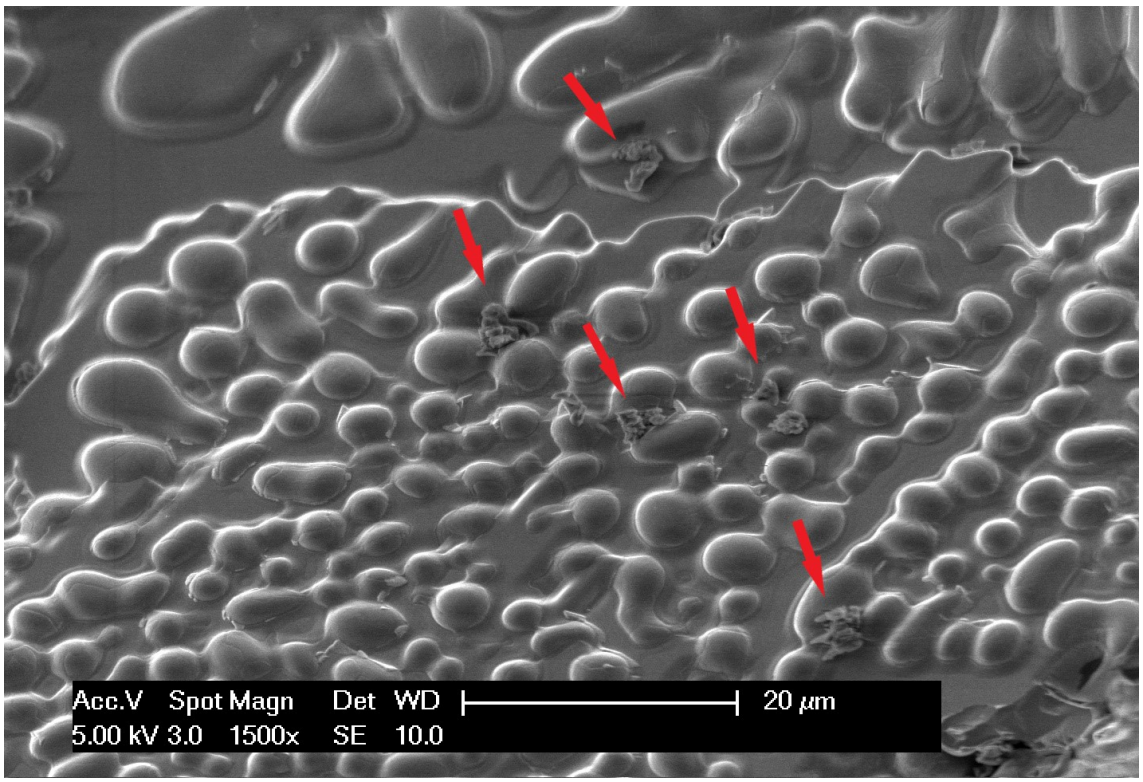


Figure 5.77: A close-up SE image of the areas marked in red in figure 5.76 showed perturbations and fragments on the surface of the plates

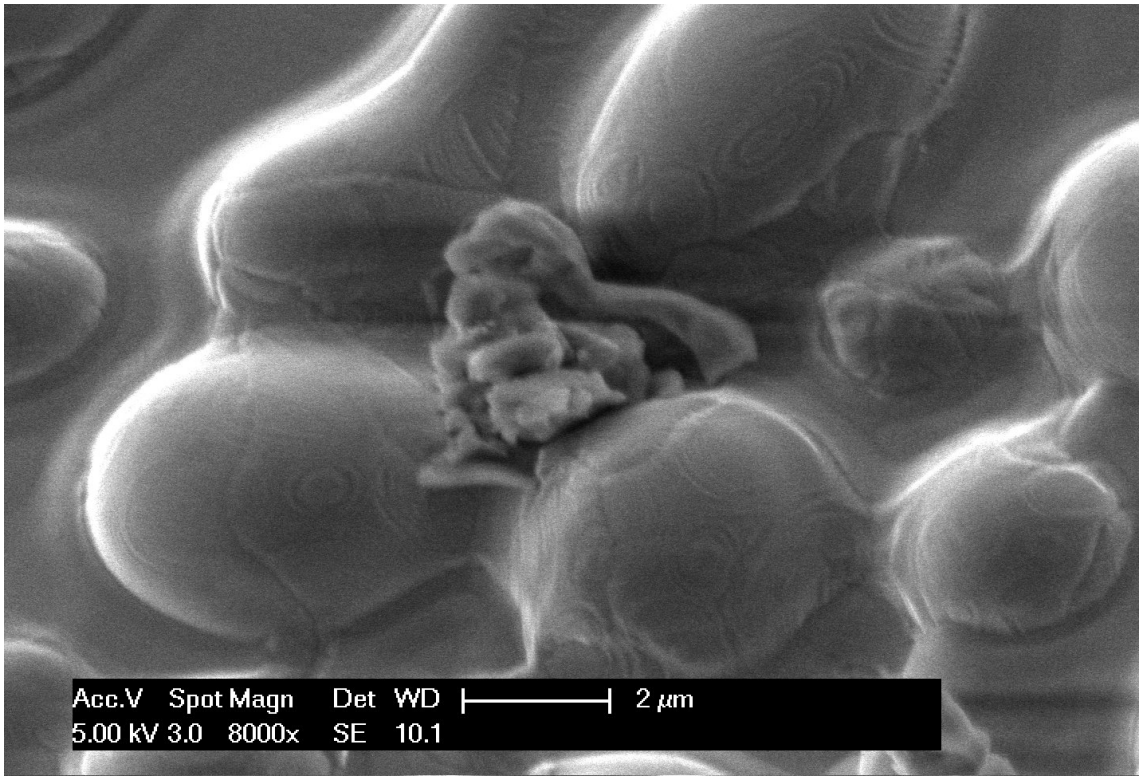
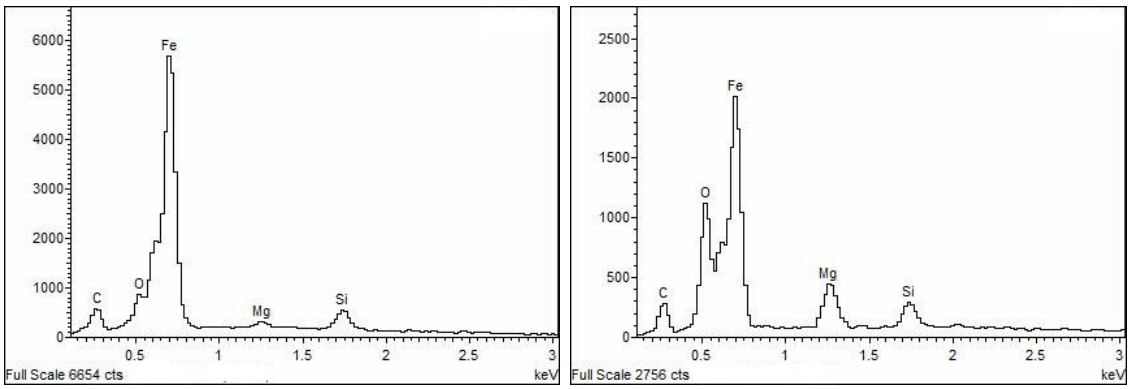


Figure 5.78: Close-up SE image of the fragments in figure 5.77



(a) The surface EDX spectrum (b) The fragment EDX spectrum

Figure 5.79: EDX analysis of the defect features shown in figure 5.77

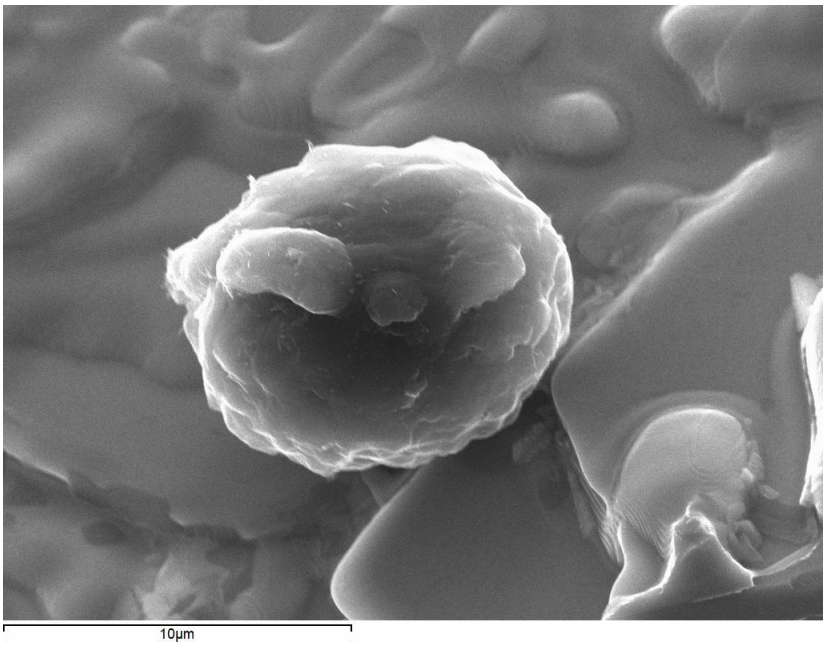


Figure 5.80: SE image of a particle nucleating on the plate of the defect shown in figure 5.74

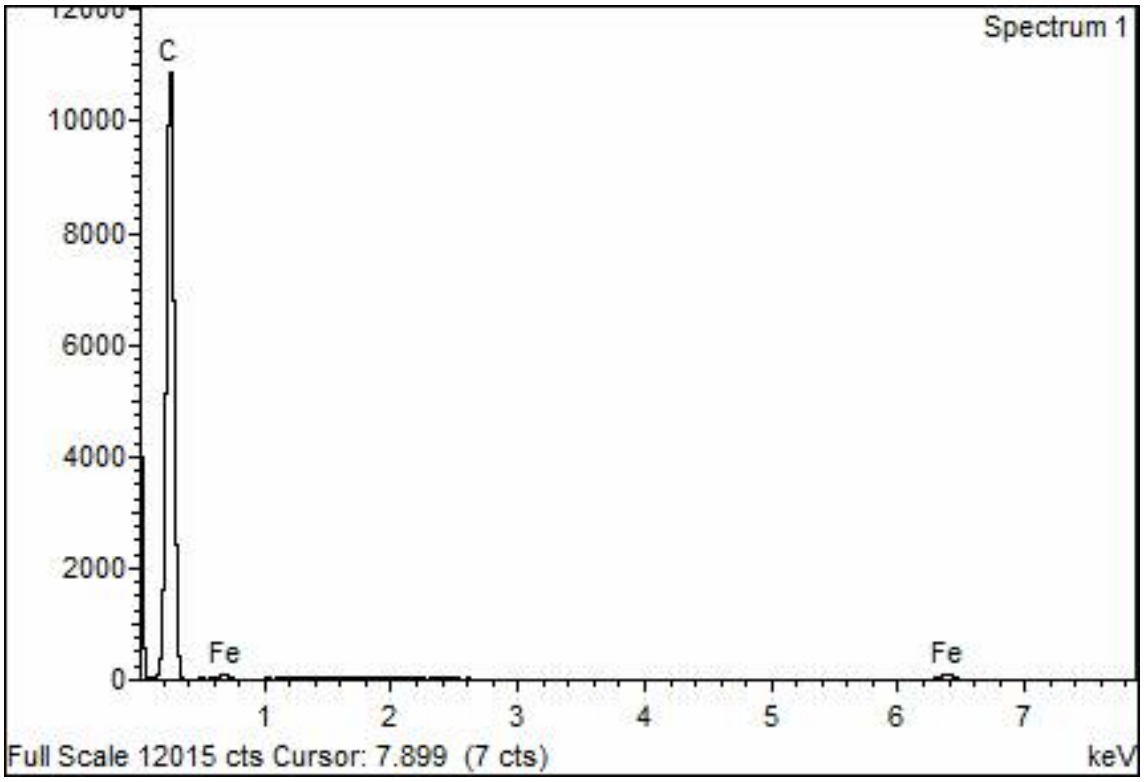


Figure 5.81: EDX spectrum of the particle shown in figure 5.80 confirmed that it was a graphite sphere

Another example of the second type of defect can be seen in figure 5.82. A BSE image of the optically bright area on the fracture surface revealed an area depleted from spheroidal graphite. It also showed, circled in red, horizontal plate defects but with a different configuration. Previously, SGI plate defects were found next to a hollowed space, as shown in figure 5.76. The source of this hollowed space was not known. The plates could be seen more clearly in the center of the SE image in figure 5.83. They resembled needles, do not have atomic bonding between their layers, and they point towards the center of the fracture surface.

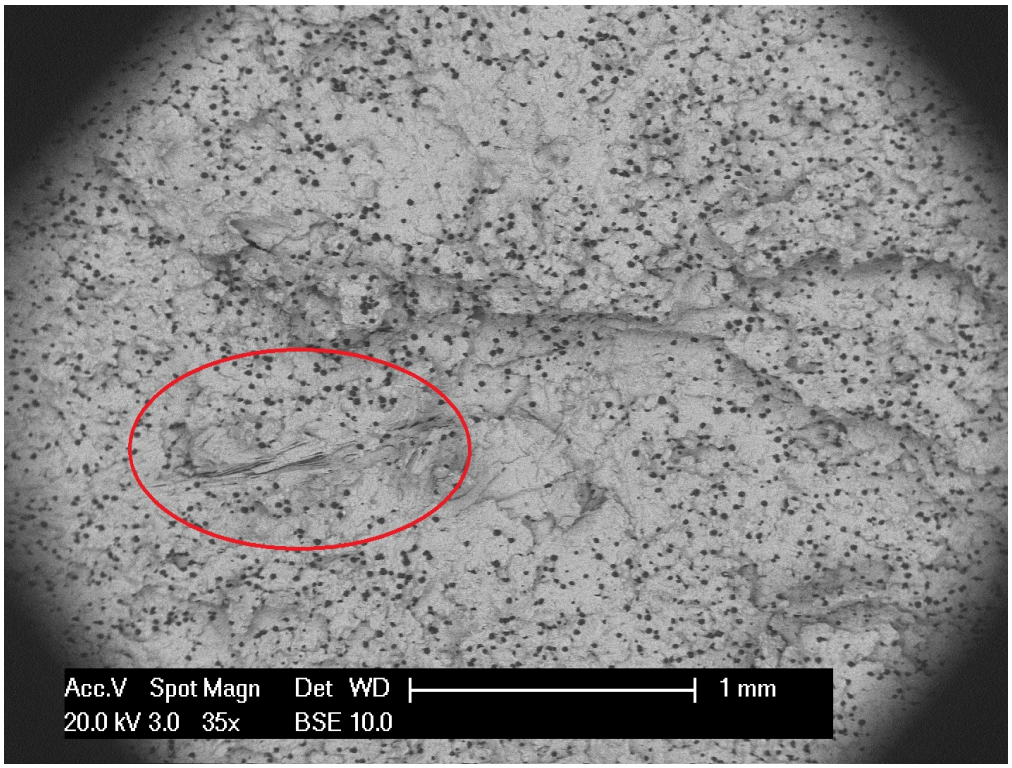


Figure 5.82: BSE image of a different plate defect marked by the red circle

oxide bifilms and casting defects

Figure 5.84 shows a shrinkage pore covered with wrinkled skin and lined with fragments between its dendrite arms. The fragments EDX analysis showed high amounts of Mg and O, and traces of Si, Cu, Sn. The EDX analysis also detected $\backsim$ 2wt. % of P. The EDX spectrum and summary of results are in figure 5.85 and table 5.26; respectively.

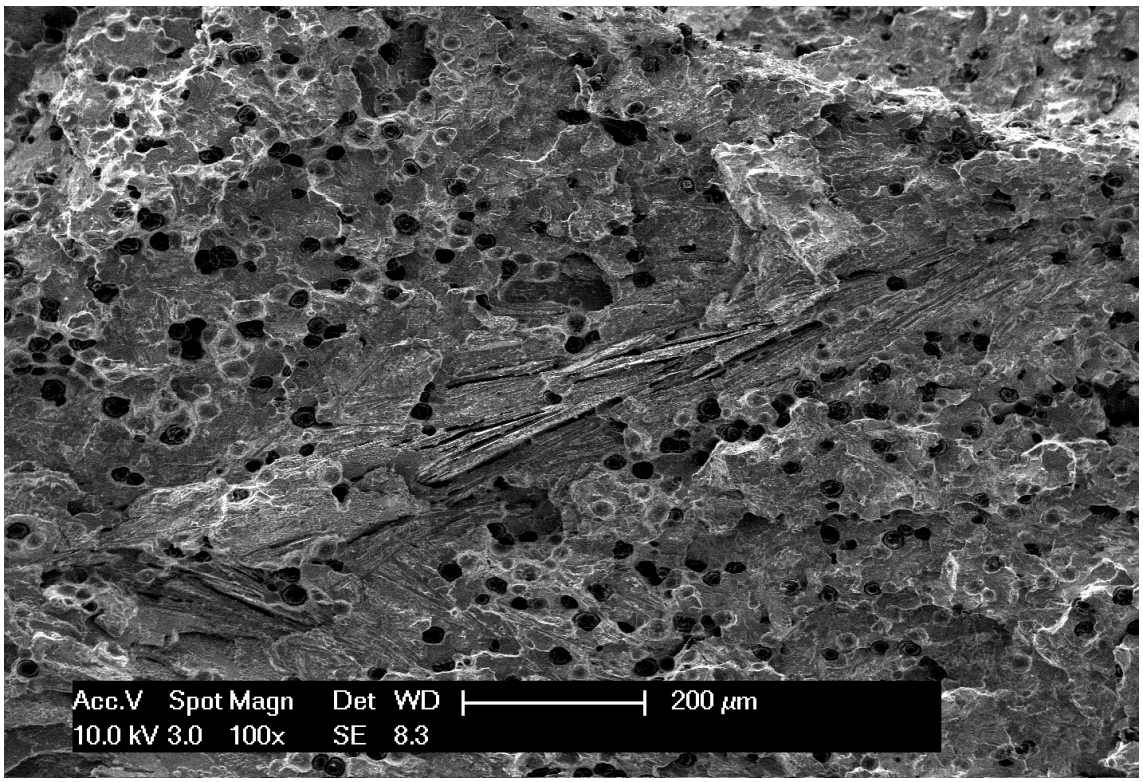


Figure 5.83: A close-up SE image of the defect shown in figure 5.82 revealed that it formed from horizontal plates

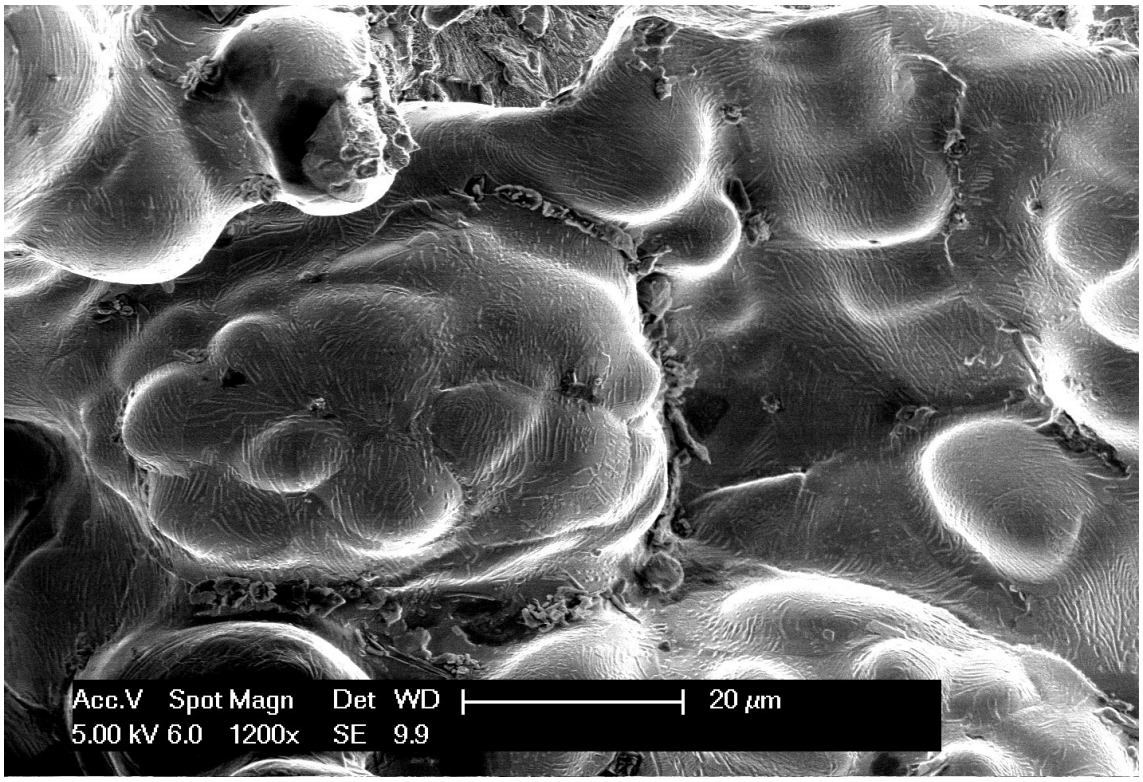


Figure 5.84: SE image of a shrinkage pore with fragments between the dendrite arms

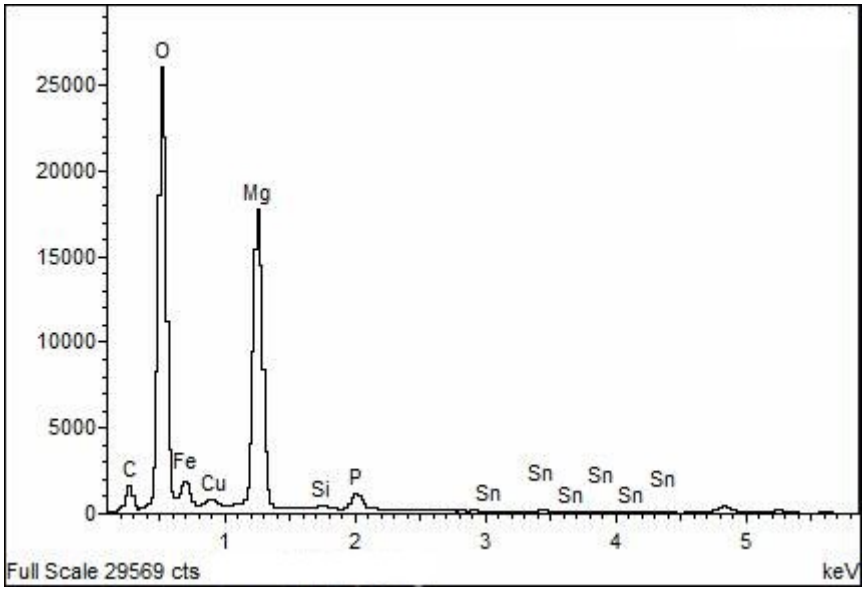


Figure 5.85: EDX spectrum of the fragments shown in figure 5.84 revealed they contained Mg and O

Element	Weight%	Atomic%
C	6.07	10.28
O	47.43	60.18
Mg	25.58	21.36
Si	0.26	0.19
P	2.37	1.56
Fe	16.68	6.06
Cu	0.74	0.24
Sn	0.86	0.15
Total	100	•

Table 5.26: EDX Chemical composition in weight% and atomic% of the fragments shown in figure 5.84

Figure 5.86 is an SE image of a symmetrical porosity on both side of the fracture surface. The porosity had wrinkled skin containing between its folds aligned light element particles, seen in figure 5.87. It also contained multiple dendrite arms as shown in figure 5.92. The EDX analysis of the porosity surface showed Mg, O and C peaks in excess of what is expected in the bulk metal. The entrained particles EDX analysis showed a large C peak which lead to the belief that the particles are graphite spheres, see figure 5.89 and table 5.28. The Mg, O, Si and Fe peaks were generated from the surrounding oxide film and bulk. A 100 µm decarburized zone was located around the porosity. Some Cu and Sn inclusions were detected between the film folds, as shown in figures 5.90 and 5.91, and table 5.29. Some areas of the porosity had circular black and thick wrinkled skin with a diameter around 50 µm, see figure 5.92. EDX analysis, (shown in figure 5.93 and table 5.30), revealed it was a graphitic film.

Element	Weight%	Atomic%
C	6.59	20.39
O	7.02	16.31
Mg	5.48	8.38
Si	1.67	2.22
Fe	79.23	52.71
Total	100	•

Table 5.27: EDX Chemical composition in weight% and atomic% of the EDX spectrum shown in figure 5.88

Element	Weight%	Atomic%
C	56.92	83.77
O	2.69	2.98
Mg	0.55	0.4
Si	0.78	0.49
Fe	39.05	12.36

Table 5.28: EDX Chemical composition in weight% and atomic% of the EDX spectrum shown in figure 5.89

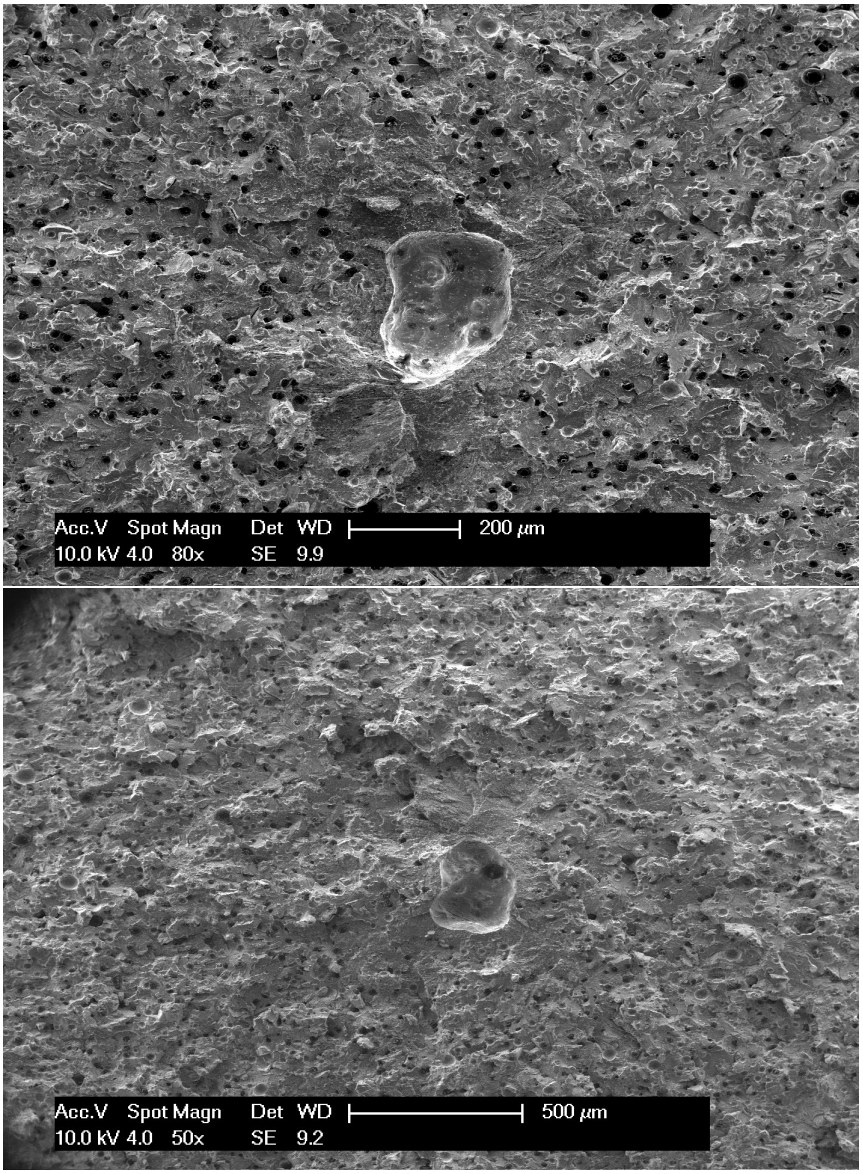


Figure 5.86: SE image of an inflated oxide bifilm

Element	Weight%	Atomic%
C	2.4	7.41
O	12.4	28.74
Mg	12.79	19.51
Si	1.68	2.22
Fe	34.5	22.9
Cu	29.15	17.01
Sn	7.08	2.21
Total	100	•

Table 5.29: EDX Chemical composition in weight% and atomic% of the spectrum shown in figure 5.91

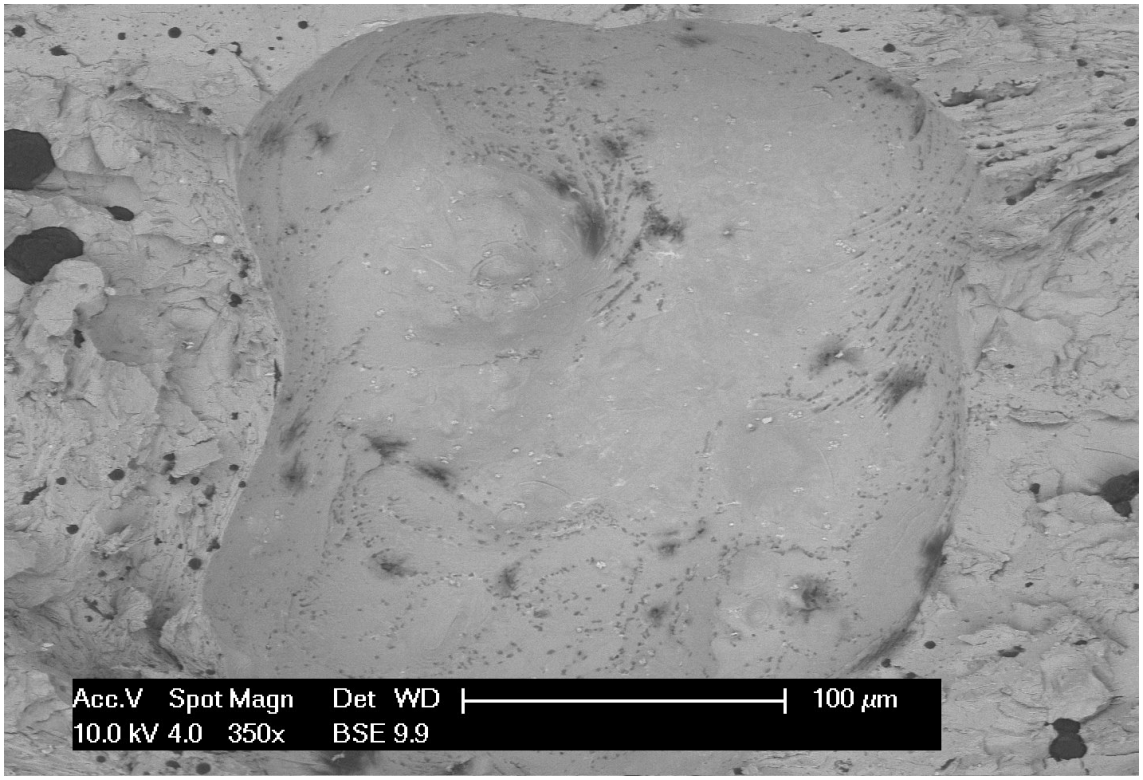


Figure 5.87: BSE image of the defect in figure 5.86 showed aligned light element particles between its folds

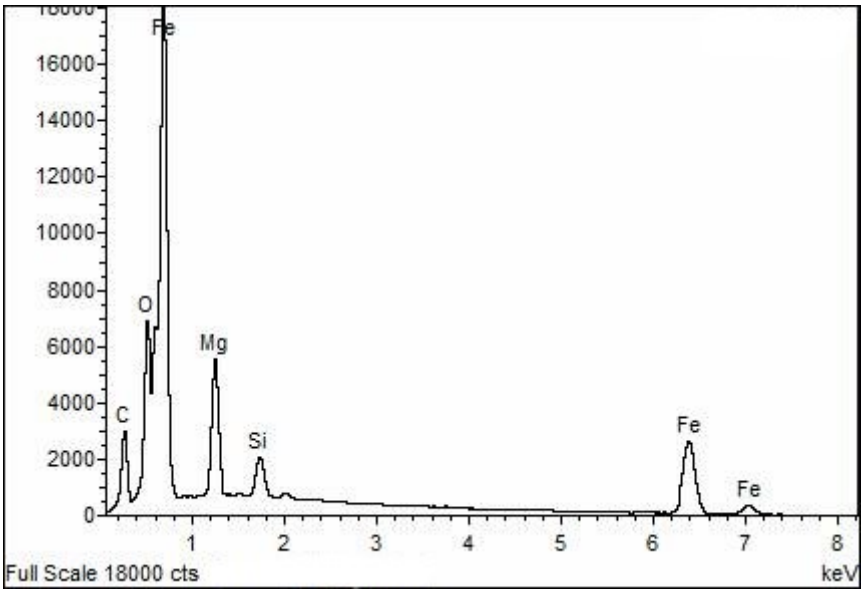


Figure 5.88: EDX spectrum from the surface of the defect shown in figure 5.87 revealed that it contained Mg, O and Si

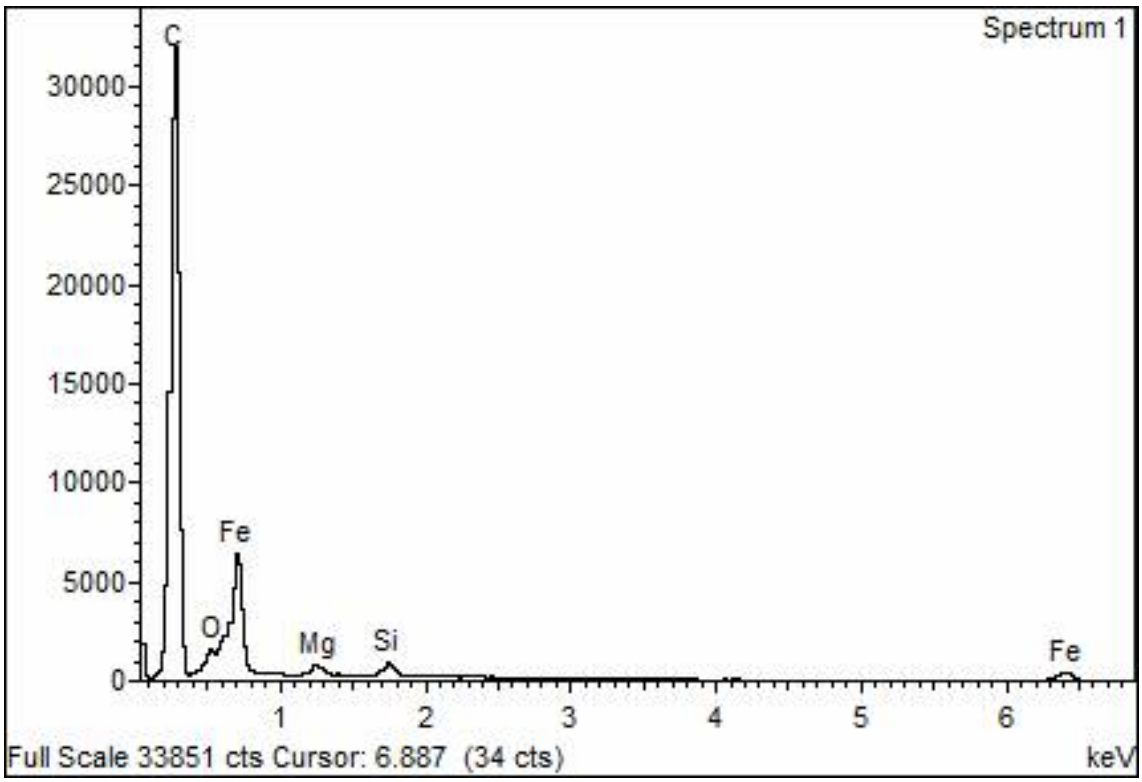


Figure 5.89: EDX spectrum of the particles shown in figure 5.87 revealed that they mainly composed of C

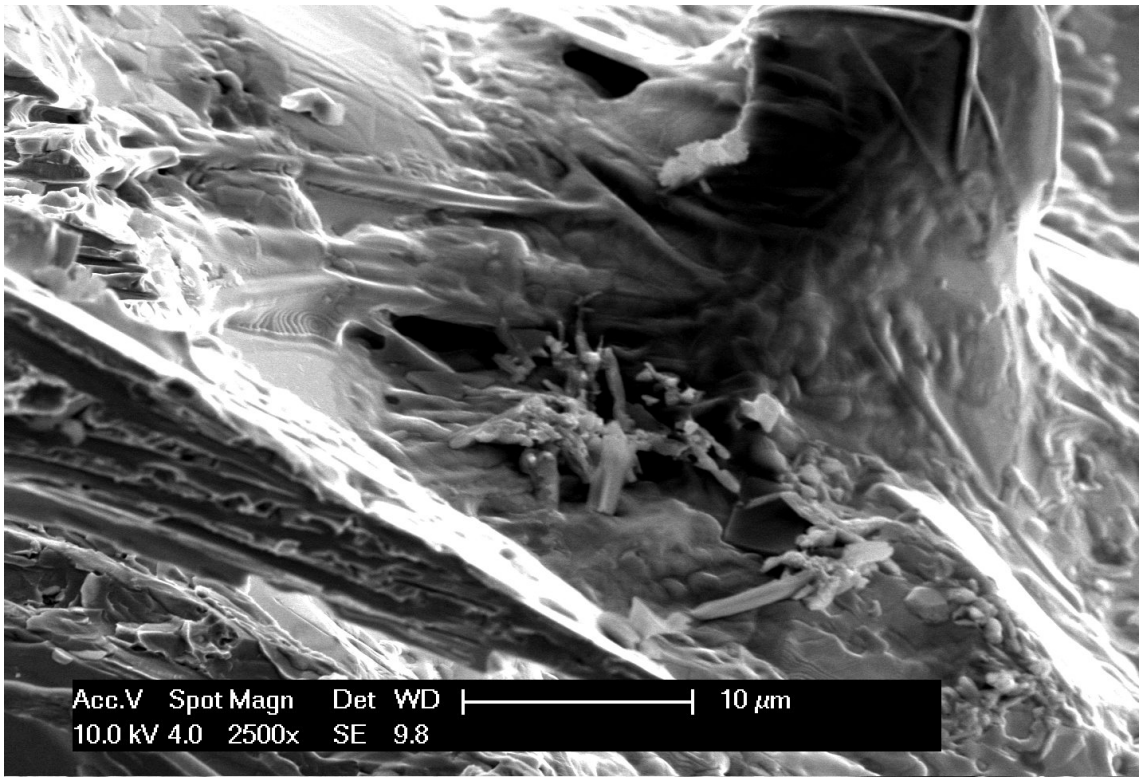


Figure 5.90: SE image of a lodged particles between the bifilm's corrugated folds

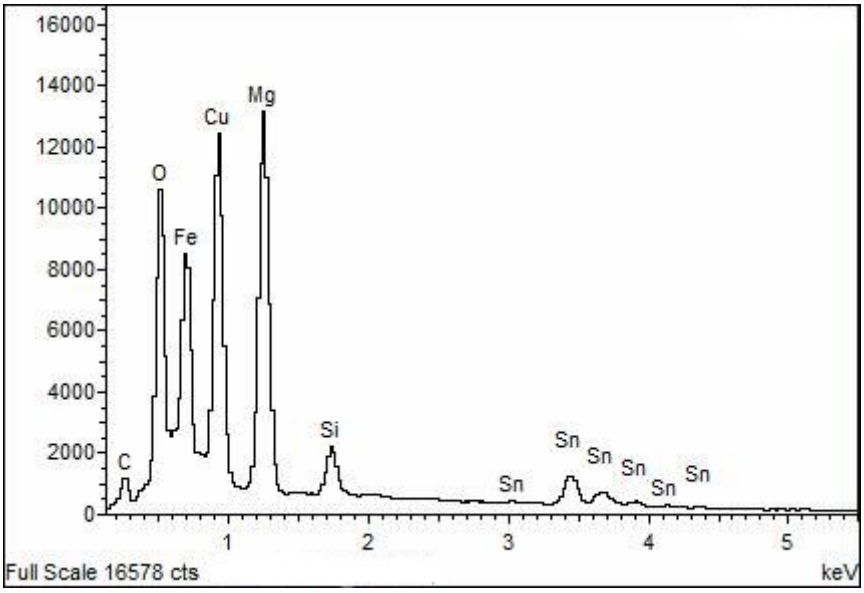


Figure 5.91: EDX spectrum of the particles shown in figure 5.90 revealed they are composed of Cu and Sn

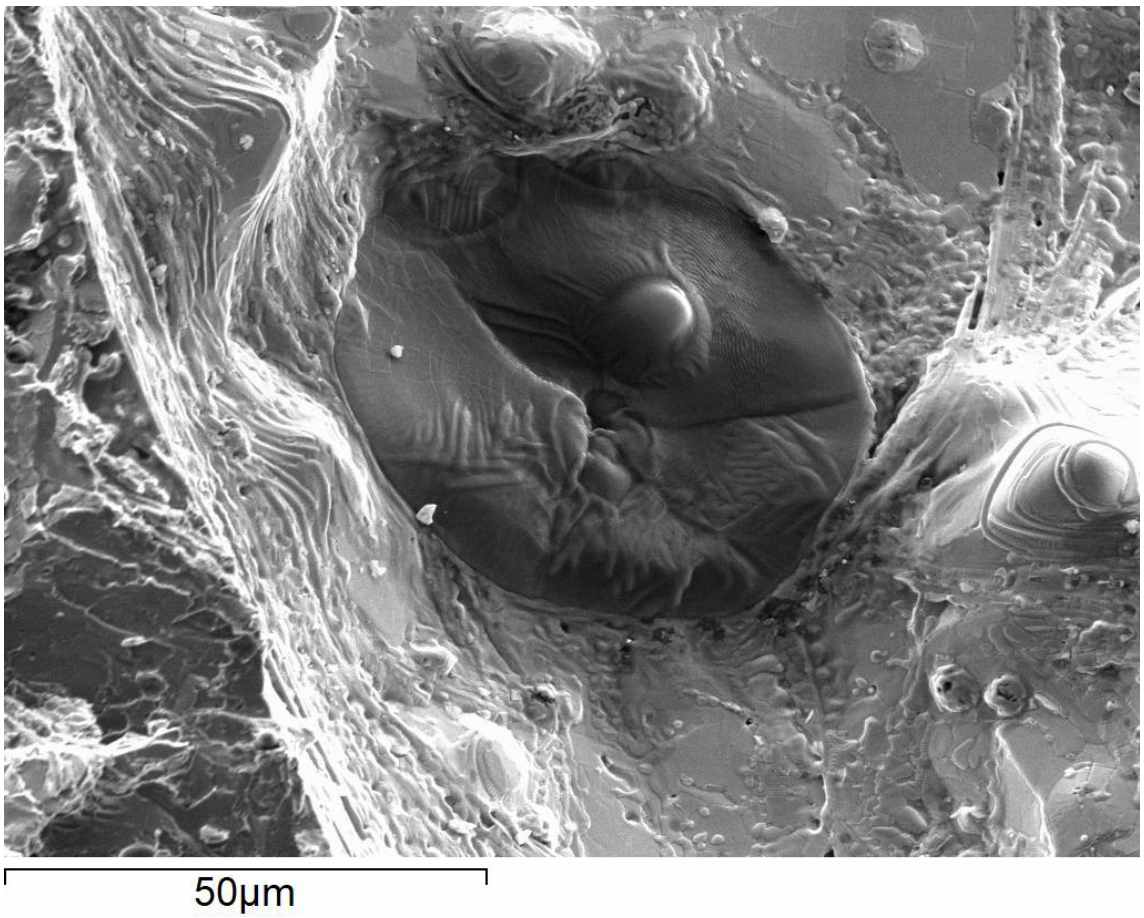


Figure 5.92: SE image of a corrugated thick black layer on the defect's surface

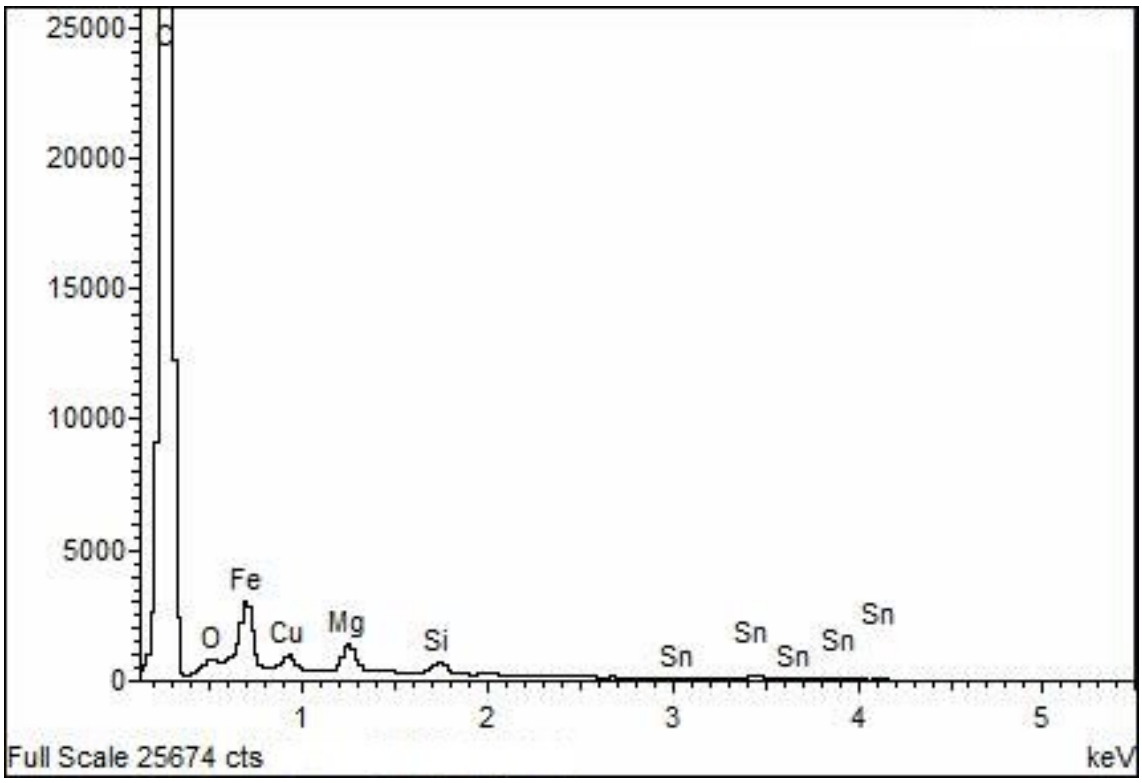


Figure 5.93: EDX spectrum of the dark layer shown in figure 5.92 showed that it is fully graphitic

Element	Weight%	Atomic%
C	74.81	91.94
O	1.7	1.57
Mg	1.02	0.62
Si	0.49	0.26
Fe	19.38	5.12
Cu	1.57	0.36
Sn	1.02	0.13
Total	100	•

Table 5.30: EDX Chemical composition in weight% and atomic% of the graphite layer shown in figure 5.92

Spheroidal graphite were found in a configuration, as shown in figure 5.94, that could be related to entrainment defects. A bubble, marked by a red arrow, 120 µm in diameter were found on the fracture surface surrounded by aligned black particles. The particles had the same colour as the surrounding graphite spheres. The particles alignment direction was parallel to the direction of bubble. This alignment is highly unusual in SGI. The trapped particles were smaller in comparison to normal spheroidal graphite size. A normal spheroidal graphite is 20 µm in diameter, the trapped particles were only 2 µm in diameter. EDX analysis of the defect area showed signals of Mg and O (figure 5.95 and table 5.31). The rest of the elements in the spectrum were Fe, Si, Cu and Sn.

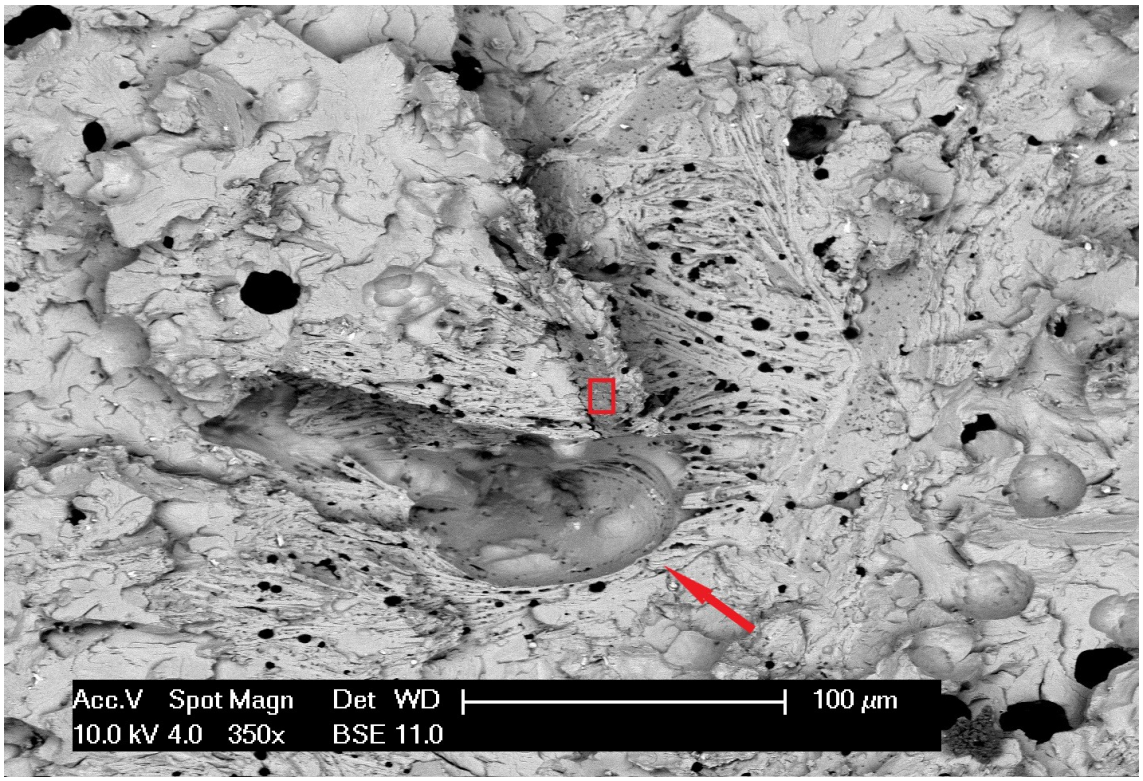


Figure 5.94: A BSE image of aligned graphite next to a bubble

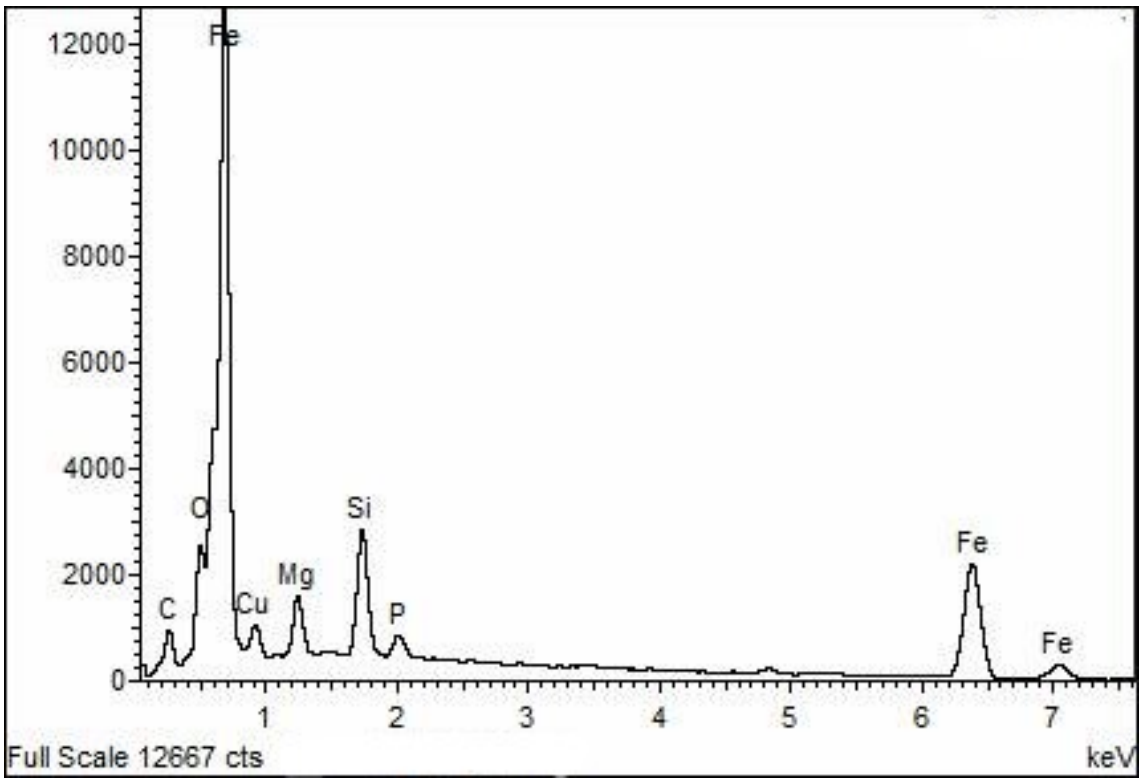


Figure 5.95: EDX spectrum from the area surrounding the bubble shown in figure 5.94 revealed that it contained Mg and O

Element	Weight%	Atomic%
C	3.05	11.17
O	3.47	9.54
Mg	2.01	3.64
Si	4.23	6.64
P	0.97	1.37
Fe	82.44	64.99
Cu	3.38	2.65
Total	100	•

Table 5.31: The EDX Chemical composition in weight% and atomic% of the area shown in figure 5.94

5.2.3 Focused Ion Beam and Transmission electron microscopy analysis

The use of optical and electron microscopy in examining SGI fracture surfaces revealed the existence of double oxide films in SGI. The type of oxide could be MgO but this cannot be fully confirmed due to the short-comings in EDX. To confirm the type of oxide and its relation to the usually observed carbon layer. A section of an oxide bifilm were taken to eliminate substrate interference. Using focused Ion Beam (FIB) milling, the film on the fracture surface in figure 5.35 was sectioned and mounted for STEM mapping to understand its chemical composition and behaviour. The bifilm was chosen due to its relatively flat surface, which make the process of milling a section from its surface, and mounting it, easier. The section location was chosen from a folded part of the bifilm as indicated in figure 5.96. To begin the process a layer of Pt was deposited on top of the desired area to protect the surface from curtaining (i.e. increasing surface roughness in the direction of the milling depth). A Ga ion source was then used for the subsequent milling. Figure 5.97 is a SE image of the hole resulting from the milling of the bifilm. Figure 5.98 shows the final section of the bifilm attached to the TEM grid (on the right side), (notice the bright Pt layer on the top). From the extracted section two folds of the bifilm were seen running all the way down. A dark area was running along the folds of the bifilm. As the section was taken from a rough fracture surface that was very difficult to navigate, some minor curtaining could be noticed.

The STEM image of the folded bifilm in figure 5.99a showed the two faces of the bifilm meeting at the top of the fold but with space in between them. After going down quarter of the way, the space diminishes and the two faces of the bifilm look like they are in full contact. The resulting element maps are in figure 5.99b, and show the detected elements in the bifilm section. Two thin films of Mg mirrored by O were captured following with the contours of the bifilm. They are not easily seen on the top of the bifilm, but some could be noticed on the top left of the map due to a dip in the bifilm surface. The two layers of Mg and O were separated at the top of

the bifilm. Then, possibly due to pressure from the solidification front, they came to contact down into the bulk. The touching of layers does not mean atomic bonding, because in bottom of the section the two layers got separated again (figure 5.99a). ImageJ, an image analysis software, was used to measure the thickness of each layer; and it was found to be around 100 nm in thickness. Due to the small thickness of the Mg and O layers, it was hard to detect it on the top part of the bifilm because the Pt deposited covered their signal. From examining the Mg and O maps it was concluded that SGI bifilms were double magnesium oxide films. A thicker C layer measuring around 1.2 µm was observed on both sides of the MgO film. It was found in the zone between the substrate and MgO film. The thickness of the C layer and its location beneath the oxide bifilm made it more detectable on the top segment of the bifilm during STEM mapping and the Pt layer had a less effect diminishing its signal. Some Si zones nanometre in size, were scattered along the Mg and O layers. Moreover, the N map showed a reminiscence of a N layer going along the Mg and O layers. The bulk signal was formed of Fe (main alloying element) with C, Si and Cu in solid solution.

Until this point, the STEM analysis had resolved the confusion stemming from SEM and EDX data. SEM and EDX data from the bifilm suggested its oxide nature, but did not specify clearly which oxide. The EDX spectra from bifilms always contained Mg, Si and substantial amounts of C. The role of C and its source was not clear, as C is available in abundance in cast iron. Another issue rose from the SEM and EDX analysis, the Al peaks in the spectra generated from the bifilms surfaces. SEM and EDX could not offer any explanation for these peaks. Due to the intensity of the signal there were no doubt that Al existed in the bifilm or at least near it. Figure 5.99a is the STEM image and figure 5.99b is the corresponding element maps of the bottom part of the bifilm. The Al map revealed some nanometre particles residing in the C layer and following the path of the bifilm. Moreover, the Si map showed similar particle locations. This meant the particles were a mix of Al and Si. They could also contain O but this was not clear as the O layer location

on the map intersects with the Si Al particles. The source of the Si was clear. It existed in enough abundance in the alloy. On the other hand, the source of Al was not clear. There is a possibility it could have originated as a impurity from the pig iron. The induction furnace and teapot ladle are only used for cast irons. Thus the possibility of contamination from Al melting is zero.

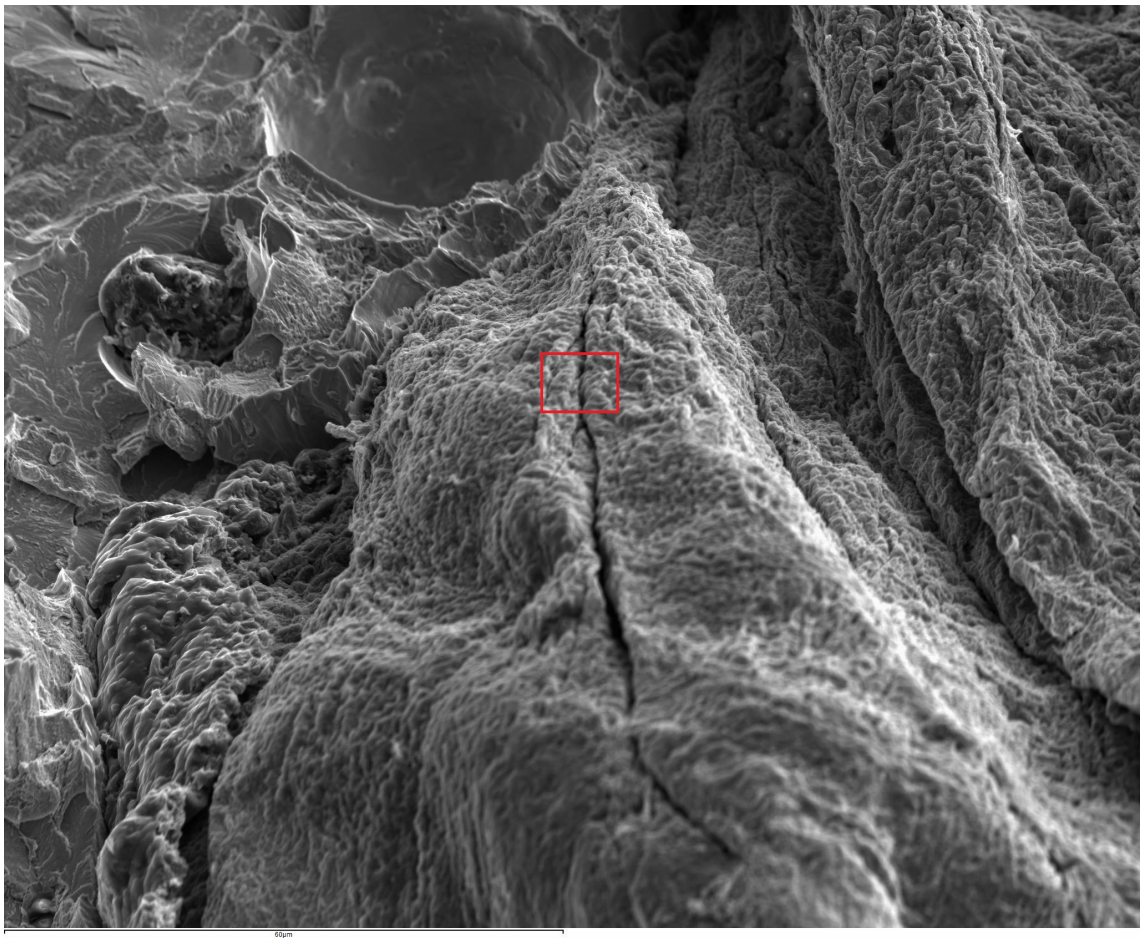


Figure 5.96: SE image of the milling location from which the TEM sample were removed, marked with a red box

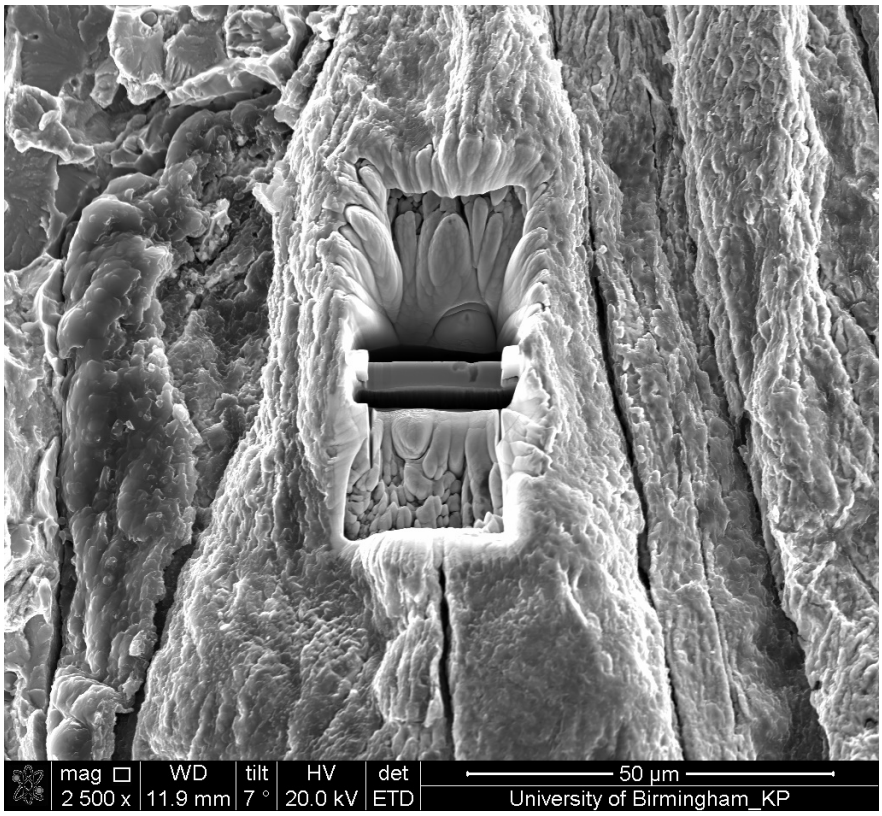


Figure 5.97: The location of the FIB milled bifilm section

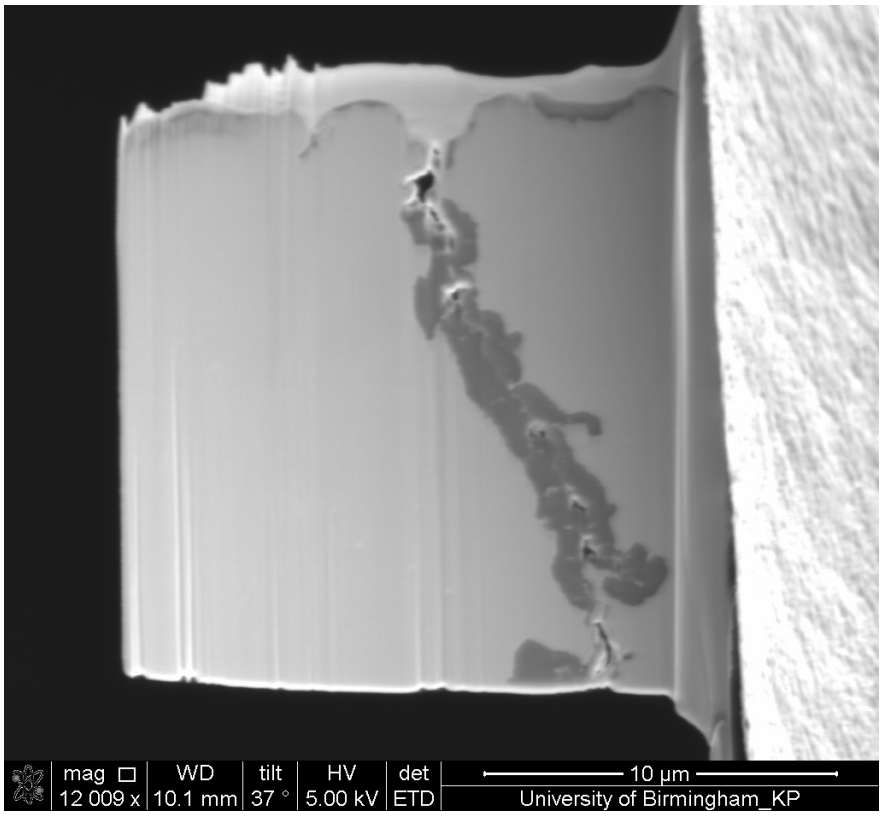
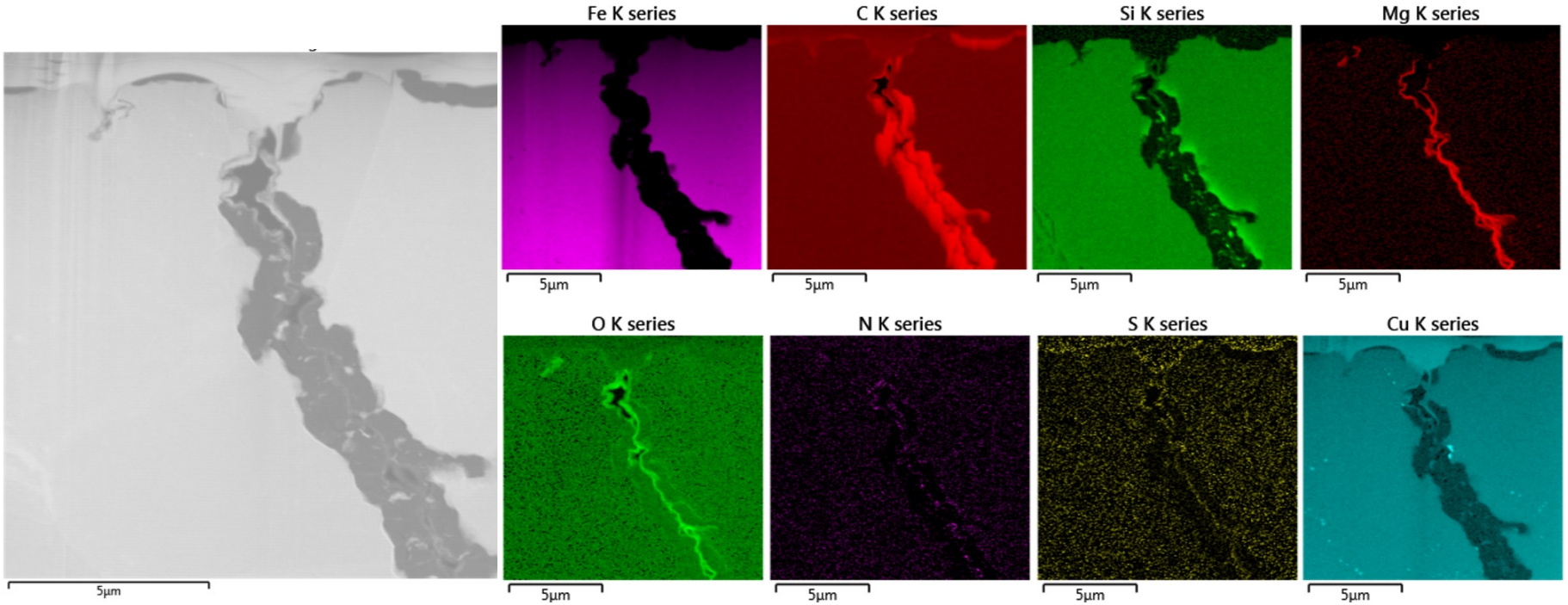


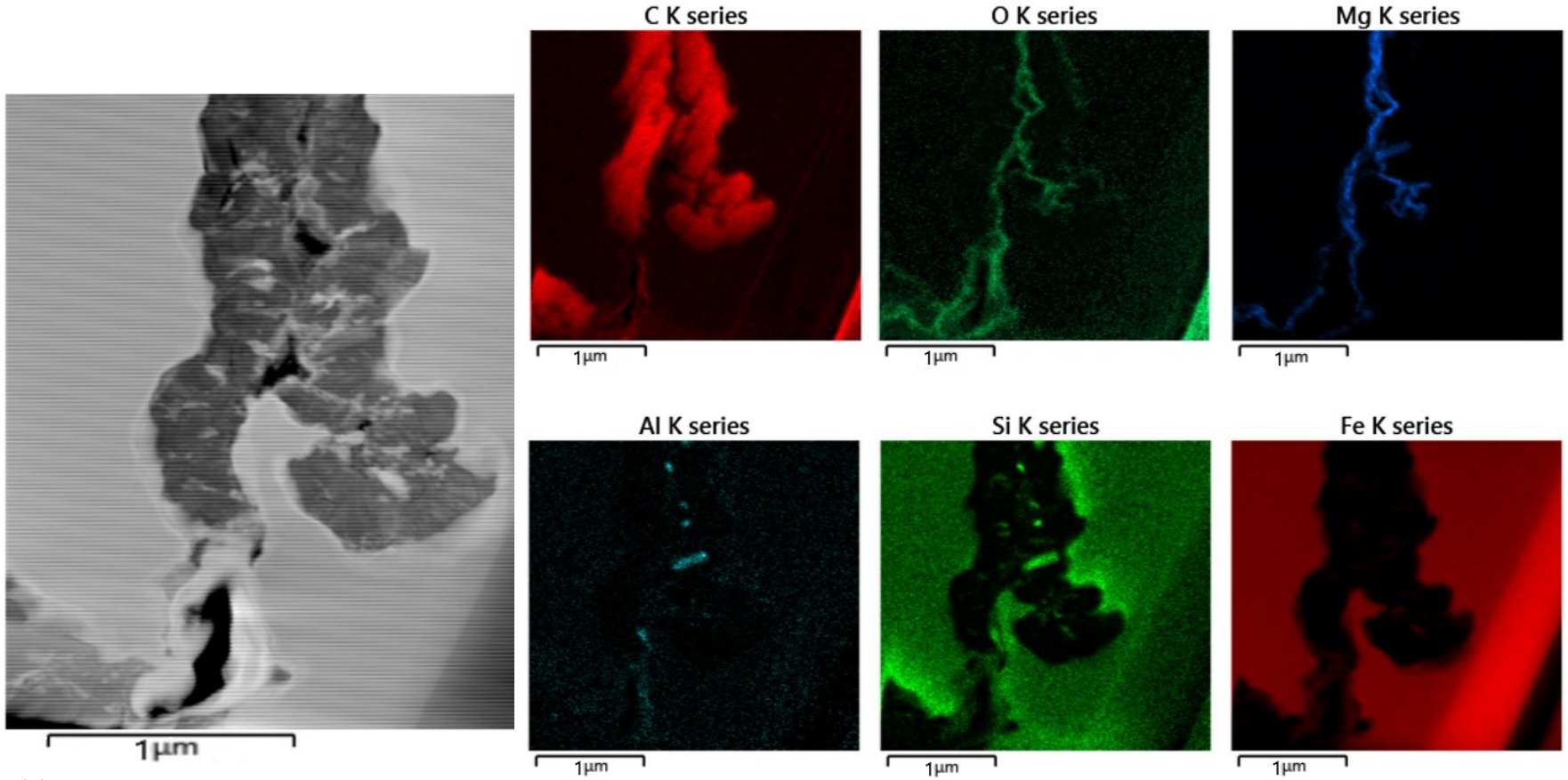
Figure 5.98: SE image of the FIB milled section of the film attached to a TEM grid



(a) STEM image of the bifilm cross-section

(b) STEM element maps of bifilm

Figure 5.99: STEM analysis of the bifilm shown in figure 5.98



(a) STEM image of the bottom section of the bifilm

(b) STEM element maps of the bottom section of the bifilm

Figure 5.100: STEM analysis of the bottom section of the same bifilm

5.3 The relation between SGI defect size and tensile properties

To understand the effect of bifilm defects on the tensile properties of SGI castings, ImageJ, an image processing software, was used to measure the area of bifilms on testbar fracture surfaces by utilizing optical and SEM images. Subsequently, the measured area of the films were plotted against the corresponding testbar UTS and %El., and the trend was revealed with linear regression, seen in figure 5.101 for the UTS and in figure 5.102 for the %El; the summary of results is in table 5.32. For the UTS, the data points were mainly clustered close to the linear trend, and the linear regression had a negative slope indicating a reduction in UTS with the increase in film area. The overall effect of the film area on %El. was the same as the UTS. The trend line had a steeper negative slope thus the effect of the bifilms on the ductility was more deleterious. The %El. data points had a bigger deviation from the linear regression than in the case of UTS. In figure 5.102, there were two data points that appeared to defy the trend. Both had a considerable film defect area but not the expected low %El. value. Figure 5.103 is an optical image of one of the testbars and it revealed an area of high density of graphite spheres around the defect.

Area of the defect (mm^2)	UTS (MPa)	%El. (pct)
0.24	709	2.5
0.28	688	3.3
0.39	787	3
0.42	718	2.3
0.82	714	2.3
0.86	641	4.1
1.07	691	4.2
1.8	587	0.7
2.15	645	1.1
2.76	609	0.8
5.95	519	0.6

Table 5.32: The area of bifilm defects with the equivalent testbar UTS and %Elongation

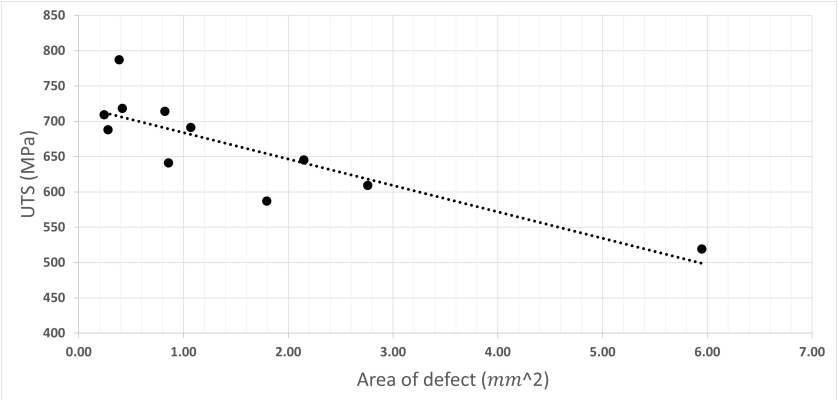


Figure 5.101: Graph between bifilm area vs UTS for SGI testbars

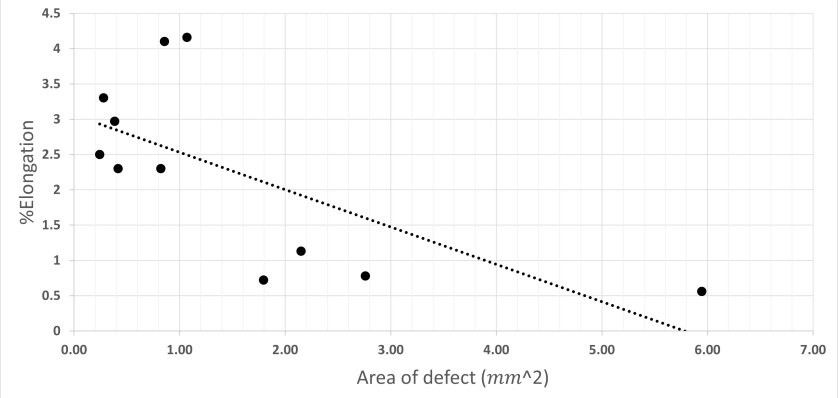


Figure 5.102: Graph between bifilm area vs %El. for SGI testbars

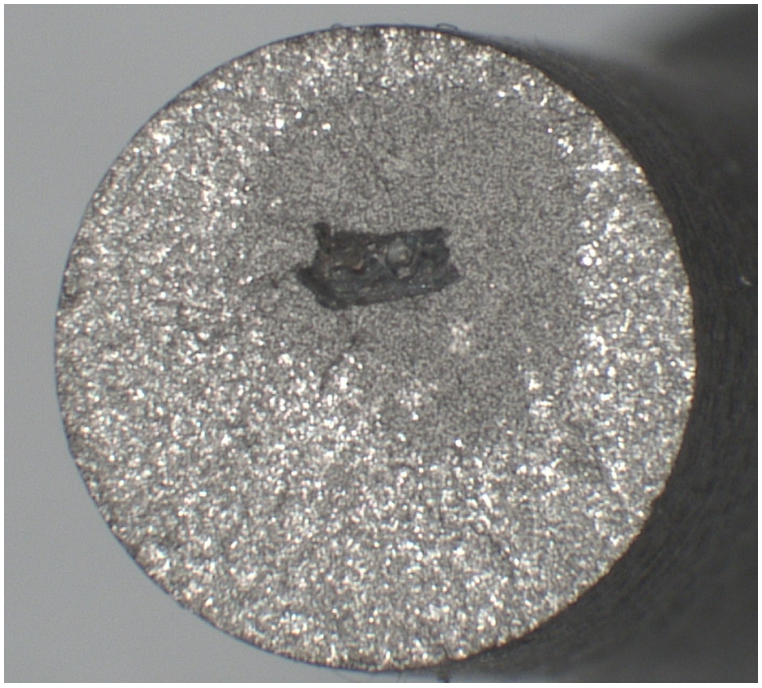


Figure 5.103: Optical image of the fracture surface of the testbar, with a bifilm defect and the highest %El. value in table 4.17, revealed a large area with a high density of spheroidal graphite around the defect

5.4 Summary

This section contained the results from the SGI tesbars sand casting experiment and they were as follows;

1. SGI UTS data had histograms trend was negatively skewed and the data fitted a 2-parameter Weibull distribution.

2. SGI %El. data histograms were positively skewed except for SGI3 and the data fitted a 2-parameter Weibull distribution, except for SGI2 it fitted a 3-parameter Weibull distribution.

3. For SGI1 UTS data VTFM m = 13, and TFM m = 22. For the %El. data VTFM m = 2.7, and TFM m = 3.6.

4. For SGI2 UTS data TFM m = 17, and QFM m = 22. For the %El. data TFM m = 1.3, and QFM m = 1.2.

5. For SGI3 UTS data VTFM m = 36, TFM m = 32, and QFM m = 50. For the %El. data VTFM m = 6, TFM m = 5, and QFM m = 7.

6. For SGI (SGI1 and SGI3) UTS data VTFM m = 16, TFM m = 26, and QFM m = 50. For the %El. data VTFM m = 2.9, TFM m = 4.1, and QFM m = 4.7.

7. Optical microscopy of SGI fracture surfaces revealed two population of defects. One characterized by its symmetrical black film (bifilm), and the other, by its symmetrical shiny surface.

8. SEM and EDX examination of the the first type of defects revealed the oxide nature of the bifilms.

9. SGI oxide bifilms were found to be different in size, topography and entraining different extrinsic inclusions (sand, slag or multiple inclusions). EDX spectra of the bifilms contained O, Si, Mg, Al and C. With one EDX spectrum containing N.

10. FIB and STEM element mapping revealed that the bifilm was MgO, and was 100 nm in thickness.

11. In addition, lustrous carbon bifilms were also detected on SGI fracture surfaces.

12. As to the second type of defects, SEM and EDX revealed what seems to be a novel symmetrical defect which combines the appearance of bubble defect, micro-shrinkage and plate defects. Its EDX spectra contained O and Mg.

13. There was an inverse correlation between the bifilm area and the UTS and %El. of SGI castings.

Chapter 6

Results for Lamellar Graphite Iron

LGI results were comprised from four sources: The first, was an experiment were LGI testbars were gravity cast in three different running system designs of resin-bonded sand moulds. The data was analysed statistically to determine the effect of the filling modes on the tensile properties, reliability and reproducibility of the castings. Subsequently the fracture surfaces were examined using SEM to determine the source of fracture. EDX was used to acquire chemical analysis of defects. The second, was also a casting experiment were LGI testbars were gravity cast iron permanent mould back filled with pure oxygen. Subsequently, the casting was examined by x-ray radiography, tensile tested, and the fracture surfaces were examined with SEM and EDX. The third was a ingot sand casting for reduced pressure test (RPT). Finally, the last results source was from industrial data.

6.1 The effect of quiescently-filled, surface turbulently filled, and very (surface) turbulently-filled moulds on the tensile properties, reproducibility and reliability of LGI

Two separate LGI grade 220 melts were cast to produce a total of 200 testbars. The first melt was denoted LGI1 and the second melts was denoted LGI2. The three filling modes were the same as the SGI experiment, and they are QFM, TFM and VTFM. LGI1 had 40 testbars from QFM and TFM. And LGI2 had 40 test bars from QFM, TFM, and VTFM (table 6.1). LGI1 was cast at the University of Birmingham; and due to the large number of testbars in LGI2, the casting was carried out in an industrial foundry.

Melt	QFM	TFM	VTFM
LGI 1	40	40	•
LGI 2	40	40	40

Table 6.1: Number of testbars in each mould type for different melts

6.1.1 Statistical analysis of LGI UTS data

The descriptive statistics of all LGI UTS data resulting from the tensile test are shown in table 6.2. Even though the two melts were from the same grade, LGI2 had higher mean UTS values than LGI1. LGI1 TFM and LGI2 QFM had a mean UTS of 258 and 257 MPa; respectively. LGI2 VTFM, LGI2 TFM and LGI2 QFM had a mean UTS of 393, 429 and 433 MPa; respectively. The average UTS for LGI1 (257.5 MPa) was lower than that of LGI2 (418 MPa), this difference could be attributed to different routes of alloy preparation between the casting laboratory and industrial foundry. LGI2 VTFM had 40 testbars cast, machined and tested, but the count in the descriptive statistics is 39. Two testbars' UTS results were omitted from the statistical analysis due to its very low UTS (103 and 269 MPa). It is good

practice in statistical analysis of cast components that no results should be ignored. A large defect - e.g. a bifilm - could be responsible for the low value and that would be important for a representative statistical analysis. However, the testbar's UTS values were removed as a result of SEM examination. It revealed that the fracture surface contained a large sand defect, see section 6.2.2. Thus the addition of the UTS result would have increased the scatter and skewed the statistical analysis.

Variable	Count	Mean	StDev	Variance	Minimum	Maximum	Range
LGI1 TFM	40	258	16	268	237	291	54
LGI1 QFM	40	257	10	53	242	270	28
LGI2 VTFM	38	396	31	941	333	447	115
LGI2 TFM	40	429	11	119	397	450	53
LGI2 QFM	40	433	17	277	378	456	78

Table 6.2: Descriptive statistics of LGI UTS (MPa) data

From the same set of UTS data Gaussian distributions were acquired and plotted, see figure 6.1.

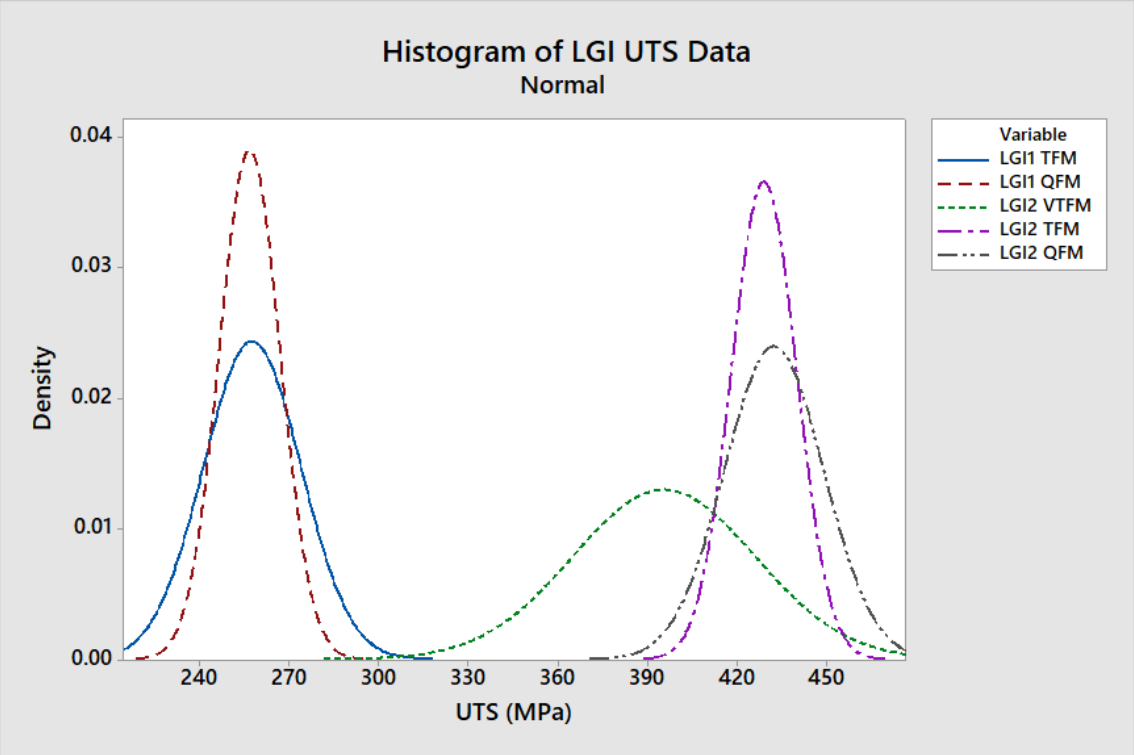


Figure 6.1: The fitted Gaussian distributions for UTS data from each mould type for different LGI melts

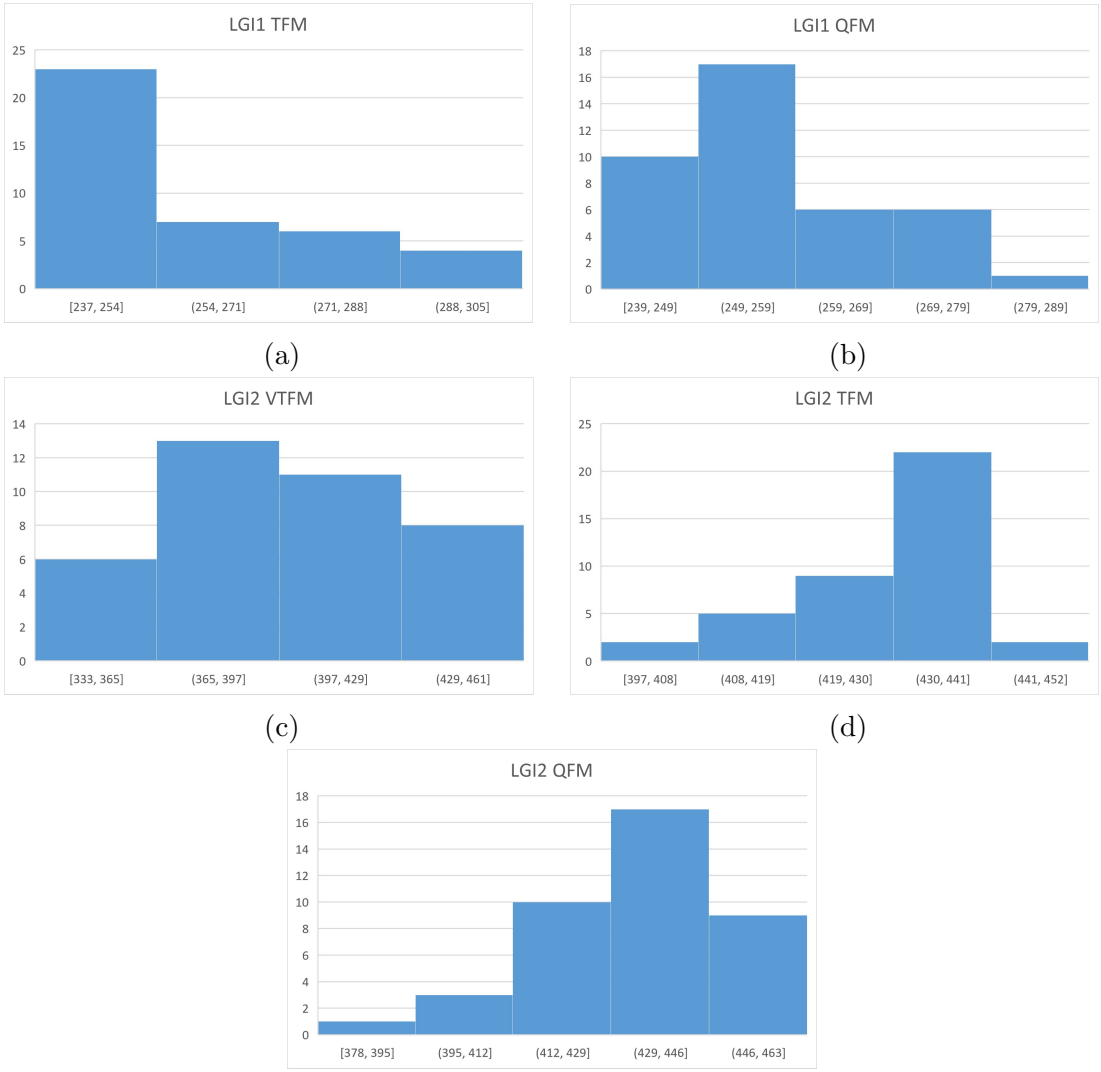


Figure 6.2: Separate histograms for UTS data. The x-axis represent the range of bins in MPa, and the y-axis represents the number of data points in each bin

The Gaussian distribution plots for LGI UTS data (figures 6.1 and 6.2) confirmed the difference between LGI1 and LGI2. LGI1 data distribution was positively skewed, on the other hand in LGI2 data distribution was negatively skewed. LGI2 TFM and LGI2 QFM UTS data sets had a positively skewed distribution. LGI1 groups were on the low side of the scale and LGI2 groups were on the high side of the scale. LGI1 QFM and LGI2 TFM had a close mean UTS, 258 MPa and 257 MPa, respectively. The data spread, represented by the range, of LGI1 QFM (28 MPa) was lower than that of LGI1 TFM (54 MPa). For LGI2, the analysis was split into two parts. Part one focused on the comparison between LGI2 VTFM vs LGI2 TFM and QFM. LGI2 VTFM had a lower mean UTS (396 MPa) and a significantly bigger spread with a range of 115 MPa. Part two examined the relation between LGI2 TFM vs LGI2 QFM. LGI2 TFM and LGI2 QFM had a close mean UTS of 429 MPa and 433 MPa, respectively. But unlike LGI1, LGI2 QFM had a bigger range than LGI2 TFM, 78 and 53 MPa; respectively. Thus, the relation between LGI2 TFM and LGI2 QFM is contrariwise mirroring that of LGI1 TFM and LGI1 QFM. The Gaussian distribution analysis also illustrated that the data sets intersected and overlapped. Thus to determine if there was a significant difference between the data sets, a student t-test was carried out between the comparable sets. The results are shown in the following table:

Two Samples		T-Value	P-Value
LGI1 TFM	LGI1 QFM	0.3	0.8
LGI2 VTFM	LGI2 TFM	6	0
LGI2 VTFM	LGI2 QFM	6.2	0
LGI2 TFM	LGI2 QFM	1.1	0.3

Table 6.3: Student's t-test results

For LGI1, the Student's t-test was carried out between LGI1 TFM and LGI1 QFM. With a t-value of 0.3 and p-value of 0.8 ($>$ the significant level of 0.05), it indicated that the null hypothesis cannot be rejected (the null hypothesis assumes the difference between the means = 0). Thus, it cannot be concluded that there is a significant difference between the means of LGI1 TFM and LGI1 QFM (table

6.3). For LGI2, LGI2 VTFM and LGI2 TFM had a t-value of 6 and a p-value of 0. As for LGI2 VTFM and LGI2 QFM, the numbers were close to the previous figures. The t-value was 6.2 and p-value was 0. This meant the rejection of the null hypothesis, concluding that there was a significant difference between the means of LGI2 VTFM and LGI2 TFM on one hand, and LGI2 VTFM and LGI2 QFM on the other. Finally, the student t-test between LGI2 TFM and LGI2 QFM resulted in t-value = 1.1 and p-value = 0.3. As 0.3 is bigger than the significant level, it cannot be concluded that there is a significant difference between their means. Nevertheless with a bigger t-value, the evidence against the null hypothesis will be bigger.

To determine which statical distribution best fitted the data sets, an Anderson-Darling (AD) test was utilized. The data sets were tested against the normal, log-normal, 2-parameter and 3-parameter Weibull distributions. The five data sets were run through the test, and each distribution resulted an AD score. The criteria applied for choosing the distribution was that the lowest the resulting AD score, the better the goodness of fit, but also taking in consideration the aims in section 5.1.1. For LGI1 TFM, the 3-parameter Weibull had the lowest AD score of 0.7. It was much lower than that of the normal, log-normal and 2-parameter Weibull of 1.8, 1.7 and 2.3, respectively. The 3-parameter Weibull also had the lowest AD score for LGI1 QFM. The score was 0.6 for 3-parameter Weibull, 1.6 for 2-parameter Weibull, 0.9 for log-normal, and 0.9 for Normal distribution. Hence for LGI1, the 3-parameter Weibull distribution was used to evaluate and compare the UTS data. Usually the target would be to use the 2-parameter Weibull distribution to align the work with the literature, but if the difference in the AD scores was high, as in the case for LGI1, this will lead to low goodness of fit and the distribution will not be a viable option. For LGI2 data sets, LGI2 VTFM UTS data had an equal AD score for the three distributions (AD score = 0.9), except for log-norm (AD score = 1). The 2-parameter Weibull had the lowest AD score for LGI2 TFM. But for LGI2 QFM, the 2-parameter Weibull had the second lowest score = 0.6. It was slightly higher than that of the 3-parameter Weibull of 0.5. Hence, the 2-parameter Weibull

distribution was chosen to evaluate and compare LGI2 UTS data. The summary of the AD test scores and the corresponding probability plots are in table 6.4 and in figures 6.3 to 6.7.

•	Normal	2-Parameter Weibull	3-Parameter Weibull	Log-normal
LGI1 TFM	1.8	2.3	0.7	1.7
LGI1 QFM	0.9	1.6	0.6	0.9
LGI2 VTFM	0.9	0.9	0.9	1
LGI2 TFM	1.1	0.7	0.8	1.2
LGI2 QFM	1.1	0.6	0.5	1.2

Table 6.4: Anderson-Darling test results

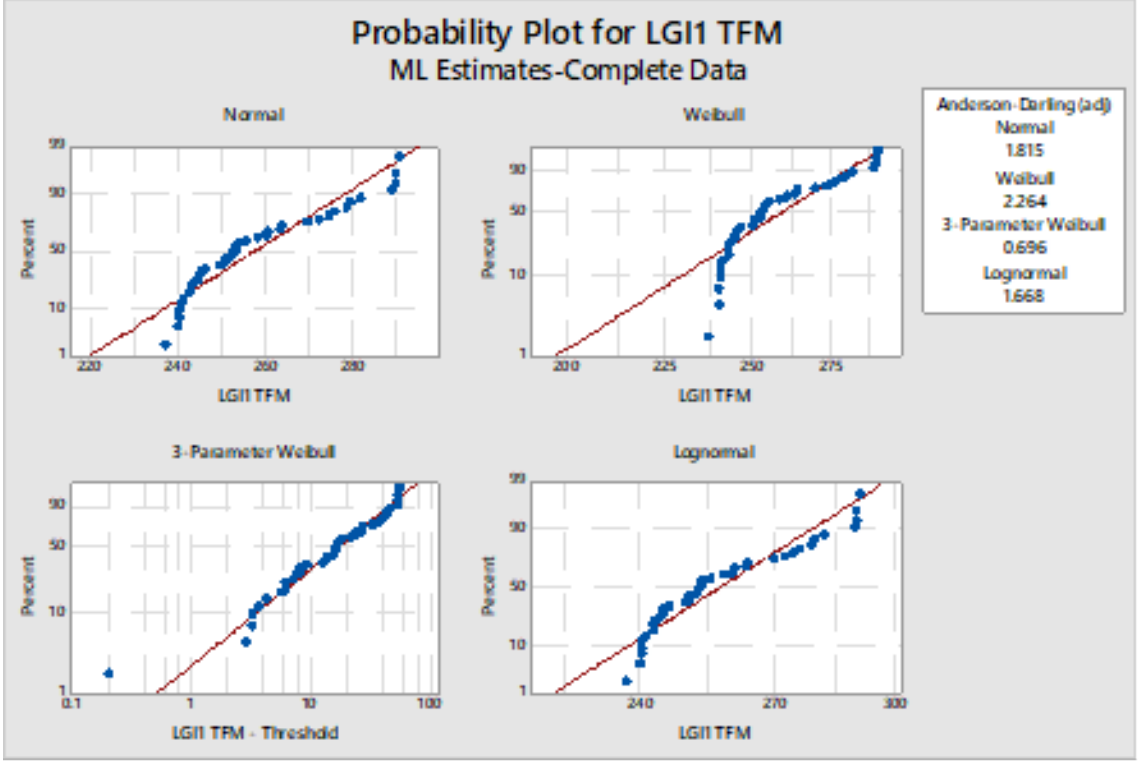


Figure 6.3: Probability plots of AD test for LGI1 TFM. The y-axis represents the cumulative probability in percent. The x-axis represents the UTS in MPa, except for the 3-parameter Weibull plot, it is the threshold value in MPa

6.1.2 Weibull Distribution analysis of LGI UTS data

The 3-parameter Weibull distribution was used to evaluate and compare LGI1 UTS data and the 2-parameter Weibull distribution was used for LGI2 UTS data. Figure 6.8 is the 3-parameter Weibull plot for LGI1 UTS data. LGI1 QFM had a higher

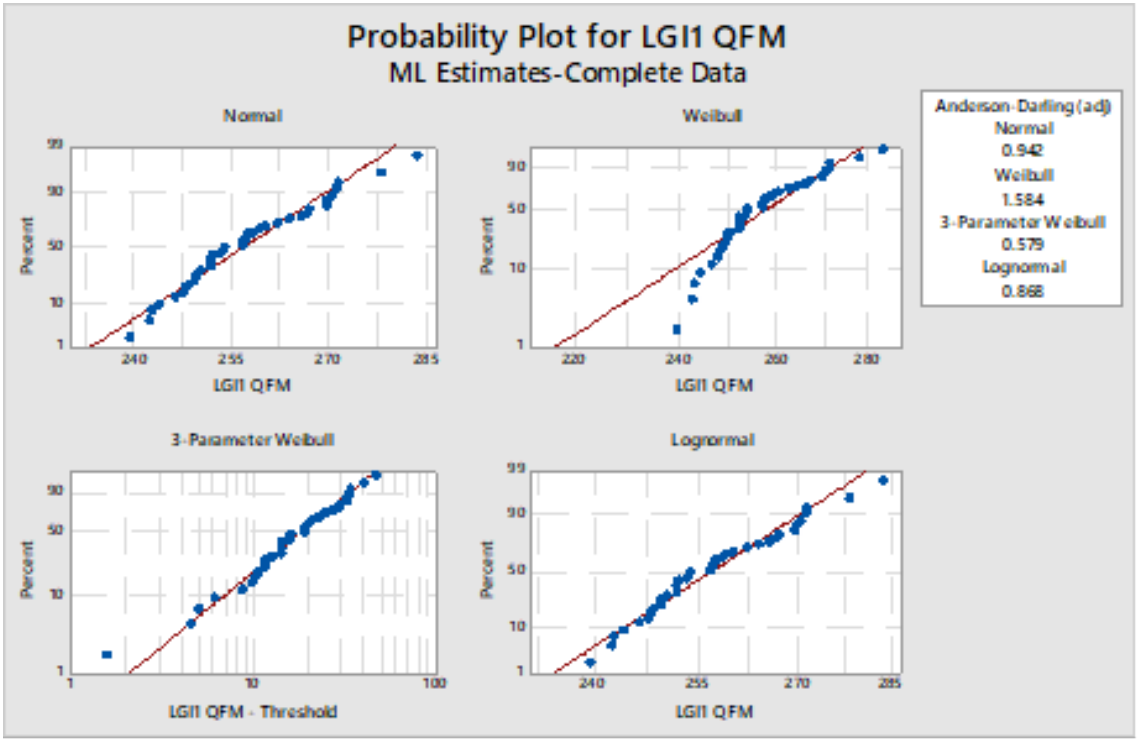


Figure 6.4: Probability plots of AD test for LGI1 QFM. The y-axis represents the cumulative probability in percent. The x-axis represents the UTS in MPa, except for the 3-parameter Weibull plot, it is the threshold value in MPa

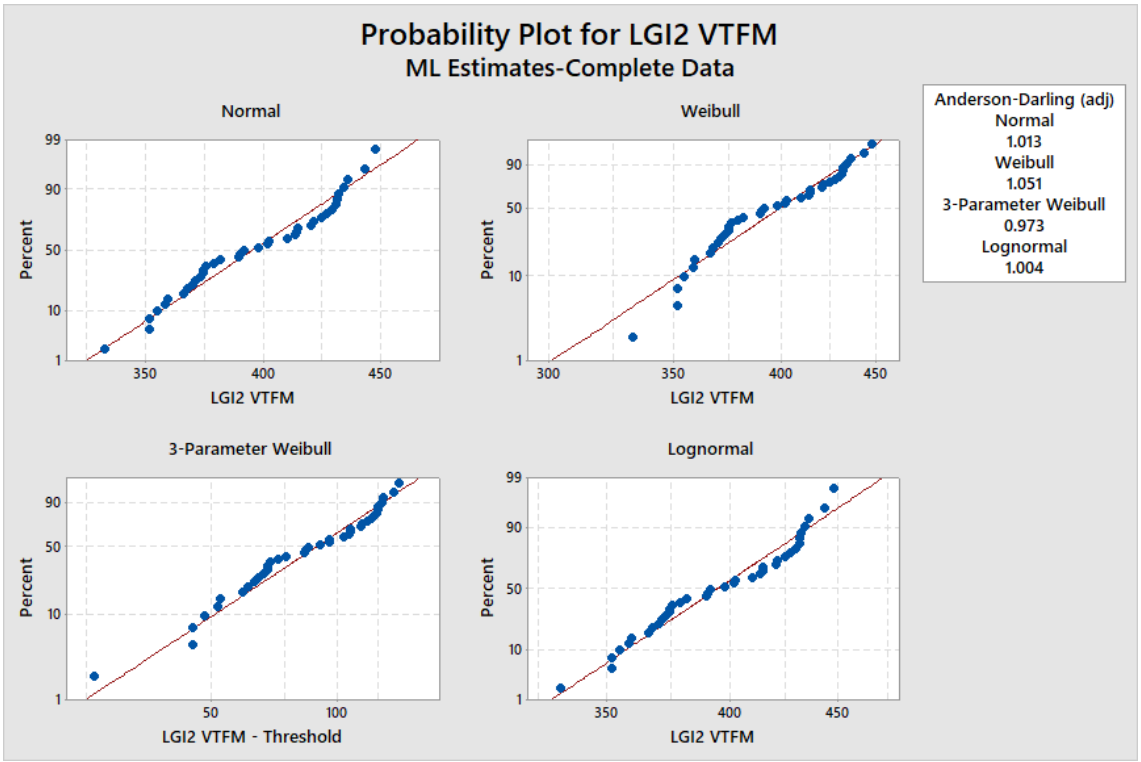


Figure 6.5: Probability plots of AD test for LGI2 VTFM. The y-axis represents the cumulative probability in percent. The x-axis represents the UTS in MPa, except for the 3-parameter Weibull plot, it is the threshold value in MPa

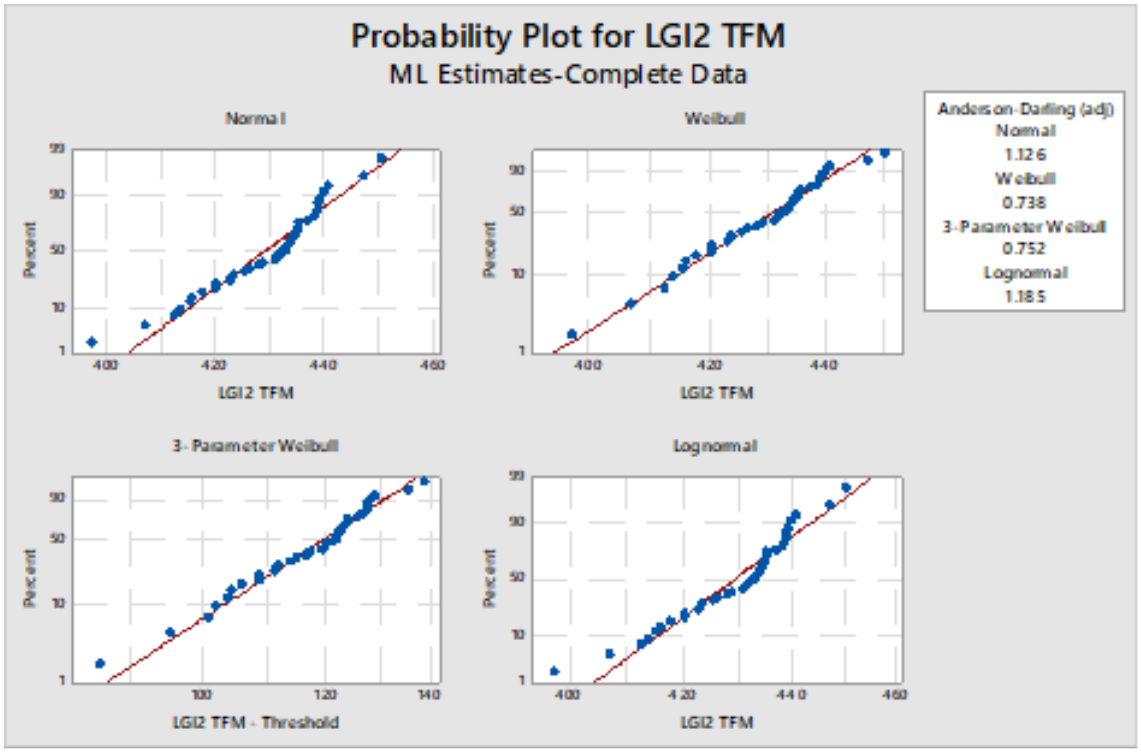


Figure 6.6: Probability plots of AD test for LGI2 TFM. The y-axis represents the cumulative probability in percent. The x-axis represents the UTS in MPa, except for the 3-parameter Weibull plot, it is the threshold value in MPa

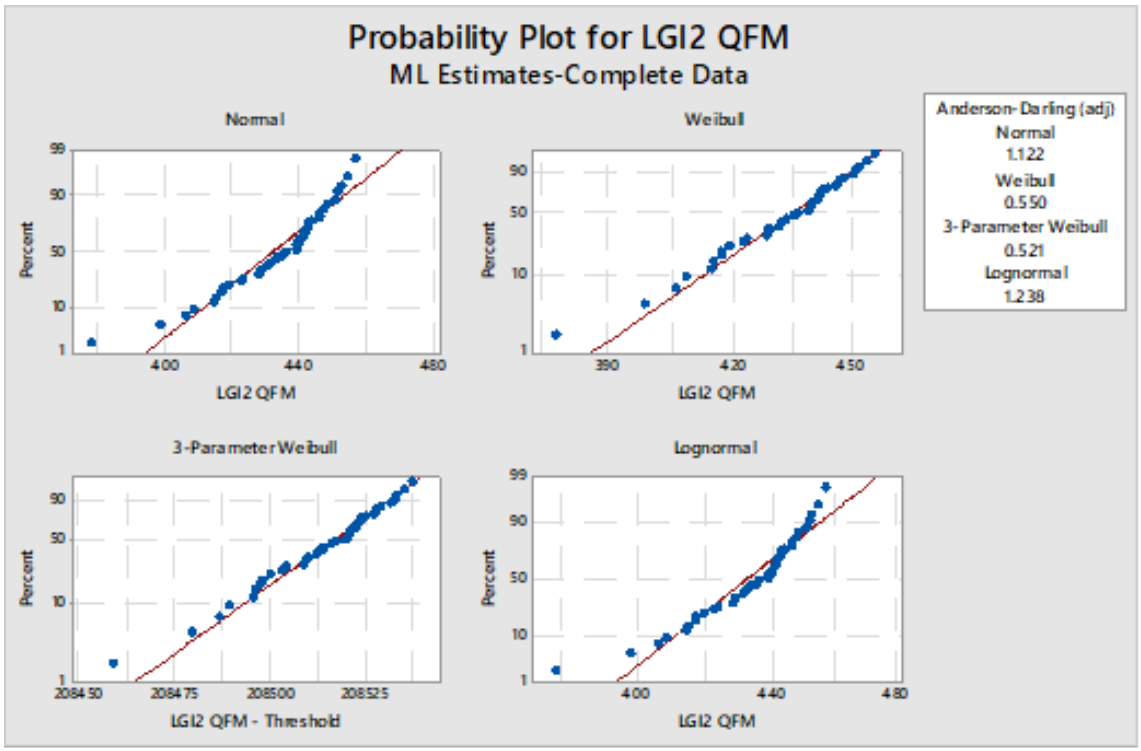


Figure 6.7: Probability plots of AD test for LGI2 QFM. The y-axis represents the cumulative probability in percent. The x-axis represents the UTS in MPa, except for the 3-parameter Weibull plot, it is the threshold value in MPa

Weibull modulus (m), almost double, than that of LGI1 TFM. LGI1 QFM m was 2, as for LGI1 TFM m was 1.2. Both data sets had the same scale parameter of 22 MPa. LGI1 thershold values were close with LGI1 TFM threshold = 237 MPa and LGI1 QFM threshold = 238 MPa. As the scale and threshold parameters are based on the tensile properties of the data, an equal scale and an almost equal threshold were expected due to the shape of the Gaussian distribution of LGI1 TFM and QFM (figure 6.1). Moreover, the 3-parameter Weibull plot for both data sets were intersecting and that was a good indication for the proximity of their UTS values. As LGI1 QFM had a higher Weibull modulus value, this meant it produced better reproducibility and reliability than LGI1 TFM. The summary of the result from the 3-parameter Weibull probability plot are in table 6.5.

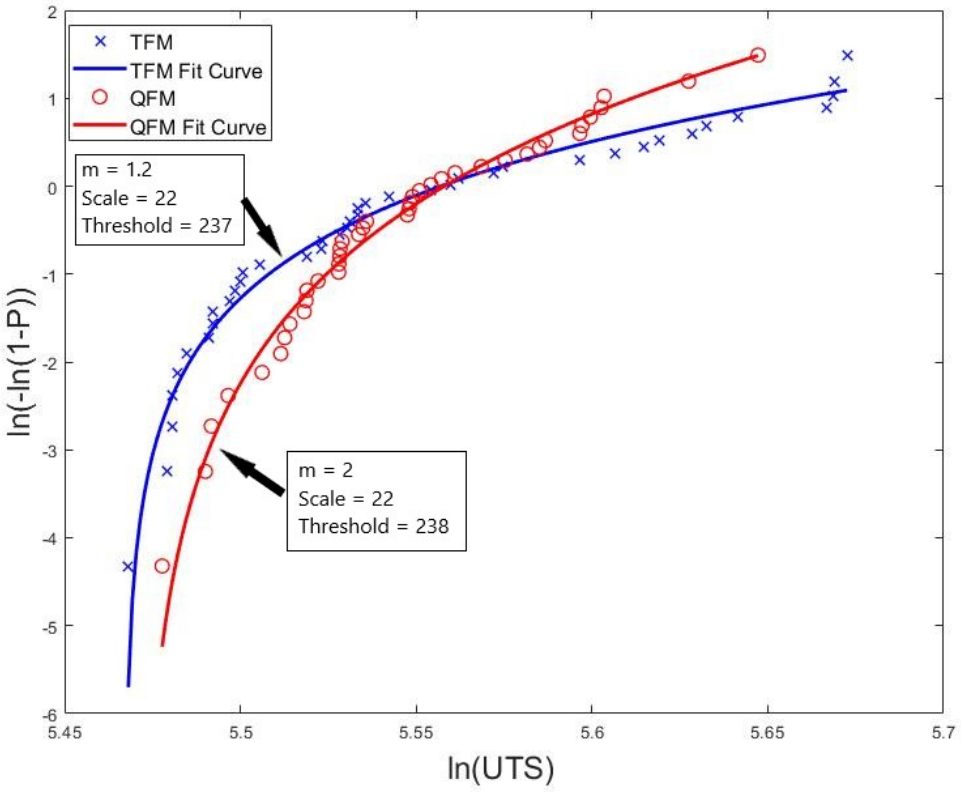


Figure 6.8: LGI1 UTS data 3-parameter Weibull probability plot

LGI2 UTS data sets showed a good fitness to the 2-parameter Weibull distribution. For all three data sets the goodness of fit test resulted in $R^2 > R^2_{0.05}$. LGI2 VTFM had the lowest Weibull modulus with m = 16. LGI2 TFM had a Weibull

Melt/Filling mode	n	m	scale (MPa)	threshold
LGI1 TFM	40	1.2	22	237
LGI1 QFM	40	2	22	238

Table 6.5: Results of the 3-parameter Weibull probability plot for LGI1 UTS data

modulus of 49 which was 50% higher than LGI2 QFM m = 32. On the other hand, the scale parameters for the three groups were almost equal, LGI3 VTFM scale parameter = 438 MPa, LGI2 TFM scale parameter = 434 MPa and LGI2 QFM scale parameter = 433 MPa. The interesting part was the reverse relation between LGI1 TFM and LGI1 QFM, vs, LGI2 TFM and LGI2 QFM. In LGI1, QFM had a higher Weibull modulus than TFM, which indicated it produced better reproducibility and reliability. In LGI2, as just mentioned, TFM had a higher m than QFM, and that indicated TFM produced better reproducibility and reliability. But in both cases, TFM and QFM produced similar UTS values. The probability plot and the summary of its results are in figure 6.9 and table 6.6.

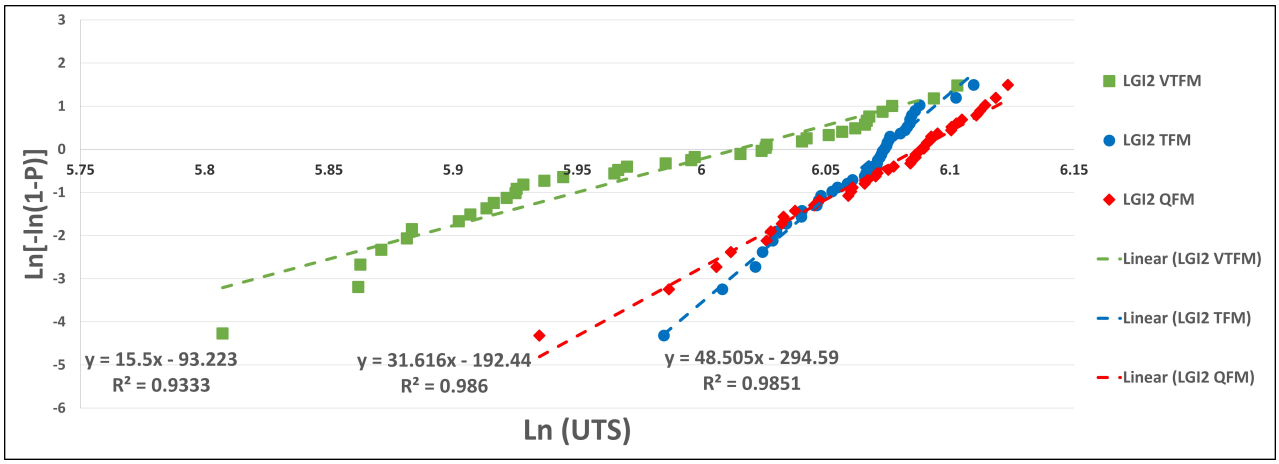


Figure 6.9: LGI2 UTS data 2-parameter Weibull probability plot

Melt/Filling mode	n	m	scale (MPa)	R^2	$R^2_{0.05}$
LGI2 VTFM	38	16	438	0.93	0.92
LGI2 TFM	40	49	434	0.99	0.92
LGI2 QFM	40	32	433	0.99	0.92

Table 6.6: Results of the 2-parameter Weibull probability plot for LGI2 UTS data

6.2 SEM and EDX examination of LGI fracture surfaces

The fracture surfaces of LGI testbars were examined with SEM and EDX to locate any entrainment defects, find the source of failure and UTS scatter. At the start of examination, an understanding of the major topographical aspects of LGI fracture surface had to be identified. This paved the way to spot any abnormal features on the fracture surfaces, which lead to finding and analysing LGI bifilm defects. More variants of bifilms defects were seen in LGI testbars cast in O enriched atmosphere.

6.2.1 LGI fracture surface topography

LGI fracture surfaces were composed of a jungle of crevasses, ledges and entangled features. Figure 6.10 is a back-scatter electrons image (BSE) of an LGI fracture surface. It showed the graphite flakes on the fracture surface in black, due to their lower atomic weight, while the bright areas represented the pearlite phase. The figure also encapsulated a rosette graphite unite, which means a stitch of the figure is what a full fracture surface will look like. This is why the the middle area of the figure had smaller features than the outer area, as it follows the growth of the graphite network.

The topography of the fracture surfaces of LGI testbars were in line with the expected brittle fracture mode of cleavages. Three distinctive features were seen on all fracture surfaces (figure 6.11):

1. fracture through the pearlite phase (marked by the red arrow).

2. fracture through the graphite/matrix interface looking at the graphite side (marked by the green arrow).

3. fracture through the graphite/matrix interface looking at the matrix side (marked by the blue arrow).

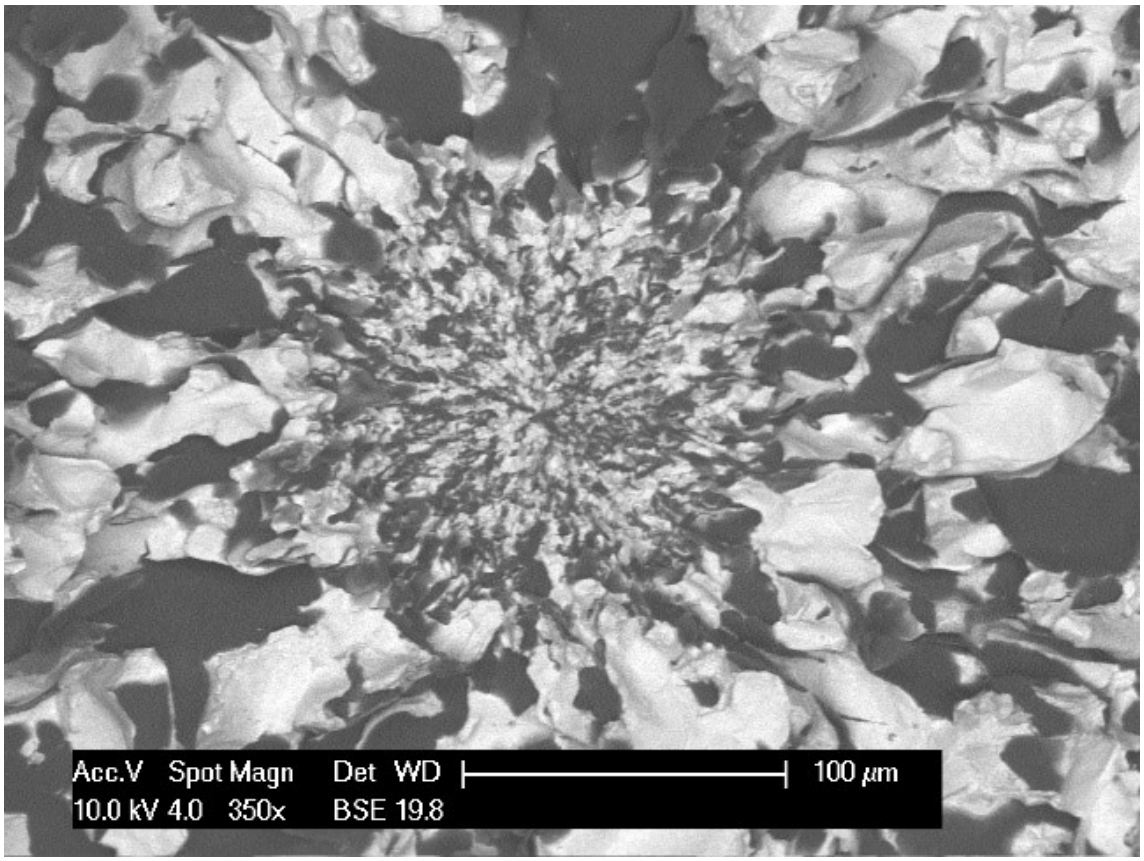


Figure 6.10: BSE image of LGI fracture surface showing the graphite flakes in black

6.2.2 Testbars containing sand inclusions

The fracture surfaces from LGI1 and LGI2 were studied by SEM and EDX. Figure 6.12 contains the SE and BSE images of the fracture surfaces with the lowest UTS in LGI2 VTFM (103 and 269 MPa). The SE image, as shown in figure 6.12a, revealed a web of multiple rounded inclusions on the surface. Most of them were covered with bright layers of charged electrons, indicating their lack of electrical conductivity. The brightness of charged electrons masked the inclusions' details. BSE imaging revealed that the web of inclusions consisted largely of light elements and their sizes ranged from 100 µm to 450 µm (figure 6.12b). The inclusions comprised of Si and O as was indicated by EDX element mapping shown in figure 6.13. The shape, behaviour and composition of the inclusions confirmed that they were silica sand inclusions. In order to study entrainment defects the caster should avoid any major casting defects as sand inclusions. With low tensile properties major defects

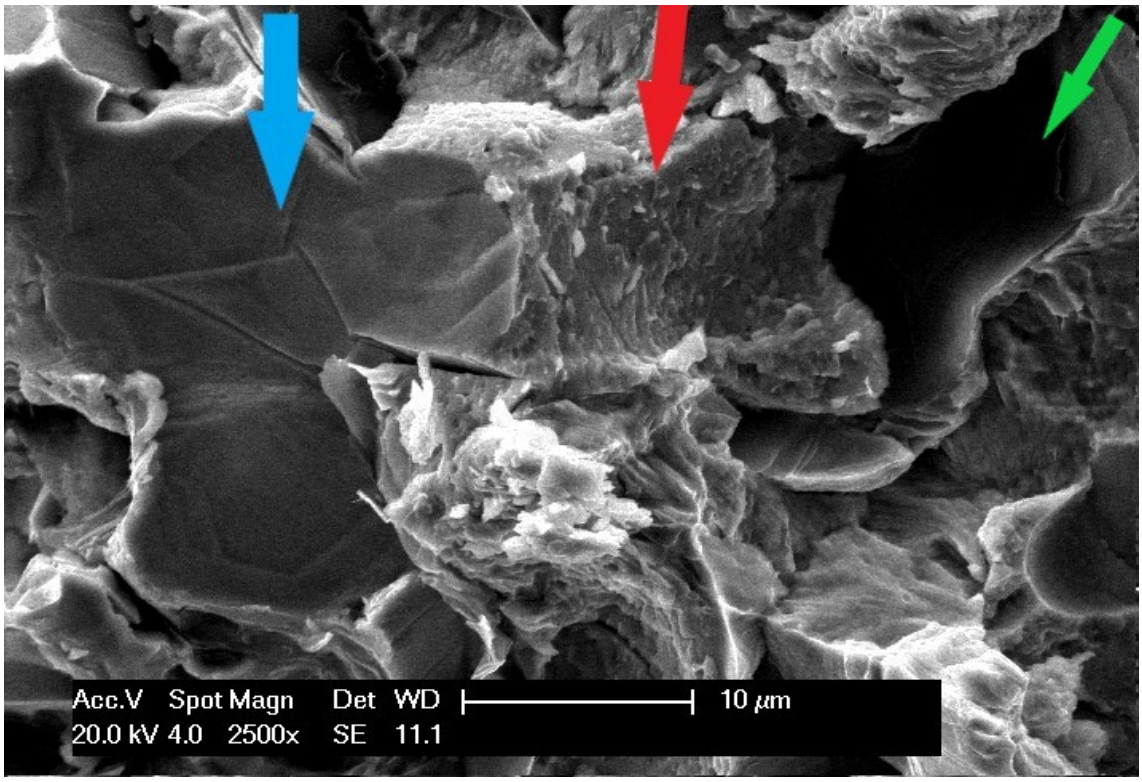


Figure 6.11: SE image of LGI fracture surface showing fracture through pearlite and graphite/matrix interface. The red arrow points to the fracture through the pearlite phase, the green arrow points to the fracture through the graphite/matrix interface looking at the graphite side, and the blue arrow points to the fracture through the graphite/matrix interface looking at the matrix side

will produce skewed statistical analysis. That will not be helpful especially while looking for smaller defects such as bifilms. Hence, the testbar UTS data points were removed from the statistical analysis.

6.2.3 Evidence of entrainment defects in LGI

The SEM and EDX analysis of the testbars fracture surfaces showed evidence of two types of entrainment defects in LGI.

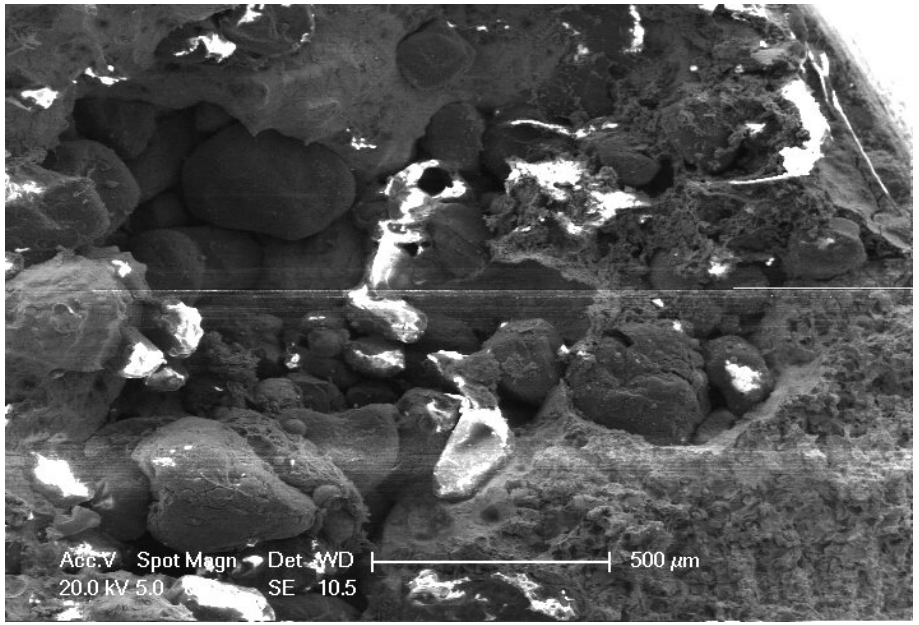
Bubble trail defect

A defect was located symmetrically on both sides of the fracture surface of the LGI testbar is captured in figure 6.14, with a closer view of its features in figure 6.15. The defect was easily detectable with an SEM as it was the only abnormality on the fracture surface. On one side the defect had a concave oval shape, a length of

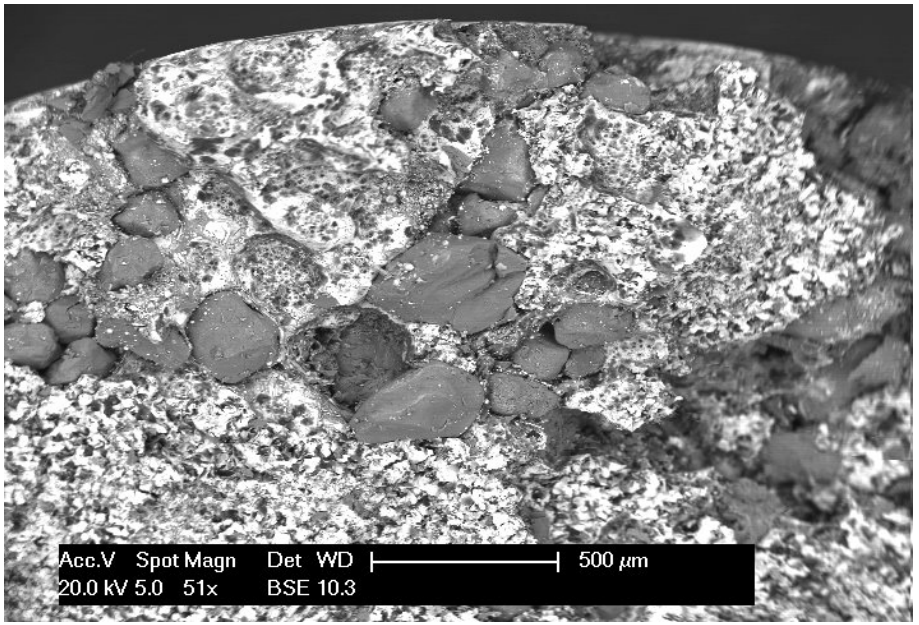
160 µm, and a width of 50 µm. The other side of the defect resembled a slit and had the same dimensions. On one side the defect was a film, mostly smooth and translucent, but in certain areas it had folds and creases (figure 6.15a). Figure 6.16a showed the thin fluted film edge-on, its thickness was estimated to be less than 100 nm. On the other side, the defect had a steeper angle with a plain smooth surface. At fist glance it did not seem to contain a film (figure 6.15b). But a closer view showed a thin patchy film on the surface (figure 6.16b). In the same figure, a green arrow pointed to some folds in the film topography and a red arrow pointed to micro-shrinkage. The EDX analysis, seen in figure 6.17, indicated that the film was composed mainly of Si and O. The amount of iron detected differed from one side to the other depending on the topography of the film (tables 6.7 and 6.8). When the film was thin, area 2, Fe content was 62.25 wt.% and when the film was thick, area 1, Fe content was 5.94 wt.%. EDX element mapping of the bifilm, seen in figures 6.18 and 6.19, confirmed that the defect was composed mostly from Si and O, as both covered the whole defect area. It is worth noting that the reason behind a less than optimal quality of the EDX elements maps in figure 6.19 was due to the defect topography. The steep angle of the defect surface meant only one side of the film could be mapped, as signals coming from the other side were blocked by fracture surface features. Hence, the absence of signals at the top half of the map was not due to the absence of a film layer, but due to EDX signal blockage. Moreover, the steep angle of the mapped surface caused the electron beam to drift with time resulting in the maps becoming hazy. The EDX analysis detected extra amounts of Mn and S that could not have been emitted from the substrate. Areas high in Mn had two distribution patterns. The first was in the mid section of the bifilm, seen in EDX element maps figure 6.18. These areas contained high density of Si and O. The second distribution pattern was areas high in Mn coupled with areas high in S.

Oxide bifilm defect

A film defect located symmetrically on both sides of a LGI fracture surface is captured in figure 6.20. The film was 500 µm in length and 250 µm in width. The defect was easily recognizable with SEM due to its size and topography. Compared to its LGI surrounding, the defect surface was relatively smooth and filled with folds and creases. An inclusion was found at the end of one of the sides of the film defect. Figure 6.21a is a close view of the film surface and it showed parts of the film folded in and the smooth surface. Figure 6.21b showed the film seen edge-on to reveal its thickness around 1 µm. Figure 6.22 is a close view of the inclusion, and showed the inclusion sandwiched between the film defect and the matrix, and it had a diameter of 200 µm. Figure 6.23 contain the EDX analysis from area 1, 2 and 3 in figure 6.22. Spectrum 1 was taken from the fracture surface matrix, spectrum 2 was taken from the film surface, and spectrum 3 was taken from the sandwiched inclusion. The corresponding chemical analysis in weight% and atomic% are in table 6.9. Note, the gold signal present in the spectrum was due to the gold coating applied to the fracture surface to reduce the charging of electrons. The EDX analysis of the inclusion (spectrum 3), in figure 6.23c and table 6.9, showed a that the major elements were C, Si, O, Al, K. The chemical composition and the appearance of the inclusion concluded that it was a silica sand particle. The chemical analysis from the fracture matrix (spectrum 1 in figure 6.23a) contained the major elements in LGI, mostly Fe (70.75 wt.%) and with lesser extent C (28.3 wt.%), Si (0.94 wt.%) and Mn (0.3 wt.%). In addition to O, the film chemical analysis (spectrum 2 figure 6.23b) contained the same elements, but with different amounts. The C, Si and Mn amounts increased to 48.67, 1.79 and 0.99 wt.%, respectively. The Fe amount decreased to 42.97 wt.% and the O was 5.57 wt.%.



(a) SE image of the first fracture surface revealed sand particles with electrons accumulation on their surface



(b) BSE image of the second fracture surface showed the inclusions were sand particles

Figure 6.12: SEM imaging of the two LGI fracture surface excluded from LGI2 VTFM due to sand inclusions

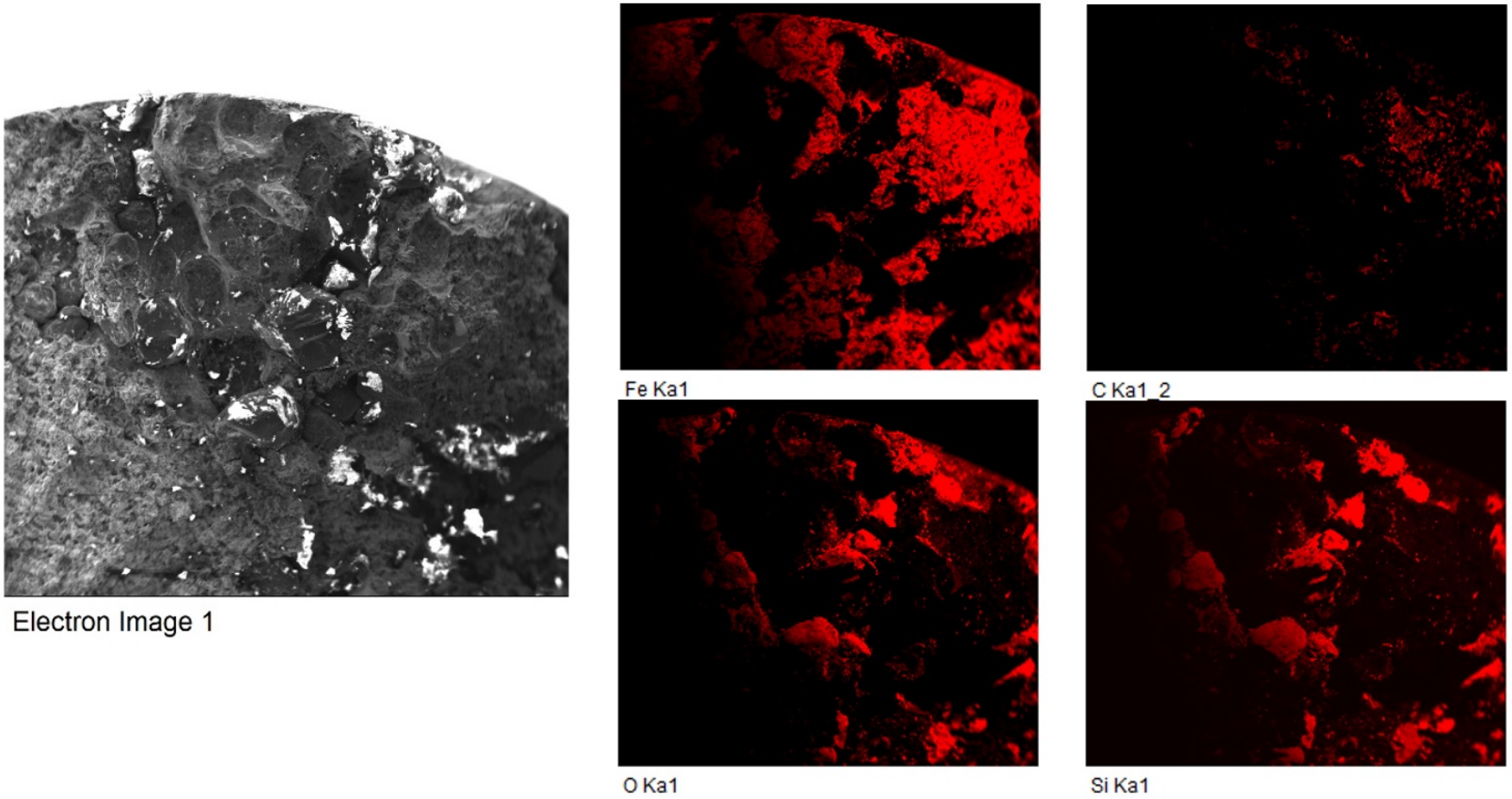


Figure 6.13: EDX element maps of the fracture surface confirmed the particles as silica sand

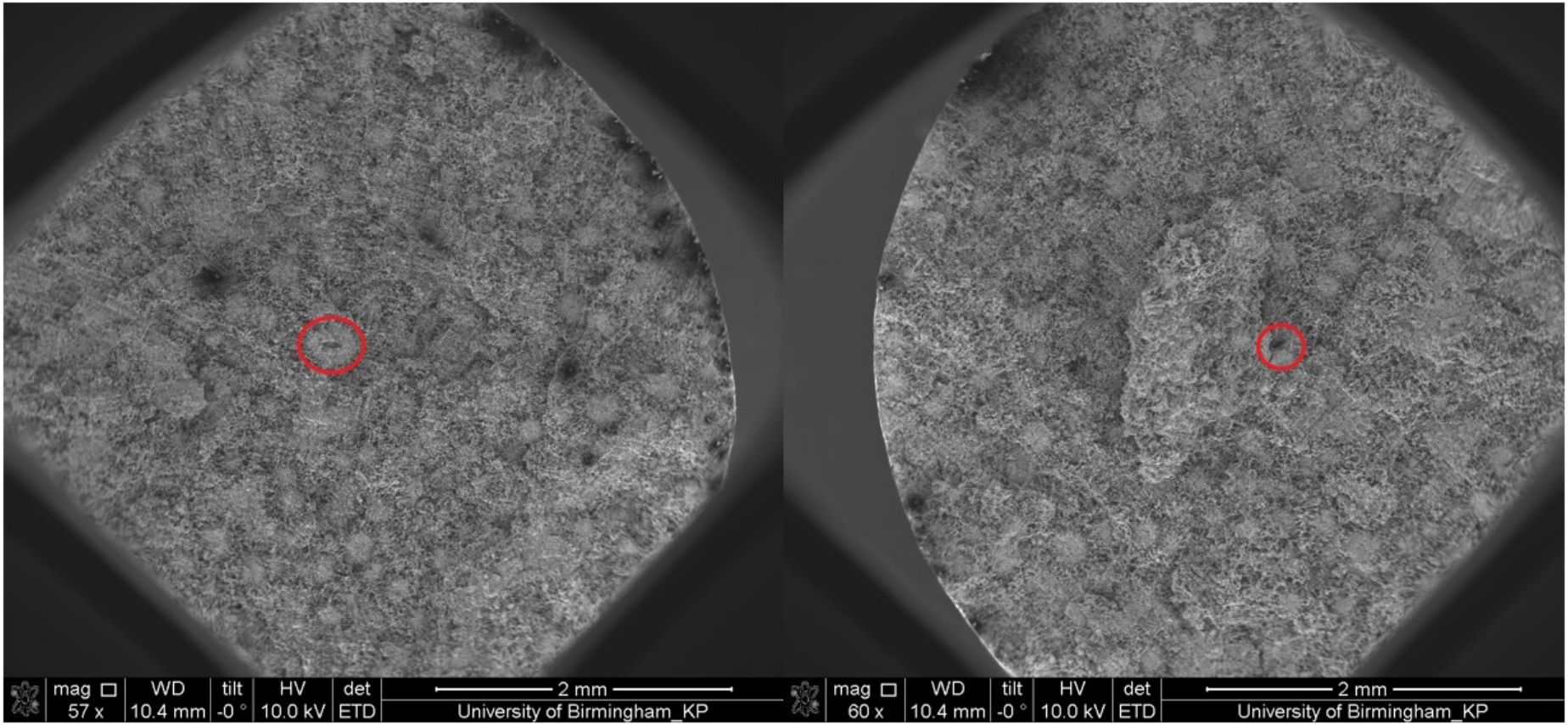
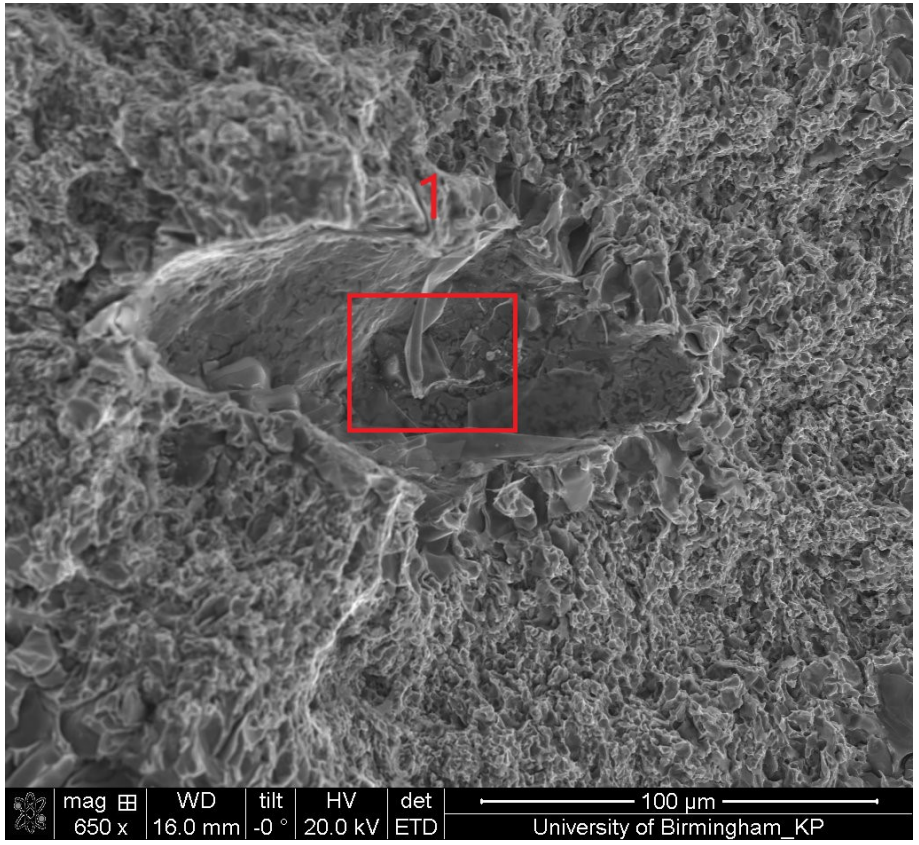
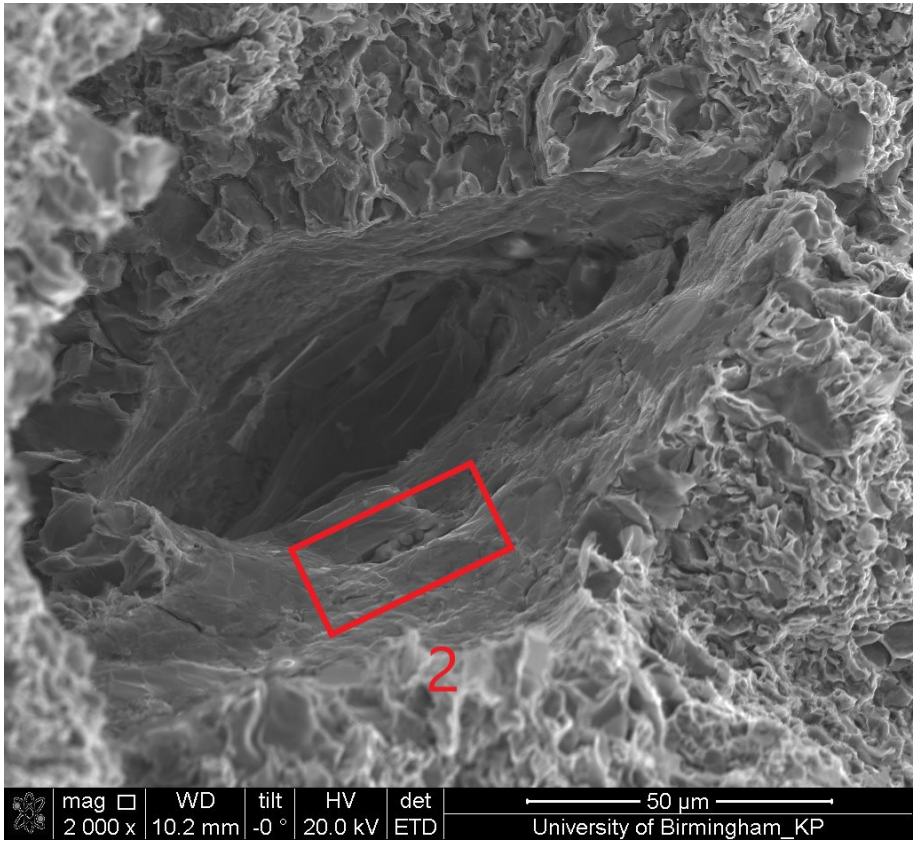


Figure 6.14: Location of a defect (red circle) on both sides of the fracture surface

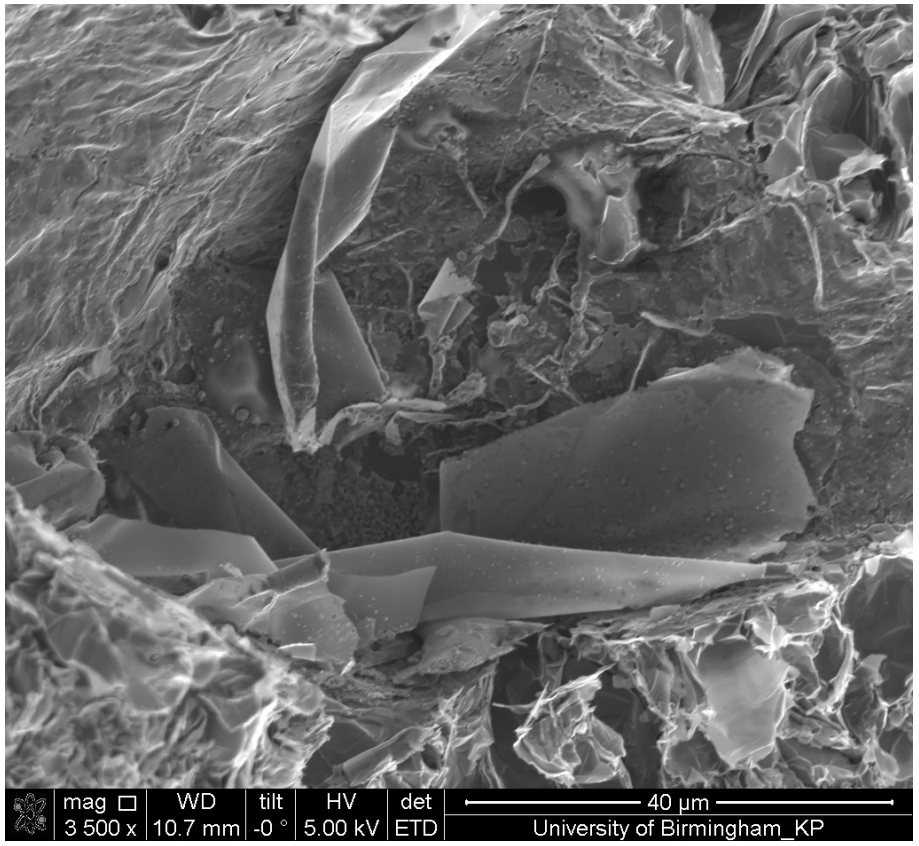


(a) The defect had a translucent film with multiple fold and creases

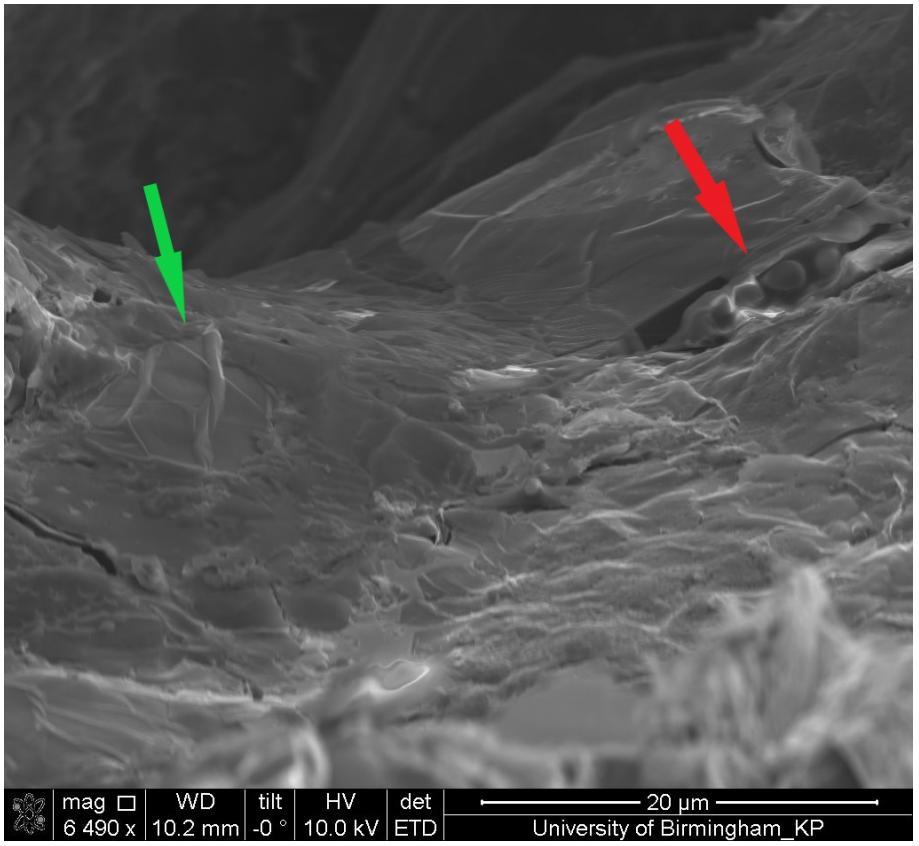


(b) The other side did not seem to have a film layer

Figure 6.15: A closer view of the defect on both sides of the fracture surfaces

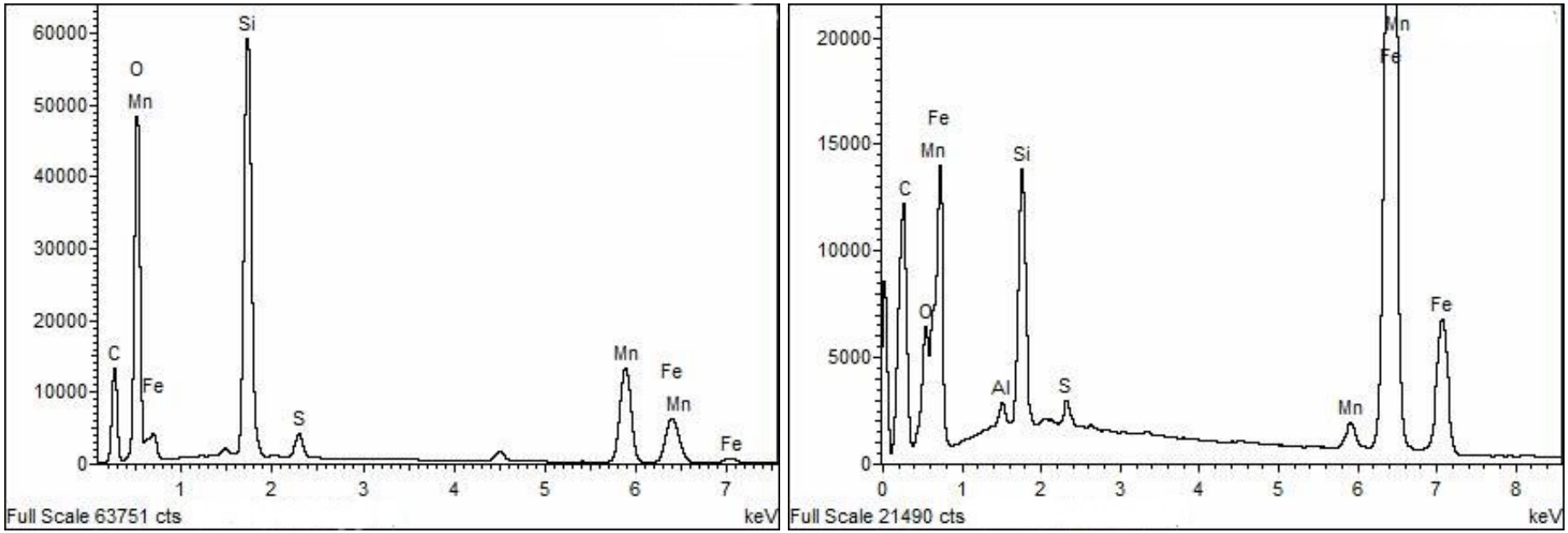


(a) A closer view of figure 6.15a showed flat and folded film areas and with part of the film edge-on



(b) A close view of figure 6.15b revealed a thin patchy film on the surface. The green arrow points to some film folds, and the red arrow points to a micro-shrinkage

Figure 6.16: A closer view of the defect on both sides of the fracture surfaces confirmed it is a bifilm nature



(a) EDX spectrum from area 1 in figure 6.15a

(b) EDX spectrum from area 2 in figure 6.15b

Figure 6.17: EDX spectrum from the bifilm

Spectrum	C	O	Si	S	Mn	Fe	Al	Total
1	25.16	43.57	13.04	0.93	11.36	5.94	-	100
2	23.8	6.8	4.87	0.47	1.32	62.25	0.48	100

Table 6.7: EDX elements composition in weight% of Area 1 and 2

Spectrum	C	O	Si	S	Mn	Fe	Al
1	37.24	48.42	8.26	0.51	3.68	1.86	-
2	52.82	11.33	4.62	0.47	1.32	62.25	0.47

Table 6.8: EDX elements composition in atomic% of Area 1 and 2

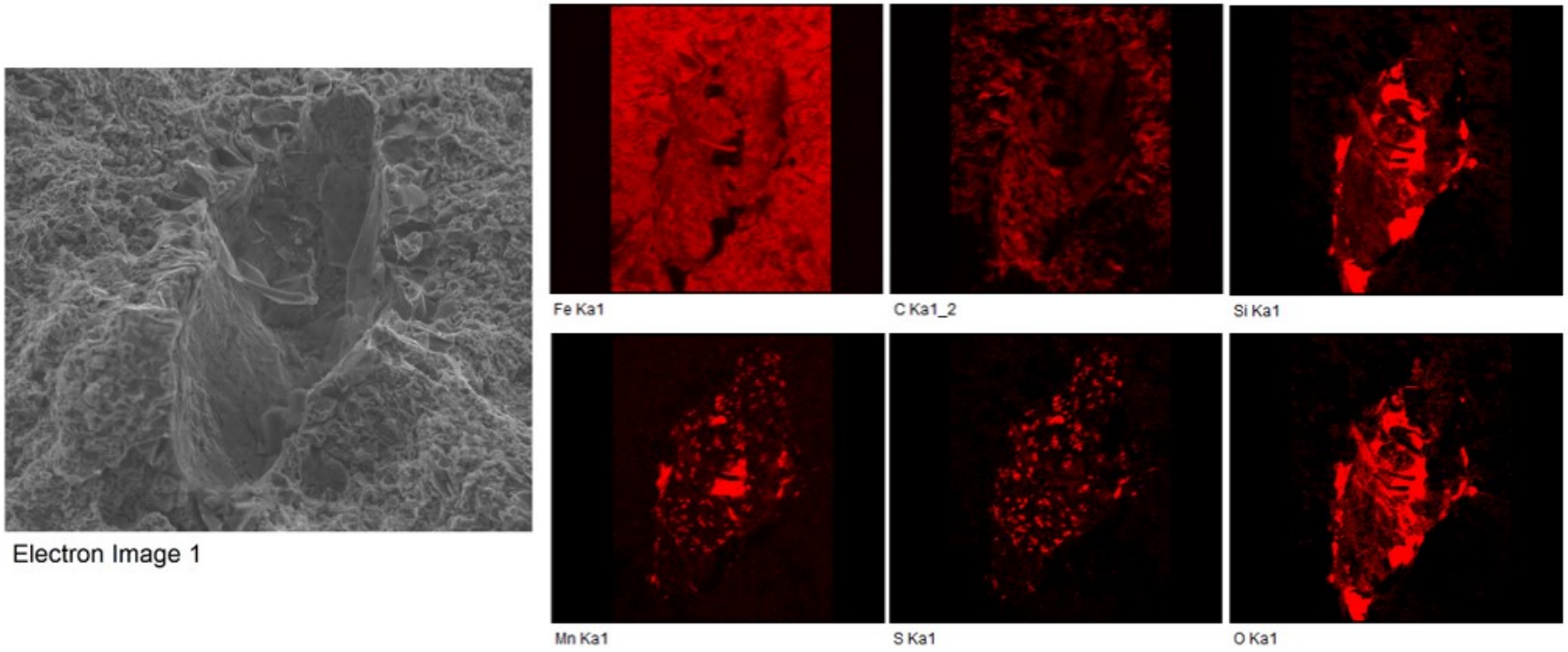


Figure 6.18: EDX element maps of the one side of the bifilm

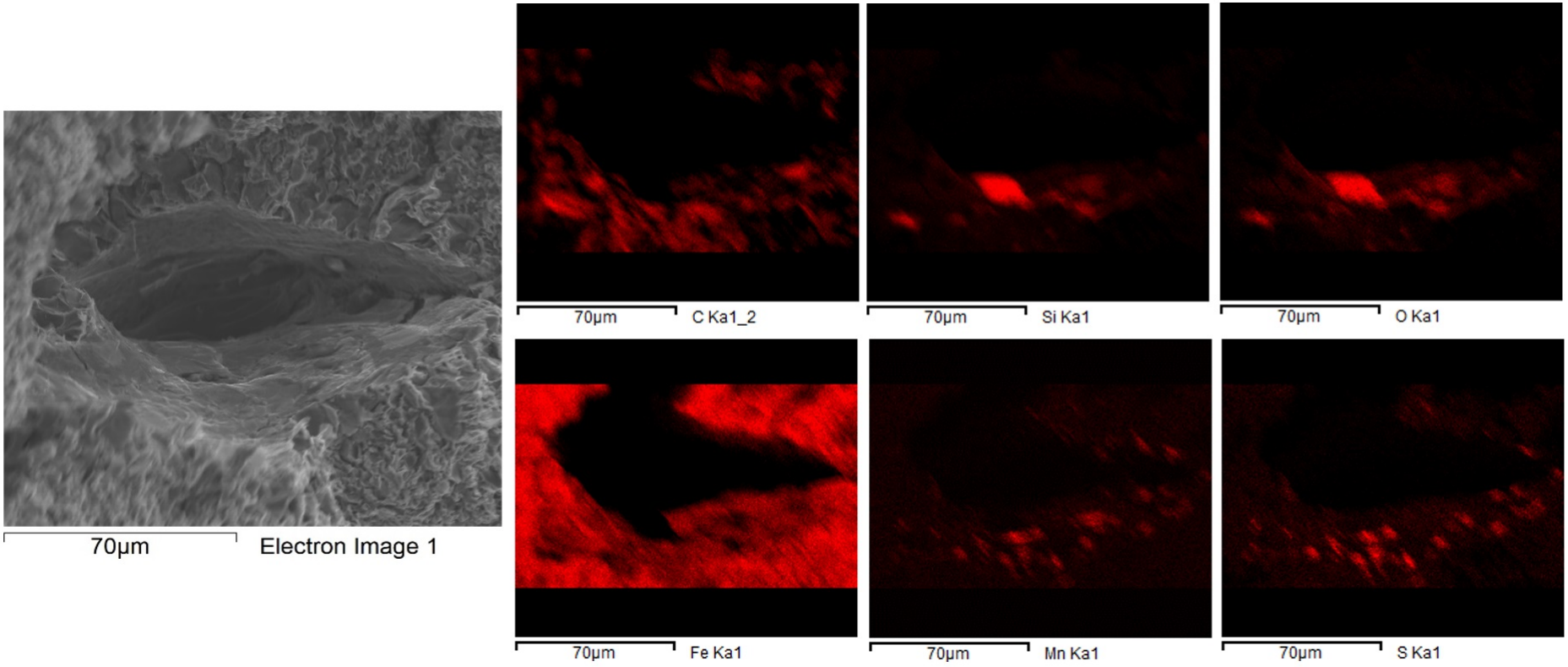
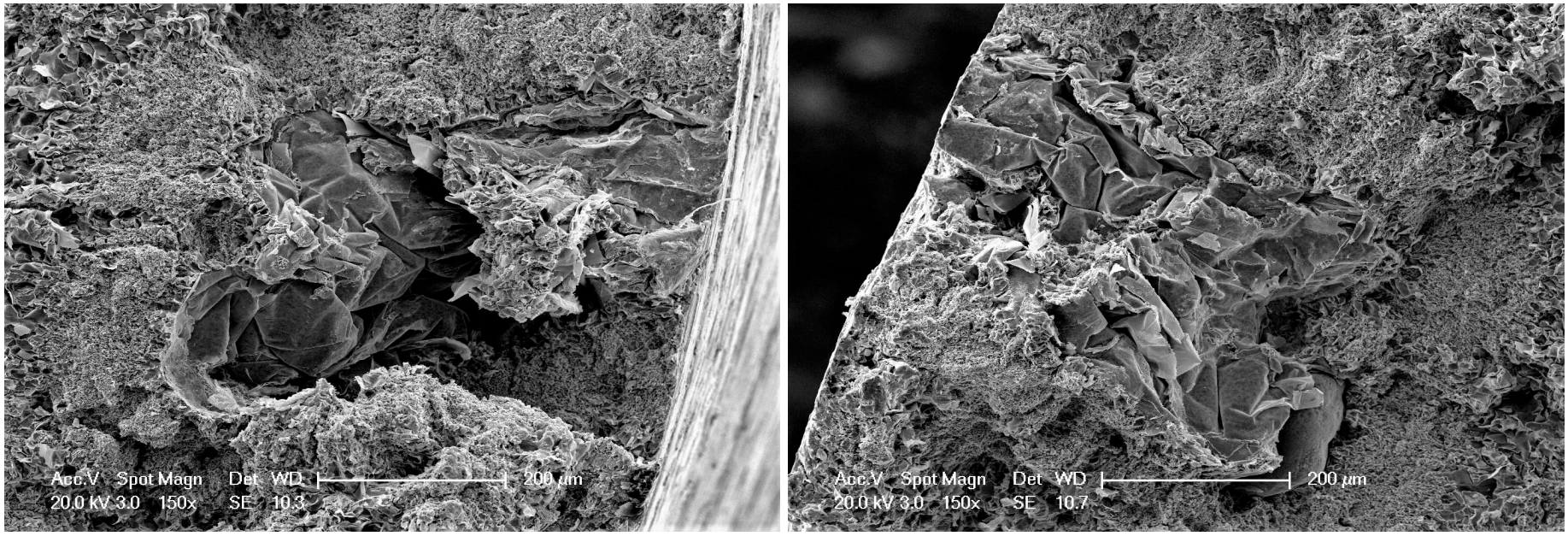
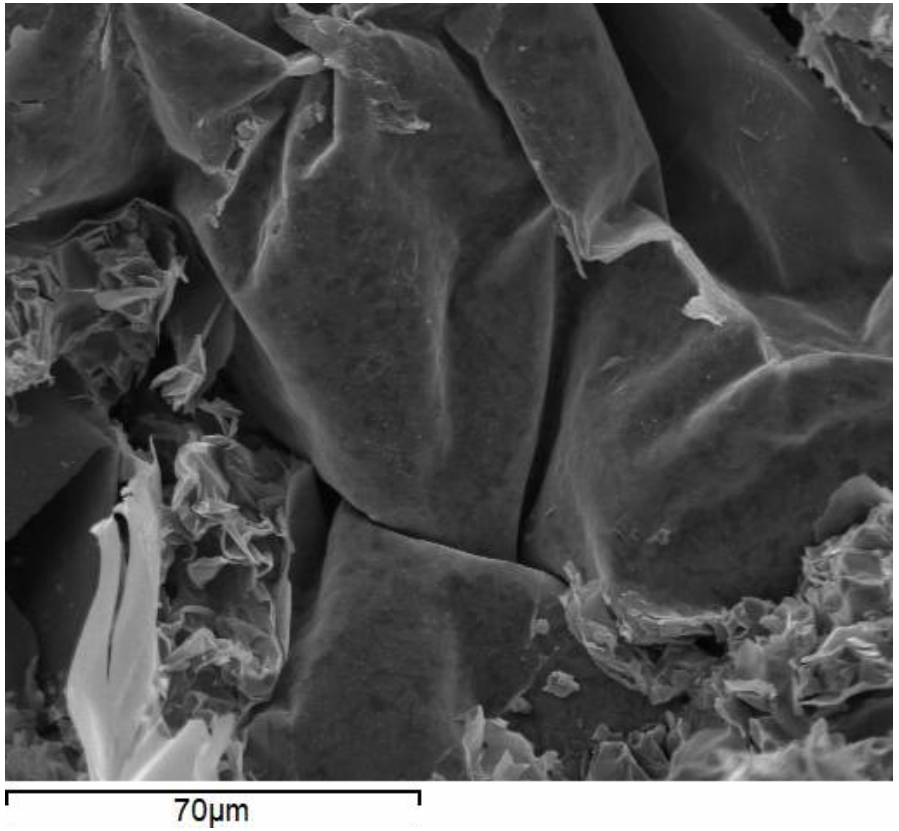


Figure 6.19: EDX element maps of the other side of the bifilm

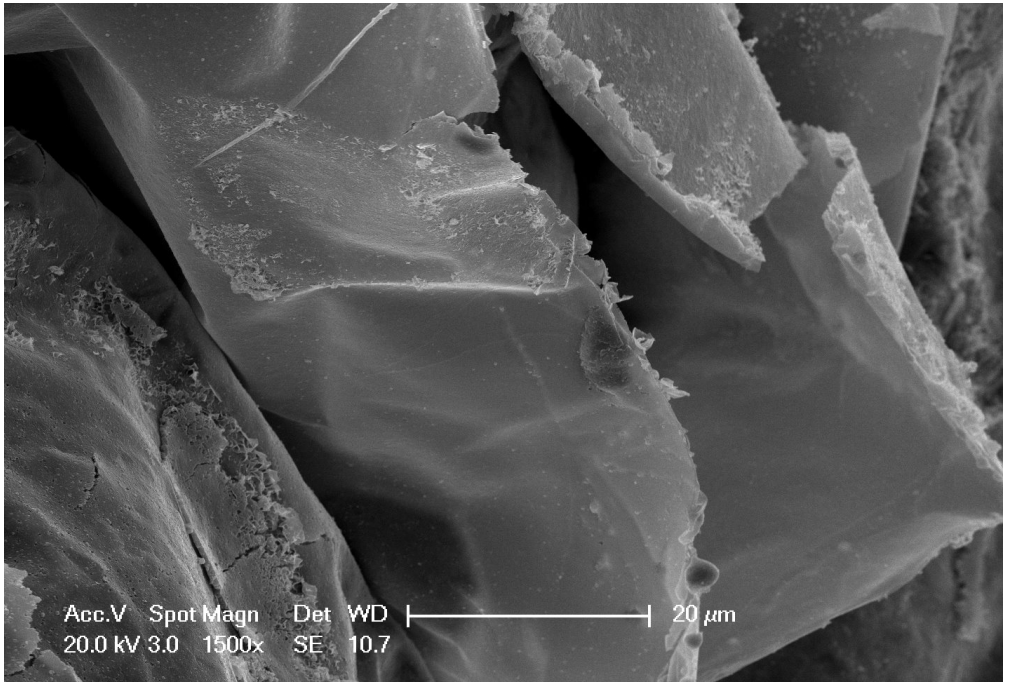


(a) (b)

Figure 6.20: A bifilm defect symmetrical on both sides of the fracture surface. Note the folds and creases of the surface pointing to the inside direction



(a)



(b)

Figure 6.21: A close view of the surface of the folded bifilm surface

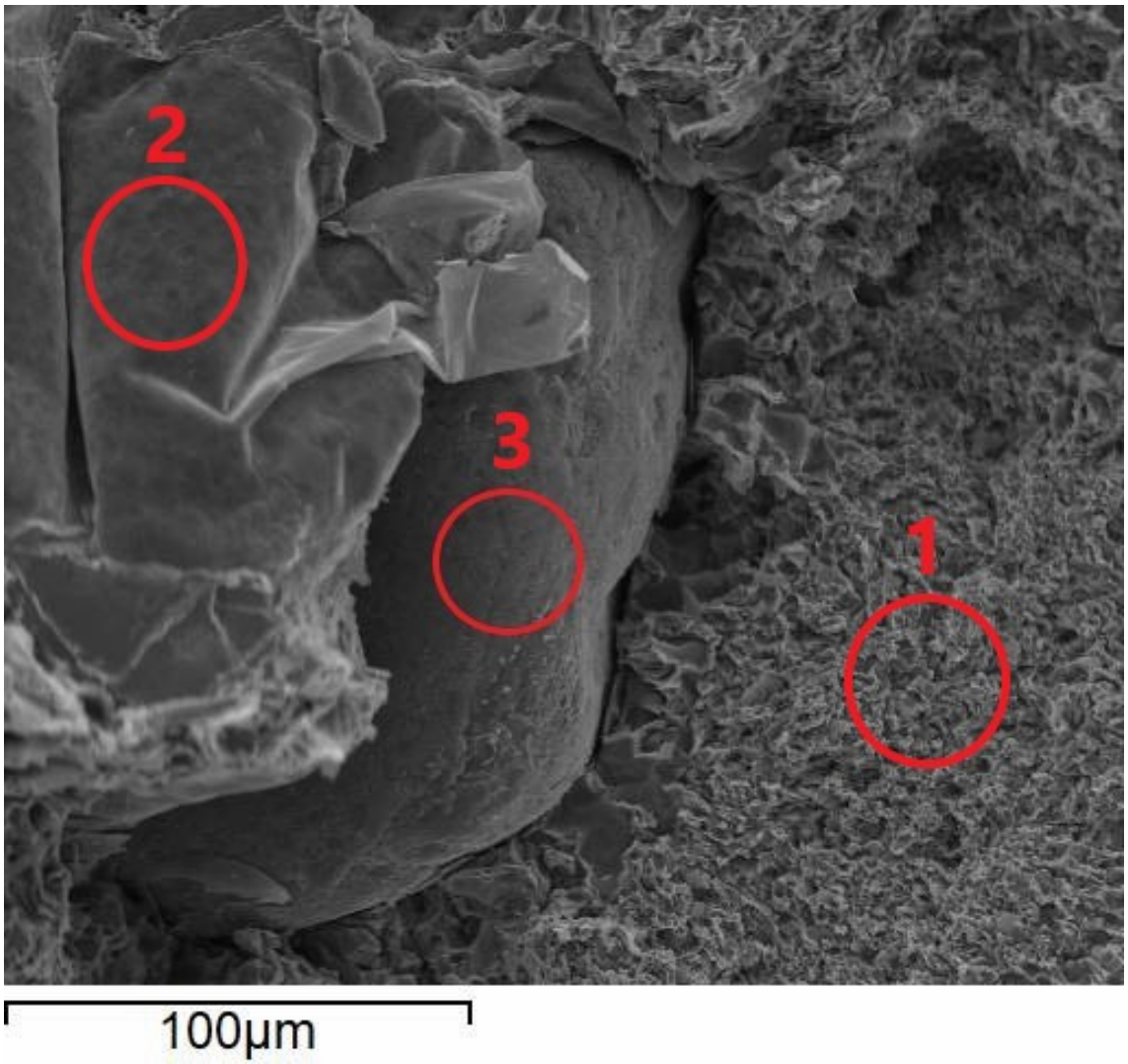
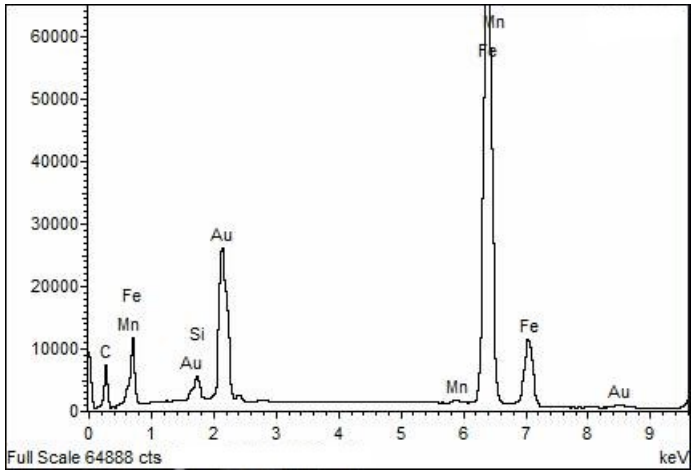


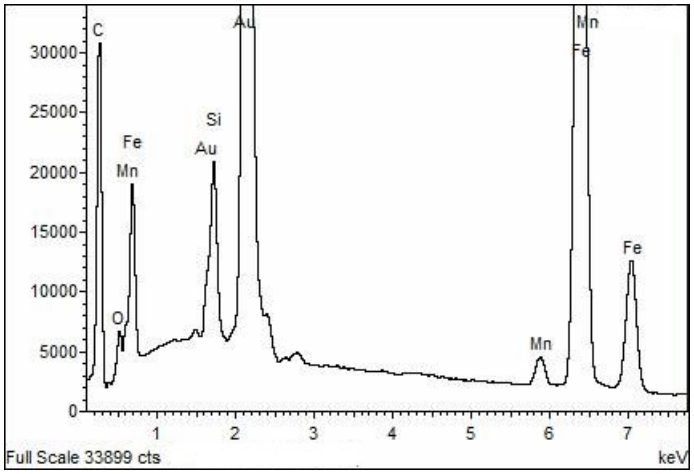
Figure 6.22: A the inclusion lodged between the bifilm and LGI matrix

•	Spectrum 1		Spectrum 2		Spectrum 3	
Element	Weight%	Atomic%	Weight%	Atomic%	Weight%	Atomic%
C	28.3	64.44	48.67	77.16	31.43	43.76
O	•	•	5.57	6.63	38.35	40.11
Si	0.94	0.92	1.79	1.22	15.5	9.23
Mn	0.3	0.15	0.99	0.34	0.36	0.11
Fe	70.75	34.64	42.97	14.65	4	1.2
Na	•	•	•	•	0.47	0.35
Al	•	•	•	•	5.04	3.12
K	•	•	•	•	4.86	2.08
Total	100	•	100	•	100	•

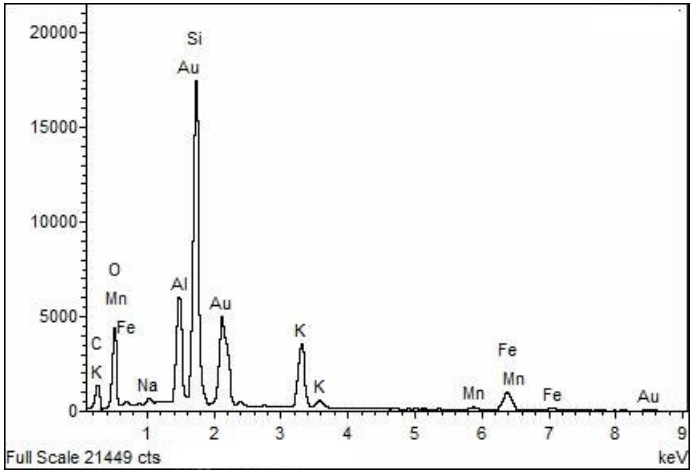
Table 6.9: EDX elements composition in weight% and atomic% from area 1, 2 and 3 in figure 6.22



(a) EDX spectrum from the fracture surface matrix (area 1)



(b) EDX spectrum from the film surface (area 2)



(c) EDX spectrum from the inclusion (area 3)

Figure 6.23: EDX analysis from different areas marked in figure 6.22

6.3 Testbars die casting in an O-rich environment

LGI grade G-220 testbars were gravity cast in a cast iron permanent mould back filled with pure oxygen. Subsequently, the casting was examined by x-ray radiography, tensile tested and the fracture surfaces were examined with SEM and EDX analysis.

Figure 6.24 shows the die with the casting. The casting body in situ contained a major misrun defect. This is a pouring defect that happens when the liquid metal does not completely fill up the cavity of the mould, resulting in partially-filled testbars. The filling was surface turbulent as indicated by the solidified CI droplets at the top of the testbar cavity. The solidified droplets also indicated the occurrence of multiple jetting events during filling. Due to the partially-filled cavity, all parts of the casting were treated as testbars.

X-ray imaging of the casting contained some light shadows, present in the downsprue (figure 6.25a), the well (figure 6.25b), runner bar and the partially-filled testbars (figure 6.25c). The light shadows are an indicator of internal casting defects, such as entrainment defects, shrinkage porosity or air bubbles.

SEM and EDX analysis of the fracture surfaces revealed multiple film defects. Figures 6.26 and 6.27 are SE images and EDX element maps of two film defects detected on the fracture surfaces. The film topography were extremely chaotic in nature carving a bath between the iron matrix. The film defects consisted mainly of Si and O but it also had a strong Fe signal, originating from the substrate. The films also contained small areas high in S that coincided with areas high in Mn. A mix of thin and thick groups of spiralling films through the iron matrix is seen in figure 6.30a. A film defect covering a part of the fracture surface is shown in figure 6.28a. The film covered the whole captured area, it was thin, translucent and it was almost only visible when it contained folds. When examined with EDX, the film emitted strong O and Si signals, with weight% of 20 and 10, respectively (figure 6.29a and table 6.10). Figure 6.28b is a high magnification view of another film surface highlighting it's topographical features. Thin, translucent, glassy and

full of folds and creases sums the totality of film defects arising in this experiment. EDX analysis of the film showed an O and a Si peaks (figure 6.29b). Table 6.11 contains the spectra elements in weight% and atomic%. The casting contained multiple shrinkage pores and with close examination of their surface, fragments and strings were found to cover their surface (figure 6.30b). The fragments and strings were microns in size and scattered between and on top of the dendrite arms. EDX analysis, seen in figure 6.31 and table 6.12, indicated that these fragments composed mainly of Si and O.

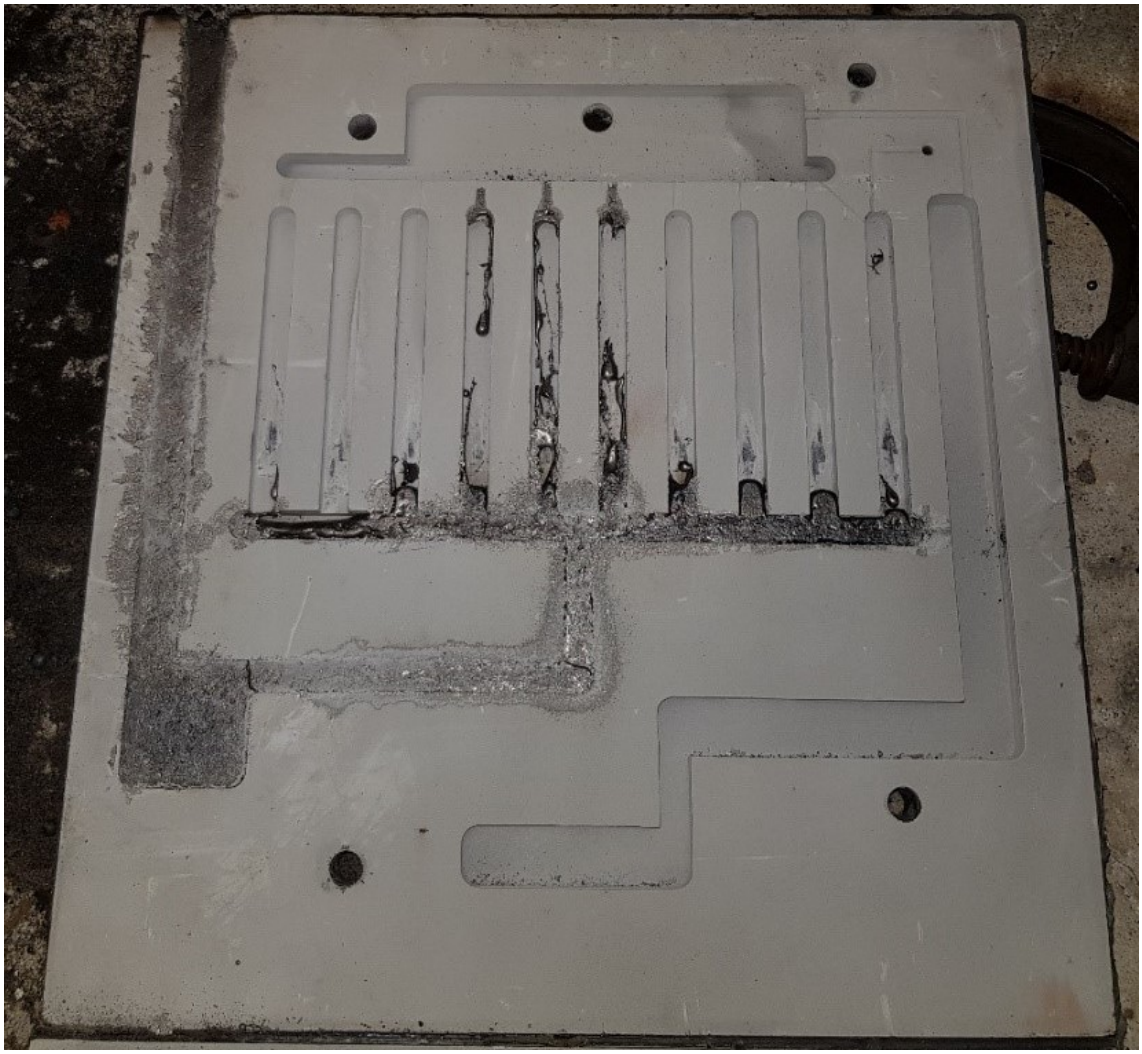
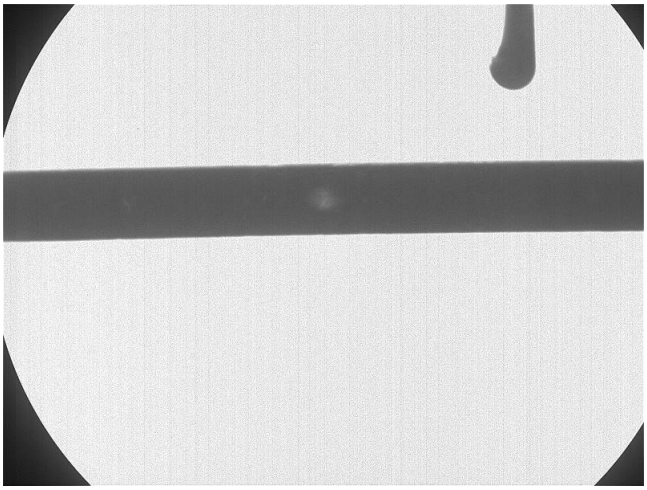
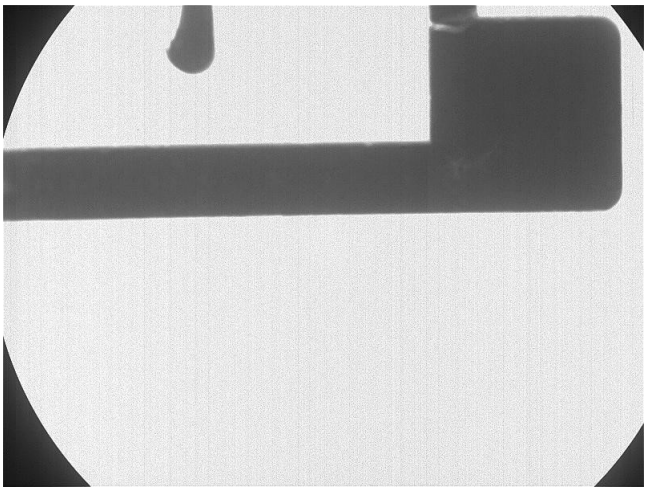


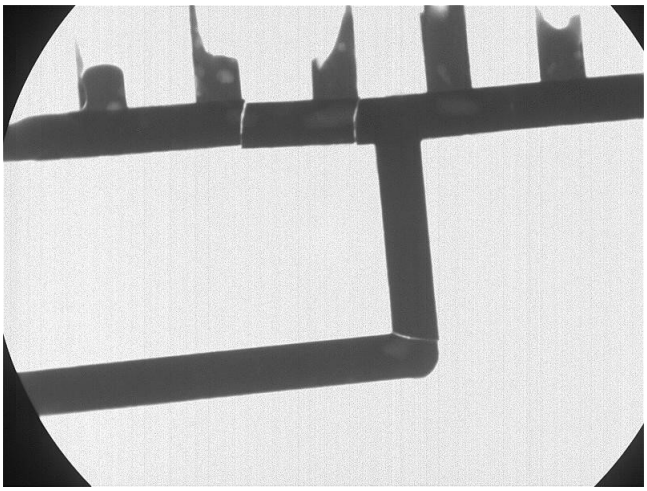
Figure 6.24: The casting appearance indicated a very surface turbulent filling



(a) X-Ray radiography image of the down sprue



(b) X-Ray radiography image of the well



(c) X-Ray radiography image of the runner bar and partially filled test bars

Figure 6.25: X-ray radiography images of the casting showed evidence of casting defects

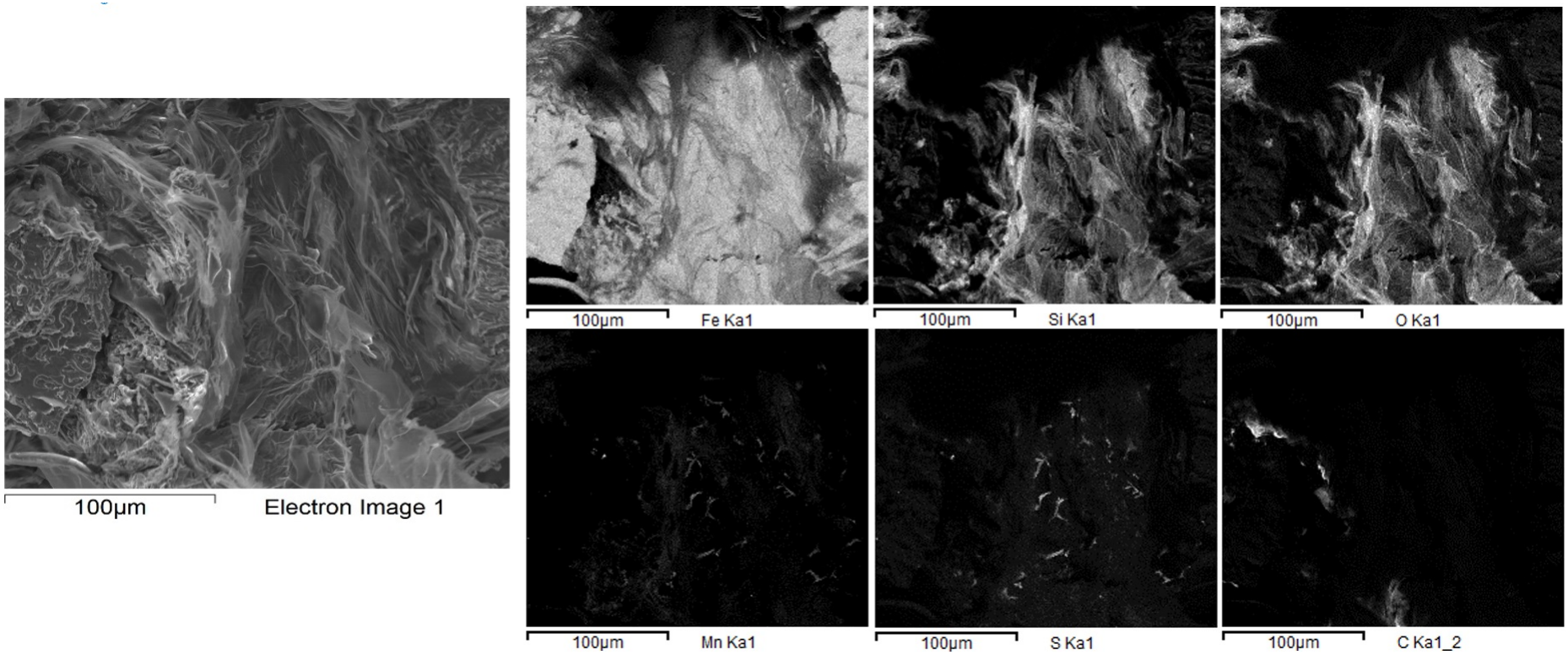


Figure 6.26: SE image of a film defect and its EDX element maps contained areas high in Si and O

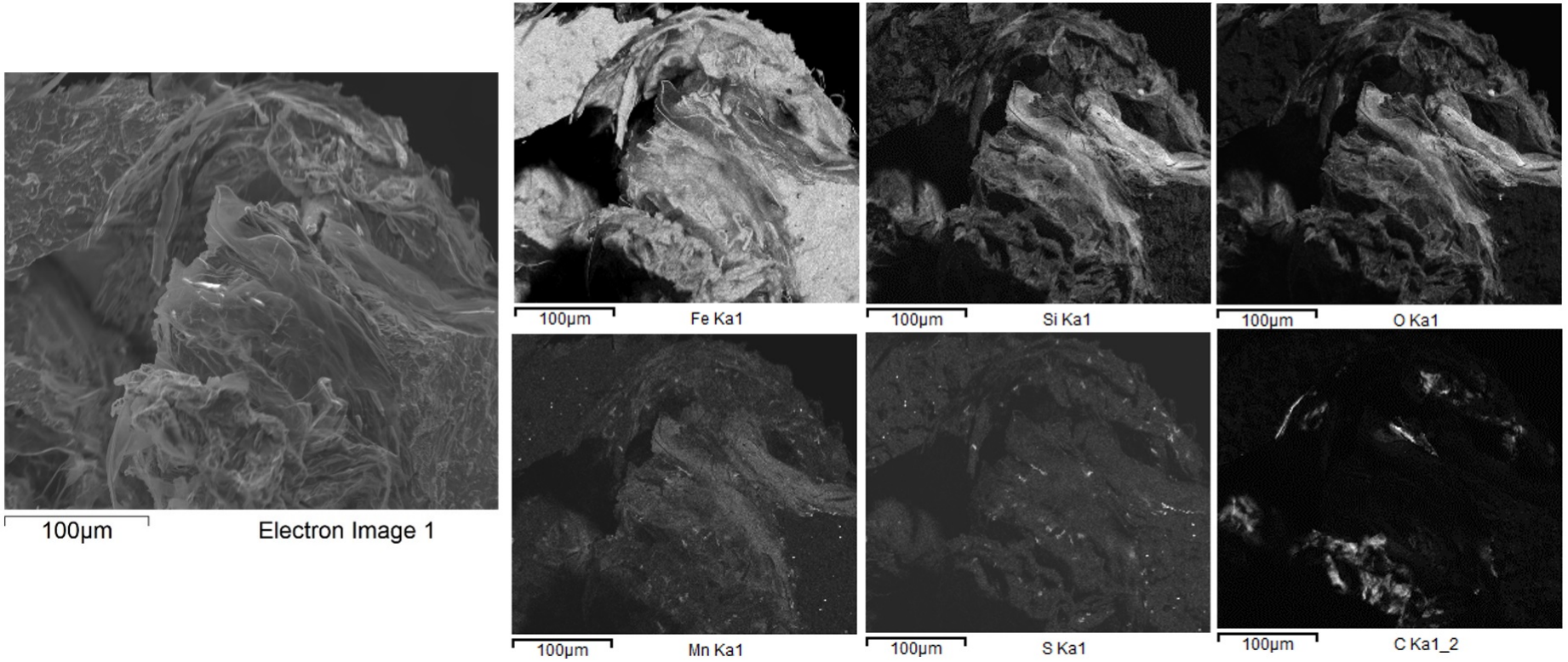
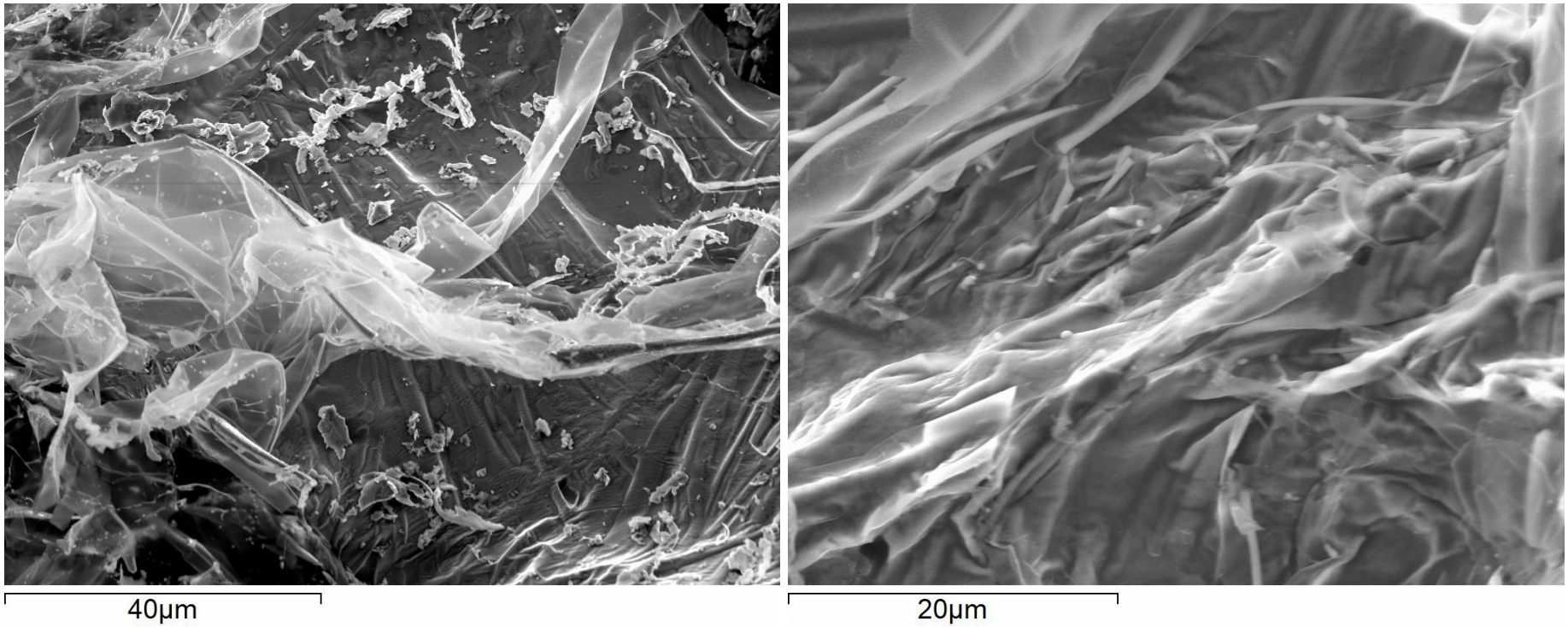


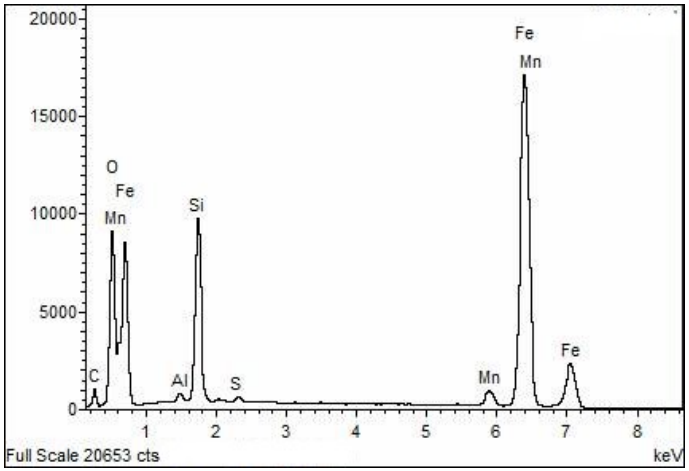
Figure 6.27: Another film defect and its EDX element maps which contained areas high in Si, O and Mn



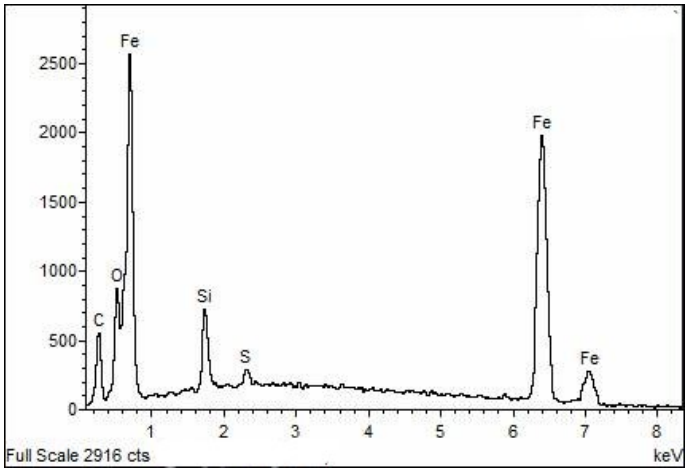
(a) SE image showed the film topography contained multiple folds

(b) A close view of the corrugated film surface

Figure 6.28: The fracture surfaces contained areas covered with creased and translucent films



(a) EDX spectrum from the film surface in figure 6.28a



(b) EDX spectrum from the film surface in figure 6.28b

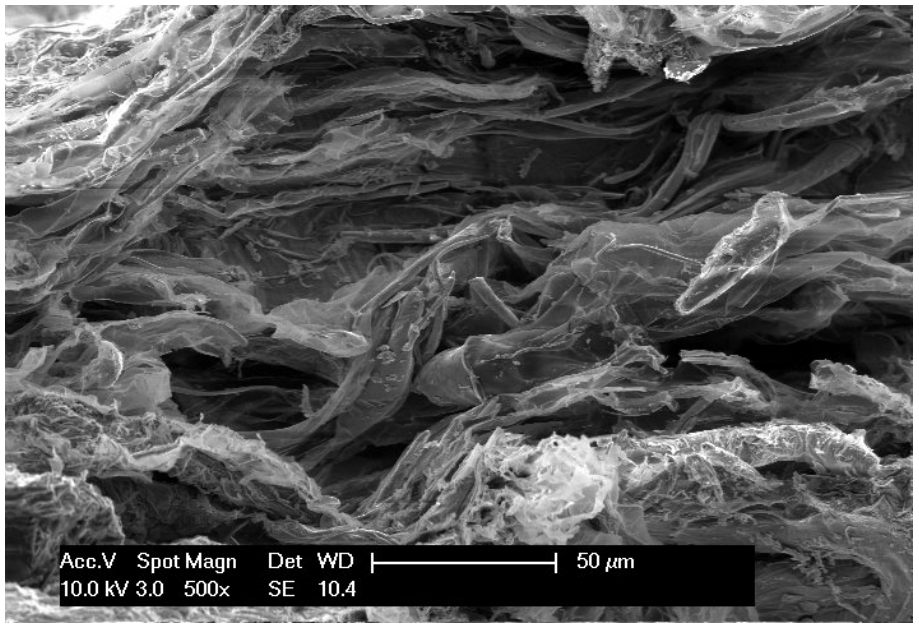
Figure 6.29: EDX analysis of the bifilms shown in figure 6.28

-	C	O	Al	Si	S	Mn	Fe	Total
Weight%	7.7	19.88	0.43	9.96	0.27	2.25	59.5	100
Atomic%	19.03	36.88	0.48	10.52	0.25	1.22	31.62	-

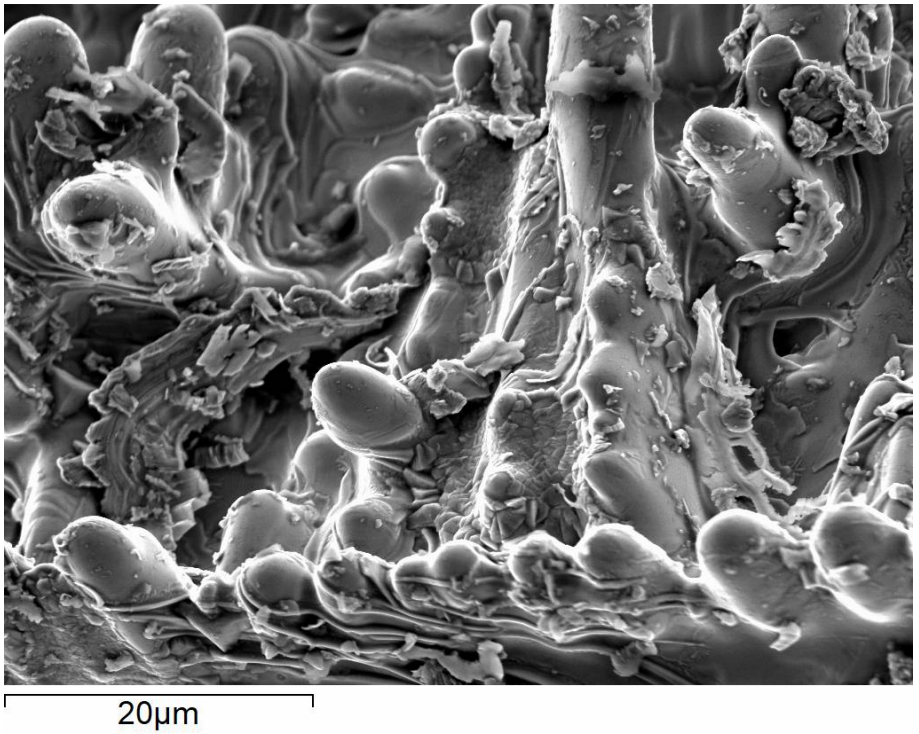
Table 6.10: EDX chemical composition in weight% and atomic% from figure 6.29a

-	C	O	Si	S	Fe	Total
Weight%	9.53	6.43	4.62	1.35	78.07	100
Atomic%	28.34	14.35	5.87	1.51	49.93	-

Table 6.11: EDX chemical composition in weight% and atomic% from figure 6.29b



(a) SE image of the fracture surface showing irregular grouping of film trails



(b) A Shrinkage pore showing dendrites covered with fragments

Figure 6.30: Different features of entrainment defects were also detected on fracture surfaces

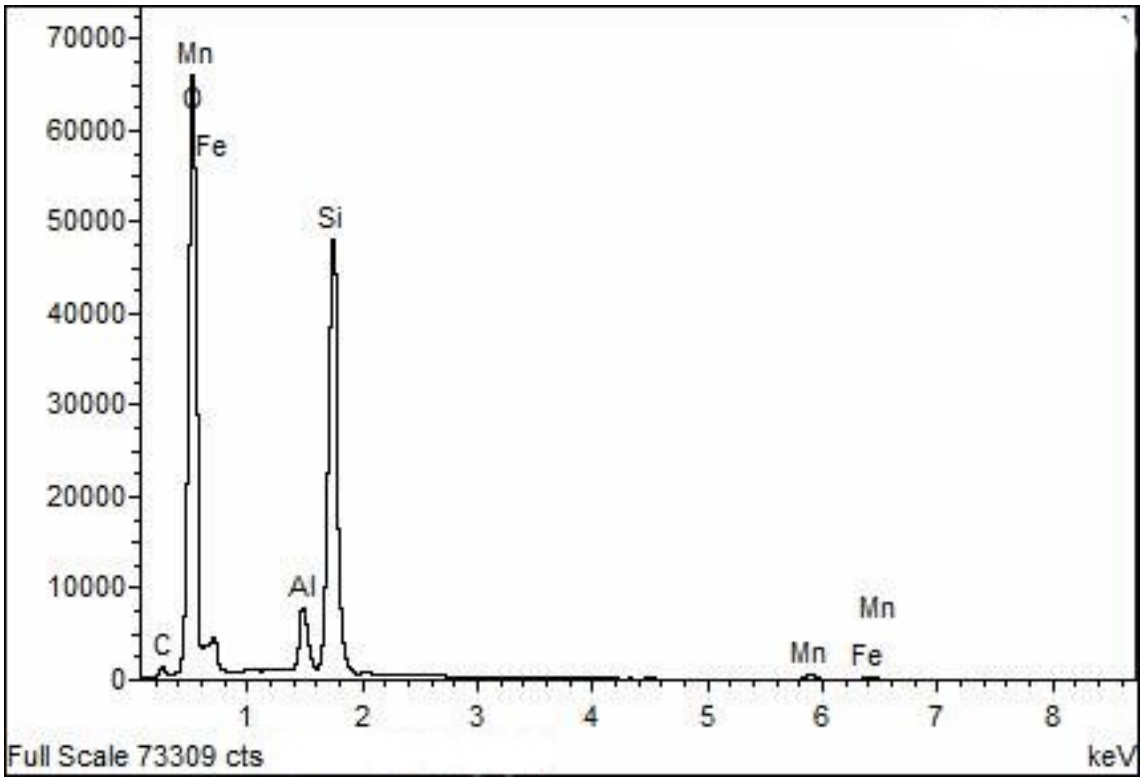


Figure 6.31: EDX spectrum from the fragments

-	C	O	Al	Si	Mn	Fe	Total
Weight%	2.61	48.68	3.51	30.32	2.15	12.74	100
Atomic%	4.56	64.23	2.74	22.79	0.83	4.82	-

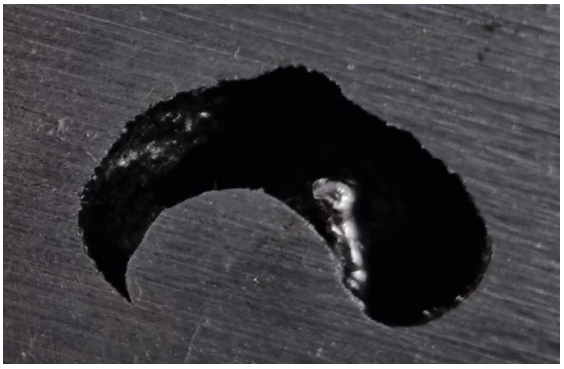
Table 6.12: EDX chemical composition in weight% and atomic% of the fragments

6.4 Reduced pressure test

LGI grade 220 ingot were gravity cast in a sand mould and solidified under reduced pressure. Subsequently, the casting was sectioned and examined for inflated bifilms. Figure 6.32a shows the sectioned ingot, and the only porosity that were observed. The porosity was located in the top section of the ingot. Figure 6.32b is close up image of the porosity and it showed an extrude inside the cavity. Figure 6.33 shows a layer and droplets of metal solidified on the bottom of the vacuum chamber though no spilling occurred during mould filling.



(a) Cross-section of the sample



(b) Close up view of the porosity showed an extrude inside it

Figure 6.32: LGI RPT sample



Figure 6.33: Droplets and a thin layer of solidified metal was found on the surface of the vacuum chamber

6.5 Industrial Data

During industry training at a commercial cast iron foundry, a surface defect was the reason behind a scraped LGI engine block (figure 6.34). The defect was a freckled metal surface in the shape of a circle with a tail attached to it. It had a total length of 60 mm and was located along the transverse section of the casting. The defect was mislabelled as a cold shut. It was not possible to extract the defect for further investigation, but an explanation of the defect and the mechanism of its occurrence will be covered in the discussion.

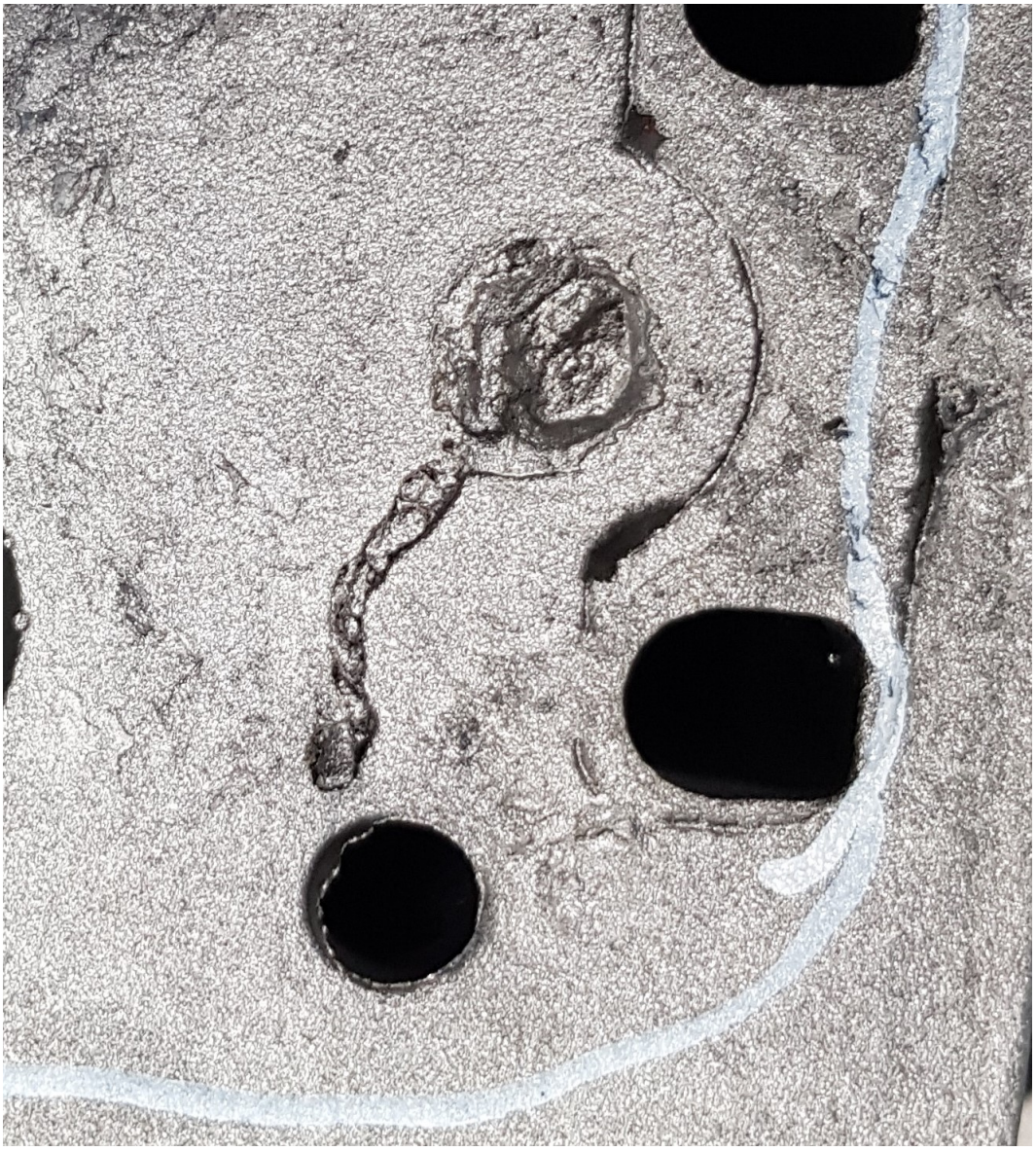


Figure 6.34: A skin defect resembles a bubble with an attached tail was the reason behind scarping LGI engine block

6.6 Summary

This section contained the results of LGI from testbars sand casting experiment, testbars die casting in an O-rich environment experiment, RPT and industrial data, and they were as follows;

1. LGI1 UTS data had positively skewed histograms and fitted a 3-parameter Weibull distribution.

2. LGI2 UTS data had negatively skewed histograms and fitted a 2-parameter Weibull distribution.

3. LGI1 UTS data for TFM had m = 1.2, and QFM had m = 2.

4. LGI2 UTS data for VTFM had m = 16, for TFM m = 49, and for QFM m = 32.

5. SEM and EDX examination of LGI fracture surfaces revealed two types of entrainment defects. Bifilms containing O, Si and Mn, and bubble trail defects containing O, Si, Mn and S.

6. LGI RPT sample contained only one porosity.

7. Industrial data showed a skin defect in a scrapped LGI engine block resembling a bubble with its tail attached.

Chapter 7

Results for Compacted Graphite Iron

In this experiment, CGI testbars were gravity cast in three different running system designs of resin bonded sand moulds. The data was analysed statistically to determine the effect of the filling mode on the tensile properties, reproducibility and reliability of the castings. Subsequently the fracture surfaces were examined using an SEM to determine the source of fracture. EDX was also used to acquire the chemical composition of any defects.

7.1 The effect of quiescently-filled, surface turbulently filled, and very (surface) turbulently-filled moulds on the tensile properties, reproducibility and reliability of CGI

Two separate melts of CGI grade 400 were cast in a commercial foundry using the the same filling modes (VTFM, TFM and QFM) used in LGI and SGI to produce a total of 200 testbars. The first melt was denoted CGI1 and the second denoted CGI2. CGI1 testbads were only produced from TFM and QFM, and CGI2 were

produced from the whole array. Table 7.1 shows the number of test bars from each type of mould in each melt.

Melt	QFM	TFM	VTFM
CGI1	40	40	•
CGI2	40	40	40

Table 7.1: Number of CGI testbars from each mould type for different melts

7.1.1 Statistical analysis of CGI UTS data

Table 7.2 shows the descriptive statistics of all CGI UTS data from the tensile testing.

Variable	Total Count	Mean	StDev	Variance	Minimum	Maximum	Range
CGI1 TFM	40	568	17	278	514	600	86
CGI1 QFM	40	581	13	174	543	603	60
CGI2 VTFM	40	574	13	169	534	594	61
CGI2 TFM	40	523	30	924	445	573	128
CGI2 QFM	40	539	26	657	484	580	96

Table 7.2: Descriptive statistics of CGI UTS (MPa) values

The descriptive statistic, shown in table 7.2. The Gaussian distribution plot of CGI UTS data, seen in figures 7.1 and 7.2, showed a difference in the behaviour between TFM and QFM. In CGI1, QFM had a higher mean UTS (581 MPa) than TFM (568 MPa). As for the range, TFM had a range of 86 MPa which was bigger than QFM's 60 MPa. In CGI2, QFM and TFM mean UTS and range had the same relation. QFM mean UTS was higher than TFM, with 539 MPa and 523 MPa, respectively; their ranges were 96 MPa and 128 MPa, respectively. Surprisingly, VTFM showed a different relation than what was expected. It was expected that VTFM would have the lowest mean UTS and the biggest range, but on the contrary it had the highest mean UTS (574 MPa) and the smallest range (61 MPa). The histograms showed that the UTS data distributions were negatively skewed. The fitted Gaussian distributions also shows the five data sets intersecting and overlapping. Thus, to determine if there was a significant difference between the data sets Student's t-test was carried out between the comparable data sets.

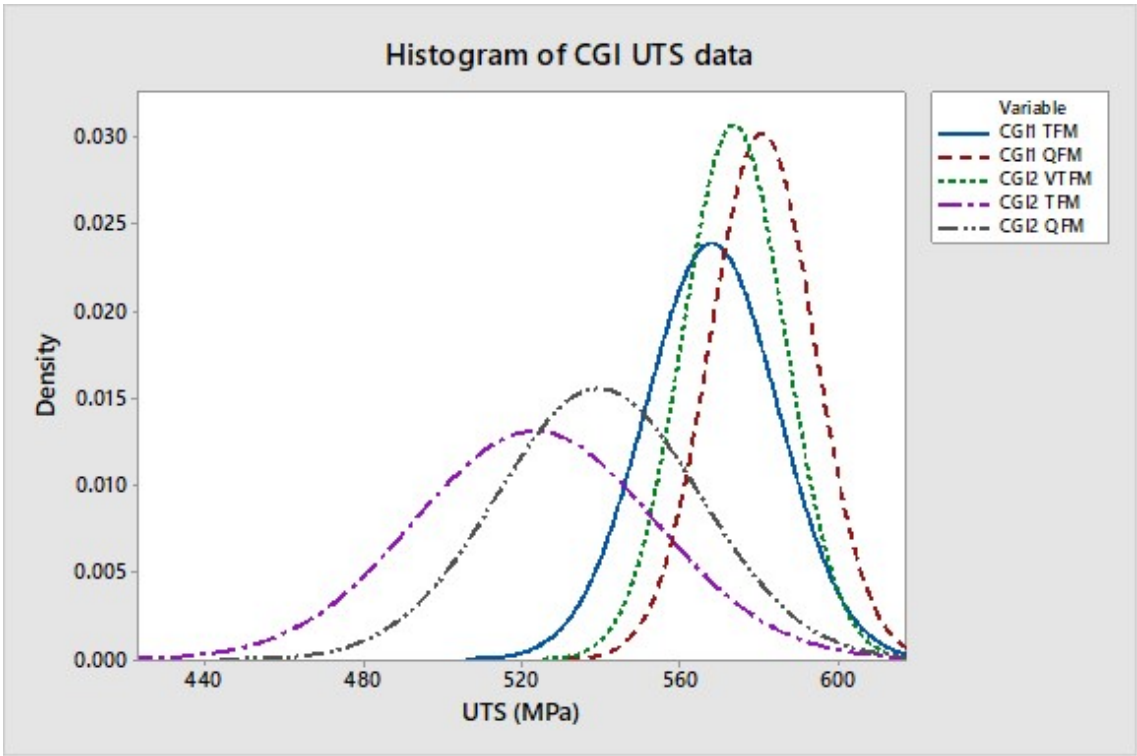


Figure 7.1: The fitted Gaussian distribution for UTS data from each mould type for different CGI melts

The Student's t-test t-values and p-values, (table 7.3), showed there was statistical significance between all data sets. The t-values were between 2.6 and 9.6, and the p-values were lower than the significant level of 0.05. Thus the null hypothesis was rejected and it was concluded that the difference between the groups' means were statistically significant.

Two Samples		T Value	P Value
CGI1 TFM	CGI1 QFM	3.8	0
CGI2 VTFM	CGI2 TFM	9.6	0
CGI2 VTFM	CGI2 QFM	7.5	0
CGI2 TFM	CGI2 QFM	2.6	0.012

Table 7.3: Student's t-test results for CGI UTS data

The Anderson-Darling test was used to test the UTS data sets against normal, log-normal, 2-parameter and 3-parameter Weibull distributions to determine which distribution had the best goodness of fit, the lowest resulting AD score the better the goodness of fit. Table 7.4 has a summary of the results. The lowest scores were for the 2-parameter and 3-parameter Weibull distribution. As a continuation for the

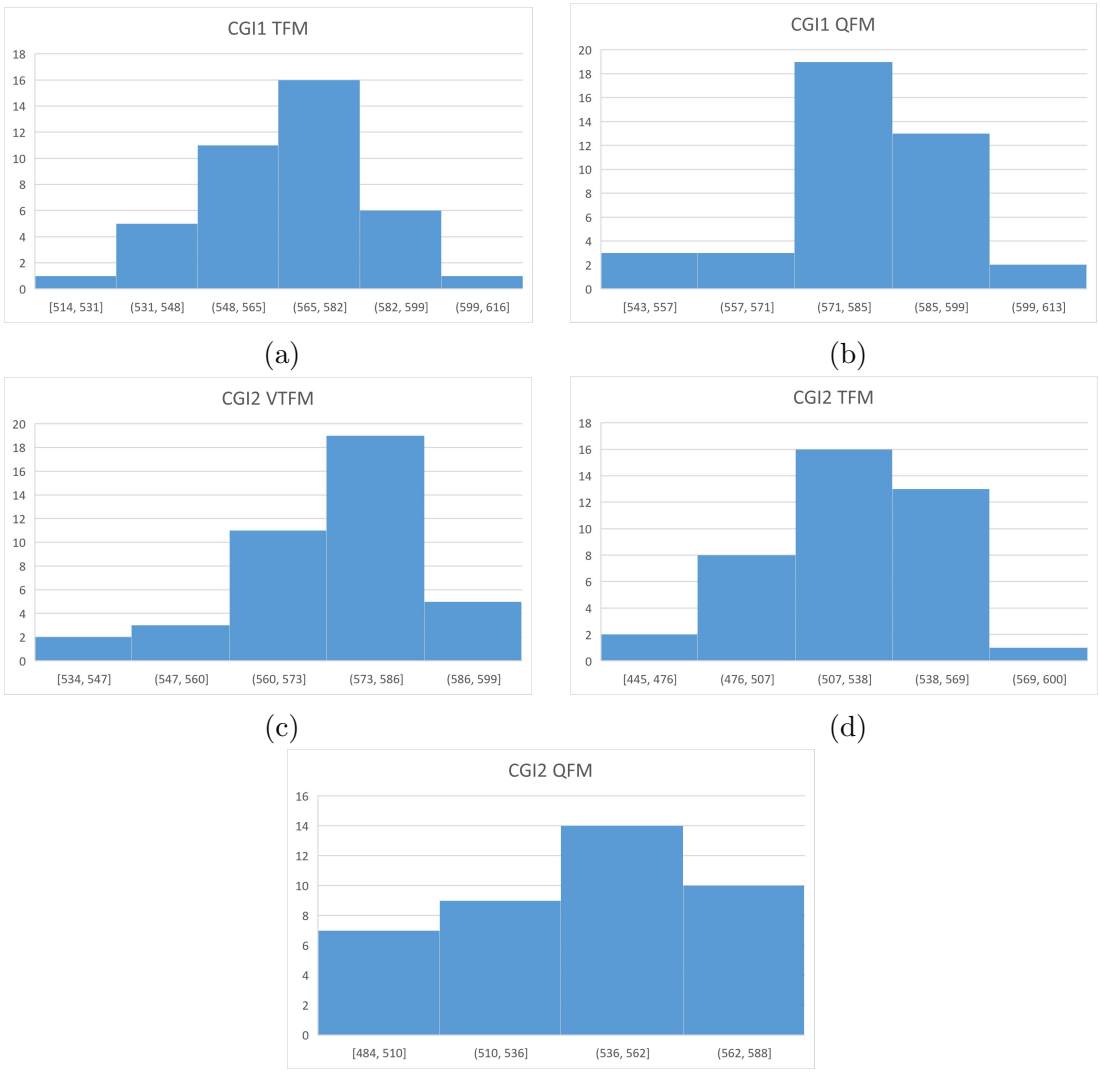


Figure 7.2: Separate histograms for UTS data. The x-axis represent the range of bins in MPa, and the y-axis represents the number of data points in each bin

previous chapters and literature, the 2-parameter Weibull distribution was used to evaluate and compare the data sets. The AD probability plots for all data sets have been shown in figures 7.3 to 7.7.

•	Normal	2-Parameter Weibull	3-Parameter Weibull	Log-normal
CGI1 TFM	0.8	0.5	0.5	0.9
CGI1 QFM	1.4	0.9	0.9	1.5
CGI2 VTFM	0.9	0.5	0.5	1
CGI2 TFM	0.7	0.7	0.7	0.7
CGI2 QFM	0.8	0.6	0.6	0.9

Table 7.4: Anderson-Darling test results for CGI UTS values

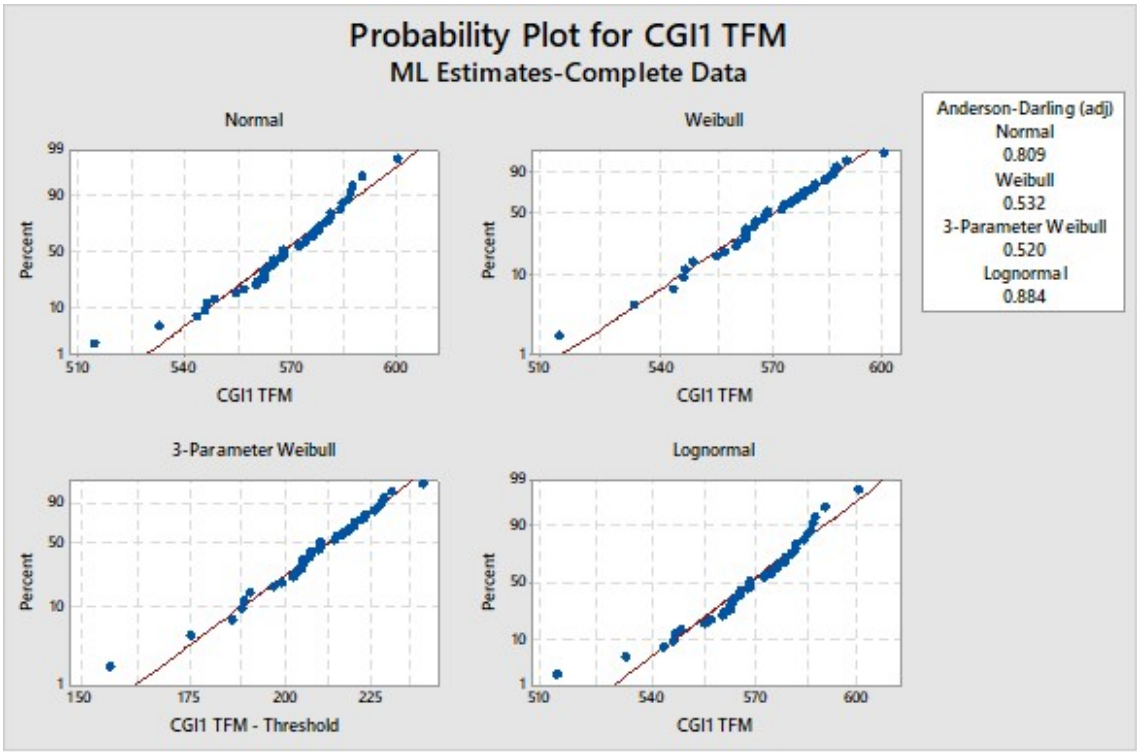


Figure 7.3: Probability plots for AD test for CGI1 TFM UTS. The y-axis represents the cumulative probability in percent. The x-axis represents the UTS in MPa, except for the 3-parameter Weibull plot, it is the threshold value in MPa

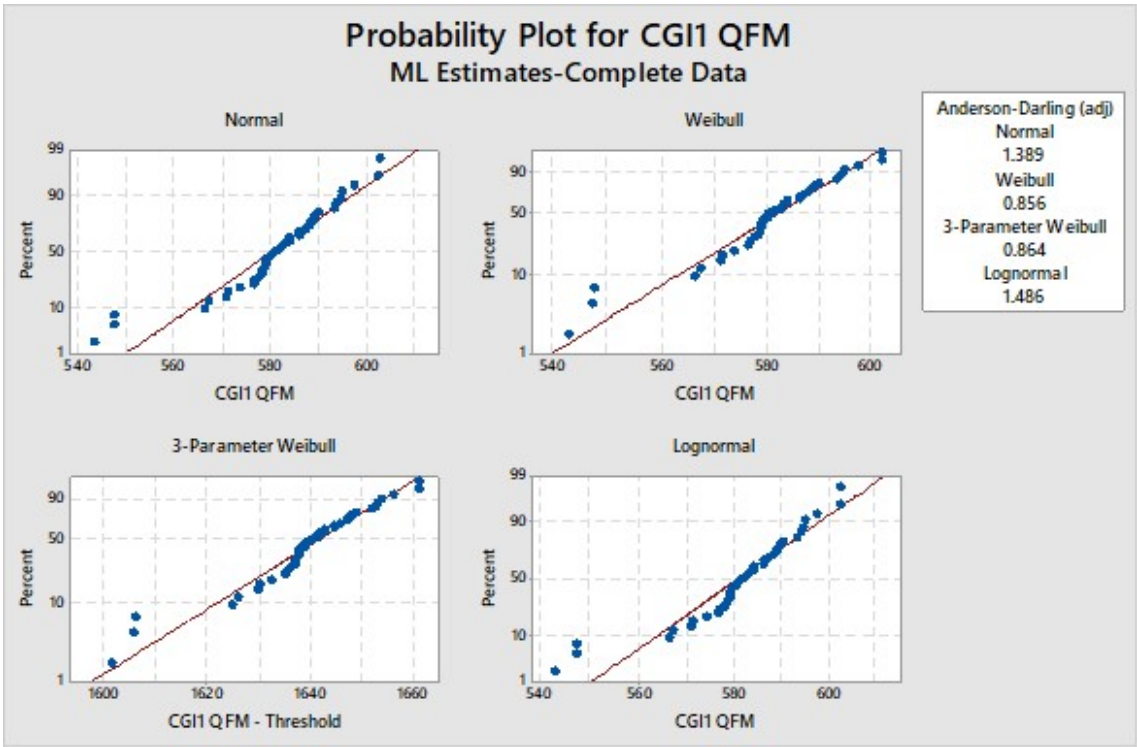


Figure 7.4: Probability plots for AD test for CGI1 QFM UTS. The y-axis represents the cumulative probability in percent. The x-axis represents the UTS in MPa, except for the 3-parameter Weibull plot, it is the threshold value in MPa

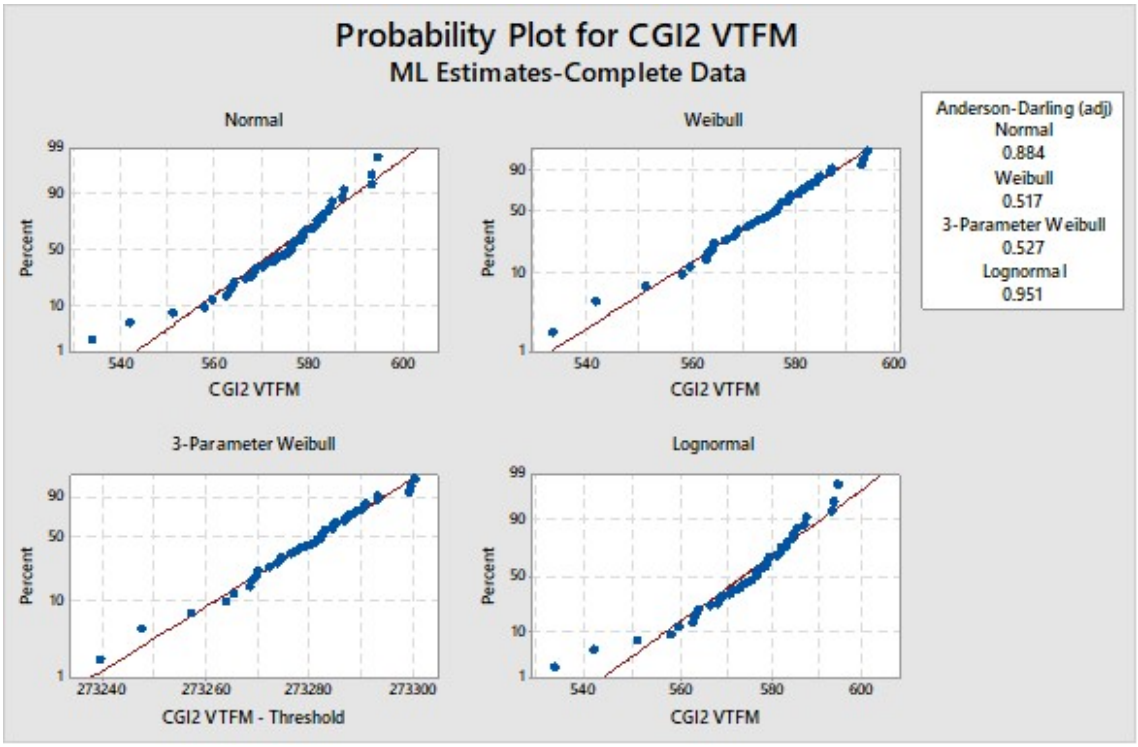


Figure 7.5: Probability plots for AD test for CGI2 VTFM UTS. The y-axis represents the cumulative probability in percent. The x-axis represents the UTS in MPa, except for the 3-parameter Weibull plot, it is the threshold value in MPa

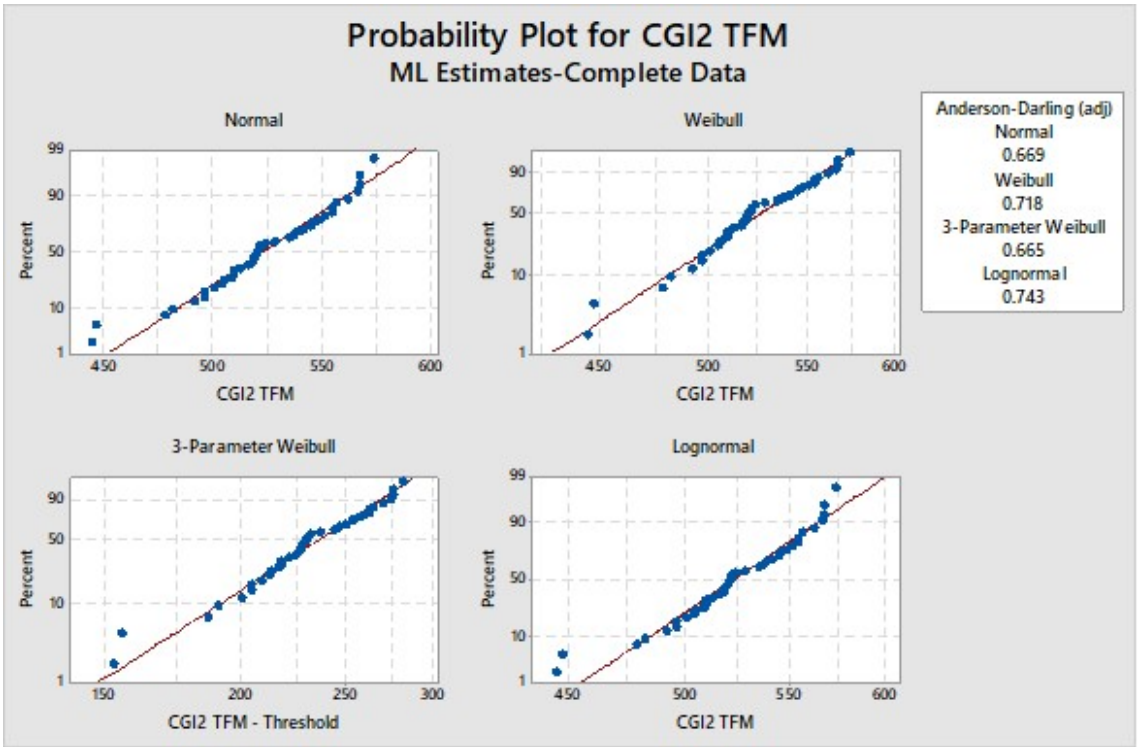


Figure 7.6: Probability plots for AD test for CGI2 TFM UTS. The y-axis represents the cumulative probability in percent. The x-axis represents the UTS in MPa, except for the 3-parameter Weibull plot, it is the threshold value in MPa

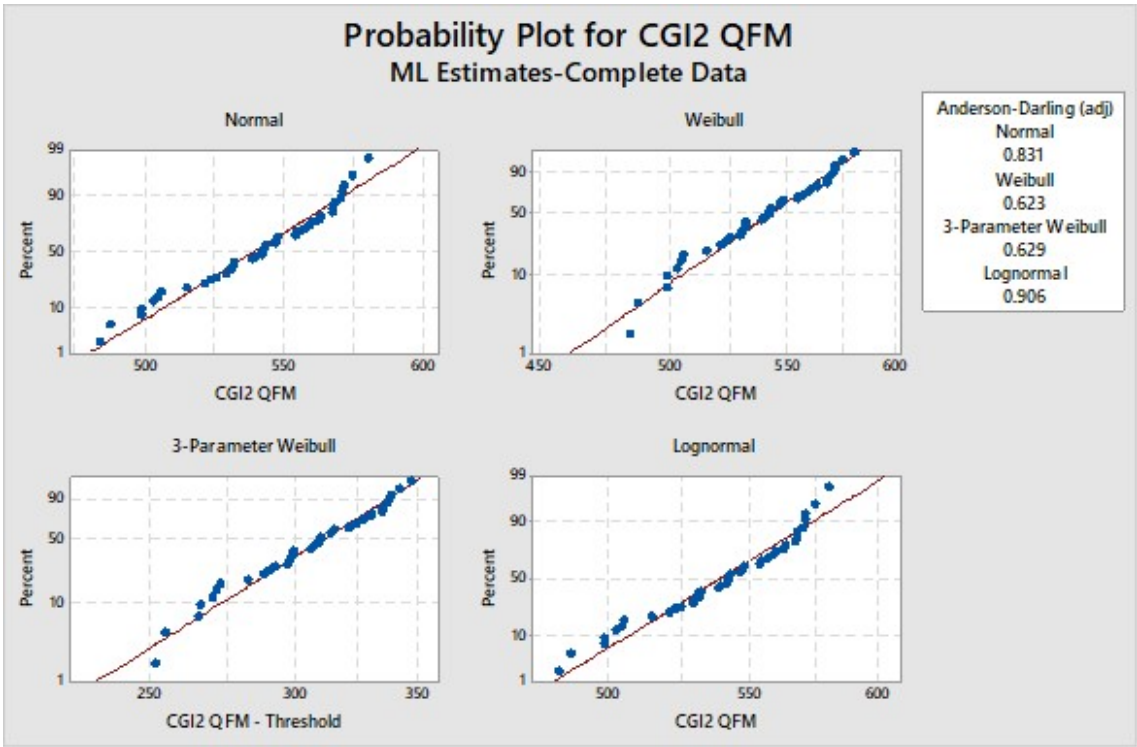


Figure 7.7: Probability plots for AD test for CGI2 QFM UTS. The y-axis represents the cumulative probability in percent. The x-axis represents the UTS in MPa, except for the 3-parameter Weibull plot, it is the threshold value in MPa

7.1.2 Statistical analysis of CGI %Elongation data

The same statistical analysis that was carried out for the UTS data was carried for the %El. data. The descriptive statistics are shown in table 7.5 and the Gaussian distribution for the %El. data is shown in figures 7.8 and 7.9. Though the mean %El. was the lowest for CGI1 QFM, it had the smallest spread, which equate to a range of 0.14. This was 3 times lower than the 2nd lowest range CGI1 TFM. Unexpectedly, CGI2 VTFM had the highest %El. mean = 0.8, but the range was around the average of all data sets. Note, that all %El. data was on the low side of % Elongation specification for the grade used.

Variable	Total Count	Mean	StDev	Variance	Minimum	Maximum	Range
CGI1 TFM	40	0.52	0.11	0.01	0.36	0.81	0.45
CGI1 QFM	40	0.44	0.03	0	0.38	0.52	0.14
CGI2 VTFM	40	0.8	0.12	0.01	0.51	1.05	0.55
CGI2 TFM	40	0.53	0.19	0.04	0.17	1.02	0.85
CGI2 QFM	40	0.53	0.16	0.03	0.23	0.88	0.65

Table 7.5: Descriptive statistics of CGI %El. (pct.) values

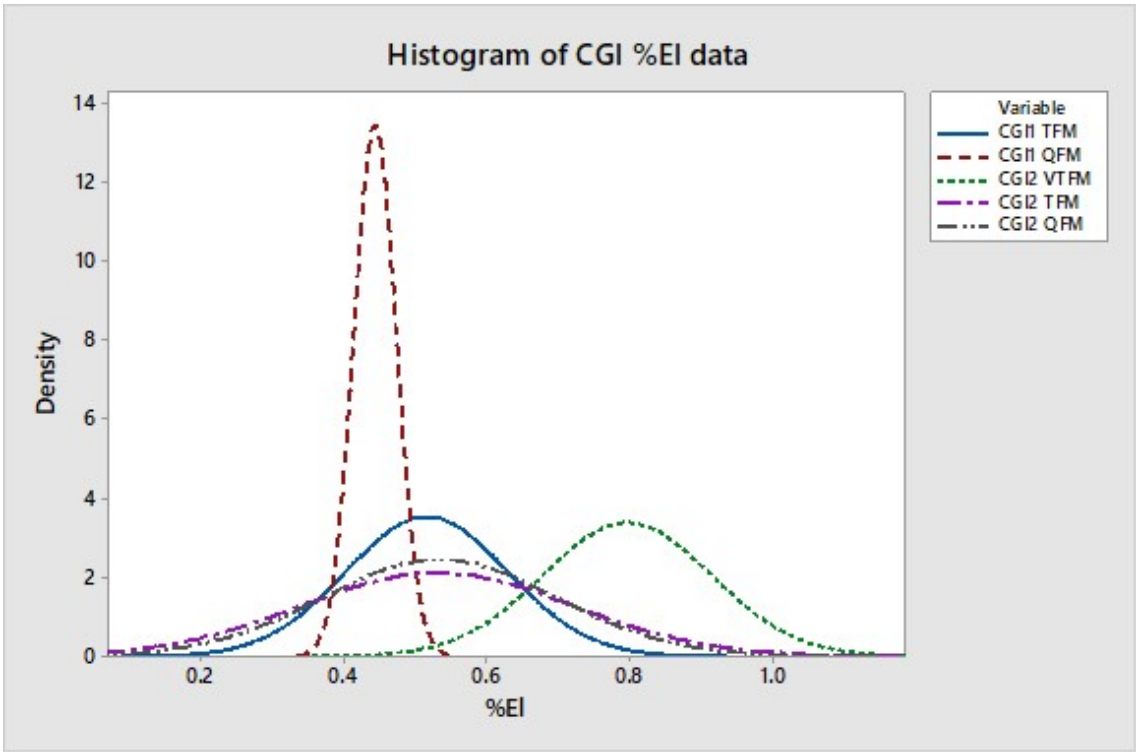


Figure 7.8: The fitted Gaussian distributions for %El. data from each mould type for different CGI melts

A Student's t-test was carried between comparable %El. data sets and the results were summarised in table 7.6. CGI1 data sets had a t-value = 3.9 and a p-value = 0 (<0.05) which meant rejecting the null hypothesis and concluding that the difference between the group means were statistically significant. For CGI2, the same conclusion was reached for VTFM against TFM and QFM, the t-values were 7.5 and 8.23, respectively, and the p-value was 0 for both. The student's t-test between CGI2 TFM and CGI2 QFM resulted in a t-value of 0.1 and a p-value of 0.93. As the P value was higher than the significant level of 0.05, the null hypothesis could not be rejected, and it could not be concluded that the difference between the means was statistically significant.

Two Samples		T Value	P Value
CGI1 TFM	CGI1 QFM	3.9	0
CGI2 VTFM	CGI2 TFM	7.5	0
CGI2 VTFM	CGI2 QFM	8.23	0
CGI2 TFM	CGI2 QFM	0.1	0.93

Table 7.6: Student's t-test results for CGI %El. data

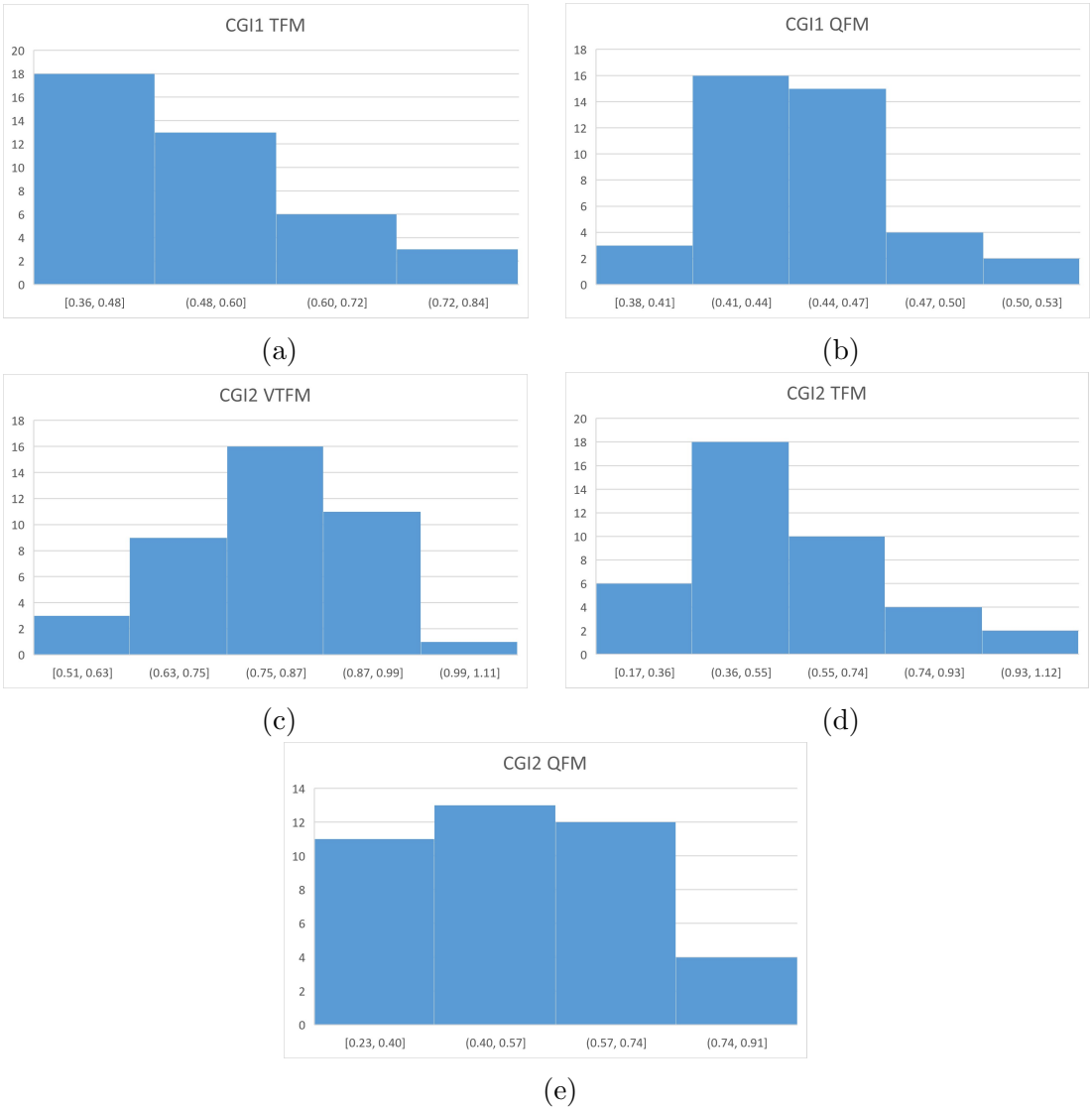


Figure 7.9: Separate histograms for %El. data. The x-axis represent the range of bins in %El (pct.), and the y-axis represents the number of data points in each bin

The Anderson-Darling test was used to test the %El. data sets against normal, log-normal, 2-parameter and 3-parameter Weibull distributions to determine which distribution had the best goodness of fit. The criteria is, the lower the resulting AD score the better the goodness of fit, with taking into consideration the aims mentioned in section 5.1.1. Table 7.4 has a summary of the results. The 3-parameter Weibull distribution had the lowest score for CGI1 TFM, while for CGI1 QFM it had a score of 0.8 which was higher than the normal and log-normal with AD score = 0.7 and 0.6; respectively. The 3-parameter Weibull distribution had the lowest AD score for CGI2 VTFM and the lowest, but equal to 2-parameter Weibull, for

CGI2 QFM. As for CGI2 TFM, the 3-parameter Weibull had the second lowest AD score after the log-normal distribution. The 3-parameter Weibull distribution was chosen to evaluate and compare the CGI %El. data. Figures 7.10 to 7.14 show the probability plot for the AD test for all of the data sets.

•	Normal	2-Parameter Weibull	3-Parameter Weibull	Log-normal
CGI1 TFM	1.2	1.5	0.5	0.7
CGI1 QFM	0.7	1.7	0.8	0.6
CGI2 VTFM	0.6	0.6	0.5	0.8
CGI2 TFM	1.3	1.2	0.9	0.7
CGI2 QFM	0.6	0.6	0.6	0.7

Table 7.7: Anderson-Darling test results for CGI %El. values

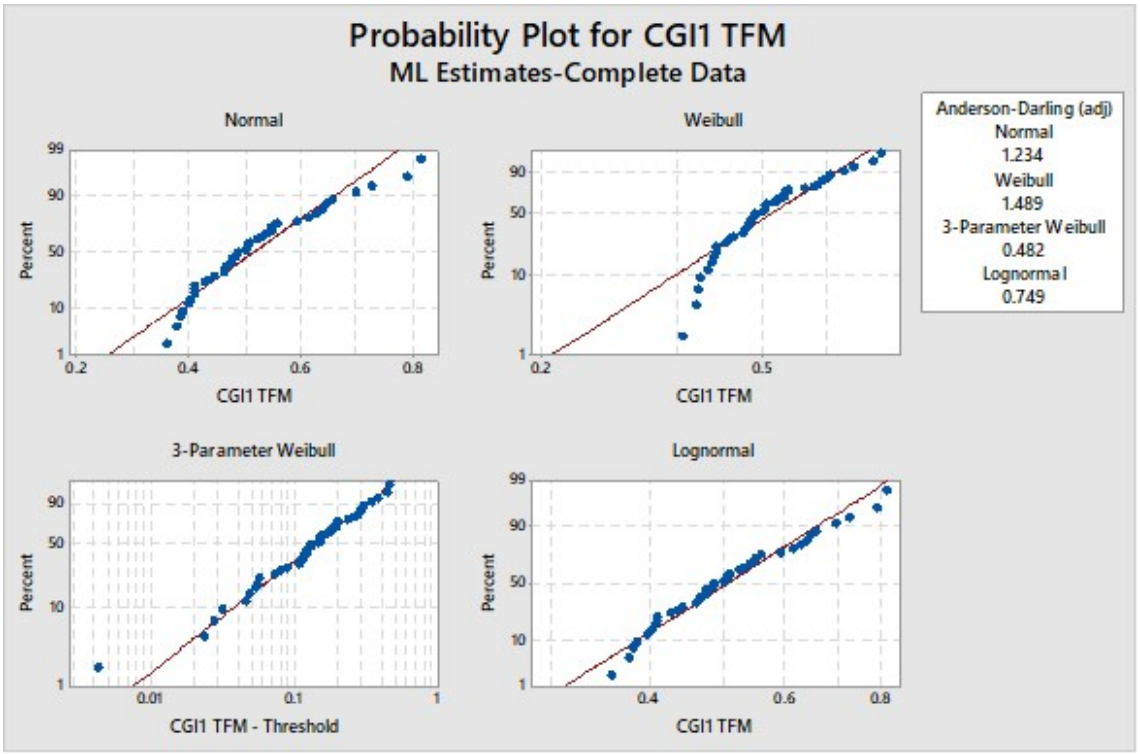


Figure 7.10: Probability plots for AD test for CGI1 TFM %El. The y-axis represents the cumulative probability in percent. The x-axis represents the %El in pct., except for the 3-parameter Weibull plot, it is the threshold value in pct.

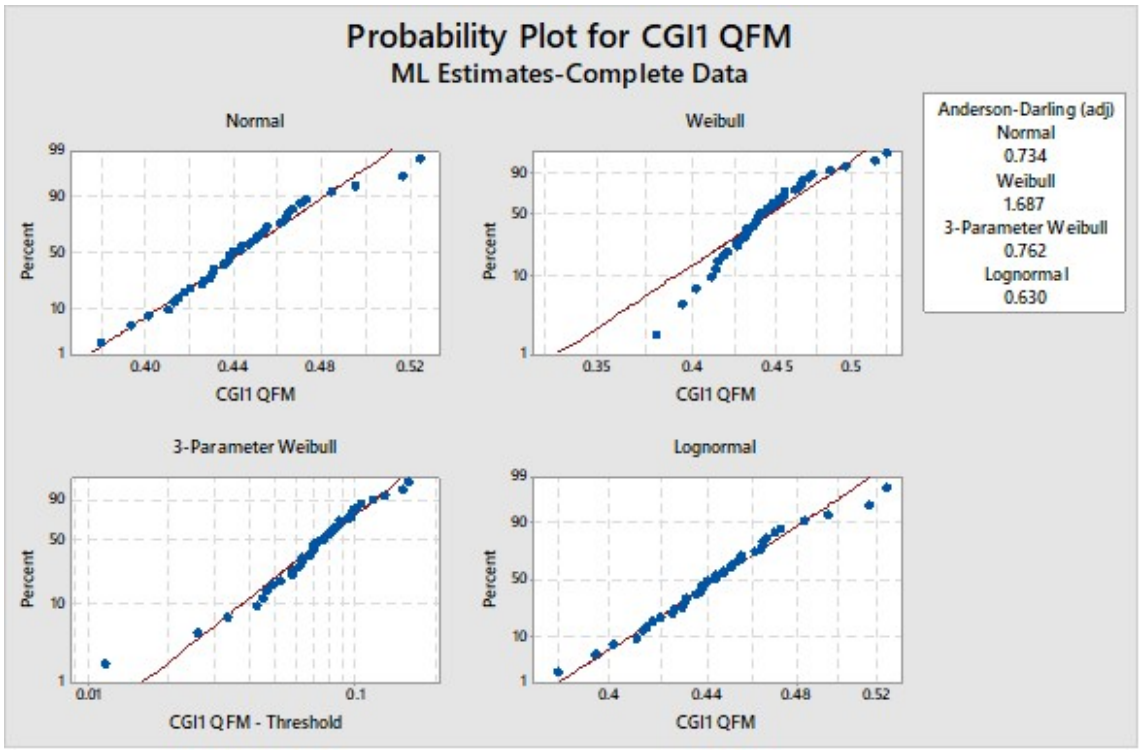


Figure 7.11: Probability plots for AD test for CGI1 QFM %El. The y-axis represents the cumulative probability in percent. The x-axis represents the %El in pct., except for the 3-parameter Weibull plot, it is the threshold value in pct.

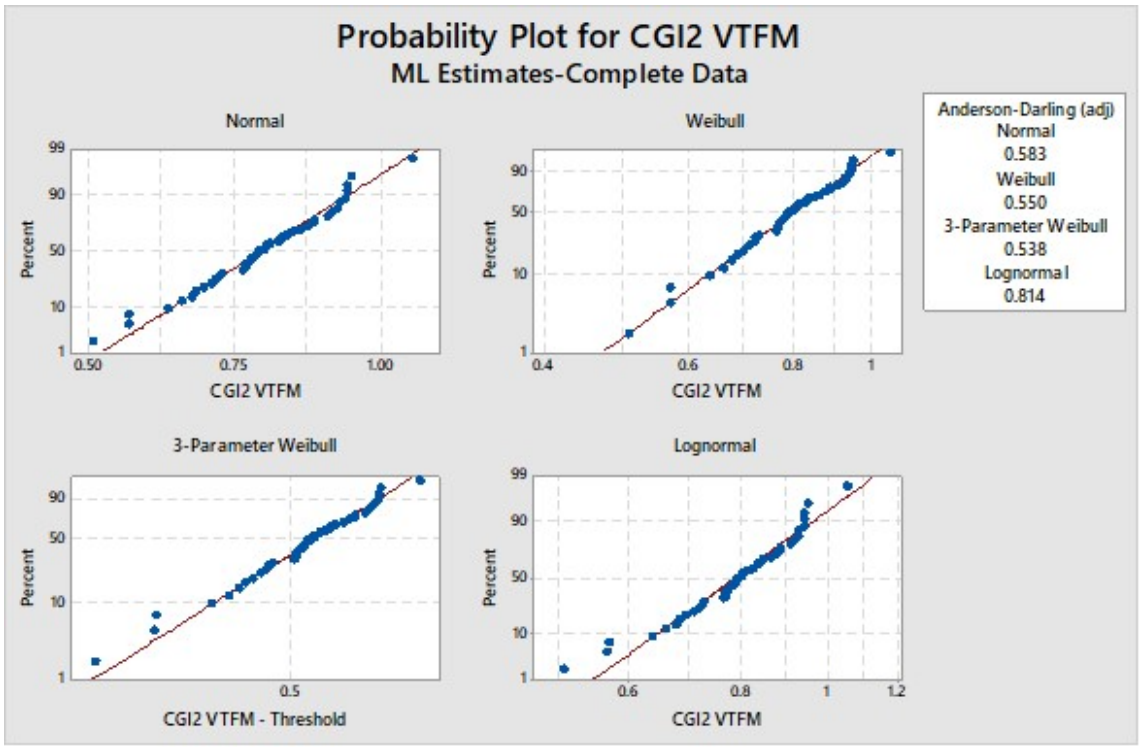


Figure 7.12: Probability plots for AD test for CGI2 VTFM %El. The y-axis represents the cumulative probability in percent. The x-axis represents the %El in pct., except for the 3-parameter Weibull plot, it is the threshold value in pct.

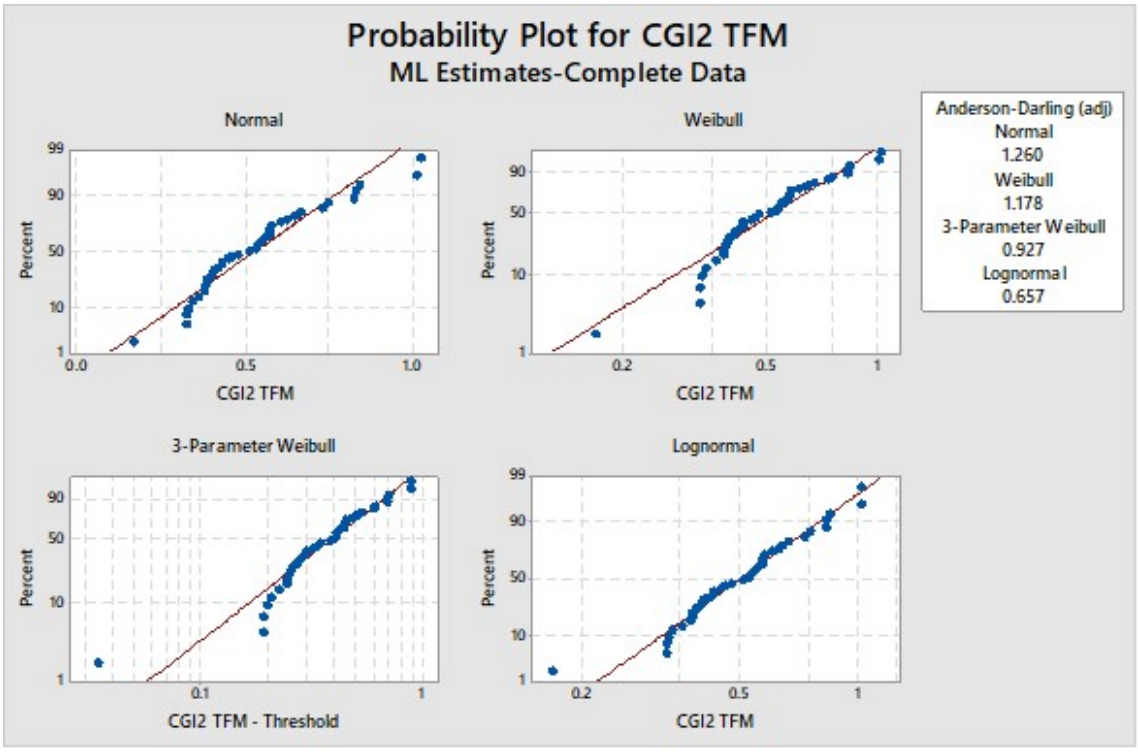


Figure 7.13: Probability plots for AD test for CGI2 TFM %El. The y-axis represents the cumulative probability in percent. The x-axis represents the %El in pct., except for the 3-parameter Weibull plot, it is the threshold value in pct.

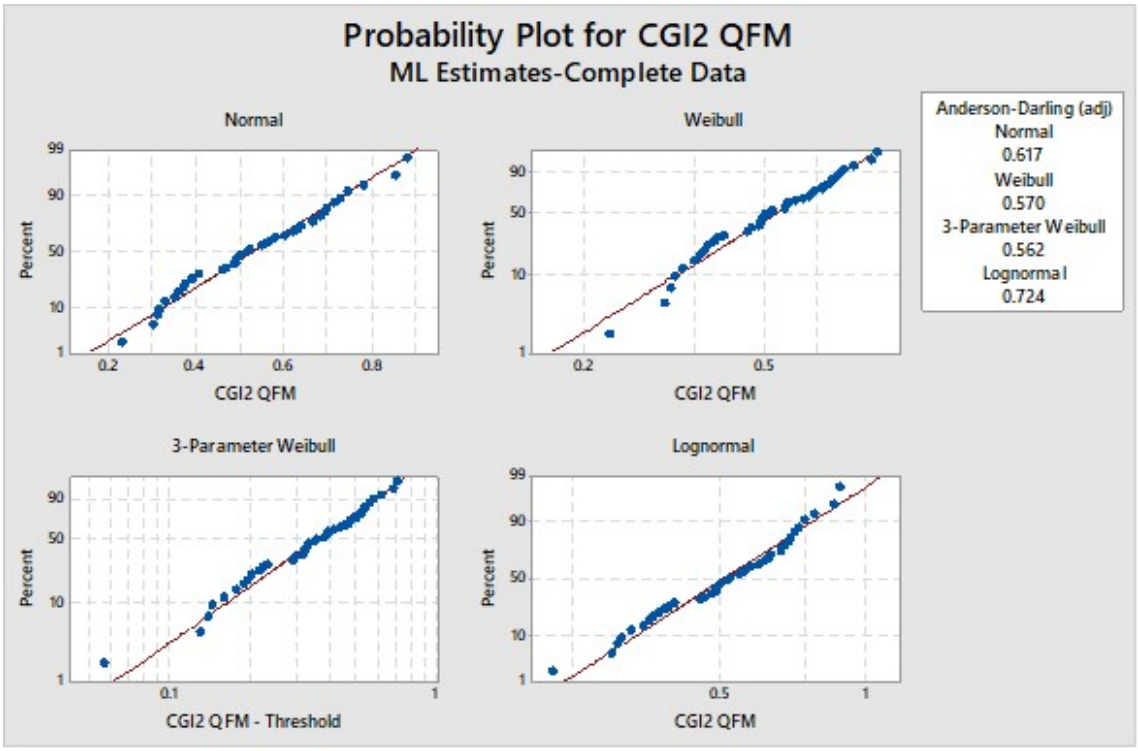


Figure 7.14: Probability plots for AD test for CGI2 QFM %El. The y-axis represents the cumulative probability in percent. The x-axis represents the %El in pct., except for the 3-parameter Weibull plot, it is the threshold value in pct.

7.1.3 Weibull distribution analysis for UTS and %El CGI data

As a result of the AD test, the 2-parameter Weibull distribution was used to evaluate and compare CGI1 and CGI2 UTS data, and the 3-parameter Weibull distribution was used for %El. data. Figure 7.15 is the 2-parameter Weibull probability plot for CGI1 UTS data. CGI1 TFM and CGI2 QFM had a good fit to the 2-parameter Weibull distribution with $R^2 > R^2_{0.05}$. CGI1 QFM had a higher Weibull modulus (m = 53) than CGI1 TFM (m = 42), a 26% increase. The scale parameter followed the same pattern and increased from CGI1 TFM to CGI1 QFM, being 570 MPa and 589 MPa; respectively. A summary of the results had been presented in table 7.8. The %El. data for CGI1 exhibited the same behaviour as the UTS data. CGI1 QFM had a higher Weibull modulus (m = 2.7) than CGI2 TFM (m = 1.5), this was an 80% increase. The threshold also experienced an increase from 0.18 to 0.37, for CGI1 TFM and CGI1 QFM; respectively. The scale parameter followed suit, as it decreased from 0.18 to 0.09 for CGI1 TFM and CGI1 QFM; respectively. The 3-parameter Weibull probability plot for the CGI1 %El. data and a summary of the results are shown in figure 7.16 and table 7.9.

For CGI2, VTFM was added to examine a more surface turbulent type of filling and to make the analysis comparable to LGI and SGI. Surprisingly the VTFM results were better than the TFM and QFM, the results are shown in figure 7.17 and table 7.10. VTFM had a higher Weibull modulus of 54 against that of TFM (m = 21) and QFM (m = 26), a 107% increase in the Weibull modulus from QFM and 157% increase from TFM. The scale parameter followed the same pattern of behaviour. CGI2 VTFM had the highest figure (578 MPa), followed by CGI2 QFM (572 MPa) and the lowest was CGI2 TFM with a scale parameter of 547 MPa. The three data sets showed good fits to the 2-parameter Weibull distribution with $R^2 > R^2_{0.05}$. CGI2 %El. data mirrored the behaviour of the UTS data. CGI2 TFM had the lowest Weibull modulus (m = 2.2), increased by 9% to 2.4 for CGI2 QFM, and increased again by 121% to 5.3 for CGI2 VTFM. The threshold was 0.17 for

CGI2 TFM, 0.13 for CGI2 QFM, and 0.26 for CGI2 VTFM. The scale parameter was 0.45 for CGI2 TFM, 0.41 for CGI2 QFM, and 0.26 for CGI2 VTFM. Therefore CGI2 VTFM had the highest performance on all parameters, and this has been shown in figure 7.18 and table 7.11.

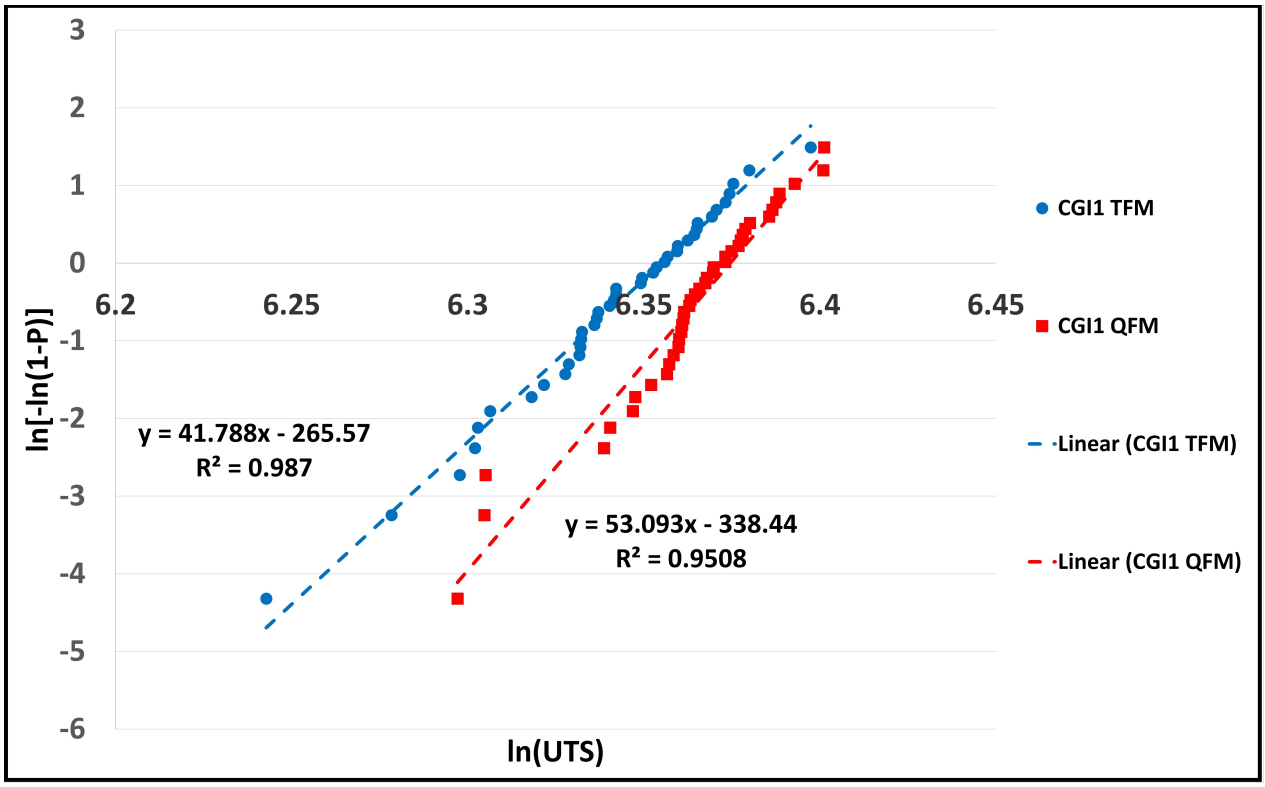


Figure 7.15: 2-parameter Weibull probability plot for CGI1 UTS data

Melt/Filling Mode	n	m	scale (MPa)	R^2	$R^2_{0.05}$
CGI1 TFM	40	42	570	0.99	0.93
CGI1 QFM	40	53	589	0.95	0.93

Table 7.8: Results of 2-parameter Weibull probability plot for CGI1 UTS data

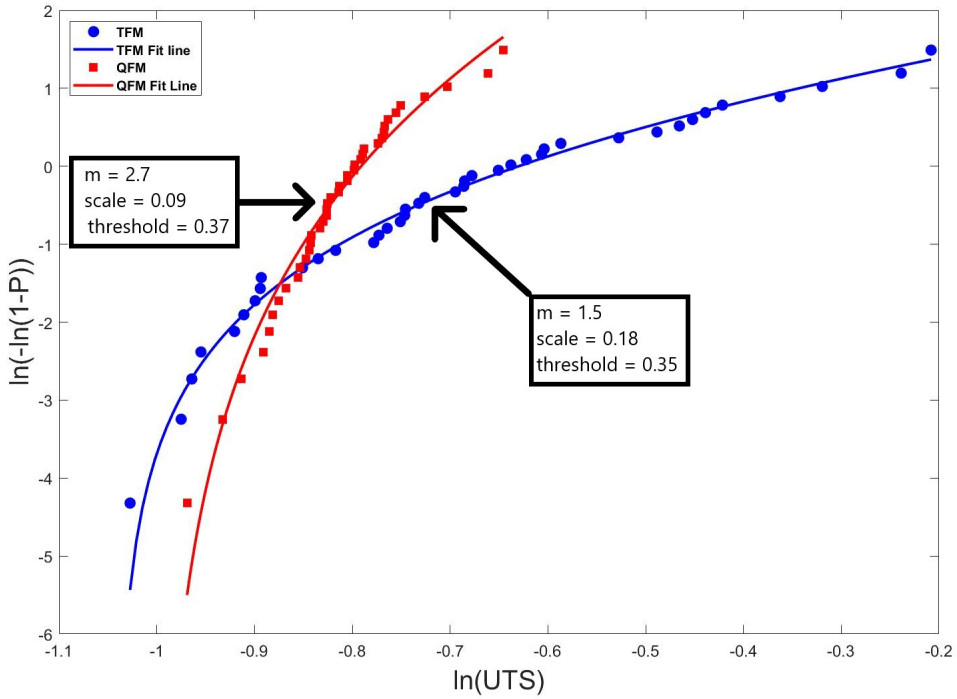


Figure 7.16: 3-parameter Weibull probability plot for CGI1 %El. data

Melt/Filling Mode	n	m	scale (pct)	threshold
CGI1 TFM	40	1.5	0.18	0.18
CGI1 QFM	40	2.7	0.09	0.37

Table 7.9: Results of 3-parameter Weibull probability plot for CGI1 %El. data

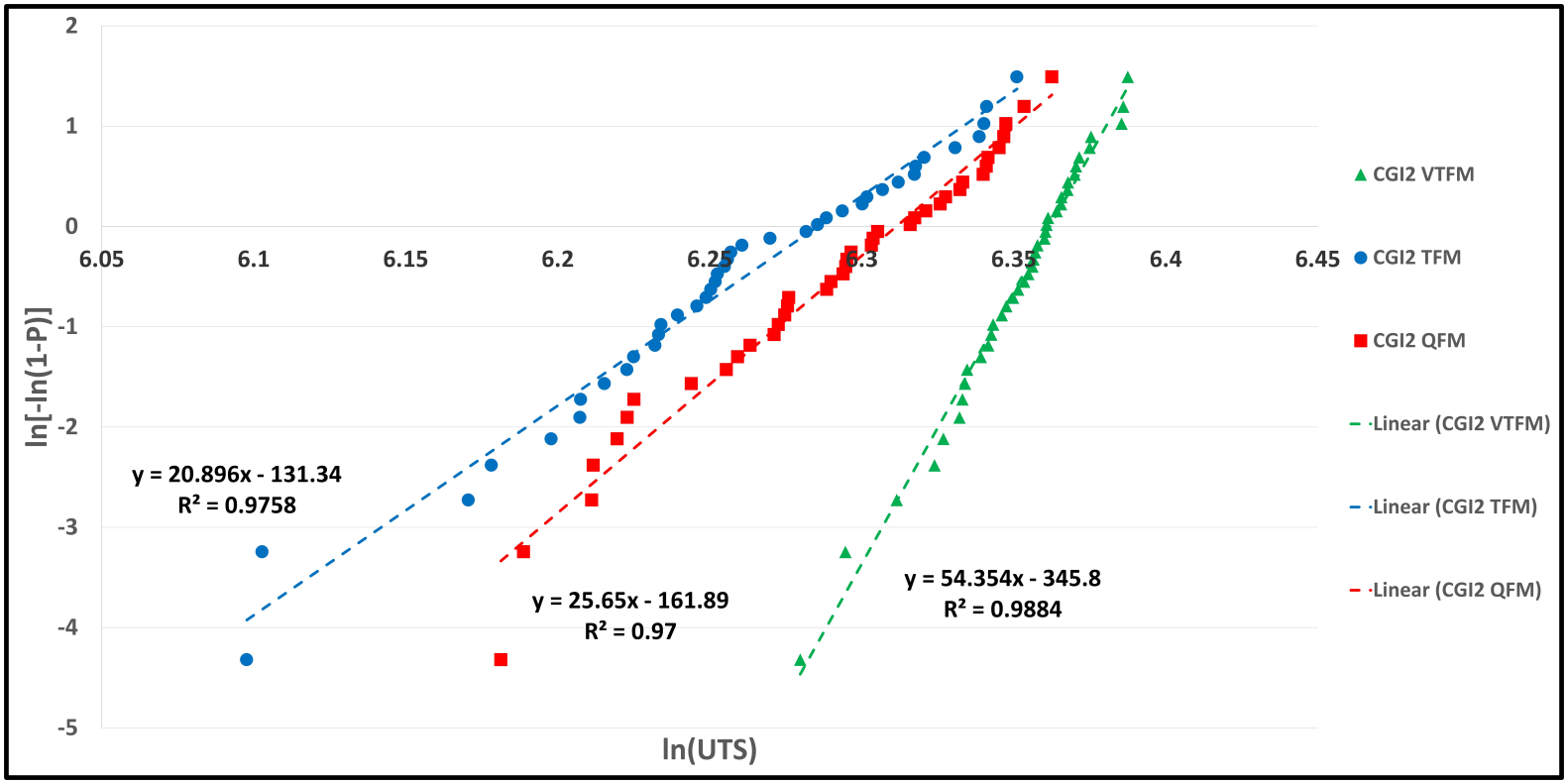


Figure 7.17: 2-parameter Weibull probability plot for CGI2 UTS data

Melt/Filling Mode	n	m	scale (MPa)	R^2	$R^2_{0.05}$
CGI2 VTFM	40	54	578	0.99	0.93
CGI2 TFM	40	21	547	0.98	0.93
CGI2 QFM	40	26	572	0.97	0.93

Table 7.10: Results of 2-parameter Weibull probability plot for CGI2 UTS data

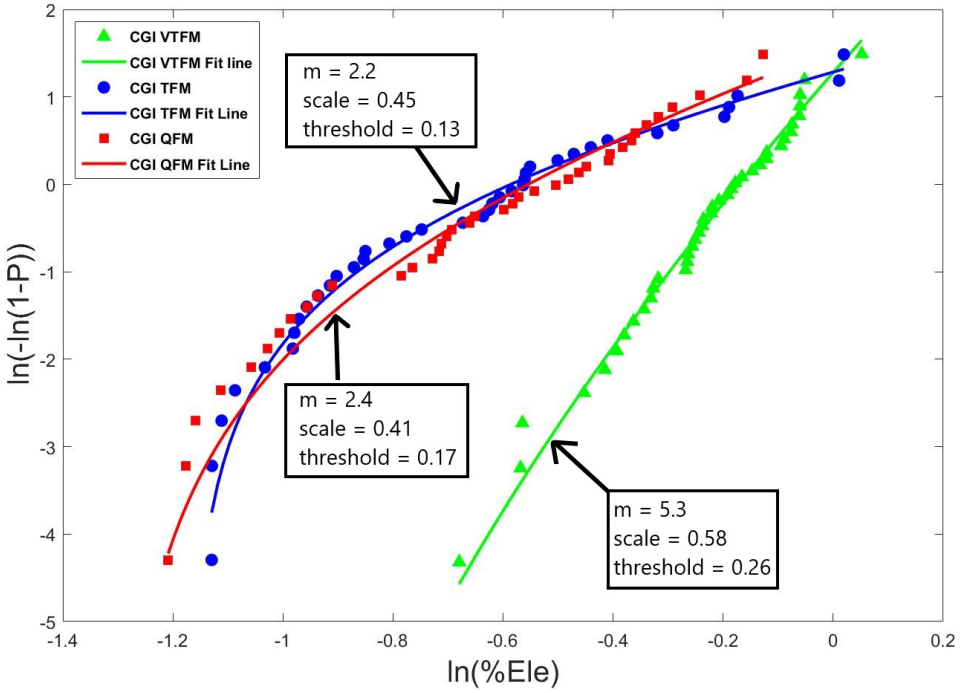


Figure 7.18: 3-parameter Weibull probability plot for CGI2 %El. data

Melt/Filling Mode	n	m	scale (pct)	threshold
CGI2 VTFM	40	5.3	0.58	0.26
CGI2 TFM	40	2.2	0.45	0.13
CGI2 QFM	40	2.4	0.41	0.17

Table 7.11: Results of 3-parameter Weibull probability plot for CGI2 %El. data

7.2 SEM and EDX examination of CGI fracture surfaces

During the examination of the fracture surfaces of the CGI castings several defects were detected, never found on CGI fracture surfaces before. The defects had a plate topography and was usually covered by a thin graphite film. There initial appearance resembled micro-shrinkage but the protruding nature of the defects distinguished them from normal micro-shrinkage observed in Al and SGI.

Figure 7.19 shows a SE image of a CGI fracture surface which showed defects scattered around the fracture surface, but mostly around the central area (marked by red circles). Note, the fracture surface is not oval, it is circular. The oval shape was a result of the big working distance (WD = 41.3 mm) and the shape of the aperture which is shown in figure 7.42. The defects had a light element content as can be seen on the BSE image in figure 7.20. It was noticed that the area around the defects were depleted of graphite. Figure 7.21 and 7.22 were SE images of the same area of the fracture surface on both sides of the same bar. As can be seen the plate defect protruded from the fracture surface and pointed mostly to the center of the fracture surface. They had different orientations, and sizes ranging from 50 μm to 250 μm.

Figures 7.23, 7.24 and 7.25 show SE and BSE images and a layered EDX map of the plate defects. The images show the plate defects to be centralized and protruding towards the middle of the testbar. The plates were covered with a light element, which the layered EDX map revealed it to be graphite. Graphite was represented in red, same color as the vermicular particles, and Fe was represented in blue. Figures (7.24 and 7.25) showed the growth of the graphite films over the whole surface of the plate defects, and the largest size found of this unique and novel defects (length = 2.7 mm).

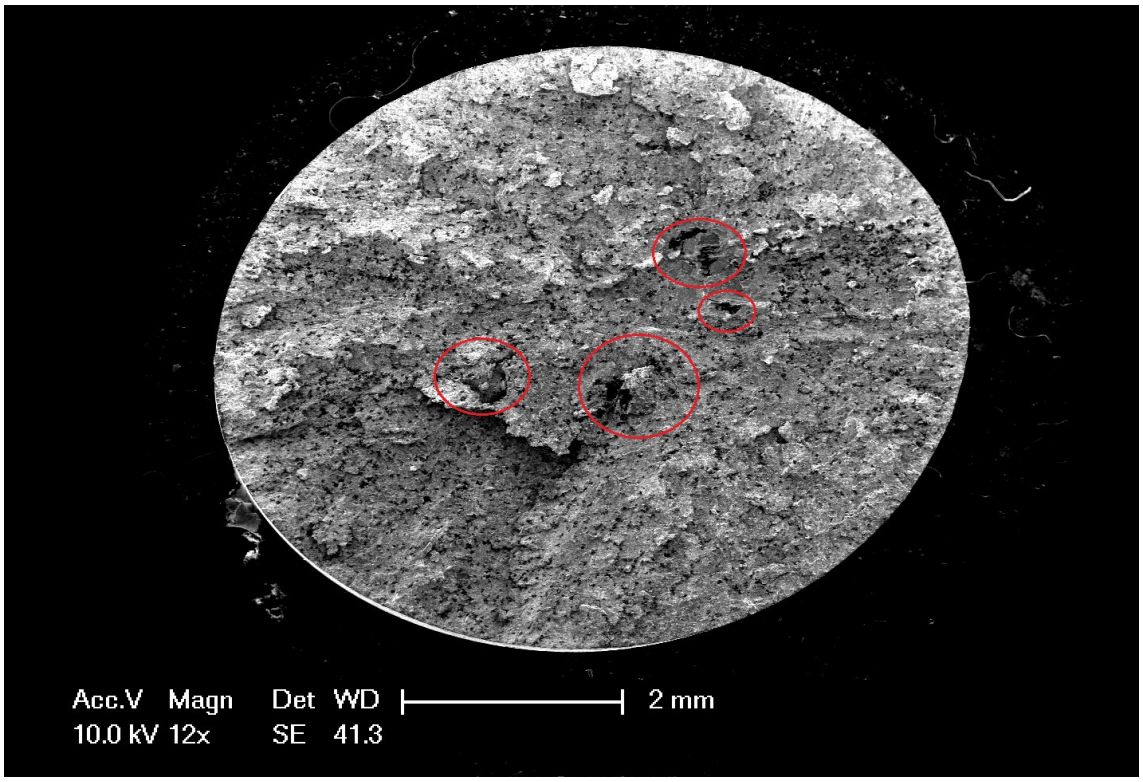


Figure 7.19: SE image of a fracture surface of CGI testbar showed four areas of defects

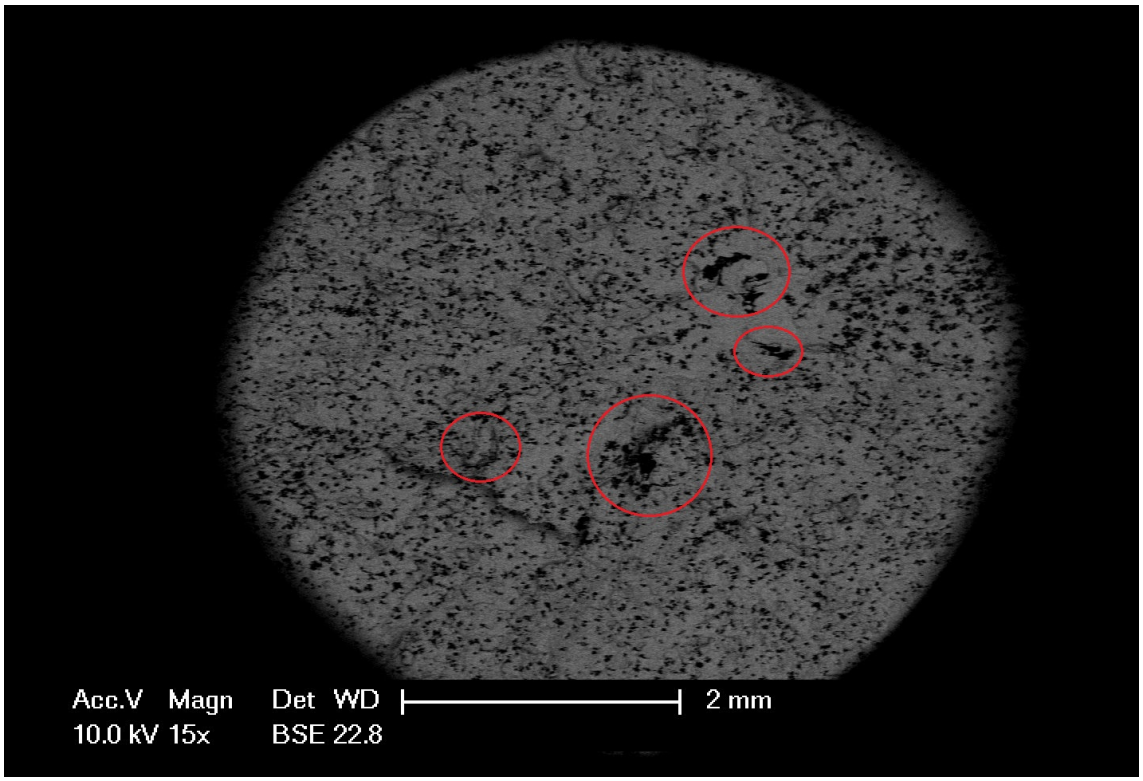


Figure 7.20: BSE image of the fracture surface shown in figure 7.19 showed four areas of defects with light elements composition, notice the areas around the defects are depleted from CG

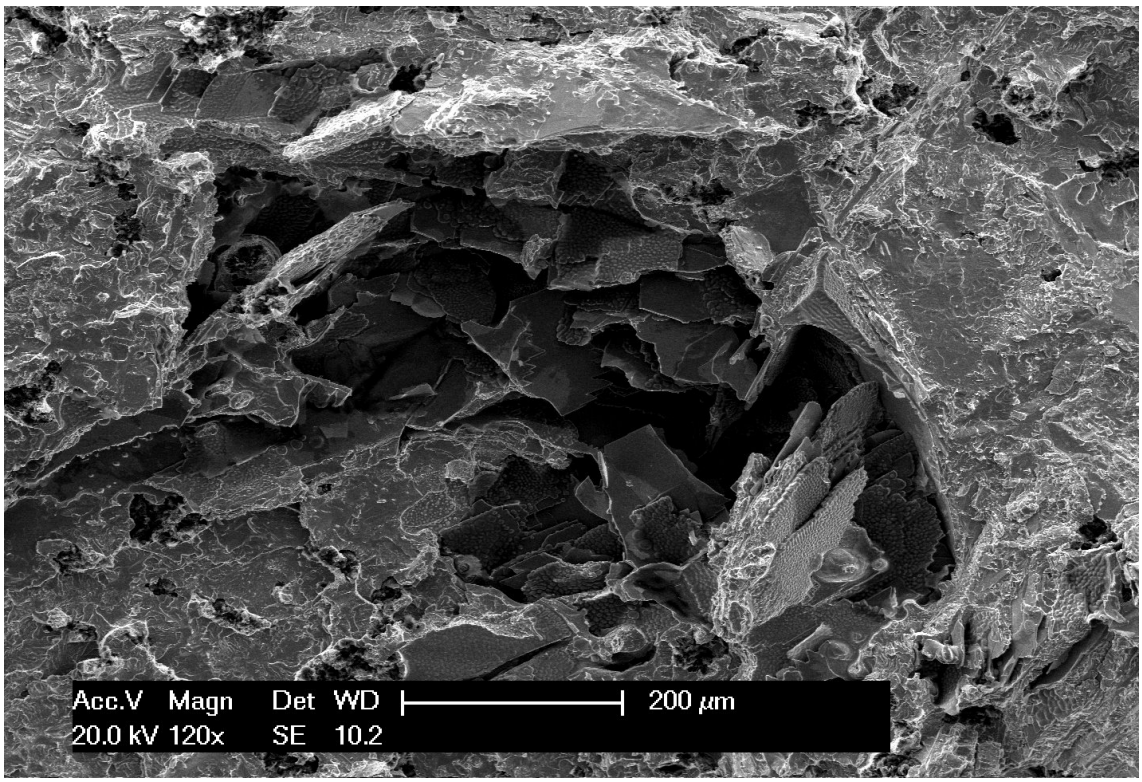


Figure 7.21: Close up SE image of the defects shown in figure 7.20 showed plate structures with perturbations on top

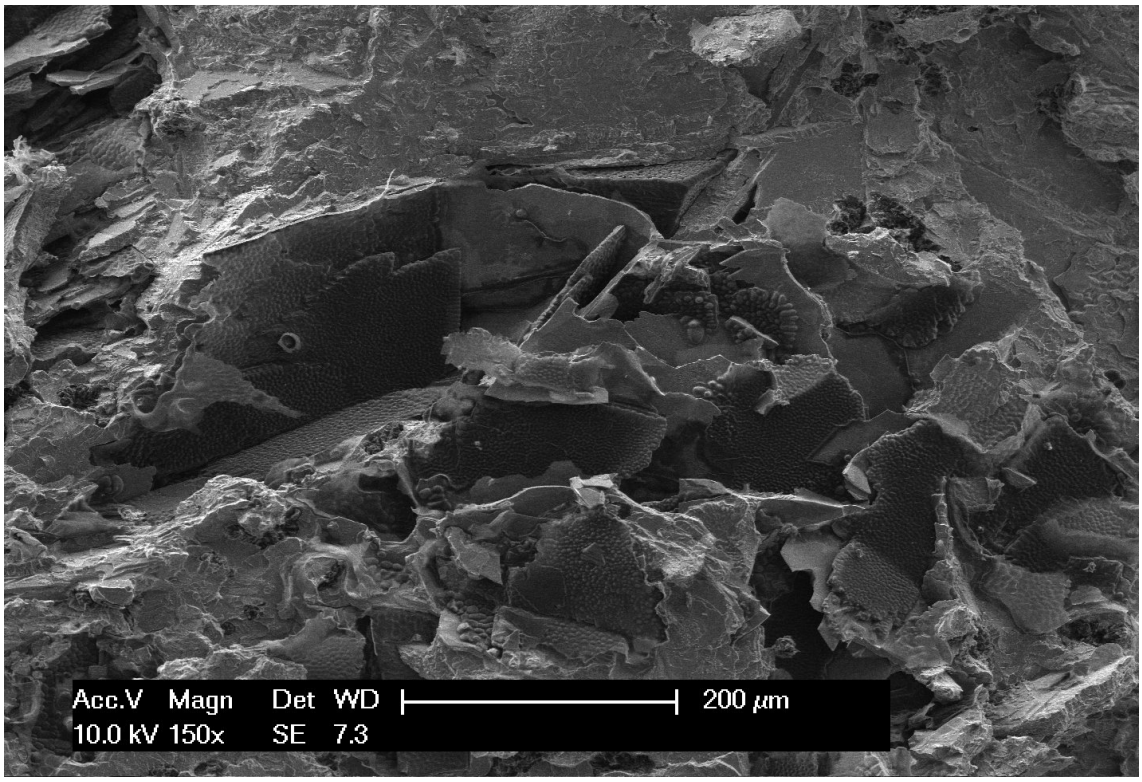


Figure 7.22: SE image of the fracture surface of the other half of the testbar showed a mirroring of the defects shown in figure 7.19

Figure 7.26 is a close-up image of the same type of defect but on a different fracture surface, and showed the film to cover only about half of the area of the plate defect. The EDX spectrum of the film had a substantial peak of carbon and two small peaks of iron and silicon (figure 7.28). The iron and silicon peaks resulted from the interaction volume of the electron beam reaching the substrate; because it penetrated through the nanometer thin, almost transparent, and light graphite film.

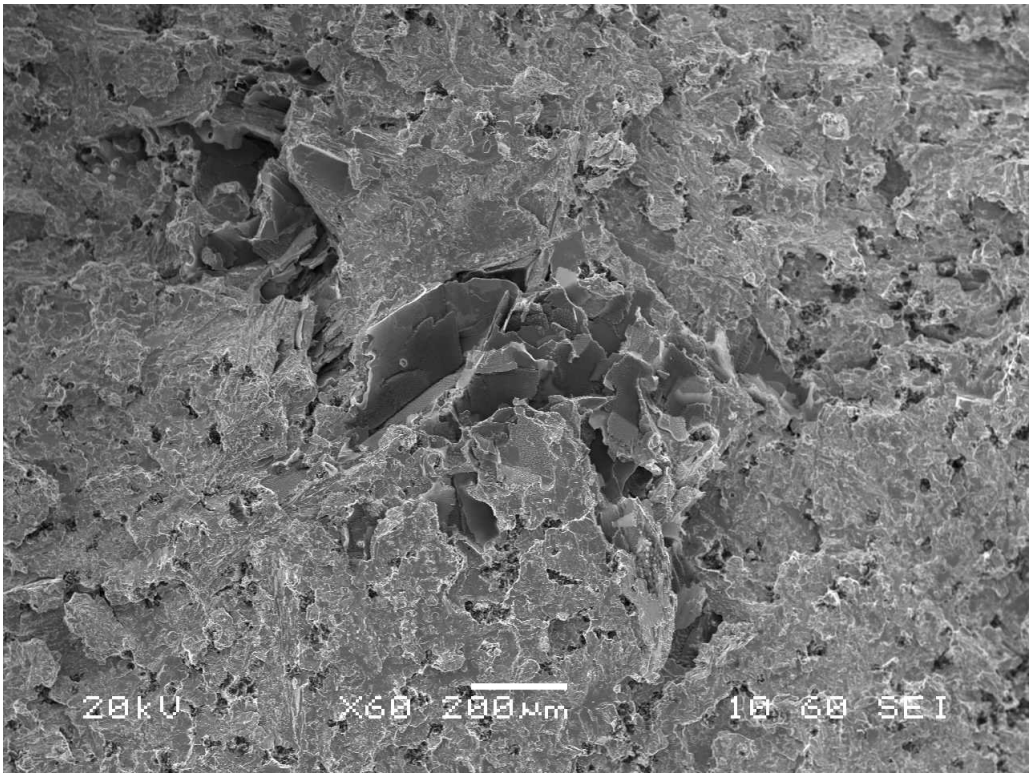


Figure 7.23: SE image of two groups of plate defects on CGI testbar fracture surface

In another plate defect, SEM imaging revealed it was also covered with a thin graphite film. The graphite film contained tens of identical star-shaped configuration, which were thicker than the original film, with diameter of 4 µm, seen in figure 7.27. They were seen on the thick side (marked by red arrows) and transparent (marked by blue arrows) side of the film (figure 7.27). Figure 7.30 is the EDX spectrum of the star marks, and it showed Mg, Si and N peaks. Figure 7.31 is the EDX element maps of the stars configuration and it confirmed that the start constituents were Si, Mg and N.

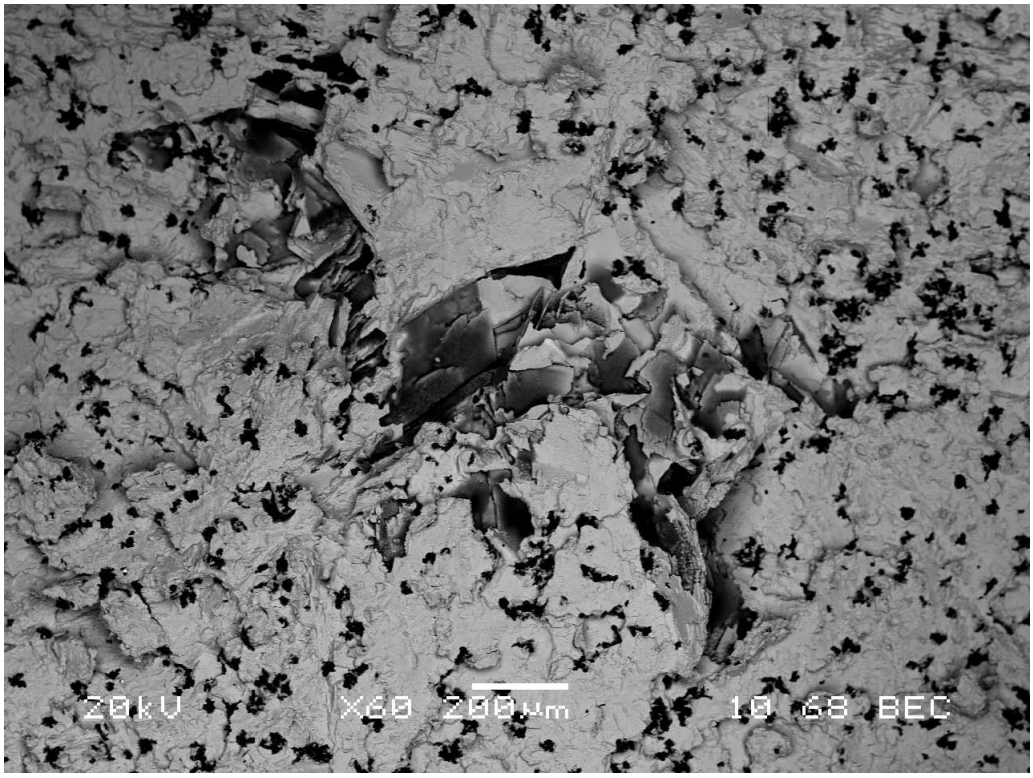


Figure 7.24: BSE image of the of plate defects shown in figure 7.23 showed the plates were covered with a light element

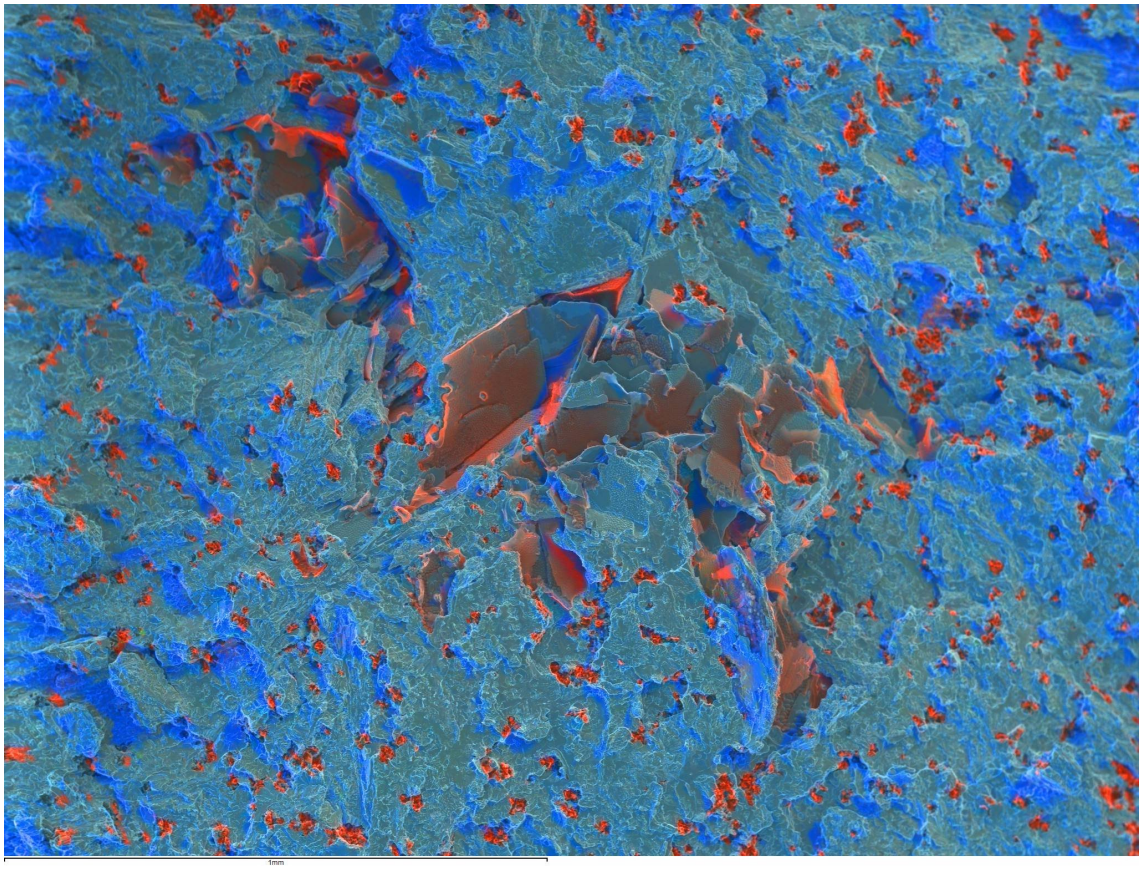


Figure 7.25: EDX layered map of the plate defects in figure 7.24 showed the plate chemical composition to be graphite

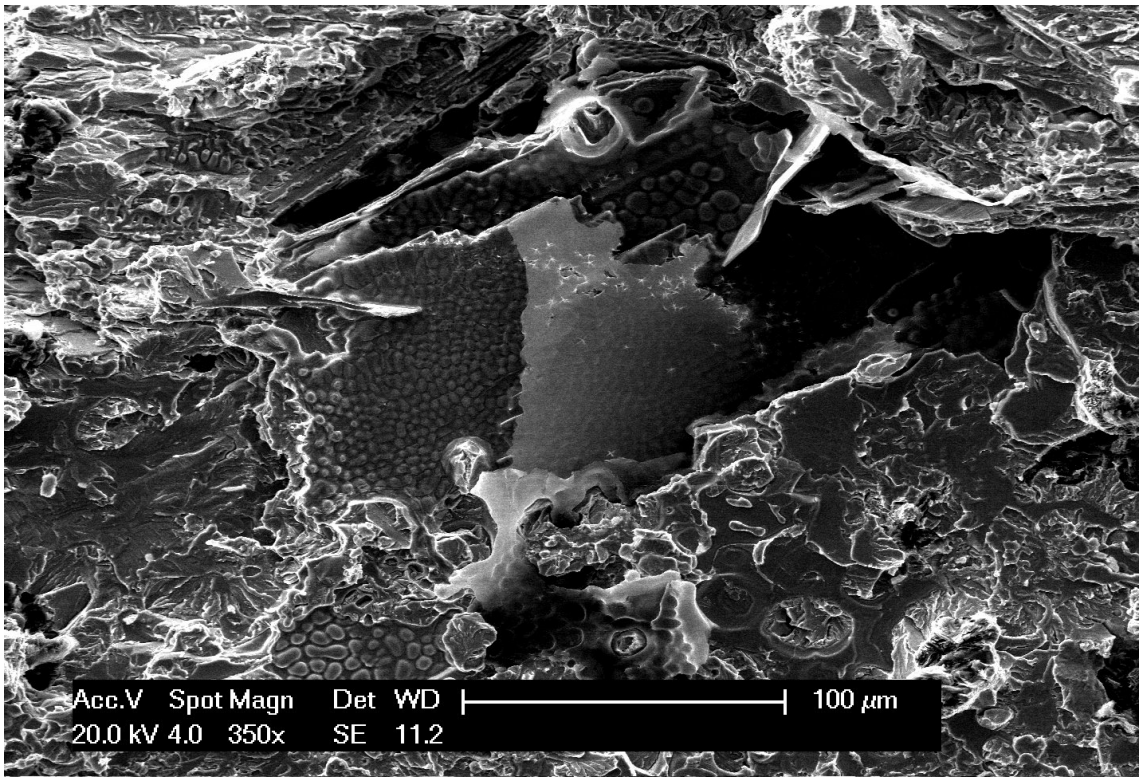


Figure 7.26: SE image of a thin film covering a plate defect

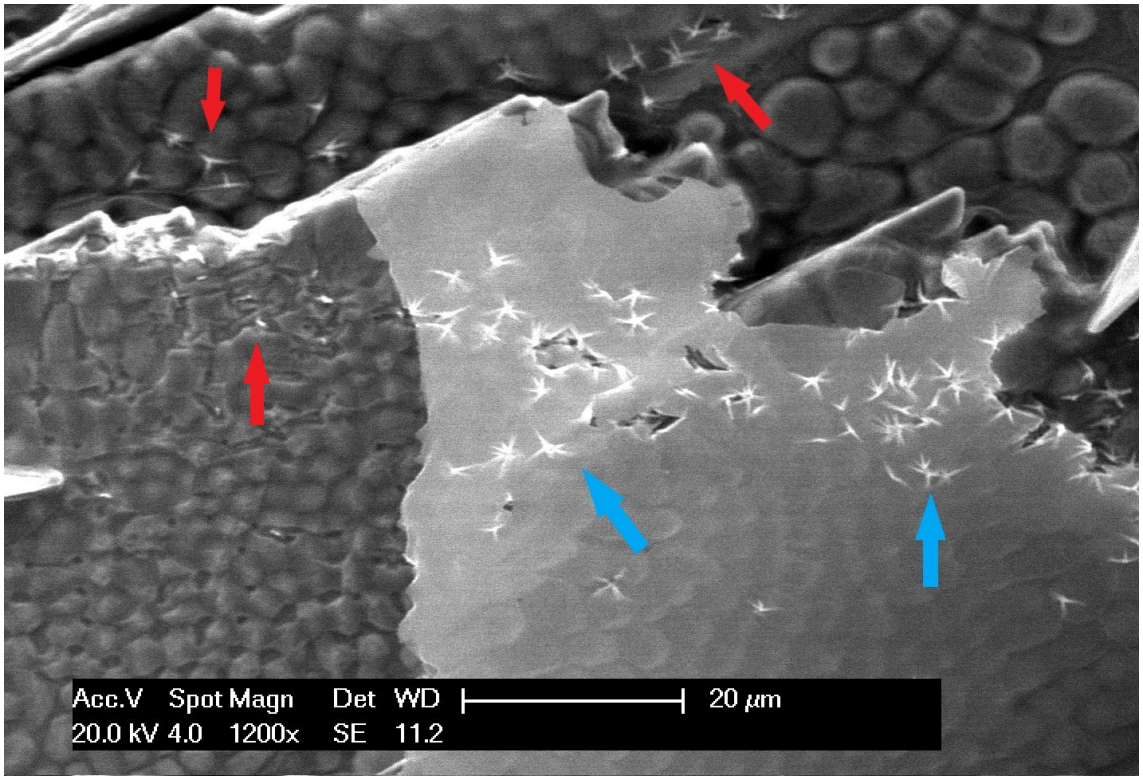


Figure 7.27: Close-up SE image of the film in figure 7.26 showed half of it to be transparent, and the other half almost transparent. The red arrows point to the star-shaped configurations on the thick side of the film. The blue arrows point to the star-shaped configurations on the almost transparent side of the film

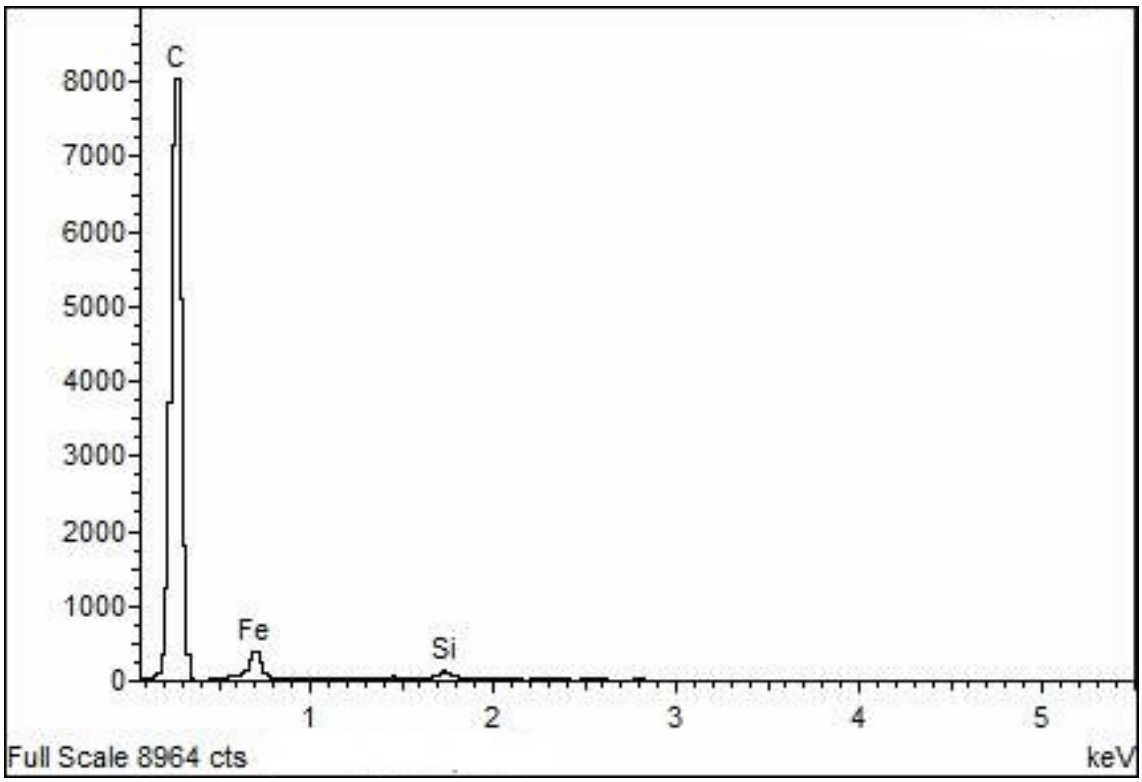


Figure 7.28: EDX analysis of the film in figure 7.27 showed it was graphitic

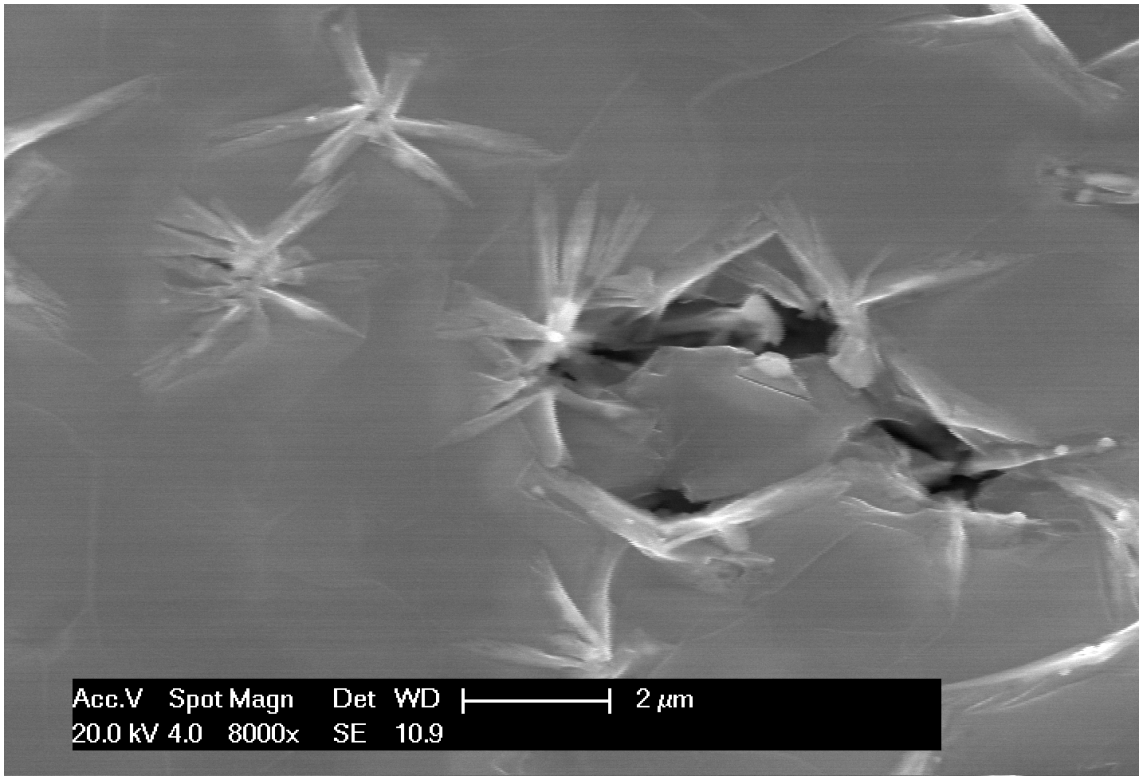


Figure 7.29: A SE image of the bright star-like configuration found on a graphite film

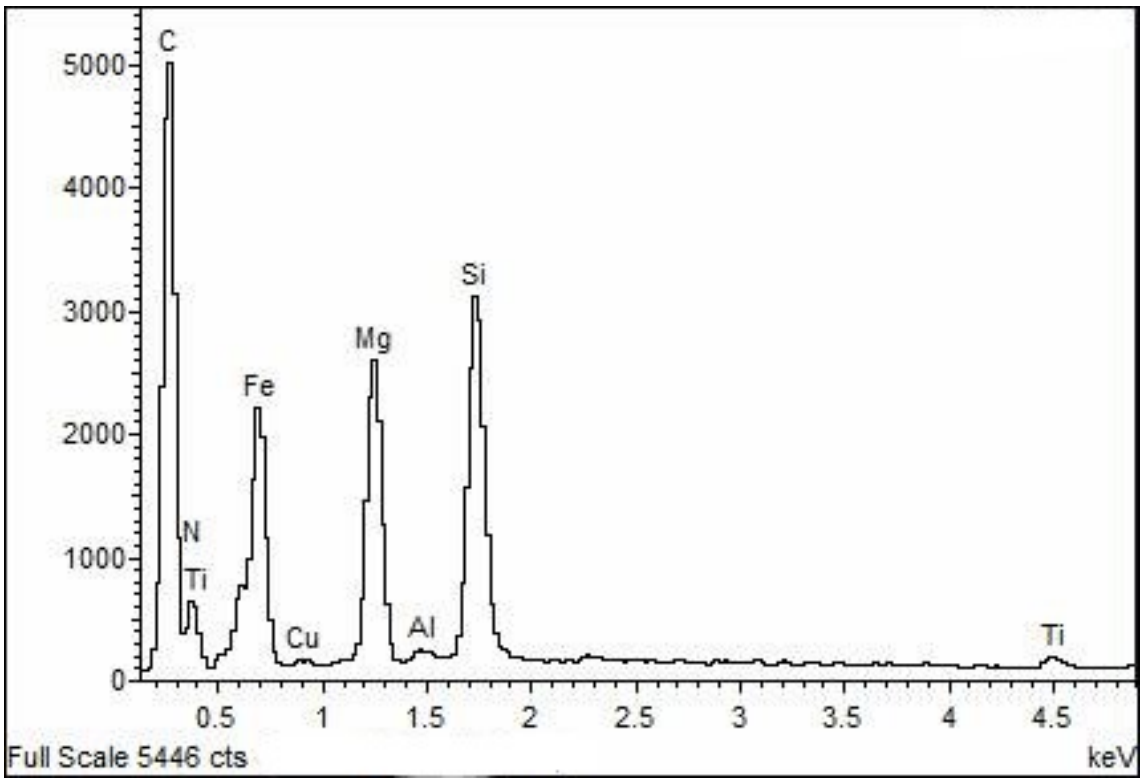


Figure 7.30: EDX spectrum of the stars configuration shown in figure 7.29

Element	Weight%	Atomic%
C	43.74	65.39
N	13.43	17.22
Mg	4.99	3.69
Al	0.12	0.08
Si	4.71	3.01
Ti	0.26	0.1
Fe	32.43	10.43
Cu	0.31	0.09
Total	100	•

Table 7.12: EDX chemical composition in weight% and atomic % of the stars configuration on the graphite film

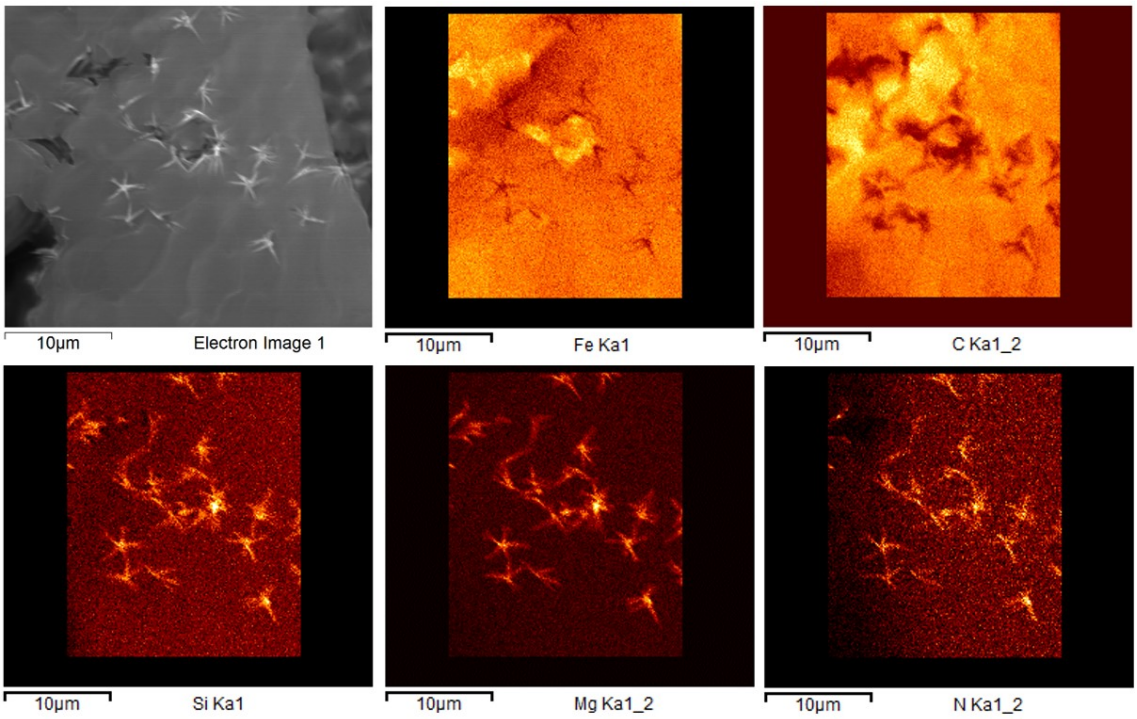


Figure 7.31: EDX element maps of the stars configuration

A different type of graphite films were also found on the fracture surfaces of CGI test bars. This type was found on top of micro-shrinkage areas, as in figure 7.32 and 7.33. It was thicker than the previous type, see figure 7.27, and had a different morphology which was distinctive with small equally spaced depressions (figure 7.34). The film appeared to hamper the solidification of the iron as can be seen from figures 7.34 and 7.33, where the dendrite arms are protruding through through the film.

•	Spectrum 1		Spectrum 2	
Element	Weight%	Atomic%	Weight%	Atomic%
C	85.43	94.76	36.67	72.84
Fe	11.53	2.75	61.8	26.4
Si	0.11	0.05	0.34	0.29
O	2.93	2.44	•	•
Mn	•	•	0.34	0.15
Cu	•	•	0.85	0.32
Total	100	•	100	•

Table 7.13: EDX chemical composition of the film and the dendrite arm shown in figure 7.34

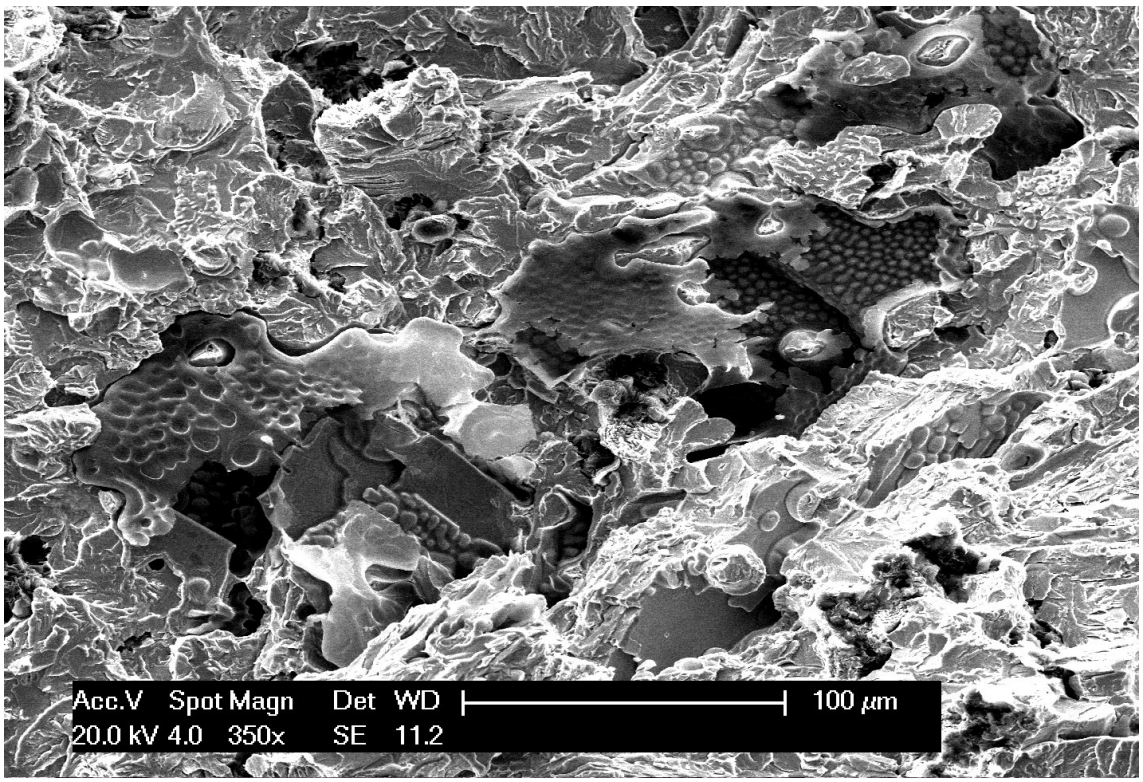


Figure 7.32: SE image of a of what looks like a micro-shrinkage defect with a graphite film

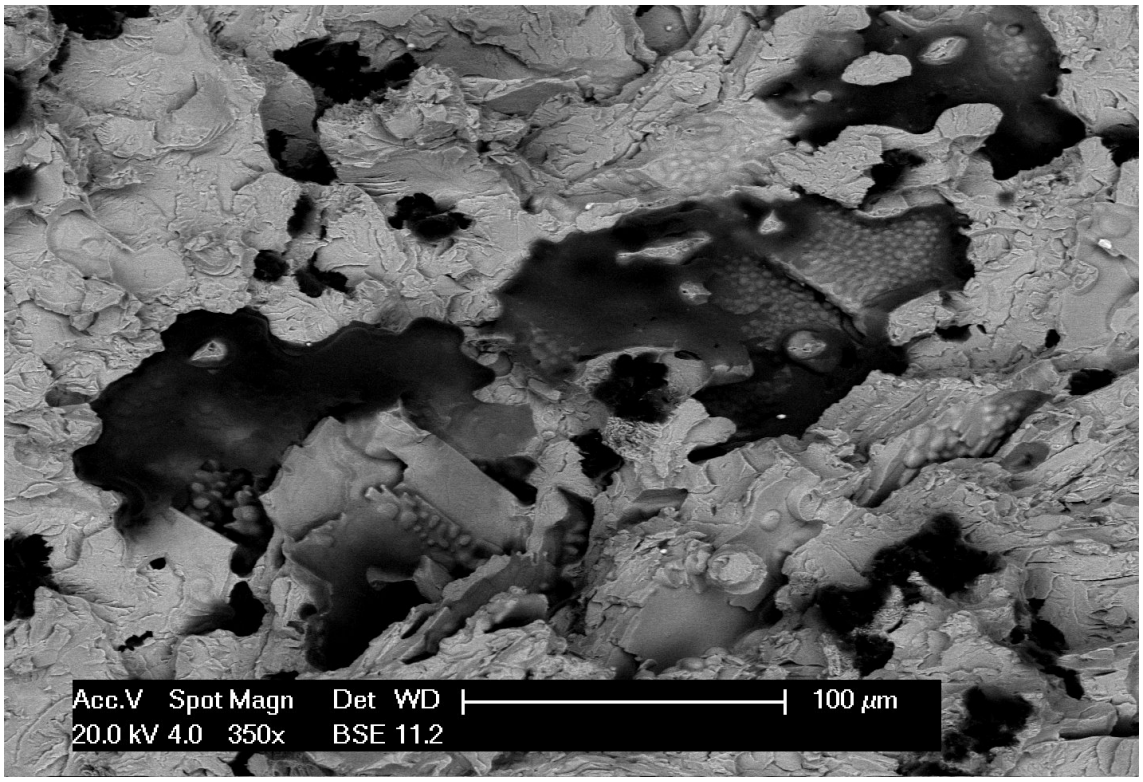


Figure 7.33: BSE image of a of graphite film covering the defect shown in figure 7.32

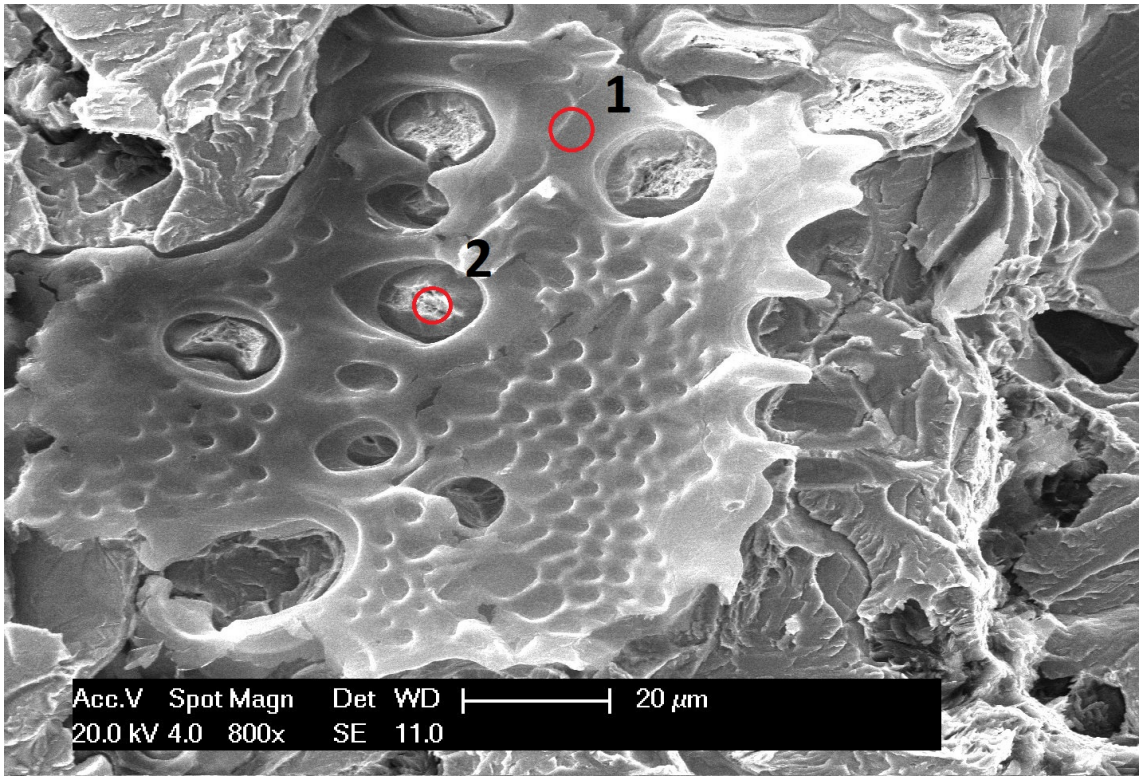


Figure 7.34: A close-up SE image of the defect shown in figure 7.32 showed a film covering part of the plates with the iron matrix impinge from it

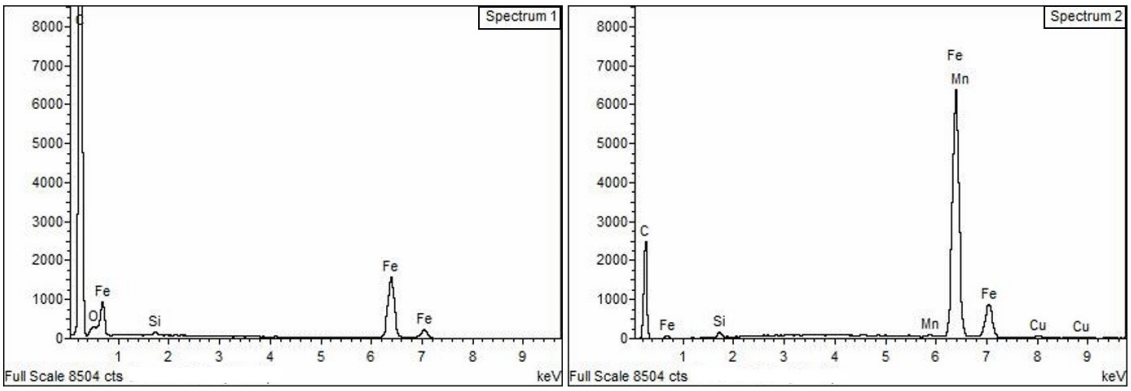


Figure 7.35: EDX spectrum of the film and the dendrite arm shown in figure 7.34

Novel folded graphite films were found scattered on the fracture surface of some CGI test bars (figure 7.36 and 7.37). They were nanometre in thickness, with about 1 µm of gap between the two folds (figure 7.38). The films were on both sides of the fracture surfaces, but vertically oriented, unlike what is usually seen in bifilm defects where their horizontal orientation can act as a crack. The film had the same rugged surface texture as seen in previous graphite films. The EDX spectrum of the film showed a large carbon peak and and a small oxygen peak; the iron and silicon peaks are products of the interaction of the electron beam with the substrate as it easily penetrated the light carbon film (figure 7.39 and table 7.14). The brightness of the graphite film seen in the SEM imaging was not due to electron charging, but due to SE edge brightness and the defect orientation towards the SE detector.

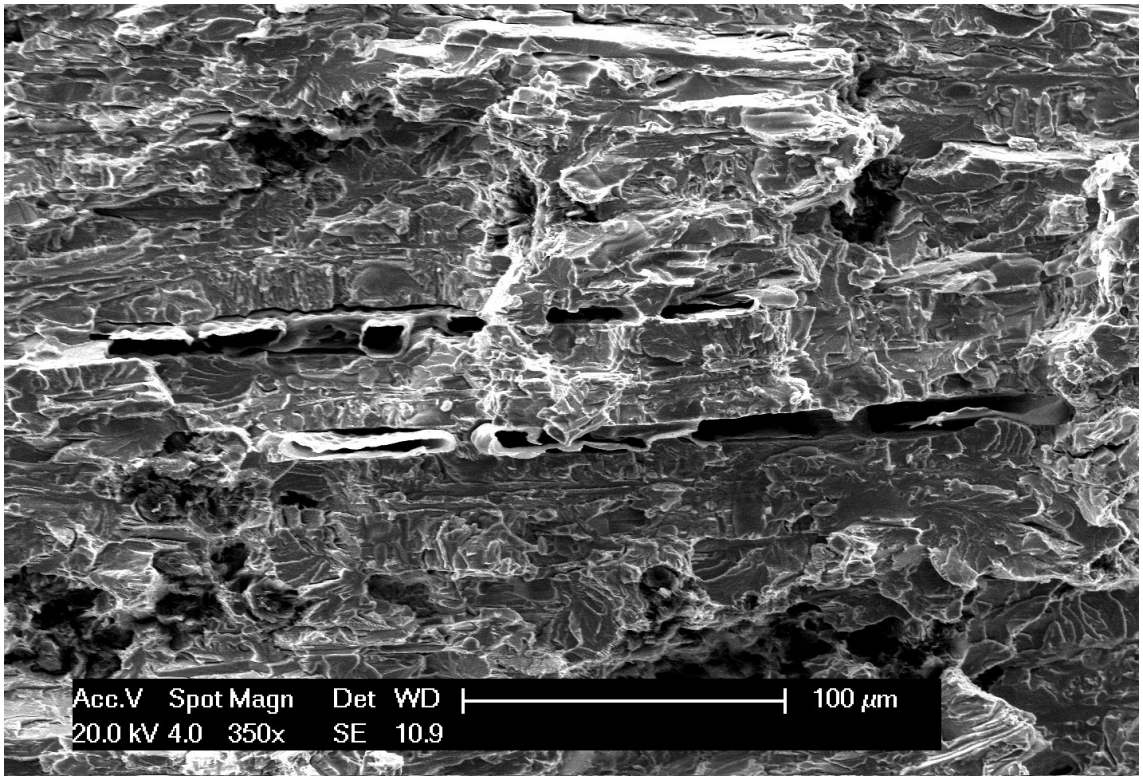


Figure 7.36: SE image of the scattered and folded graphite films

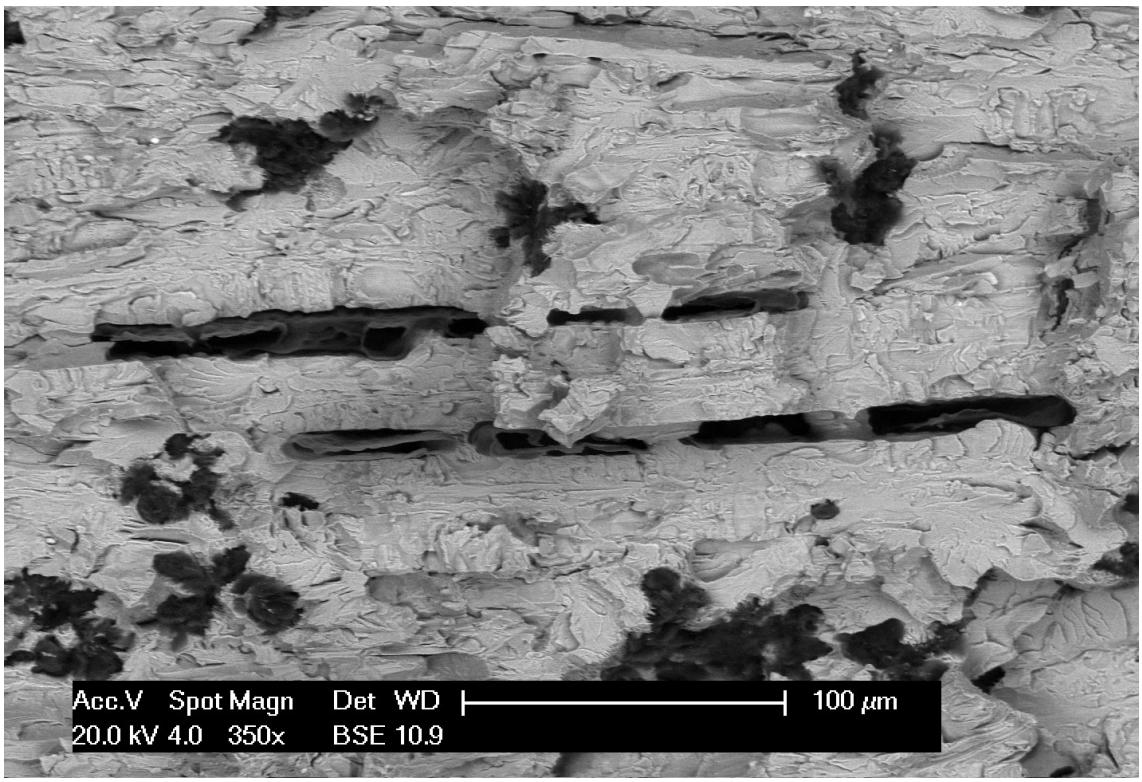


Figure 7.37: BSE image of the scattered and folded graphite films shown in figure 7.36

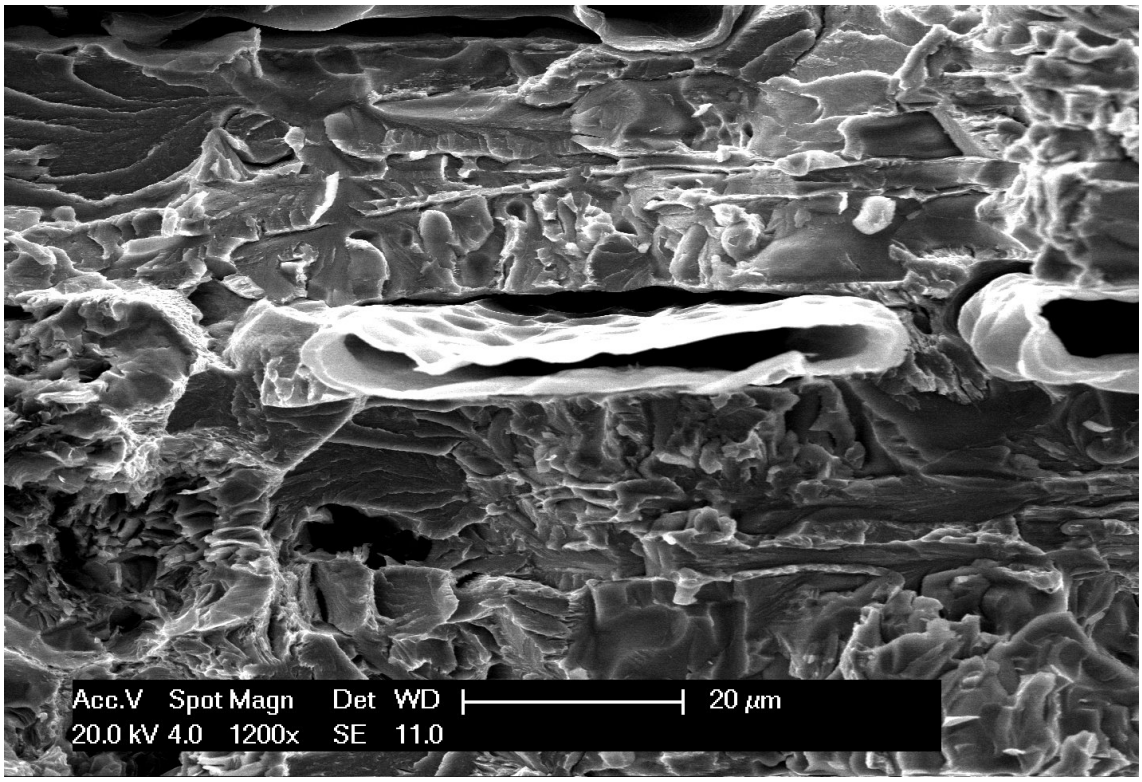


Figure 7.38: Close up SE image of folded graphite film revealing the empty space between its folds

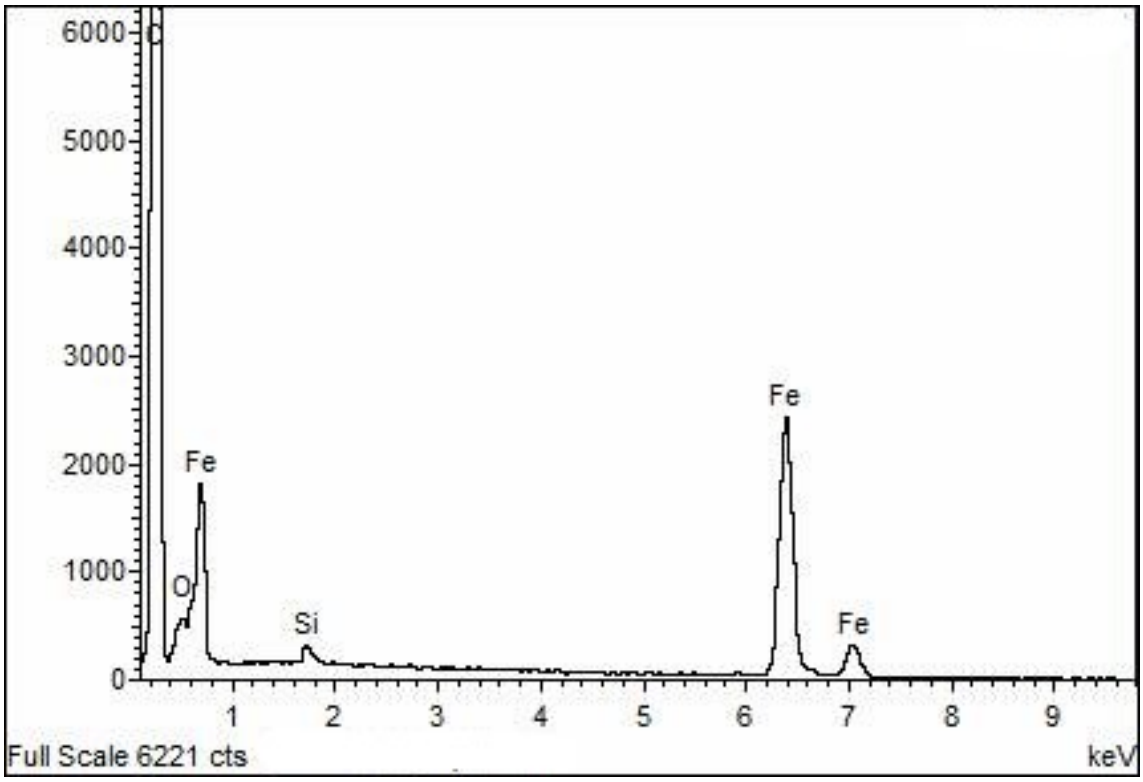


Figure 7.39: EDX spectrum of the folded graphite films

Element	Weight%	Atomic%
C	83.78	93.93
O	3.54	2.98
Si	0.16	0.08
Fe	12.52	3.02
Total	100	•

Table 7.14: EDX chemical composition of the folded graphite films

7.3 The relation between CGI defect size and tensile properties

To understand the effect of the defects on the mechanical properties of CGI castings, ImageJ, an image processing software, was used to measure the area of the defects found on testbar fracture surfaces by utilizing SE images. Subsequently, the measured area of the defect were plotted against the corresponding testbar UTS and %El., and the trend was revealed with linear regression, seen in figure 7.40 for the UTS and in figure 7.41 for the %El.; the summary of results is in table 7.15. For the UTS, the data points were mainly clustered close to the linear trend, and the linear regression had a negative slope indicating a reduction in UTS with the increase in the area of the defect. The overall effect of the defect area on %El. was the same as the UTS. The trend line had a similar negative slope thus the effect of the defects on the ductility was deleterious. The data points had a bigger deviation from the linear regression than in the case of UTS. Figure 7.42 is a BSE image of a defect-free CGI fracture surface, and it showed webs of vermicular graphite.

Area of the defect (mm^2)	UTS (MPa)	%El. (pct)
0.516	514	0.377
0.123	533	0.379
0.061	543	0.381
0.049	546	0.385
0.032	547	0.463
0.011	587	0.465
0.023	590	0.504
0.006	598	0.522
0.008	602	0.59

Table 7.15: The area of CGI defects with the equivalent testbar UTS and pct elongation

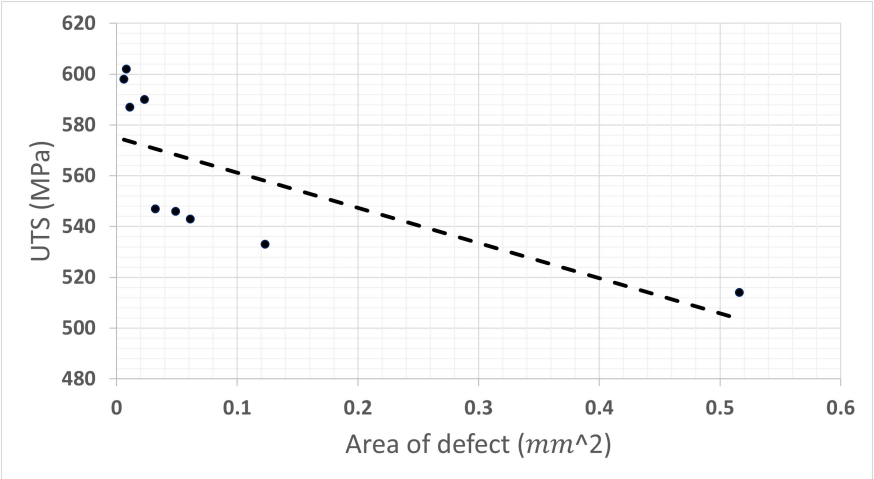


Figure 7.40: Graph between defect area vs UTS for CGI testbars

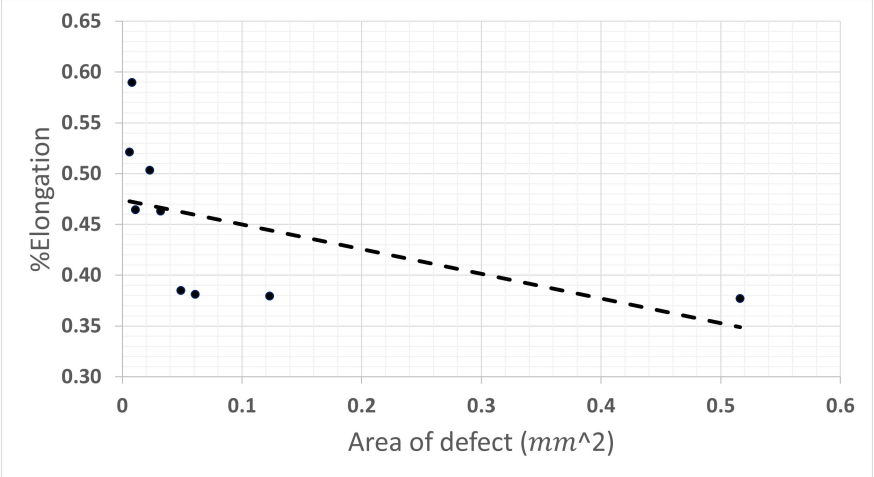


Figure 7.41: Graph between defect area vs %El. for CGI testbars

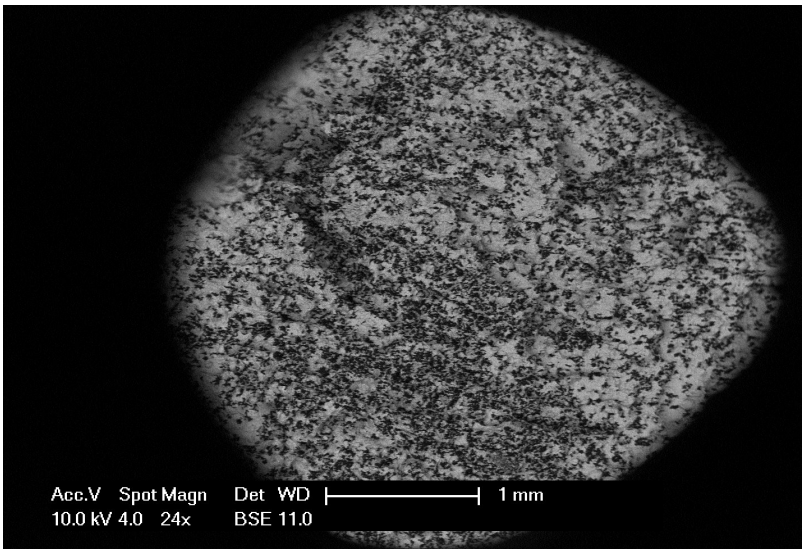


Figure 7.42: BSE image of a CGI fracture surface demonstrates the difficulty of finding small defects between the dense web of vermicular graphite

7.4 Summary

This section contained the results from the CGI testbars sand casting experiment and they were as follows;

1. CGI UTS data had negatively skewed histograms and fitted a 2-parameter Weibull distribution. As for CGI %El. data, it had positively skewed histograms and fitted a 3-parameter Weibull distribution.

2. CGI1 UTS data TFM m was 42, and QFM m was 53. CGI1 %El. data TFM m was 1.5, and QFM m was 2.7.

3. CGI2 UTS data VTFM m was 54, TFM m was 21, and QFM m was 26. For %El. data VTFM m was 5.3, TFM m was 2.2, and QFM m was 2.4.

4. SEM and EDX examination of CGI fracture surfaces revealed a defect that resembled a micro-shrinakge, was characterized by its plate topography, and was covered by thin graphite films.

5. There was an inverse correlation between the defect area and the UTS and %El. of CGI castings.

Chapter 8

Discussion

The discussion of the study is divided into four parts: 1) types of entrainment defects observed in cast irons, 2) the effect of surface turbulence on the tensile properties, reproducibility and reliability of cast irons, 3) the relationship between the defect size and cast irons tensile properties, and 4) the effect of mould design features on surface turbulence, and the potential of entrainment defects for flotation in cast irons.

8.1 Entrainment defects in cast irons

This section examines and discusses the different types of entrainment defects observed in cast irons, their chemical composition, structure, and formation process, utilizing results from optical, scanning and transmission electron microscopy. As well as highlighting the similarities between entrainment defects in cast irons the more intensively studied entrainment defects in aluminium alloys are included.

8.1.1 Entrainment defects in SGI

Entrained surface films are well recognized microstructural defects. In SGI, oxide and carbonaceous entrained surface films were observed. Initially they would form on the surface of liquid metal when it reacts with the atmosphere, then they are entrained into the casting as a result of surface turbulent filling of the mould. Sur-

face films are flexible and deformable, and tend to compress and bend by surface turbulence. The action of folding of surface films, dry side to dry side, will trap air or mould gases between the folds, and behave like a crack defect inside the final casting, categorized as an entrainment defect. As mentioned in the literature review (see section 2.1.2) there are several types of entrainment defects. The current study found evidence that SGI castings contained several types of entrainment defects which were: (a) bifilms (oxide and carbonaceous), (b) inflated bifilms, (c) bifilms entraining sand inclusions (d) bifilms entraining surface debris (slag), and (e) complex bifilms entraining multiple inclusions.

Oxide bifilms

Oxide bifilms were observed on the fracture surfaces of SGI testbars, mostly in testbars produced from moulds containing surface turbulence. Large oxide bifilms, visually recognizable (1 mm or more in length), were observed in testbars from TFM and VTFM castings. Optical images of the fracture surfaces, shown in figures 5.28 and 5.31, show the defects symmetrically on both sides of the fracture surfaces. This indicated the doubled over nature of SGI bifilm defects. Imaging of the defects showed no sign of atomic bonding between the two internal sides of the defects, even when folded inside the melt, as shown in figure 5.98. Thus the bifilms acted as pre-existing cracks that have been opened up during fracture, and played a role in the reduction of the mechanical properties of the castings. The internal crack features of the SGI bifilms were also observed after machining of the testbars revealed some bifilms preserved below the surface, as shown in figure 5.29.

The maximum length of the oxide bifilm defects observed in the casting, excluding fragmented bifilms, varied from a few microns (see figure 5.35), to 5 mm as shown in figure 5.51. Their size depended on the filling system used and the volume of surface turbulence in the mould. Large and chaotic bifilms, shown in figures 5.28, 5.103, 5.41, 5.48, 5.51 and 5.63, were detected in VTFM and TFM testbars. Their large size compared to other types of defects produced significant effects on

the mechanical properties of the casting. These defects were similar to the oxide bifilm crack-like defects found on the fracture surface of Al alloys testbar (28, 89, 94). SEM images showed that large oxide bifilms were caused by considerable surface turbulence that have occurred in the runner systems. The absence of large-folded oxide bifilms in QFM (filtered casting) shows the effects of filters on decreasing oxide bifilm defects in SGI. However the presence of oxide bifilm defects was observed seldomly in QFM (the only one is shown in figure 5.35), therefore there is evidence that oxide bifilms can still occur even with the use of filters. These results were consistent with the effect of filters on the reduction of bifilm defects in aluminium alloys (91, 93).

The EDX analysis of oxide bifilms (see figures 5.40a, 5.45b, 5.49, 5.52, 5.57, 5.62a and 5.65) showed Mg, O, Si, Al and C signals originating from the film surface. Due to the lack of the depth resolution of EDX analysis as its signals are emitted from an interaction volume which is mostly below the surface, the chemical composition of the film layer could not be resolved, but the oxygen content indicated the oxide nature of the bifilm. The FIB milling and lift out technique, coupled with STEM mapping (figures 5.96, 5.97, 5.98, 5.99 and 5.100) showed that MgO was the main oxide contributor in SGI bifilms. This finding was consistent with the expectation that MgO has the lowest free energy formation according to the Ellingham diagram (144) and hence is the most stable surface oxide expected in SGI. Furthermore, the results corroborate the findings in the literature that MgO is the cause of casting defects in SGI (76, 78, 79, 140). However these results have not previously been described as oxide bifilm defects. Though SEM images portrayed the bifilm to be thick, the thickness of the MgO film layer that was revealed by STEM was only 100 nm thick (shown in figures 5.99 and 5.100). The STEM analysis also explained the C signals seen in EDX spectra, as it revealed a graphite layer nucleated on the wetted surface of the bifilm. This layer could have given SGI oxide bifilms their thick and dark surface look (figures 5.55 and 5.38). This result could be evidence to support the idea of Campbell (162) that oxide bifilms play a part in the graphite

morphology of cast irons. For Si and Al, STEM mapping showed faint particles of Al and Si following the contours of the MgO film layer. Thus it is not clear if the Si and Al were parts of the structure of the oxide film or just precipitates. Evidence from EDX analysis, especially in the element maps shown in figures 5.49, 5.52 and 5.58, suggested that Si contributed to the chemical constituents, forming a magnesium silicate $MgSiO_3$ or Mg_2SiO_4 bifilm, which is also a stable film (142). The close-up EDX element map in figure 5.58 showed the same behaviour of graphite nucleation on the wetted surface of a magnesium silicate bifilm.

Nitrogen was only detected in one of the oxide bifilms observed on the fracture surfaces of SGI testbars (see figures 5.41, 5.42, 5.39, 5.44 and 5.45a). EDX element mapping showed that the area of nitrogen coincided with the same area of Mg and Al. This interesting finding shows that similar to aluminium oxide bifilms, as hypothesised by Nyahumwa et al. (94), and confirmed by multiple studies (95, 96, 97, 98, 102), the entrapped atmosphere in SGI bifilms might gradually be consumed by reacting with the surrounding liquid metal, when the majority of oxygen is depleted. Subsequently the liquid metal might react with the entrapped nitrogen forming either aluminium nitride (more stable) or magnesium nitride according to the following:

$$3Mg + N_2 \rightarrow Mg_3N_2 \tag{8.1}$$

$$2Al + N_2 \rightarrow AlN \tag{8.2}$$

Lustrous carbon bifilms

Lustrous carbon bifilms, (an example is shown in figures 5.32, 5.66 and 5.67), were observed only in the upper grip section of two testbars. Hence, the bifilms did not affect the tensile test results. EDX analysis, shown in figure 5.69 and table 5.23, showed carbon to be the main element in the bifilm, with only a small amount of oxygen, silicon and iron. Lustrous carbon films form from the breaking of carbona-

ceous gases at the hot surface of liquid iron, depositing a film of pyrolytic carbon (147), which will be laid down as a rigid mechanical barrier between the metal and the mould (67). Surface turbulence could then entrain the surface film as a crack-like defect. Figure 5.68 showed lustrous carbon bifilms rigid enough to block the growth of dendrites. Campbell and Naro (62) suggested that the film is deposited on a precursor thin oxide film. Thus, a combination of FeO and SiO_2 films as a precursor could explain the observed oxygen, silicon and iron peaks in the EDX spectra, and the EDX mapping of the film, shown in figures 5.70 and 5.71, and corroborate the assumption made by Campbell and Naro (62).

The location of the lustrous bifilms at the upper grip section of the testbars could possibly be explained by the following factors: the potential of entrainment defects flotation, as shown in the section 8.4.2, and the fast dendritic growth from the bottom of the mould, due to the higher rate of heat transfer from the base, pushing the defect upwards. The location of the bifilm could also indicate that it could have served as a barrier to interdendritic growth. Oxide bifilms in aluminium were observed to cause reduced feed-ability by becoming suspended between the α-aluminium dendrites (163). Figures 5.72 and 5.73, show fragmented lustrous carbon films on the dendrites of shrinkage pores found near the lustrous carbon bifilms. The fragments could have originated from a lustrous carbon bifilm that tore during shrinkage formation. As shrinkage reduces pressure in local regions and acts to unfurl bifilms, the reduced pressure would stretch the film over the dendrites and pull the bifilm halves into the interdendritic region, leaving only the fragments draped over the dendrites. The evidence and mechanism of bifilm inflation under reduced pressure has been observed in aluminium castings in the literature (16, 24, 31, 32).

Plate defects

Plate defects were observed symmetrically on both sides of the fracture surfaces, as shown in figures 5.33, and their formation could be attributed to oxide bifilms. The defect structure were only visible with SEM and they had a distinguishable visual

pattern as shown in figure 5.34. The plate defects were the source of failure in test-bars cast in VTFM and TFM, but they were less deleterious to the tensile properties than to bifilms. This could be due to the nature of their orientation relative to the direction of tensile loading. The plate defects had a vertical orientation, (shown in figures 5.74, 5.76, 5.82 and 5.83), with the direction of loading. The tensile force would act parallel to the plane of the defect and perpendicular to the crack front, and hence be converted to a shear force (sliding mode). As for bifilm defects (i.e. planar cracks) they had a horizontal orientation perpendicular to the direction of tensile loading, which would make it easier for opening (opening mode).

SEM and EDX results, as shown in figures 5.77, 5.78 and 5.79, and table 5.25, show evidence of what appears to be fragmented MgO bifilms on the defect surface. This suggested that the plates could have grown on thin oxide bifilms, nm thick, that were pushed ahead of growing dendrites, (unravelled and flattened). The gaps found between the plates were a sign that dendrites were unable to grow through the layer of air between the bifilms. The mechanism of fragmented bifilm formation due to entrained bifilms and growth of shrinkage was explained in section 8.1.1. In SGI, the contraction force of solidification would need to exceed the expansion generated by graphite precipitation to initiate shrinkage. The layered element map of plate defects, shown in figure 5.75, showed the area around the defect to be depleted from spheroidal graphite, which could have aided the formation of the defect. The vertical orientation of the defect could be possibly explained due to a combination of the higher rate of heat transfer from the base of the casting, and the anchoring of the bifilm to the mould wall. The grains growing vertically from the base would grow faster and further, vertically aligning the bifilms. Flotation could have played a part driving the bifilms to the mould wall and encouraging their vertical orientation.

Figures 5.80 and 5.81 show a graphite sphere found on the surface of the defect. According to previous studies (164, 165) the size and smooth surface of the graphite suggested it to be primary graphite that nucleated in the liquid. Its location on the bifilm indicated the possibility that the bifilm could have prevented it from

growing by blocking secondary crystallization. The same phenomena was reported by Stawarz and Dojka (85) in high alloyed cast iron.

Plate defects/fracture were also reported in SGI castings (166, 167). Such fractures were attributed to large and coarse dendrites, and aligned graphite nodules that were located in large planes alongside the dendrites. The study carried out by Gagne and Golle (166) reported that an essential feature of the defect was areas that contained non-uniformly distributed oxide inclusions high in Mg and Si. They also were puzzled by the formation of the dendritic nature of the plates and suggested that these form would require a restriction of growth in one direction. The observed inclusions and dendretic growth could both be explained by the bifilm theory. Entrained oxide bifilms could have served as a barrier to dendrite growth before being torn into fragments by the hydrostatic pressure. Moreover, an SEM image presented in the study, (figure 8.1), showed what appeared to be an area next to the dendrites of the plate defect covered by what seems to be a light film. Although no EDX analysis was carried over the film, the brightness of the film area could be explained by the charging of electrons on the non conducting film surface. Campbell (142) claimed that plate fracture and aligned graphite nodules in SGI are evidence of bifilm defects; especially if the iron was cast at a low temperature that allowed the surface film to be solid before entrainment. Thus, the results in this study further support the idea that plate defects in SGI are a result of entrainment of surface oxide films.

Inflated bifilms (Oxide bifilms and casting defects)

The surface film entrained in the bulk metal in a bifilm form due to surface turbulence could be responsible for the nucleation of shrinkage and gas pores. In this instance the entrainment defect would be designated as an inflated bifilm. SEM and EDX examination of shrinkage pores found in SGI2 samples, shown in figures 5.84 and 5.85, and table 5.26, show accumulations of fragments containing Mg and O, occurring between the dendrite arms of a shrinkage pore. The existence of the

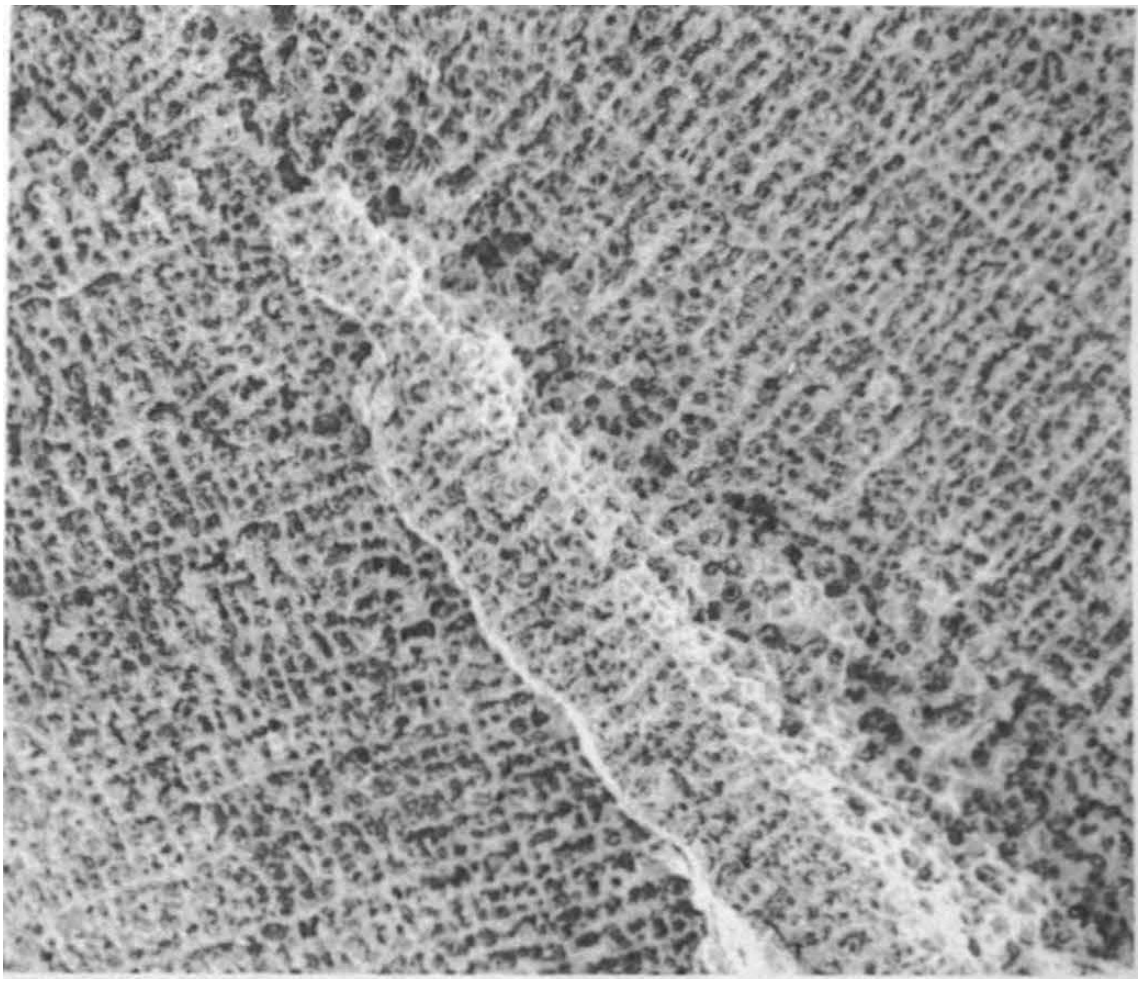


Figure 8.1: SE image of a recorded SGI plate defect (166), note the bright area that resembles a light film covering a part of the dendrites

fragments suggested that a MgO bifilm could be the nucleation site of the shrinkage pore. Shrinkage during solidification in an enclosed volume will act to open the bifilm. The bifilm will expand to preserve the loss in volume created during solidification contraction. The inflation process will unfold the bifilm until transferring it to a significant crack. As was seen and discussed with lustrous carbon bifilms and plate defects, the size of the shrinkage would probably result in an equivalent hydrostatic strain (negative pressure). The reduced pressure would pull the extended bifilm stretching it over the dendrites and eventually tearing it into fragments. Oxide bifilms torn into fragments due to shrinkage forces have been previously observed in aluminium castings (33, 168) and in magnesium castings (6, 39).

Unlike the opening of bifilms due to shrinkage growth, if the opening took place at an early stage of freezing, the defect would attempt to open not surrounded by

any dendrites but appear as a gas pore. The SEM analysis of what appeared to be gas pores, (examples shown in figures 5.86, 5.87), showed an inflated oxide bifilm symmetrically on both sides of the fracture surface. The EDX analysis result of the inflated bifilm showed that MgO (see figure 5.88 and table 5.27) was the main constituent of the bifilm. Further examination showed more evidence supporting the defect bifilm origin theory. BSE imaging of the bubble, shown in figure 5.87, revealed multiple small folds on the surface; more apparent on the top right corner of the image. Graphite particles were found aligned along the folds (see figure 5.89 and table 5.89). Their size (less than 1 µm) indicated that they were primary graphite that were trapped between the folds of the bifilm. Their subsequent growth would have been blocked by the surrounded oxide bifilm folds. Similar configurations were also observed in a different defect. Figures 5.94 and 5.95 show what appears to have been a bubble trying to push through multiple young MgO bifilms that have entrained small-aligned graphite spheres between their folds.

Nucleation of secondary phases were also observed on the surface of inflated bifilms. A circular graphite corrugated layer that was a part of the surface of the inflated bifilm (see figures 5.92 and 5.93, and table 5.30) showed that it was possible for the graphite nucleated on the wetted surface of a bifilm to grow as a film. The graphite volume expansion due to precipitation was accommodated by the free surface provided by the pore. CuSn intermetallics were another secondary phase particles that nucleated on the folds of the bifilms (see figures 5.90 and 5.91, and table 5.30). Cu and Sn were added to the melt to promote a pearlitic structure, increasing the tensile strength and hardness.

The observations discussed in this section are consistent with the behaviour of bifilms in aluminium alloys. Griffiths and Raiszadeh (96) suggested that oxide bifilms in Al could act as nucleation sites for gas porosity. Work carried out by Campbell (20, 169) and Tiryakioğlu (21) showed it was not possible for gas pores to nucleate homogeneously or heterogeneously in liquid aluminium. The origin of gas pores was attributed to the unfurling of bifilms due to gas precipitation. Thus it was

concluded, if surface turbulence were eliminated, the control of hydrogen content in the melt would be unnecessary. Moreover, the growth of different types of secondary phase particles and intermetallic compounds on the wetted surface of bifilms were a common feature of bifilms in Al alloys. $\alpha - Fe$, $\beta - Fe$ (23, 29, 36, 37), $TiAl_3$ (35), Sr rich phases (22, 170) and $CuAl_2$ (22) were found to precipitate on entrained bifilms.

Bifilm entraining sand inclusions

Moulding sand, an extrinsic inclusion, could be entrained into the liquid metal due to surface turbulence. SEM and EDX analysis of oxide bifilms found on the fracture surfaces of SGI testbars showed evidence of SGI bifilms entraining sand inclusions (see figures 5.53, 5.54 and 5.57). All the oxide bifilms containing sand inclusions were found in testbars produced with moulds containing surface turbulence (VTFM and TFM). Filling systems that had been poorly designed allowed air to accompany the liquid metal. This problem happens due to the over-sized cross-section area of the running system that remain unfilled with metal. As the VTFM and TFM design allowed significant surface turbulence, air can be seen mixing with the melt in the running systems for both mould designs, as shown in the real time X-ray radiography in figures 4.10 and 4.11. The air gaps would allow the liquid metal to ricochet back and forward in the channel causing mechanical impact to the mould walls and creating erosion. Liquid metal ricochets were observed at the end of the runner bar in TFM and the filter print in VTFM. The liquid metal then heats the mould surface and burns away the binder while bouncing back and fourth. The mechanical and heat erosion will peel sand grains from the mould wall. The oxidised surface of the liquid metal will then adhere to the sand grains. As the liquid surface folds over, the sand grains will be enfolded into the oxide bifilm. The entrainment of moulding sand by surface film in SGI is consistent with Fox and Campbell who observed oxide bifilms entraining sand inclusions in Al alloys (16).

Bifilm entraining surface debris

Solid slag, another extrinsic inclusion, could also be entrained into the liquid metal due to surface turbulence. SEM and EDX analysis of oxide bifilms found on the fracture surfaces of SGI testbars evidence of SGI bifilms entraining solid slag (see figures 5.60, 5.61, 5.62, and table 5.22). The slag inclusion was found between the folds of the oxide bifilm and composed of S and CaO, which are common constituents in SGI slag (75, 171). The inclusions could have originated from remnants of the dry slag formed on the surface of liquid SGI held in the ladle or the furnace; which would be removed before pouring using flux. The entrainment of extrinsic inclusions by surface films in SGI is consistent with the finding of Lofaj et. al (82) in SGI castings (the inclusions were debris), and with findings in aluminium castings by Emamy et al. (17) (the inclusions were alumina particles).

Complex bifilm entraining multiple inclusions

Finally, there was evidence that SGI bifilms could entrain multiple inclusions as an integral part of the defect. SEM and EDX analysis of an opened oxide bifilm on the fracture surface of an SGI testbar (see figures 5.63, 5.64 and 5.65) revealed an oxide bifilm entraining moulding sand, and several types of SGI slag (CaO, Al_2O_3 and K_2O) (75, 171). Although no visual evidence of such behaviour was found in the aluminium literature, this finding supports the assumption made by Campbell (4) that an entrainment defect could form from a surface film entrapping different inclusions. Moreover, the results are an example of the complexity that could be present in many bifilms that is entrained in bulk as pre-existing cracks.

Summary

In summary, the examined fracture surfaces of the testbars revealed evidence that SGI castings contained several types of entrainment defects. The defects were mostly in testbars cast with surface turbulence. The entrainment defect were mainly caused by oxide films (magnesia and magnesium silicate), but evidence of lustrous carbon

bifilms was also present. The magnesia bifilm was found to be nanometres in thickness and there was evidence showing that lustrous carbon films grew on a precursor oxide film. Moreover, entrainment defects in SGI showed similarities in behaviour to entrainment defects in aluminium: 1) it could form from several constituents, 2) it could act as nucleation sites for shrinkage and gas pores, 3) it could entrain different types of inclusions, 4) the wetted surface of the defect could act as a nucleation site for precipitates, and 5) the entrapped atmosphere in SGI bifilms might gradually be consumed by reaction with the surrounding liquid metal. Finally, evidence was presented that plate defects/fracture in SGI castings could form as a result of oxide bifilms.

8.1.2 Entrainment defects in LGI

As mentioned in the literature review (see section 2.7.1) when casting LGI in an oxidising environment, the falling temperature during pouring and mould filling will ensure the surface film will be liquid. If surface turbulence occurs and the liquid surface film becomes entrained in the metal it will spherodise into droplets. The droplets have a lower density than the melt, thus they will agglomerate and rapidly float out. Thus entrainment of surface films in LGI should not lead to entrainment defects which would act as pre-existing cracks that will reduce the mechanical properties, reproducibility and reliability of castings. The current study found no evidence of wide-spread entrainment defects on the fracture surface of LGI testbars cast in TFM and VTFM. Unlike the SGI results, the defects present in the LGI results were the only ones found on the fracture surface of LGI testbars. They were only present in samples cast with surface turbulent filling. Their features and formation mechanisms were indicative of their late arrival into the liquid metal. Thus, this study confirms the assumption derived in the literature. The types of entrainment defects observed in LGI were (a) bifilms (oxides), and (b) bubble trail defects.

Oxide bifilms

Oxide bifilms were observed on the fracture surfaces of LGI testbars. SEM images of the fracture surfaces, shown in figure 6.20, show the defects occur symmetrically on both sides of the fracture surfaces. This indicated the doubled over nature of LGI bifilm defects. Imaging of the defects showed no sign of atomic bonding between the two internal faces of the defects. Thus the bifilms acted as pre-existing cracks that had been opened up during fracture, and played a role in the reduction of the tensile properties of the testbar. The surface contained the distinctive folded feature of a bifilm defect (figure 6.21). SEM and EDX analysis (see figures 6.22 and 6.23c) showed a sand particle lodged between the bifilm and the iron matrix. The direction of the bifilm folds, shown in figure 6.20, coupled with the location of the sand grain, suggested that the bifilm could have originated from a mould blow that blew the sand grain inside the liquid. The comparison between the EDX analysis of the LGI matrix and bifilm (see figure 6.23a and 6.23b and table 6.9) suggested that the film is an iron silicate, possibly containing some manganese in solution. The same EDX analysis of the bifilm showed higher carbon content than the LGI matrix, which could indicate the nucleation of a carbon layer on the wetted surface of the bifilm, as was observed in SGI bifilms.

The sand inclusions presented in figures 6.12 and 6.13 provided additional evidence for the late arrival of bifilm defects in LGI. It showed that sand entrained during LGI filling due to the forces generated by surface turbulence, as explained in section 8.1.1, were not enveloped by oxide bifilms. This suggested that inclusions entrained during filling of LGI were not affected by surface films due to their liquid nature.

A chaotic form of oxide bifilms were observed on the fracture surface of LGI testbars that solidified white, (see figures 6.26, 6.27, 6.28 and 6.30a), due to casting with severe turbulent filling (the evidence is presented in figure 6.24), in a highly oxidising environment (the die was backfilled with pure oxygen), and quick solidification. The films were extensive, distorted, folded, contained creases, and to a

large extent were thin and translucent, which were all indicators of their formation environment. The quick solidification time retained the bifilms in their positions, eliminating any effect of flotation, and did not allow sufficient time for thickening. Although EDX analysis results (see figures 6.26, 6.27, 6.29, and tables 6.10 and 6.11) could not unambiguously specify the bifilm constituents due to the interaction with the substrate; some indications could be drawn. The bifilms in figures 6.26 and 6.28b could be either composed of iron silicate ($2FeO - SiO_2$) due to the Fe, Si and O content present in the EDX spectrum, or SiO_2 if the Fe signal originated from the substrate. The bifilm in figures 6.27 and 6.28a contained the same elements plus Mn, and this could indicate a $SiO_2 - FeO - MnO$ composition. This low temperature molten phase (1066°C) was reported in the literature (see section 2.7.1). The low melting temperature suggested that if the film was entrained in a relatively slowly solidifying environment, and due to the high surface energy and low viscosity of the liquid metal, the entrained liquid films should spheroidize in seconds and buoyancy will carry them to the surface. Finally, figures 6.30b and 6.31 show fragmented oxide bifilms draped over the dendrites of a shrinkage pore. The fragmentation of bifilm defects due to the growth of shrinkage porosity was discussed in details in section 8.1.1, and the results are in agreement with the literature (33, 168).

As mentioned in the literature review, the reduced pressure test (RPT) was developed to examine the quality of aluminium melts in relation to oxide bifilm content (16, 24, 30, 31, 32, 33). Under reduced pressure the compacted nature of the bifilm would inflate to a sphere observable with the unaided eye. Figure 6.32 show the result of LGI RPT, and it did not reveal any inflated bifilms; further supporting the findings from the testbar casting experiment. The only porosity found probably originated from the forces of the strong vacuum acting on the surface of the liquid metal. A layer of solidified metal were found on the surface of the vacuum chamber indicating a strong negative pressure, enough to dislodge some of the liquid out of the mould, as shown in figure 6.33.

Bubble trail defects

Bubble trail defects form when severe surface turbulence causes entrainment of large bubbles or core blows forcing bubbles into the melt causing surface turbulence. The bubbles will be caught between the bifilm folds but their greater buoyancy will overcome the resistance of the oxide film, and will float to the surface. Figure 6.34 shows what could be evidence of bubble trail defects in LGI. Similar to bubble trail defects observed in aluminium alloys (15), the defect comprised of a bubble head and its attached tail. The diameter of the bubble (10 mm) suggested a size large enough to allow it to float to the surface. The size of the bubble could also indicate it to have originated from a core blow (169). The wrinkled skin of the defect is a result of the oxide surface of the bubble collapsing when reaching the surface, (the mechanism is shown in figure 8.2). Although the conclusion is derived only from visual analysis of the defect, the finding is consistent with that of Campbell (72) who observed bubble trail defects in LGI. He attributed the source of the defects to core blows.

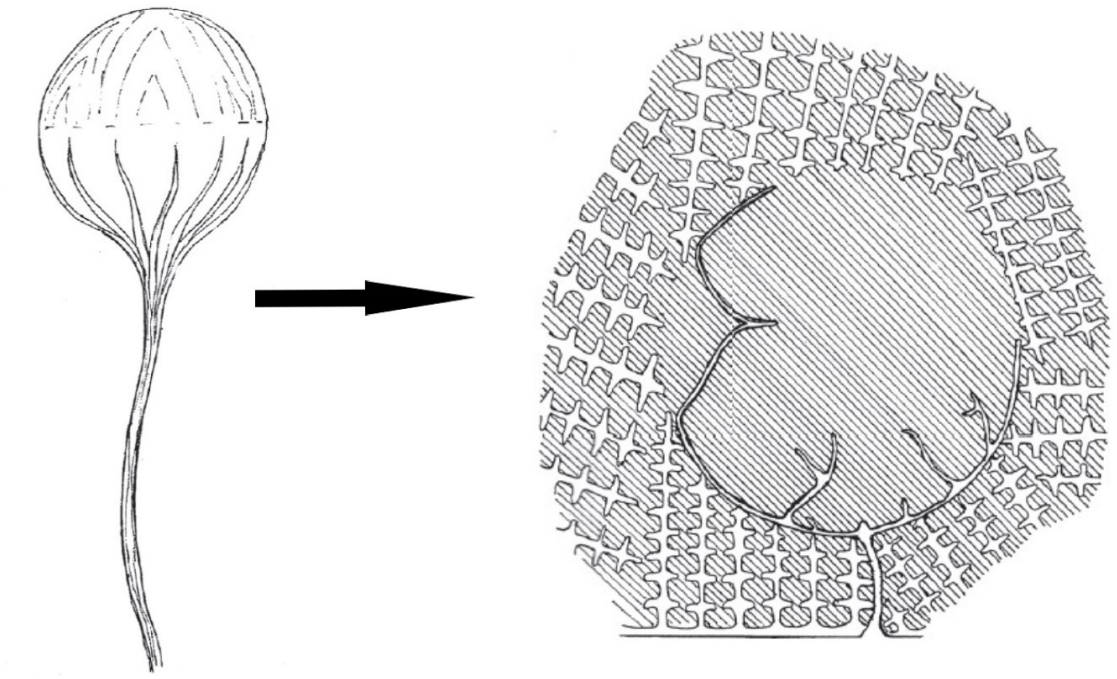


Figure 8.2: A schematic illustration showing the shape transformation from a bubble trail to a collapsed surface bubble

Smaller bubbles could also be entrained to form bubble trail defects. Figures 6.14 and 6.15 show a defect that resembled a symmetrical bubble head that was sectioned due to tensile fracture, as illustrated in figure 8.3. The top part contained folded films which could have developed after the bubble came to rest, and the tension created by the flotation to the bubble surface dissipated. Moreover, thin films were found on the surface of the bottom section, as shown in figure 6.16. EDX analysis of the two sides of the defect, (see figures 6.17, 6.8 and 6.19), showed symmetry in the chemical composition, but with smaller amounts of the film constituents on the bottom half due to the thinness of the film (tables 6.7 and 6.8). The EDX analysis suggested that the defect was composed mainly of a silica film (SiO_2), which would explain its glassy and translucent features, possibly with some parts composed of manganese silicate ($Mn - SiO_2$). Film defects containing the same elements were observed in LGI (72), and in high alloyed cast iron (86). Areas of Manganese Sulphide (MnS) were found nucleated on the surfaces of the defect. As previously mentioned, the growth of secondary phase particles on the wetted surface of entrainment defects is a common feature of entrainment defects in Al alloys (22, 23, 29, 35, 36, 37, 170), and were observed in SGI (see section 8.1.1).

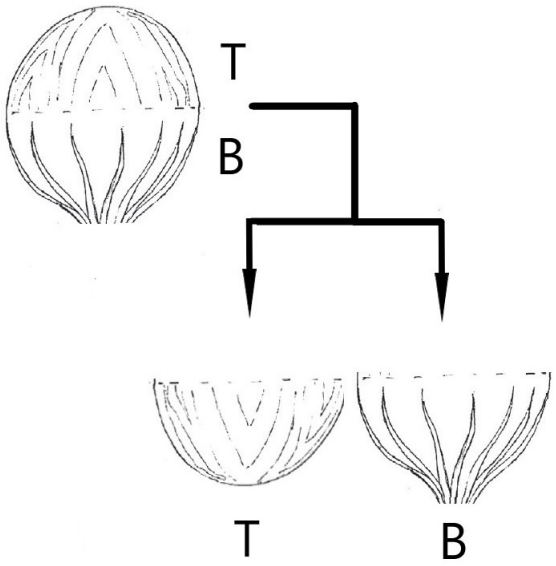


Figure 8.3: A schematic illustration showing head of the bubble splitting into two sections. The top section is in figure 6.15a, and the bottom section is in figure 6.15b

To conclude this section, the study found occasional evidence of entrainment defects in LGI. The defects were in samples cast with surface turbulence, or contained surface turbulent events. They were either oxide bifilms, or bubble trail defects. In agreement with the literature, it was evident that LGI castings could be insensitive to entrainment defect formation.

8.1.3 Entrainment defects in CGI

As was mentioned in the previous sections, surface films played an essential role in the formation of entrainment defects. In contrast to LGI, the chemical composition of CGI listed in table 3.4 had the same main elemental constituents as LGI (table 3.3), with only one difference, the small amount of Mg required to obtain the shape of the compacted graphite. By contrast to SGI, the residual Mg amount in CGI (average 0.01 wt.%) is one fifth of that of SGI (average 0.05 wt.%) (table 3.2). As stated in the literature, the small amount of Mg added to SGI for treatment stabilizes the surface film during mould filling, which could lead to the rise of entrainment defects. It is not clear if the even smaller amount of Mg in CGI would act in the same manner, or the surface film in CGI would be liquid during mould filling similar to LGI. The SEM and EDX analysis of the testbar fracture surfaces cast in TFM and VTFM point towards the latter, as, and unlike SGI, the results did not reveal any of the entrainment defects listed in section 2.1.2.

That being said, the current study found a novel defect on the fracture surfaces of the testbars with the lowest tensile properties in CGI2 TFM, (see figures 7.19, 7.20, 7.23, 7.26, 7.27, 7.32), that could be related to surface turbulence and entrainment defects. The biggest defect, in area, (see figures 7.21 and 7.22) was observed in the testbar with the lowest UTS in CGI1 (514 MPa), but the testbar was above the required standard for the grade (minimum UTS required = 450 MPa).

The defects had a distinctive protruding plates structure, which contained perturbations, and had a symmetrical location on both sides of the fracture surfaces (see figures 7.21 and 7.22 and 7.34). SE images (see figures 7.26, 7.27, 7.32), BSE

imaging (figure 7.24, and 7.34) and EDX analysis (see figures 7.25, 7.28 and 7.36) showed the defect surface was covered with a layer of graphite that was translucent in some locations. The defect could be explained as a form of microshrinkage, as the perturbations on the plates could be secondary dendrite arms, and the graphite film could be due to the diffusion of carbon into the free surface created by the shrinkage void. But the topography of microshrinkages recorded with SEM imaging in CGI literature (172, 173, 174, 175) did not reveal any plate structures. Thus, another possible explanation of the structure could be that the plates grew on, and stretched, a precursor young oxide bifilm (possibly nm in thickness, similar to SGI MgO bifilms shown in section 5.2.3), and each plate could represent a dendrite arm (the mechanism is described in section 2.1.3). Figures 7.29, 7.30 and 7.31, and table 7.12, show evidence of formations containing Mg, Si and N on a film located by the area of the plate defect. That raises the possibility of the presence of a $MgSiN_2$ film. In future investigations, it might be possible to use FIB milling, lift out techniques, and STEM element mapping on a vertical section taken from the plates to shed a light on such hypothesis.

Finally, some micron sized, thin, folded over, carbon films, with a vertical orientation, were observed on some fracture surfaces covering the surface of pores, as shown in figures 7.36, 7.37, 7.38 and 7.39. It seems possible that the films formed due to carbon diffusion through the iron to the surface of the pore. As the inside of the pore could not be observed due to the orientation of the defect, the pore origin (shrinkage or gas) could not be confirmed.

In summary, the study found no evidence of entrainment defects in CGI. A novel plate structured defect, that could be explained by bifilm theory, was found in a few testbars cast in TFM. On the whole, it was evident that CGI castings could be insensitive to entrainment defect formation.

8.2 The effect of surface turbulence on the tensile properties, reproducibility and reliability of cast irons

8.2.1 The effect of surface turbulence on the tensile properties, reproducibility and reliability of SGI

SGI statistical analysis was performed and presented in section 5.1. SGI1 and SGI3 castings belonged to the same grade (500/7), thus their discussion has been combined, as were their results. SGI3 castings were a different grade (700/2), and their results have been discussed separately.

Regarding SGI1 and SGI3, the results showed that the UTS values followed the 2-parameter Weibull distribution, and that with the increase in surface turbulence, samples had more scatter at the low end of the distribution. This was illustrated in the UTS histograms shown in Figures 5.2a, 5.2b, 5.2e, 5.2f and 5.2g. The Student's t-test performed showed that the comparable distributions had significantly different means (table 5.3). From the Weibull plot of SGI1 and SGI3 combined data, denoted SGI, and shown in figure 5.26, a Weibull modulus of 50 for QFM samples, compared with 26 for the TFM samples, and 16 for VTFM samples, indicating a higher degree of reproducibility and reliability in UTS values. It is the outlying lower UTS TFM and VTFM values that resulted in the lower Weibull moduli. The UTS means followed the same behaviour and decreased with the increase in surface turbulence, from 769 MPa for QFM, to 745 MPa for TFM, and to 739 MPa for VTFM. The UTS means showed a significantly lower sensitivity compared to the Weibull modulus. The improvement in mean UTS from VTFM to QFM was 4.7%, on the other hand, the Weibull modulus improved by 212.5 %. With regards to the %El. data, the values showed a similar trend as that of UTS values. The %El. values followed the 2-parameter Weibull distribution, and showed an increase in reproducibility and reliability, represented by the Weibull modulus, with the reduction in surface

turbulence, as shown in figure 5.27 and table 5.18. The values of the mean %El. also increased accordingly (table 5.17), showing less sensitivity to surface turbulence than the Weibull modulus.

In the case of SGI2, the UTS values showed a similar behaviour to SGI1 and SGI2. The UTS histograms showed a negatively skewed distribution, as shown in figures 5.2c and 5.2d. The TFM samples had more scatter at the lower end of the distribution compared with QFM. The values also followed the 2-parameter Weibull distribution (figure 5.21). However, unlike SGI3, the Student's t-test did not conclude that the distributions' means were significantly difference. Nevertheless, the Weibull distribution showed that the performance of the two sets of data were not equivalent. The Weibull modulus increased, although slightly as shown in table 5.22, with the reduction of surface turbulence, (TFM = 17 and QFM = 22), indicating a higher degree of reproducibility and reliability. With respect to %El. data, the QFM values did not follow a 2-parameter Weibull distribution, as shown in figure 5.22 and table 5.11, but when the distribution was applied, it showed an increase in the Weibull modulus from 2.6 for TFM to 3.8 for QFM. This was a larger degree of increase than exhibited in UTS values. On the other hand, when the comparison was carried out using the 3-parameter Weibull distribution, the relationship between the two data sets was inverted, and the Weibull modulus values were almost equal (TFM = 1.3 and QFM = 1.2). As the only different parameter between the two distributions was the threshold, this result showed the effect of the threshold value on the sensitivity of the Weibull modulus, and was consistent with that of Fok et al. (123) and Zahedi et al. (37) who observed the same behaviour in aluminium castings.

As shown in the previous paragraph, SGI2 data did not show significant improvement from TFM to QFM exhibited in the combined SGI1 and SGI3 data. This discrepancy could be attributed to some differences in casting routes. SGI1 and SGI3 were cast in a commercial foundry, while SGI2 was cast at the University of Birmingham. The casting processes were mostly similar: melting was done

in an induction furnace, melts were produced with the sandwich process, used the same nodulariser, inoculant material, sand grade, and resin type. However, there were two main differences. The first difference was the charge. The foundry charge was composed of 50% SGI returns/scrap, and 50% pig iron. For the casting in the University of Birmingham, the charge was 100% CGI returns. As discussed previously in section 8.1, oxide bifilms were more evident in SGI castings, thus SGI returns could be a source of old oxide bifilms. The second difference was the size of the ladle. The foundry used a preheated ladle with a capacity of 1000 kg for a 500 kg melt. For the casting in the University of Birmingham, the ladle used was much smaller, 30 kg capacity with 20 kg melt. The significantly smaller melt size dictated a faster treatment process to maintain the superheat, and reduce the fade effect. As a consequence, this could have resulted in more turbulent reactions in the moulds, reducing the quality of the castings from the two types of moulds, masking the effect of surface turbulence. Hence, the data must be interpreted with caution. Furthermore, as explained in the previous section, the differences between the melt routes were also evident from the defects observed on the fracture surfaces of the testbars.

To conclude, due to the tighter controls in the commercial foundry, and it being representative of industrial conditions, the combined results of SGI1 and SGI3 would accurately describe the effect of surface turbulence on the tensile properties, reproducibility and reliability of SGI casting. This showed the deleterious effect of surface turbulence on the tensile properties, reproducibility and reliability of SGI castings, with the reproducibility and reliability showing significant deterioration than mean tensile properties.

8.2.2 The effect of surface turbulence on the tensile properties, reproducibility and reliability of LGI

LGI statistical analysis was performed and presented in section 6.1. Although LGI1 and LGI2 testbars were from the same grade (220), their data was not combined in

the results, because, similar to SGI, LGI testbars were cast in both the University of Birmingham (for LGI1), and a commercial foundry (for LGI2). Subsequently, the tensile properties of LGI2 were considerably higher than LGI1.

LGI1 UTS data was the only case in the study to have positively skewed histograms, as shown in figures 6.2a and 6.2b, but the reason was unclear. The Mean UTS values were equal (TFM UTS = 258 MPa and QFM UTS = 257 MPa), and the Student's t-test did not conclude that the distributions' means were significantly difference. LGI1 UTS data followed the 3-parameter Weibull distribution, as shown in figure 6.8. The 3-parameter Weibull plot showed the two data sets had similar distributions and intersected, but the Weibull modulus increased from TFM to QFM by 67%. This increase might be due to the highest four UTS values in TFM increasing the scatter. Hence, it could be concluded from the LGI1 castings that the difference in surface turbulence between TFM and QFM did not cause a major effect on the tensile properties, but decreased the reproducibility and reliability.

Turning now to LGI2, the UTS data of TFM and QFM data showed similar trends to LGI1, but the addition of VTFM showed a notable negative effect of surface turbulence on the tensile properties, reproducibility and reliability of LGI castings. LGI2 UTS histograms were negatively skewed, as shown in figures 6.2c, 6.2d and 6.2e. Mean UTS values for TFM and QFM were, similar to LGI1, almost equal (TFM UTS = 429 MPa and QFM UTS = 433 MPa), and the Student's t-test did not conclude that the distributions' means were significantly difference. On the other hand, VTFM mean UTS was lower from the average UTS means of TFM and QFM, and was significantly different from TFM and QFM, as shown in tables 6.2 and 6.3; respectively. In contrast to LGI1, LGI2 UTS data followed a 2-parameter Weibull distribution, as shown in figure 6.8. Almost the same degree of increase in the Weibull modulus (53%) as LGI1 was observed, but unlike LGI1 it was from QFM to TFM, and was driven by the lowest 3 UTS values in QFM. Though the reason behind this rather contradictory result is not clear, the result might indicate that another factor other than surface turbulence between TFM and QFM could be

relevant. Nevertheless, the results still showed that surface turbulence between TFM and QFM did not cause a major effect on the tensile properties. Despite this, the increased surface turbulence in VTFM showed a notable deleterious effect on tensile properties (9% decrease), and a significant deleterious effect on the reproducibility and reliability (67% decrease), compared to the highest values of mean UTS and Weibull modulus, respectively. The fracture surface examination of VTFM testbars did not reveal any noticeable defects that could contribute to a such degree of degradation.

In summary, the results did not show clear evidence of the effect of surface turbulence on the tensile properties, reproducibility and reliability of LGI casting, but it showed an indication that at higher level of surface turbulence the mean UTS is slightly reduced, and the reproducibility and reliability is significantly reduced.

8.2.3 The effect of surface turbulence on the tensile properties, reproducibility and reliability of CGI

The CGI statistical analysis was performed and presented in section 7.1. CGI1 and CGI2 belonged to the same grade (400), and were cast in the same commercial foundry, thus their discussion was combined.

CGI UTS data had negatively skewed histograms (figure 7.2), which indicated their fit to the Weibull distribution, and the Student's t-test showed that the comparable distributions had significantly different means (table 7.3). TFM and QFM showed similar behaviour in CGI1 and CGI2. The UTS data 2-parameter Weibull probability plot, see figures 7.15 and 7.17, showed that the Weibull modulus increased from TFM to QFM by almost the same percentage, 26% in CGI1, and 24% in CGI2; which indicated an increase in the reproducibility and reliability. The Mean UTS values showed the same trend but only increased slightly by an average of 14 MPa or 2% (table 7.5). The greater degree of increase in the reproducibility and reliability is likely related to the TFM data containing more scatter at the low end of the distribution. Thus, it appeared from TFM and QFM UTS data

that the increase in surface turbulence leads to a reduction in the tensile properties, reproducibility and reliability.

Surprisingly, VTFM UTS data contradicted that conclusion. The VTFM UTS data showed a higher mean UTS 574 MPa (6% increase), and a significantly higher Weibull modulus 54 (108% increase), than QFM (mean UTS = 539 and m = 26). This unexpected result could not be attributed to any experimental error as CGI1 and CGI2 castings were done under tight controls and close observation. Moreover, the fracture surface examination did not reveal any noticeable defects that could contribute to the decrease in scatter from QFM to VTFM. This resultwas also in great contrast to the effect of VTFM in LGI and SGI. Note that the only difference between VTFM and QFM was the existence of a ceramic foam filter, which acted to reduce surface turbulence during filling. Thus, if only comparing the tensile data from CGI2 VTFM and CGI2 QFM, the findings of this study suggested that the filter had a deleterious effect on the quality of the castings. This outcome is contrary to previous studies carried out in aluminium (13, 91, 94) which have suggested that ceramic foam filters increase the mechanical properties, reproducibility and reliability of castings.

With regards to the %El. data, the data showed a similar trend as that of the UTS data. The %El. data followed the 3-parameter Weibull distribution, and showed an increase in reproducibility and reliability, with the reduction of surface turbulence from TFM to QFM, as shown in figures 7.16 and 7.18. The values of the mean %El. also increased accordingly (table 7.5), showing less sensitivity to surface turbulence than the Weibull modulus. VTFM produced higher reproducibility, reliability and %El. performance than QFM. The above arguments put forth for UTS results could also be applicable to the %El. performance of the testbars.

In summary, the results showed that up to a certain level of surface turbulence, there was a negative effect on the tensile properties, reproducibility and reliability of CGI castings. After that level, the results suggested that surface turbulence had a positive effect on tensile properties, reproducibility and reliability of CGI castings.

8.3 The relationship between cast iron tensile properties and defect size

This section discusses the results examining the relationship between defect size and tensile properties of SGI and CGI presented in section 5.3 and 7.3; respectively. With regards to LGI, the number of defects was not sufficient for analysis.

The deleterious effects of entrainment defects on tensile properties of SGI

SGI results showed that with an increase of entrainment defect area the tensile properties deteriorated, as shown in figures 5.101 and 5.102. Nerveless, the %El. data had a larger deviation from the linear regression than UTS data, and it contained two data points that appeared to defy the trend.

The larger deviation could be due to errors in the measurements of the extensometer. Since the testbar had a round geometry, the touch extensometer had only two point contact with the surface of the gauge length. Moreover, to eliminate any surface sites for crack propagation, and to ensure the testbar would only fail due to subsurface features, the gauge length was polished with fine grit paper during machining to remove any marks from the machining tool. Combining point touch extensometer, smooth gauge surface, and a relatively hard SGI led to some extensometer slipping, which could have affected the measurements. The measurement errors would translate into %El. data deviating from the linear regression.

With regards to the two data points that appeared to defy the trend, both had a considerable film area but not the expected low %El. value. This point highlights one of the main issues the author noticed while studying the behaviour of cast irons. Cast iron behaviour is complicated, not in any way easily predictable and in many instances cannot be explained with simple direct relations. This stems from the many variables that can affect the behaviour and properties of cast irons. Regarding this instance, even though the two film areas were lying in the middle of the ascending order of measured values (see table 5.32), the test bars had the highest

%El. values. The two test bars had approximately 4 times the area of the smallest film, but was 70% higher in %El, as shown in table 5.32. The examination of the fracture surface explained the contradictory behaviour. Figure 5.103 is the optical microscopy image of the fracture surface of one of the two testbars in question. It revealed an area around the defect, eight times the size of the bifilm, with a high density of spheroidal graphite. In SGI there is a direct positive correlation between nodule count (SG density) and ductility (%El.). Thus, even though the bifilm defect will reduce the ductility, the high density of SG will counter the negative effect of the bifilm and increase the ductility, resulting in positive net ductility.

Finally, SGI is chosen and used mainly for applications requiring a certain degree of ductility, and this is one of the main aspects in which it differs from LGI and CGI. In this regard, figure 5.102 showed that with a large defect area (approaching $7mm^2$) the ductility of SGI will be rendered almost negligible, making the alloy behaviour completely brittle. Thus, a small hidden defect in an SGI component could lead to a catastrophic failure.

The deleterious effect of plate defects on tensile properties of CGI

CGI results showed that with the increase in the plate defect area the tensile properties deteriorated, as shown in figures 7.40 and 7.41. Similar to SGI, the %El. data had a bigger deviation from the linear regression than the UTS data. In addition to the reasons mentioned for SGI, The measured %elongation values for CGI were all below 1%. The low measurements may have exacerbated the effect of extensometer slipping errors causing deviation from the linear trend.

The search for defects on CGI fracture surfaces was more challenging than SGI. When examining fracture surfaces for defects, the use of BSE imaging was preferred by the author. BSE imaging smoothed topographical features and removed edge brightness. This simplified the appearance of the fracture surface and helped the author identify any abnormal features. This was the case for SGI but with lesser extent for LGI and CGI. The difference in effectiveness was due to the morphology

of the graphite. CGI fracture surfaces were tightly packed with vermicular graphite, see figure 7.42, thus small sized defects were hard to notice. This could have affected the total measured defect area causing deviation from the linear trend. ‘

The previous section has shown that the tensile properties of SGI decreased with the increase of entrainment defect area. As for CGI, the tensile properties decreased with the increase of plate defect area.

8.4 Entrainment of surface films due to mould design features, and the potential of entrainment defect flotation

The section below is divided into two parts, part one will discuss the effect of the testbar cavity and empty filter print on entrainment volume, using the results arising from the analysis of mould filling using X-ray radiography, computer simulation and recorded ingate velocities. Part two will discuss the potential for entrainment defect flotation in cast iron considering the mould design, solidification behaviour, and the properties of liquid metal and entrainment defects.

8.4.1 Effect of mould design features on surface turbulence and entrainment of surface film in cast iron

Surface turbulence has been defined as the disturbance of the liquid surface such that the surface finds itself submerged and incoperated into the bulk of the metal, as an entrainment defect (oxide bifilm defect). Equations 2.3 and 2.4 (described in section 2.1.1) have been used to assess the critical ingate velocity associated with surface turbulence. Equation 2.4 gives the general critical ingate velocity, listed in figure 2.4, using only the physical properties of the liquid metal (surface tension and density), and not requiring a knowledge of the radius as in equation 2.3. Since the radius of the chancel could dictate the radius of the liquid (L), and affect the

surface tension (γ), the equation could be inapplicable in certain cases. For example, in thin wall castings a faster filling velocity would be needed to avert filling defects such as misruns and micro jetting. As for thicker wall castings, if the filling velocity is too high, the surface tension cannot contain the high liquid pressure due to the high filling velocity and entrainment of the surface film would occur. Thus, and according to equation 2.4, higher ingate velocities are tolerated in thin wall casting without causing surface turbulence and entrainment, as the liquid metal would be constrained by a thin wall or a small diameter testbar during metal flow.

With regard to the effect of the testbar cavity in the turbulently filled mould (TFM) and very (surface) turbulently-filled mould (VTFM) on the entrainment of surface film. In TFM, the ingate generated velocity (1.46 m/s), as calculated in section 4.2.1, was higher than the critical ingate velocity for iron (4) (0.45 m/s), which meant, according to equation 2.4, entrainment of the surface film was expected. This was observed and shown with real time X-ray radiography and computer modelling in figures 4.11i and 4.14, respectively. As for VTFM, the liquid metal fell into the empty filter print and generated continuous surface entrainment, as shown with real time X-ray radiography and computer modelling, in figures 4.10 and 4.13 respectively. With this in consideration, the diameter of the testbar cavities could play a role in damping the severity of surface entrainment. The diameter of the testbar cavities in the VTFM and TFM, shown in figures 3.6 and 3.7b, were 11 mm. These were 1 mm thicker than that what is considered to be thin wall castings (width = 10 mm). Thus the filling behaviour inside the testbar cavities was mostly quiescent, as shown by real time X-ray radiography in figure 4.11i for the TFM, and in figure 4.10h for the VTFM.

The reduction of ingate velocity effect, (i.e. surface turbulence) on the reproducibility and reliability of castings due to casting thickness was demonstrated in work done by Green (13) using a Weibull analysis approach to study the effect of filling on the UTS of 2L99 Al alloy castings. Testbars with 30 mm diameter cast in top-filled moulds produced unreliable castings with Weibull modulus of 12; however,

a value of 55 was achieved when the testbars were only 12 mm in diameter. The reduced testbar diameter would constrain the surface of the liquid metal, producing a reliable casting from surface turbulent (top-filled) running system with a high ingate velocity during filling.

Moving on now to consider the effect of the empty filter print in VTFM on the entrainment of surface film. The measured ingate velocity in the VTFM (0.12 m/s), as calculated in section 4.2.1, was less than the critical ingate velocity of iron (4) (0.45 m/s), which should indicate a tranquil fill with no entrainment of surface films. However, the large empty volume of the filter print connected to the downsprue exit, as shown in figure 3.7b, played a critical role in the entrainment of surface films. The narrow channel between the filter print and the runner bar constrained the flow of liquid metal, and reduced the out flow volume from the filter print; this allowed the liquid metal to dwell and build up a reservoir (figure 4.10e). The combination of the dwelling liquid metal reservoir and continuous plunging jet from the pouring basin increased the number of severe entrainment defects, as seen from X-ray radiography of the filter print in figure 4.10. The defects would then be carried in the bulk flow into the testbars and could cause a deterioration in the casting quality. This suggested that even though VTFM ingate velocity would not allow surface entrainment, the empty filter print would cause the mould to produce castings containg entrainment defects.

These observations are in agreement with those obtained by Reilly et al. (152) using computer modelling. The study modelled the formation of entrainment defects during the filling of two identical moulds, one with a filter, and one without. The result showed that the persistent plunging jet from the downsprue impinged on the fluid in the partially-filled filter print and created a continuous high volume of entrainment defects. This might be expected to result in the proportion of entrainment defects created in the runner bar being almost negligible compared to the proportion created in the filter print. The study of Reilly et al. (152) found that entrainment generated in the filter print was two thirds of the entrainment gener-

ated in the pouring basin. Lai et al. (153) used computer modelling to examine the effect of different casting stages on the severity of entrainment of surface films. The modelling relied on measuring the free surface area generated in each stage as an indicator of the volume of entrainment. The liquid metal fluid motion in the pouring basin was found to potentially generate 3.7 times the amount of surface film entrainment generated during filling with a high ingate velocity of 1.0 m/s. Combining the results from Lai et al. (153) with those from Reilly et al. (152), it can be assumed that the filter print in the VTFM generated entrainment volume 2.46 times the amount generated during filling with an ingate velocity of 1.0 m/s. The addition of this figure to the results from the X-ray radiography (figure 4.10e), and MAGMASOFT^{TM} simulation (figure 4.13a), and the fact that the ingate velocity of TFM was 1.46 m/s and QFM was 0.12 m/s, it is to be expected that VTFM would generate more amount of entrainment than the TFM, and subsequently mare than QFM.

This section has reviewed the features of moulds that may affect the amount of surface film entrainment generated during filling. It was found that the diameter of the testbars in TFM and VTFM could reduce the amount of entrainment. And due to the empty filter print in VTFM, evidence (152, 153) was found that supported the assumption that VTFM would generate the most mount of entrainment amount compared to TFM and QFM.

8.4.2 Entrainment defects flotation in cast irons

In addition to the mould features, the type of alloy could have an effect on the entrainment process; as some alloys could be more sensitive to entrainment defects, resulting in lower mechanical properties, while others could be insensitive. The sensitivity of an alloy to entrainment defects could be tied to the potential of the defect for flotation. The entrained surface films expected and observed in cast irons were discussed in the literature (section 2.2.2 and 2.7), and were found to be either carbonaceous defects (lustrous carbon), or oxides (MgO and SiO_2). Since

the defects are much lighter than iron, their potential for flotation is examined in this section.

Flotation of bifilms would not take place until the forces of bulk turbulence largly dissipate. Therefore, before calculating the flotation time, the liquid metal transition time from bulk turbulence to quiescence was examined. According to Flemings (154), and following equation 8.3, convection introduced by the momentum of pouring will dissipate after a period of time (t_e) due to the dissipation of local eddies of size l. Solidification would not have progressed far by this time. Turbulent eddies are characterized by the flow length scale (L), and can be estimated by equation 8.4 (155). Using equations 8.4 and 8.3, the calculated time for bulk turbulence conditions inside the testbar cavity to be dissipated (t_e) was equal to 0.584 s, as shown in table 8.1. After that period of time, the flow should be in a laminar condition, and the flotation times of the different types of bifilms can be calculated using Stokes Law.

According to Stokes Law, the terminal velocity of, and the time taken for, particles to float out of a liquid is proportional to the density difference between the liquid and the solid as described in equation 8.5 (156). Table 8.2 shows some calculated times of travel for the distance of vertical flotation from the bottom to the top of the testbar (100 mm), and horizontal flotation from the center of the testbar to the mould wall (5.5 mm). The values were calculated depending upon what assumptions were made about the age and size of the bifilm defects, as stated in the following sections.

Let us now consider the age. Only MgO bifilms were expected to have two populations, young and old, due to the stable nature of the oxide during remelting cast irons containing MgO, as was observed by Lai et al. (39). On the other hand, SiO_2 bifilms can not grow old. In the event of remelting cast irons containing a population of silicate bifilms, the liquid metal will reach temperatures where CO is preferentially formed, and any SiO_2 will be reduced into silicon and dissolved into the melt; with the oxygen combining with the carbon to form CO.

With regards to lustrous carbon films, they are initially 5 μm thick, but could grow to be approximately 10 μm thick (62). This further growth can happen when the film is trapped between the casting and mould, as shown in figure 2.47. Liu and Loper (157) observed lustrous carbon films up to 300 μm which consisted of stacks of thin films with a thickness around 10 μm. As the growth mechanism of lustrous carbon films depends on their location trapped between the casting and the mould, thicker lustrous carbon films do not have the potential to form entrainment defects, unless a disruption to the mould metal interface occurs (e.g. core blows). Similar to silicate bifilms, when lustrous carbon bifilms are reintroduced into the melt, they will diffuse into the iron and disappear. Thus, they cannot be introduced into new castings as old bifilms.

Turning now to the size of the entrained bifilms, for simplicity, the bifilm size was assumed to be a disk shape with a diameter of 2.5 mm. Bifilms are more likely to have a higher surface area-to-volume ratio than a spherical shape. I.e. to be more lens-shaped and could even be an extensive film. The effect of variations in the aspect ratio of the bifilms on their flotation rate is difficult to take into account. Thus, as a guide, Stokes Law, valid for spherical particles, has been used. Young oxide bifilm defect thickness was assumed to be 1 μm (3), which meant the total thickness of the oxide layer was 2 μm. As previously stated, lustrous carbon film thickness is expected to be 5 μm (62), and that meant the thickness of film layer in the defect is 10 μm. The old magnesia bifilm film layer was assumed to have the same thickness (10 μm) (142). The nature of entrainment defects is that they contain an interior atmosphere. Therefore the thickness of air layer had to be taken in consideration. For young bifilms the entrapped air layer was assumed to be 2 μm due to the limited consumption of entrained air compared to older oxide bifilms (94). Hence for old bifilms, an entrapped air layer of 1 μm was considered reasonable (3). The values of the density and dynamic viscosity of cast iron are shown in table 8.4. The lustrous carbon density stated in table 8.3 is represented by pyrolytic graphite density (147). Finally, by utilizing Stokes Law in equation 8.5, the predicted floating

terminal velocity of lustrous carbon, SiO_2 and MgO bifilms were calculated, and the vertical and horizontal flotation times were obtained as shown in table 8.2.

From the combined result of $t_e \backsimeq 0.6$ s, and the maximum predicted floating terminal velocity for the different types of cast iron bifilm defects $\backsimeq 0.6$ s, it could be assumed that entrained bifilms would have sufficient time either to float out, or to adhere to the mould wall, before solidification occurs. Hence, the flotation of bifilms could be a factor in reducing the deleterious effect of entrainment defects in cast irons. The same phenomena was recorded by Halvaee (158) in a study which showed that a 20 mm thick plate casting of Cu-10Al alloy appeared to be remarkably resistant to entrained oxide bifilms associated with an increased critical ingate velocity, showing bend test properties unaffected by ingate velocities. In this case, there would be a large density difference between the oxide film (3960 kg/m^3), (and an oxide film defect containing air would have a lower density than this value), and the Cu-Al melt (6590 kg/m^3), and therefore the buoyancy of the oxide bifilms may cause them to float out of the liquid metal, thus effectively migrating out of the center of the casting and perhaps sticking to the mould wall. Moreover, the effect of flotation of oxide bifilms were also observed in lighter alloys that contained bifilm defects of a greater density than the melt. In aluminium alloys, improved casting quality was attributed to flotation of bifilms when the melt was held quiescently in a crucible under atmospheric pressure (159). The same effect was also observed with short solidification times in thin wall aluminium sand castings. Chen et al. (160) found that alumina and spinel (Al_2MgO_4) bifilms were concentrated in the top side of horizontal testbars with a height of only 10 mm. The high concentration of bifilms, which was attributed to flotation before solidification, reduced the ultimate bending strength of the upper side of the testbars.

In summary, the analysis and the evidence from the literature presented in this section suggested that cast irons could be less sensitive to entrainment defects due to defect flotation.

$$t_e \backsimeq \frac{l^2}{\nu} \tag{8.3}$$

t_e: time till dissipation of local eddies, l: length of local eddies, and ν: kinematic viscosity

$$l = 0.07L \text{ (L is the characteristic length)} \tag{8.4}$$

$$V = 2gr^2(d_l - d_p)/9\mu \tag{8.5}$$

V: terminal velocity, g: acceleration due to gravity, r: particle radius, d_l: liquid density, d_p: particle density, and μ: fluid viscosity

Characteristic length (L) for the testbar (m)	0.011
eddies length (l) (m)	0.00077
t_e for testbar (s)	0.584

Table 8.1: Dissipation time of turbulent eddies

Entrainment defect type	Lustrous Carbon	SiO_2	MgO	
Assumed conditions	Young	Young	Old	Young
Diameter of defects (mm) shape assumed to be a disk	2.5	2.5	2.5	2.5
Thickness of film layer (μm)	10 (62)	1 (3)	10 (142)	1 (142)
Thickness of air layer (μm) (94)	2	2	1	2
Density of entrained defect (d_p) (kg/m^3)	1816	884	3254	1194
Predicted floating terminal velocity (m/s)	2.47	2.93	1.77	2.78
Distance	Flotation time (s)			
For distance of 100 mm (vertical travel)	0.04	0.034	0.056	0.036
For distance of 5.5 mm (horizontal travel)	0.002	0.0019	0.0031	0.002

Table 8.2: Estimated density and flotation times of entrained bifilms for various assumptions concerning the bifilm thickness and the volume of the entrained air

Material	Density (kg/m^3)
Lustrous carbon	2180 (147)
SiO_2	2650 (161)
MgO	3580 (161)
Air	1.22
Cast iron (d_l)	6900 (74)

Table 8.3: Density values

Cast iron dynamic viscosity ($N.s/m^2$)	0.007 (74)
Cast iron kinematic viscosity (m^2/s)	$1.01 * 10^{-6}$
Acceleration due to gravity (m/s)	9.81

Table 8.4: Properties employed

Chapter 9

Conclusions

This study set out to examine the effect of surface turbulent filling on the tensile properties, reproducibility and reliability of cast irons, focussing on the formation of entrainment defects, as follows;

9.1 Cast iron alloys and mould designs

1. Weibull statistics were found to accurately describe the distributions of tensile properties of SGI, LGI and CGI alloys made with VTFM, TFM, and QFM running system designs.

2. It was found that the relatively small diameter (11 mm) of the testbars in TFM and VTFM could reduce the volume of surface entrainment during filling. Additionally, an empty filter print in VTFM would generate higher volumes of entrainment defect than in a TFM runner bar.

3. Analysis of entrainment defects, their geometry and density, and cast iron density and viscosity suggested that cast irons could be less sensitive to entrainment defects due to increased defect flotation.

9.2 Spheroidal graphite iron

1. The use of surface turbulent mould filling methods when casting SGI alloys can result in premature failure of castings. Alternatively, high integrity castings can be achieved using quiescent filling techniques.

2. Tensile test results showed that surface turbulent filling had a deleterious effect on the tensile properties, reproducibility and reliability of SGI testbars. Regarding UTS, QFM had a mean UTS = 769 MPa, 3% higher than TFM (745 MPa), and 5% higher than VTFM (734 MPa). QFM UTS Weibull modulus (m = 50) was 92% higher than TFM (m = 26) and 212% higher than VTFM (m = 16) . With regards to %El., QFM had a mean %El. = 3.5, 6% higher than TFM (%El. = 3.3), and 30% higher than VTFM (%El. = 2.7). QFM %El. Weibull modulus (m = 6.7) was 63% higher than TFM (m = 4.1) and 131% higher than VTFM (m = 2.9).

3. The samples with the lowest tensile properties were found to contain film defects. Their symmetrical appearance, on either side of the fracture surface, showed them to have originated from the entrainment of surface film (oxide or carbonaceous) that have folded onto each other, but remained unbounded to form an entrainment defect.

4. Entrainment defects found in SGI were of the following types:

   (a) Bifilms (either magnesia, magnesium silicate, or lustrous carbon)

   (b) Inflated bifilms

   (c) Bifilms entraining inclusions, (either sand, slag or multiple inclusion types)

5. STEM element mapping of magnesia bifilm revealed it had a thickness $\backsimeq$ 100 nm.

6. The results suggested that entrainment defects in SGI behaved in a similar manner to entrainment defects in aluminium in the following respects:

(a) They could act as nucleation sites for shrinkage and gas pores.

(b) Their wetted surfaces could act as nucleation sites for precipitates, (C and CuSn).

(c) Nitrogen detected on the surface of an SGI bifilm showed that the entrapped atmosphere in SGI bifilms could, similarly, gradually be consumed by reaction with the surrounding liquid metal.

7. Fragmented oxide films found on plate defect/fracture surfaces in SGI strongly suggested that SGI plate defects/fractures were attributable to oxide bifilms.

8. There was an inverse correlation between the entrainment defect area and the tensile properties of SGI castings. It was found that with an increase of entrainment defect area the UTS and %El. were decreased.

9.3 Lamellar graphite iron

1. Tensile test results of TFM and QFM testbars showed mixed evidence of the effect of surface turbulence on the tensile properties, reproducibility and reliability of LGI castings. Nevertheless, VTFM testbars showed an indication that a higher level of surface turbulence would negatively impact the reproducibility, reliability and the tensile properties of LGI castings. VTFM testbars compared to QFM/TFM testbars had on average 8% lower mean UTS (VTFM mean UTS = 396 MPa, and QFM/TFM mean UTS = 431 MPa), and 60% lower Weibull modulus (VTFM m =16 and QFM/TFM m = 41).

2. The study found no evidence that entrainment defects were the cause of the deterioration in the mean UTS and Weibull modulus of VTFM compared to QFM.

3. Evidence of entrainment defects were seldomly found in LGI castings, and SEM/EDX analysis suggested they were:

(a) Oxide bifilms (either SiO_2, $2FeO - SiO_2$, or $SiO_2 - FeO - MnO$)

(b) Bubble trail defects

4. Finally, and in agreement with the literature, this study suggested that entrainment defects should not be a cause of concern in LGI castings, unless they form in the late stages of filling, because of the liquid nature of LGI surface films.

9.4 Compacted graphite iron

1. Tensile test results showed mixed evidence of the effect of surface turbulence on the tensile properties, reproducibility and reliability of CGI castings. The tensile properties, reproducibility and reliability increased with a decrease of surface turbulence from TFM to QFM. On average, the mean UTS increased by 3%, and the Weibull modulus increased by 26%. However, VTFM produced better tensile properties, reproducibility and reliability than QFM. The mean UTS increased by 6% (from 539 MPa to 574 MPa) and the Weibull modulus increased by 108% (from 26 to 54).

2. This study found no evidence of entrainment defects in CGI.

3. Novel defects, with plate structures that resemble a form of microshrinkage, and that could be explained by bifilm theory, were observed on the fracture surfaces of the testbars with the lowest tensile properties.

4. There was an inverse correlation between plate defect area and the tensile properties of CGI castings. It was found that with the increase in plate defect area the UTS and %El. decreased.

Chapter 10

Future Work

1. Surface turbulence filling and entrainment defects were found to negatively influence the tensile properties, reproducibility and reliability of SGI castings. A natural progression of this work is to analyse the effect of surface turbulence on the fatigue properties.

2. The evidence suggested that the deleterious effect of VTFM on LGI casting was not caused by entrainment defects. Further investigation into the reason could reveal different negative outcomes of surface turbulence filling other than the formation of entrainment defects.

3. In terms of CGI castings, the VTFM produced better quality castings than QFM. Further studies need to be carried out in order to validate the outcome, and to examine more closely the link between severe surface turbulence and the microstructure of CGI castings. As the only difference between VTFM an QFM was the ceramic foam filter, further research should be undertaken to explore how filters affect CGI castings. The outcome from both investigations will be a benefit to automotive foundries.

4. In regards to the novel plate defects in CGI, further work using FIB milling, lift out technique, and a STEM element mapping on a vertical section taken from the plates is required to determine whether the plates grew on a stretched bifilm substrate.

5. With regards to the reduced pressure test, it was clear that the LGI sample did not contain inflated bifilms. A further study could apply the same test to CGI and SGI castings, to examine the potential for entrainment defect formation. Subsequently, the test could be utilized to measure melt quality, especially for SGI.

Bibliography

[1] Report MCS. Census of World Casting Production. In: Modern Casting. The American Foundry Society; 2020. p. 28–30.

[2] Campbell J. The consolidation of metals: the origin of bifilms. Journal of Materials Science. 2016 1;51:96–106.

[3] Campbell J. Castings. Elsevier; 2003.

[4] Campbell J. Entrainment. In: Complete Casting Handbook. Elsevier; 2015. p. 17–90.

[5] Runyoro J, Boutorabi SMA, Campbell J. Critical Gate Velocities for Film-Forming Casting Alloys: A Basis for Process Specification. AFS Transactions. 1992;100:225–234.

[6] Lai NW. Critical Ingate Velocity in Mg and Al alloy [PhD thesis]. School of Metallurgy and Materials University of Birmingham; 2004.

[7] Xiao Z, Peng Y, Liu C. Modelling study of the entrapment phenomena at the slag-metal interface in the gas-stirred ladle. Chinese Journal of Metal Science and Technology. 1987;3(4):187–193.

[8] Yin J, Guo S, Ersson M, Jönsson PG. An Experimental and Numerical Study of the Free Surface in an Uphill Teeming Ingot Casting Process. Steel Research International. 2020 6;91.

[9] Birch J. Computerized properties data for zinc casting alloys. Die Casting Engineer. 1995;39(3).

[10] Divandari M, Campbell J. A new technique for the study of aluminum oxide films. Aluminum Trans. 2000;2(2):233–238.

[11] Campbell J. The Melt. In: Complete Casting Handbook. Elsevier; 2015. p. 3–15.

[12] Divandari M, Campbell J. Oxide film characteristics of Al–7Si–Mg alloy in dynamic conditions in casting. International Journal of Cast Metals Research. 2004;17(3):182–187.

[13] Green NR, Campbell J. Influence of oxide film filling defects on the strength of Al-7Si-Mg alloy castings. Transactions of the American Foundrymen's Society. 1994;102:341–348.

[14] Cao X, Campbell J. Oxide inclusion defects in Al-Si-Mg cast alloys. Canadian Metallurgical Quarterly. 2005;44:435–448.

[15] Divandari M, Campbell J. Mechanisms of Bubble Trail Formation in Castings. Transactions of American Foundry Society. 2001;109(01):1–10.

[16] Fox S, Campbell J. Liquid metal quality. International Journal of Cast Metals Research. 2002;14(6):335–340.

[17] Emamy M, Razaghian A, Kaboli S, Campbell J. Statistical analysis of tensile properties of cast A357/Al 2O3 MMCs. Materials Science and Technology. 2010 feb;26(2):149–156.

[18] Campbell J. Cavitation in liquid and solid metals: role of bifilms. Materials Science and Technology. 2015 mar;31(5):565–572.

[19] Campbell J. An overview of the effects of bifilms on the structure and properties of cast alloys. Metallurgical and Materials Transactions B: Process Metallurgy and Materials Processing Science. 2006 dec;37(6):857–863.

[20] Campbell J. Entrainment defects. Materials Science and Technology. 2006 feb;22(2):127–145.

[21] Tiryakioğlu M. The effect of hydrogen on pore formation in aluminum alloy castings: Myth versus reality. Metals. 2020;10(3).

[22] Miresmaeili SM, Campbell J, Shabestari SG, Boutorabi SMA. Precipitation of Sr-rich intermetallic particles and their influence on pore formation in Sr-modified A356 alloy. Metallurgical and Materials Transactions A. 2005 sep;36(9):2341–2349.

[23] Cao X, Campbell J. The nucleation of Fe-rich phases on oxide films in Al-11.5Si-0.4Mg cast alloys. Metallurgical and Materials Transactions A: Physical Metallurgy and Materials Science. 2003;34 A(7):1409–1420.

[24] Dispinar D, Campbell J. Critical assessment of reduced pressure test. Part 1: Porosity phenomena. International Journal of Cast Metals Research. 2004;17:280–286.

[25] Garcia-Garcia O, Sanchez-Araiza M, Castro-Romn MJ, Escobedo BJ. Analysis of a Confluence Weld Defect in an Aluminum Casting Alloy. In: P N C, M T, J C, editors. Shape Casting: 2nd International Symposium. TMS Annual Meeting and Exhibition Orlando; 2007. p. 109–116.

[26] Mi J, Harding RA, Campbell J. The tilt casting process. International Journal of Cast Metals Research. 2002;14(6):325–334.

[27] Campbell J. Thin wall castings. Materials science and technology. 1988;4(3):194–204.

[28] Green NR, Campbell J. Statistical distributions of fracture strengths of cast Al7SiMg alloy. Materials Science and Engineering A. 1993;173(1-2):261–266.

[29] Cao X, Campbell J. Effect of precipitation of primary intermetallic compounds on tensile properties of cast Al-11.5Si-0.4Mg alloy. Transactions of the American Foundry Society. 2000;108:391–400.

[30] Fox S, Campbell J. Visualisation of Oxide Film Deffects During Solidification of Aluminium Alloys. Scripta mater. 2000;43:881– 886.

[31] Dispinar D, Campbell J. Critical assessment of reduced pressure test. Part 2: Quantification. International Journal of Cast Metals Research. 2004;17:287–294.

[32] Dispinar D, Campbell J. Reduced Pressure Test (RPT) for Bifilm Assessment. In: Shape Casting: 5th International Symposium; 2014. p. 243–251.

[33] Esfahani HB, Raiszadeh R, Doostmohammadi H. Weibull verification of reduced pressure test as a tool for assessing Al melt quality. International Journal of Cast Metals Research. 2017 3;30:87–95.

[34] Divandari M, Campbell J. Morphology of oxide films of Al-5Mg alloy in dynamic conditions in casting. International Journal of Cast Metals Research. 2005;18(3):187–192.

[35] Cao X, Campbell J. Precipitation of primary intermetallic compounds in liquid Al 11.5Si 0.4Mg alloy. International Journal of Cast Metals Research. 2000;13:175–184.

[36] Cao X, Campbell J. Effect of precipitation and sedimentation of primary alpha-Fe phase on liquid metal quality of cast Al-11.1Si-0.4Mg alloy. International Journal of Cast Metals Research. 2004;17:1–11.

[37] Zahedi H, Emamy M, Razaghian A, Mahta M, Campbell J, Tiryakioğlu M. The effect of Fe-rich intermetallics on the Weibull distribution of tensile properties in a cast Al-5 Pct Si-3 Pct Cu-1 Pct Fe-0.3 Pct Mg alloy. Metallurgical and Materials Transactions A: Physical Metallurgy and Materials Science. 2007 apr;38(3):659–670.

[38] Bahreinian F, Boutorabi SMA, Campbell J. Critical gate velocity for magnesium casting alloy (ZK51A). International Journal of Cast Metals Research. 2006;19(1):45–51.

[39] Griffiths WD, Lai NW. Double oxide film defects in cast magnesium alloy. Metallurgical and Materials Transactions A: Physical Metallurgy and Materials Science. 2007 jan;38(1):190–196.

[40] Li T, Davies JMT, Zhu X. Revealing the structure and evolution of entrained oxide film in Mg–Y alloy castings. Journal of Materials Science. 2021 10;56:16671–16685.

[41] Wang L, Rhee H, Felicelli SD, Sabau AS, Berry JT. Oxide Film and Porosity Defects in Magnesium Alloy AZ91. In: Shape Casting: 3rd Intern. Symp; 2009. p. 348.

[42] Mirak AR, Divandari M, Boutorabi SMA, Taylor JA. Effect of oxide film defects generated during mould filling on mechanical strength and reliability of magnesium alloy castings (AZ91). International Journal of Cast Metals Research. 2012 jun;25(3):188–194.

[43] Halvaee A, Campbell J. Critical mold entry velocity for aluminum bronze castings. In: One Hundred First Annual Meeting of the American Foundrymen's Society, Rosemont; 1997. p. 35–46.

[44] Song H, Zhang L, Shen H, Cao F, Zhao X, Gu X, et al. Morphology and fracture of oxide bifilm defects in nickel-aluminium bronze. Journal of Materials Research and Technology. 2021;10:926–934.

[45] Mi J, Harding RA, Wickins M, Campbell J. Entrained oxide films in TiAl castings. Intermetallics. 2003;11(4):377–385.

[46] Cox M, Wickins M, Kuang JP, Harding RA, Campbell J. Effect of top and bottom filling on reliability of investment castings in Al, Fe, and Ni based alloys. Materials Science and Technology. 2000 11;16:1445–1452.

[47] Rashid AKMB, Campbell J. Oxide defects in a vacuum investment-cast Ni-based turbine blade. Metallurgical and Materials Transactions A: Physical Metallurgy and Materials Science. 2004;35 A(7):2063–2071.

[48] Campbell J, Tiryakioğlu M. Bifilm defects in Ni-based alloy castings. Metallurgical and Materials Transactions B: Process Metallurgy and Materials Processing Science. 2012;43:902–914.

[49] Fuchs GE, Kaplan MA. Investigation of Oxide Bifilms in Investment Cast Superalloy IN100: Part I. Mechanical Properties. Metallurgical and Materials Transactions A: Physical Metallurgy and Materials Science. 2016 may;47(5):2346–2361.

[50] Kaplan MA, Fuchs GE. Investigation of Oxide Bifilms in Investment Cast Superalloy IN100: Part II. Characterization. Metallurgical and Materials Transactions A: Physical Metallurgy and Materials Science. 2016 5;47:2362–2375.

[51] Campbell J. Discussion of "Investigation of Oxide Bifilms in Investment Cast Superalloy IN100 Parts I and II"*. Metallurgical and Materials Transactions A: Physical Metallurgy and Materials Science. 2017 10;48:5151–5153.

[52] Zhang YN, Cao X, Wanjara P, Medraj M. Oxide films in laser additive manufactured Inconel 718. Acta Materialia. 2013 10;61:6562–6576.

[53] Attard B. Internal Document; 2021. Scanning electron microscopy images.

[54] Ang ASM, Berndt CC, Sesso ML, Anupam A, Praveen S, Kottada RS, et al. Plasma-sprayed high entropy alloys: microstructure and properties of AlCoCrFeNi and MnCoCrFeNi. Metallurgical and Materials Transactions A. 2015;46(2):791–800.

[55] Harding RA. Towards more reliable investment castings. International Journal of Cast Metals Research. 2006;19(5):289–301.

[56] Griffiths WD, Cox M, Campbell J, Scholl. Influence of counter gravity mould filling on the reproducibility of mechanical properties of a low alloy steel. Materials Science and Technology. 2007;23:137.

[57] Klinger C, Bettge D. Axle fracture of an ICE3 high speed train. Engineering Failure Analysis. 2013 12;35:66–81.

[58] Naro RL, Tenaglia RD. Formation and control of lustrous carbon surface defects. Transactions of the American Foundrymen's Society. 1977;85:65–74.

[59] Goodrich GM. Cast Iron Microstructure Anomalies and Their Causes. Transactions of the American Foundrymen's Society. 1997;105:669–683.

[60] Fasoro AA. Lustrous carbon defect in grey cast iron [Masters thesis]. School of Metallurgy and Materials, University of Birmingham; 1998. J. Campbell.

[61] Naro RL. Formation and Control of Lustrous Carbon Surface Defects in Iron and Steel Castings. Transactions of the American Foundrymens Society. 2002;1:815–834.

[62] Campbell J, Naro RL. Lustrous carbon defects in grey iron. Transactions of the American Foundry Society. 2010;114:277–282.

[63] Habibollahzadeh A, Campbell J. Surface film on liquid grey cast iron a study by SEM. AFS Transactions. 2003;p. 675–684.

[64] Sun W, Bates CE. Visualizing Defect Formation in Gray Iron Castings Using Real Time X-Rays. Transactions of American Foundry Society. 2003;111(03-092):1–9.

[65] Naro RL. Porosity defects in iron castings from mold-metal interface reactions. AFS transactions. 1999;107:839–851.

[66] Naro RL. Influence of Chemical Binder Core Sand Contamination on Green Sand Molding Properties- 25 Years of Controversy. In: Transactions of the American Foundry Society and the One Hundred Eighth Annual Metalcasting Congress; 2004. p. 527–545.

[67] Naro RL. Battling the Elusive Lustrous Carbon Defect. Modern casting. 2003;93(5):32–35.

[68] Chakherlou TN, Mahdinia YV, Akbari A. Influence of lustrous carbon defects on the fatigue life of ductile iron castings using lost foam process. Materials and Design. 2011 1;32:162–169.

[69] Jezierski J, Jureczko M, Dojka R. The impact of process factors on creating defects, mainly lustrous carbon, during the production of ductile iron using the lost-foam casting (LFC) method. Metals. 2020 8;10:1–15.

[70] Regordosa A, Llorca-Isern N. Microscopic characterization of different shrinkage defects in ductile irons and their relation with composition and inoculation process. International Journal of Metalcasting. 2017 10;11:778–789.

[71] Takemoto Y, Mizumoto M, Kinno K. Internal Porosity Defects in Ductile Cast Irons. International Journal of Metalcasting. 2021 7;15:916–929.

[72] Campbell J. Leakage defects via bubble trails in grey iron castings. International Journal of Metalcasting. 2007 jan;1(1):7–16.

[73] Modaresi A, Safikhani A, Noohi AMS, Hamidnezhad N, Maki SM. Gating system design and simulation of gray iron casting to eliminate oxide layers caused by turbulence. International Journal of Metalcasting. 2017;11(2):328–339.

[74] Stefanescu DM. ASM Handbook: Cast Iron Science and Technology. Volume 1A. ASM International; 2017.

[75] Gagné M, Paquin MP, Cabanne PM. Dross in Ductile Iron: Source, formation and explanation. In: 68th World Foundry Congress 2008, WFC 2008; 2008. p. 101–106.

[76] Haque R, Din TU, Campbell J. Effect of liquid velocity of the properties of flake and shoroidal graphite iron; 2001. Inernal Document.

[77] Campbell J. Fatigue Fracture of Ductile Cast Irons. International Journal of Metalcasting. 2008;2:43–46.

[78] Shirani M, Härkegård G. Casting defects and fatigue behaviour of ductile cast iron for wind turbine components: A comprehensive study. Materialwissenschaft und Werkstofftechnik. 2011;42:1059–1074.

[79] Nilsson KF, Blagoeva D, Moretto P. An experimental and numerical analysis to correlate variation in ductility to defects and microstructure in ductile cast iron components. Engineering Fracture Mechanics. 2006 6;73:1133–1157.

[80] Lofaj F, Metten L, Sande AVD, Nilsson KF, Eriksson A. Ductile cast iron inserts for spent nuclear fuel disposal: digital radiography. Metallic Materials. 2007;45:27–34.

[81] Minnebo P, Nilsson KF, Blagoeva D. Tensile, compression and fracture properties of thick-walled ductile cast iron components. Journal of Materials Engineering and Performance. 2007;16:35–45.

[82] Lofaj F, Metten L, Sande AVD, Nilsson KF, Eriksson A. Ductile cast iron inserts for spent nuclear fuel disposal: radiography and fractography. Metallic Materials. 2007;45:17–26.

[83] Vokal V, Nilsson K, Minnebo P. Characterization of defects and graphite types in ductile cast iron by image processing and its relation to mechanical properties. Metallic Materials. 2008;46:39–49.

[84] Nilsson KF, Vokál V. Analysis of ductile cast iron tensile tests to relate ductility variation to casting defects and material microstructure. Materials Science and Engineering A. 2009;502:54–63.

[85] Dojka M, Stawarz M. Bifilm defects in Ti-inoculated chromium white cast iron. Materials. 2020 7;13.

[86] Stawarz M, Dojka M. Bifilm inclusions in high alloyed cast iron. Materials. 2021 6;14.

[87] Hsu FY, Wang KN, Li CL. Bifilm defects in ductile-iron support bracket castings. International Journal of Cast Metals Research. 2017 5;30:148–158.

[88] Dai X, Yang X, Campbell J, Wood J. Effects of runner system design on the mechanical strength of Al-7Si-Mg alloy castings. Materials Science and Engineering A. 2003 8;354:315–325.

[89] Dai X, Yang X, Campbell J, Wood. Influence of oxide film defects generated in filling on mechanical strength of aluminium alloy castings. Materials Science and Technology. 2004 4;20:505–513.

[90] Aubrey LS, Schmahl JR, Cummings M. Application of advanced reticulated ceramic foam filter technology to produce clean steel castings. Transactions of the American Foundrymen's Society. 1993;101:59–69.

[91] Sirrell B, Campbell J. Mechanism of Filtration in Reduction of Casting Defects Due to Surface Turbulence During Mold Filling. Transactions of the American Foundrymen's Society. 1997;105:645–654.

[92] Bäckman J, Svensson IL, Maeda Y. Influence of filter on the mould filling of aluminium melts in vacuum-sealded moulds. Ingenjörshögskolan; 1999.

[93] Ardekhani A, Raiszadeh R. Removal of double oxide film defects by ceramic foam filters. Journal of materials engineering and performance. 2012;21(7):1352–1362.

[94] Nyahumwa C, Green NR, Campbell J. Effect of Mold-Filling Turbulence on Fatigue Properties of Cast Aluminum Alloys. Transactions of the American Foundrymen's Society. 1998;106:215–223.

[95] Raeiszadeh R. A Method to Study the Behavour of Double Oxide Film Defects in Aluminium Alloy [PhD thesis]. School of Metallurgy and Materials University of Birmingham; 2005.

[96] Griffiths WD, Raiszadeh R. Hydrogen, porosity and oxide film defects in liquid Al. Journal of Materials Science. 2009 jul;44(13):3402–3407.

[97] Raiszadeh R, Griffiths WD. A Method to Study the History of a Double Oxide Film Defect in Liquid Aluminum Alloys. Metallurgical and Materials Transactions B. 2006;37B:865–871.

[98] El-Sayed M. Double Oxide Film Defects and Mechanical Properties in Aluminium Alloys [PhD thesis]. School of Metallurgy and Materials University of Birmingham; 2012.

[99] Aryafar M, Raiszadeh R, Shalbafzadeh A. Healing of double oxide film defects in A356 aluminium melt. Journal of Materials Science. 2010 6;45:3041–3051.

[100] Amirinejhad S, Raiszadeh R, Doostmohammadi H. Study of double oxide film defect behaviour in liquid Al-Mg alloys. International Journal of Cast Metals Research. 2013 12;26:330–338.

[101] Bakhtiarani FN, Raiszadeh R. The behaviour of double oxide film defects in Al-4.5 wtJournal of Materials Science. 2011 3;46:1305–1315.

[102] El-Sayed MA, Salem HAG, Kandeil AY, Griffiths WD. Determination of the lifetime of a double-oxide film in al castings. Metallurgical and Materials Transactions B: Process Metallurgy and Materials Processing Science. 2014;45:1398–1406.

[103] Campbell J. Properties of Castings. In: Complete Casting Handbook. Elsevier; 2015. p. 447–528.

[104] Weibull W. A Statistical theory of the Strength of materials. The Royal Swedish Institute for Engeniring Research. 1939;15.

[105] Weibull W. A statistical distribution function of wide applicability. Journal of applied mechanics. 1951;18(3):293–297.

[106] Peirce FT. Tensile Tests for Cotton Yarns v.—"The Weakest Link" Theorems on the Strength of Long and of Composite Specimens. Journal of the Textile Institute Transactions. 1926;17(7):T355–T368.

[107] Hallinan Jr AJ. A review of the Weibull distribution. Journal of Quality Technology. 1993;25(2):85–93.

[108] Quinn JB, Quinn GD. A practical and systematic review of Weibull statistics for reporting strengths of dental materials. dental materials. 2010;26(2):135–147.

[109] Bantle M, Kolsaker K, Eikevik TM. Modification of the Weibull distribution for modeling atmospheric freeze-drying of food. Drying Technology. 2011;29(10):1161–1169.

[110] Sullivan JD, Lauzon PH. Experimental probability estimators for Weibull plots. Journal of Materials Science Letters. 1986;5(12):1245–1247.

[111] Lawless JF. Statistical models and methods for lifetime data. vol. 362. John Wiley & Sons; 2011.

[112] Khalili A, Kromp K. Statistical properties of Weibull estimators. Journal of materials science. 1991;26(24):6741–6752.

[113] Tiryakioğlu M, Hudak D. Unbiased estimates of the Weibull parameters by the linear regression method. Journal of materials science. 2008;43(6):1914–1919.

[114] Tiryakioğlu M, Hudak D, Ökten G. On evaluating Weibull fits to mechanical testing data. Materials Science and Engineering: A. 2009;527(1-2):397–399.

[115] Nyahumwa C. Multiple Defect Distributions On Weibull Statistical Analysis Of Fatigue Life Of Cast Aluminium Alloys. African Journal of Science and Technology (AJST) Science and Engineering Series. 2005;6:43–54.

[116] Byczynski GE. The strength and fatigue performance of 319 aluminum alloy castings [PhD thesis]. School of Metallurgy and Materials, University of Birmingham; 2002.

[117] Tiryakioğlu M. Weibull Analysis of Mechanical Data for Castings II: Weibull Mixtures and Their Interpretation. Metallurgical and Materials Transactions A: Physical Metallurgy and Materials Science. 2015 jan;46(1):270–280.

[118] Nyahumwa C, Green NR, Campbell J. Influence of casting technique and hot isostatic pressing on the fatigue of an Al-7Si-Mg alloy. Metallurgical and Materials Transactions A: Physical Metallurgy and Materials Science. 2001 feb;32(2):349–358.

[119] Hudak D, Tiryakioĝlu M. On comparing the shape parameters of two Weibull distributions. Materials Science and Engineering A. 2011;528:8028–8030.

[120] Shewhart WA. Economic control of quality of manufactured product. Macmillan And Co Ltd, London; 1931.

[121] Tiryakioğlu M, Campbell J. Weibull analysis of mechanical data for castings: A guide to the interpretation of probability plots. Metallurgical and Materials Transactions A: Physical Metallurgy and Materials Science. 2010;41(12):3121–3129.

[122] Holland Jr FA, Zaretsky EV. Investigation of Weibull statistics in fracture analysis of cast aluminum. In: Failure Prevention and Reliability Conference; 1989. p. 246–254.

[123] Fok SL, Mitchell BC, Smart J, Marsden BJ. A numerical study on the application of the Weibull theory to brittle materials. Engineering Fracture Mechanics. 2001;68(10):1171–1179.

[124] of Defense USD. Military Handbook: Metallic Materials and Elements for Aerospace Vehicle Structures. vol. 1. US Department of Defense; 1990.

[125] Upadhyay SK, Mukherjee B. Assessing the value of the threshold parameter in the Weibull distribution using Bayes paradigm. IEEE Transactions on Reliability. 2008;57(3):489–497.

[126] Anderson TW, Darling DA. A test of goodness of fit. Journal of the American statistical association. 1954;49(268):765–769.

[127] D'Agostino R. Goodness-of-fit-techniques. Routledge; 2017.

[128] Stephens MA. EDF statistics for goodness of fit and some comparisons. Journal of the American statistical Association. 1974;69(347):730–737.

[129] D'Agostino I, Ralph B. Test for normal distribution. New York: Marcel Dekker Inc.; 1986.

[130] Tiryakioğlu M. On estimating Weibull modulus by moments and maximum likelihood methods. Journal of materials science. 2008;43(2):793–798.

[131] Elliot R. Liquid metal preparation. In: Cast Iron. Butterwort & Co., England; 1988. p. 46–90.

[132] Katz S, Mcinnis DE, Brink DL, Wilkinson GA. Determination Of Aluminum In Malleable Iron From Measured Oxygen. In: Trans. Am. Foundrymens Soc.; 1980. p. 835–844.

[133] Neumann F, Dötsch E. Thermodynamics of Fe-C-Si melts with particular emphasis on the oxidation behavior of carbon and silicon. Giessereiforschung. 1975;27(1):318–38.

[134] Bramley A, Haywood FW, Cooper AT, Watts JT. The diffusion of non-metallic elements in iron and steel. Transactions of the Faraday Society. 1935;31:707–734.

[135] Monroe R. Porosity in Castings. Transactions of American Foundry Society. 2005;4:245–273.

[136] Campbell J. Melting. In: Complete Casting Handbook. Elsevier; 2015. p. 769–796.

[137] Brown J. Resin bonded sand. In: Foseco ferrous foundryman's handbook. Butterworth-Heinemann; 2000. p. 167–203.

[138] Brown J. Molten metal handling. In: Foseco ferrous foundryman's handbook. Butterworth-Heinemann; 2000. p. 130–145.

[139] Brown J. Filtration and the running and gating of iron castings. In: Foseco ferrous foundryman's handbook. Butterworth-Heinemann; 2000. p. 245–271.

[140] Heine RW, Loper CJ, Rosenthal PC. Principles of metal casting. McGraw-Hill; 1967.

[141] Heine RW. Major aspects of processing cast irons. Transactions of American Foundrymens Society. 1996;104:89–95.

[142] Campbell J. Casting Alloys. In: Complete Casting Handbook. Elsevier; 2015. p. 223–340.

[143] Brown J. Ductile iron. In: Foseco ferrous foundryman's handbook. Butterworth-Heinemann; 2000. p. 70–89.

[144] Ellingham HJT. Reducibility of oxides and sulphides in metallurgical processes. Journal of the Society of Chemical Industry. 1944 May;.

[145] Holtzer M, Górny M, Dańko R. Microstructure and properties of ductile iron and compacted graphite iron castings: the effects of mold sand/metal interface phenomena. Springer; 2015.

[146] Bindernagel I, Kolorz A, Orths K. Controlled additions of hydrocarbon components to molding sand mixtures improve casting surface finish. Transactions of the American Foundrymen's Society,. 1975;83.

[147] Draper AB. Lustrous Carbon in Moulding Sand. Transactions of the American Foundrymen's Society. 1976;84:749–764.

[148] International A. Standard Test Methods for Tension Testing of Metallic Materials. ASTM International; 2012.

[149] Fourie JT. High contamination rates from strongly adsorbed hydrocarbon molecules and a suggested solution. Optic 52. 1978;1:91–95.

[150] Hren JJ. Specimen contamination in analytical electron microscopy: sources and solutions. Ultramicroscopy. 1978;3(4):375–380.

[151] Goldstein JI, Newbury DE, Michael JR, Ritchie NWM, Scott JHJ, Joy DC. Scanning electron microscopy and X-ray microanalysis. Springer; 2017.

[152] Reilly C, Green NR, Jolly MR, Gebelin JC. The modelling of oxide film entrainment in casting systems using computational modelling. Applied Mathematical Modelling. 2013 10;37:8451–8466.

[153] Lai NW, Griffiths WD, Campbell J. Modelling of the potential for oxide film entrainment in light metal alloy castings. In: Modeling of Casting, Welding and Advanced Solidification Processes-X; 2003. p. 415–422.

[154] Flemings MC. Solidification Processing. Materials Science and Engineering Series. McGraw-Hill; 1974.

[155] Bird RB, Stewart WE, Lightfoot EN. Transport phenomena. vol. 1. John Wiley & Sons; 2006.

[156] Szekely J. Fluid flow phenomena in metals processing. Elsevier; 2012.

[157] Liu S, Loper Jr CR. Morphology of Kish Graphite. Transactions of the American Foundrymen's Society. 1990;98:385–394.

[158] Halvaee A. Invistigation of the critical mould entry velocity in aluminum bronzes [PhD thesis]. School of Metallurgy and Materials, University of Birmingham; 1995.

[159] Raiszadeh R, Griffiths WD. The behaviour of double oxide film defects in liquid Al alloys under atmospheric and reduced pressures. Journal of Alloys and Compounds. 2010 2;491:575–580.

[160] Chen Q, Griffiths WD. The investigation of the floatation of double oxide film defect in liquid aluminium alloys by a four-point bend test. International Journal of Cast Metals Research. 2019 7;32:221–228.

[161] Railsback LB. Some Fundamentals of Mineralogy and Geochemistry. Athens, Georgia 30602-2501 U.S.A; 2006.

[162] Campbell J. A hypothesis for cast iron microstructures. Metallurgical and Materials Transactions B: Process Metallurgy and Materials Processing Science. 2009 dec;40(6):786–801.

[163] Campbell J, Tiryakioğlu M. Review of effect of P and Sr on modification and porosity development in Al–Si alloys. Materials Science and Technology. 2010;26(3):262–268.

[164] Stefanescu DM, Alonso G, Larranaga P, De la Fuente E, Suarez R. On the crystallization of graphite from liquid iron–carbon–silicon melts. Acta Materialia. 2016;107:102–126.

[165] Stefanescu DM, Alonso G, Larranaga P, De la Fuente E, Suarez R. Reexamination of crystal growth theory of graphite in iron-carbon alloys. Acta Materialia. 2017;139:109–121.

[166] Gagne M, Goller R. Plate Fracture In Ductile Iron Castings. Transactions of the American Foundrymen's Society. 1983;91:37–46.

[167] Heckmann CJ, Stets W, Wolf G. Plate fracture of nodular cast iron. Key Engineering Materials. 2011;457:367–373.

[168] El-Sayed MA, Hassanin H, Essa K. Bifilm defects and porosity in Al cast

alloys. International Journal of Advanced Manufacturing Technology. 2016 sep;86(5-8):1173–1179.

[169] Campbell J. Porosity. In: Complete Casting Handbook. Elsevier; 2015. p. 341–415.

[170] Chen Q, Griffiths WD. The Effect of Sr Modifier Additions on Double Oxide Film Defects in 2L99 Alloy Castings. Metallurgical and Materials Transactions A: Physical Metallurgy and Materials Science. 2017 nov;48(11):5688–5698.

[171] Kaczmarek ER, Leitermann R, Heine RW. Pinhole and slag casting defects in ductile iron processing. AFS Transactions. 2003;p. 67–75.

[172] Vazehrad S, Elfsberg J, Diószegi A. On factors influencing macro shrinkage porosity formation in compacted graphite iron. In: Materials Science Forum. vol. 790-791. Trans Tech Publications Ltd; 2014. p. 429–434.

[173] Fonseca FCVD. Porosity Analysis On Compacted Graphite Iron [Masters thesis]. The Faculty of Engineering, University of Porto; 2017.

[174] Ramos AK. Shrinkage Porosity Formation during Solidification in Compacted Graphite Iron [Master thesis]. Santa Catarina State University; 2018.

[175] Boeri RE, López G, Tenaglia NE, Massone JM. Solidification, Macrostructure and Shrinkage Formation of Ductile and Compacted Irons. International Journal of Metalcasting. 2020 10;14:1172–1182.

Appendix A

A.1 Tensile test results for SGI

Table A.1: Tensile test reuslts for SGI1

SGI1 TFM			SGI1 VTFM		
No.	UTS (MPa)	%El. (pct.)	No.	UTS (MPa)	%El. (pct.)
1	786	3.4	1	701	1.7
2	749	2.8	2	609	0.8
3	686	1.6	3	677	1.5
4	646	1.1	4	750	2.0
5	775	4.3	5	664	1.2
6	811	4.0	6	728	1.9
7	749	NA	7	696	1.5
8	717	1.8	8	723	1.9
9	773	2.4	9	647	1.1
10	641	1.5	10	587	0.7
11	771	4.1	11	659	1.3
12	808	3.9	12	730	2.2
13	797	5.5	13	787	3.0
14	756	3.4	14	767	2.7
15	775	3.2	15	625	1.1
16	756	2.4	16	772	2.8

17	732	3.3	17	778	2.8
18	691	2.2	18	661	1.5
19	778	4.2	19	519	0.6
20	751	2.5	20	729	2.2
21	741	4.5	21	749	2.8
22	776	4.9	22	790	3.3
23	671	2.5	23	702	1.9
24	695	2.9	24	801	3.5
25	734	4.2	25	779	3.1
26	717	2.5	26	743	2.6
27	763	3.6	27	774	3.0
28	676	2.9	28	744	2.2
29	712	2.6	29	790	3.6
30	735	4.4	30	758	2.8
31	727	3.8	31	689	1.8
32	702	2.1	32	674	1.8
33	691	2.4	33	750	2.6
34	742	3.6	34	647	1.3
35	754	3.7	35	674	1.6
36	740	2.8	36	752	3.2
37	733	3.2	37	689	1.9
38	745	3.5	38	712	1.9
39	795	3.3	39	769	3.2
40	777	3.3	40	823	4.0

Table A.2: Tensile test reuslts for SGI2

SGI2 TFM			SGI2 QFM		
No.	UTS (MPa)	%El. (pct.)	No.	UTS (MPa)	%El. (pct.)
1	819	1.4	1	780	0.6
2	789	1.1	2	803	0.8
3	880	1.4	3	749	0.6
4	793	0.8	4	776	0.6
5	791	1.1	5	817	0.8
6	836	1.7	6	738	0.5
7	808	0.9	7	781	0.6
8	809	1.2	8	801	0.7
9	841	1.6	9	809	0.7
10	725	0.5	10	847	1.0
11	664	0.5	11	761	0.6
12	842	1.2	12	797	0.8
13	816	1.5	13	867	1.2
14	802	1.3	14	865	1.2
15	787	0.8	15	881	1.4
16	724	0.5	16	766	0.6
17	726	0.6	17	722	0.5
18	904	2.7	18	823	0.9
19	823	1.6	19	820	0.8
20	811	1.3	20	830	0.8

Table A.3: Tensile test reuslts for SGI3

SGI3 VTFM			SGI3 TFM			SGI3 QFM		
No.	UTS (MPa)	%El. (pct.)	No.	UTS (MPa)	%El. (pct.)	No.	UTS (MPa)	%El. (pct.)
1	760	3.1	1	813	3.1	1	775	3.6
2	774	3.6	2	757	4.1	2	781	3.9
3	735	3.2	3	733	4.7	3	765	4.2
4	760	4.4	4	716	4.0	4	738	3.5
5	795	4.0	5	749	3.0	5	792	4.1
6	786	3.8	6	774	3.5	6	792	4.0
7	763	3.9	7	745	4.7	7	749	3.9
8	764	4.0	8	679	2.5	8	767	4.0
9	787	3.9	9	752	3.7	9	774	3.6
10	748	3.0	10	805	3.1	10	763	3.4
11	725	2.5	11	783	2.4	11	790	3.1
12	745	2.8	12	740	3.7	12	761	2.7
13	766	3.4	13	715	4.0	13	735	2.7
14	767	3.9	14	724	4.3	14	736	3.2

15	788	3.3	15	772	3.4	15	797	3.4
16	754	2.8	16	750	2.8	16	806	3.9
17	768	4.1	17	743	4.8	17	767	4.1
18	776	4.0	18	742	4.4	18	768	3.7
19	727	2.6	19	760	4.1	19	772	3.9
20	782	3.8	20	776	2.3	20	775	4.0
21	754	3.3	21	794	3.4	21	780	3.6
22	767	3.1	22	747	4.7	22	760	3.7
23	759	3.4	23	730	5.0	23	765	3.4
24	765	3.2	24	688	3.3	24	758	3.7
25	800	3.5	25	762	3.3	25	802	3.6
26	774	3.1	26	755	3.6	26	788	3.2
27	734	2.9	27	692	3.8	27	782	4.0
28	751	3.0	28	723	4.5	28	767	4.4
29	751	3.0	29	735	4.0	29	769	4.1
30	714	2.3	30	753	2.3	30	780	2.6
31	718	2.3	31	750	1.9	31	757	3.3

32	782	3.4	32	768	3.2	32	742	2.5
33	771	3.3	33	738	2.8	33	767	3.6
34	756	2.9	34	740	3.3	34	764	3.4
35	786	2.9	35	776	2.5	35	789	3.5
36	674	1.6	36	736	2.1	36	789	2.1
37	788	3.9	37	709	2.5	37	769	3.4
38	775	3.5	38	731	3.0	38	747	2.9
39	778	3.6	39	746	3.1	39	730	2.1
40	734	2.7	40	755	2.1	40	746	2.5

A.2 Tensile test results for LGI

Table A.4: Tensile test reuslts for LGI1

LGI1 TFM		LGI1 QFM	
No.	UTS (MPa)	No.	UTS (MPa)
1	237	1	239
2	240	2	242
3	240	3	243
4	240	4	244
5	240	5	246
6	241	6	248
7	242	7	248
8	243	8	248
9	243	9	249
10	244	10	249
11	244	11	249
12	245	12	250
13	245	13	252
14	246	14	252
15	249	15	252
16	250	16	252
17	250	17	252
18	252	18	253
19	252	19	253
20	252	20	254
21	253	21	257
22	253	22	257
23	254	23	257
24	255	24	257

25	258	25	257
26	260	26	258
27	260	27	259
28	263	28	260
29	264	29	262
30	269	30	264
31	272	31	265
32	274	32	266
33	276	33	267
34	278	34	269
35	279	35	270
36	282	36	270
37	289	37	271
38	290	38	271
39	290	39	278
40	291	40	284

Table A.5: Tensile test reuslts for LGI2

LGI2 VTFM		LGI2 TFM		LGI2 QFM	
No.	UTS (MPa)	No.	UTS (MPa)	No.	UTS (MPa)
1	103 R	1	397	1	378
2	269 R	2	407	2	398
3	333	3	412	3	406
4	351	4	413	4	408
5	352	5	415	5	414
6	355	6	416	6	415
7	358	7	417	7	417
8	359	8	420	8	417

9	366	9	420	9	419
10	368	10	423	10	422
11	370	11	423	11	423
12	371	12	423	12	428
13	373	13	425	13	429
14	374	14	426	14	429
15	375	15	428	15	431
16	376	16	429	16	431
17	379	17	431	17	433
18	382	18	431	18	433
19	390	19	431	19	435
20	390	20	432	20	436
21	392	21	433	21	439
22	398	22	433	22	439
23	402	23	433	23	440
24	402	24	434	24	440
25	410	25	434	25	440
26	413	26	434	26	441
27	414	27	435	27	441
28	414	28	435	28	442
29	420	29	435	29	442
30	421	30	435	30	443
31	425	31	437	31	444
32	427	32	438	32	446
33	429	33	438	33	446
34	431	34	439	34	447
35	431	35	439	35	448
36	432	36	439	36	451

37	434	37	440	37	451
38	436	38	440	38	452
39	443	39	447	39	454
40	447	40	450	40	456

A.3 Tensile test results for CGI

Table A.6: Tensile test reuslts for CGI1

CGI1 TFM			CGI1 QFM		
No.	UTS (MPa)	%El. (pct.)	No.	UTS (MPa)	%El. (pct.)
1	590	0.59	1	603	0.52
2	578	0.81	2	602	0.46
3	568	0.61	3	577	0.44
4	563	0.66	4	584	0.42
5	586	0.63	5	566	0.45
6	565	0.73	6	595	0.50
7	555	0.70	7	586	0.44
8	548	0.64	8	578	0.44
9	600	0.56	9	582	0.43
10	556	0.79	10	588	0.48
11	581	0.50	11	571	0.44
12	580	0.48	12	594	0.45
13	514	0.38	13	547	0.38
14	587	0.47	14	589	0.45
15	587	0.50	15	547	0.39
16	584	0.41	16	588	0.43
17	581	0.43	17	571	0.44
18	574	0.47	18	579	0.52
19	575	0.41	19	578	0.46
20	572	0.53	20	580	0.43
21	560	0.55	21	574	0.43
22	562	0.50	22	590	0.47
23	565	0.40	23	576	0.41
24	568	0.46	24	583	0.43
25	564	0.54	25	579	0.43
26	562	0.41	26	577	0.45
27	543	0.52	27	594	0.44
28	576	0.55	28	579	0.43
29	560	0.64	29	587	0.47
30	567	0.51	30	581	0.47
31	581	0.46	31	593	0.46
32	533	0.38	32	579	0.45
33	584	0.48	33	580	0.45
34	572	0.43	34	598	0.46
35	546	0.44	35	543	0.40
36	578	0.47	36	586	0.45
37	576	0.36	37	567	0.41
38	568	0.47	38	589	0.41
39	546	0.38	39	583	0.44
40	562	0.40	40	584	0.42

Table A.7: Tensile test reuslts for CGI2

CGI2 VTFM			CGI2 TFM			CGI2 QFM		
No.	UTS (MPa)	%El. (pct.)	No.	UTS (MPa)	%El. (pct.)	No.	UTS (MPa)	%El. (pct.)
1	573	0.80	1	567	0.75	1	505	0.37
2	577	0.89	2	567	1.01	2	553	0.68
3	559	0.86	3	478	0.38	3	560	0.73
4	570	0.88	4	546	0.83	4	556	0.78
5	534	0.57	5	556	0.66	5	571	0.85
6	575	0.66	6	504	0.41	6	567	0.71
7	579	0.93	7	554	1.02	7	580	0.88
8	583	0.94	8	524	0.64	8	542	0.62
9	584	0.94	9	554	0.84	9	571	0.75
10	587	0.93	10	566	0.62	10	570	0.69
11	566	0.72	11	509	0.38	11	568	0.70
12	564	0.68	12	509	0.43	12	531	0.39
13	563	0.73	13	522	0.58	13	504	0.46
14	581	1.05	14	541	0.82	14	538	-0.02

15	574	0.64	15	447	0.33	15	529	0.50
16	563	0.57	16	535	0.47	16	574	0.50
17	579	0.94	17	551	0.73	17	547	0.64
18	558	0.71	18	516	0.46	18	499	0.38
19	582	0.76	19	528	0.51	19	521	0.31
20	576	0.85	20	445	0.17	20	523	0.40
21	542	0.70	21	521	0.34	21	547	0.49
22	571	0.81	22	496	0.32	22	563	0.63
23	578	0.91	23	510	0.42	23	525	0.48
24	562	0.79	24	518	0.54	24	532	0.52
25	594	0.78	25	482	0.32	25	559	0.49
26	572	0.72	26	562	0.57	26	539	0.60
27	584	0.95	27	521	0.57	27	562	0.66
28	568	0.79	28	496	0.45	28	531	0.47
29	576	0.77	29	519	0.38	29	554	0.56
30	569	0.77	30	513	0.36	30	484	0.36
31	551	0.67	31	500	0.37	31	530	0.37

32	585	0.80	32	492	0.40	32	498	0.35
33	581	0.84	33	519	0.57	33	542	0.56
34	583	0.83	34	538	0.61	34	541	0.52
35	568	0.51	35	573	0.53	35	567	0.55
36	594	0.78	36	537	0.39	36	543	0.31
37	578	0.82	37	548	0.53	37	515	0.30
38	593	0.92	38	545	0.56	38	546	0.58
39	587	0.89	39	517	0.55	39	502	0.33
40	577	0.77	40	505	0.43	40	487	0.23

A.4 MATLAB^{TM} code for plotting the 3-parameter Weibull distribution

```
function []=WeibullPlot(lnUTS1,lnminusln1minusP1,lnUTS2,lnminusln1minusP2,lnUTS3,lnminusln1minusP3)
    xlsData=xlsread('WeibleResults.xlsx');
    m1=input('m value for first dataset:');
    sigma_01=input('sigma_0 for first dataset:');
    sigma_t1=input('sigma_t for first data set:');
    m2=input('m value for second dataset:');
    sigma_02=input('sigma_0 for second dataset:');
    sigma_t2=input('sigma_t for second data set:');
    m3=input('m value for third dataset:');
    sigma_03=input('sigma_0 for third dataset:');
    sigma_t3=input('sigma_t for third data set:');
    xq1=linspace(exp(min(lnUTS1)),exp(max(lnUTS1)),200);
    xq2=linspace(exp(min(lnUTS2)),exp(max(lnUTS2)),200);
    xq3=linspace(exp(min(lnUTS3)),exp(max(lnUTS3)),200);
    myfit1=(m1*log(xq1-sigma_t1))-(m1*log(sigma_01));
```

```
    myfit2=(m2*log(xq2-sigma_t2))-(m2*log(sigma_02));
    myfit3=(m3*log(xq3-sigma_t3))-(m3*log(sigma_03));
    figure('Name','Weibull Plots');
    plot(lnUTS1,lnminusln1minusP1,'b.',log(xq1),myfit1,'b',lnUTS2,lnminusln1minusP2,'r.',
    log(xq2),myfit2,'r',lnUTS3,lnminusln1minusP3,'c.',log(xq3),myfit3,'c')
    xlabel('ln(%Ele)')
    ylabel('ln(-ln(1-P))')
    legend('CGI QFM','CGI QFM Fit line','CGI TFM','CGI TFM Fit Line',
    'CGI VTFM','CGI VTFM Fit Line','Location','northwest')
end
```